Pressure Fluctuations in a High-Reynolds-Number Turbulent Boundary Layer over Rough Surfaces of Different Configurations

Liselle A. Joseph

Dissertation submitted to the Faculty of the
Virginia Polytechnic Institute and State University
in partial fulfilment of the requirements for the degree of

Doctor of Philosophy
in
Aerospace Engineering

William J. Devenport, Chair
W. Nathan Alexander
Aurélien Borgoltz
Theodore M. Farabee
K. Todd Lowe
Roger L. Simpson

August 23, 2017
Blacksburg, Virginia

Keywords: turbulent boundary layer, pressure spectra, zero-pressure gradient, rough walls, scaling laws

Pressure Fluctuations in a High-Reynolds-Number Turbulent Boundary Layer over Rough Surfaces of Different Configurations

Liselle A. Joseph

(ABSTRACT)

The pressure fluctuations under a high Reynolds Number, rough-wall, turbulent, boundary layer have been studied in the Virginia Tech Stability Wind Tunnel. Rough surfaces of varying element height (1-mm, 3-mm), shape (hemispheres, cylinders) and spacing (5.5-mm,10.4-mm,16.5-mm) were investigated in order to ascertain how the turbulent pressure fluctuations change with changes in roughness geometry. Rough surfaces which contain two types of elements are investigated and relationships between the combination surface and the individual surfaces have been uncovered. Measurements of the wall pressure fluctuations were made using pinhole microphones and hotwire measurements were made to obtain the velocity and turbulence field.

Among the principal findings is the development of two scaling laws for the low frequency pressure fluctuations. Both of these are based on the idea that the defect between the edge velocity and some local boundary layer velocity sustains the pressure fluctuations in the outer regions of the flow. The first scaling uses the broadband convection velocity as the local velocity of the large scale pressure fluctuations. The second scaling uses the mean boundary layer velocity. Both these scalings appear more robust than the previously proposed scalings for the low frequency region and are able to scale the pressure spectra of all the data to within 3.5-dB.

In addition, it was proven that the high frequency shear friction velocity scaling of Meyers *et al.* [1] is universal to rough surfaces of different element shape and density. Physical insights into the shear friction velocity, on which this scaling is based, have been revealed. This includes an empirical formula which estimates the element pressure drag coefficient from the roughness density and the Reynolds number.

The slopes in the mid-frequency region were found to vary with element density and microphone location such that a useful scaling could not be determined for this region. The possibility of an overlap region is explored and the expectation of a -1 slope is disproved. It is hypothesised that an evanescent decay of the mid-frequency pressure fluctuations occurs between their actual location and the wall where they are measured. A method for accounting for this decay is presented in order to scale the pressure fluctuations in this region.

Lastly, a piecewise interpolation function for the pressure spectrum of rough wall turbulent boundary layers was proposed. This analytical function is based on the low frequency scaling on mean velocity and the high frequency scaling of Meyers *et al.* The mid-frequency is estimated by a spline interpolation between these two regions.

This work was supported by the National Science Foundation and the Office of Naval Research.

Pressure Fluctuations in a High-Reynolds-Number Turbulent Boundary Layer over Rough Surfaces of Different Configurations

Liselle A. Joseph

(GENERAL AUDIENCE ABSTRACT)

Most flows of practical interest are turbulent in nature, typically occurring next to a rigid surface such as a submarine hull or aircraft wing. This boundary layer flow is of engineering importance because its pressure fluctuations are the source of unwanted structural vibrations and undesired acoustic noise. From a purely scientific perspective, it is useful to study the turbulent pressure fluctuations in order to learn more about the workings of the region of the flow closest to the surface.

Turbulent flow over smooth walls has been researched extensively. However, one cannot ignore the fact that surfaces of practical interest are not smooth. Thus, it is important to account for the effect of roughness on the turbulent boundary layer. It has been found that there are significantly greater pressure fluctuations over rough walls when compared to smooth walls. Consequently the extent of vibrations and noise which occur in rough walls is larger than that experienced in smooth walls.

The present study seeks to shed light on the nature of the rough-wall turbulent boundary layer through wind tunnel experiments. The nature of the velocity, pressure fluctuations, and turbulence within the boundary layer are examined as well as the existence of universal relationships which are applicable to all rough-wall turbulent boundary layers. A method for predicting the pressure fluctuations (to within 4-dB) over a specific rough wall is also proposed.

For my brother

Cornelius Keith Joseph

who also wanted to make advances in science

Acknowledgements

First, and above all, I thank the Lord for His continual provision and guidance. He has blessed me with this research opportunity and with wonderful people who have contributed to the success of my degree.

I must express my sincere gratitude to my academic advisor, Dr. William Devenport, for being my guide and advocate. I count it a blessing to have been your student because you are a true teacher, educating my whole person. You saw my potential when I didn't and taught me so much more than engineering and research. Thank you for showing me how to be a good leader and a better person.

I also thank the rest of my committee: Dr. Nathan Alexander, Dr. Aurélien Borgoltz, Dr. Ted Farabee, Dr. Kevin Lowe, and Dr. Roger Simpson. You have improved my work with your critical assessment, direction and suggestions. I especially want to thank Dr. Aurélien Borgoltz for serving as my unofficial co-advisor. I am fortunate to have benefited from your immense knowledge and direction, and I am incredibly grateful for your constant encouragement. In addition, I thank Dr. Stewart Glegg for his contributions in developing equations for the evanescent pressure decay hypothesis proposed in this work.

I would be remiss if I did not acknowledge the outstanding contributions of technicians of the AOE Machine Shop, in particular Mr James A. Lambert and Mr Cameron J. Hollandsworth. Your ideas, expertise and commitment went well past your daily duties and I greatly appreciate your work ethic. Very special thanks is also due to Mr Bill P. Oetjens, the Stability Wind Tunnel Engineer, who assisted during the wind tunnel tests. A special acknowledgement must be made to Mr Tim Meyers who worked on this project before me, and helped me get up to speed on it. He was also instrumental during the wind tunnel testing, when he worked as the Wind Tunnel Research Engineer.

I thank all the graduate students of CREATe with whom I have had the pleasure of working. You all have created a supportive and productive work environment, and have become dear friends. In particular, I would like to thank Nick Molinaro who played an integral role in the hotwire measurements and wind tunnel tests. I am also indebted to Agastya Balantrapu, Ian Clark and Anthony Millican for their constant assistance during the testing phase and to Matt Ruda for proof-reading sections of this dissertation. You have all made my graduate school experience rich and enjoyable.

Finally I express my heartfelt gratitude to my parents and siblings for their support and prayers. I also acknowledge the support and encouragement of my family and friends in Grenada, and the unparalleled counsel of my trusted personal advisors: Dr. H. Pat Artis and Dr. Rita Klein. You believed in me every step of the way, and kept me going in the toughest moments.

Thank you all,

Liselle

Contents

List of Figures

List of Tables

1. Introduction

1.1 Motivation

Most flows of practical interest are turbulent in nature, typically occurring next to a rigid surface such as a submarine hull or aircraft wing. These wall-bounded flows have been researched for decades and are found to have characteristics which vary depending on several factors. Flows such as these are of engineering importance because the pressure fluctuations which are inherent to a turbulent boundary layer can produce unwanted structural vibrations, or act as a source of undesired acoustic noise. Furthermore, a study of these pressure fluctuations can reveal much about the not-well-understood turbulent structure of the near-wall region.

Turbulent flow over smooth walls has been researched extensively, and much has been learned in the past few decades. Pressure spectra, for example, have been used to ascertain the pressure levels in the flow as well as predict the type of coherent structures present. The goal of such studies has been to better understand the nature of smooth-wall turbulent flow from the velocity and pressure spectra. However, one cannot ignore the fact that most surfaces are not hydrodynamically smooth. This has led to another large field of study: the nature of turbulent flow over rough walls. It has been found that there are significantly greater pressure fluctuations over rough walls when compared to smooth walls. Consequently the extent of vibrations and noise which occur in rough walls is larger than that experienced in smooth walls. Therefore, as with smooth walls, the pressure fluctuations are of particular interest.

The all-encompassing goal of roughness research is to develop a quantitative scheme which, given the specific features of the roughness, is able to predict how the boundary layer will be affected by a rough surface.

1.2 Turbulent Flow over Smooth Walls

The most simple case of turbulent flow would be that over a smooth, flat plate aligned with the flow as shown in fig. 1.1. In this case there is a zero pressure gradient and the turbulent flow is two dimensional. The y-coordinate increases upward from the wall and the free-stream flow, U_e, and the mean flow are in the x-direction. This canonical case is the focus of the present work.

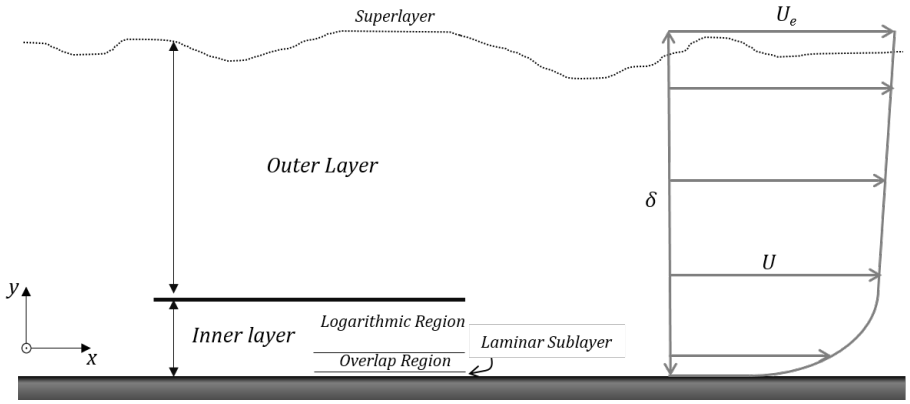

Figure 1.1: Schematic of a portion of the 2-D turbulent boundary layer over a flat plate, showing co-ordinate system and parts of the boundary layer

In general, the turbulent boundary layer is thought to consist of an inner and an outer region as depicted by fig. 1.1. Close to the wall viscosity controls the vertical transport of momentum and away from the wall turbulence controls the vertical transport of momentum. In the outer region the length scale is the boundary layer thickness, δ, and the length scale in the inner region is ν/U_τ, where ν is the kinematic viscosity and U_τ is the friction velocity. $U_\tau = \sqrt{\tau_w/\rho}$ where τ_w is the wall shear stress and ρ is the fluid density. It is believed that the region closest to the wall, called the laminar sublayer, is a region in which turbulence is suppressed by viscosity. This is in order to damp the velocity fluctuations in accordance with the no-slip condition at the wall. At laboratory Reynolds numbers this region is about 1% of the entire boundary layer thickness and encompasses $y^+ < 5$ where $y^+ = yU_\tau/\nu$ (y is the vertical distance from the wall). Above the thin laminar sublayer is the buffer layer or the 'overlap' layer which extends from $5 \leq y^+ < 30$. This is essentially a blending region in which the laminar sublayer merges with the logarithmic region above. The logarithmic region is typically said to extend from $30 \leq y^+ < 300$ and is governed by the *law of the wall* (discussed in § 1.2.1). These three layers (viscous sublayer, buffer region, logarithmic region) make up the inner layer. Above the logarithmic region is the outer layer where the *law of the wake* (discussed in § 1.2.1) applies. Therefore the turbulent boundary layer can be thought of as having 1) an innermost laminar sublayer, which has a length scale of ν/U_τ and a velocity scale of U_τ, 2) a wall-dominated layer (buffer region and semi-logarithmic region) with length scale y and velocity scale u_τ, 3) an outer region with length scale δ and velocity scale U_e, and 4) a superlayer which is the thin region of interface between the turbulent and the non-turbulent flow [2, 3].

One of the most significant characteristics of turbulent flow is the general *swirling* nature of the flow [3]. These swirls (typically referred to as eddies) can be thought of as organised motions of lumps of fluid in a localised region. Turbulent flow is unique in that there exists a wide range of eddy sizes at a given time and in a given location of the flow. Turbulent motions are therefore said to have a wide range of scales - in both time and space. The

size of these turbulent motions range from scales on the order of the height of the boundary layer, δ, to Kolmogorov scales at which dissipation occurs [4]. The size of the smallest scales changes with Reynolds number such that as Reynolds number increases the small scales become smaller [4].

The energy cascade postulates that kinetic energy enters the flow at the largest scales of motion and is transferred to smaller and smaller scales until it is dissipated by viscous action at the very smallest scales. This concept describes the large eddies as unstable, which cause them to break up into smaller eddies, which in turn break up into even smaller eddies until the length scale is small enough that the eddies can be considered stable [4]. Dissipation then occurs due to molecular viscosity. The distribution of the eddies of varying size within the boundary layer is a topic under much discussion. One would expect that the random nature of turbulent flow would result in eddies of varying sizes existing at various locations throughout the boundary layer. However, the appearance of universal scalings (which will be discussed in § 1.5) points toward the larger eddies existing in the outer region of the boundary layer while the smaller eddies exist in the near-wall region. Researchers agree that this is most likely the case [5, 6]. This would mean that, according to the energy cascade, the most energetic part of the boundary layer is the outer layer because this is where the large scales exist. However, this is contradicted by researchers such as Klebanoff [7], Raupach [8] and Robinson [9] (among many others) who state categorically that the near-wall region is the source of nearly all the turbulent kinetic energy (TKE) in the boundary layer. This high level of TKE in the near-wall region is attributed to the interactions of turbulent structures which create high levels of turbulence.

Because the turbulent motions associated with the eddies are stochastic, they are generally characterised using statistical concepts. For simplicity of analysis, turbulence is usually considered statistically stationary, homogeneous and isotropic. Turbulence is stationary if all mean quantities are invariant under a translation in time. Homogeneity implies that all the statistics of the flow are invariant when shifted in position (translations) [4]. Isotropic turbulence is statistically invariant under rotations and reflections as well as translations.

1.2.1 The Mean Flow over Smooth Walls

In the outer region of the turbulent boundary layer, the velocity profile is given by the velocity-defect law:

$$\frac{U_e - U}{U_\tau} = G\left(\frac{y}{\delta}\right) \tag{1.1}$$

where, U_e is the free-stream velocity and U is the local velocity. In the inner region, the velocity profile is given by the *law of the wall*:

$$\frac{U}{U_\tau} = F\left(\frac{yU_\tau}{\nu}\right) \tag{1.2}$$

These can be combined [3] to obtain:

$$\frac{U}{U_\tau} = G\left(\frac{y}{\delta}\right) + \frac{U_e}{U_\tau} \tag{1.3}$$

$$\frac{U}{U_\tau} = F\left[\left(\frac{y}{\delta}\right)\left(\frac{\delta U_\tau}{\nu}\right)\right] \tag{1.4}$$

Based on the structure of the boundary layer described at the beginning of § 1.2, it follows that there must exist a region between the inner and outer layers where both these equations are valid. The only function which satisfies the summation of eq. (1.3) and the multiplication of eq. (1.4) simultaneously is the logarithmic function [3]. Thus we obtain the following equations for this overlap/buffer region:

$$\frac{U_e - U}{U_\tau} = A \log\left(\frac{y}{\delta}\right) + B \tag{1.5}$$

$$\frac{U}{U_\tau} = A \log\left(\frac{yU_\tau}{\nu}\right) + C \tag{1.6}$$

where eq. (1.5) is the logarithmic velocity profile expressed in outer-layer variables and eq. (1.6) is expressed in inner-layer variables [10]. B and C are constants for the smooth-wall turbulent boundary layer. These equations can be (and are usually) further re-written with a natural logarithm and using the constant $\kappa = \ln(10)/A$ which is called the von Kármán constant [3]. The final equation is:

$$\frac{U}{U_\tau} = \frac{1}{\kappa} \ln\left(\frac{yU_\tau}{\nu}\right) + C \tag{1.7}$$

Different values of κ and C have been reported but all are in the vicinity of κ=0.40 and C=4.9 [3]. Equation (1.7) clearly shows that the overlap region of the turbulent boundary layer must have a semi-logarithmic velocity profile, which is supported by experimental data [11].

The *law of the wake* was introduced by Coles [12] to describe the mean velocity profile in the outer region. This relation is shown in eq. (1.8):

$$\frac{U}{U_\tau} = \frac{1}{\kappa} \ln\left(\frac{yU_\tau}{\nu}\right) + C + \frac{\Pi}{\kappa} W\left(\frac{y}{\delta}\right) \tag{1.8}$$

where, $\Pi = \kappa B/2$ is the wake parameter which Coles [12] gives a value of 0.51.

Fig. 1.2 shows the mean velocity profile for the turbulent boundary layer over a smooth wall. It plots the result of the equations for the laminar sublayer and logarithmic region. This result is compared with experimental data obtained by Awasthi [11]. Fig. 1.2 shows that the result of the equations discussed in this section agree with experimental results, which speaks toward their accuracy.

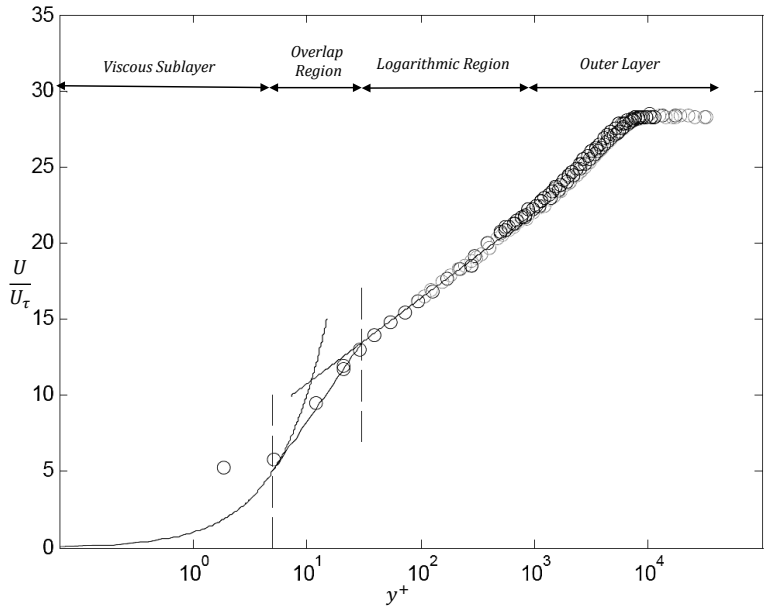

Figure 1.2: Mean velocity profile over a smooth wall [11]. ——is result from equations and ○ is experimental data

1.2.2 Mechanics of Turbulent Flow over Smooth Walls

Research has shown that turbulent boundary layers are composed of organised, coherent structures. However the specific structures which exist and the processes involved in their formation, interactions and demise are not widely agreed upon. In fact, a large range of possible structures and conceptual models have been proposed in the literature in order to explain observed experimental phenomenon. Unfortunately experimental detection of detailed features of the different structures has been limited by spatial resolution and the intrusive character of instrumentation. Nevertheless, it is known that structures differ in their geometry and their evolutionary dynamics. Robinson [9] completed a comprehensive review of the literature and summarises all reported coherent structures into eight classes:

1. Low speed streaks in the viscous sub-layer
2. Ejections of low speed fluid from the near-wall region
3. Sweeps of high speed fluid from the outer region to the near-wall region
4. Vortical structures
5. Sloping near wall shear layers
6. Near wall “pockets”
7. Large-scale motions capped by three-dimensional bulges at the interface of the turbulent and potential flows

8. Shear layer "backs" of large-scale outer-region motions

The existence of these structures are supported by many researchers such as Chu [13] and Falco [14].

It is important to take a look at the nature of these structures in order to develop a physical understanding of pressure fluctuations. This will better enable us to interpret the pressure spectrum. The interactions of these structures with each other within the boundary layer is not well documented and apparently not well understood. The first four motions on Robinson's list are most commonly reported, and will therefore be discussed here.

Low-Speed Streaks

Streaky structures were first identified during flow visualisation studies in the 1950's and in several studies since then [15, 16]. They are found in the viscous sublayer and buffer layer of *every* turbulent boundary layer [17]. Essentially these streaks are composed of elongated regions of high- and low-speed fluid [18]. In a flat plate, smooth-wall turbulent boundary layer the low-speed streaks have a streamwise velocity approximately $1/2$ the local mean velocity while the velocity of the high-speed streaks is roughly $3/2$ the local mean speed [16].

Low-speed streaks are of particular interest because it was found that they are able to lift away from the wall and interact with flow in the buffer region in a process called 'bursting'. This interaction produces turbulence and occurs quite suddenly. According to *continuity* this ejection of fluid from the wall must be accompanied by a slow flow of high-momentum fluid to the near-wall region, which is the mechanism by which energy is supplied to these layers [18]. Viscous forces then dissipate this energy. Kline *et al.* [16] found that transverse streak spacing increases with the distance from the wall outside the viscous sublayer, a result which has been supported by other researchers in the following years [19, 17].

The formation of low-speed streaks is not well understood.In a low-Reynolds number study, Robinson [9] stated that the most likely cause was quasi-streamwise vortical elements convecting downstream. These vortices leave near-wall, low-speed fluid trailing from the upward rotating side of the vortex and high-speed fluid trailing from the downward rotating side thus forming a streak. However this premise may be incomplete in light of Lee's [20] findings that high shear rate alone is able to produce low speed streaks (in flows which do not have vortical elements). Furthermore Chu [13] states categorically that his simulations show that streamwise vortices are not required to produce streamwise streaks. Hence it appears that the effect of vortical structures on streak formation may simply be to enhance their evolution. This conclusion makes sense considering the high shear rate associated with a quasi-streamwise vortex as it moves both high- and low- speed fluid. Also, numerous studies have proven that streaks and quasi-streamwise vortices are closely linked and frequently occur in the vicinity of each other [21]. Other researchers [14, 22] have observed that pairs of low speed streaks are formed in response to a sequence of high-speed eddies in the outer region interacting

with the wall. Chu [13] also found that long, low-speed streaks are formed in pairs due to interactions of typical eddies (ring-like eddies) over the wall.

Some of the hydrogen bubble flow-visualisation images of Kline [16] are shown in fig. 1.3. In these images the view is from the top of the boundary layer looking toward the wall. The flow is moving from the top of the images to the bottom with the wire used to create the turbulent boundary layer at the top of the image. Clearly low speed streaks are seen in the laminar sublayer and buffer region of the boundary layer but these disappear into the logarithmic layer (fourth image where $y^+ = 38$).

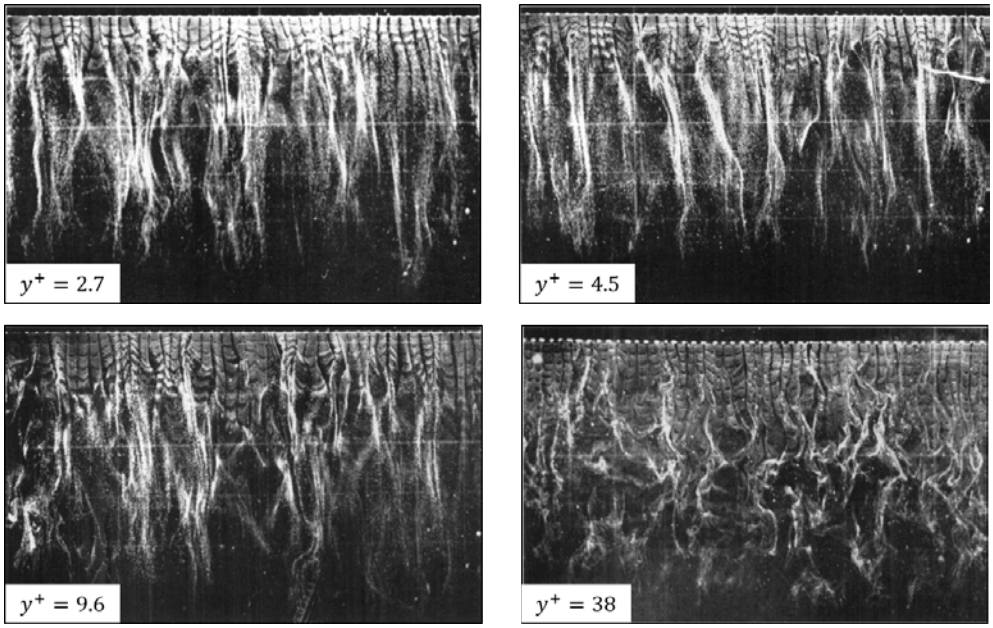

Figure 1.3: Low speed streaks seen in laminar sublayer and buffer region by hydrogen bubble flow visualisation [16]

Sweeps and Ejections

Intermittently, a parcel of fluid near the wall will move into the faster moving fluid away from the wall. This is called an ejection. This event has $u < 0$ and $v > 0$. In a similar way a parcel of fast-moving fluid away from the wall will move into the slower moving fluid near the wall. This is called a sweep and has $u > 0$ and $v < 0$. In this way ejections and sweeps maintain turbulent mixing and contribute to the Reynolds shear stress.

Sweeps and ejections have been detected and discussed extensively [23, 24, 8, 9, 25, 26]. Both processes are observed in the buffer region [9] and sublayer of the boundary layer. These motions are thought to arise from the rotation of vortical structures in the buffer layer. Quasi-streamwise single vortices or vortex-pairs can generate both sweeps and ejections (sweep-ejection pairs) because as they rotate they push some of the flow upward (from the

upward rotating side) as well as draw flow downward (from the downward rotating side) [9]. This is depicted in fig. 1.4

Sweeps and ejections in smooth wall flows are intense but infrequent (approximately occurring 10% of the time [24, 25]). They are the main form of momentum transport in the turbulent boundary layer. Sweep events in particular bring high momentum fluid towards the wall and are therefore a source of TKE and turbulent motions [24, 9].

In relation to wall pressure fluctuations, sublayer sweeps have high-pressure regions beneath them [17] which is consistent with the idea of high-speed fluid impacting with the wall. Similarly a sweep-ejection pair will result in low wall pressure because of the presence of quasi-streamwise vortices (which have low pressure cores) which produce the pair.

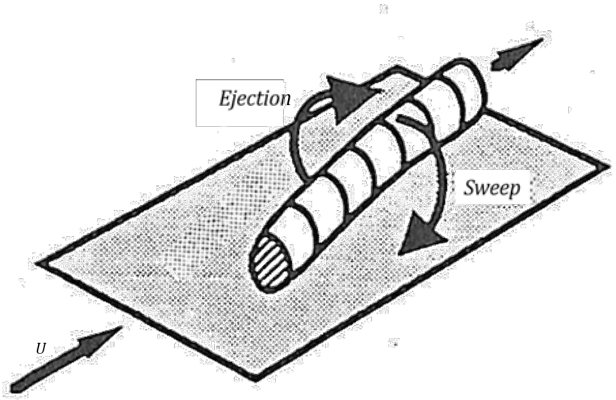

Figure 1.4: Quasi-streamwise vortex in buffer region, generating sweeps and ejections as it rotates and convects downstream [9].

Vortical Structures

Researchers agree that different vortical structures exist in the turbulent boundary layer but the type of structures, their formation, and their interactions are still highly debated. It is however agreed that these structures play a key role in the production of boundary layer turbulence. Vortical structures can be defined as any instantaneous vortex which forms a complex three-dimensional shape [17]. They have been proposed to take the form of hairpins, horseshoes, rings, arches and streamwise vortices.

The hairpin vortex is probably the most discussed coherent motion in turbulence research. It can be asymmetric (called cane vortices) or symmetric having the typical hairpin-like shape. It has been suggested that they originate in the near wall region as vortical "tornadoes" [27] and grow outward extending through a large part of the boundary layer. Evidence of hairpins in the outer region was provided by the flow visualisation work of Head and Bandyopadhyay [28]. They proposed that, as the Reynolds number increases, horseshoe structures are stretched to create the characteristic hairpin-shaped vortex. The heads of these elongated features are typically inclined to the wall at a characteristic angle of 40°-50°at high Reynolds numbers [29, 28, 27]. An alternative view was proposed by Ahn [30] who suggested that the hairpin vortex is generated from a initial disturbance which grows and generates a shape in the streamwise direction. It soon develops a vortex head, rises from the wall and bends back in the shear flow. A hairpin vortex is shown in fig. 1.5-c.

Figure 1.5: Schematic of features composing the outer region of turbulent boundary layer. (a) Loop (low Re); (b) Horseshoe (low-moderate Re); (c) Hairpin (moderate-high Re) [28].

Hairpin shape is highly dependent on Reynolds number. For example the existence of these hairpin vortices was not supported by the low Reynolds number investigation of Robinson [9]. This is most likely because hairpin vortices in general are strongly affected by the Reynolds number and tend to become skinnier and narrower as the Reynolds number increases [29, 28]. This is also depicted by the evolution of vortices shown in fig. 1.5.

Head and Bandyopadhyay [28] postulated that the large scale structures in the boundary layer are in fact collections of hairpin-shaped vortices. This hypothesis was later validated by the Particle Image Velocimetry (PIV) work of Adrian [31] which revealed quantitative evidence of 'packets' of hairpin vortices. He suggested that these originate in the near-wall region and grow to span a significant portion of the boundary layer (sometimes as much as δ). This suggests that the smaller flow structures may in fact organise to create the large scale motions [31, 21].

The horseshoe vortex, similar to the hairpin vortex, is another commonly discussed coherent motion in turbulence research. As with its hairpin counterpart, there are conceptual models about its existence and formation but little experimental evidence to support either. Head [28] suggests that horseshoes form from the stretching of vortex loops as the Reynolds number increases (much like the stretching of hairpins with Reynolds number). Black [32] proposed a conceptual model for the formation of this type of vortex in which horseshoe vortices evolve from vortex structures resembling closed loops or rings. As the vortex develops outward and downstream, it eventually leaves behind its wall-ward transverse element so that the ring is broken and the horseshoe shape is formed. The horseshoe vortex is represented in fig. 1.5-b.

Other vortical structures discussed in turbulence research include vortex rings, arch vortices and quasi-streamwise vortices. Ring vortices, such as shown in fig. 1.6, are toroidal in shape with most of the angular velocity (and vorticity) concentrated near to the core. It has been suggested that these rings are formed from "pinch-off" of hairpin vortices [14]. Arch vortices occur predominantly in the near-wall region at the tops (or sides) of near-wall low-speed streaks [9] as shown in fig. 1.7.

It is presumed that they are formed because of the roll-up of the shear layer which exists between the high- and low-speed fluid. These vortices then tend to grow and move outward due to inviscid circulation lift, $L = -\rho U \Gamma$ [17], moving progressively into higher velocity

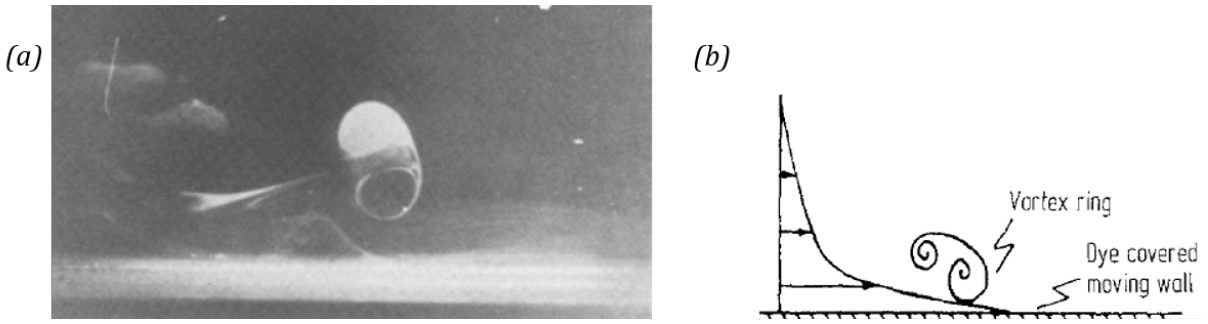

Figure 1.6: (a) Smoke visualisation and (b) schematic of ring vortex in buffer region [13].

fluid so that the upward lift vector is maintained. Quasi-streamwise vortices, as shown in fig. 1.4, have been observed as solitary eddies or in counter-rotating pairs [21]. They are dominant in the near-wall region where their close association with low-speed streaks is widely accepted. These structures are important in the production of TKE in the buffer region [9]. The specific mechanisms behind their formation is yet unknown but several propositions have been made. It is possible that they arise from the break-off of a leg (or neck) of a vortex arch as it convects and stretches downstream [9]. Alternatively they may arise when fluid impacting the wall rolls up into into a near-wall streamwise vortex [9]. As with their formation, the question of how they grow to fill the entire boundary layer is still open [21].

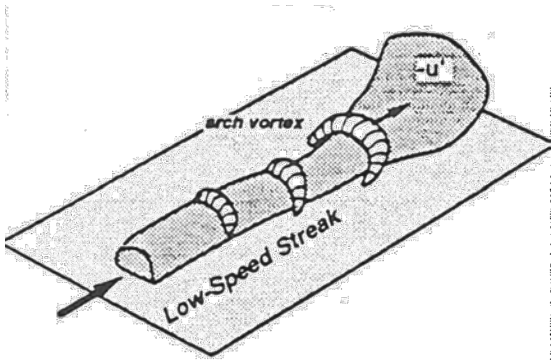

Figure 1.7: Schematic of arch vortices astride low-speed streaks [17].

While clear distinctions have been made concerning hairpin and horseshoe vortices in literature, it must be stated that these structures (along with cane vortices, omega-shaped vortices and even quasi-streamwise vortices) are most likely all variations of a common flow structure [31]. The cited differences in geometry may simply be characteristic of different stages of evolution through the flow.

1.3 Turbulent Flow over Rough Walls

The more practical problem of a turbulent flow over a rough surface is quite different from that of the smooth wall case. The ways in which the presence of roughness changes the aerodynamic characteristics of the flow is a thriving research topic, and very little is widely agreed upon. However it has been accepted that the main effect of roughness is to disrupt the mean velocity profile.

1.3.1 The Mean Flow over Rough Walls

In general, roughness has the effect of changing the mean velocity profile near the wall. In the outer region roughness only indirectly affects the mean velocity by increasing C_f but this is accounted for in the U_τ scaling [3]. In the logarithmic region, experiments show that roughness shifts the logarithmic portion of the mean velocity profile down and to the right, but without changing its slope [29, 3]. This shift, which corresponds to an increase in C_f and therefore an increase in U_τ, is captured in eq. (1.9) by the roughness function $\Delta U/U_\tau$ [33] and is also shown in fig. 1.8. Equation (1.9) is the law of the wall for rough walls [34, 35, 3].

$$\frac{U}{U_\tau} = A \log\left(\frac{yU_\tau}{\nu}\right) + C - \frac{\Delta U}{U_\tau} \tag{1.9}$$

Here constants A and C are considered to be the same as in the smooth wall equations, eq. (1.3) and eq. (1.4). The laminar sublayer is said to disappear for large roughness Reynolds numbers, $k_g^+ = U_\tau k_g/\nu$ [3]. However some researchers believe that roughness only changes the sublayer's thickness and character [23] forming a rough-wall counterpart commonly referred to as the *roughness sublayer* [8], where viscosity is still dominant.

In eq. (1.9) $\Delta U/U_\tau = 0$ for an aerodynamically smooth surface ($k_g^+ \leq 5$) [37]. For transitionally rough flows ($5 \leq k_g^+ \leq 70$) Dvorak [35] developed curves for $\Delta U/U_\tau$ in terms of k_g^+ and λ, the sparseness ratio (discussed in § 1.8). For the completely rough regime ($k_g+ \geq 70$) eq. (1.9) the right-hand side of eq. (1.9) is independent of viscosity. This means, as discussed before, the only source of drag is form drag produced by the pressure distribution on the

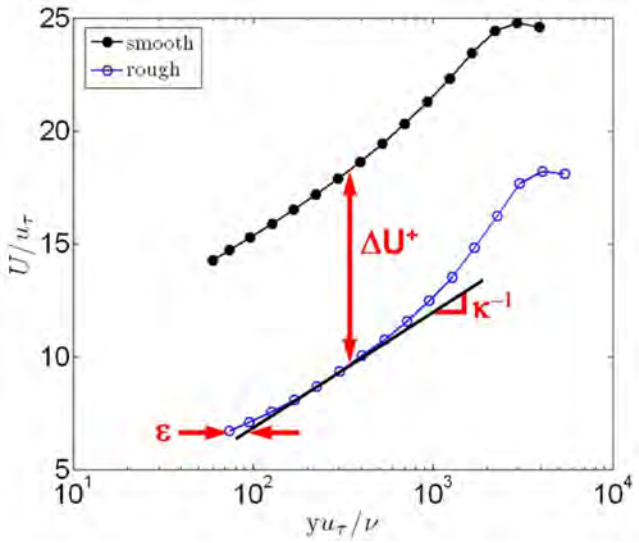

Figure 1.8: Effect of a roughness on the mean velocity profile [36].

roughness elements. For this regime the law of the wall becomes eq. (1.10) [38].

$$U^+(y) = \frac{1}{\kappa}\log\left(\frac{y}{k_g}\right) + C - \left(\frac{\Delta U}{U_\tau} - \frac{1}{\kappa}\log\left(\frac{k_g U_\tau}{\nu}\right)\right) \tag{1.10}$$

Roughness also has the effect of displacing the mean streamlines away from the wall by a constant *displacement height*, ε [24, 36]. This effect is due to the presence of the roughness elements and their wakes and can be accounted for by including the displacement height in the rough-wall law of the wall, eq. (1.9). This gives a modified law of the wall for rough surfaces

$$\frac{U}{U_\tau} = A\log\left[\frac{(y+\varepsilon)U_\tau}{\nu}\right] + C - \frac{\Delta U}{U_\tau} \tag{1.11}$$

The effect of ε on the velocity profile is also shown in fig. 1.8.

This classical way of accounting for roughness by using this roughness function $\Delta U/U_\tau$ has been called into question by some. For example, unlike with smooth walls, research has shown that the von Kármán constant κ (and therefore A in eq. (1.9)) may not be a constant for rough walls [39, 24, 40, 21, 36] as this classical approach suggests.

The rough-wall law of the wake is given in eq. (1.12) [33].

$$\frac{U}{U_\tau} = \frac{1}{\kappa}\ln\left(\frac{yU_\tau}{\nu}\right) + C - \frac{\Delta U}{U_\tau} + \frac{\Pi}{\kappa}W\left(\frac{y}{\delta}\right) \tag{1.12}$$

1.3.2 Categorising Rough Wall Flows

One of the earliest works on the effect of surface roughness on a turbulent boundary layer was conducted by Nikuradse [37] in 1950 studying pipes roughed with graded sand. He stated that flow over rough surfaces produce vortices which cause either pressure or suction depending on the aperture of the vortices. Obviously this will in turn affect the pressure field and the measured pressure fluctuations. Nikuradse [37] also defined $k^+ = k_s U_\tau/\nu$, a dimensionless parameter, where k_s was the actual sand-grain diameter used in his pipe studies. He found that for $k_s > 70$ the 'pipe loss coefficient' was dependent on k_s alone but for values below 70 the Reynolds number was also a significant factor. The first regime with $k_s > 70$ was termed 'fully rough' while the second with $5 < k_s < 70$ was termed 'transitionally rough'. The regime with $k_s < 5$ were called 'hydraulically smooth' since the roughness did not appear to have an effect on the pressure loss (because roughness peaks are within the laminar sublayer) [37]. Later Schlichting coined the term "equivalent sand-grain roughness" for k_s while using the findings of Nikuradse to correlate various types of "non-sand" roughness (rivets, bumps, and protuberances etc.). This term essentially refers to features of the roughness (height, spacing, etc.) that has the "equivalent" effect as a uniform layer of actual sand-grains of diameter k_s. The value of k_s is usually greater than the geometric roughness height, k_g. Since then the

concept of equivalent sand-grain roughness has been widely used and accepted in roughness research. It should be noted that the equivalent sand-grain roughness, k_s, is dependent on the aerodynamic effects of the flow over the roughness and not on the roughness geometry alone. It can therefore be determined from the roughness defect expressed in eq. (1.13) [41].

$$\frac{\Delta U}{U_\tau} = -5.75 \log \frac{k_s U_\tau}{\nu} + 3.4 \tag{1.13}$$

Flow regimes are still categorised as hydrodynamically smooth, transitionally rough, and fully rough today. The determining factor for each flow regime is the extent to which the roughness disrupts the mean flow. This effect is now quantified by the roughness Reynolds number, $k_g^+ = k_g U_\tau / \nu$. When k_g^+ is less than 5 the viscous sublayer is undisturbed by the roughness elements and the flow is considered smooth. On the other extreme the flow is considered fully rough if k_g^+ is greater than 40 [23] (Jiménez [42] suggests that this value should be 50). In this case viscous effects are negligible [23] and the roughness elements project into the log-layer [1]. The fully rough regime is of most practical significance and, according to Meyers *et al.* [1], the regime where universal scalings will become most apparent if they exist. Below $k_g^+ = 40$ the viscous sublayer is only partially altered by the presence of roughness and the flow is termed transitionally rough. In this regime both form drag on the roughness elements (as with the fully-rough regime) and viscous drag are thought to be important [23] (though recent works [1] have challenged this premise).

Roughness can also be divided into two classes: *k-type* and *d-type* roughness. Fig. 1.9 demonstrates the major difference between k-type and d-type roughness. K-type describes roughness where k_s is proportional to the dimensions of the roughness [42]. The effect of k-type roughness is to shift the logarithmic region of the mean velocity profile by a distance k_s. This type of roughness is of greatest practical importance. On the other hand the k_s value of d-type roughness is not proportional to the dimensions of the roughness but is instead proportional to the boundary layer height [42]. D-type roughness exhibits "extreme mutual sheltering" [42] and tend to sustain stable recirculation vortices between their elements (as shown in fig. 1.9). These vortices isolate the the outer flow from the roughness [42]. Geometrically, d-type roughness is usually closely packed 2-D square groove roughness (or 2-D ribs) [43, 42, 44] such as that shown in fig. 1.9. Wood further [44] differentiates between these two types of roughness using λ/k, stating that for λ/k values greater than 4 the roughness is k-type. He used roughness with $\lambda/k = 2$ which is d-type roughness.

1.3.3 Wall Similarity

As with the smooth wall, the turbulent boundary layer over rough walls is composed of an outer and an inner region. Many researchers believe that at sufficiently high Reynolds numbers both the rough wall and the smooth wall turbulent boundary layers are structurally similar outside the viscous or roughness sublayer [45, 8, 33]. This hypothesis is called *wall similarity*.

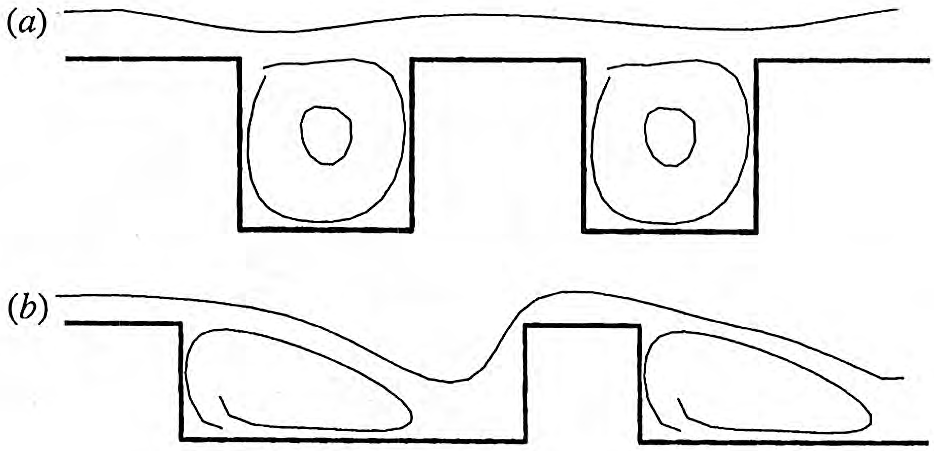

Figure 1.9: Comparison of (a) d-type and (b) k-type slotted walls (flow from left to right) [42].

The experimental work of Schultz [33] for example, which compared the measurements of smooth wall flows with that of flows ranging from transitional to fully rough regimes, found that the mean flow of smooth and rough walls showed excellent agreement in the 'overlap' and outer regions of the boundary layer. In fact, the Reynolds stresses, velocity triple products and quadrant decomposition of the Reynolds stresses all show similar good agreement for smooth and rough walls. This, he stated, provides "compelling support" for the concept of wall similarity as it proves that turbulence effects are limited to the near-wall region alone.

The underlying premise of wall similarity is that if there is a large enough separation between the scales of the largest turbulent eddies and the roughness length scales then the outer layer will be independent of the roughness geometry and, in fact, any features of the surface. In other words, the outer layer will not be able to 'see' the roughness and therefore not be affected by its presence at all. This is a very compelling idea in rough-wall turbulent boundary layer research because it means that, since the outer flow does not 'see' the roughness, the scaling for the outer flow will be completely independent of length scales based on roughness geometry.

It is important to note that the concept of wall similarity is only valid at high Reynolds numbers ($Re_\theta > 50{,}000$) and with relatively small roughness heights, k_g [33]. At high Reynolds numbers the boundary layer will be composed of a large number of structures of varying length scales. The larger the Reynolds number, the wider the range of scales which will be observed [4]. The requirement of small roughness height to boundary layer thickness is discussed at length by Jiménez [42]. He states that δ/k_g must be greater than 40 (experimental results suggest that this value is closer to 80 [42]) in order for any similarity laws to be observed. He also states that this ratio can be thought of as a direct measure of the effect of the roughness on the logarithmic layer — large ratios mean there is little effect

and wall similarity is valid. Contrary to Jiménez [42], Flack [45] postulates that δ/k_s is a more appropriate parameter to indicate whether the roughness will have a significant effect on the logarithmic region of the turbulent boundary layer. Notwithstanding the work of Meyers *et al.* [1] has shown that the combination of high Reynolds numbers and relatively small roughness heights does indeed produce scale separation. Under experimental conditions which met the two aforementioned criteria they were able to establish a *triple scaling hypothesis* based on observations of three distinct scaling regions, as opposed to two. It is believed that this was possible because large scale separations were achieved between δ, k_g and ν/u_τ. The triple scaling hypothesis is discussed further in § 1.7. As an aside it should be mentioned that decreased δ/k_g increases the friction velocity and in turn the drag. This is the case because the lower ratio means increased roughness area for increased form drag and also more intense mixing of the rough wall flow with the remainder of the shear layer [46].

It must be stated that there have been studies in which the outer region of the flow was clearly altered by the presence of the roughness [47, 48]. However in all these cases the Reynolds number was relatively low thereby violating the basic assumptions of wall similarity.

1.3.4 Mechanics of Rough Wall-Bounded Flows

Organised motions in rough wall-bounded flows bear some similarities to that of the smooth wall. However, as one would expect, the presence of roughness disrupts as well as creates motions. Of the eight types of motions identified by Robinson [9] (and listed in § 1.2.2) this section will focus on five of these motions and how the presence of roughness changes their behaviour (compared to the smooth-wall case).

It should be noted that while the subsequent discussion is a general description of some of the known organised motions in some rough-wall bounded turbulent flows, the geometry (height, density, shape etc.) of the roughness greatly affects the structures in the flow.

Low-Speed Streaks

Longitudinal low-speed streaks and the bursting process have been observed in rough-wall bounded flows [18, 8], occurring similarly to the smooth-wall processes. However these have only been observed in d-type roughness and when the roughness spacing is sufficiently large such that there is reattachment of flow between roughness elements. In the case of d-type roughness, elements are located close enough together so that a "pseudo wall" is formed by the tops of adjacent roughness elements. It is near this pseudo wall that the low-speed streaks are observed. Similarly when elements are far enough apart so that the separated region behind roughness elements can re-attach to the wall before encountering another element, low-speed streaks are observed close to the wall. In both these cases it

is believed that low-speed streaks are observed because the pseudo wall and the surface between roughness elements behave dynamically like the smooth-wall [8]. In all other types of rough wall flow the presence of roughness disrupts the near-wall flow to the extent that low-speed streaks are non-existent [18, 8].

Sweeps and Ejections

Unlike low-speed streaks, sweeps and ejections are present in the turbulent boundary layer irrespective of surface condition [15, 8]. However roughness induces changes in the intensity and distribution of the ejections and sweeps [23]. In his flow visualisation experiments using hydrogen bubbles, Grass [15] observed these sweep and ejection events in smooth wall-bounded flows (as was observed by Kline [16]), transitionally-rough (2-mm sand-grains) and fully-rough (9-mm pebbles) flows. He found that unlike smooth-wall ejections which involved the propulsion of fluid from low-speed streaks in the viscous sublayer, rough-wall ejections involved the expulsion of low-momentum fluid which was trapped between roughness elements. This makes sense considering the absence of low-speed streaks in most rough-wall boundary layer flows. Additionally Grass observed that rough-wall ejections appeared particularly violent (almost vertical expulsions of fluid) and were identifiable throughout the majority of the flow. Ligrani [23] concurred with this observation during his investigation of flow over spherical roughness. He stated that ejected fluid rises almost vertically pushing a large amount of fluid far from the wall, compared to smooth-wall flows. However rough-wall sweeps remained confined to the near-wall region [15].

In rough-wall flows sweep and ejection events occur much more frequently than in the smooth-wall flow [24, 25, 36]. According to Rusche [25], who studied the structure of turbulent flow over sparsely-spaced hemispheres and cubes, these events occur approximately 38% of the time (compared with 10% in the smooth-wall case). This value is in the vicinity of that found by both Hopkins [24] and Varano [36]. This increase in sweep and ejection motions indicates that in rough-wall boundary layers there is increased mixing and a marked rise in energy and momentum exchange between the inner and outer regions. With regard to momentum transfer close to the wall it has been suggested by Nakagawa *et al.* [49], from their investigation into the flow over glass-bead roughness in an open channel water flow, that sweep events are more important than ejections. They further stated that the importance of sweeps in momentum transfer increases with increasing roughness and decreasing distance from the wall. Nakagawa *et al.* further postulated that sweeps and ejections occur in very short periods of time, and this time decreases with increasing roughness and decreasing distance from the wall.

In general, Rusche [25] found that these sweeps and ejections are most likely to occur behind roughness elements (agreeing with the findings of Grass) with sweeps occurring slightly below the roughness height and ejections occurring slightly above the roughness height. Hopkins [24], in a study of the turbulent structure of flow over densely-packed hemispheres, reported

that ejections occur approximately 2-6% more often than sweep events.

Liu [18] hypothesises that the bursting process in rough wall-bounded flow is again (as with the smooth-wall) a dominant source of turbulence and turbulent energy but also states that the rough-wall case requires much more energy extraction from the mean flow in order to maintain vortical motions occurring between roughness elements.

Vortical Structures

The vortical structures in rough-wall flows are not as easily described as those in smooth-wall flows mainly because there is much less information available. Intuitively one would expect there to be are significantly more vortical structures in rough-wall flows because of the wakes of elements and the fact that structures are formed as the shear flow manoeuvres around the elements. However, Tomkin's [21] PIV measurements revealed reduced streamwise length scales in rough walls when compared to smooth walls, which suggests that the roughness actually
tends to disrupt the vortex organisation So it would seem that the creation, and evolution of vortical structures is not well understood in rough-wall flows. Nevertheless it is known that vortices are highly dependent on the roughness geometry. In fact it has been shown that the roughness elements tend to introduce vortical structures in the flow that are consistent with the roughness scale [51, 21]. Surprisingly most of the reported structures in rough wall flows are the same as those described in the smooth wall flow, but with variations in size, location and shape.

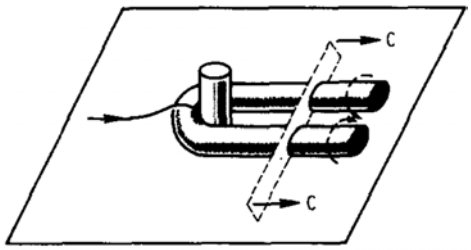

Figure 1.10: Horseshoe vortex around the base of cylindrical element in turbulent boundary layer [29]

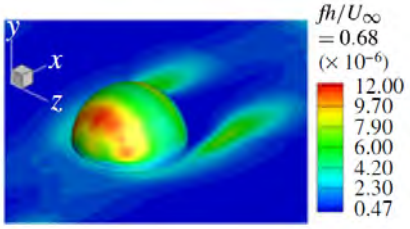

Figure 1.11: Simulated isocontours of the power spectral density of pressure fluctuations showing horseshoe vortex around the base of hemispherical element in turbulent boundary layer [50]

It is widely reported that horseshoe vortices form at the base of roughness elements of varying shapes and sizes [29, 51, 38, 25, 52] as shown in fig. 1.10 and fig. 1.11. In his examination of the turbulence structure downstream of isolated cylinders and Gaussian shaped spikes, George [38] found that, for both element shapes, a horseshoe vortex is formed at the nose of the element. Their formation is due to large adverse pressure gradient in the vicinity of the upstream junction

between the wall and the roughness element. This causes the flow to separate and the near-wall shear layers to roll up into the horseshoe vortex [53]. Experiments and simulations have identified this small region of separated flow upstream of roughness elements [36, 50]. Horseshoe vortices exist very close to the wall and, according to Bennington [51], are on the order of the size of the roughness element from which they emanate. Bandyopadhyay [29] (who refers to these as necklace vortices) emphasises that these structures remain parallel to the wall. Additionally, the horseshoe vortex produces a significant downwash velocity which is highly dependent on shape and size of the element [51]. This downwash velocity draws high-momentum fluid toward the wall which contributes to the increased shear stresses observed in rough wall flows and adds to the production of turbulent kinetic energy [51, 25]. The structure itself only persists for a short distance downstream (3-5 element diameters [38]) before viscosity causes it to dissipate [51, 38, 25]. In the case of distributed roughness horseshoe vortices form on each element. However the strength and coherence of the structures formed around downstream elements is significantly less than that found around upstream elements [25, 52, 50]. This is most likely due to increased shear layer interactions (e.g. interactions between wakes of different elements) as the flow moves downstream.

George [38] also found that flow separates at the top of roughness elements producing a pair of counter-rotating vortices which convect downstream for a significant distance (tens of element diameters). He plotted contours of the streamwise vorticity over cylinders which captured the presence of these vortices, as shown in fig. 1.12. These vortices induce large downwash velocities which, along with the convergence of the flow forced around the roughness element, contribute to a marked increase in wall shear stress. These interactions also enhance the Reynolds normal stress levels as well as the Reynolds shear stresses. The magnitude and extent of these stresses was found to be dependent on element size. Bennington [51] also observed these smaller vortices on the sides and top of his cubical roughness. He attributed them to the shear layers rolling up at the edges of the elements. The existence of these vortices are said to be intermittent while the horseshoe vortex is a permanent fixture at the base of the roughness element [29].

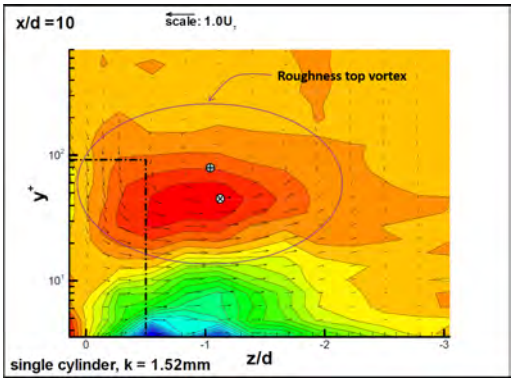

Figure 1.12: Contours of vorticity showing a single rotating vortex off the top right corner of a cylindrical element. View is looking upstream at a spanwise cut through the element. Cylinder is outlined by dashed lines [38]

Other vortical structures reported in the literature include the arch vortex [51] which was observed by Bennington directly downstream of cube elements. He ascribed their formation to the separation and shear layer roll-up created near the sharp edges of the element. As is proposed for the smooth walls, it is believed by some that vortex packets exist in the rough

wall flows and these are similar to that of the smooth wall packets [21].

The preceding description of vortical structures is for k-type roughness. In the case of d-type roughness large vortices form between roughness elements [18]. These slow-moving structures remain in the grooves and enforce a no-slip condition for the flow over the d-type roughness. It was observed that the vortices between d-type roughness elements occasionally display vortex-like swirling motions but only within the confines of the adjacent elements.

Wall-similarity dictates that the dominant vortical structures in the rough-wall flow be similar to that of the smooth-wall flow, except in the roughness sublayer [8]. This would suggest that in flows with high Reynolds numbers and high δ/k_g the roughness elements produce structures that are of the order of k_g or smaller. These structures are also confined to the roughness sublayer.

Large-Scale Outer-Layer Motions

It is worth mentioning that according to some researchers the properties of large-scale bulges and motions in the outer region of the boundary layer over a rough wall are similar to that observed over smooth walls. This, according to the theory of wall-similarity, is expected [8].

1.4 Velocity and Turbulence Statistics

Apart from the boundary layer thickness, some of the most important parameters in analysing any turbulent boundary layer are the displacement thickness

$$\delta^* = \int_0^\delta \left(1 - \frac{U}{U_{ref}}\right) dy \tag{1.14}$$

the momentum thickness

$$\theta = \int_0^\delta \left(1 - \frac{U}{U_{ref}}\right) \frac{U}{U_{ref}} dy \tag{1.15}$$

the friction velocity

$$U_\tau = \sqrt{\frac{\tau_w}{\rho}} \tag{1.16}$$

and the skin friction coefficient

$$C_f = \frac{\tau_w}{{}^1\!/_2 \rho U_{ref}^2} \tag{1.17}$$

Therefore measurements of the mean velocity and the wall shear stress are of utmost importance in any experimental boundary layer analysis. Hotwire probes are commonly used in

measuring velocity statistics. In fact quad-wire probes (four-sensor hotwires) are able to give measurements of all three components of velocity as well as the Reynolds stresses. Naturally there are limitations and special considerations in using these instruments, which have been chronicled by many researchers [11, 54, 55, 56, 57].

The most challenging parameter to estimate is the wall shear stress. Typically two approaches are taken to derive this parameter: fitting methods, which use inherent assumptions, or independent methods [36]. The most reported fitting method in the literature is that of Schlichting [58] which has been used by Blake [41], Aupperle and Lambert [59], Meyers *et al.* [1] among many others. It involves optimising U_τ and k_s to achieve the best fit to the mean velocity profile shown in eq. (1.9), with $\frac{\Delta U}{U_\tau}$ as defined in eq. (1.13).

Varano [36] did an extensive study into the most reliable method for estimating τ_w and found that fitting methods tend to over-predict U_τ and are highly dependent on the chosen value of κ. He postulated that an independent method using an integral momentum balance was more reliable. This method requires measurements of velocity (such as would be obtained by hotwires of LDV instrumentation) but is based on the integral momentum balance of eq. (1.18)

$$\frac{C_f}{2} = -\frac{\partial}{\partial x}\int_0^{Y_1}\frac{U^2}{U_e^2}dy + \frac{U(Y_1)}{U_e}\frac{\partial}{\partial x}\int_0^{Y_1}\frac{U}{U_e}dy - \frac{\partial}{\partial x}\int_0^{Y_1}\frac{\overline{u^2}-\overline{v^2}}{U_e^2}dy - \frac{\overline{uv}}{U_e^2} + \frac{\nu}{U_e^2}\frac{\partial U}{\partial y}\bigg|_{Y_1} \tag{1.18}$$

This equation assumes zero-pressure gradient and two-dimensional flow. The turbulent shear stress term in eq. (1.18) was shown to dominate the C_f value for small Y_1, such that the two were almost equal at the peak of the Reynolds stress values. Therefore, this term could be used to estimate U_τ because it would follow that the peak in the Reynolds shear stress value would occur when it is equal to U_τ. This method was also used by Meyers *et al.* [1] to verify the Schlichting fit described above.

Using these methods with hotwire/LDV measurements can produce mean velocity profiles such as is shown in figs. 1.1 and 1.2. More complicated profiles, such as the Reynolds stress profiles, can also be created and analysed from more advanced experimental techniques. These profiles have been described in depth by Marusic *et al.* [60]. They showed that the turbulence intensity profile of high-Reynolds number smooth wall boundary layers measured at different facilities around the world showed a similar natural-logarithm slope of -1.2 – -1.3. These results are shown in fig. 1.13.

Fernholz and Finley [61] also did an in-depth assessment of data looking at the trends in Reynolds stresses at high-, mid- and low Reynolds numbers. For high Reynolds numbers they found that outer-region similarity was observed with both the $\overline{u'^2}/U_\tau^2$ and $\overline{v'^2}/U_\tau^2$ profiles. Inner region similarity was observed only for $\overline{u'^2}/U_\tau^2$ in the viscous sublayer and buffer layer, which they took to confirm that there is no semi-logarithmic region for $\overline{u'^2}/U_\tau^2$. There was a clear peak in the $\overline{u'^2}/U_\tau^2$ and $\overline{v'^2}/U_\tau^2$ profiles but the $\overline{w'^2}/U_\tau^2$ profile did not show very clear peaks. Fig. 1.14 presents plots of the Reynolds stress components from this study.

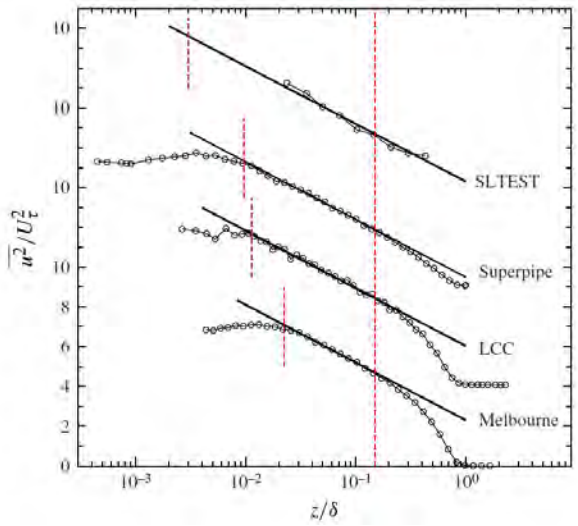

Figure 1.13: Streamwise turbulence intensity of smooth wall boundary layer measured at Melbourne wind tunnel (Re_τ = 18,010), LCC (Re_τ = 68,780), Princeton Superpipe (Re_τ = 98,190), SLTEST (Re_τ = 628,000) [60]

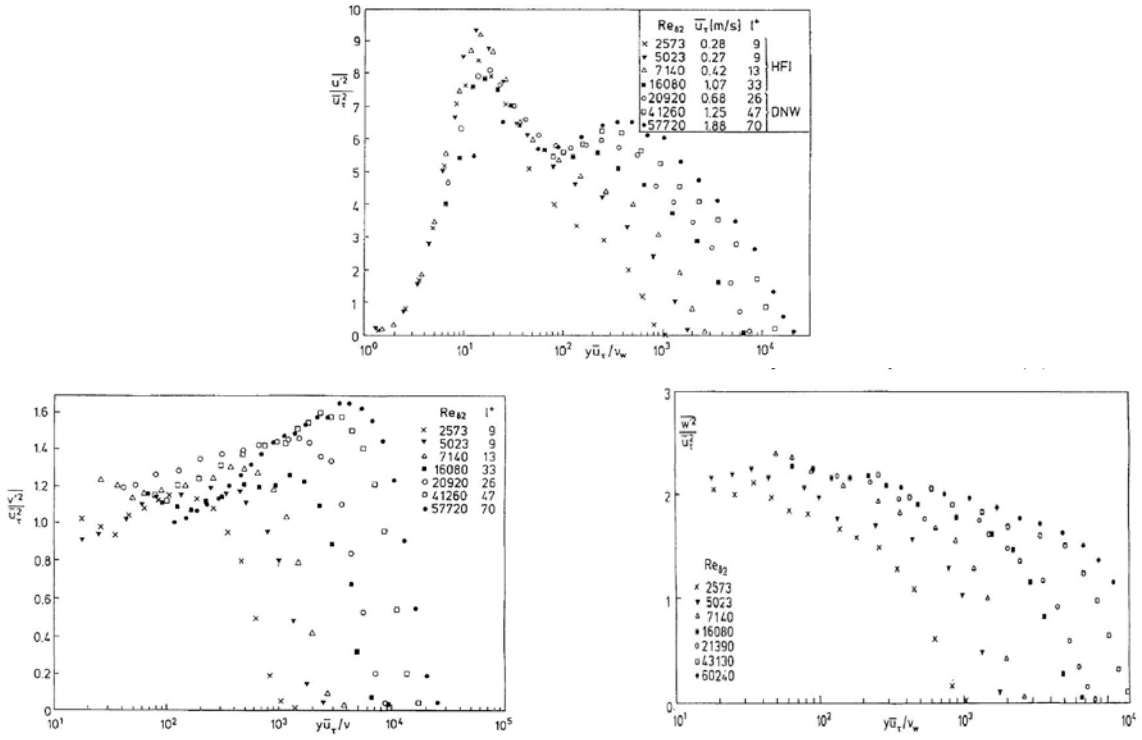

Figure 1.14: Variation of (a) x-component (b) y-component (c) z-component of Reynolds stress normalised on inner-scales [61]

1.5 Wall Pressure Fluctuations

Wall pressure fluctuations are inherently present in turbulent flow. Most researchers agree that they arise and are sustained by turbulent velocity fluctuations [62, 63, 64, 65, 30, 66]. According to Willmarth [66] pressure-producing organised motions tend to convect downstream at speeds which are proportional to their wavelength, thereby resulting in velocity fluctuations. These structures will eventually decay. He cites the production and convection of the turbulent structures as the source of pressure fluctuations in turbulent flow. Another theory is that the mean shear-turbulence interaction, which occurs as turbulence is convected, is the source of pressure fluctuations [41, 67]. Again this theory is not independent of the first two since shear cannot exist without variation in velocity. It is therefore conceivable that the shear-interactions occurring naturally in a turbulent flow because of velocity fluctuations will also result in pressure fluctuations. Thus the wall shear level is integral when considering the pressure fluctuations because it affects the overall wall pressure level [67].

The pressure fluctuations are obtained by solving a form of Poisson's equation [30, 68, 69, 62]. Goody [69] gives a detailed analysis of how the Navier-Stokes and continuity equations for an incompressible fluid with constant density and constant viscosity can be broken down to obtain the correct form of Poisson's equation. Then using a Reynolds decomposition the fluctuating pressure component can be isolated from the mean pressure component in this equation.The final equation from Goody, which is valid for all points in the flow, is given in eq. (1.19) where p is the fluctuating pressure term.

$$\nabla^2 p = -\rho\left[2\frac{\partial \overline{U_i}}{\partial x_j}\frac{\partial u_j}{\partial x_i} + \frac{\partial^2}{\partial x_i \partial x_j}(u_i u_j - \overline{u_i u_j})\right] \tag{1.19}$$

In eq. (1.19) the first term on the right, which represents the turbulence-mean-shear interaction, is referred to as the rapid term because it is presumed to respond more quickly to changes in the mean flow than the second term. Conversely the second term, which represents the turbulence interaction itself, is usually called the slow term because it only responds to changes in the flow after the mean flow alters the turbulence.

Goody [69] goes on to rewrite eq. (1.19) to give the pressure fluctuation on the wall, which is the objective when looking at pressure fluctuations in turbulent boundary layers.

$$p = \frac{\rho}{\pi}\oint_\Omega \left[\frac{\partial \overline{U_i}}{\partial x_j}\frac{\partial u_j}{\partial x_i}\right]\frac{d\Omega}{r_S} + \frac{\rho}{2\pi}\oint_\Omega \left[\frac{\partial^2}{\partial x_i \partial x_j}(u_i u_j - \overline{u_i u_j})\right]\frac{d\Omega}{r_S} \tag{1.20}$$

where $d\Omega$ is the differential volume element. As with eq. (1.19), the first term of eq. (1.20) is typically referred to as the rapid term while the second term is referred to as the slow term.

According to Bull and Thomas [70] wall-pressure fluctuations in a turbulent boundary layer should be measured using transducers which meet two criteria. The first is that the transducer should be smaller than the smallest length scale of the fluctuations in order to prevent high-frequency attenuation which is observed when instruments with large sensing areas are used. The attenuation is due to the spatial averaging of the signal across the sensing area resulting in length scales smaller than the length of the sensing area are lost. The second requirement is that the transducer must form a smooth, continuous surface with the wall in order for it to be non-intrusive and have its sensing area tangent and flush with the wall. The most used transducer in this field of research is and has been the pinhole microphone, an instrument which Bull and Thomas [70] specifically stated was not ideal because of the flow disturbance which results from the presence of the pinhole. Nevertheless, countless researchers have used this transducer in order to obtain previously unattainable high-frequency data and admit that this data can be trusted because, as concluded by Willmarth [62], the observed high frequency signal is not an artefact of the pinhole alone (if at all).

A pinhole microphone is a microphone with sensing area reduced by the use of a pinhole cap in order to meet criteria 1 of Bull and Thomas [70]. Corcos [71, 72] did extensive investigations into the effect of transducer sensing area on the resolution of turbulent pressures at the wall of a boundary layer. He developed a scheme to correct the measured power spectra for the high-frequency attenuation which occurs due to non-zero transducer size [71]. This correction is still being used today but is only considered as a rough guide. Corcos also found that for sensors with large sensing area to boundary layer thickness there is an increase in attenuation as the cube of the transducer face linear dimension [72]. Schewe [64] and Gravante [73] also studied the effect of transducer size on the resolution of the measured pressure fluctuations. Schewe's [64] investigation was carried out in a wind tunnel which was specifically designed for acoustic measurements using small transducers of the Sell type (a category of electrostatic microphones, made of a light conductive membrane and a counterelectrode, which works like a capacitor in that sound waves create fluctuations in capacity which are transformed to voltage fluctuations). He used the dimensionless parameter $d^+ = dU_\tau/\nu$, with values ranging between 19 and 333, to represent transducer size (where d is the pinhole diameter). The actual size of the five microphones used was $1 < d <$ 18-mm. He found that the smallest size transducer tested ($d^+ = 19$) was sufficient to resolve the structures of the turbulent pressure fluctuations. Gravante [73] used a variety of pinholes with high sensitivity microphones to obtain wall pressure measurements. He was able to do this down to a resolution of $d^+ = 2$ with a total range of d^+ between 2 and 27. He found that the smallest transducer size required to measure the spectrum with no spatial averaging effects is between $d^+ = 12 - 18$.

Spectral analysis is used to study the measured pressure fluctuation data. This provides a means of looking at all the scales present in the flow by working in the frequency domain. In this way spectral analysis gives quite a lot of information about the flow in apparently simple spectral plots. Additionally, the existence of any universal scaling laws will be most apparent through spectral analysis which simultaneously shows all the scales present in the flow.

1.6 Spectral Features of Smooth Wall Pressure Fluctuations

The discussion of this section will be limited to the results of pressure fluctuations measured on a smooth-wall under a zero-pressure gradient, turbulent boundary layer. This canonical case has been extensively studied and is fairly well-understood.

An important concept in the analysis of pressure fluctuations is that of scaling. Scaling is useful when a function is self-similar, which means it maintains the same shape/form under a wide variety of conditions [74]. Due to the large range of scales present in turbulent boundary layers the concept of self-similarity is not easily applied. As discussed at the beginning of § 1.2 the inner and outer layers have different length scales and so, traditionally, the boundary layer has been scaled as two independent layers. This is called the two-layer model [74, 75] and is depicted in fig. 1.15 using the pressure spectra of Farabee and Cassarella [76].

It has been found that the high-frequency portion of the pressure spectra collapses when scaled on wall variables such as τ_w (as pressure scale) and ν/U_τ^2 (as timescale). The result

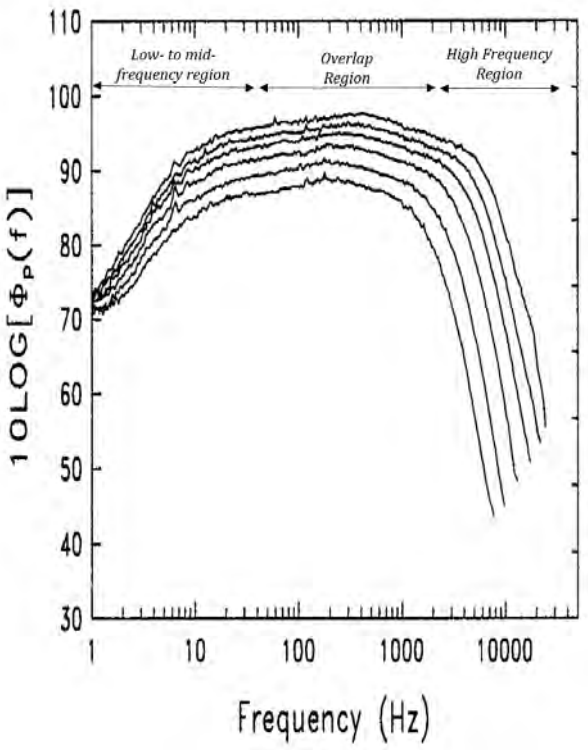

Figure 1.15: Two-Layer Model of smooth-wall pressure spectra (spectra obtained from Farabee and Cassarella [76]).

is that the high-frequency data collapse into a narrow band which decays as ω^{-5}. This result for the high-frequency range is well documented and agreed upon in the literature [78, 69, 74, 73, 1, 79]. The mathematical basis for the -5 decay has been detailed by Blake [77] and is based on the physical argument of the defect law. The defect law scaling on U_τ, which is valid in the inner region and the outer regions of the boundary layer, means that the pressure scale for the boundary layer should be $\rho^2 U_\tau^4$. He extends this to obtain an expression for the spectrum of wall pressure at a point caused by convected turbulence. The spectrum is shown in fig. 1.16, a diagram replicated from the work of Blake [77], where the high frequency limit is shown as decaying with a slope of ω^{-5}.

This result further suggests that the motions which generate the high-frequency pressure fluctuations (small wavelength eddies) are close to, and therefore highly influenced by, the wall [5]. The high-frequency region is generally considered to collapse on the Kolmogorov smooth-wall scaling where the pressure spectrum, $\Phi(\omega)$, and the frequency, ω, are normalised as $\Phi(\omega)U_\tau^2/\tau_w^2\nu$ versus $\omega\nu/U_\tau^2$. This scaling was applied on several data sets by Goody [69] and the result is shown in fig. 1.17. The figure shows that he obtained a fair collapse of the high-frequency data, within uncertainty, and obtained the expected slope of -5.

It is believed that the spectra in the low- to mid-frequency range scale on the outer region

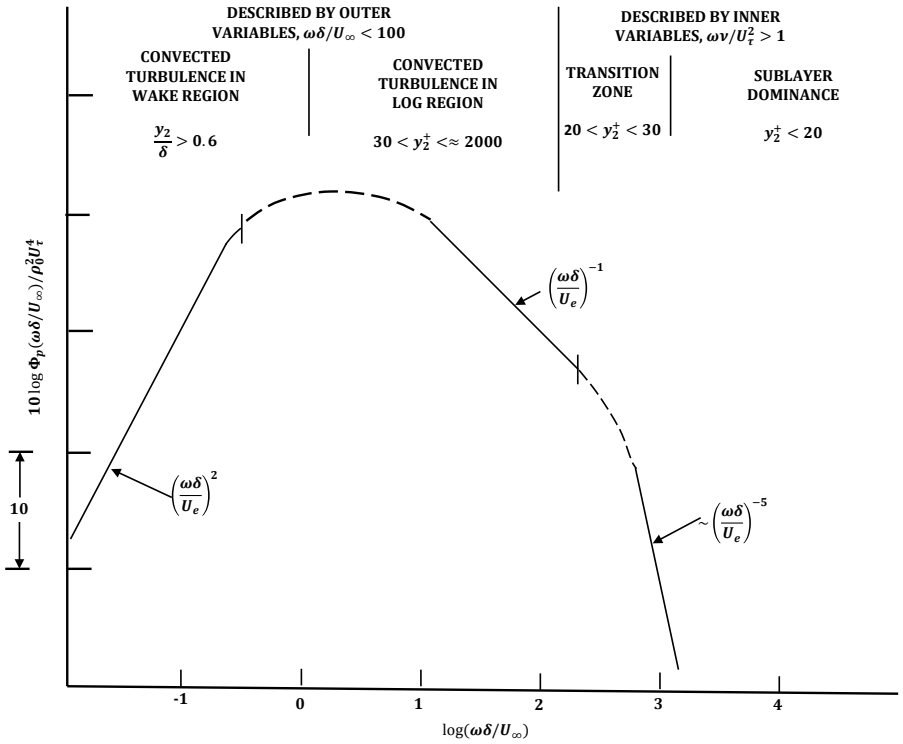

Figure 1.16: Frequency spectrum of wall pressure fluctuations at a point. Diagram reproduced from the work of Blake [77]

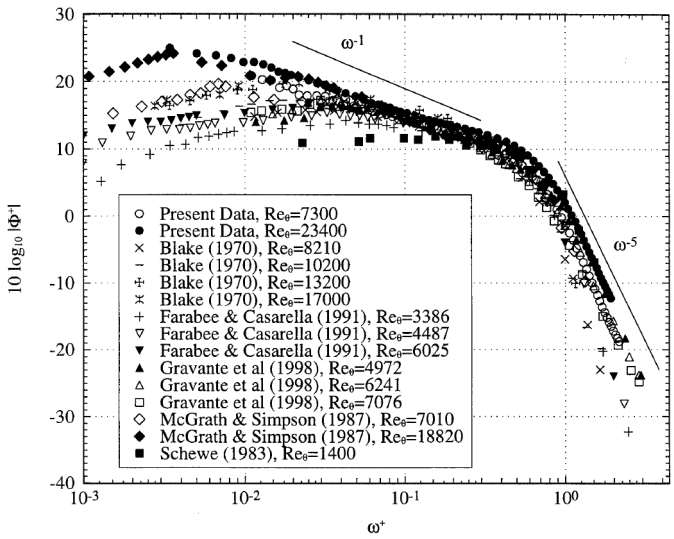

Figure 1.17: Smooth-wall pressure spectra under two-dimensional, zero-pressure-gradient, turbulent boundary layers scaled using Kolmogorov's Smooth Wall Scaling [69].

variables. The low- to mid-frequency range is therefore thought to coincide with the outer region of the flow. In the very low-frequency region ($\omega\delta/U_\tau < 2$) the spectrum is observed to increase, as ω^2, to a shallow maximum [76, 80]. This was again proven by Blake [77] who showed that in the low-frequency limit his equation for the wall pressure spectrum varies as ω^2. This is depicted by fig. 1.16. The value of this maximum is highly dependent on Reynolds number [81, 1] but it typically occurs at $\omega\delta/U_\tau \cong 2$. In the low- to mid-frequency range after the maximum the spectrum starts to decrease. Unlike the high-frequency region the scaling for the low- to mid-frequency is not widely agreed upon. Scalings include the *classical smooth-wall scaling* which is $\Phi(\omega)U_\tau/\tau_w^2\delta$ versus $\omega\delta/U_\tau$ and Blake's scaling [41]. Blake's outer region scaling resembles the classical smooth-wall scaling except that he uses the edge velocity U_e instead of the friction velocity, U_τ, and the displacement thickness, δ^*, is used instead of the boundary layer thickness, δ. Blake's outer scaling (also called the *the mixed outer scaling*) is $\Phi(\omega)U_e/\tau_w^2\delta^*$ versus $\omega\delta^*/U_e$ and is used extensively throughout the literature. Both these outer scalings have shown reasonable collapse with smooth wall data but neither have been able to collapse the very low-frequency region [69]. Fig. 1.18 shows a fair collapse of low- to mid- frequency data (from different sources) by Goody [69] using the Classical Outer Scaling.

The two-layer model with the inner and outer scales implies that there must exist a universal 'overlap' region where the inner and outer regions blend and in which both the inner and outer scalings apply. It has been argued [41, 82] that the spectrum in this 'overlap' region must decay as ω^{-1}. This 'overlap' region and the resulting -1 slope was proven to be dimensionally sound by Blake [77]. Again because of the defect law, the pressure scale for both the high and low frequency is $\rho_0 U_\tau^2$. Following the work of Panton [82] the spectrum at low frequencies

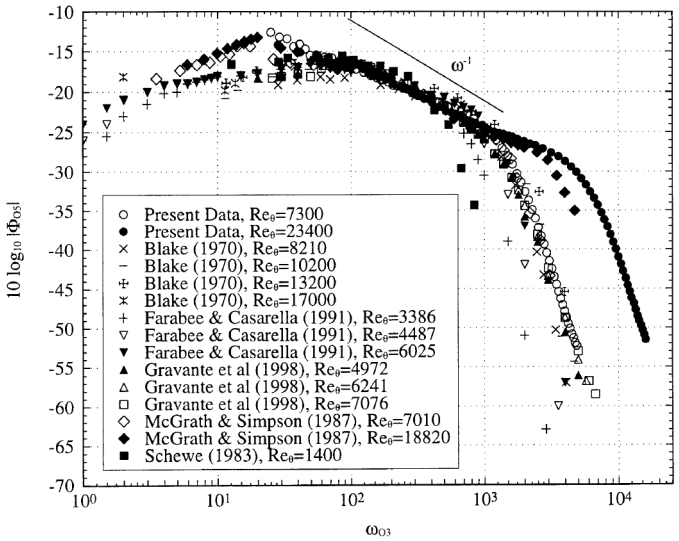

Figure 1.18: Smooth-wall pressure spectra under two-dimensional, zero-pressure-gradient, turbulent boundary layers scaled using Classical Outer Scaling [69].

will have the form

$$\frac{G_{pp}(\omega)}{(\rho_0 U_\tau^2)^2}\frac{U_e}{\delta} = g_o\left(\frac{\omega\delta}{U_e}\right) \tag{1.21}$$

At the high frequencies the pressure spectrum will scale based on $\rho_0 U_\tau^2$. The small near-wall structures will convect at speeds proportional to U_τ. Thus the high-frequency portion of the spectrum will have the form

$$\frac{G_{pp}(\omega)}{(\rho_0 U_\tau^2)^2}\frac{U_\tau^2}{\nu} = g_i\left(\frac{\omega\nu}{U_\tau^2}\right) \tag{1.22}$$

In the mid-frequency region both these scalings must exist simultaneously so

$$\frac{\delta}{U_e}g_o\left(\frac{\omega\delta}{U_e}\right) = \frac{\nu}{U_\tau^2}g_i\left(\frac{\omega\nu}{U_\tau^2}\right) \tag{1.23}$$

which is only possible if

$$g_o\left(\frac{\omega\delta}{U_e}\right) \propto \left(\frac{\omega\delta}{U_e}\right)^{-1} g_i\left(\frac{\omega\nu}{U_\tau^2}\right) \propto \left(\frac{\omega\nu}{U_\tau^2}\right)^{-1} \tag{1.24}$$

This means that when plotted on a log-log scale the pressure spectrum in the 'overlap' region must have a -1 slope. This -1 slope has not been observed in experimental work. Most measurements show a spectral decay between -0.7 and -0.8 [41, 69, 83, 1]. There have been simulations which support the existence of the ω^{-1} region [84] as well as the experimental work of Klewicki *et al.* [81] on high Reynolds number atmospheric boundary layers. The fact that ω^{-1} region is not realised experimentally is usually attributed to the relatively low Reynolds number of many laboratory scale flows. However, the high Reynolds number

investigations of Forest [85] and Meyers *et al.* [1] also did not produce the ω^{-1} region. This implies that either the reasoning behind the existence of this region is somehow flawed, or the convergence to a -1 slope at high Reynolds number is extremely gradual [85].

While there has been consensus on the two-layer model there are some researchers who believe that this model may in fact be incomplete. Farabee and Cassarella [76] carried out experiments to determine the regions of turbulence activity within the boundary layer that contribute to various spectral regions of the wall pressure field. They identified four characteristic regions in the pressure spectra: 1) a very low-frequency region with ω^{-2}) a region where there is a maximum level occurring in the mid-frequency range (which arises from sources in the outer region, 3) an 'overlap' region with ω^{-1} (which arises from sources in the logarithmic region) and 4) a high-frequency range (which arises from sources in the buffer layer) that decreases rapidly. It should also be noted that not may other works have obtained data at the very low frequencies achieved by Farabee and Cassarella [76] (shown in fig. 1.15). Brungart [6] and Smol'yakov [79] obtained results which agreed with the findings of Farabee and Cassarella. Smol'yakov [79] developed a method for calculating the spectra of pseudo-sound wall pressure fluctuations in turbulent boundary layers at different Reynolds numbers. His calculations revealed the four characteristic frequency ranges: low-frequency, mid-frequency, universal range and high-frequency. The universal range was first named by Bradshaw [86] who used dimensional analysis to show that ω^{-1} exists in this universal region. This four-layer model is clearly not very different from the two-layer model and 'overlap' region discussed previously.

In-depth reviews of the works related to pressure fluctuations in turbulent flows are given by Willmarth [62], Fernholz [61], and Bull [68].

1.6.1 Empirical Spectral Model of Surface Pressure Fluctuations

Goody [74] developed an empirical spectral model for predicting smooth wall pressure fluctuations similar in functional form to the Chase-Howe model:

$$\frac{\phi(\omega)U_e}{\tau_w^2\delta} = \frac{C_2(\omega\delta/U_e)^2}{\left[(\omega\delta/U_e)^{0.75} + C_1\right]^{3.7} + \left[C_3 R_T^{-4/7}(\omega\delta/U_e)\right]^7} \tag{1.25}$$

The model ensures that the pressure spectrum collapses to a universal curve at low frequencies when normalised using τ_w as the pressure scale and δ/U_e as the timescale. This region varies as ω^2. The model also ensures that the spectrum collapses as ω^{-5} at high frequencies when normalised on τ_w as the pressure scale and ν/U_τ^2 as the timescale. In the mid-frequency, Goody chose the constants in eq. (1.25) so that a slope of -0.7 would be obtained. This was in accordance with the results of experiment and not the theoretical -1 slope. The constants

suggested are

$$C_1 = 0.5 \qquad C_2 = 3.0 \qquad C_3 = 1.1$$

R_T is the ratio of the outer timescales to the inner timescales, $(\delta/U_e)/(\nu/U_\tau^2)$ and controls the size of the 'overlap' range (as opposed to the Reynolds number). The effectiveness of the Goody model in predicting the smooth wall pressure spectrum is shown in fig. 1.19.

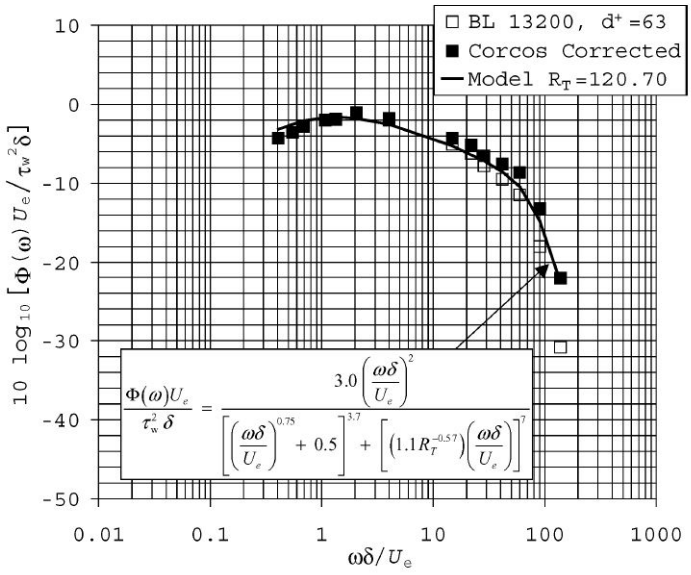

Figure 1.19: Effectiveness of Goody model compared to experimental data, obtained from Goody [74]

1.6.2 Temporal and Spatial Correlations

In addition to characterising the spectral features of wall pressure fluctuations, it is valuable to characterise relationships existing between two points within the pressure field. Time delay cross correlations and spatial correlations are best for such analyses.

The time delay cross correlation function is defined as in eq. (1.26).

$$R_{ab}(\tau) \equiv E[a(t)b(t+\tau)] \tag{1.26}$$

where $x(t)$ and $y(t)$ are stationary, zero-mean value, random signals. This function is the first step in determining insightful parameters like the covariance, the cross correlation coefficient, the cospectrum and quad-spectrum, the coherence, and the phase spectra.

The coherence and phase spectrum are probably the most useful of these for studying temporal correlations within a pressure field. The coherence is defined in eq. (1.27) and the phase spectrum is defined in eq. (1.28).

$$\gamma_{xy}(\omega)^2 = \frac{\left|S_{xy}(\omega)\right|^2}{S_{xx}(\omega)S_{yy}(\omega)} \tag{1.27}$$

$$\theta_{xy}(\omega) = \tan^{-1}\left(\frac{\Im[S_{xy}(\omega)]}{\Re[S_{xy}(\omega)]}\right) \tag{1.28}$$

Streamwise coherence values have been used by past researchers [63, 76, 87] to infer the extent of the turbulent eddies in the streamwise direction. For example, the coherence maps of Forest [87] confirm Bull's [63] finding that the larger turbulent eddies (low frequency content) persist for greater distances than the smaller eddies (high frequency content). This is because an eddy will lose coherence in the time taken for it to travel a distance which is proportional to its wavelength [63, 76]. Plots of the coherence decay over streamwise distance, such as fig. 1.20 from Forest, support this finding. While a perfect collapse has not been reported, the overall de-correlation of wall pressure fluctuations as the flow convects downstream is clear [76]. The collapse is typically better at frequencies above $26 \geq \omega\delta/U_\tau \geq 46$ (cut-off frequency) and breaks down at low frequencies [76, 87]. This collapsed decay curve was modelled by Corcos [71] as shown in eq. (1.29).

$$\Gamma(\omega, \xi) = e^{-C_1|\theta(\omega,\xi)|} \tag{1.29}$$

where C_1 is a constant and $\theta(\omega, \xi)$ is the phase spectrum as a function of the streamwise separation distances (ξ) and the phase convection velocity (U_{cp}).

$$\theta(\omega, \xi) = \omega\xi/U_{cp} \tag{1.30}$$

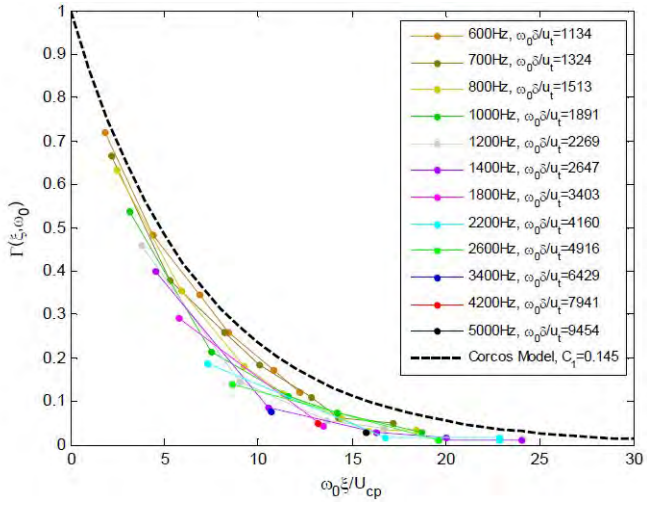

Figure 1.20: Decay of the smooth wall pressure spectra coherence with phase angle for for fixed frequencies [87]

The effectiveness of this model is also shown in eq. (1.29). C_1 is reported in the literature between 0.10 and 0.19 [63].

The phase spectrum of the smooth wall shows that the phase increases with increasing streamwise separation ξ [87]. For fixed separation distances the phase angle tends to increase with frequency. Forest postulates that this means that similarly sized turbulent eddies moving faster towards the outer portions of the boundary layer would be the first to de-correlate, while similarly sized eddies moving more slowly would tend to be more stable.

Blake [41] used the phase angle to calculate phase convection velocities according to

$$U_{cp} = \frac{s\omega}{\theta(\omega, \xi)} \tag{1.31}$$

where s is the separation distance – ξ in streamwise direction and η in spanwise. U_{cp} is useful in assessing coherence loss. Blake [41] found that U_{cp} for the smooth wall can be as high as $0.8U_e$ and asymptotes to $0.53U_e$ at large separations.

Trends in both the convection velocity and the coherence indicate that the small-scale components of the pressure field convect slowly downstream at speeds of the order of $0.5U_e$ and de-correlate quite quickly. On the other hand large-scale components are convected rapidly at about 0.8 – 0.9 U_e and tend to lose coherence slowly [63].

Spatial correlations reveal the spatial structure of the pressure field and are obtained in much the same way as the temporal correlations. For example, consider flow along a line with points x_1 and $x_1' = x_1 + \Delta x_1$. The correlation between velocity fluctuations measured at the same time at x_1 and x_1' is given by eq. (1.32)

$$R_{22}(x_1, x_1') \equiv E[u_2(x_1)u_2(x_1')] \tag{1.32}$$

The flow can be assumed to be homogeneous if the average properties only vary on a scale much larger than the scale of its turbulence. For a boundary layer flow homogeneity can be assumed because the scale over which the boundary layer is growing is much larger than the scale of the boundary layer thickness (the size of the largest turbulent eddies).

The Fourier transform of the spatial correlation function in the homogeneous direction produces the wavenumber spectrum. It is also possible to expand the correlation function between two points to consider both space and time. This will produce the wavenumber frequency spectrum based on the space-time correlation function of eq. (1.33) (assuming homogeneous, stationary flow).

$$R_{pp}(s, \tau) \equiv E[p(x, t)p(x + s, t + \tau)] \tag{1.33}$$

Much work [63, 78, 88, 76, 89] has been done in the wavenumber frequency spectrum to reveal quite interesting characteristics of the smooth wall turbulent boundary layer. This representation of the flow is particularly favoured because it gives direct physical understanding

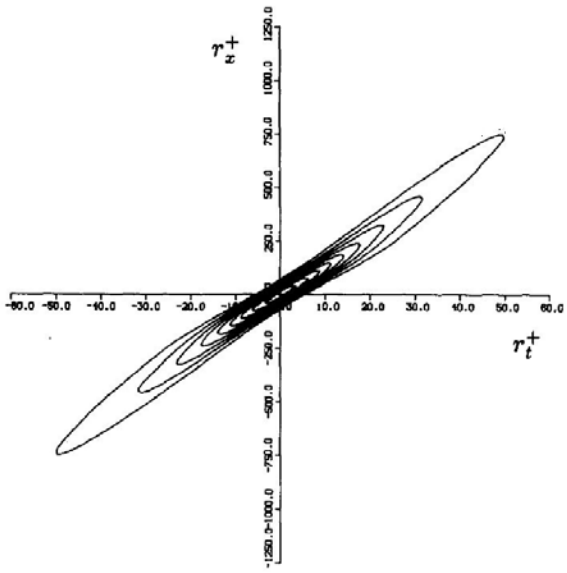

Figure 1.21: Contour plot of space-time correlation of wall-pressure fluctuations as a function of spatial (ordinate) and temporal (abscissa) separations [78]

of the wavelengths and frequencies of interest. Both the wavenumber frequency spectrum and the space-time correlation capture information about the scale, intensity and convection velocity of the eddies in the turbulent boundary layer. A typical space-time correlation for wall pressure fluctuations in a smooth wall turbulent boundary layer is shown in fig. 1.21 [78].

The shape of the contours tell a great deal about the nature of the flow. The elongated form of the correlation function is referred to as the *convective ridge* where most of the energy of the flow is concentrated. The slope of the convective ridge changes along its length, because it is a measure of the convection velocity of the eddies relative to the spatial separations. For small separations the level of correlation is high because the eddies have only travelled a short distance and therefore have not had much time to evolve. In addition the small eddies will contribute most to the correlation in this region [63] because their size is on the order of the small separation distance. Since these eddies are close to the wall and slow-moving, the slope of the centre of the ridge is smaller than at the edges of the ridge. The typical value of the convection velocity for this region is $U_c \approx 0.6U_e$ [41, 78, 54]. Conversely, the large scale eddies contribute substantially to the correlation toward the edges of the convective ridge because they are able to persist over larger distances than the small eddies. Since the large eddies are in the outer regions of the boundary layer where the flow is moving faster, the edges of the convective ridge tend to have a larger slope (U_C). Typically $U_c \approx 0.8U_e$ [41, 78, 54] in this region. The magnitude of the correlation also tends to be lower in this region because the eddies can evolve significantly over the large spatial separations.

Spatial and temporal correlations are obtained from using two or more pressure transducers to simultaneously measure the flow.

1.7 Spectral Features of Rough Wall Pressure Fluctuations

One direct consequence of the presence of roughness is that it intensifies the pressure fluctuations in the boundary layer. Overall the roughness causes a rise in both the wall shear stress [1] and the form drag [47] which in turn increases the pressure fluctuations. The roughness elements themselves shed vortices (as discussed in § 1.3.4) thereby introducing local sources of pressure fluctuations in the flow [50]. Additionally pressure fluctuations are created on the front of the roughness elements as the existing turbulence in the flow impinges on the surface [50]. At the back of elements a low-pressure fluctuation zone is formed as the flow separates [50]. Yang & Wang [50] physically interpreted their simulations to mean that the lower-frequency pressure fluctuations were generated by the impingement of the upstream wakes on the roughness elements. The high frequency pressure fluctuations he attributed to vortices produced at the edge of the roughness elements.

Despite the importance, only a few studies have focused on the pressure fluctuations associated with rough-wall turbulent boundary layers. These have aimed to develop scalings for the rough-wall pressure fluctuations as was done for the smooth-wall pressure fluctuations. To date no universal scaling has been found which collapses the pressure spectra of different Reynolds number flows at all frequencies.

However there have been significant advances in identifying scaling characteristics in different frequency ranges. By all accounts the rough-wall pressure spectrum has a roughly similar form to that measured over the smooth wall (see § 1.6 for smooth-wall discussion). There is a shallow maximum at low frequencies, a mid-frequency region where the slope may appear nearly constant, and a high frequency region with an approximate slope of -5. These features can be seen in fig. 1.22.

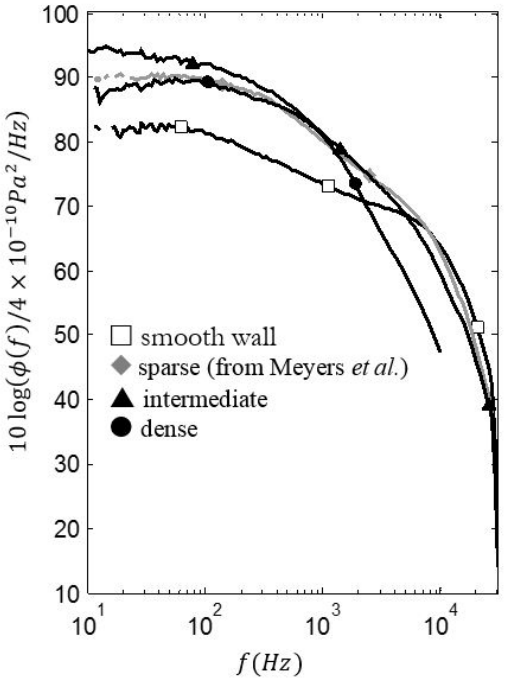

Figure 1.22: Effect of roughness on the pressure spectrum at 40-ms^{-1}, taken from Joseph *et al.* [90]

Despite these similarities some important differences exist. The absolute value of the pressure spectrum at low- and mid-frequencies tends to be significantly higher in the rough wall cases than in the smooth wall case at the same speed. This can be seen from the experimental data of fig. 1.22. This is expected because, as discussed before, roughness tends to intensify the pressure fluctuations. However at the high-frequencies the smooth-wall is observed as having higher absolute values. Additionally the maximum observed in the low-frequency region occurs at a higher frequency in rough-wall flows than in smooth-wall flows, a trend which apparently increases with increasing roughness height [59, 1]. At low frequencies the pressure spectra show levels that increase with increasing roughness size. The mid-frequency region also appears to have a higher slope than in the smooth-wall case [85, 1].

The Outer Region

On the basis of wall-similarity one would expect that the scaling in the outer region (low-frequency region) of the flow be the same for both smooth and rough walls. As discussed in § 1.6 the two scalings commonly used are the *classical smooth-wall scaling*, $\Phi(\omega)U_\tau/\tau_w^2\delta$ versus $\omega\delta/U_\tau$, and the outer scaling of Blake [41], $\Phi(\omega)U_e/\tau_w^2\delta^*$ versus $\omega\delta^*/U_e$. Both these scalings have showed acceptable collapse for most rough-wall pressure spectra [41, 85, 1], as can be seen in fig. 1.23 which applies these scalings for the data sets of Blake [41], Aupperle and Lambert [59], Varano [36] and Meyers *et al.* [1]. On close inspection, it is believed that there is considerable room for improvement when certain data sets (such as Varano's [36]) are considered.

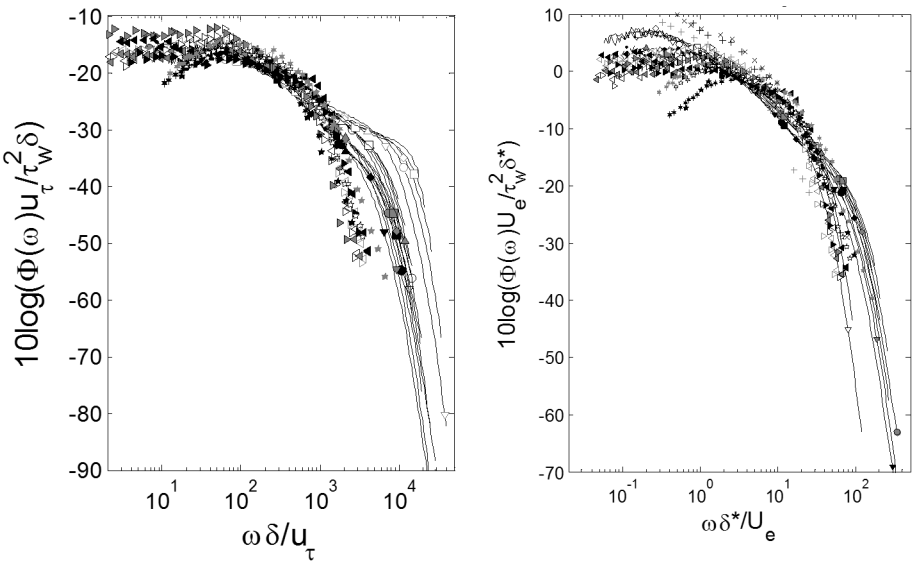

Figure 1.23: (a) Classical Outer Scaling and (b) Blake's [41] Outer Scaling applied to data sets of Blake [41], Aupperle and Lambert [59], Varano [36] and Meyers *et al.* [1]

The Inner Region

In the mid- to high-frequency region there has been considerably more work done to achieve a useful and universal scaling law. One of the first notable studies to this end is the work of Aupperle and Lambert [59]. The roughness consisted of sparsely populated, uniformly distributed sand particles on a stiff test panel. The grit particles were randomly spread over the test panel with an average spacing of 4.6 diameters and measurements were made using ceramic transducers with sensing diameter of 0.7-mm and pinhole microphones with sensing diameter of 0.5-mm. Three different surface roughness (grade 36, 12 and 4 grit particles) were tested, along with the smooth wall case, at a speed of 50-ms^{-1}. The boundary layer thickness varied from 28-38-mm during these experiments, depending on the type of roughness. The roughness Reynolds numbers ranged from 81 to 858 suggesting, by the criteria of Jiménez [42], that all cases were in the fully rough regime. However the δ/k_g values were considerable low, ranging from 10 (grade 4 case) to 56 (grade 36 case). Therefore only the grade 36 case could be expected to be free of transitional effects. There were also issues with acoustic disturbances in the test section, due to blower noise, which limited the low frequency content to above 200-Hz. Despite these limitations Aupperle and Lambert were able to develop an inner scaling based on the friction velocity, U_τ, the equivalent sand-grain roughness, k_s, the shear stress, τ_w and the skin friction coefficient, C_f. The inner scaling proposed is $\Phi(\omega)U_\tau/(\tau_w^2 k_s C_f)$ versus $\omega k_s/U_\tau$. While this empirical scaling is dimensionally correct there appears to be little physical basis for it. The success of this scaling has been marginal at best, as seen in fig. 1.24.

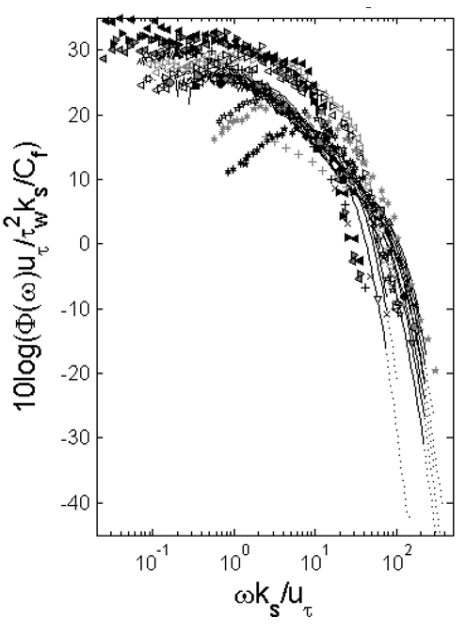

Figure 1.24: Aupperle and Lambert's [59] Inner Scaling applied to data sets of Blake [41], Aupperle and Lambert [59], Varano [36] and Meyers *et al.* [1]

While shown to work with some data sets (like that of Meyers *et al.*) this scaling clearly needs improvement when applied to others (Blake [41], Varano [36]). In fact, even the data of Aupperle and Lambert presented in this work failed to show collapse at the highest frequency which casts doubt on its viability as an inner scaling. These apparent shortcomings are most likely because the flow was not free of transitional effect and so a complete view of the pressure fluctuation behaviour could not be observed. Apart from the inner scaling, Aupperle and Lambert found that the exact placement of the roughness elements around the transducers had almost no effect on the resulting autospectrum, a finding which is consistent

with later findings by Smith [56]. They also pointed out that at low frequencies the pressure spectrum increased with increasing roughness size.

Another major work is that of Blake [41] who investigated the turbulent boundary layer wall-pressure fluctuations on smooth and rough walls. He used pinhole microphones which were three times smaller than that used in any other work at that time. This afforded him the ability to look into the influence of high frequency eddies because of the improved high frequency resolution of the microphones. Three rough fetches were tested – sparsely packed small roughness, densely packed large roughness and densely packed small roughness – each at two speeds of 38- and 50-ms^{-1}. All the cases tested produced fully-rough flows with roughness Reynolds numbers ranging from 170 to 410. The δ/k_g ratios were however fairly small, ranging from 26 to 42. The relative location of the measurement transducer to the surrounding roughness elements, which may be an important consideration in developing an inner scaling based on roughness geometry, was not reported or included in the analysis. Blake proposed both an outer (discussed in § 1.6 and § 1.7) and an inner region scaling. The inner scaling is based on the friction velocity, U_τ, the shear stress, τ_w and the geometric roughness height k_g. It is $\Phi(\omega)U_\tau/\tau_w^2 k_g$ versus $\omega k_g/U_\tau$. This is basically the same as his smooth wall scaling with the exception of the length scale, which he took as the geometric roughness height, and the velocity, which he took to be the friction velocity rather than the free stream. These substitutions are logical since k_g was thought to be the appropriate length scale, and U_τ the appropriate velocity scale, in the inner region. Additionally these changes were made because Blake theorised that at high frequencies the pressure fluctuations should scale on Strouhal Number of the roughness elements.

Blake also reasoned that τ_w is the only external stress on the boundary layers (for a zero pressure gradient flow), and so it follows that τ_w should determine the level of fluctuating pressure exerted on a wall by eddy motion in the boundary layer. This scaling showed acceptable collapse for the small roughness cases but did not work well with his large roughness cases. Nevertheless many researchers have used Blake's inner scaling since, and reported reasonable success [85, 1, 36] as illustrated in fig. 1.25.

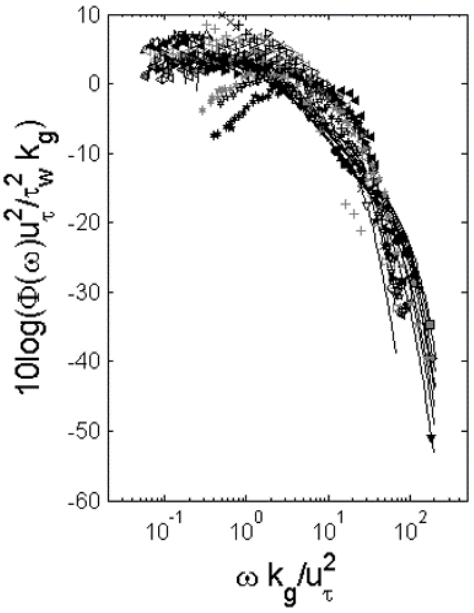

Figure 1.25: Blake's [41] Inner Scaling applied to data sets of Blake [41], Aupperle and Lambert [59], Varano [36] and Meyers *et al.* [1]

More recently Varano [36] proposed another inner scaling during his work with sparse roughness in turbulent boundary layers. He

tested 1-mm radius hemispheres under a 43-mm thick boundary layer at 20- and 27-ms^{-1}. The hemispherical elements were ordered in square arrays with transducers placed at the centre of this arrangement. There were issues with his low frequency spectral content because the boundary layer on the ceiling of his facility merged with the boundary layer of the floor. Special care was taken with this placement because Varano found that the location of the transducer relative to the elements affected the measured pressure spectra at high frequencies (contrary to the findings of both Aupperle and Lambert [59] and Smith [56]). While not his main goal, he was able to modify Blake's [41] inner scaling, which worked reasonably well with his data but was not perfect, to produce a new scaling: $\Phi(\omega)/\rho^2 U_e^3 k_g$ versus $\omega k_g/U_e$.

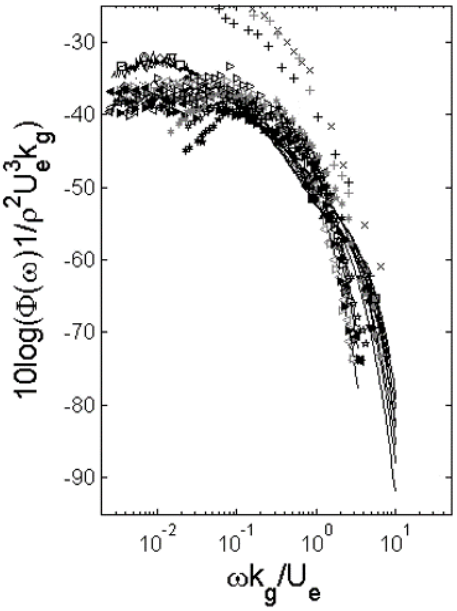

Figure 1.26: Varano's [36] inner scaling applied to data sets of Blake [41], Aupperle and Lambert [59], Varano [36] and Meyers *et al.* [1]

This scaling is applied to different data sets in fig. 1.26 where a fair collapse is obtained. Varano's argument for the new scaling was based on the assumption that U_τ should be proportional to U_e in the fully rough regime such that

$$\frac{\Phi U_\tau}{\tau_w^2 k_g} = \frac{\Phi}{\rho^2 U_\tau^3 k_g} \propto \frac{\Phi}{\rho^2 U_e^3 k_g} \tag{1.34}$$

This allowed him to substitute U_e into Blake's scaling to obtain his new high frequency scaling. The success of his attempt at a scaling may be due to the fact that a significant amount of Varano's data was in the fully-rough regime ($k_g^+ \approx 52 - 74$ and $\delta/k_g \approx 30 - 64$).

Alternative Model for the Pressure Spectrum

The premise of two scaling regions in the rough wall boundary layers, an inner and an outer region, has since been brought into question by the work of Meyers *et al.* [1]. They investigated the pressure spectrum of the turbulent boundary layer over 1-mm and 3-mm ordered hemispheres as well as 3-mm quasi-randomly distributed hemispheres. The ordered hemispheres were arranged in square arrays with 16.5-mm separation (centre to centre). All three rough surfaces had the same sparseness ratio, λ, of 0.052. The hemispheres themselves were molded epoxy resin on a substrate made of paper and Kevlar or fibreglass Velocity fluctuations were measured using single- and four-sensor hot-wire anemometers. Surface

pressure fluctuations were measured using 1/8-in B&K microphones fitted with 1/2-mm pinhole caps. Following the work of Varano [36] microphones were placed in the centre of the four element array, as far as possible from adjacent roughness elements. Boundary layer velocity measurements were made at free-stream velocities of 30- and 60-ms^{-1} and pressure fluctuation measurements were made at free-stream velocities of 20-, 30-, 40-, 50- and 60-$ms^{-}1$ for all cases. This resulted in roughness Reynolds numbers ranging from 91 to 507 and δ/k_g values from 72 to 212, such that all cases were in the fully-rough flow regime. The boundary layer height ranged from 201- to 231-mm.

The first major contribution of this work is the proposal of the triple scaling hypothesis which states that the rough-wall turbulent boundary layer is believed to have three well-defined scaling regions: a low-frequency range where δ and U_e are important; a mid-frequency range where k_g and U_τ are important; and a high-frequency range where ν/u_τ and U_ν (defined as the shear friction velocity) are important. It is believed that the reason for the emergence of these three distinct regions is the large scale separation ($\delta \gg k_g \gg \nu/u_\tau$) obtained due to high k_g^+ and δ/k_g. Meyers *et al.* [1] further hypothesised that if the roughness had two or more distinct and widely separated scales then even more scaling regions might emerge.

In the low-frequency region the pressure spectrum obtained for both the smooth- and the rough-wall was found to scale on outer variables, collapsing best with the classical outer scaling (discussed in § 1.6 and § 1.7). This region typically ranged between $20 \gtrsim \omega\delta/U_\tau \gtrsim 800$. The scaling of Blake [41] and Varano [36] were equally successful in collapsing the mid-frequency region of the rough-wall pressure spectra producing a region of -4/3 slope. This region is observed between $3 \gtrsim \omega k_g/U_\tau \gtrsim 20$ for the cases investigated but was observed to grow with Reynolds number. Collapse in the high-frequency range was obtained by a high-frequency scaling based on a new parameter they called the shear friction velocity, U_ν. This parameter can be thought of as the friction velocity in the boundary layer without the contribution of the pressure drag on the roughness elements. This physical meaning explains why U_ν would be chosen to scale the near-wall region which, because of scale separation, is unaffected by the roughness. Naturally U_ν has the same value as U_τ for the smooth-wall case and is always smaller than U_τ in the rough-wall case. The proposed scaling is $\Phi(\omega)U_\nu/\tau_\nu^2\nu$ versus $\omega\nu/U_\nu$ where $\tau_\nu = \rho U_\nu^2$, a modified wall shear stress. It is was developed based on the smooth-wall viscous scaling, $\Phi(\omega)U_\tau^2/\tau_w^2\nu$ versus $\omega\nu/U_\tau^2$ (discussed in § 1.6), because the high-frequency region of the rough-wall pressure spectra closely resembled the viscous dissipation region of the smooth-wall pressure spectra. When this new scaling was applied it convincingly collapsed the high-frequency region of all the data into a small band with a slope of -5. The scaling appears to be robust; it was applied to the independent data of Blake [41], Aupperle and Lambert [59] and Varano [36] and the result was a similar collapse of the data into a narrow band with a -5 slope. This collapse is shown in fig. 1.27.

With the new insights from Meyers *et al.* it is clear that any high-frequency scaling must include some reference to viscosity because this controls the smallest scales of turbulence [91, 1]. This suggests that the scalings of Blake [41], Aupperle and Lambert [59] and Varano [36] would be more appropriately categorised as mid-frequency scalings.

While this appears to be a significant advancement in the field, the versatility of this new hypothesis and high-frequency scaling is fairly untested. Its success with different roughness density, roughness shape, and two-scale roughness is still to be determined. The effect of transducer location relative to roughness element, which might prove to be important to the small scales in the boundary layer, was also not addressed in this work. Furthermore, not much explanation of the characteristics new U_ν parameter was given. It is unclear whether U_ν is a local or global parameter. At its root, U_ν is the scaling velocity inferred from the correlation of the highest frequency portion of the wall pressure spectrum. It is therefore a local quantity. However, the interpretation presented by Meyers *et al.* is that U_ν is a friction velocity that excludes pressure drag effects, which implies an area averaged quantity.

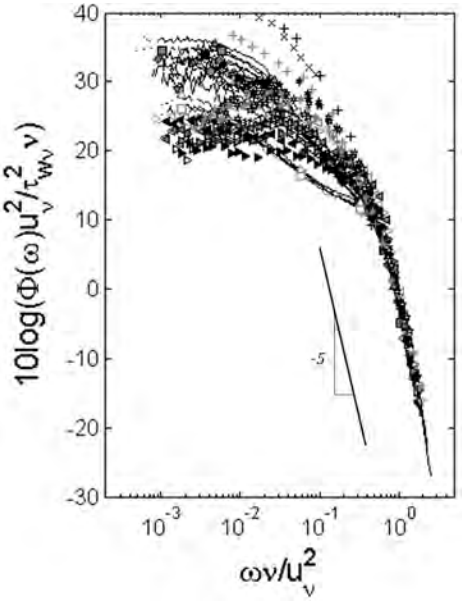

Figure 1.27: High frequency scaling of Meyers *et al.*'s [1] applied to data sets of Blake [41], Aupperle and Lambert [59], Varano [36] and Meyers *et al.* [1]

The 'Overlap' Region

As discussed for the smooth-wall pressure spectra, it is expected that an 'overlap' region must exist between scaling regions. This 'overlap' region must have a slope of ω^{-1} and comprise of scales from both scaling regions. This value for the slope has yet to be realised in experimental work for smooth-walls or rough-walls. Even the high Reynolds number work of Meyers *et al.* which had large scale separation did not achieve this value. Again this suggests that the premise of an ω^{-1} region might be flawed or approached extremely gradually with increasing Reynolds number, considering a slope of -1 has been reported by Klewicki [81].

It should be mentioned that if the hypothesis of an 'overlap' region with ω^{-1} slope is valid, then based on the results of Meyers *et al.* [1] it is conceivable that there might be two 'overlap' regions in a rough-wall boundary layer in which the roughness scale is uniform. Much like the analysis of eqs. (1.22) and (1.24) and § 1.6, the 'overlap' region would dictate that the scalings on either side of the 'overlap' region both apply in the 'overlap'. The result would again be a slope of -1, assuming that the pressure scales are the same. Taking this argument one step further one can speculate that with sufficient scale separation there might be even more 'overlap' regions in the flow, coinciding with the junction of each independent

scaling region. However, this could only be observed at extremely high Reynolds numbers and over a surface with multi-scale roughness.

1.7.1 Temporal and Spatial Correlations

Unlike with smooth walls, the body of knowledge relating to space-time correlations for the rough wall turbulent boundary layer is limited. What is known is that roughness decreases the streamwise extent of the eddies [47]. In addition, the actual coherence of the structures in the rough wall have generally been found to be lower for rough wall flows than for smooth walls [89]. Despite these differences, Forest [87] showed that the coherence decay of fig. 1.20 is applicable to rough walls.

Surface roughness was found to broaden the convective ridge of the wall pressure space-time correlation [87]. This is indicative of rough elements reducing the convection velocity. Compared to the smooth wall flow, convection velocities are indeed lower for a rough wall flow [89], between $0.78U_e$ and $0.84U_e$ [87]. This is due to the rough elements retarding the mean boundary layer flow.

1.8 Effect of Roughness Geometry

It has been established that one effect of roughness as it relates to the turbulent boundary layer is to intensify the pressure fluctuations. However the specific effect of different geometric parameters of the roughness - height, arrangement, shape, spacing - is still an active topic of research.

Height and Arrangement Effects

The most important role of roughness height, k_g, has already been discussed: scale separation. The height of the roughness compared to the boundary layer height dictates whether the flow is fully-rough and the extent to which scale separation is observed. Additionally it has been reported by Blake [41] that the roughness height influenced the medium and very small scale turbulent structures as observed in his pressure spectrum. Similarly Meyers *et al.* [1] found that the mid-frequency range for their 1-mm hemispheres had a slope which was markedly lower than that of their 3-mm hemispheres. So it would seem that the slope of the mid-frequency region changes depending on the roughness height. This suggests that k_g is the dominant length scale in this range and affects the way in which energy is transferred between structures in this region.

With regard to the arrangement of the roughness elements it was reported by Meyers *et al.* [1] that their 3-mm random and 3-mm ordered roughness showed nearly identical pressure

fluctuation results. Similarly George tested circular cylinders arranged in square and diagonal patterns. He found in general the differences between the two patterns were minimal and only observed within about $3k_g$ above the wall. Waigh and Kind [92] also reported similar results. These results are by no means convincingly conclusive but they do suggest that the roughness arrangement may not play a critical role in the turbulent boundary layer structure (and the pressure fluctuations).

Roughness Density Effects

The sparseness of roughness elements is another important geometric quantity. It is characterised by a parameter called the sparseness ratio, λ, defined as the ratio of forward projected area of the elements to the planform area that they cover. When λ is small elements tend to be widely separated while a high λ value means a more dense distribution. Bettermann [34] developed a geometric roughness function for the rough surface drag on densely spaced roughness. Similarly Dvorak [35] proposed a function which correlated the elements streamwise width and element spacing with roughness drag for sparsely distributed roughness geometries (square or round rods, sand, screens, and staggered rows of spheres). Both of these correlations were based on the log-law intercept of the rough-wall mean velocity profile (which is the last term of eq. (1.10)):

$$f(\lambda) = \left(\frac{\Delta U}{U_\tau} - \frac{1}{\kappa} \log \left(\frac{k_g U_\tau}{\nu} \right) \right) \tag{1.35}$$

In their correlations Bettermann and Dvorak both interpreted λ as the ratio of the total surface area to roughness area. Later Simpson [46] modified these correlations to obtain single variable, generalised functions in λ (eq. (1.36) and eq. (1.37)).

$$f(\lambda) = 12.24 \ln \lambda^{-1} - 17.35, \lambda^{-1} < 5 \tag{1.36}$$

$$f(\lambda) = -2.85 \ln \lambda^{-1} + 5.95, \lambda^{-1} > 5 \tag{1.37}$$

However he used the frontal area normal to flow instead of the roughness area, leading to the current definition of λ (note that Simpson defines λ as the planform area to the total roughness frontal area normal to the flow, the inverse of the present definition). Simpson's interpretation of λ in these equations appear to be physically sound because the form drag (which is represented by $f(\lambda)$) should be about proportional to the roughness frontal area [46]. So not surprisingly he achieved better data agreement than Bettermann and Dvorak. This is seen in fig. 1.28 where eq. (1.36) and eq. (1.37) (representing the rough surface drag) are plotted with experimental data versus the sparseness ratio. In both Dvorak's and Simpson's papers, as well as in fig. 1.28, it is shown that as λ increases so does the drag ($f(\lambda)$) until it peaks at approximately $\lambda = 1/7$ when elements are so close together that adjacent

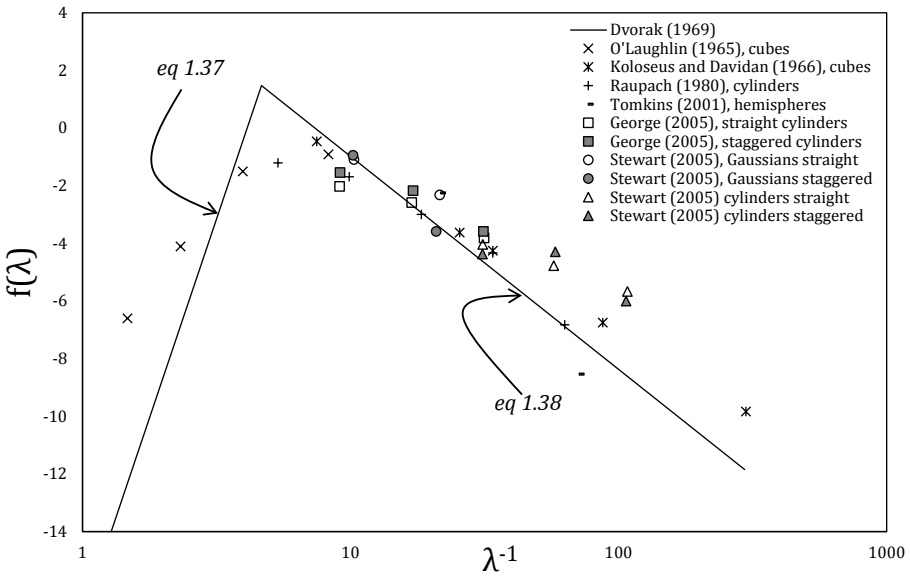

Figure 1.28: Variation of Dvorak-Simpson correlation function with roughness density

elements start sheltering each other. Up to this point the total drag can be considered as a linear combination of the increased drag due to each element [36] (assuming discrete elements). After this point the drag starts to decline because of the increased sheltering effect [1].

Because it essentially delineates the region when sheltering starts to occur, λ is also used to differentiate between k-type and d-type roughness. D-type roughness usually has $\lambda \approx 0.5$ [42] and displays extreme mutual sheltering. K-type roughness is further categorised using λ as either sparse ($\lambda < 0.15$) or dense ($0.15 < \lambda < 0.5$) [42]. The dense k-type roughness can also exhibit mutual sheltering but to a lesser extent than d-type roughness.

Most roughness research is done on fairly sparsely distributed roughness or single elements so the information about the structure of the flow over densely packed roughness is limited. Hopkins [24] attempted to shed some light on this topic in his study of boundary layers over densely distributed surface roughness. Both smooth and rough surfaces were tested at speeds of 20 and 27 m/s. Hemispherical roughness with spacings of 2.38-mm and 2.75-mm (k_g=1-mm), and three sandpaper roughness of grit values of 40 ($k_g \approx$ 0.86-mm), 100($k_g \approx$ 0.26-mm), and 150($k_g \approx$ 0.20-mm) were used. He was able to achieve δ/k_g values on the order of 40 or greater.While it is concerning that the roughness heights and shape were also varied in this test, Hopkin's results do shed light on some basic effects of the roughness density.

A major finding of his work is that in dense roughness cases there exists a large portion separated low-momentum fluid between the wall and up to approximately 70% of the element height. Hopkins explained that this region is a direct result of the close-packed nature of

dense roughness which also tends to inhibit the occurrence of streamwise vortices. Both these findings were fundamentally different from previous experiments done on sparse roughness [93, 94, 36]. Hopkins also noted that the sweep and ejection events occurred over longer fractions of time for dense roughness than for smooth walls. Additionally ejections occurred 2-6% more than sweeps. The latter finding is supported by the work of Raupach [95] who found that the stable recirculating vortices which form in the spaces between dense roughness (more specifically d-type roughness) tend to limit the occurrence of sweeps in the roughness sublayer so that ejections tend to dominate. The pressure spectrum of Hopkins data did not collapse on the scaling of either Blake [41] or Varano [36]. In fact Hopkins found no normalisation which adequately scaled the data. This suggests that scaling on a parameter which somehow takes into account the sparseness or element spacing might be necessary for dense roughness.

While widely accepted there is still some that believe λ to be an incomplete characterisation of the roughness sparseness. Waigh and Kind [92] used a different parameter to characterise the roughness sparseness. They postulated that λ was not sufficient to separate the dense and sparse roughness regimes. They proposed what they thought was a better parameter, Λ, which is defined as the ratio of the total volume over the surface (up to the height k_g) to the effective volume of the roughness elements.

As it relates to the pressure fluctuations Blake [41] observed that the large scale structures were affected by the roughness separation. Similarly Varano [36] stated that the element spacing was not an important factor when scaling in the high-frequency range of his surface pressure spectrum.

Shape Effects

In practical applications the shape of roughness is mostly irregular. This is modelled in research by the use of regular shapes which closely resemble the practical roughness. Common shapes investigated are hemispheres [51, 24, 85, 1, 25, 21, 36], circular cylinders [93, 96, 95, 25, 94, 21, 50, 97] and cubes [51, 25, 98, 52, 50]. Many other less common shapes have also been analysed, like spheres [35, 23], pebbles [15], Gaussian spikes [51, 99, 94], wire mesh [39, 100, 35] and cones [51]. Another common roughness fetch is sand-grain/grit-paper [59, 41, 35, 100, 15, 24, 56]. Of these extensive studies only a few have focused solely on the effect that the specific geometry has on the turbulence structure, namely the works of Stewart [94] and Bennington [51].

Stewart [94] studied the turbulent flow over four fetches of Gaussian spikes and six fetches of circular cylinders. For both Gaussian spike surfaces the elements were 2.54-mm in height with and base diameter of 2.54-mm and spaced 5.49-mm from each other. They were oriented differently in the flow: the first fetch was aligned straight on with the flow while the second was staggered. The circular cylinders all had base diameters of 1.98-mm, but three different heights are studied: 0.38-mm, 0.76-mm, and 1.52-mm. Cylinders of each height were also

aligned straight and staggered relative to the flow. In this way Stewart was able to look into the effects of both shape, height and orientation of the elements. He used Laser Doppler Velocimetry (LDV) to obtain data at an edge velocity of 27.5-ms^{-1}. Stewart found that the flows over both surfaces were similar and consistent with the mechanics described in § 1.2.2. However he did find that the cylindrical elements produced more well-defined, high peaks in the turbulent stresses than did the Gaussian spikes. This, he thought, was due to interface between the low-speed fluid (near the wall) and the high speed fluid (above the element) at the flat tops of the cylindrical elements. He stated that the Gaussian element, because it was pointed, allowed mixing over a large range of heights which reduced the peaks in the turbulent stresses. However it is more likely that the cylinders produced higher peaks in the turbulent stresses because their upper edges produce a larger pair of counter-rotating vortices than does the Gaussian spike. This would mean more shear layer interactions and therefore higher shear stresses. This aligns with the ideas of Rusche [25] who found that elements with smooth edges (like his hemispheres) create gradual slopes in the turbulence data while elements with sharp edges (like his cubes and Stewart's cylinders) create sharp changes in the turbulence, more closely resembling the behaviour of real roughness. Tomkins [21] also found that the shape of the roughness had a significant effect on the vortex shedding during his studies of cylinders and hemispheres.

Bennington [51] investigated the effects of various shaped roughness elements in two-dimensional high Reynolds number turbulent boundary layers. Single roughness elements included a 0.1-in high cone, a cone with spatial variations equal to the smallest sublayer structure length scale ($12\nu/U_\tau$), which he called fine-grooved; cone with spatial variations equal to 2.5 times the smallest sublayer structure length scale, which he called large grooved; 0.1-in high Gaussian bump; a hemisphere with base diameter of 0.11-in; a cube of edge length 0.068-in, front face aligned 90° to the flow; and a cube of edge length 0.068-in, front face aligned 45° to the flow. These elements are shown in fig. 1.29.

He also tested a fetch of distributed Gaussian elements with constant spacing of 0.216-in in order to give $\lambda = 0.088$. LDV measurements were taken for each of these cases at free-stream speed of approximately $27.5ms^{-1}$. For all the single elements, a horseshoe vortex was observed at the front base of the element. He also found that the cube oriented 45° relative to the flow produced a stronger downstream vortex pair than the cube oriented 90° relative to the flow (also observed by Castro and Robins [101]). In addition an arch vortex was detected directly downstream of the cube elements. Like Varano [36], Bennington observed high levels of TKE close to the downstream height-level of the elements. The largest magnitude was observed with the cube at 45° followed by the cube at 90°, the fine grooved element, cone, large grooved, Gaussian, and finally the hemisphere element. He therefore concluded that the elements which have sharp edges tend to produce the highest levels of TKE near the downstream height of the element. This energy appeared to be diffused most readily by the elements with sharp edges and peaks, namely the cone and cubes. The 'peakiness' of the element also appeared to have a direct correlation to the decay of circulation which was found to be proportional to $(x/d)^{-1.12}$. In terms of vorticity the cube at 90° showed the

largest magnitude of streamwise vorticity with the cube at 45° slightly less. Bennington presents detailed conceptual models for the flow around each roughness shape investigated, accounting for recirculation regions, vortical elements, downwash regions etc.

Yang *et al.* [50] also reported that for their cuboids the sharp frontal edges induced unsteady flow separation which he said produced strong pressure fluctuations. In addition Yang *et al.* [52] found that the vortical structures created near cylinders, hemispheres and cubes were

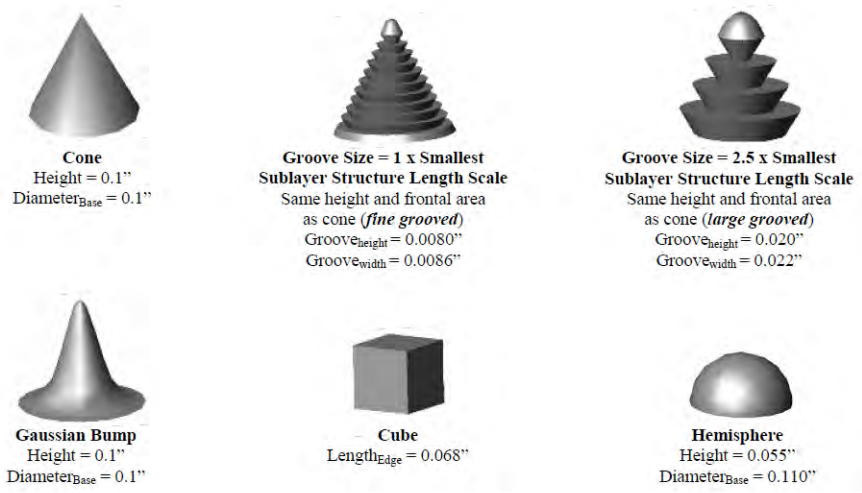

Figure 1.29: Shapes of roughness elements investigated by Bennington [51]

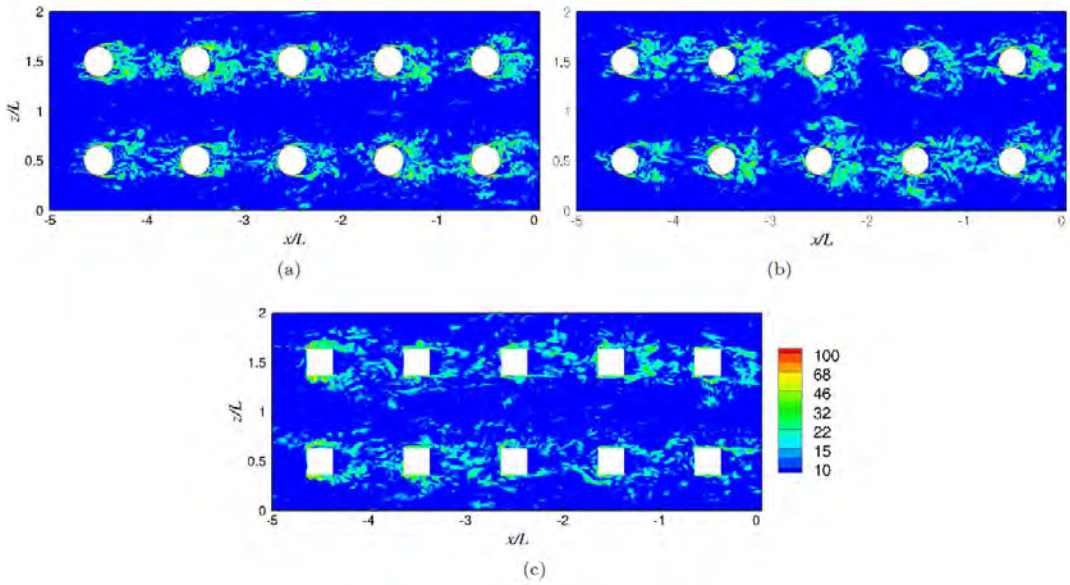

Figure 1.30: Isocontours of vorticity magnitude for (a) hemispherical, (b) cylindrical and (c) cuboidal fetches [52]

noticeably different. These results were part of a DNS study on unsteady forces and acoustic dipole sources in hemispherical, cubical and cylindrical roughness fetches. The rough surfaces consisted of elements 4.3-mm high arranged 25.4-mm apart. The fetch was 4 elements in the spanwise direction and 10 elements in the streamwise direction. The edge velocity was 13.7-ms^{-1} which produced k_g^+ of 140. Their findings on vorticity are shown in fig. 1.30. It is seen that the wake of the hemispheres are more confined than that of cylinders, most likely because the flow over cylinders tend to separate earlier than hemispheres. The cubes induce flow separation at the front edges causing more intense vortical structures at the sides, while the back of the element is shielded. This is also observed for the cylinders but to a lesser extent. Thus it is can be said that the flow over the cylinders appear to be an intermediate flow between that of the hemispheres and the cubes.

Considering these findings it would seem that when it comes to shape of elements, peaks and sharp edges affect the flow physics most.

1.9 Summary of Literature

A wide range of studies involving experiments, simulations, and analytical methods have been reviewed. The consensus is that the presence of roughness of different types introduces distinct differences between smooth wall and rough wall flows. Overall the pressure spectra of smooth and rough walls have similar shape: a slow-rising low frequency region, a rapidly decaying high frequency region, and a slowly-decaying mid-frequency or 'overlap' region. At low- and mid-frequencies the pressure fluctuations in rough wall boundary layers are typically higher than that in smooth wall boundary layers.

Currently it is believed that the smooth and rough wall flows comprise of an outer region, where δ is the length scale and the velocity scale is U_e. In the inner region of the smooth wall flow the length scale is ν/U_τ and the velocity scale is U_τ. The accepted smooth wall pressure scale is ρU_τ^2 for all regions, based on the fact that U_τ is an effective scaling in the defect law. In the rough wall flow k_g has been considered as an inner layer length scale instead of ν/U_τ because it is believed that the roughness eliminates the laminar sublayer altogether. In this way it is believed that the inner region of the smooth and rough walls are fundamentally different.

Scaling for the smooth wall flow appears to be satisfactory. The rough wall scalings present more discrepancies and less convincing collapses. This latter assessment is however purely subjective. To date almost no work has been done into properly defining the uncertainties associated with the current scalings, for a given data set. This means that the assessment of the success of a given scaling has been based on subjective user-inspection of the resulting collapse. While this is an important part of analysis, it would be more prudent to be able to compare the success of scalings on a more consistent and less user-dependent basis. A valid option would be to evaluate the uncertainty of the scaling parameters and the data and

use this to delimit the maximum width of an acceptable collapse. Such analysis will better distinguish a successful collapse from an unsuccessful one, and better equip us to improve the present scalings.

The ideal 'outer' scaling should be one which works for both the smooth and the rough wall. This requirement is based on the wall-similarity theory. From the works reviewed, the classical outer scaling appears effective for the smooth wall but is less successful for the rough wall flow, despite being one of the two (Blake's outer scaling [41] being the second) best available options at the present time. We must therefore take another look at these low frequency scalings in order to (1) adequately quantify the effectiveness of the current scalings independent of user-bias (2) obtain a more acceptable collapse for a wider range of data and (3) find a scaling which is equally effective for smooth and rough wall flows.

The recent work of Meyers *et al.* [1] has introduced the high frequency portion of the spectrum as opposed to an 'inner' region. This is based on their triple scaling hypothesis. The apparent success of their new high frequency scaling on U_ν cannot be denied. However this scaling is fairly new and is untested on data sets which include roughness of various shapes and element spacings.

The mid-frequency/'overlap' region warrants a much closer examination. The study of Meyers *et al.* [1] achieved the highest Reynolds numbers of any laboratory experiment reviewed here. This means that they have achieved the largest scale separation to date, allowing them to observe the 'overlap'/mid-frequency region more clearly than any other researcher. This is the reason that their triple scaling hypothesis is promising and their proposition of a mid-frequency (as opposed to an an 'overlap') region warrants a closer look. With the success of their high-frequency scaling, we know that the previously called 'inner' scalings are in fact mid-frequency scalings. Among the most successful of these are that of Blake [41], Forest [87] and Varano [36]. Yet, there is still much to be desired in terms of tightest of the resulting collapse. As stated before these scalings still need to be evaluated based on an independent criteria for success, thereby removing user-subjectivity.

The triple scaling hypothesis does not support the 'overlap' hypothesis. The latter is a concept developed for smooth wall flows and extended to rough wall flows. However this extension may not be appropriate because the interstitial flow created by roughness will certainly result in differences in the mid-frequency/'overlap' region between the smooth and rough walls. The presence of roughness will affect the mechanics of the flow and produce vortical structures and events which are not present on the smooth wall. Therefore, the rough wall mid-frequency region may not be an 'overlap' region. This is supported not just by physical intuition, but by the high Reynolds number spectra of Meyers *et al.*. These have shown that the so-called 'overlap' region is markedly different for the rough wall compared to the smooth wall and so does not have a universal form.

Next steps in this field must include deciphering the workings of the mid-frequency region. The 'overlap' concept is unlikely because it is does not account for interstitial flow effects of the roughness elements themselves. The alternative triple scaling hypothesis proposes

that the mid-frequency is governed by k_g and U_τ but this is yet to be proven. Current mid-frequency scalings which are based on k_g and U_τ are less than satisfactory. We must explore the possibility that measures of roughness element geometry other than k_g – frontal projected area, sparseness ratio, shape, peakiness etc. – are important parameters as well. The effect of roughness element spacing (roughness density) on the pressure spectrum appears to be less studied than other geometric features such as shape. Of the studies reviewed concerning dense roughness, it was found that the pressure spectrum does not collapse using currently known scalings. More efforts toward finding a relationship between roughness element spacing and the rough-wall pressure spectrum is required.

Once more is known about the mechanics of the mid-frequency region we can then address the rigour of the -1 slope expectation. The fact that it has not been achieved in experiment, even at high Reynolds numbers as that achieved by Meyers *et al.* casts some doubt on the validity of this requirement itself. The explanation of Meyers *et al.* that the -1 slope is probably approached slowly with increasing Reynolds number is possible. However, it is more likely that the -1 slope argument is, at some level, flawed because there should at least be some variation or progression toward this slope between experiments. Instead we see that the slope is consistently between -0.7 and -0.8 for experiments with widely varying Reynolds numbers. Much work is needed here.

1.10 Scope and Aim of Present Work

The main objective of this work is to provide insights into the nature of the turbulent pressure fluctuations over any rough wall. This is a complex problem. The approach taken here is to

1. broaden the understanding of the flow structure of a turbulent boundary layer over rough surfaces of varying geometries. Specifically we will seek to
   (a) infer the presence of organised motions near rough elements based on the pressure field measured at different locations relative to the elements
   (b) reveal the effect of rough surfaces of different element shape and spacing on the turbulence statistics and typical boundary layer parameters
   (c) identify characteristic flow features from the pressure spectrum of rough surfaces of different geometries
   (d) detail the relationship between the pressure spectrum of single-scale rough surfaces with that of two-scale rough surfaces (which are combinations of the single-scale surfaces)
2. uncover the effect of rough surfaces of different geometries on the space-time correlation of the wall-pressure fluctuations. Steps will be taken to

(a) infer, from streamwise and spanwise spatial separations, the persistence of turbulent eddies in the boundary layer over various kinds of rough surfaces

(b) explore the role that roughness geometry plays on the convection velocity of turbulent eddies in the boundary layer

3. identify the scaling laws that govern the time-spectrum of wall pressure fluctuations in various frequency ranges. More specifically we will

(a) determine whether the high frequency shear friction velocity scaling of Meyers *et al.* (2015) [1] is universal to rough surfaces of different shape and roughness density

(b) determine whether estimates of the roughness drag coefficient can be used to usefully predict the shear friction velocity for rough surfaces of different shape and density

(c) shed light on the nature of the shear friction velocity

(d) identify the parameters that govern the pressure spectrum at low frequencies, and thus the associated source of these pressure fluctuations

(e) assess the effectiveness of the presently proposed mid-frequency roughness scalings, as it relates to rough surfaces of different shape and density

(f) evaluate the mid-frequency region as an 'overlap' region where the low-frequency and high-frequency scaling both apply

(g) determine the extent to which the location of the pressure measurement within the depth of a rough surfaces influences the pressure measured and its scaling

(h) explore the effectiveness of scalings laws which govern single-scale roughness when applied to two-scale rough surfaces

4. develop an interpolation function for the pressure spectrum of rough wall flows which is sufficiently universal to be of practical use.

To achieve these goals the high-Reynolds number turbulent flow over eight rough surfaces is examined. Measurements of the wall pressure fluctuations were made using pinhole microphones and hotwire measurements were made to obtain the velocity field. The smooth wall will also be investigated as a control for the rough cases.

2. Apparatus and Instrumentation

2.1 Virginia Tech Stability Wind Tunnel

All the data presented in this work was measured in the Virginia Tech Stability Wind Tunnel. It is a continuous, closed-circuit, single-return, subsonic facility. The circuit, shown in fig. 2.1, comprises of a motor driving a fan, an air exchange tower, settling chamber, and a removable test section.

An outstanding feature of this wind tunnel is that it produces good flow uniformity and has significantly low turbulence levels for a facility of its size – on the order of 0.03% or less. As of 2006, hot-wire anemometry measurements of free stream turbulence as a function of flow speed indicated that turbulence levels are as low as 0.016% at 12-ms^{-1} and increase with speed, rising to 0.031% at 57-ms^{-1}.

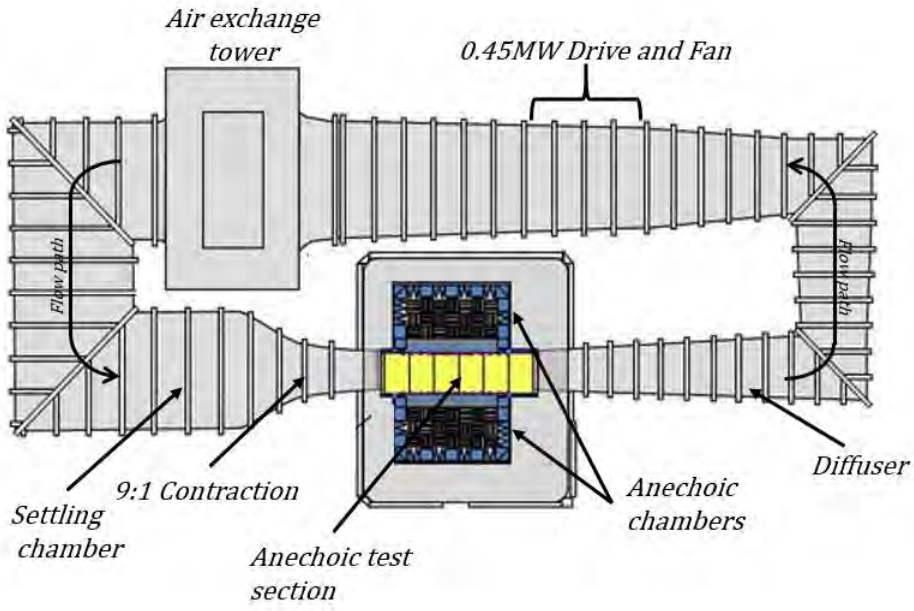

Figure 2.1: Schematic showing full circuit of the Virginia Tech Stability Wind Tunnel (adapted figure, courtesy of VT AOE department)

2.1.1 Stability Wind Tunnel Circuit

The Virginia Tech Stability Wind Tunnel is capable of producing flow speeds up to 80-ms^{-1} and, not accounting for blockage in the test section, Reynolds numbers per meter of approximately 5,000,000. The system is powered by a 0.45-MW variable DC motor which drives a 4.3-m propeller with maximum rotation of 600-RPM. The fan is lined with Delrin® to reduce the tip gap from about 15±4-mm to about 7±3-mm. The speed in the circuit is regulated using a custom designed Emerson VIP ES-6600 SCR Drive which interfaces with the computer-controlled data acquisition system of the tunnel.

As shown in fig. 2.1, downstream of the fan and motor is an air exchange tower. This facilitates temperature stabilisation as it is open to the atmosphere. Following the flow path, there is then a 5.5-m × 5.5-m settling chamber housing seven turbulence-reducing screens. These screens are credited with the extremely low turbulence levels discussed before. A 9:1 contraction nozzle further reduces the turbulence levels while simultaneously accelerating the flow to the test speed. The flow then enters the removable test section. There are two removable test sections in use in the Stability Wind Tunnel: an anechoic test section and an aerodynamic, hard-wall test section. Both test sections are 7.3-m long and have a 1.83-m square cross section. The test section is housed indoors, enclosed inside a sealed steel building (control room). The downstream end of the test sections are outfitted with sidewall slots which serve to equalise the pressure inside the control room with the static pressure of the test section. The data presented in this study was collected in the anechoic test section which is discussed in detail in § 2.1.2.

A 3° diffuser is directly downstream of the test section, with eight 0.16-m high vortex generators at its entrance. The vortex generators minimise separation and are mounted 0.4-m from the corners of the channel. The possibility of separation and corner stall is further reduced by a series of turning vanes installed in the four corners of the wind tunnel circuit. These direct the flow through the circuit and comprise of diagonal vanes typically spaced 0.3-m apart, except for the turning vanes immediately upstream of the settling chamber which are spaced 0.056-m apart.

In order to reduce noise reflection some parts of the wind tunnel circuit are acoustically treated. 25-mm thick melamine is used to line the side walls and ceiling of the diffuser while the walls between the diffuser and the drive and fan are lined with 50-mm thick melamine and urethane foam. Additionally 50-mm urethane foam is used to line the walls and floor of the section between the air exchange tower and the settling chamber as well as the walls of the section of the settling chamber upstream of the turbulence-reducing screens.

2.1.2 Anechoic Test Section

The aeroacoustic test section of the Stability Wind Tunnel is shown in figs. 2.2 and 2.3. It consists of the main test section and two anechoic chambers, one on each of the starboard

Figure 2.2: Upstream view looking downstream of the anechoic test section of the Virginia Tech Stability Wind Tunnel

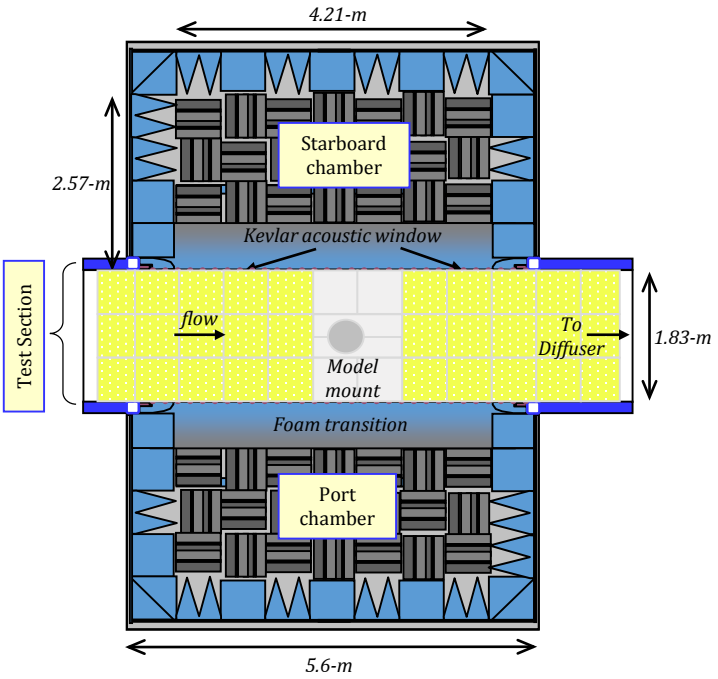

Figure 2.3: Schematic showing the anechoic test section and chambers of the Virginia Tech Stability Wind Tunnel

and port side of the test section. These chambers are 4.21-m long, 2.57-m deep and 3-m high and are lined with 0.61-m foam wedges.

Both side walls of the test section are made of 4.21-m long tensioned Kevlar panels. The Kevlar enables the walls to simultaneously contain the flow while remaining almost completely transparent to sound [102]. This enables sound generated inside the test section to freely propagate into the anechoic chambers where it can be measured using acoustic instrumentation. The floor and ceiling panels of the test section are made almost completely of Kevlar-covered metal perforate panels. Underneath the perforate are 0.45-m sound absorbent foam wedges which minimise the reflections from the supporting structure of the test section. The work of Devenport *et al.* [102], which fully describes the aeroacoustic features of this test section, found that the flow along the Kevlar walls is well-behaved with minimal blockage effects. They were also able to determine, by the use of transfer functions between a noise source and microphones placed in these chambers, that the facility is anechoic above 180-Hz.

2.1.3 Semi-Anechoic Configuration of Virginia Tech Stability Wind Tunnel

In the semi-anechoic configuration, the starboard Kevlar wall of the test section along with a portion of the roof and ceiling panels are replaced with hard walls. A photograph, from upstream looking downstream, of the test section in semi-anechoic configuration is shown in fig. 2.4 and a top-down schematic is presented in fig. 2.5.

As can be seen in fig. 2.4, the twelve floor and twelve ceiling perforate panels nearest the starboard wall were replaced with equivalent sized solid aluminium plates. These aluminium panels enable the starboard Kevlar wall to be replaced with a series of six Lexan panels. These panels align to form a continuous 1.78-m high and 7.32-m long test surface. The Lexan panels are attached to the aluminium floor and ceiling panels by 50.8-mm wide, 25.4-mm high 80/20 mounting rails. These rails enable each Lexan panel to be independently adjusted in the streamwise direction, so as to ensure that the wall is continuous, and in the wall-normal direction, in order to create a near zero-pressure gradient test surface.

80/20 slotted aluminium beams frame the Lexan panels and provide structural support. Each Lexan panel is 1.22-m $\times$ 1.78-m and 13-mm thick except for the panel furthest downstream which is 1.11-m $\times$ 1.78-m and 13-mm thick. Since the full height of the test section is 1.83-m, a 25.4-mm gap is created between the top/bottom of the hard wall and the ceiling/floor. This gap is bridged using a 1.6-mm thick, 90° aluminium extruded angle. This angle is attached to the test section wall using double sided tape and streamlined to the wall, floor and ceiling with 0.08-mm NASHUA All Weather aluminium foil tape. After installation, if any gaps were found between consecutive panels of the hard wall, these were taped over using 0.04-mm thick edging and reinforcing tape (3M 8411).

As opposed to the fully anechoic configuration, the default location of the hard wall is approximately 0.1-m further into the test section than the original Kevlar wall. This reduces the width of the test section from 1.83-m to 1.73-m. A curved fairing is used to smoothly transition the flow between the two surfaces. This fairing is made of wooden ribbing overlaid with black ABS plastic as is shown in the forward right side of fig. 2.4. Its full dimensions are detailed in the works of Forest [87] and Awasthi [11]. The fairing is bolted to the tunnel contraction, with its upstream edge approximately 2.4-m from the leading edge of the test section. This upstream edge is faired to the contraction using 1.5-mm thick aluminium sheets. Similarly the junction between the fairing and the hard wall is covered with a 0.25-mm thick brass shim. All junctions between the contraction fairing, shim, floor and ceiling were sealed using foil tape (which can be seen in fig. 2.4).

The turbulent boundary layer was initiated by two 19-mm high, 90° aluminium angles. These are mounted on the fairing, 1.2-m and 2.1-m upstream of the hard wall leading edge, as shown in fig. 2.4. The trips were secured in place using screws and double-sided tape, and their junction with the contraction was sealed with foil tape.

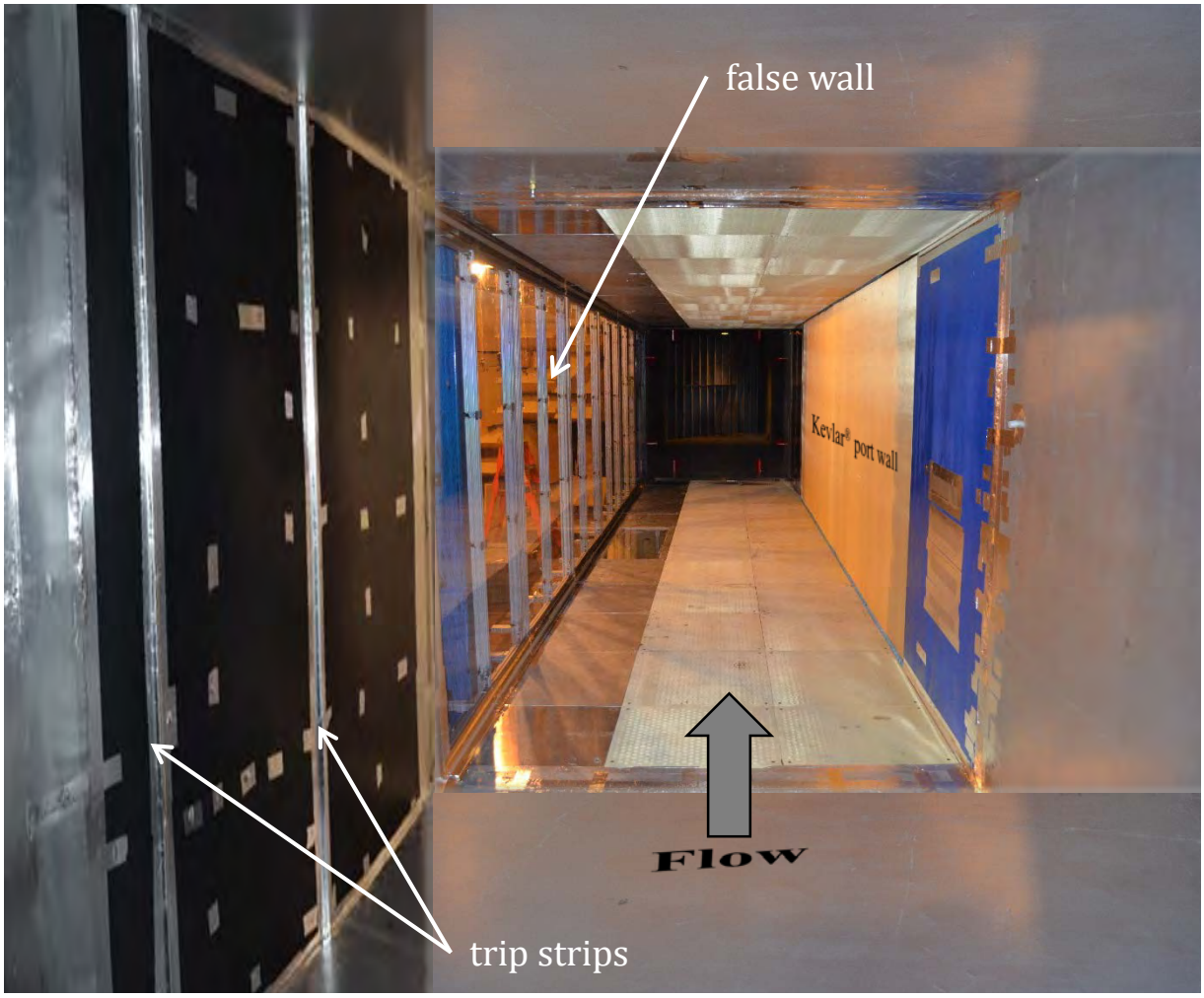

Figure 2.4: View from upstream looking downstream of the Stability Wind Tunnel's test section in semi-anechoic configuration - hard wall on the left, Kevlar wall on left

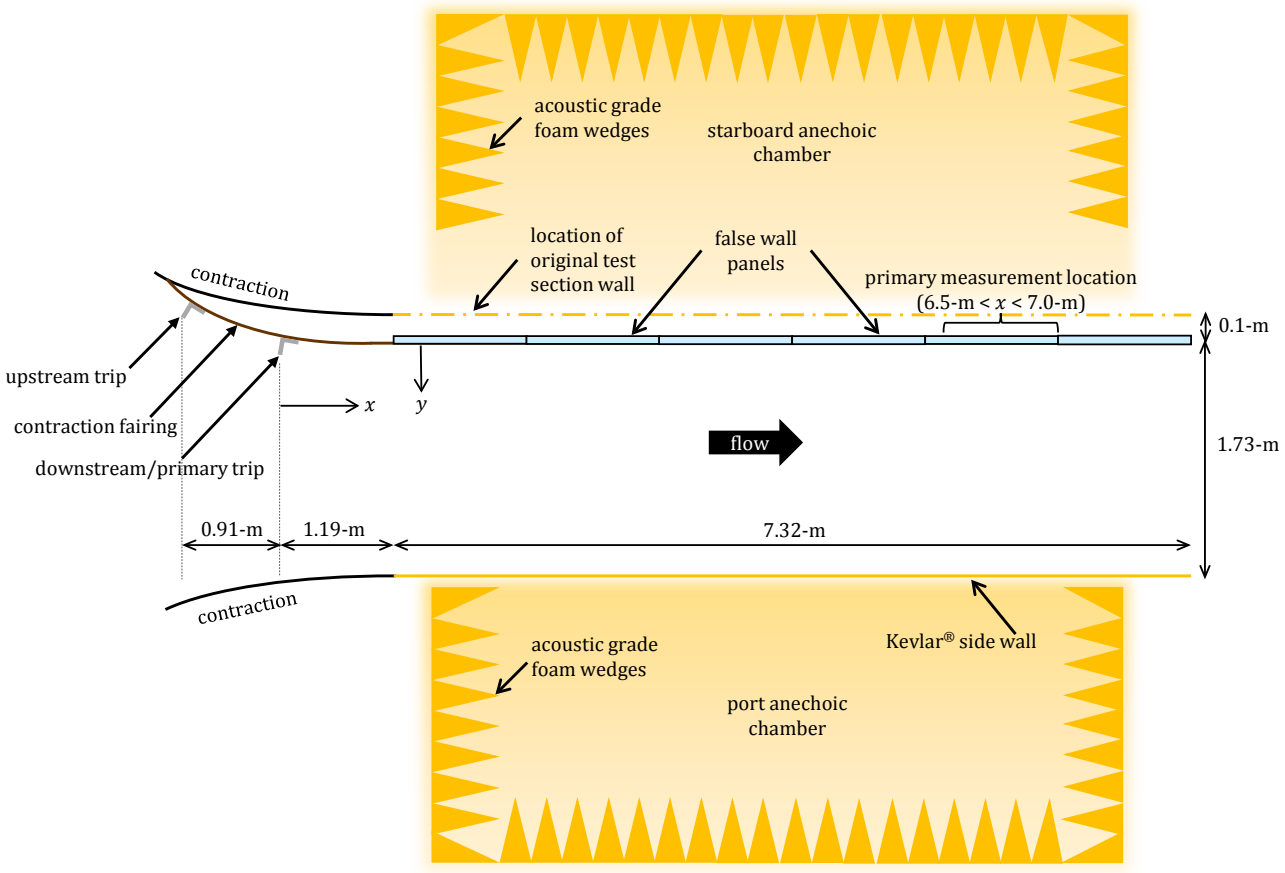

Figure 2.5: Schematic of the Stability Wind Tunnel's test section in semi-anechoic configuration

Pressure taps in the contraction (2.51-m upstream of the start of the test section) and settling chamber are used to measure the free-stream static and stagnation pressures as well as the free-stream velocity. The ambient temperature is obtained from a thermocouple in the wind tunnels contraction.

The coordinate system which will be used in this work is shown in fig. 2.5. The origin is on the wall at the downstream (primary) trip, 0.921-m from the wind tunnel ceiling. The x-component is in the streamwise direction, increasing downstream. The y-component is the wall-normal direction, increasing through the boundary layer. The z-component is from the centreline of the hard wall panels (0.921-m from the ceiling) increasing toward the ceiling of the test section.

Further details of the design and fabrication of the hard wall and contraction fairing can be found in the works of Forest [87] and Awasthi [11].

2.2 Rough Surfaces

A total of five roughness fetches were tested for this work. Including the smooth wall, this produces a total of six test surfaces. The configuration of these surfaces, their fabrication and installation in the Stability Wind Tunnel will be described in the following sections. The surfaces of Meyers *et al.* [1] will also be detailed as these complete the data set which will be analysed in this work.

2.2.1 Fabrication

Roughness fetches were fabricated using the method first reported by Forest [87] and described extensively by Meyers [103]. An HDPE mold was machined for each of the surfaces, with indentations of the exact size and shape of the elements desired. The mold was 1.83 $\times$ 1.24-m in size and therefore produces identical roughness fetches of this size. A portion of the mold used to produce the densely packed hemispheres is shown in fig. 2.6.

Epoxy resin in a 3:1 ratio was poured unto the greased (with Smooth-On Ease Release spray) mold so that the epoxy filled the indentations in the mold completely. Two sheets of 1.22-m wide Canson 50-lb sketch paper were then overlaid on the epoxy-covered mold, ensuring that there were no gaps between neighbouring sheets. The paper was smoothed to remove excess epoxy before a second layer of epoxy was applied over the paper. Then a sheet of 9-oz, 1.27-m wide, 0.254-mm thick, satin weave fibreglass (style 6781 S2-Glass) was laid over the epoxy and smoothed to remove the excess epoxy. This fibreglass-paper composite acts as the substrate for the rough elements once they are formed. The fetch was then left to dry for twenty-four hours.

The fetches were removed from the mold by carefully lifting the substrate upward starting from one corner of the mold. The result is perfectly shaped masses of cured epoxy securely attached to the fibreglass-paper substrate. However, in the case of the cylindrical elements removal by lifting from one corner of the mold resulted in elements which sheared off the substrate quite easily. This was due to the edges of the cylinders being caught in the cylindrical indentations during removal. Hence a method for removing the cylindrical fetch in a perfectly vertical upward motion was required. An aluminium sheet was therefore attached to the back of the fetch while still in the mold. Then using suction cups the entire set up was lifted vertically out of the mold using an engine hoist. This removal method successfully preserved the shape of the cylinders and their bond to the substrate.

The fetches were then cut to size and adhered to 3-mm thick aluminium panels, 1.8 $\times$ 1.2-m in dimension, using silicone (except for the cylinders, which were already attached to aluminium plates). Each fetch was cut so that there was a 12.7-mm overhang of the roughness fetch on the downstream end of each aluminium plate. Correspondingly each fetch was offset downstream such that the upstream end of the fetch was a 12.7-mm smooth surface. This ensured that, when aligned next to each other, the downstream 12.7-mm of the upstream roughness fetch would lay over the adjacent downstream fetch thereby ensuring a smooth transition between the roughness on adjacent panels.

Finally each rough panel was inspected to ensure that missing and damaged elements were replaced, and that all edges were well attached to the aluminium and smoothly cut. For each configuration six roughness-covered aluminium panels were made.

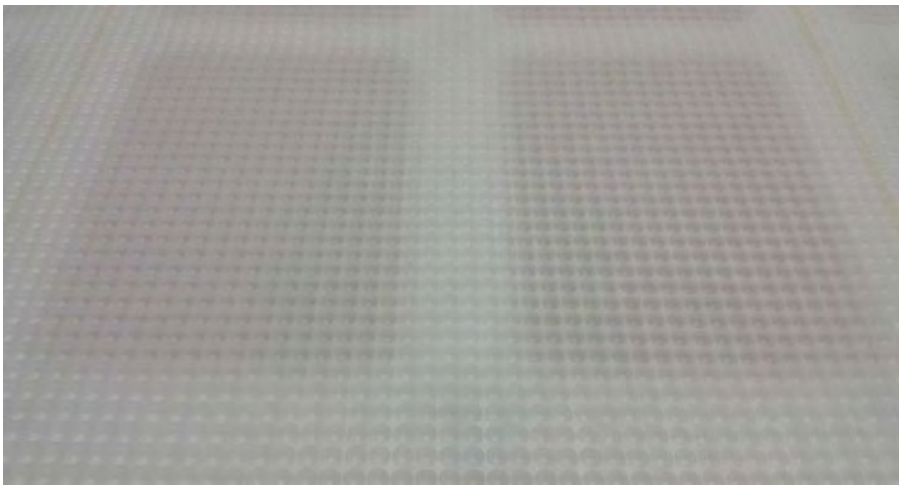

Figure 2.6: HDPE mold with hemispherical indentations used to manufacture the 3-mm densely-spaced hemispheres

2.2.2 Roughness Configurations

Fetches tested in this work all comprise of ordered, discrete elements. In all cases the rough fetches consisted of square arrays of elements, carefully spaced so as to produce the desired sparseness ratio, λ. Recall that

$$\lambda = \frac{\text{frontal projected area of element}}{\text{planform area of element}} = \frac{A_f}{A_w}$$

These configurations are summarised in table 2.1 which also includes the specifications of the configurations of Forest [87] and Meyers [103], who investigated the effect of roughness height, k_g, and roughness distribution (ordered or random).

Fig. 2.7 also describes the different element areas and geometric features in diagrammatic form. The shape of the roughness element is either hemispherical or cylindrical. d is the diameter of the base of the element. k_g is the geometric roughness height. The orientation parameter describes the angle of the elements to the oncoming flow. If the roughness elements are oriented such that the rows of the pattern are parallel to the flow direction, the orientation is termed straight. This is the case for all but one configuration. If the rows of the pattern are oriented at an angle of 45°to the flow the configuration is termed staggered.

s is the spacing between upstream and downstream elements, measured from the centre of each element. For the staggered configuration this means that the planform area will be determined from a fraction of this distance ($s/\sqrt{2}$) as shown in fig. 2.7. Throughout this work reference will be made to a 'four element array'. This is applicable to the straight orientation and refers four elements in a square pattern, separated by a distance s in both the streamwise and spanwise directions. For the staggered configuration, the four element array is oriented 45°to the flow. A_w is the element planform area which is the square planform area $s \times s$ around a single element (or the area enclosed by a four element array). A_f is the frontal projected area of the element and is the area that the flow 'sees' when encountering the roughness element. For the hemispheres, A_f is the area of half a circle and for the cylinder, A_f is a rectangle. V_e is the geometric volume of a single element, based on its shape.

Recall that the roughness has the effect of displacing the mean streamlines away from the wall by a constant displacement height, ε [24, 38, 94, 36] (see § 1.3.1 for discussion on this effect). This quantity is challenging to estimate because it comprises of the volume of the roughness elements, their upstream separation region, and their wakes. Stewart [94], Hopkins [24] and Varano [36] achieved reasonable results for this parameter by using the roughness element volume, V_e, with the volume of the upstream and downstream separation regions to obtain a total volume, V_t. The separation regions were modelled as half cones that extended upstream by an element height k_g and downstream by some value H_{ds}, which was determined from their LDV measurements. The final estimate of ε was found from eq. (2.1).

$$\varepsilon = \frac{V_t}{A_p} = \frac{1}{A_p}(1/6\pi k_g^3 + V_e + 1/6\pi k_g^2 H_{ds}) \tag{2.1}$$

In the present study the extent of the upstream separation region could be estimated as a half-cone as described above. However, we have no measurements from which to estimate the downstream separation region, H_{ds}. Hence we consider a modified displacement height, ε^* which accounts only for the displacement effect of the element. In this way,

$$\varepsilon^* = \frac{V_e}{A_p} \tag{2.2}$$

which can be thought of as the height of the layer that would be formed if all the roughness elements were to be melted down to cover the surface. The value of this parameter is included in table 2.1 for each surface.

We will first examine the surfaces of Forest [87] and Meyers [103]. These are shown in fig. 2.8 where each image is of a rectangular patch of roughness approximately 50×58-mm^2 ($h \times w$). We will then examine the rough surfaces tested in the current work. These are designed based on the surfaces of Forest and Meyers in order to produce useful and systematic comparisons. Fig. 2.9 presents images of the actual rough surfaces tested in the present study, again on a 50×58-mm^2 area.

Sparse, Ordered, 3-mm Hemispheres

The sparse, ordered roughness of Forest [87] consisted of hemispherical elements of 3-mm radius. The rows of elements were aligned parallel to the flow direction and each element had a volume of 56.5-mm^3. The element centre-to-centre spacing was constrained to 16.5-mm which produced a sparseness ratio, λ, of 0.052. A photograph of the roughness elements of this surface is shown in fig. 2.8a.

Sparse, Random, 3-mm Hemispheres

Following from Forest, Meyers [103] designed a surface of hemispherical elements of 3-mm radius. Thus the element volume and areas were the same as that on Forest's surface of sparse, 3-mm hemispheres. However, Meyers' aim was to test the dependence of the wall pressure fluctuation field on the distribution of roughness elements. Thus his elements were pseudo-randomly distributed on the surface according to a MATLAB algorithm. The algorithm's only restriction on element location was that elements should not be within 4-mm of the pressure transducers. Also, the average element density was designed to be 0.052 to match that of Forest's surface. The resulting surface is shown in fig. 2.8b.

Table 2.1: Summary of complete set of rough surfaces under consideration in this work

Surface Descriptor	d (mm)	k_g (mm)	Shape	Orientation	s (mm)	A_f (mm^2)	A_w (mm^2)	λ	V_e (mm^3)	ε^* (mm)
Past data sets										
1-mm ordered, sparse [87]	2	1	hemisphere	straight	5.5	1.57	30.3	0.052	2.1	0.07
3-mm ordered, sparse [103]	6	3	hemisphere	straight	16.5	14.1	272.3	0.052	56.5	0.21
3-mm random, sparse [103]	6	3	hemisphere	random	16.5	14.1	272.3	0.052	56.5	0.21
Current data sets										
Intermediately-spaced	6	3	hemisphere	straight	10.4	14.1	108.2	0.13	56.5	0.52
Densely-spaced	6	3	hemisphere	straight	6.5	14.1	42.3	0.33	56.5	1.34
Cylinders	4.71	3	cylinders	straight	16.5	14.1	272.3	0.052	52.3	0.19
Multi-height	2, 6	1, 3	hemisphere	straight*	16.5*	14.1*	272.3*	0.104	40.8	0.30
Multi-shape	6	3	hemisphere, cylinders	staggered	16.5	14.1	136.1	0.104	54.4	0.40

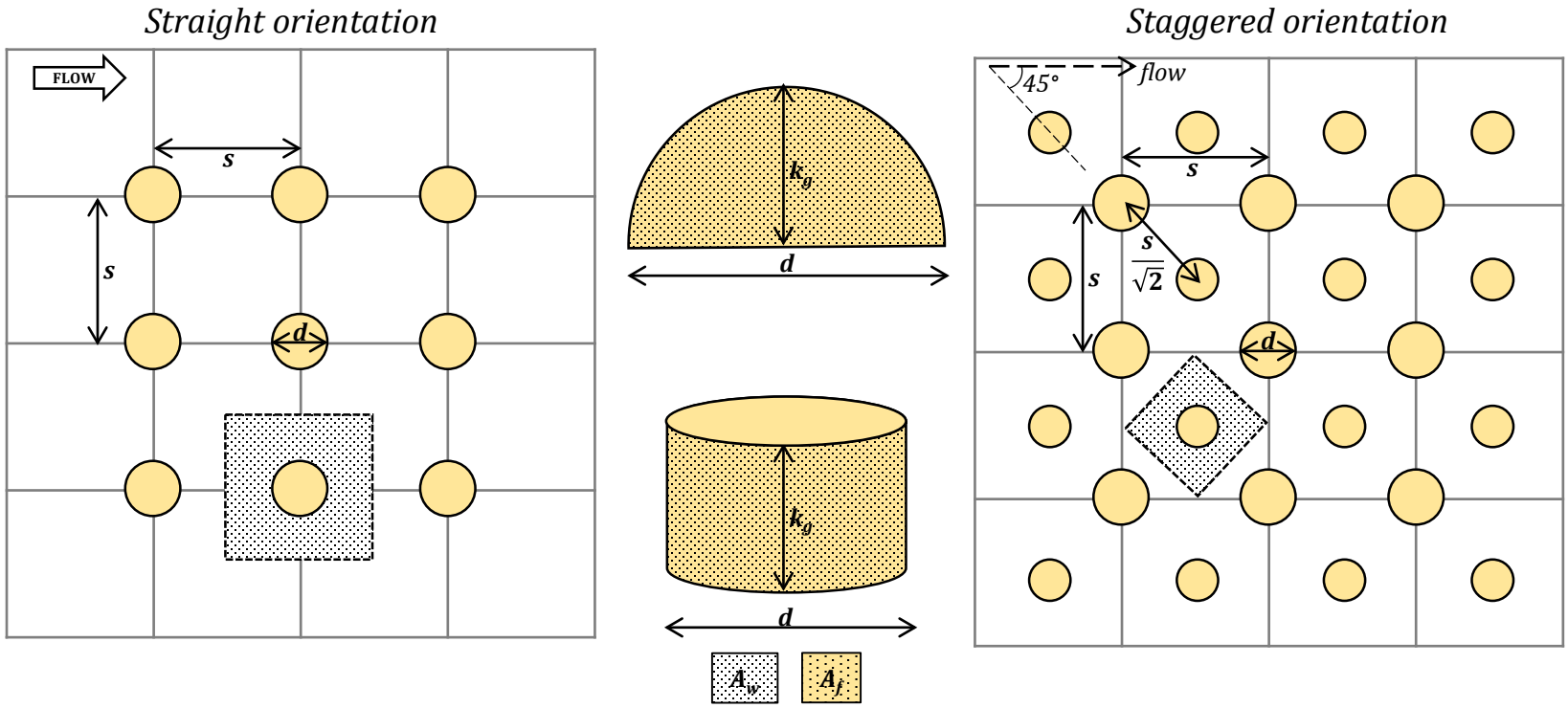

Figure 2.7: Diagram of the important geometric parameters on rough surfaces

Sparse, Ordered, 1-mm Hemispheres

Meyers [103] also designed a surface of straight-oriented hemispheres of 1-mm radius. This was to investigate the effect of roughness height on the pressure field in the turbulent boundary layer. The centre-to-centre spacing of these hemispheres was set to 5.5-mm so that the resulting sparseness ratio matched that of Forest's 3-mm hemispherical surface – 0.052. In this way a one-to-one comparison could be made. The sparse, 1-mm hemispheres are depicted in fig. 2.8c.

Intermediately-Spaced Hemispheres

The intermediately-spaced roughness consists of hemispherical elements of 3-mm radius. Thus the elements have the same frontal projected area as the 33-mm ordered hemispheres of Forest [87]. The element centre-to-centre spacing was constrained to 10.4-mm which produced a sparseness ratio, λ, of 0.13. λ of 0.13 was deliberately chosen because it is sufficiently close to the peak of the Dvorak-Simpson plot (fig. 1.28) while still being in the regime where drag increases with number of elements. For the remainder of this paper this surface will be referred to as the 'intermediate' roughness case. A photograph of the roughness elements of this surface is shown in fig. 2.9a.

Densely-Spaced Hemispheres

The second rough surface was also made up of square arrays of 3-mm hemispheres, matching the frontal projected area of the 3-mm ordered hemispheres of Forest [87]. However the element centre-to-centre spacing was reduced to 6.5-mm in order to obtain a sparseness ratio of $\lambda = 0.33$. Like the intermediately-spaced hemispheres, this λ was intentionally selected because it occurs after the peak in the Dvorak-Simpson plot (fig. 1.28). Based on this correlation, this surface should exhibit decreased drag due to element-to-element sheltering. This rough surfaces is shown in fig. 2.9b and will be referred to hereafter as the 'dense' roughness case.

Cylinders, Sparsely Distributed

In order to investigate the effect of element shape a surface of cylindrical roughness elements was fabricated. The elements were ordered in square arrays and are presented in fig. 2.9c. Each cylindrical element was 3-mm tall, in order to match the k_g of Meyers' sparse hemispheres, and 4.71-mm in diameter, in order to match the frontal projected area of Forest's sparse hemispheres. The centre-to-centre element spacing was set to 16.5-mm, as was done by Meyers *et al.* [1], producing the same sparseness ratio of 0.052.

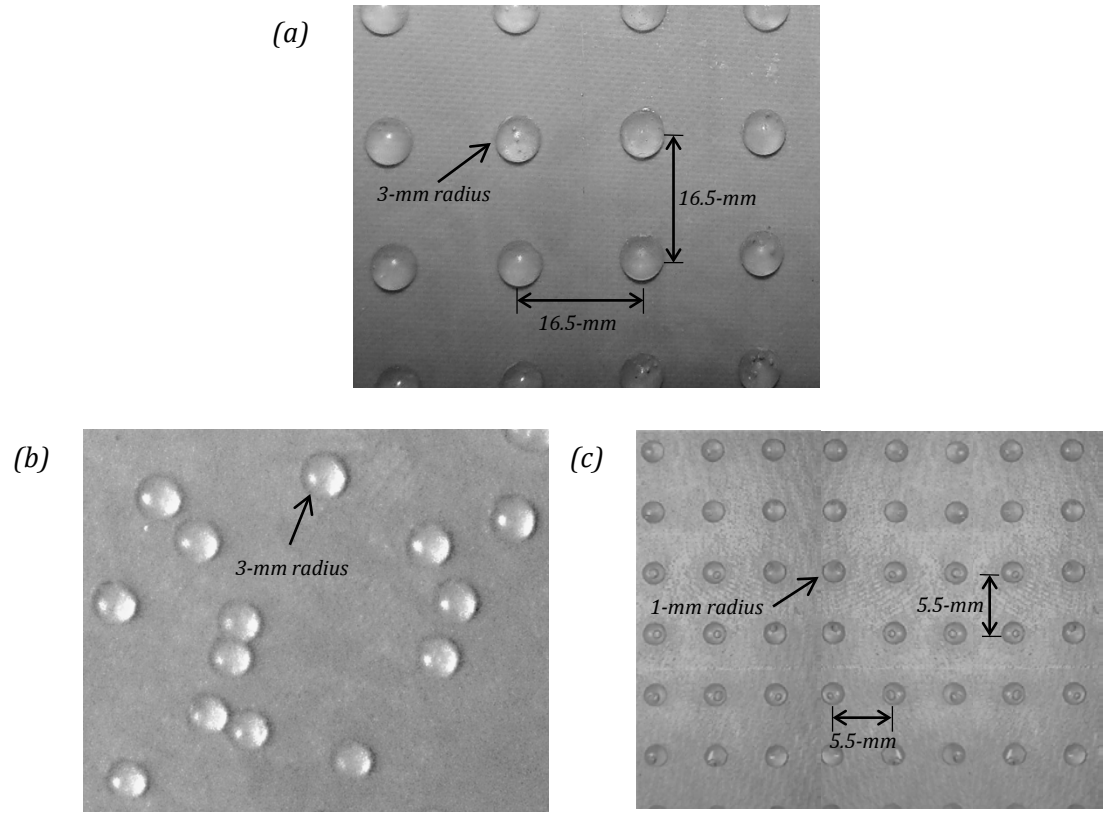

Figure 2.8: Geometry of roughness fetches of Forest [87] and Meyers [103]. (a) sparse, ordered, 3-mm hemispheres (b) sparse, random, 3-mm hemispheres (c) sparse, ordered, 1-mm hemispheres

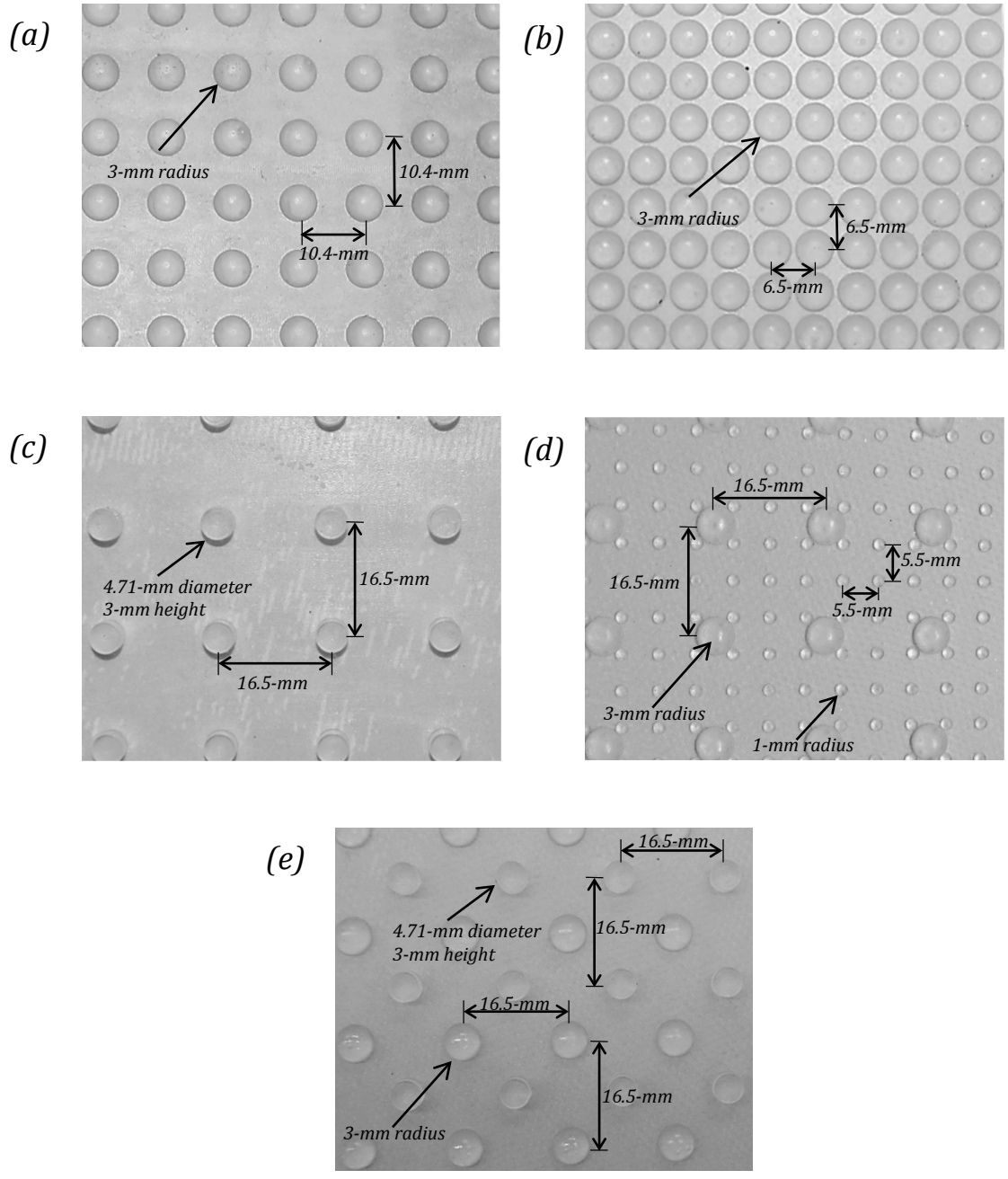

Figure 2.9: Geometry of roughness fetches. (a) intermediately-spaced hemispheres (b) densely-spaced hemispheres (c) cylinders (d) multi-height rough surface: 1-mm and 3-mm hemispheres (e) multi-shape rough surface: 3-mm hemispheres and cylinders

Multi-height (k_g = 3-mm, 1-mm) Hemispheres

The fourth surface investigated had hemispherical elements with two roughness heights, k_g = 1-mm and 3-mm. These were chosen based on the sparse, ordered 1-mm of Meyers [103] and the 3-mm roughness fetches of Forest [87]. Essentially the 1-mm surface of Meyers *et al.* was replicated, with same sparseness ratio (λ =0.052) and element centre-to-centre spacing (5.5-mm). Between these elements, the sparse 3-mm ordered elements were inlaid, as shown in fig. 2.9d. The sparseness ratio of these elements also matched that of Meyers *et al.* (λ =0.052) as did the element centre-to-centre spacing (16.5-mm). The result was a surface with a sparseness ratio twice that of the individual 1-mm and 3-mm sparse ordered roughness, λ =0.104, and which is a superposition of these roughness fetches. The goal of testing such a surface is to ascertain how the pressure field changes when two roughness heights exist, and whether, in any sense, the flow can be characterised as having the combined or summed properties of the flows over the 1-mm and 3-mm component surfaces.

Multi-Shape (hemispheres and cylinders) Roughness

Another composite roughness fetch combined the sparse, ordered 3-mm fetch of Forest [87] with the sparse, 3-mm cylinder fetch described above. The aim of testing this fetch is to investigate the pressure field of a roughness fetch which has elements of different shapes, and to determine how one component shape contributes to the pressure field relative to the other. This surface should reveal whether the pressure field over elements of different shapes is a superposition of each component surface or some other combination of the individual pressure fields. This fetch replicated the cylindrical roughness exactly and overlaid the 3-mm sparse roughness in the centre of a four element array of cylindrical elements. The result is shown in fig. 2.9e. Separately, both the cylinders and hemispheres had k_g =3-mm and element centre-to-centre spacing of 16.5-mm. When combined this increased the sparseness ratio to λ =0.104.

2.2.3 Subsets of Rough Surfaces

Along with the surfaces of Forest [87] and Meyers [103], the present rough surfaces form a set which allows us to systematically compare the effect of different geometric parameters on the pressure field. Fig. 2.10 outlines the full data set in the form of logical subsets of surfaces corresponding to specific geometric parameters.

The effect of roughness element density will be revealed by comparisons of Forest's sparse 3-mm hemispheres, and the current intermediate and dense 3-mm hemispheres. These three surfaces have the same k_g and geometric shape. The only variable is the element density which is represented by λ. More insights into the roughness element density can be revealed by comparing surfaces of common λ but different shape and k_g. Thus the multi-height,

multi-shape and intermediate surfaces can be compared since they have $\lambda \sim 0.1$. Likewise the sparse 3-mm hemispheres, random 3-mm hemispheres, 1-mm hemispheres, and 3-mm cylinders can be compared since they all have $\lambda = 0.052$. These comparisons will tell us how important the roughness element density is compared to the other geometric parameters.

Comparisons of the 3-mm hemispheres of Forest and the present 3-mm cylinders will shed light on the effect of roughness element shape on the turbulent boundary layer. These two surfaces have the same k_g, A_f, A_w, and λ and differ only in terms of element shape. The difference in element shape results in a small difference in element volume and thus ε^* between these surfaces as well.

The multi-height surface can be compared with the 1-mm sparse hemispheres of Meyers and the 3-mm sparse hemispheres of Forest. Since these uniform surfaces have been superposed to produce the multi-height surface, comparison of these three surfaces will reveal how different

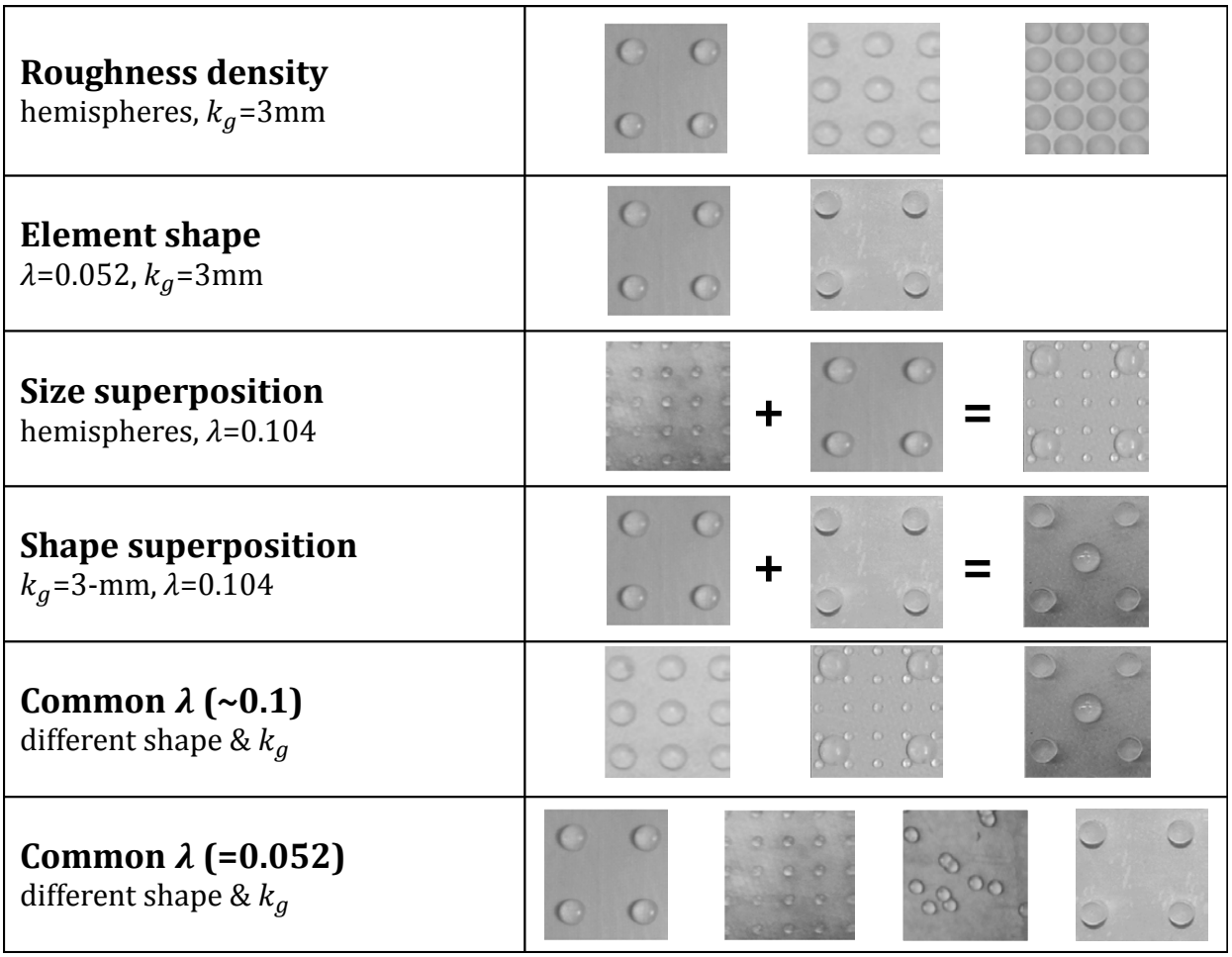

Figure 2.10: Full data set in the form of logical subsets of surfaces corresponding to specific geometric parameters

k_g on the same surface impact the pressure field. We will learn whether superimposing different k_g on one surface results in a pressure field which is a summation or average of the individual surface pressure fields. It is also possible that only the pressure field of the largest k_g matters. During these comparisons we should bear in mind that, while the shape of the roughness elements is common among all surfaces, λ of the multi-height surface is twice that of the uniform surfaces.

Similar prospects arise from comparing the multi-shape surface with its component surfaces – the sparse 3-mm hemispheres and 3-mm cylinders. k_g is the same for these surfaces and again we must keep in mind that the multi-shape surface has λ twice that of the uniform surfaces. The main variable is the element shape. This comparison will tell us whether having different element shapes on the same surface results in a combination of the individual pressure field or an average of these. Another possibility is that one element shape overshadows the other and contributes more to the pressure field than the other.

This systematic approach to the current problem is expected to reveal new relationships between roughness geometry and pressure fluctuations.

2.2.4 Installation in Stability Wind Tunnel

Each Lexan panel of the hard wall was fitted with a roughness fetch 1.22-m $\times$ 1.78-m in dimension. The leading edge of the most upstream fetch was aligned with the leading edge of the most upstream hard wall panel at x=1.19-m. A fairing, 3.3-mm high and 40-mm wide, was then installed between the most upstream roughness fetch and the contraction fairing in order to smooth the junction between the fetch and the contraction. The six roughness fetches together formed a continuous 7.32-m long, 1.76-m high rough surface, which can be seen in fig. 2.11. In all cases the hard wall was covered with upward to of 50,000 elements, and as many as 400,000 elements (in the case of the densely-packed hemispheres).

It was also ensured that the rough elements between adjacent panels aligned in the streamwise direction. This was achieved by aligning the elements of adjacent panels when the roughness was attached to the aluminium plates. Furthermore small adjustments in the z direction were made to compensate for any misalignment once the fetches were in place on the hard wall. A smooth transition was created between adjoining panels due to the 12.7-mm downstream overhang described in § 2.2.1. Super-glue was used to bond the overhang to the 12.7-mm gap on the upstream end of the downstream panel. Additionally this prevented flow from becoming trapped between the fetch and the Lexan panel, thereby undermining the integrity of the set up. An example of the transition and the typical streamwise alignment achieved is shown in fig. 2.12. In all cases streamwise misalignment of adjacent panels was less than 5-mm.

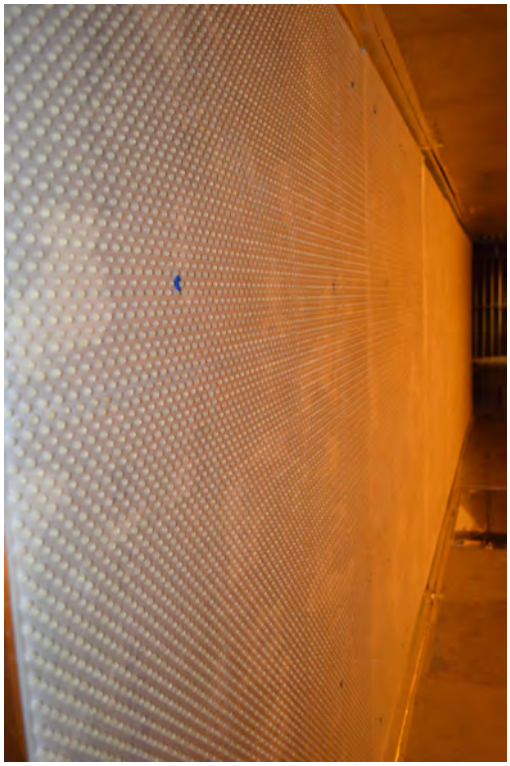

Figure 2.11: Full scale roughness (cylinders) mounted in the Stability Wind Tunnel (view from upstream looking downstream)

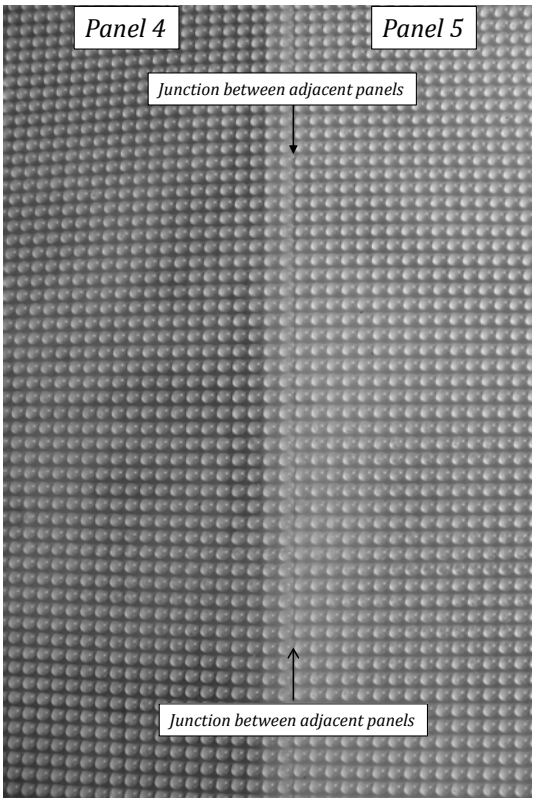

Figure 2.12: Junction of adjacent panels (4th and 5th in this case) showing element alignment and how downstream overhang creates smooth transition

2.3 Boundary Layer Velocity Instrumentation

To understand and scale the pressure fluctuations in the rough-wall turbulent boundary layer, measurements of the velocity and turbulence statistics are required. These parameters were derived from velocity measurements made during the experiments. This section details the specifications of the hotwires and flattened Pitot probes used to make these measurements, including the data acquisition and processing methods.

2.3.1 Single Hotwire Instrumentation

An Auspex AHWU-100 constant temperature single hotwire probe was used to measure the mean velocity within the boundary layer. This instrument produces measurements of velocity in one direction based on the convective heat transfer of the wire. The hotwire probe is the fourth resistor which completes a Wheatstone Bridge. In order to keep the error voltage of the bridge to zero the temperature of the hotwire is adjusted to produce the required resistance. As the flow moves over the probe, the temperature decreases resulting in an increase in the bridge voltage in order to maintain a constant resistance (temperature). The change in voltage can be related to the fluid velocity through the King's law calibration (see § 2.3.3). Thus, the faster the flow, the higher the voltage.

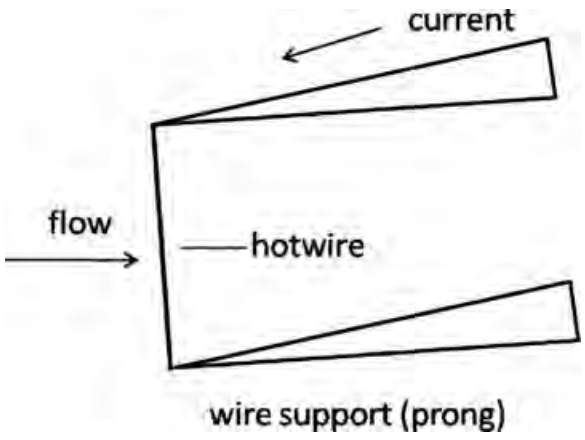

Figure 2.13:
Diagram of a single hotwire probe

Fig. 2.13 is a diagram of a typical single hotwire sensor supported by prongs. The specific probe used in this experiment consists of two prongs, each 15-mm long, connected by a thin Tungsten wire. The wire is 1.2-mm long and 5-μm in diameter. The probe is shown in fig. 2.14 being used simultaneously with a flattened Pitot probe (described in § 2.3.6). In this way the data of the single hotwire probe could be validated.

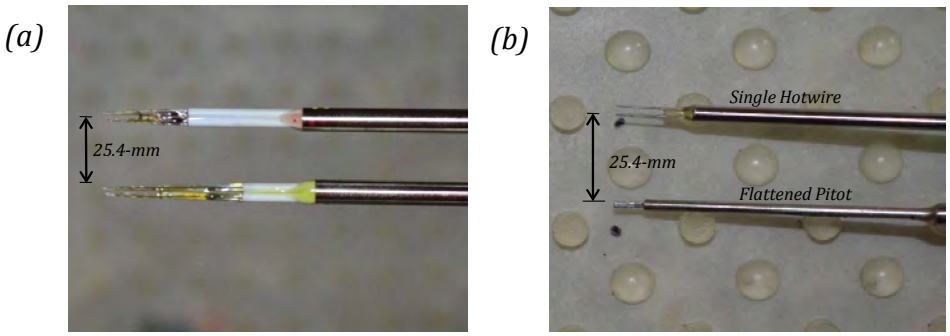

Figure 2.14: (a) Quad-wire probes arranged in two-point configuration (b) Single hotwire (top) and flattened Pitot (bottom) probes

2.3.2 Quad-wire Instrumentation

The mean velocity and velocity fluctuations in the boundary layer were measured using four sensor hotwire anemometer (quadwire) probes. A diagram of this type of probe, adapted from Wittmer *et al.* [57], is presented in fig. 2.15. Four sensor hotwires are capable of simultaneous three-component velocity measurements from a fairly small measurement volume. They are able to measure low turbulence levels and velocity spectra because they give continuous, low-noise signals. They also have less gradient errors than instrumentation such as triple wire probes, and through calibration, errors associated with large flow angles and prong interference can be reduced.

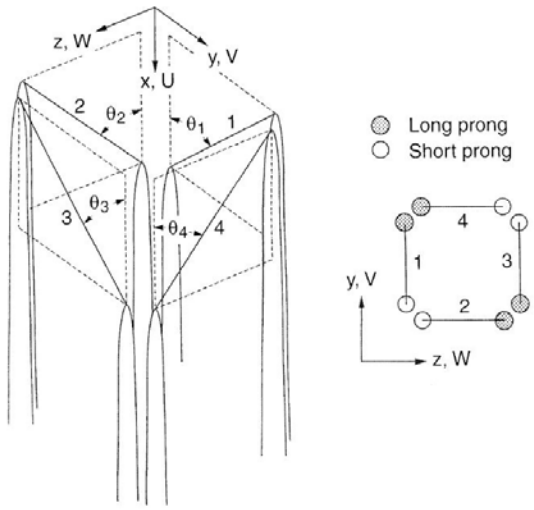

Figure 2.15: Diagram of a four-sensor (quad) hotwire probe adapted from Wittmer *et al.* [57]

The four-sensor probes were traversed in the test section on a three-axis traverse with 0.025 mm resolution. The four sensor hotwire, Auspex Corporation model AVOP-4-100, is able to measure the three-components of flow velocity with a 0.5-mm^3 measurement volume. This system was calibrated for flow angles and the measured velocities were corrected using the lookup table method of Wittmer *et al.* [57] and King's law (see § 2.3.3). The quad-wire is shown in fig. 2.14a. Here two quadwires are being used in tandem in order to validate the measured data.

The four component hotwire system was operated by a Dantec Dynamics Streamline Con-

stant Temperature Anemometry (CTA) system. Because each sensor on the four sensor probes requires a separate bridge module to operate, four Dantec 90C10 CTA modules were installed in a Dantec 90N10 frame. Each CTA bridge was found to have a flat frequency response up to 10-kHz. Output signals were recorded using NI-9239 cDAQ modules. Two four-channel DAQ modules were required for this test because two quadwire probes were to be used. These were installed in an NI 9174 USB cDAQ chassis which allowed all eight channels to be sampled simultaneously, up to 50-kHz at an accuracy of 0.03% of the measurement. The NI-9239 DAQ modules have a range of ±10-V at a 24-bit resolution. They are also equipped with a built in anti-aliasing filter which produces an alias-free bandwidth of 22.6-kHz.

2.3.3 Hotwire Calibrations

Both the single hotwire and quad-wire probes required velocity calibrations in order to relate the changes in circuit voltage to velocity. This calibration is based on King's law, shown in eq. (2.3), where E is the voltage across the wire, U is the velocity of the flow normal to the wire and A, B, and n are constants. For hotwire probes, and in this experiment, n is assumed to be 0.45. A and B were found by measuring the voltage, E, obtained for a number of known flow velocities and performing a least squares fit for the values of A and B which produce the best fit to the data.

$$E^2 = A + BU^n \tag{2.3}$$

The initial velocity calibration was done in a uniform 1-in diameter jet, at speeds from 9.6 – 30.8-ms^{-1}. This jet is powered by a Baldor M3613T 5-horsepower motor, using a Rockwell Automation VTAC-9 controller, and Cincinnati Fan HP Series II blower. During the experiment velocity calibrations were regularly performed in the free stream of the Stability Wind Tunnel (roughly at the centre of the test section). This was necessary because single runs are typically longer than 30 minutes, and thus there is some temperature drift, and because the range of the initial velocity calibration was limited to 30.8-ms^{-1}. In the Stability Wind Tunnel voltages were generally acquired at speeds from 8-ms^{-1} up to 62-ms^{-1}. At each velocity the exact flow velocity was computed using the reference instrumentation and the output voltages from each of the sensors on the probe were recorded.

In addition to the velocity calibration, the quad-wire probes also required calibrations to account for the angle of the probe relative to the oncoming flow. Therefore, these calibrations were done for each probe and after every sensor repair. The calibration method used was adopted from Wittmer *et al.* [57]. Calibrations were carried out in the same uniform jet used for the initial velocity calibrations, at a flow speed of 20±0.5-ms^{-1} (fan frequency of 17-Hz). Phase II planetary turntables, operated using two Applied Motion HT23-553 high torque stepper motors, were used to vary the probe pitch and yaw. Using this system pitch and yaw angles were varied from -45° to 45° in 5° increments, with an accuracy within 0.25°.

This produced a matrix of over 600 independent angular positions at which the flow velocity was measured (using a pressure transducer with a rated accuracy of 0.01-inWC) along with the outputs of each sensor. Velocity calibrations were completed before and after each angle calibration to account for temperature drift.

2.3.4 Installation in Stability Wind Tunnel

All velocity probes were mounted to and traversed using a computer-controlled three-axis traverse system. This system was set up in the test section of the Stability Wind Tunnel and is capable of moving independently in the x, y and z directions. The three axis traverse is shown, from upstream looking downstream, in fig. 2.16. It consists of four streamwise rails, two of which attach to the ceiling and two of which mount to the floor, which allows for streamwise movement. Two spanwise (vertical) rails are fastened to these and a wall-normal (horizontal) rail is then mounted between the vertical rails. The horizontal rail is able to traverse vertically and allows instrumentation attached to it to be traversed across the span of the test section.

The hotwire probes were fitted to a metal sting arm which was attached to the horizontal rail, as shown in fig. 2.17. The sting arm is sturdy enough to damp out large vibrations and is designed at a permanent yaw angle of 28° to the streamwise centreline of the test section. This, and other dimensions of the sting arm, are presented in the top-view diagram to right of fig. 2.17. The sting arm is shown as a dimensioned drawing. The actual probe holder is mounted approximately 10.3-cm further toward the starboard wall than the tip of sting arm itself. An image of the probe holder is included with the drawing (on the same scale) of the sting arm so that the attachment can be seen. This extension further increased the reach of the probes toward the wall which ensured that the probes were not yawed into the wall more than 4°. In this configuration the sting arm can securely support two probes simultaneously, as shown in the perspective view of fig. 2.17, so that two-point measurements could be taken. Overall, the hotwire probes were installed approximately 0.55-m upstream of the wall-normal and spanwise rails (main body) of the three axis traverse. The location of the sting arm and the probe holder is also depicted by a red dashed box in fig. 2.16. The connecting wires of the probes were secured to the sting arm using electrical tape. In fact, the entire sting arm was taped over using a combination of electrical and foil tape. This served to both secure the wires and to improve the streamline of the sting arm.

The hotwire probes were traversed from the free-stream (approximately 356-mm from the wall) through the boundary layer by exponential increments up to a distance 3-mm from the wall, taking data at each increment. The traversing distance could be measured within an resolution of ±0.0125-mm. The boundary layer velocity measurements were made at approximately 7.0-m downstream of the trip, at three spanwise locations: z=0-m and ±0.304-m.

Figure 2.16: Upstream view looking downstream at the three-axis traverse system installed in the test section of the Stability Wind Tunnel

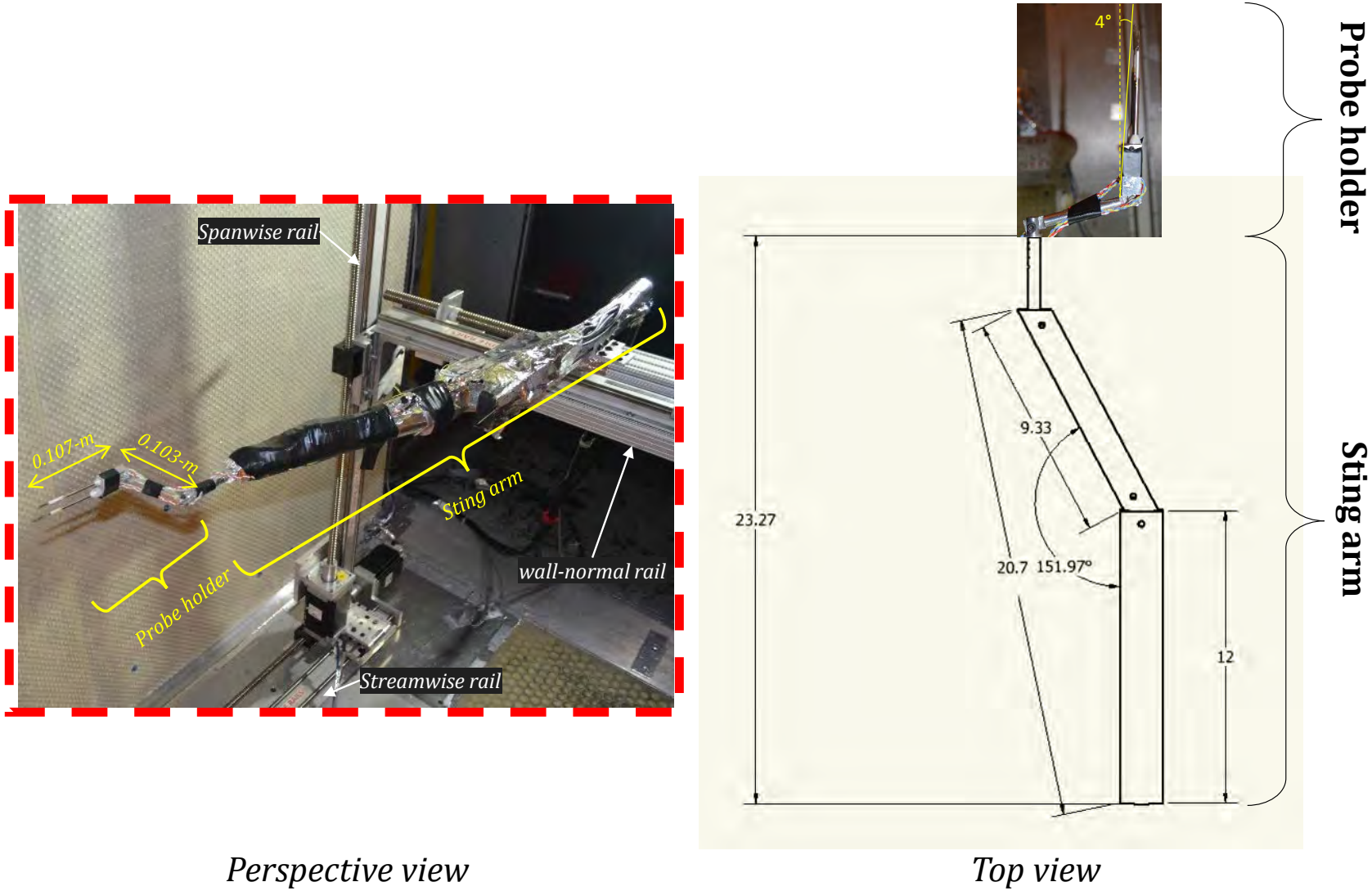

Figure 2.17: Traversing sting arm with mounted two-point probes shown in perspective view from the port wall (left image) and a view from the top (right diagram). NOTE: units of drawing is inches.

All velocity data was acquired and processed using MATLAB scripts written in-house [55]. The acquisition process was automated to take 50 records at a sampling rate of 50-kHz at every measurement location within the boundary layer.

2.3.5 Uncertainty Estimates

The uncertainty estimates for the single hotwire and quadwire results were obtained by applying the methods detailed by Ma [104] to the present instrumentation and flow conditions. The primary sources of uncertainty come into play with the A/D conversion, velocity calibration, velocity component estimation, angle calibration, averaging and normalisation. Specific equations for each step of the analysis is omitted here but can be found in the work of Ma [104].

Conservative estimates of uncertainty for the quadwire are given in table 2.2. Similarly estimates of uncertainty for the single hotwire are given in table 2.3. For both single and quad-wire the uncertainty in the dynamic pressure and the static pressure is estimated as 2.49-Pa. Temperature uncertainty is estimated to be 0.28-K. The absolute uncertainty in the traversing distance is 0.0125-mm.

Table 2.2: Relative uncertainty estimates for the quadwire results, obtained according to the work of Ma [104]

Quantity	Percentage Uncertainty (20:1 odds)
U/U_{ref}	1%
V/U_{ref}	12%
W/U_{ref}	17%
u^2/U^2_{ref}	2%
v^2/U^2_{ref}	12%
w^2/U^2_{ref}	12%
uv/U^2_{ref}	20%
vw/U^2_{ref}	20%
uw/U^2_{ref}	9%

Table 2.3: Relative uncertainty estimates for the single hotwire results, obtained according to the work of Ma [104]

Quantity	Percentage Uncertainty (20:1 odds)
U/U_{ref}	1%
u^2/U^2_{ref}	2%

Table 2.4: Relative uncertainty estimates for the flattened Pitot results (jitter analysis)

Quantity	Percentage Uncertainty
U/U_{ref}	1%

A well-known source of experimental error in hot-wire anemometry measurements is the spatial filtering of velocity fluctuations. This occurs when the sensing length of the probe, l, is larger than the smallest turbulence length scale. This is obviously not achievable in experimental work. The study of Ligrani and Bradshaw [105] stated that for smooth walls in order to resolve the viscous scales (ν/U_τ), $l^+ = lU_\tau/\nu$ <20. For the present study, the smallest l^+ values are approximately 70. Thus, based on the criteria of Ligrani and

Bradshaw, the nearest wall structures are certainly under-resolved. However, the goal of this study was to reveal the outermost form of the velocity and turbulence profiles where the resolution effects are minimal. Measurements were made starting at 3-mm above the wall, which corresponds to a maximum y^+ of 225 and 450 for 30-ms^{-1} and 60-ms^{-1} respectively (across all surfaces). Wittmer *et al.* [57] made four-sensor probe measurements of in a fully developed pipe flow under similar conditions and found that the Reynolds shear stress were underestimated by 8%, 4% and 1% at y^+ of 300, 450 and 600 respectively. Comparing this to the present results we expect that the error in under-resolving the measurements will be less than the uncertainty in the measurements, as listed in table 2.2. Therefore we can expect negligible spatial filtering effects in the region of the flow measured using the quadwire.

2.3.6 Flattened Pitot

In addition to the hotwires discussed previously, flattened Pitot measurements were made of the mean velocity profiles in the boundary layer. The probe itself had a 1-mm × 0.3-mm aperture (wall-parallel × wall-perpendicular). This system was traversed by the same three-axis traverse used to locate the hotwire probes. An Esterline NetScanner Model 98RK pressure scanner recorded the output signal. The flattened Pitot is shown in fig. 2.14b. It is being used simultaneously with the single hotwire probe. In this way the data of the hotwire probe could be validated.

2.4 Pressure Instrumentation

2.4.1 Mean Pressure Measurements

The mean wall pressure was measured using twenty four 1/4-mm diameter pressure taps embedded in the aluminium floor and ceiling panels closest to the hard wall (see fig. 2.4). The pressure taps were located between x=1.6 – 8.1-m and between y=0.25 – 0.36-m away from the hard wall (refer to fig. 2.5). An Esterline NetScanner Model 98RK pressure scanner, with range of ±10-inWC, resolution of ±0.003 and an accuracy of 0.05%, was used to record the mean pressure data. This pressure scanner was also used to record the ambient pressure in the starboard chamber (used as a reference pressure) and the free stream static and stagnation pressures.

The mean pressure measurements were the first series of data collected as it was used to establish the zero-pressure gradient. To do this, measurements were made at speeds between 30-ms^{-1} and 70-ms^{-1} for the smooth wall. The data obtained was used to iteratively adjust the hard wall panels to obtain the near zero-pressure gradient. Understandably achieving a perfect zero-pressure gradient was limited by the resolution to which the 1.78-m high panels of the hard wall could be adjusted and also the effects of the port-side Kevlar wall on the test

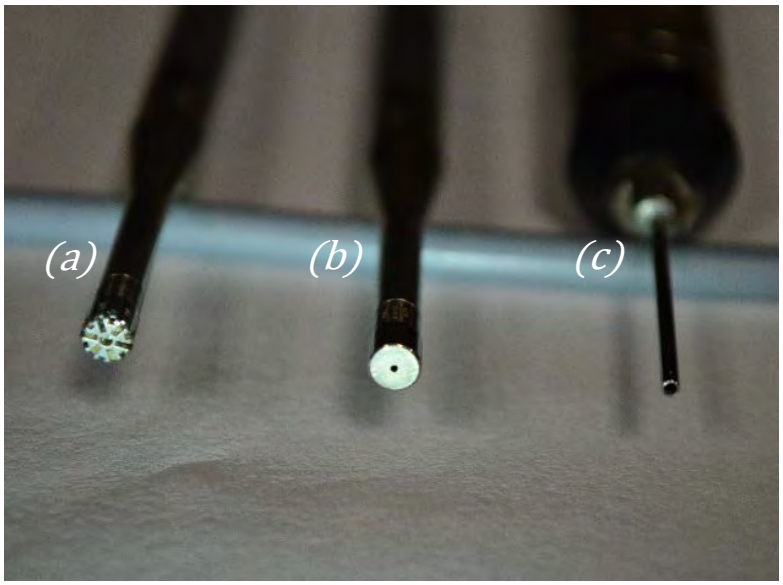

Figure 2.18: Microphones used during this experimental campaign: (a) B&K 4138-A-015 ⅛-in microphone with factory-provided salt-and-pepper cap (b) B&K 4138-A-015 ⅛-in microphone with pinhole cap (c) B&K 4182 probe microphone

section pressure. Nevertheless adjustments were made until the average gradient achieved was less than $dC_p/dx \approx$-0.005-m^{-1} (equal to the value obtained by Meyers *et al.* [1]). Results from this process are presented in § 3.1.

Mean pressure measurements were made simultaneously with the surface pressure (microphone) measurements for all surfaces tested. Thus it could be ensured that the near-zero pressure gradient was maintained from test case to test case.

2.4.2 Surface Pressure Fluctuation Measurements

The fluctuating pressure on the wall was measured using seven Bruel & Kjaer (B&K) 4138-A-015 ⅛-in microphones. The microphones were fitted with pinhole caps to reduce their sensing area, as shown in fig. 2.18b. This is important in reducing the spatial averaging of structures which are smaller than the microphone sensing area.

Because of the finite size of the pinhole, attenuation of the highest frequencies will become important. This attenuation is due to loss in resolution of the microphone. The frequency at which this occurs varies for each rough surface and for each Reynolds Number. A pinhole size of 0.5-mm was suggested by Devenport *et al.* [106] as being sufficiently small to resolve the small scale structures while mitigating attenuation. Consequently, in all but one case, the microphones used in the present experiments were outfitted with 0.5-mm pinhole caps. The exception to this was when testing the intermediately-spaced rough surface. One of the

microphones was outfitted with a 0.25-mm diameter pinhole in order to validate the use of the 0.5-mm pinhole cap.

A comparison of the pressure spectrum from both pinhole sizes, for the densely-packed roughness at 30-ms^{-1}, is shown in fig. 2.19. The dashed line represents the 0.25-mm pinhole result and the solid lines is the 0.5-mm pinhole result. In the low- and mid-frequency regions the size of the pinhole does not appear to have a great effect. However, at high frequencies the extremely low level of the raw signal from the 0.25-mm microphone (because of increases in viscous losses) results in a clear non-physical dip in its spectrum between 8,000 and 10,000-Hz. So, even though the 0.25-mm pinhole microphone had better spatial resolution, its frequency response was limited to a lower frequency than the 0.5-mm pinhole microphone. Similar problems were encountered with the intermediate roughness measurements. As a result the measurements of the 0.25-mm pinhole microphone were omitted from the final averaged spectral data.

Following from Meyers *et al.* [1], the results of Gravante *et al.* [73] were used to determine the frequency limit, f_{max}, at which the present system of microphones begins to under-resolve the highest frequency pressure fluctuations. Gravante *et al.* [73] found that in order to avoid spectral attenuation at any frequency the ideal d^+ values must be less than 18. Here $d^+ = dU_\tau/\nu$ and $f^+ = f\nu/U_\tau^2$ where d is the pinhole diameter. For the present work it was assumed that d^+ varies inversely with the maximum frequency for which the attenuation is less than 2-dB. Then using the results of Gravante *et al.* ($d^+ \approx 26.6$ for $f^+ \approx 0.22$) the frequency limit, f_{max}, for the present data was estimated. d^+ values were found to vary between 30 (for the smooth wall) and 100 (for the densely-packed roughness) for the 0.5-mm pinhole. The 0.25-mm pinhole produced smaller d^+ values between 15 and 51. Larger values correspond to higher speeds which result in higher U_τ values. A summary of the results is shown in table 2.5.

According to Gravante *et al.* [73] the limit of the f^+ values will decrease with increasing d^+ which is what is observed. The frequency limits found increased with speed and with decreasing pinhole size. In the following chapters data above the marked limits are eliminated from analysis and not plotted.

A Bruel & Kjaer (B&K) 4182 probe microphone, with a 0.75-mm sensing area, was used as the reference microphone. The data of this microphone allows for the identification and removal of the wind tunnel background acoustics from the signal of the other microphones. The probe microphone is also shown in fig. 2.18c. All microphones were powered by B&K Type 3050-A-060 LAN-XI modules, which also handled the data acquisition and signal conditioning.

Table 2.5: Summary of 0.5-mm microphone pinhole (expressed in wall units) and the corresponding frequency limits on wall-pressure fluctuation estimated using the results of Gravante *et al.* [73]

		30-ms^{-1}	40-ms^{-1}	50-ms^{-1}	60-ms^{-1}	70-ms^{-1}
Smooth Wall	d^+	29.3	37.6	45.7	53.7	61.5
	f_{max} (kHz)	13.5	17.5	21.5	25.5	29.6
Intermediately-spaced	d^+	43.2	56.7	69.6	82.1	94.0
	f_{max} (kHz)	18.4	24.7	31.0	37.2	43.5
Densely-spaced	d^+	41.3	53.9	66.0	77.7	88.9
	f_{max} (kHz)	17.9	23.8	29.8	35.7	41.7
Cylinders	d^+	43.7	57.2	70.1	82.6	94.6
	f_{max} (kHz)	18.6	24.8	31.0	37.3	43.5
Multi-height	d^+	41.0	53.9	66.4	78.5	90.4
	f_{max} (kHz)	18.0	24.0	30.0	36.0	42.0
Multi-shape	d^+	43.5	57.3	70.4	83.1	95.3
	f_{max} (kHz)	18.9	25.4	31.9	38.3	44.8

2.4.3 Microphone Calibration

The effect of the pinhole cap on the microphone is not only to reduce spatial averaging, but it also alters the microphone frequency response. This is due to the fact that the pinhole

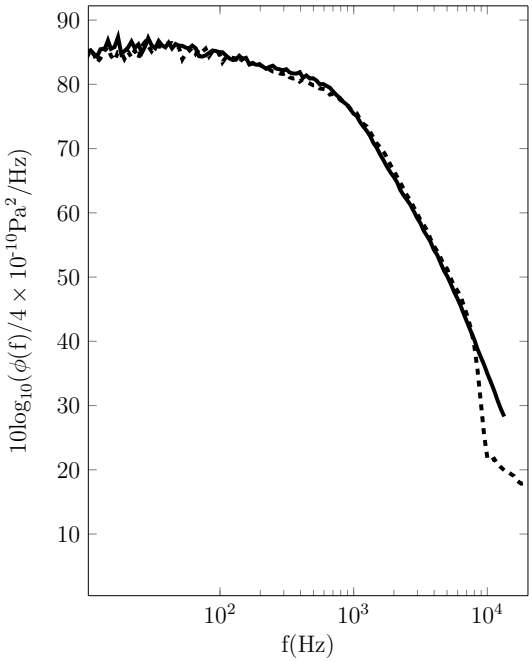

Figure 2.19: Effect of 0.25-mm pinhole microphone (——) compared with the 0.5-mm pinhole microphone (- - - -) on the measured pressure spectrum of densely-packed at 30-ms^{-1}

cap's aperture and cavity together act as a *Helmholtz resonator* [54]. The pinhole cavity behaves as a second-order system resulting in a resonant peak in the amplitude response of the microphone. For the purposes of this work the acoustic resistance of the pinhole cavity is assumed to be constant.

A calibration scheme was designed according to the work of Mish [107] to account for the change in microphone response. The set up for the calibration is shown in fig. 2.20. Before the calibration was started, a B&K type 4228 Pistonphone operating at 250-Hz was used to measure the sensitivity of each microphone. Then in an anechoic chamber, white noise was produced using the Agilent E1432 digitiser and a University Sound ID60C8 speaker. This signal is ideal for calibration because it has a flat frequency response up to 25.6-kHz. The output from the white noise generator to the speaker is $V_1(t)$.

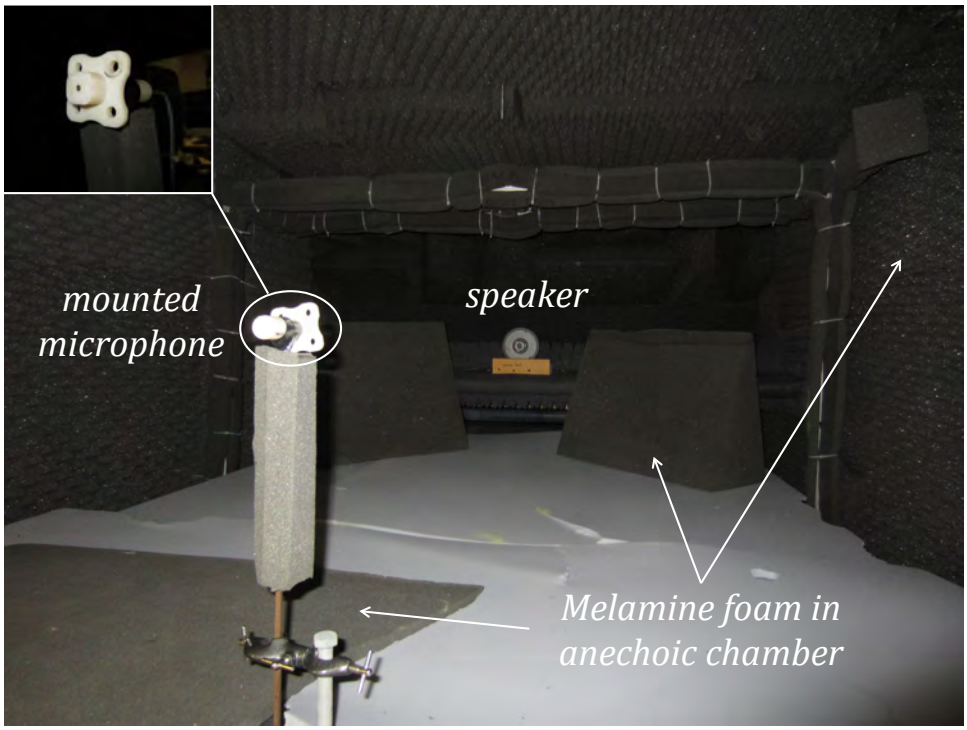

Figure 2.20: Microphone and speaker set up in the anechoic chamber to calibrate the pinhole microphone's amplitude and phase response

An unaltered factory-provided B&K microphone with salt-and-pepper cap (see figure fig. 2.18a) was used as a reference microphone. This microphone has a known flat response, $H_{ref}(\omega)$, with a sensitivity which is determined from Piston phone calibrations. The reference microphone was installed 2.06-m away from the speaker and in-line with the centre of the speaker (a laser was used to ensure this placement). The pinhole microphone was later mounted in a 3-D printed microphone holder , in the same position as the reference microphone. It was ensured that the face of the microphone was flush with the face of the holder (see image in

the upper left corner of fig. 2.20). The output of the speaker, $P_s(t)$, was then measured by the microphone and recorded as $V_2(t)$.

The following schematic shows the steps involved in the calibration process.

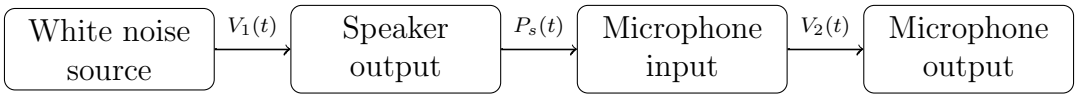

Essentially a calibration in the frequency domain is

$$\text{output signal} = \text{input signal} \times \text{calibration function}$$

so the speaker transfer function, which is a combination of the speaker response and the acoustics of the specific set up (anechoic chamber, speaker, microphone holder etc.), can be obtained from

$$\begin{aligned}\text{speaker transfer function} &= \frac{\text{reference mic input (speaker output)}}{\text{white noise signal}} \\ &= \frac{\text{reference mic output/reference mic response}}{\text{white noise signal}}\end{aligned}$$

Therefore using the reference microphone as described above provides the speaker transfer function, $S_p(\omega)$, by eq. (2.4)

$$S_p(\omega) = \frac{E\left[\frac{V_2(\omega)}{H_{ref}(\omega)} \cdot V_1^*(\omega)\right]}{E\left[V_1(\omega)V_1^*(\omega)\right]} = \frac{G_{PV_1}^{(a)}}{G_{V_1V_1}^{(a)}} \tag{2.4}$$

Note that the superscript (a) denotes the calibration using the reference microphone, $E[\,]$ is the expected value and G_{pp} is the spectrum as defined by Bendat and Piersol [108].

Following this same procedure (shown in the schematic) the reference microphone was replaced by each of the pinhole microphones. The set up remained unaltered except for the changing of microphones so the speaker response found from eq. (2.4) is the same for the pinhole mic calibrations. Again great care was taken to ensure that the face of the pinhole cap aligned with the face of the microphone holder. The calibration can be found from the frequency domain relation

$$\text{mic output signal} = \text{speaker output signal} \times \text{mic calibration function}$$

and we know from the reference mic study that

$$\text{speaker output signal} = \text{white noise signal} \times \text{speaker response}$$

so

$$\text{mic calibration function} = \frac{\text{mic output signal}}{\text{white noise signal} \times \text{speaker transfer function}}$$

This produces eq. (2.5), where the superscript b denotes values from the test using the pinhole microphones.

$$C(\omega) = \frac{E\left[V_2(\omega) \cdot V_1^*(\omega)\right]}{E\left[V_1(\omega) \cdot V_1^*(\omega)\right]} \cdot \frac{1}{S_p(\omega)} = \frac{G^{(b)}_{V_2V_1}}{G^{(b)}_{V_1V_1}} \cdot \frac{G^{(a)}_{V_1V_1}}{G^{(a)}_{PV_1}} \tag{2.5}$$

Note that the reference microphone was later outfitted with a pinhole cap and calibrated by the same process as the other pinhole microphones. Hence the amplitude and phase calibration for all seven pinhole microphones were obtained using the calibration set-up shown in fig. 2.20 and the calibration function defined by eq. (2.5).

The resulting calibration curves, for amplitude and phase, are shown in fig. 2.21a-b. Resonant peaks are observed in the amplitude calibration curves at natural frequencies which depend on the pinhole diameter – 16-kHz for the 0.5-mm pinhole and 8-kHz for the 0.25-mm pinhole. The magnitude of the resonant peak also depends on pinhole diameter such that the 0.5-mm pinhole microphones have an average maximum amplitude of approximately 15-dB and the 0.25-mm pinhole has a maximum amplitude of approximately 7.5-dB. These plots are noisy because of uncertainty associated with background acoustic contamination and at low frequencies uncertainty associated with the low efficiency of the speaker overwhelm the results. This is clear from the spikes observed at all frequencies, which are about 2dB on average but can be as large as 29-dB at frequencies below 1-kHz.

To reduce uncertainty and eliminate the spurious low frequency uncertainty, the microphone calibrations were smoothed using a curve-fit algorithm. First the algorithm eliminates widely scattered data below 1-kHz. Then using a Fourier-transformed transfer function of the form shown in eq. (2.6), a fit was created such that the error between the fit and the data was minimised

$$R(\omega) = \frac{b_1\omega^n + b_2\omega^{n-1} + ... + b_{n+1}}{a_1\omega^m + ... + a_2\omega^{m-1} + a_3} \tag{2.6}$$

This was done by iteratively choosing values of n and m which would minimise the error and, at the same time, enforce that the amplitude and phase curves flat-lined at zero at the low frequencies. Both the n and m indices were set to 2 such that 3 terms were used in the numerator or denominator. The smoothed calibration curve for a select microphone is shown in fig. 2.21c-d. Here the curve fit (solid, black line) is compared to the original data collected (solid, grey line). We can see that the fit appears to go through the middle of the noisy data at all frequencies up to the Nyquist frequency and the curves both level off to zero below 3-kHz.

The shape of the resonant peak in the calibration curve has been found to depend on the flow speed [1]. Figs. 2.22 to 2.25 show this dependence for the 3-mm sparse cylinders at speeds

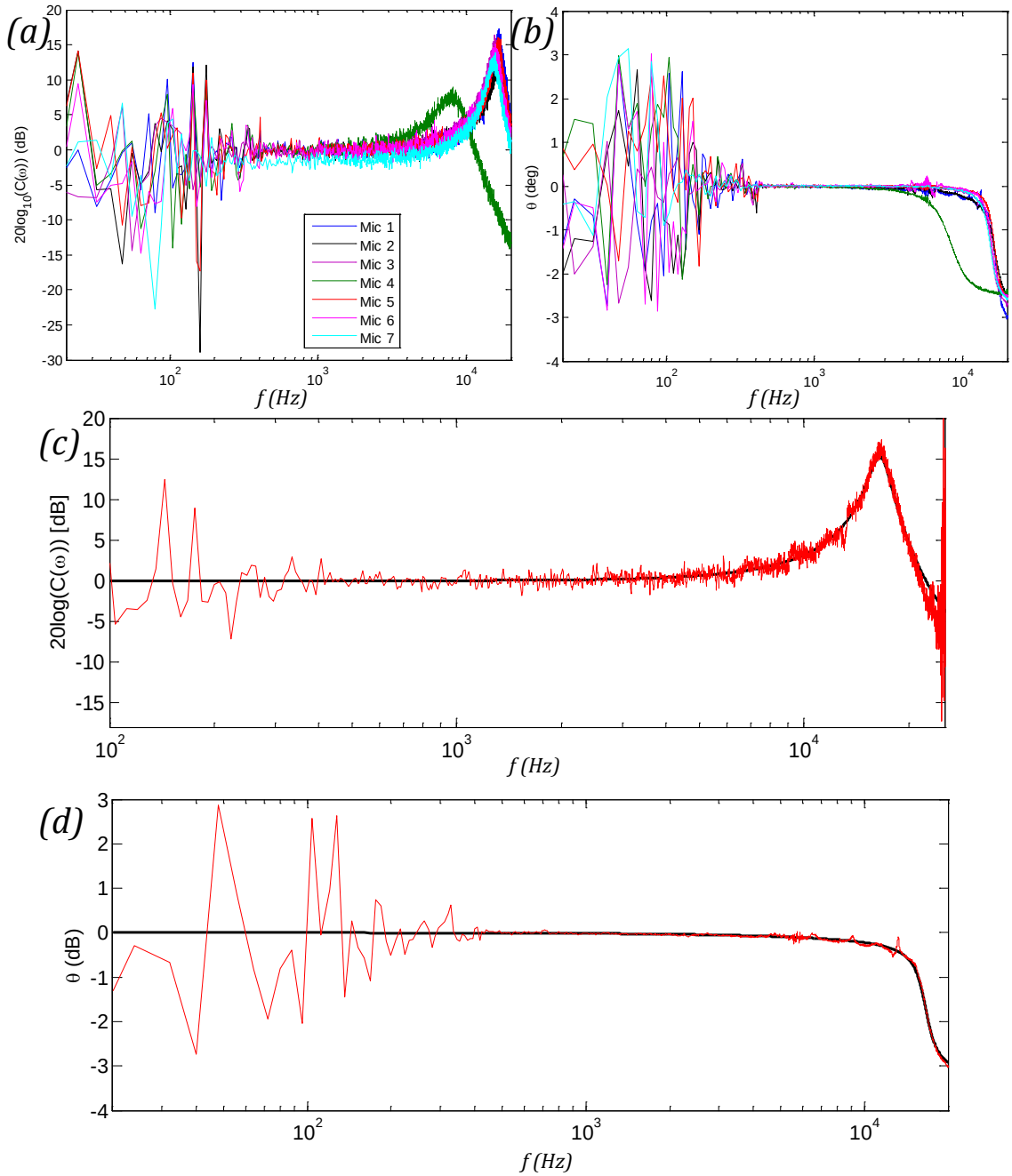

Figure 2.21: (a) Amplitude and (b) phase calibration curve for all 0.5-mm pinhole microphones tested and the 0.25-mm pinhole microphone (mic # 4 ——). Smoothed (c) amplitude and (d) phase calibration curve for a single 0.5-mm pinhole microphone (——) compared to the untransformed curves (——)

between 30-ms^{-1} and 70-ms^{-1}. In fig. 2.22 the uncalibrated pressure spectrum is shown at all speeds and we can clearly see the resonant peak at about $f=$ 16-kHz for all speeds. Taking a closer look at the peaks themselves in fig. 2.23 we immediately see that the shape is slightly different from speed to speed. The magnitude of the peak relative to the rest of the spectrum also increases with increasing speed. The differences in shape of the peak are subtle so we overlay the spectra from different speeds in fig. 2.24 and zoom in on these in fig. 2.25. It is clear in this last figure that there is a narrowing of the resonant peak with increasing flow speed. In addition, there is a slight shift of the peak to higher frequencies (by about 0.1-kHz) from the 30-ms^{-1} case to the 70-ms^{-1} case. Note that the y-axes of figs. 2.24 and 2.25 are deliberately left blank since the curves are artificially overlaid such that the magnitudes of the spectra are meaningless.

The observations of figs. 2.22 to 2.25 can be explained by the fact that as we increase flow speed, we increase Reynolds number, which decreases the relative magnitude of the viscous effects.This effect is not captured in the microphone calibration process described above. Following the work of Forest [87], the microphone calibrations were optimised during post-processing to account for the effect of flow speed on the damping of the resonant peak. This was done by adjusting both the system damping (a_2 in eq. (2.6)) and a_1 in eq. (2.6). The basic idea is to multiply the microphone calibration frequency scale by a small factor until the irregularities in the measured spectra after application of the anechoic chamber calibration (residual from resonant peak) are eliminated. This was done by iteratively adjusting the multiplication factors until we find values which produce the minimum RMS of the disturbances (using MATLAB's *fminsearch* function) in the vicinity of the resonant peak. These multiplication factors are then applied to the calibration to optimise it. The multiplier for a_1 was typically 10%. On the other hand, the damping factor varied by as much as 40% at 70-ms^{-1} for some surfaces.

Fig. 2.26 shows the variation with speed of the multiplicative factors used in optimising one microphone for the smooth wall case at 30-ms^{-1}. Here we see that the damping factor varies much more than the a_1 multiplier. Furthermore, we see a decrease in the damping factor with increases in speed, consistent with the observation that as the Reynolds number is increased the damping effect of the pinhole on the microphone system is reduced.

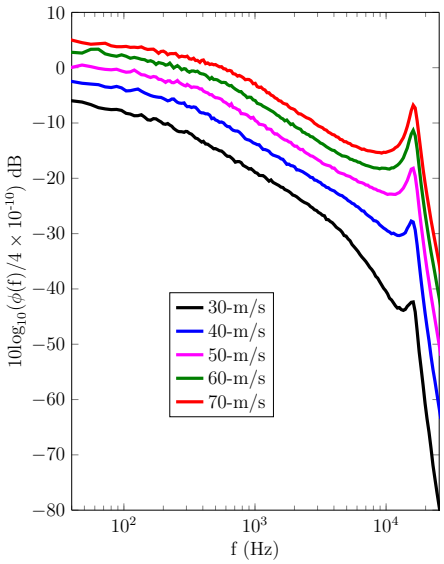

Figure 2.22: Effect of speed on the resonant peak of the uncalibrated pressure spectrum measured over a select rough surface (sparse, 3-mm cylinders in this case), at speeds between 30-ms^{-1} and 70-ms^{-1}

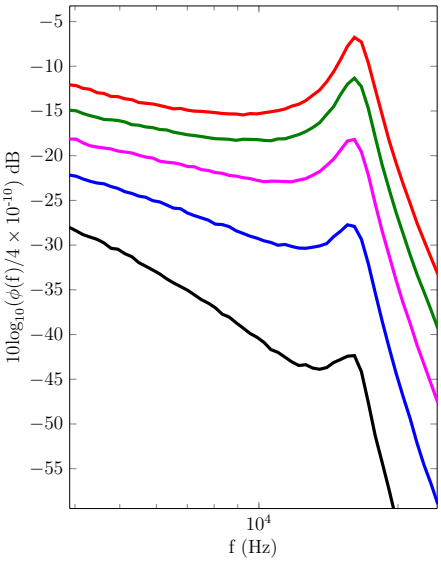

Figure 2.23: Enlarged plot of resonant peaks from fig. 2.22. Line colours same as in fig. 2.22

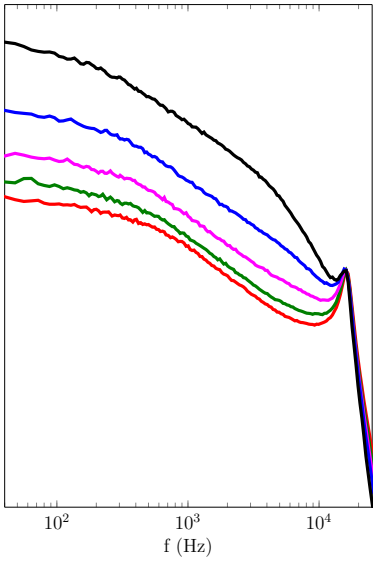

Figure 2.24: Uncalibrated pressure spectrum from fig. 2.22 overlaid for all speeds between 30-ms^{-1} and 70-ms^{-1}. Line colours same as in fig. 2.22

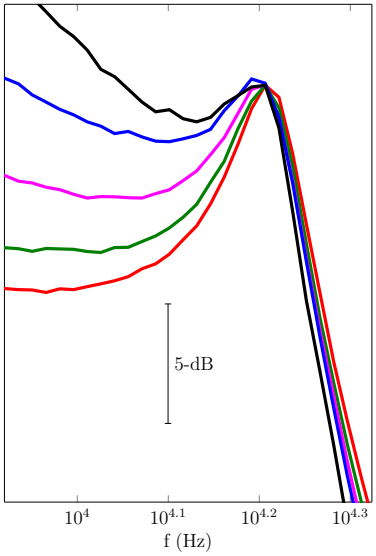

Figure 2.25: Enlarged plot of resonant peaks from fig. 2.24. Line colours same as in fig. 2.22

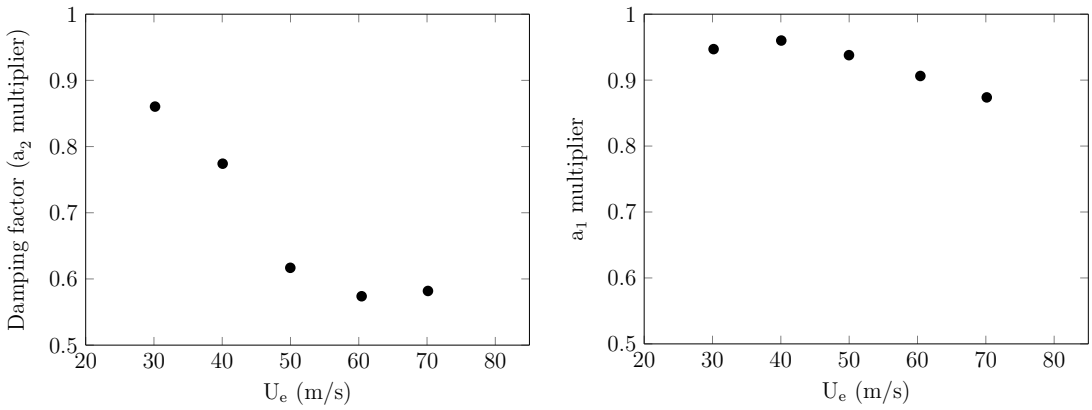

Figure 2.26: Variation with speed of the multiplicative factors for (a) a_1 and (b) a_2 of eq. (2.6)) which were used to optimise the calibration functions for each microphone

This optimisation process was done for each microphone, for every test case, and was successful in about 93% of cases. In the other 7% of cases, mainly for the densely-packed rough surface, the algorithm for minimising the RMS disturbances failed. This is because the algorithm searches in an expected region for the resonant peak and optimises within that region. In the case of the dense roughness in particular, the large slope differences in the spectra made this difficult. The result was that the multiplication factors did not adequately remove the resonant peak. There were obvious 'kinks' visible in the spectrum in the vicinity of the natural frequency of 16-kHz. To correct this a second MATLAB algorithm was implemented which allowed a user to interactively adjust the multiplicative factors, between 0 and 2.5, while observing the resulting changes to the spectrum. This allowed the user to specify the multiplication factors which sufficiently removed the resonant peak, based on their inspection of the spectrum, as opposed to leaving this determination up to the *fminsearch* function. This method proved to be more reliable for the spectra with steep slopes and in most cases removed the resonant peak completely. However at 60-ms^{-1} and 70-ms^{-1} over the densely-packed rough surface, even this process was not able to perfectly optimise the calibration curves. Remnants of the resonant peak still remained. In these two cases the spectra were manually clipped to remove these artefacts and all data above the natural frequency.

Appendix A details an experiment which was carried out in an attempt to capture and quantify the effect of the shear stress on the microphone response. The aim of this experiment was to quantify the effect of damping on the resonant peak and subsequently apply a correction to the spectra which was more reliable than the optimisation described above. These goals could not be fully achieved because the shear stresses produced were small. Nevertheless the methodology of the experiment is sound. Much more work and further experiments like these are critical because this damping effect due to increased flow speed has not been addressed in the literature. Yet, its effect on the quality of the final data could be substantial.

2.4.4 Installation of Surface Pressure Transducers in Stability Wind Tunnel

Microphones were installed in the 5th panel of the hard wall (measurement area shown in fig. 2.5), between 6.3-m and 7.0-m from the downstream trip. As depicted in figs. 2.27 and 2.28, microphones were installed in eight streamwise locations (the seven microphones were moved around to achieve this) and seven spanwise locations. The reference microphone was permanently placed at x=7.0-m and z=-0.347-m. This position was 0.15-m away from the nearest measurement microphone in spanwise direction. From the work of Forest [87] the length of the largest spanwise coherent structures observed over the rough and smooth walls were $\sim \delta^* \sim$ 0.033-m. Hence the 0.15-m separation distance was deemed sufficiently far away from the measurement microphones to ensure that cross-correlations could isolate the wind tunnel background acoustics.

The fifteen locations shown in fig. 2.27 and fig. 2.28 were carefully chosen to obtain the maximum number of unique separation distances between microphones, while also ensuring that microphones were not placed behind roughness elements. This is important for obtaining the two-point correlations discussed in chapter 4 and verifying the homogeneity of the wall pressure field. Multiple measurement locations also reduces uncertainty in the wall-pressure time spectra by averaging.

3-D printed holders made it possible to easily install and remove the delicate microphones in the hard wall (into the Lexan panels, through the aluminium and into the test section). Clay was used to fill in any gaps between the microphone holders and the rough wall substrate (see fig. 2.30) as well as to smooth over the head of the bolts which held the rough panels in place (see fig. 2.28). Great care was taken to ensure that the surface of the microphones were flush with the substrate of the rough surface or the smooth wall. This was done using a perfectly straight edge.

The placement of roughness elements around the microphone was also rigorously considered during the installation process. Typically, the microphone holders were smooth requiring rough elements to be attached individually using super glue. However in some cases roughness elements were printed directly unto the microphone holders to ensure that the placement of the microphones with the surrounding rough elements was accurate. This method also better preserved the alignment of the rough elements on the holder with the surrounding elements (more so than attaching the elements by hand). An example of the alignment achieved can be seen in fig. 2.29 for the dense roughness case.

As a standard practice microphone holders were designed so that the microphones would be as close as possible to the centre of a four element array because this has been established [87, 1, 109] to be the optimum measurement location. Before the roughness fetches were installed, careful measurements were made to design the holes on the 3-D printed microphone holders in the centre of the four element array. However, once installed in the test section the adjustments in wall location naturally offsets the microphone location relative to the

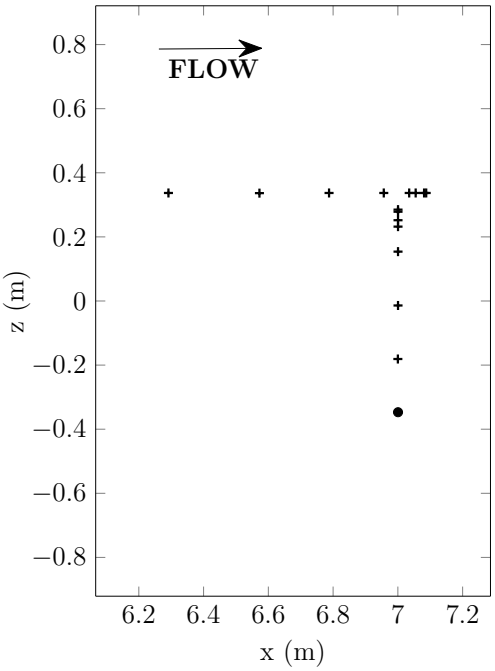

Figure 2.27: Diagram of microphone locations (+) in both streamwise and spanwise directions and the reference microphone (●)

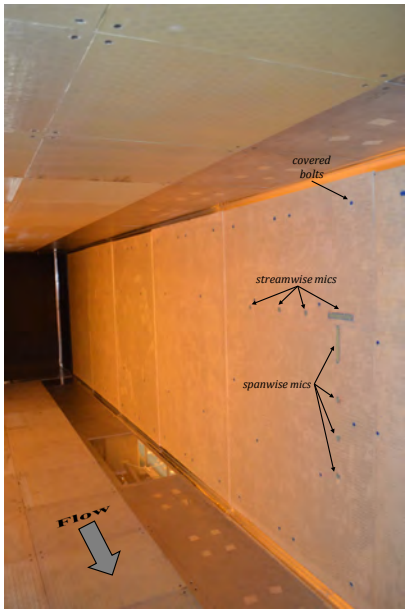

Figure 2.28: Microphone mounts (spanwise array and streamwise array) in panel 5, surrounded by cylindrical rough elements

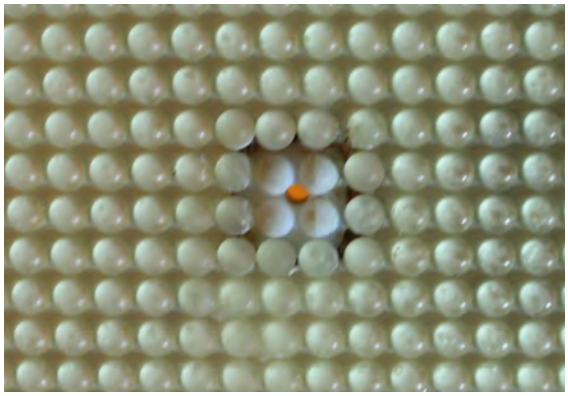

Figure 2.29: Alignment of 3-D printed microphone mount with surrounding (dense) roughness

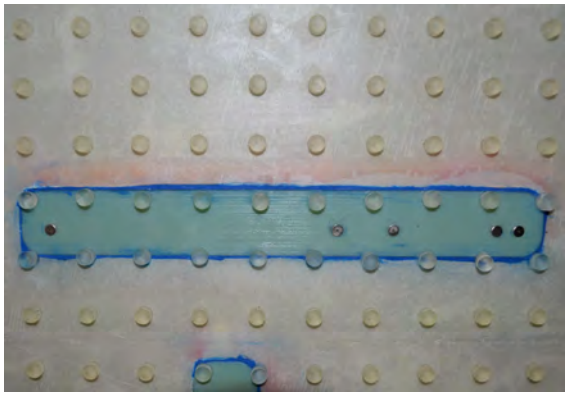

Figure 2.30: Streamwise microphone holder (with microphones installed) with blue clay used to fill the seam with the substrate

surrounding roughness. In this way, there is variation in microphone location relative to the roughness elements.

Figs. 2.31 to 2.35 present images of all the microphone locations for all surfaces that were tested during this work. Each of these figures includes specific element-relative locations for the eight streamwise microphone locations (horizontal array) and the seven spanwise microphone locations (vertical array). The microphones in these arrays are in the order and orientation outlined by fig. 2.27. Note that the microphones are installed in some images while in others they are not.

Fig. 2.31 shows that in the streamwise configuration only three microphones are installed the middle of the four element array of cylinders – mics #1, #7 and #8. The others in this array are slightly offset from the centre by 1 to 3-mm. Microphone #2 was designed to be offset from mic #1 by 5-mm so this microphone was expected to be offset. This is the case for all surfaces. In the spanwise array of microphones, mics #2, #6 and #7 are in the middle of the four element array. Again all other microphones are offset from the centre by 1-3-mm.

In the case of the intermediate roughness shown in fig. 2.32 the offset from the middle of the four element array was more significant than in the case of the cylinders. This is due to decreased spacing between elements. For this reason offsets on the intermediate surface which are of the same size as on the surface of cylinders are more distinct and result in microphones being very close to the elements. Mic #3 in the streamwise array is roughly in the middle of the four element array. All other microphones, in both configurations, are offset from the centre. Decreased spacing also means that parts of the offset microphones are more likely to be behind roughness elements. This is true for both the streamwise (mics #4 and #6) and spanwise arrays (mics #2, #4, #5, #6, #7). However, the pinhole itself is always open to the flow.

The difficulties with the intermediate roughness are further increased on the densely packed rough surface which has even smaller spaces between adjacent elements. On this surface the spacings is so small that the microphone was either in the middle of a four element array or behind an element. For this reason the rough elements were printed on the microphone holders themselves. We see in fig. 2.33 that this guarantees the microphones are in the middle of the four element array. This is true for mics #1-#5 and mic #7. Mic #6 and mic #8 are offset enough so that the pinhole would be behind the element. To circumvent this the element in front of mic #8 was removed completely and the element in front mic #6 was clipped. In the spanwise array mics #1-#5 were in the middle of the four element array. For mic #6 an upstream element was clipped to ensure the microphone wouldn't be behind the element, and for mic#7 surrounding elements were again removed to allow the microphone to sense the flow.

In the case of the multi-scale surfaces, microphone holders were designed to place microphone at different locations relative to the different kinds of elements on the surface. This was done with the aim of detecting variations in the pressure field due to the different ele-

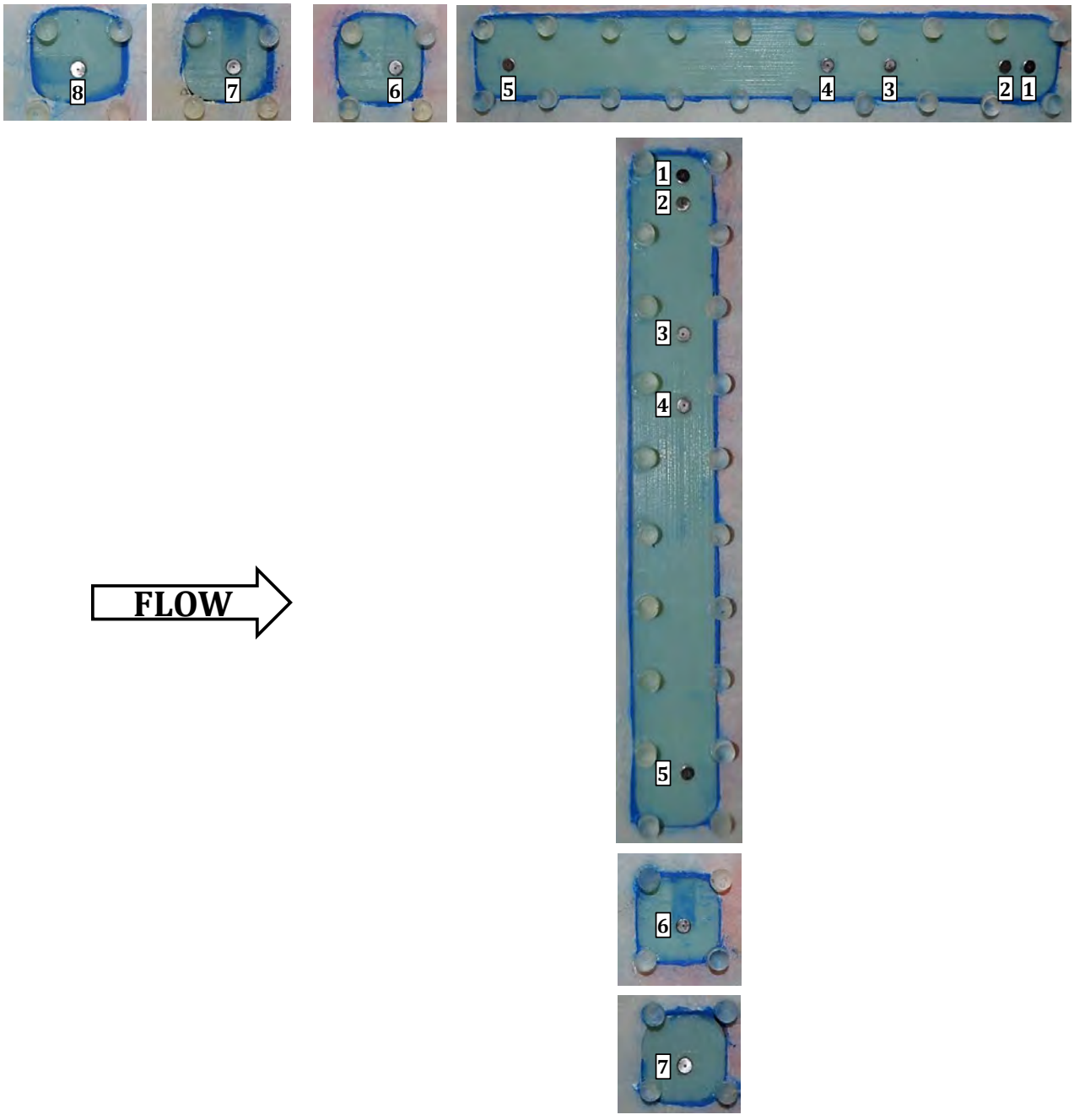

Figure 2.31: Microphone placement relative to the cylindrical elements in both the streamwise (horizontal) and spanwise (vertical) configurations. Refer to fig. 2.27 for microphone locations on the hard wall panel.

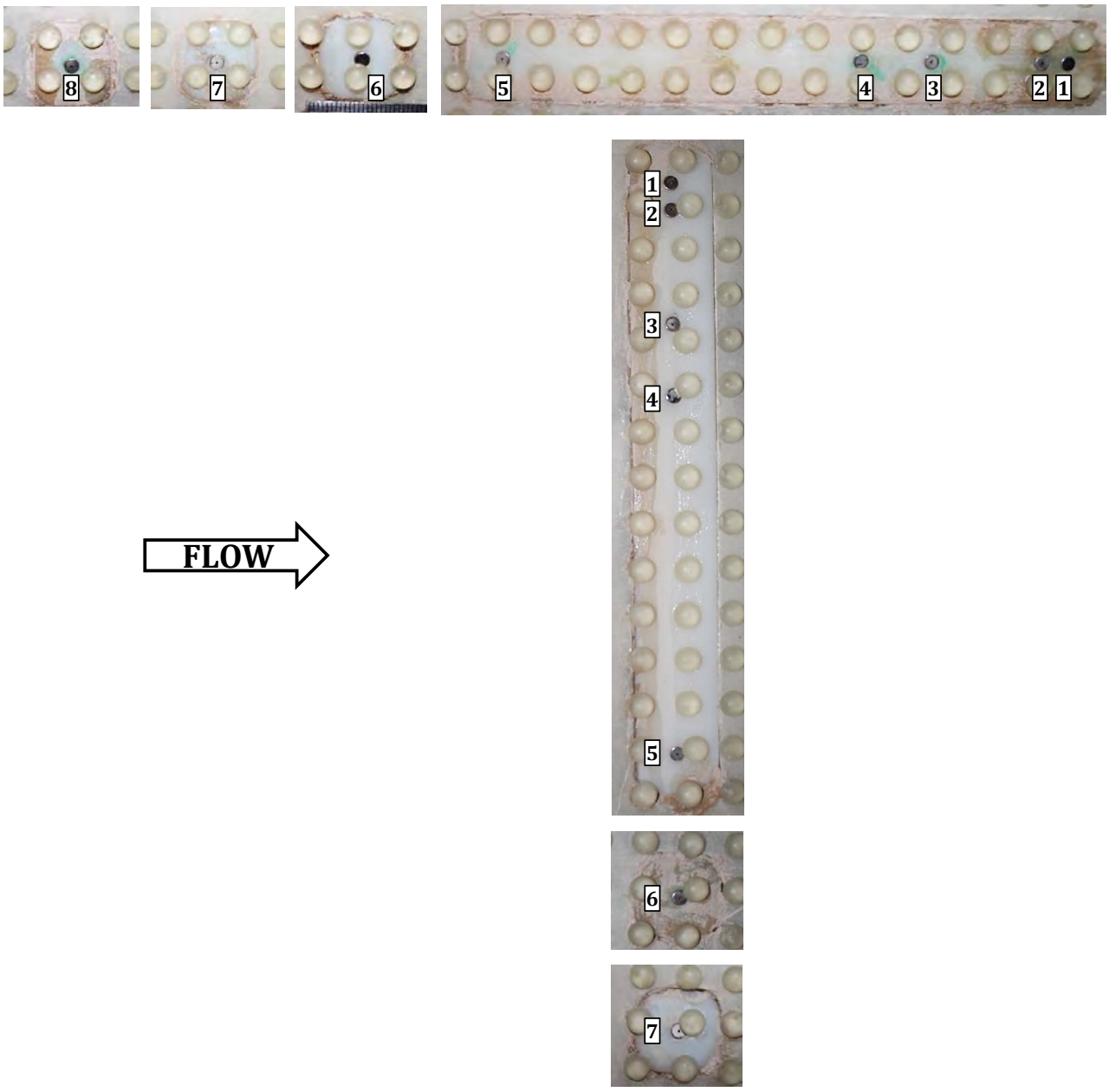

Figure 2.32: Microphone placement relative to the intermediately spaced 3-mm hemispheres in both the streamwise (horizontal) and spanwise (vertical) configurations. Refer to fig. 2.27 for microphone locations on the hard wall panel.

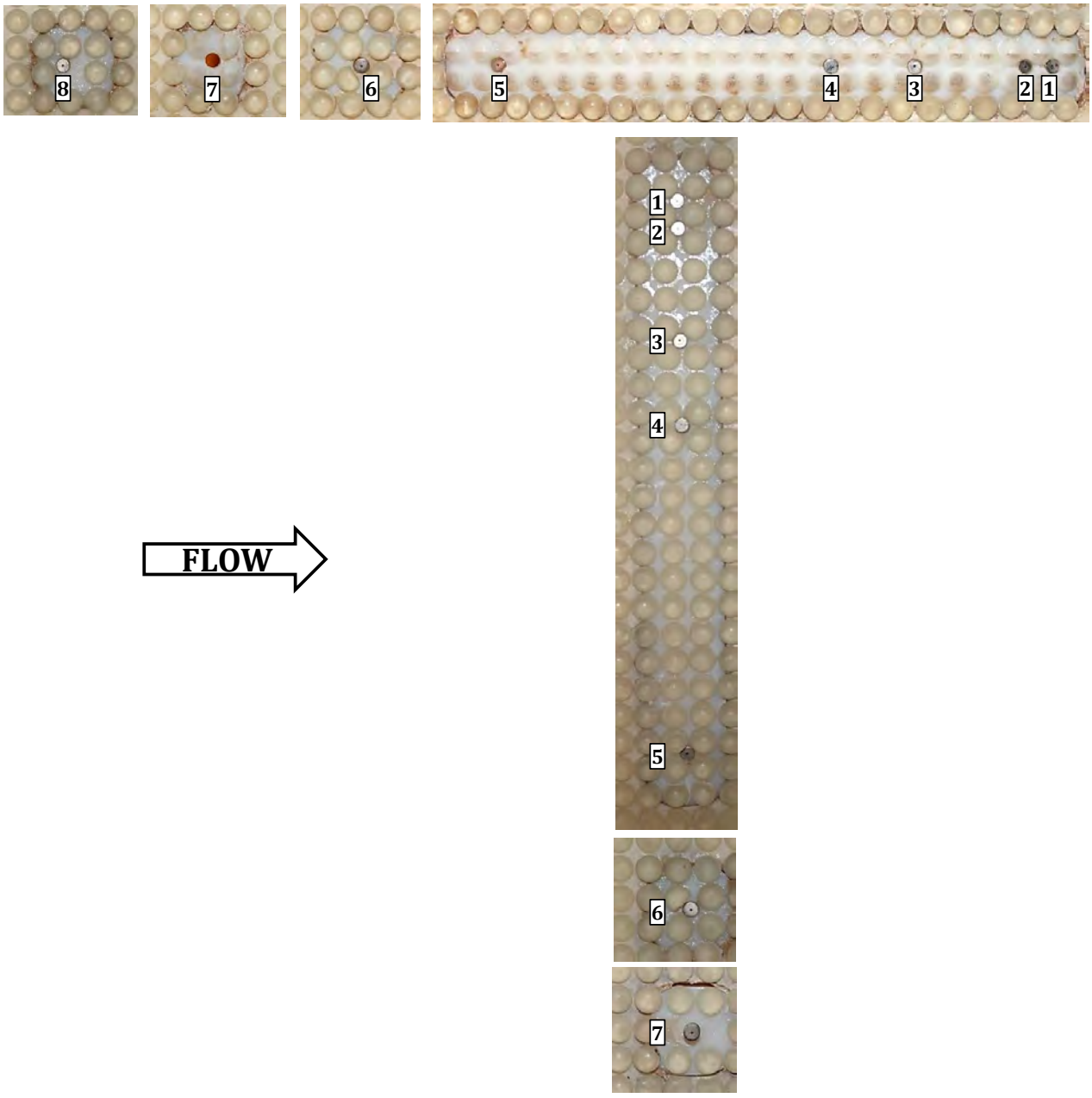

Figure 2.33: Microphone placement relative to the intermediately spaced 3-mm hemispheres in both the streamwise (horizontal) and spanwise (vertical) configurations. Refer to fig. 2.27 for microphone locations on the hard wall panel.

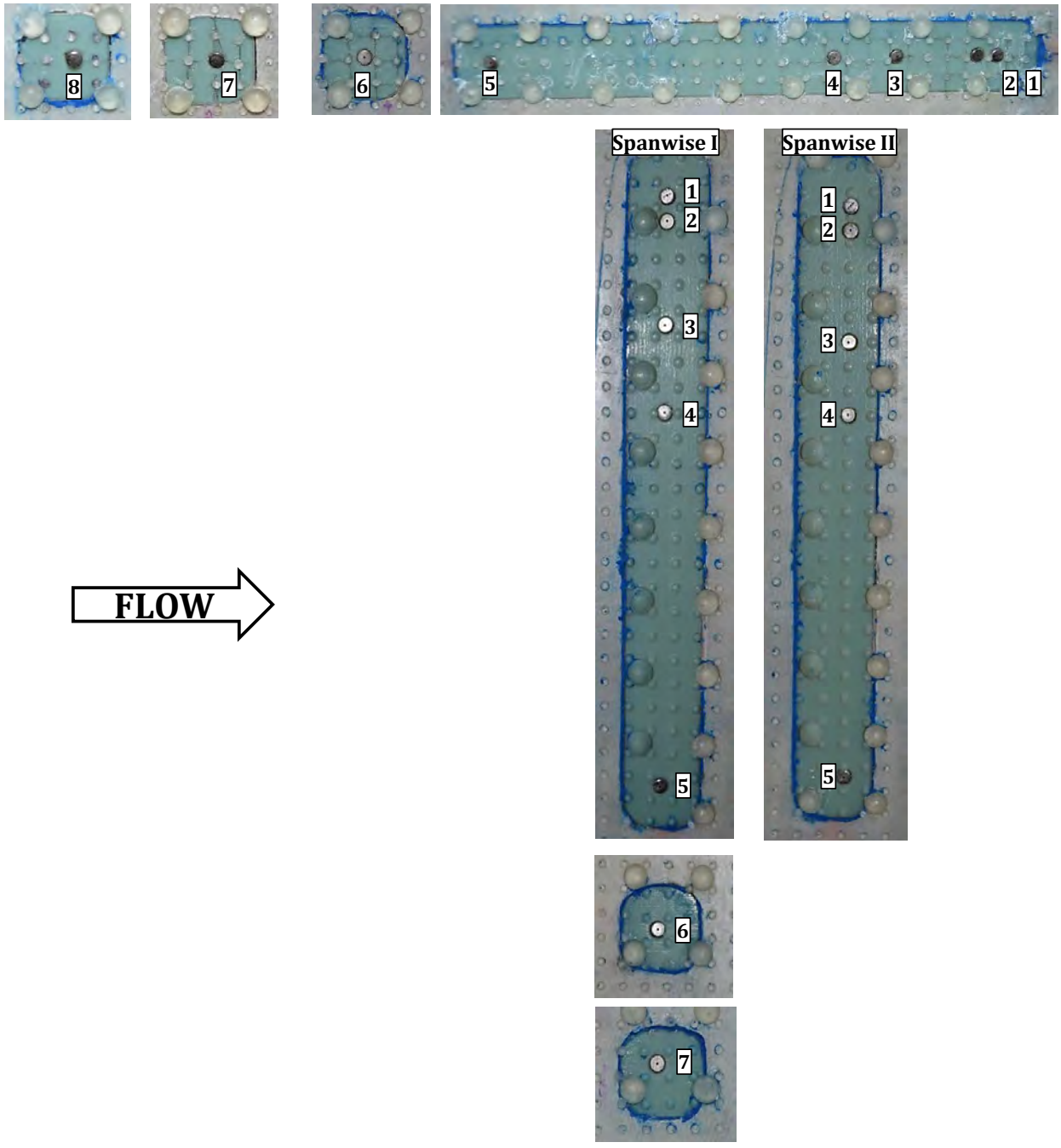

Figure 2.34: Microphone placement relative to the 1-mm and 3-mm hemispheres on the multi-height surface in both the streamwise (horizontal) and spanwise (vertical) configurations. Refer to fig. 2.27 for microphone locations on the hard wall panel.

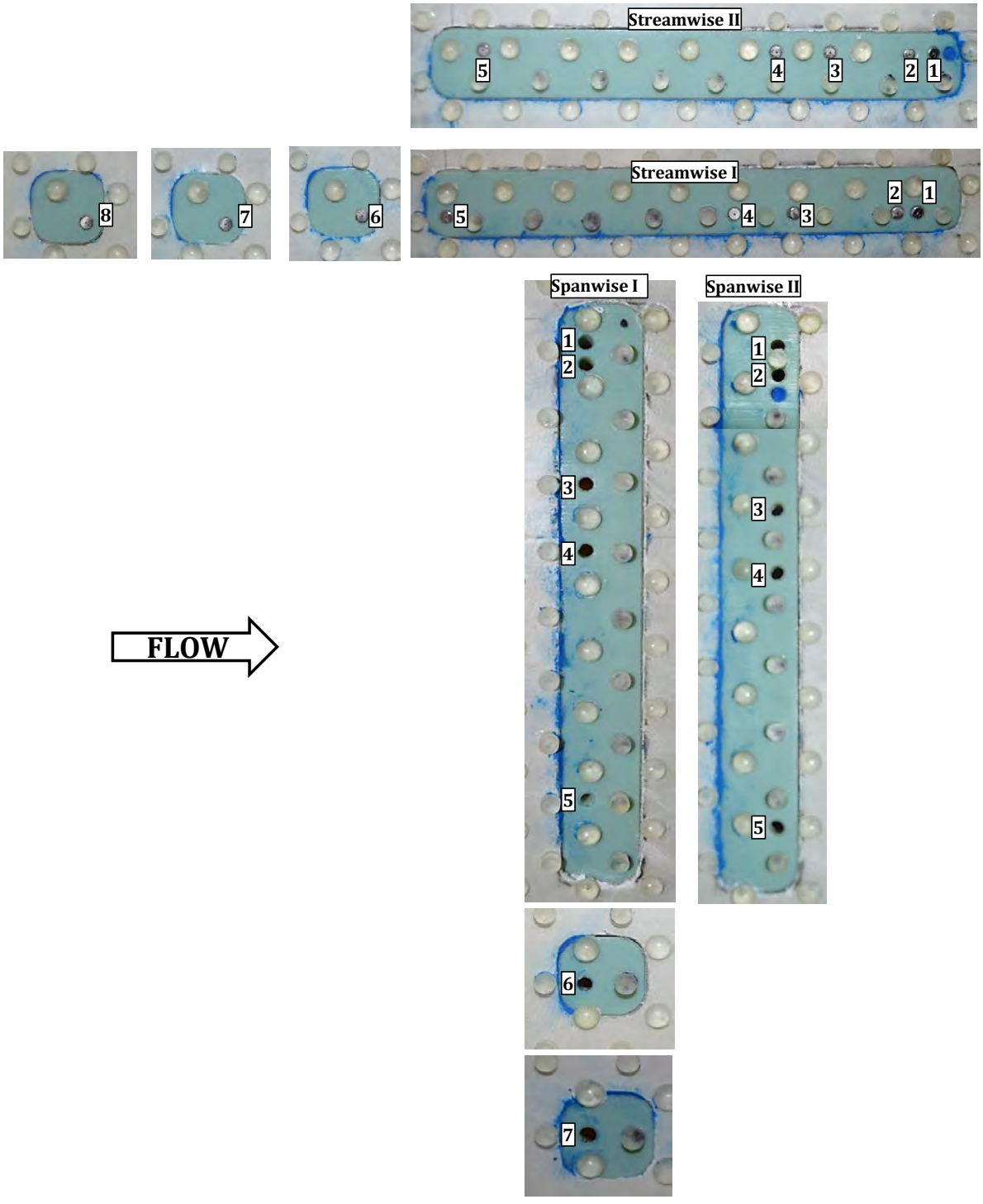

Figure 2.35: Microphone placement relative to the cylindrical and hemispherical elements on the multi-shape surface in both the streamwise (horizontal) and spanwise (vertical) configurations. Refer to fig. 2.27 for microphone locations on the hard wall panel.

ments. Fig. 2.34 shows the different microphone locations on the multi-height surface. The streamwise array of microphones was designed so that mics #1-#6 were between two streamwise 1-mm elements and equidistant (in the spanwise direction) between two 3-mm elements. This location will henceforth be referred to as being 'in the vicinity of 1-mm elements'. Mics #7 and #8 were installed in place of a 1-mm element. This was done in order to measure the pressure field in the middle of a four element array of 3-mm hemispheres. This location is defined as 'in place of 1-mm element'. Note that the image presented in fig. 2.34 for streamwise mic #8 is one in which the microphone was inserted 1-mm into the flow. This is simply because pictures were not taken of the microphone when it was inserted flush with the wall. The data was collected with the microphone flush with the wall, despite what is shown in this image.

For this surface two spanwise configurations, spanwise I and spanwise II, were tested. The difference between these two configurations is that configuration I is approximately 3-mm upstream of the mics in configuration II. This means that spanwise I placed all microphones, except mic #4, in the middle of a four element array of 1-mm hemispheres. The relative distance to the 3-mm element varied among these mics. Mic #2 was placed directly downstream a 3-mm hemisphere. It should be noted that fig. 2.34 shows a missing 3-mm hemisphere close to mic #5 in the spanwise I configuration. After taking these pictures, this inconsistency was discovered and an element was glued into this spot before taking data. Spanwise II includes microphones 'in the vicinity of 1-mm elements' and 'in place of 1-mm element' but further downstream than spanwise I.

In much the same way, the microphone holders for the multi-shape surface were designed to place microphones at different locations relative to the different elements. There were two streamwise and two spanwise configurations. Recall that this surface is categorised as staggered (see fig. 2.7). Streamwise I and spanwise I both place the microphones downstream the cylinders, in the middle of a staggered four element array (comprising of 2 cylinders and 2 hemispheres). This is true of all microphones except mic #6-#8 of the streamwise I configuration. These microphones were installed in place of a cylinder such that they were in the middle of a 'straight' (see fig. 2.7) four element array. Streamwise II and spanwise II microphones #1-#5 downstream the hemispherical elements, in the centre of a staggered four element array.

These diverse locations on the different surface will provide us with useful information about the pressure field around different elements. It will allows us to uncover characteristics of the local flow around elements of different geometries. These effects are examined in detail in § 3.7.

2.4.5 Data Acquisition and Signal Processing

Data Acquisition System: PULSE

All microphone data were acquired using a B&K type 3050-A-060 Pulse Analyser. Once the microphones were connected to the 6-channel input modules (B&K Type 3050-A-060 LAN-XI) the settings of each microphone and the data acquisition are controlled through the Pulse Analyser interface. For all measurements the frequency span was set to 25.6-kHz – a sampling rate of 65536-Hz for 32-s. The factory-documented microphone sensitivity was applied to the data during acquisition. This would be corrected to the actual sensitivity (obtained using the Pistonphone) during post-processing. Therefore the amplitude gain of the microphones was calibrated daily using the Pistonphone (as discussed in § 2.4.3). As a final step the Pulse Analyser was used to export the data collected from each channel of the acquisition system into a MATLAB data file.

Signal Processing

Starting with the sensitivity-corrected, time-series data the first step of processing is to obtain the power spectra density (PSD). This produces the frequency spectrum of each signal so that the different scales of the boundary layer can be better identified. This was done using a Hanning window and 50% overlap. The data from each microphone was divided into 511 records each of length 8192 and the Fourier transform of each record was computed. The one-sided PSD was then found from the average of the Fourier transforms as in eq. (2.7).

$$\Phi_{pp}(f) = \frac{2E[X_p^* X_p]}{T_r F_s} \tag{2.7}$$

where X_p is the Fourier transform, T_r is the record length, N_{rec} is the number of records and F_s is the sampling rate.

The calibration function developed in eq. (2.5) is then applied to the PSD of each pinhole microphone according to eq. (2.8).

$$\Phi_{pp_{cal}} = \frac{\Phi_{pp}}{C^* C} \tag{2.8}$$

Fig. 2.36 shows the effectiveness of the calibration process to remove the resonant peak from the PSD, for the cylindrical roughness at 30-ms^{-1}.

In an effort to reduce uncertainty a frequency averaging scheme was employed to smooth the PSD. The data was binned with twelve logarithmically spaced bins per octave. Fig. 2.37 shows the effectiveness of this process to smooth the spectrum. The grey line shows the spectrum before binning and the black line shows the smoothed, binned spectrum.

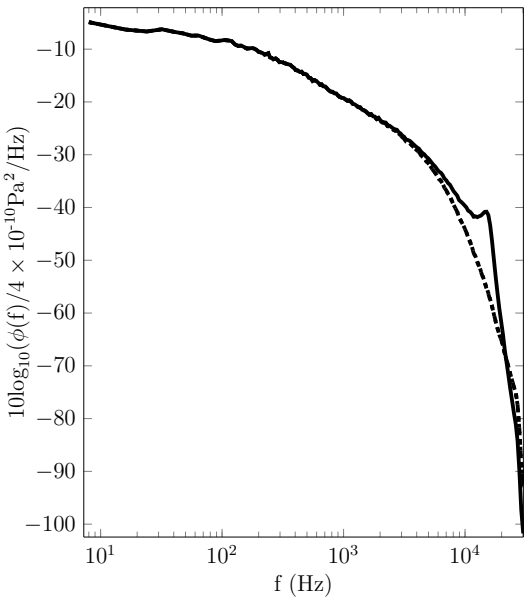

Figure 2.36: Power spectral density for the cylindrical rough surface (——) compared with power spectral density for the cylindrical rough surface with applied calibration (-·-·-) at 30-ms^{-1}

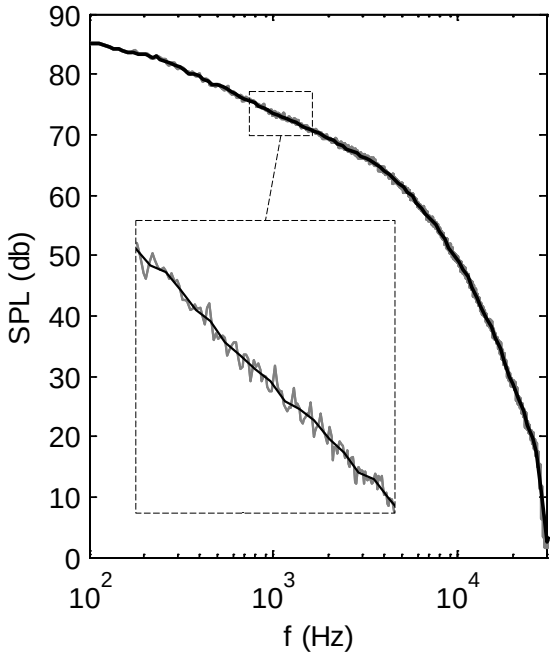

Figure 2.37: Power spectral density for the cylindrical rough surface with no frequency averaging (——) compared with the binned spectrum (——) at 30-ms^{-1}

After this the background noise of the wind tunnel is isolated and subtracted from the PSD of the reference microphone. This produced the hydrodynamic spectrum (background subtracted spectrum). According to Horne [110] the measured wall pressure spectrum, $\phi_{pp}^{(m)}$, can be expressed as the sum of the wall pressure spectrum due to turbulence, $\phi_{pp}^{(t)}$, and the wall pressure spectrum due to background noise, $\phi_{pp}^{(b)}$ as shown in eq. (2.9).

$$\phi_{pp}^{(m)} = \phi_{pp}^{(t)} + \phi_{pp}^{(b)} \tag{2.9}$$

Consider two points in the flow, i, and a reference point, r, which are sufficiently far away from each other. We have

$$\phi_{p_ip_r}^{(m)} = \phi_{p_ip_r}^{(t)} + \phi_{p_ip_r}^{(b)} \tag{2.10}$$

The component of the pressure spectrum due to turbulence will be uncorrelated between these points, which will be reflected in the cross-spectrum such that $\phi_{p_ip_r}^{(t)} = 0$. On the other hand the wall pressure spectrum due to background noise will be correlated. Therefore the acoustically subtracted wall pressure autospectrum at location i is simply a subtraction of the measured cross-spectrum between i and r from the measured autospectrum at location i

$$\begin{aligned} \phi_{p_ip_i} &= \phi_{p_ip_i}^{(m)} - \phi_{p_ip_r}^{(m)} \\ &= \phi_{p_ip_i}^{(t)} + \phi_{p_ip_i}^{(b)} - \phi_{p_ip_r}^{(b)} \end{aligned} \tag{2.11}$$

Furthermore, $\phi_{p_ip_r}^{(b)} = \phi_{p_ip_i}^{(b)}$ because the background noise will be the only part of the signal correlated between i and r, assuming the background noise is perfectly correlated between i and r. We would expect this to occur when.... So eq. (2.11) becomes $\phi_{p_ip_i} = \phi_{p_ip_i}^{(t)}$ which is the isolated wall pressure spectrum due to turbulence.

If we consider two points other than the reference location, i and j for example, the method above can be expanded to produce background subtracted cross spectra between these points. It has been established that the only part of the signal from any location which will be correlated with the signal at the reference location, r, is the background acoustics. Therefore $\phi_{p_ip_r}^{(a)} = \phi_{p_jp_r}^{(a)}$ for all locations. Based on this and eq. (2.11), eq. (2.12) shows the acoustic cancellation scheme used for the cross spectrum between two locations.

$$\phi_{p_ip_r}^{(m)} = \phi_{p_ip_r}^{(t)} + \phi_{p_ip_r}^{(b)} \tag{2.12}$$

The average of the background acoustic signal taken at the two locations is what is subtracted from the cross spectrum. This reduces bias in the result related to microphone locations.

Microphone pressure spectra were further reduced by removing the data points which showed low signal to noise ratio. The coherence between the measurement microphones and the reference microphones was found as in eq. (2.13).

$$\gamma_{noise}^2 = \frac{\left|(\phi_{p_ip_r}^{(m)})^2\right|}{\left|\phi_{p_ip_i}^{(m)}\right|\left|\phi_{p_rp_r}^{(m)}\right|} \tag{2.13}$$

Consider again the reference microphone, r, and a measurement microphone at location i. Equation (2.13) uses the wall pressure spectrum with acoustic noise included ($\phi_{pp}^{(m)}$) for each of these microphones. Therefore this equation can be used to identify the correlated background noise between the measurement and reference microphones. This means that high coherence, γ^2_{noise}, values would indicate a low signal to noise ratio (SNR). Therefore at frequencies with $\gamma^2_{noise} > 0.03$, the data were discarded. The effect of this process was most clearly observed at frequencies below 40-Hz. The discrimination value of 0.03, which corresponds to an SNR of-15-dB, was chosen based on eq. (2.14) from Glegg and Devenport [54]. This equation was derived by equating the coherence with its uncertainty estimate to ascertain the significant coherence (maximum allowable) based on the number of records of data.

$$N_{rec} \geq 8\frac{(1-\gamma^2_{noise})^2}{\gamma^2_{noise}} \tag{2.14}$$

Another step taken to preserve the quality of the data which will be used in this analysis was to remove any data points which had an associated uncertainty of more than 3-dB. The detailed uncertainty analysis is presented in § 2.4.6. Again the effect of this filtering is greatest at low frequencies, below 40-Hz. These filtering methods also served to remove the very low frequency data which corresponds to length scales larger than the test section width (U_c/f >1.73) since these are not flow-related.

Finally the autospectrum from the spanwise array of microphones were arithmetically averaged to produce a single pressure spectrum for each of these runs. Great care was taken in selecting which microphones would be included in this average. Individual microphone results were inspecting along with high resolution images of the microphone at the time of the run. If a microphone's results showed marked deviation from that of the other microphones, which could be explained by an artefact in the set-up, then this microphone's autospectrum was not included in the final average. For example, it was found that there was a gap between the microphone holder and the rough surface for a particular microphone during some runs (see fig. 2.38). This resulted in some flow leakage which lowered the pressure spectrum of that microphone significantly (see fig. 2.39). For this reason, this microphone's result was not used in any analysis. Similarly, there were cases where a change in the slope of the spectrum consistent with the slope change observed with the microphone being inserted into the flow (this will be discussed in depth in § 6.3.4) was observed. Again, these data were discarded.

2.4.6 Uncertainty Estimates

In order to analyse the final wall-pressure spectra in the subsequent chapters, an estimate of the uncertainty associated with the final spectrum is warranted. As discussed in the previous section, there are several steps taken in processing the measured wall-pressure data. The

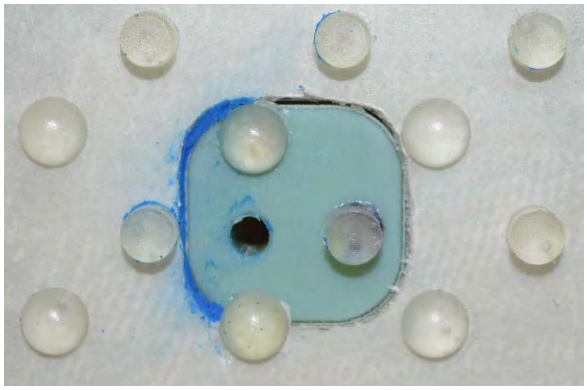

Figure 2.38: Partially filled seam between microphone holder and rough surface which may have led to lower pressure spectrum (see fig. 2.39)

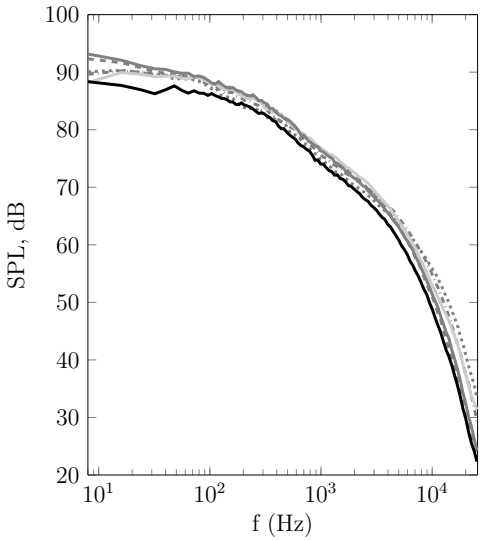

Figure 2.39: Autospectrum from seven microphones in spanwise array at 30-ms^{-1}. Mic 7 (——) is an outlier at all frequencies because of leakage (see fig. 2.38) and was not included in the final average.

approach taken here is to estimate the uncertainty during each step of the signal processing procedure (refer to § 2.4.5 for details).

We begin with the uncertainty estimate in the single sided wall-pressure spectrum as given by Glegg and Devenport [54] and shown in eq. (2.15).

$$\delta(\Phi_{pp}) = \frac{2\Phi_{pp}}{\sqrt{N_{rec}}} \tag{2.15}$$

This estimate is at 95% confidence level and is based on the number of independent spectral averages, N_{rec}, taken. In the present case N_{rec} is the number of records used in the spectral estimate (511).

In determining the uncertainty in the calibration function we refer to eq. (2.5). In this case the uncertainty will be

$$\delta(C) = \frac{\Phi^b_{V_2V_1}}{\Phi^b_{V_1V_1}} \cdot \frac{\Phi^a_{V_1V_1}}{\Phi^a_{PV_1}} \sqrt{\left(\frac{\delta(\Phi^b_{V_2V_1})}{\Phi^b_{V_2V_1}}\right)^2 + \left(\frac{\delta(\Phi^a_{V_1V_1})}{\Phi^a_{V_1V_1}}\right)^2 + \left(\frac{\delta(\Phi^b_{V_1V_1})}{\Phi^b_{V_1V_1}}\right)^2 + \left(\frac{\delta(\Phi^a_{PV_1})}{\Phi^a_{PV_1}}\right)^2} \tag{2.16}$$

The uncertainty in the calibration spectra will be the same as shown in eq. (2.15). Thus

eq. (2.16) becomes

$$\delta(C) = \frac{4}{\sqrt{N_{rec}}} C(\omega) \tag{2.17}$$

and is, as one would expect, a function of frequency.

To apply the calibration to the wall-pressure spectra, eq. (2.8) is used. The uncertainty associated with this is therefore

$$\delta(\Phi_{pp_{cal}}) = \frac{\Phi_{pp}}{C \cdot C^*} \sqrt{\left(\frac{\delta(\Phi_{pp})}{\Phi_{pp}}\right)^2 + \left(\frac{\delta(C)}{C}\right)^2 + \left(\frac{\delta(C^*)}{C^*}\right)^2} \tag{2.18}$$

Substituting eqs. (2.15) and (2.17) into eq. (2.18) we find that the uncertainty in the spectrum after the calibration is applied is

$$\delta(\Phi_{pp_{cal}}) = \frac{6}{\sqrt{N_{rec}}} \Phi_{pp_{cal}} \tag{2.19}$$

After applying the calibration the spectrum was smoothed by averaging to twelve bins per octave. The uncertainty associated with this averaging is given by

$$\delta(\Phi_{pp_{cal,bin}}) = \frac{1}{N_{avg}} \sqrt{\delta(\Phi_{pp_{cal_1}})^2 + \delta(\Phi_{pp_{cal_2}})^2 + ... + \delta(\Phi_{pp_{cal_{N_{avg}}}})^2} \tag{2.20}$$

where N_{avg} is the number of data points averaged per bin. This number will be different for each bin because the bins are logarithmically spaced. Simplified, this equation becomes

$$\delta(\Phi_{pp_{cal,bin}}) = \frac{6}{N_{avg}\sqrt{N_{rec}}} \sqrt{\sum_{i=1}^{N_{avg}} (\Phi_{pp_{cal}})_i^2} \tag{2.21}$$

Now we find the uncertainty in the hydrodynamic spectra (background subtracted spectra). The hydrodynamic spectrum is

$$\Phi_{hh} = \Phi_{pp_{cal,bin}} - \Phi_{bb_{bin}} \tag{2.22}$$

where $\Phi_{bb_{bin}}$ is the spectrum of the background acoustics smoothed to twelve bins per octave (but no calibration applied since this is the data from the reference probe microphone). So the uncertainty in this operation would be

$$\delta(\Phi_{hh}) = \sqrt{\delta(\Phi_{pp_{cal,bin}})^2 + \delta(\Phi_{bb_{bin}})^2} \tag{2.23}$$

We can find $\delta(\Phi_{bb_{bin}})$ from eqs. (2.15) and (2.20) as

$$\delta(\Phi_{bb_{bin}}) = \frac{2}{N_{avg}\sqrt{N_{rec}}} \sqrt{\sum_{i=1}^{N_{avg}} (\Phi_{bb})_i^2} \tag{2.24}$$

Substituting eqs. (2.21) and (2.24) into eq. (2.23), the result is

$$\delta(\Phi_{hh}) = \frac{2}{N_{avg}\sqrt{N_{rec}}}\left(3\sqrt{\sum_{i=1}^{N_{avg}}(\Phi_{pp_{cal}})_i^2} - \sqrt{\sum_{i=1}^{N_{avg}}(\Phi_{bb})_i^2}\right) \tag{2.25}$$

A more useful expression of this uncertainty would be in dB, so we convert eq. (2.25) as follows

$$\begin{aligned}
\Phi_{hh_{dB}} =& \frac{10}{\ln(10)}\ln\left(\Phi_{hh}\right) \\
\delta(\Phi_{hh_{dB}}) =& \frac{10}{\ln(10)}\frac{\delta(\Phi_{hh})}{\Phi_{hh}} \\
\delta(\Phi_{hh_{dB}}) =& \frac{20}{\ln(10)N_{avg}\sqrt{N_{rec}}}\frac{1}{\Phi_{hh}}\left(3\sqrt{\sum_{i=1}^{N_{avg}}(\Phi_{pp_{cal}})_i^2} - \sqrt{\sum_{i=1}^{N_{avg}}(\Phi_{bb})_i^2}\right)
\end{aligned} \tag{2.26}$$

For a single microphone the average uncertainty obtained from eq. (2.26) is 1.5-dB below frequencies of 100-Hz (maximum of 3-dB) and 0.1-dB at frequencies above 20-kHz (minimum of 0.08-dB). Fig. 2.40 shows how the uncertainty (shaded region) varies for a select microphone measurement taken at 30-ms^{-1} on the cylindrical rough surface.

Finally the uncertainty in taking the average of the autospectrum over a number of microphones, N_{mic}, is found as

$$\begin{aligned}
\delta(\Phi_{HH}) =& \frac{1}{N_{mic}}\sqrt{\delta(\Phi_{hh_{dB_{mic1}}})^2 + \delta(\Phi_{hh_{dB_{mic2}}})^2 + ... + \delta(\Phi_{hh_{dB_{micN}}})^2} \\
\delta(\Phi_{HH}) =& \frac{1}{N_{mic}}\sqrt{\sum_{j=1}^{N_{mic}}\delta(\Phi_{hh_{dB}})_j^2}
\end{aligned} \tag{2.27}$$

Equation (2.27) shows that taking the average of the spectra from different microphones decreases the uncertainty from that obtained in eq. (2.26), as one would expect. The average uncertainty obtained from eq. (2.27) is 0.5-dB below frequencies of 100-Hz and 0.05-dB at frequencies above 20-kHz. This uncertainty estimate does not take into account variations in the pressure gradient, microphone position, etc. or the uncertainty associated with optimising the calibration. A repeatability study revealed that these factors raises the uncertainty to about 2-dB.

2.5 Summary of Test Cases

The data which is the primary focus of this work was collected during two wind tunnel campaigns. The first of these, campaign I, was conducted in 2015 and involved testing

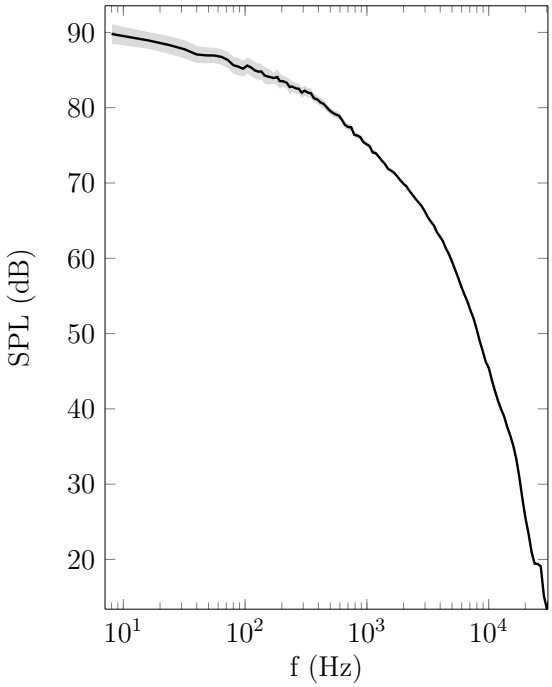

Figure 2.40: Uncertainty band (shaded area) in dB for a select microphone measurement taken on the cylindrical rough surface at 30-ms^{-1}

of the intermediately-spaced and densely-spaced rough surfaces. In 2016 campaign II was implemented to investigate the turbulent boundary layer over the cylinders and composite rough surfaces. A summary of the data obtained in each campaign is given in table 5.1.

In addition to these data, the data of Forest [87] and Meyers [103] will be included the analyses of this work. Their data set can be reviewed in § 2.2.2.

Table 2.6: Summary of test cases completed in the present work

Surface	Campaign	Measurements Taken	Speeds, ms^{-1}	Flow density (ρ), kg m^{-3}	Viscosity (ν), m^2 s^{-1} $\times 10^{-5}$
Smooth wall	I, II	Pressure Fluctuations	[30,40,50,60,70]	[1.06, 1.05, 1.04, 1.03, 1.03]	[1.79, 1.80, 1.82, 1.84, 1.86]
	I	Hotwire	[30,60]		
	I, II	Flat-head Pitot	[30,60]		
Intermediately-spaced	I	Pressure Fluctuations	[30,40,50,60,70]	[1.11, 1.09, 1.08, 1.06, 1.05]	[1.65, 1.69, 1.72, 1.76, 1.79]
	II	Hotwire	[30,60]		
	II	Flat-head Pitot	[30,60]		
Densely-spaced	I	Pressure Fluctuations	[30,40,50,60,70]	[1.10, 1.08, 1.07, 1.06, 1.04]	[1.67, 1.71, 1.74, 1.78, 1.81]
	II	Hotwire	[30,60]		
	II	Flat-head Pitot	[30,60]		
Cylinders	II	Pressure Fluctuations	[30,40,50,60,70]	[1.11, 1.10, 1.08, 1.07, 1.05]	[1.65, 1.68, 1.71, 1.75, 1.78]
		Hotwire	[30,60]		
		Flat-head Pitot	[30,60]		
Composite height	II	Pressure Fluctuations	[30,40,50,60,70]	[1.09, 1.08, 1.07, 1.05, 1.04]	[1.70, 1.73, 1.76, 1.79, 1.82]
		Hotwire	[30,60]		
		Flat-head Pitot	[30,60]		
Composite shape	II	Pressure Fluctuations	[30,40,50,60,70]	[1.10, 1.08, 1.07, 1.05, 1.03]	[1.68, 1.72, 1.76, 1.80, 1.84]
		Hotwire	[30,60]		
		Flat-head Pitot	[30,60]		

3. Surface Pressure Spectra

3.1 Mean Pressure on the Wall

The aim of this work is to investigate the turbulent boundary layer over rough walls with *zero pressure gradient*. As with most experiments, such conditions cannot be created perfectly and the result is a near-zero pressure gradient. This small pressure gradient is slightly different in each campaign. Fig. 3.1 presents the near-zero pressure gradient created for both campaigns at select speeds: 30-ms^{-1} and 60-ms^{-1}. This plot presents the pressure coefficient, C_p, measured by the pressure taps in the floor and ceiling. In this figure the dotted line demarcates the bounds of the measurement region. The streamwise array of microphones are distributed between these two lines and the spanwise array of microphones is distributed along the line at x=7.0-m. Velocity measurements were also taken along the line at x=7.0-m.

The variation in mean pressure coefficient for each case tested during campaign I, shown in fig. 3.1a, has regions of both slightly favourable and slightly adverse pressure gradients. All three cases appear to have almost identical pressure gradient along most of the wall. The largest differences in coefficient of pressure between the cases are observed within the measurement region (between 6.3-m and 7.0-m). These differences are on average 1×10^{-2}. The pressure gradients appear to be smallest for the smooth wall case and largest for the dense cases. On average $dC_p/dx \approx -0.002$-m^{-1} with the largest gradient observed being -0.01-m^{-1} for the rough wall cases at 60-ms^{-1}. In the measurement region there is a slight favourable streamwise pressure gradient of approximately -0.01-m^{-1} for the rough wall cases. This will result in a slight acceleration of the flow ($1.01\times10^{-9} \leq -(\nu/U_e^2)(dU_e/dx) \leq 2.63\times10^{-9}$). Outside the measurement region accelerations drop to as low as $-(\nu/U_e^2)(dU_e/dx) = 1.67\times10^{-10}$.

Similarly, the variation in mean pressure coefficient for each case tested during campaign II, shown in fig. 3.1b, also has regions of both slightly favourable and slightly adverse pressure gradients. All cases appear to have almost identical pressure gradient along most of the wall. The largest differences in mean pressure coefficient between the cases ($\sim 5\times10^{-3}$) are again observed within the measurement region. In the measurement region the pressure gradient was smallest for the smooth wall case although the gradient for the cylindrical surface and the multi-shape surface were almost as small $\sim 5\times10^{-4}$. The largest gradient was observed for the multi-height surface $\sim 5\times10^{-3}$. In all cases there is a slight favourable pressure gradient in the measurement region, which will result in an acceleration of $7.3\times10^{-10} \leq -(\nu/U_e^2)(dU_e/dx) \leq 1.2\times10^{-9}$. Outside the measurement region the accelerations drop to as low as $-(\nu/U_e^2)(dU_e/dx) = 6.1\times10^{-13}$.

In both campaigns the pressure gradient achieved was similar to that of most other re-

searchers and so we expect accelerations of the flow over the wall to also be at most equal to that experienced in other works. For example the average acceleration experienced in campaign I was 4 times lower than that of Meyers *et al.* [1]. Similarly, the works of Varano [36] and his colleague Hopkins [24] in the Virginia Tech Small Boundary Layer Wind Tunnel reported maximum accelerations of -$(\nu/U_e^2)(dU_e/dx)$ *sim* 4.6×10^{-9} and -$(\nu/U_e^2)(dU_e/dx)$ *sim* 2.3×10^{-9} respectively.

3.2 Flow Uniformity

In the smooth wall configuration, the flattened Pitot was traversed in the y and z directions at x=7.0-m. Data was collected inside a measurement rectangle with dimensions of 0.305 × 0.318-m ($y \times z$) at 30-ms^{-1} and 0.305 × 0.381-m at 60-ms^{-1}. The normalised velocity (U/U_{ref}) maps obtained are presented in fig. 3.2. These figures are the view from upstream looking downstream at a cross section of half the width of the wind tunnel test section (at

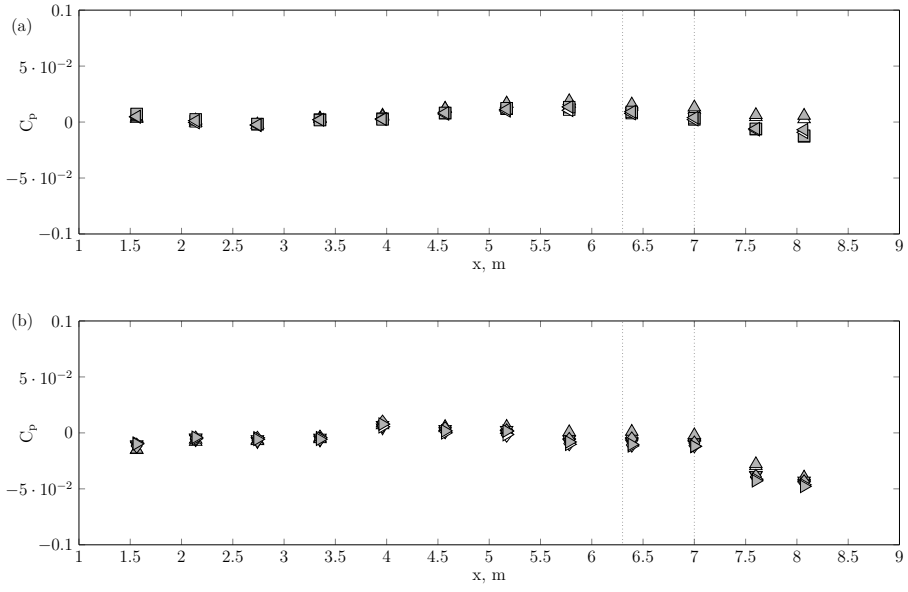

Figure 3.1: Near-zero pressure gradient achieved during (a) campaign I and (b) campaign II for each surface tested: △ smooth wall at 30-ms^{-1}; ▲ smooth wall at 60-ms^{-1}; □ intermediate roughness at 30-ms^{-1}; ■ intermediate roughness at 60-ms^{-1}; ◁ dense roughness at 30-ms^{-1}; ◀ dense roughness at 60-ms^{-1}; ▽ cylindrical roughness at 30-ms^{-1}; ▼ cylindrical roughness at 60-ms^{-1}; ◇ multi-height roughness at 30-ms^{-1}; ◆ multi-height roughness at 60-ms^{-1}; ▷ multi-shape roughness at 30-ms^{-1}; ▶ multi-shape roughness at 60-ms^{-1}; - - - - bounds of measurement area

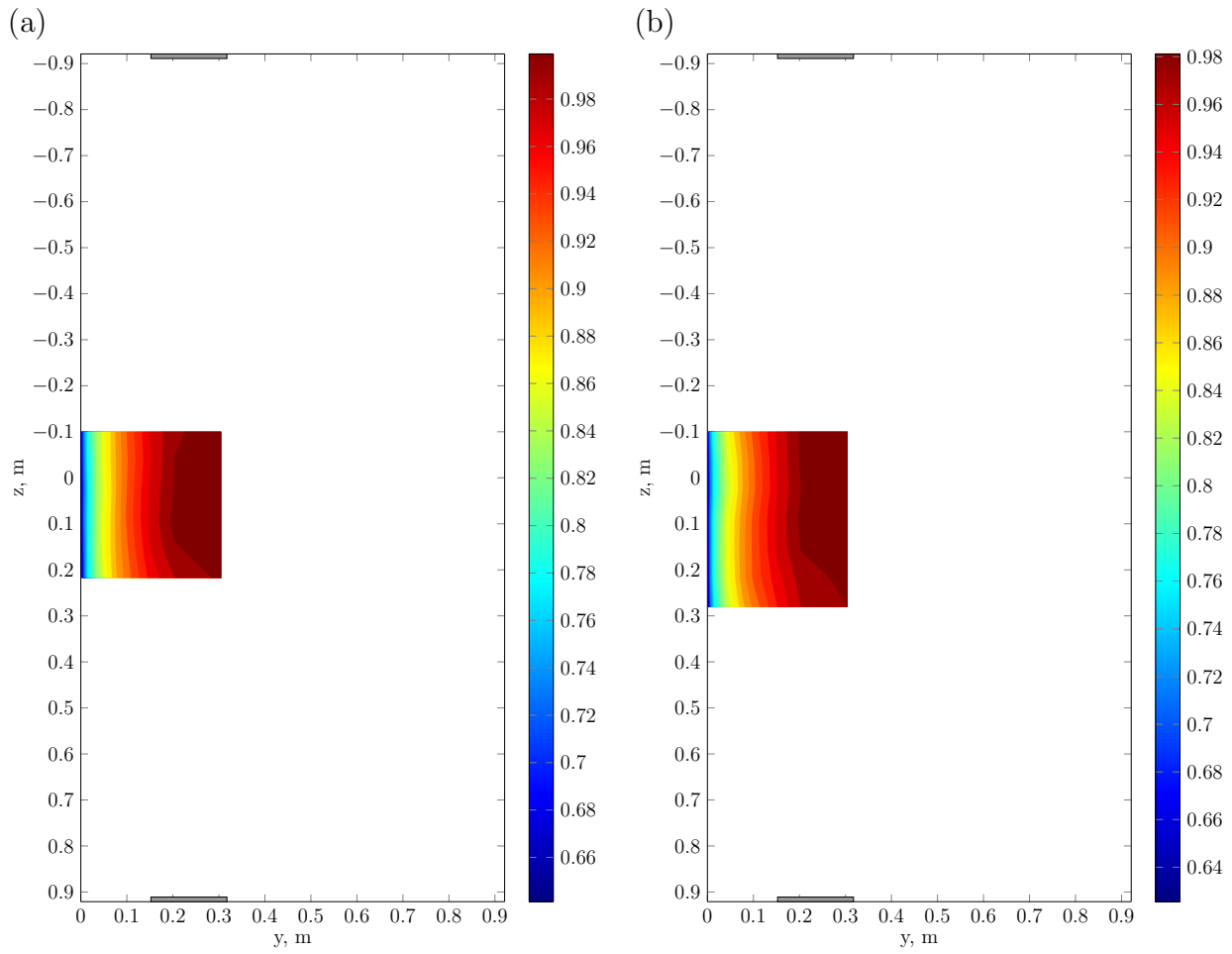

Figure 3.2: Contours of U/U_{ref} in the boundary layer measured at x=7.0-m using the flattened Pitot at (a) U_{ref}=30-ms^{-1} and (b) U_{ref}=60-ms^{-1} (flow into page). ▬ is the cross section of the streamwise legs of the three-axis traverse.

x=7.0-m). At the top and bottom of the plots the cross section through the streamwise legs of the three-axis traverse can be seen as a grey box (drawn to scale).

At both speeds the flow is uniform within 0.15-m of the wall. Above y=0.15-m the flow begins to show some non-uniformity ($dU/dz \approx 2.7$-s^{-1}). This is more pronounced closer to the floor and ceiling compared at z=0-m. The reason for this non-uniformity may be the three-axis traverse. While the bulk of the traverse is downstream of the measurement location, the streamwise legs do extend to x=7.0-m. The effect of the 10-cm tall legs on the flow is obviously greater closer to them, but almost non-existent at z=0-m. Apart from this non-uniformity the flow at both the high and low speeds appear to be uniform.

The implications of the non-uniformity from the three-axis traverse is not dire for our purposes. For the velocity measurements, data was collected close to x=7.0-m where the effect

of the traverse is not evident. In the case of the pressure measurements, the traverse is not installed in the wind tunnel so it is expected that the flow would be uniform over the bulk of the wall and out to y=0.305-m.

3.3 Homogeneity of the Flow

The rough wall turbulent boundary layer is by nature inhomogeneous. However it is possible for the flow well above the roughness tops to be homogeneous in layers parallel to the wall. This would mean that at different points along the same streamwise line (fixed x but variable z) the pressure spectrum is the same for a given frequency.

Figs. 3.3 and 3.4 presents the raw pressure spectra for different microphones mounted at the same spanwise location (x=7.0-m as shown in fig. 2.27) measuring pressure fluctuations simultaneously at 30-ms^{-1}. These plots are presented for all the surfaces tested and are representative of the results for speeds up to 70-ms^{-1}. Different coloured curves represent data from different microphones in the spanwise array and correspond to the numbers assigned to the spanwise array of microphones in figs. 2.31 to 2.35. In this way we can relate the spectrum to the microphone locations relative to the roughness elements. Note that for the multi-scale surface the spanwise I configuration (see figs. 2.31 to 2.35) is considered here. Figs. 3.3 and 3.4 also include the corresponding uncertainty band (shaded region around each line) for each spectrum.

As discussed in § 2.4.5 the data from each microphone was carefully appraised before including it in the following analysis. For instance, fig. 3.3a-b present data from only five of the seven microphones used on the intermediate and dense roughness. In both cases mic # 4 was eliminated because of the loss in resolution experienced due to the use of the 0.25-mm pinhole (see discussion in § 2.4.2). Mic #7 was not included because there was some leakage around the microphone holder due to a gap between the holder and the roughness fetch. This can be seen in figs. 2.32 and 2.33. Similarly fig. 3.3d shows that only five of the seven microphones were chosen for the multi-shape surface. Mic #1 was removed because its face was not aligned flush with the surface of the wall, while mic #6 was removed due to some leakage between the microphone holder and the roughness fetch. § 2.4.5 contains further detailed discussions on how data quality from each microphone was evaluated.

For all surfaces, in the low-frequency region all microphones have about the same spectrum, within the uncertainty. This tells us that the outer region of the boundary layer, well above the roughness tops, is homogeneous. For the smooth wall case of fig. 3.4a this agreement extends to the mid- and high-frequency regions. This means that not only is the flow over the smooth wall uniform (shown in § 3.2) but also homogeneous in layers parallel to the wall.

For the rough wall cases, the agreement in the mid- and high-frequency regions is not as convincing. There are significant variations in these inner regions of the flow suggesting that

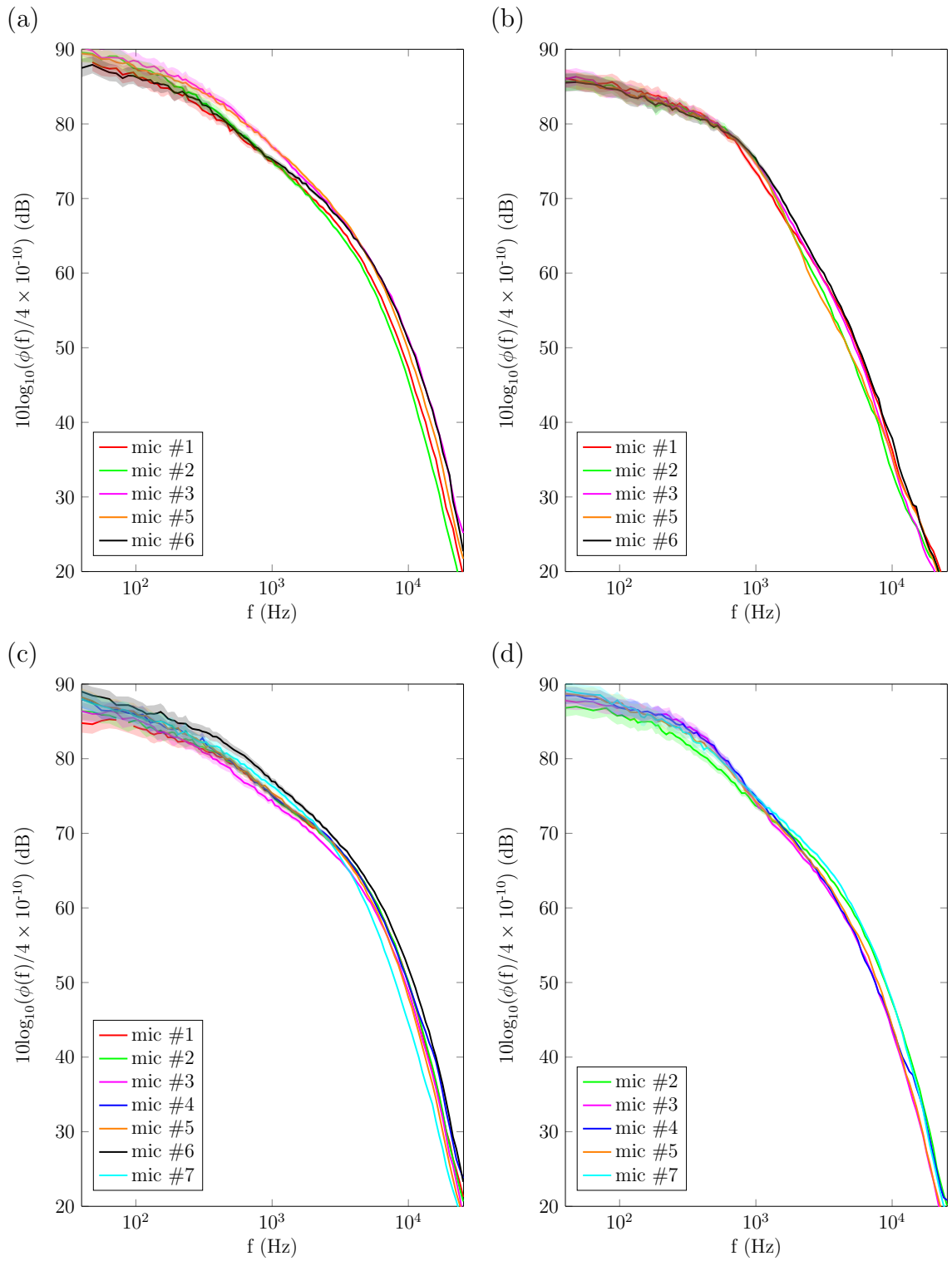

Figure 3.3: Raw pressure spectra from different microphones in spanwise configuration on the (a) intermediately-spaced rough surface (b) densely-spaced rough surface (c) multi-height surface and (d) multi-shape surface at 30-ms^{-1}

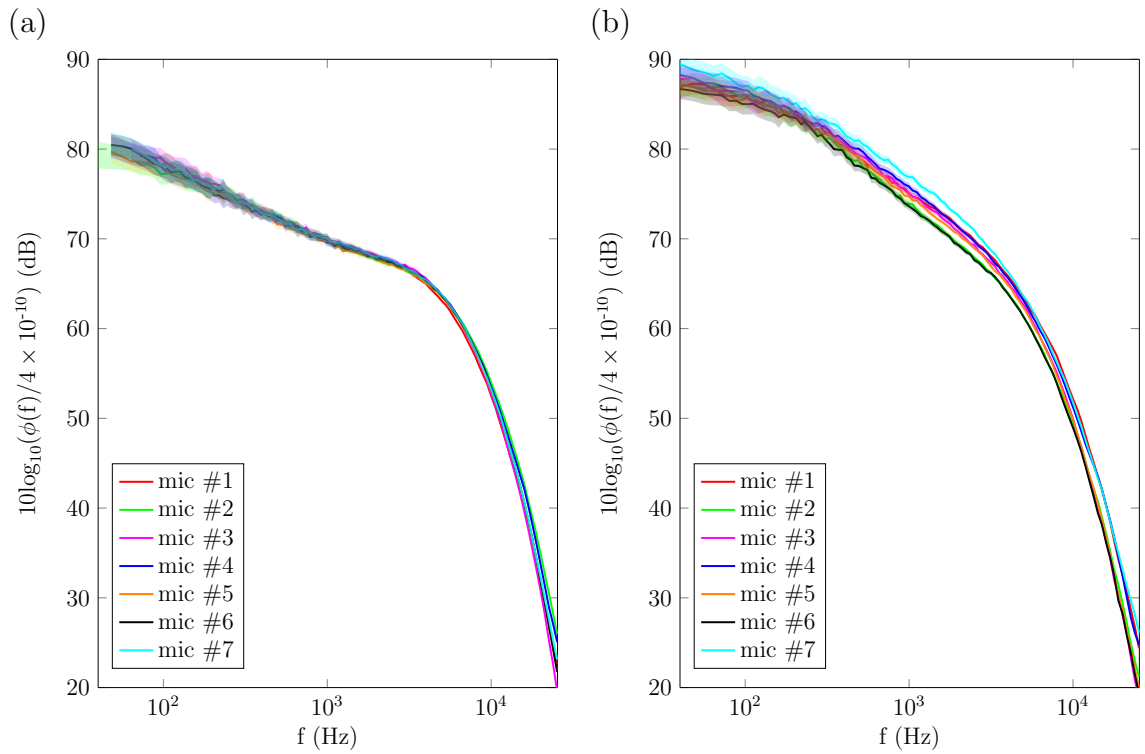

Figure 3.4: Raw pressure spectra from different microphones in spanwise configuration on the (a) smooth wall (b) cylinders at 30-ms^{-1}

the flow is non-homogeneous in these layers. This should not be surprising considering how the presence of the roughness disrupts the structures of the smooth wall flow. Furthermore, recall from § 2.4.4 that few microphones were installed in exactly the same element-relative location. A quick review of figs. 2.31 to 2.35 shows that the microphones in the spanwise configurations are typically 1 to 3-mm offset relative to the centre of a four element array. With these variations in microphone location we cannot expect to see perfect alignment of curves in the mid- and high-frequency regions. It should also be pointed out that as the sparseness ratio λ is increased (elements are more closely packed), the spread among microphones becomes larger. This is most likely because there is more complex flow features (from merged vortical structures, wakes, and separated regions etc.) on the denser surfaces than on the sparse surfaces, which means that even small variations in mic location on the denser surfaces will show significant differences in flow features. We will take a closer look at the variations in the mid- and high-frequency regions due to discrete roughness elements in § 3.7.

To account for inhomogeneity in developing universal scalings, we will consider only the averaged pressure spectrum over the spanwise microphones. The spread in microphone data shown figs. 3.3 and 3.4 is typical of the spread observed for every test run. Therefore these will not be presented in full here.

3.4 Boundary Layer Development

The boundary layer develops over the wall as the flow moves downstream. At some distance downstream, we expect the rate of development to be sufficiently slow that locally the boundary layer appears streamwise homogeneous. This means that the boundary layer profile will be about the same at different streamwise points in the flow.

Figs. 3.5 and 3.6 presents the raw pressure spectrum for different microphones mounted in the streamwise array ($\sim z$=0.337-m as shown in fig. 2.27) measuring pressure fluctuations simultaneously at 30-ms^{-1}. These plots are presented for all the rough surfaces tested and include the uncertainty band (shaded region) for the spectra. Each microphone is represented by a coloured line and the microphone numbers correspond to those defined in figs. 2.31 to 2.35. The x distance between the first and last microphone in the array is 0.8-m.

Figs. 3.5 and 3.6 show that the pressure spectrum measured by different microphones at different streamwise locations varies in the mid- and high-frequency regions. However, this variation is consistent with that of the inhomogeneity discussed in § 3.3. The variation in the low frequency region is, as before, minimal. This is true of all surfaces and tells us that within the 0.8-m measurement region the flow can be considered to be streamwise homogeneous.

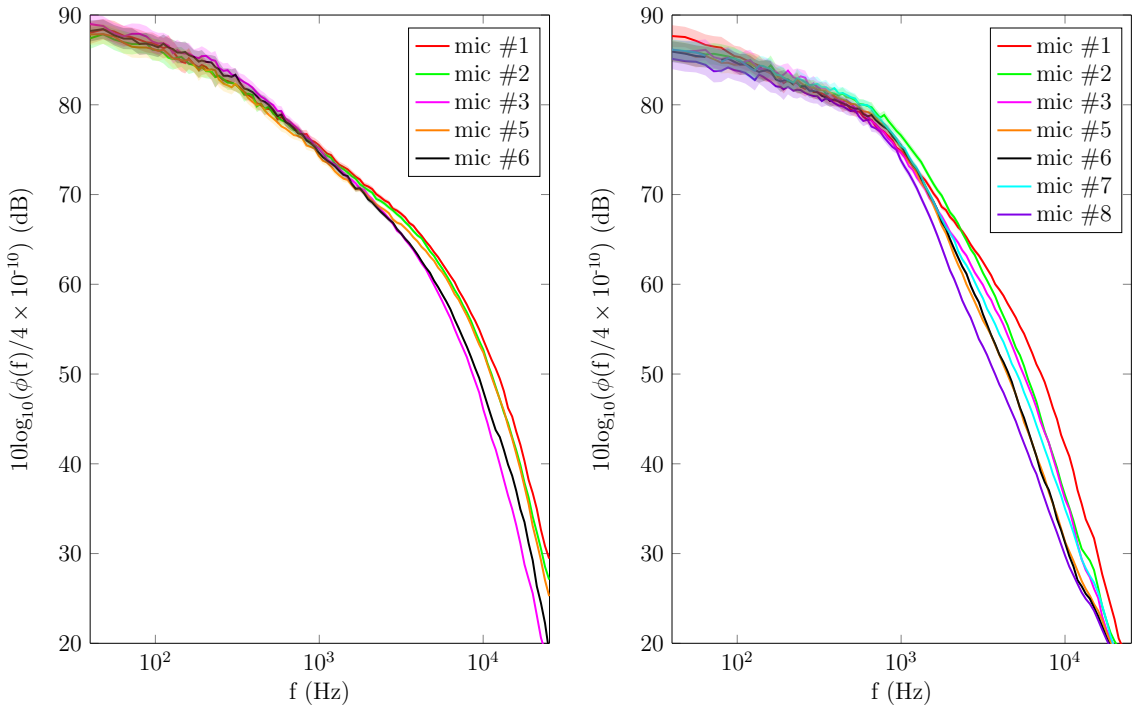

Figure 3.5: Raw pressure spectra from different microphones in streamwise configuration on the (a) intermediately-spaced and (b) densely-spaced rough surfaces at 30-ms^{-1}

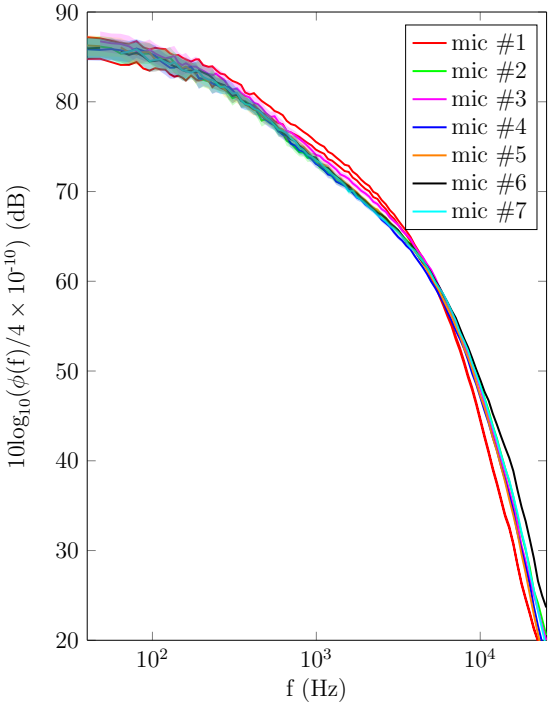

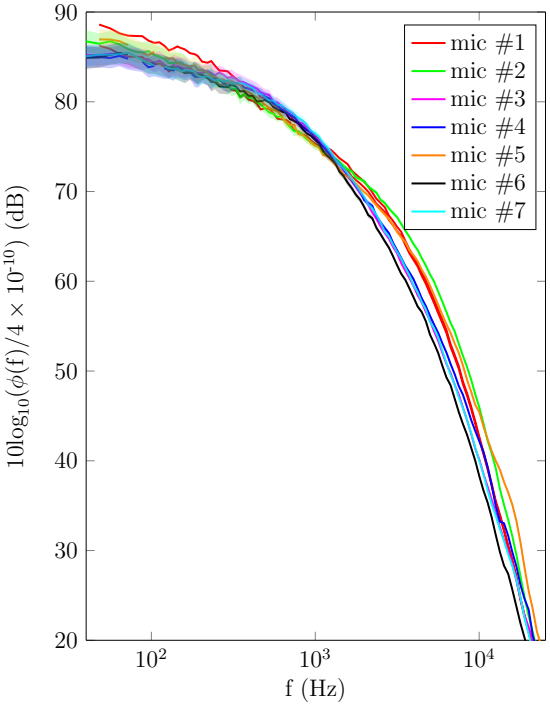

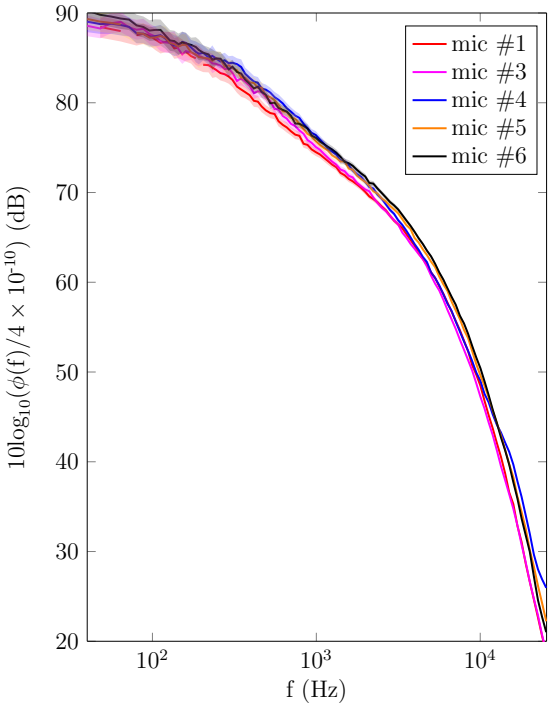

Figure 3.6: Raw pressure spectra from different microphones in streamwise configuration on the (a) cylinders (b) multi-height surface and (c) multi-shape surface at 30-ms^{-1}

Therefore streamwise and spanwise arrays of microphones should produce identical results, with some variations due to differences in microphone location relative to the elements. Recall that figs. 2.31 to 2.35 showed that the microphones in each of these configurations were installed at slightly different locations relative to the surrounding elements.

Figs. 3.7 and 3.8 presents the pressure spectra measured by the spanwise array of microphones versus that measured by the streamwise array of microphones. In these figures, the solid lines represent the averaged spectrum measured by the spanwise array of microphones. The dotted lines are the averaged spectra measured by the streamwise array of microphones. The process for averaging the data was explained at the end of § 2.4.5.

Fig. 3.7a shows the agreement between spanwise and streamwise measured spectra for the smooth wall. Not surprisingly, these agree fairly closely with a maximum deviation of about 1-dB occurring at frequencies above 20-kHz. The results for the intermediate and dense rough surfaces are presented in fig. 3.7b-c. These also show fair agreement between the streamwise and spanwise measurements with a maximum of deviation of about 2-dB observed, for both surfaces, above 10-kHz. Similar variations are seen in fig. 3.8a for the cylinders and in fig. 3.8b for the multi-height surface. The maximum deviations on these surfaces are 3-dB and 7-dB respectively. The results from the multi-shape surface is presented in fig. 3.8c-d. In fig. 3.8c measurements were taken behind the cylinder by both the spanwise and streamwise arrays of microphones. In this case the maximum deviation between the two conflagrations is 1.5-dB. and hemisphere respectively. Fig. 3.8d presents the spectra measured behind the hemispheres on the multi-shape surface. Variations between spanwise and streamwise results is at most 3.5-dB in this case.

We conclude that the deviations observed between spanwise and streamwise microphone measurements are most likely due to the differences in measurement location relative to the roughness elements.

3.5 Reproducibility & Repeatability

A test of the reproducibility of the data is only possible for the densely packed hemispheres. This was the only surface on which microphone data was collected during both test campaigns. Fig. 3.9 presents the comparison of the data from both tests. The agreement in the low frequency is good. The agreement in the mid and high frequency is less convincing but that is because the microphones were installed in different element-relative locations during the two tests. As such the mid-frequency region is affected, which in turn affects the high frequency region. Nevertheless, the slope changes occur at the same frequencies for all speeds, and the magnitude differences due to microphone location are less than 2-dB. Overall, the reproducibility of the data was considered acceptable.

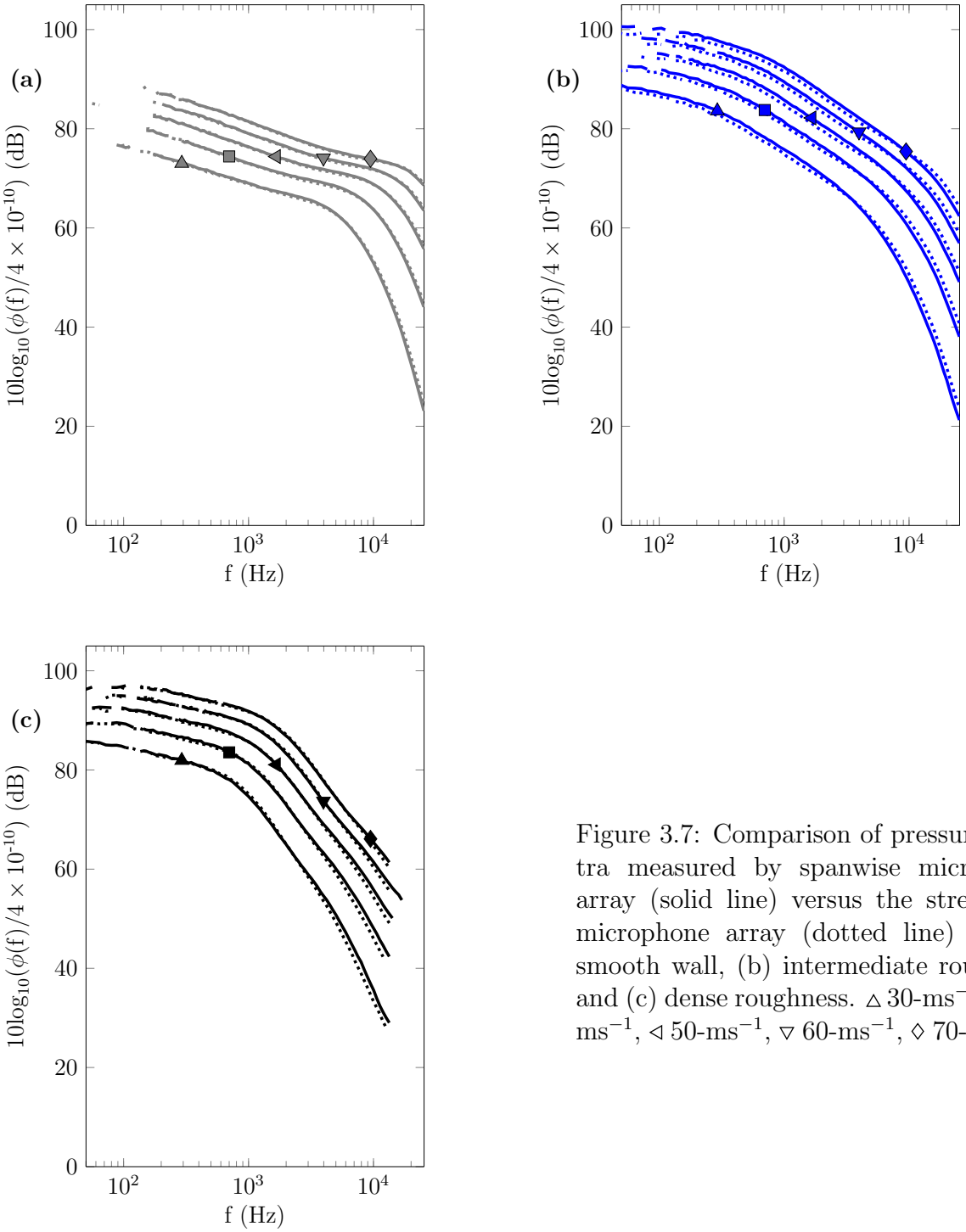

Figure 3.7: Comparison of pressure spectra measured by spanwise microphone array (solid line) versus the streamwise microphone array (dotted line) for (a) smooth wall, (b) intermediate roughness and (c) dense roughness. $\triangle$ 30-ms^{-1}, $\square$ 40-ms^{-1}, $\triangleleft$ 50-ms^{-1}, $\triangledown$ 60-ms^{-1}, $\diamond$ 70-ms^{-1}

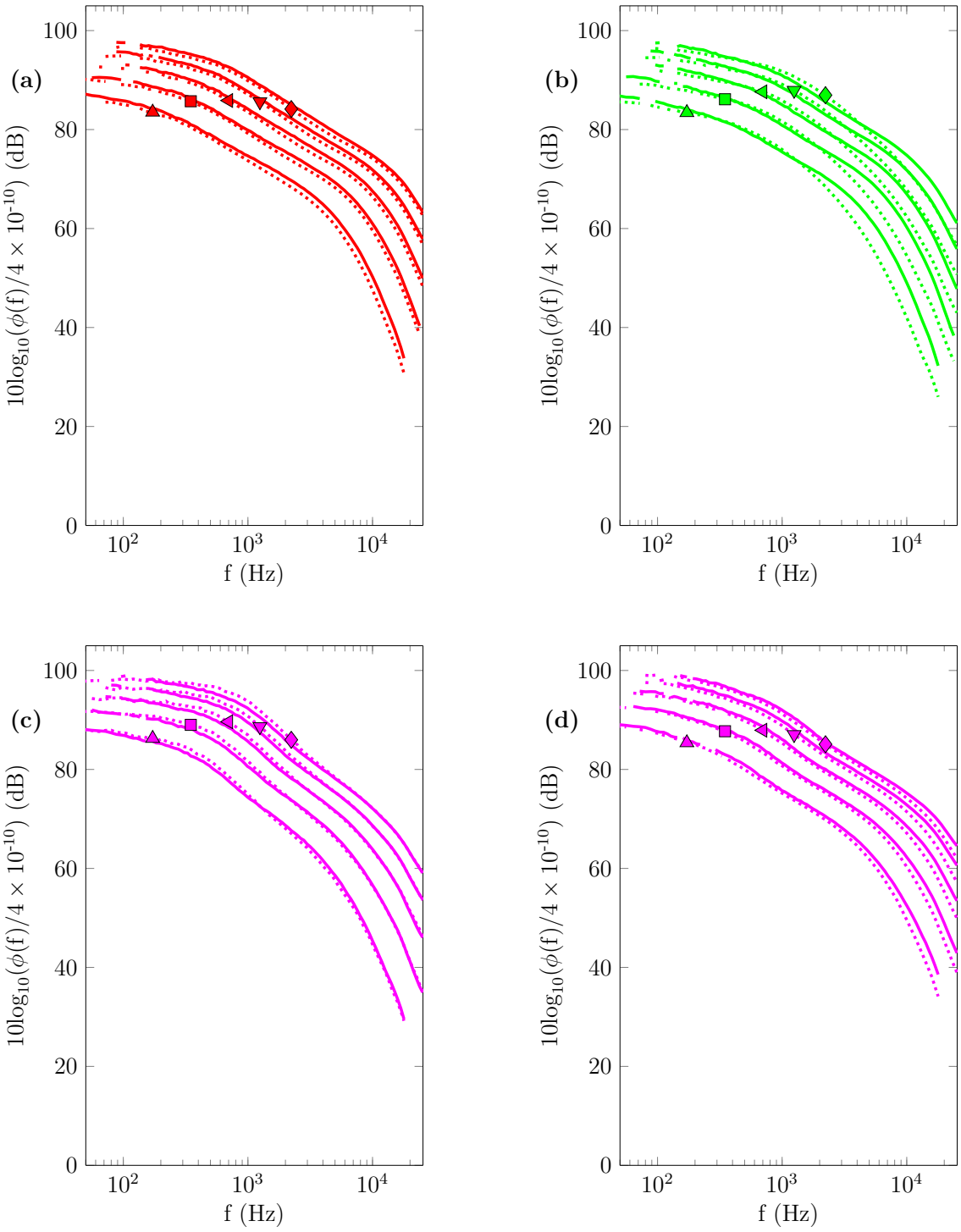

Figure 3.8: Comparison of pressure spectra measured by spanwise microphone array (solid line) versus the streamwise microphone array (dashed) for (a) cylinders, (b) multi-height surface, in vicinity of 1-mm elements, (c) multi-shape surface, behind cylinders and (d) multi-shape surface, behind hemispheres. $\triangle$ 30-ms^{-1}, $\square$ 40-ms^{-1}, $\triangleleft$ 50-ms^{-1}, $\triangledown$ 60-ms^{-1}, $\diamond$ 70-ms^{-1}

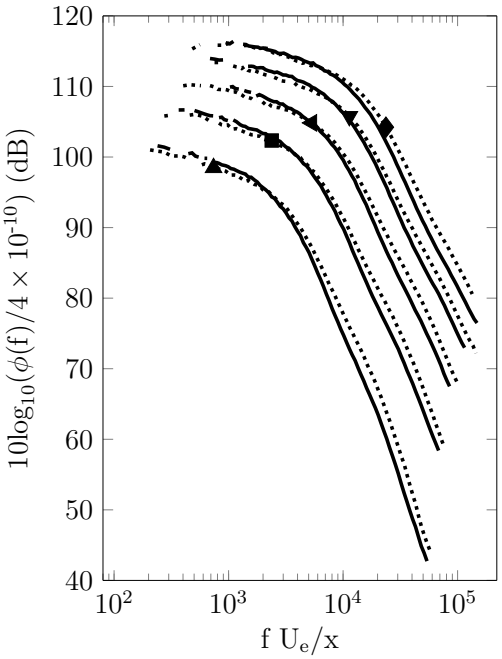

Figure 3.9: Reproducibility study showing agreement between repeated microphones measurements on the dense surface. ·····was measured during Campaign I and ——was collected during Campaign II. ▲ 30-ms^{-1}, ■ 40-ms^{-1}, ◀ 50-ms^{-1}, ▼ 60-ms^{-1}, ♦ 70-ms^{-1}

Figs. 3.10 and 3.11 present the data which was collected multiple times during the same test campaign. These data include measurements made on the dense roughness, cylinders, multi-height and multi-shape surfaces. They also include spanwise and streamwise configurations, as well as different microphone locations. Spectra are presented at speeds between 30-70-ms^{-1}. In all cases, the agreement between data taken at different times during the same test campaign is convincing. There are no significant deviations. Overall the repeatability of the measurements appears good.

3.6 Averaged Pressure Spectra

The pressure spectra measured on the smooth and rough walls in the spanwise configuration (x=7.0-m and variable z) are presented in figs. 3.12 and 3.13. These spectra have been background subtracted, binned to 12$^{\text{th}}$ octave bands, and calibrated for the effect of the pinhole cap (techniques detailed in § 2.4.5). The frequency in Hz is plotted on the x-axis and the power spectral density of pressure is plotted on the y-axis in dB.

Some of the plots of figs. 3.12 and 3.13 contain vertical lines which mark the frequency limit above which attenuation of the highest frequencies becomes important. This attenuation

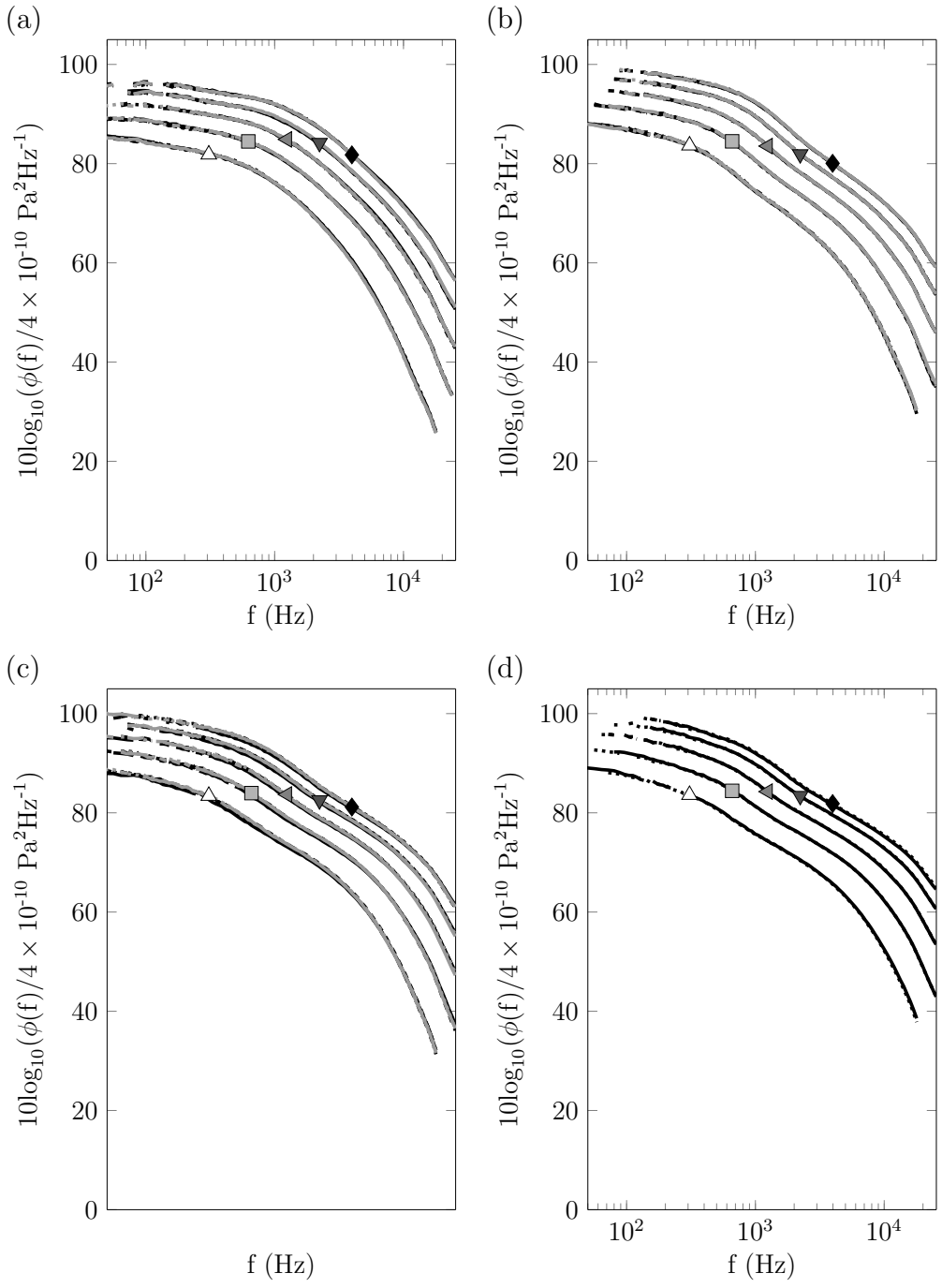

Figure 3.10: Repeatability study showing agreement between repeated microphones measurements. (a) six runs, at all speeds, on the multi-height surface in streamwise configuration (b) six runs, at all speeds, on the multi-shape surface in spanwise configuration (c) six runs, at all speeds, on the multi-shape surface in streamwise configuration (d) two runs, at all speeds, on the multi-shape surface behind hemispheres. △ 30-ms^{-1}, □ 40-ms^{-1}, ◁ 50-ms^{-1}, ▽ 60-ms^{-1}, ♦ 70-ms^{-1}

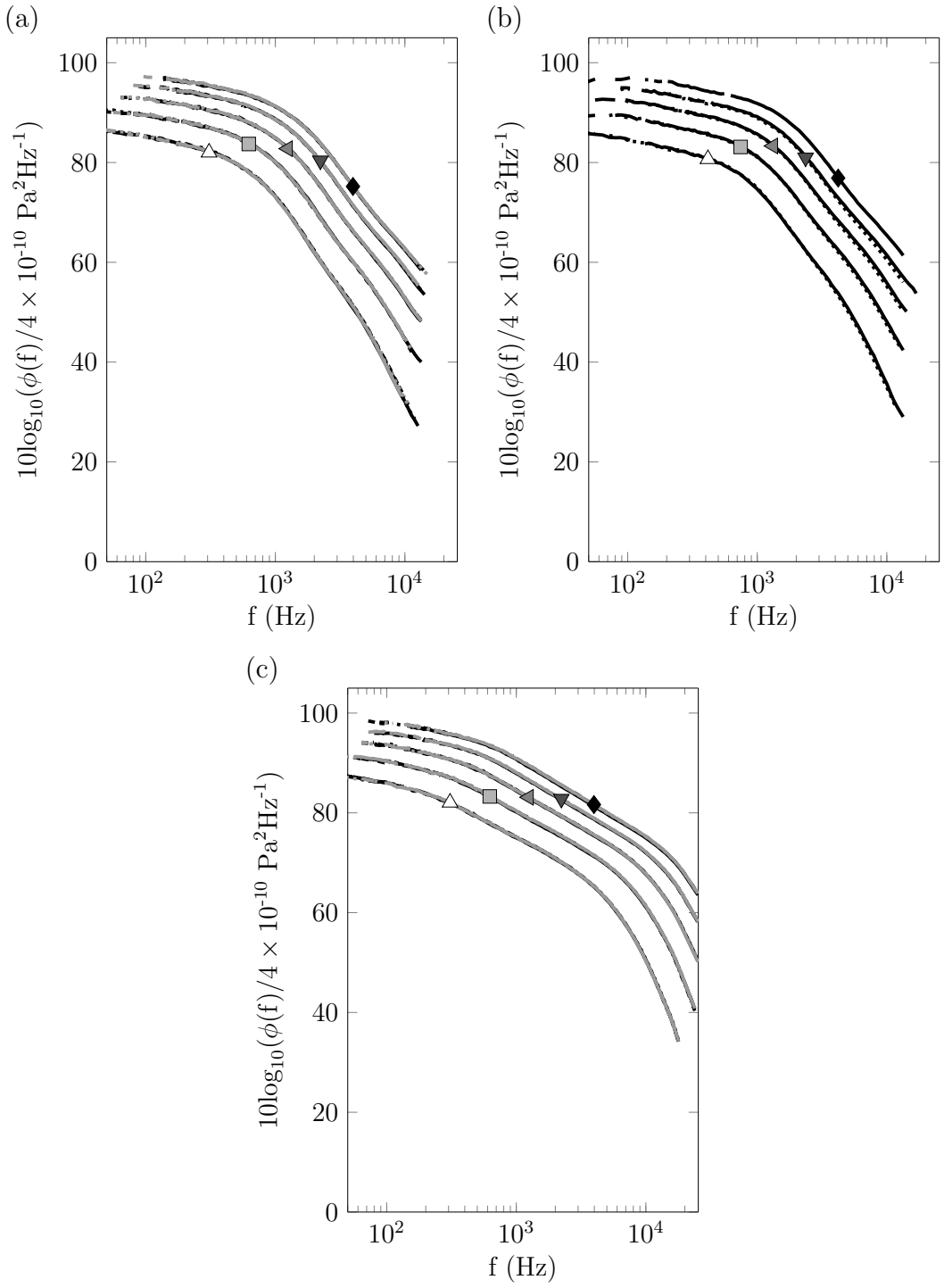

Figure 3.11: Repeatability study showing agreement between repeated microphones measurements. (a) six runs, at all speeds, on the dense surface during 2016 campaign (b) two runs, at all speeds, on the dense surface during 2015 campaign (c) six runs, at all speeds, on the cylindrical surface. △ 30-ms^{-1}, □ 40-ms^{-1}, ◁ 50-ms^{-1}, ▽ 60-ms^{-1}, ♦ 70-ms^{-1}

of the high-frequency data is due to the finite size of the pinhole which results in loss of resolution (see § 2.4.2 for in-depth discussion). At higher speeds this frequency tends to be above the Nyquist frequency and thus not shown on the figures. Refer to table 2.5 for the list of frequency limit values for each speed, for each surface. From this point the portion of the spectra above these frequency limits will be omitted from consideration.

In the case of the dense roughness presented in fig. 3.13b, an additional frequency cut-off was enforced. This cut-off was necessary because the process of optimising the calibration for changes in damping was not fully effective. Remnants of the resonant peak were present in the spectra resulting in non-physical slope changes. The spectra was carefully inspected and clipped to remove these inconsistencies. This process and the considerations made during clipping were discussed in the last paragraphs of § 2.4.3. Fig. 3.13b presents the spectra with this cut-off already applied.

Qualitatively, the general form of the spectra of the rough wall and the smooth wall is quite similar. Due to the background subtraction of the low frequency content, most of the spectra presented in figs. 3.12 and 3.13 do not capture the initial positive slope region which is typically observed at low frequencies (see fig. 1.15). Nevertheless, the shallow maximum

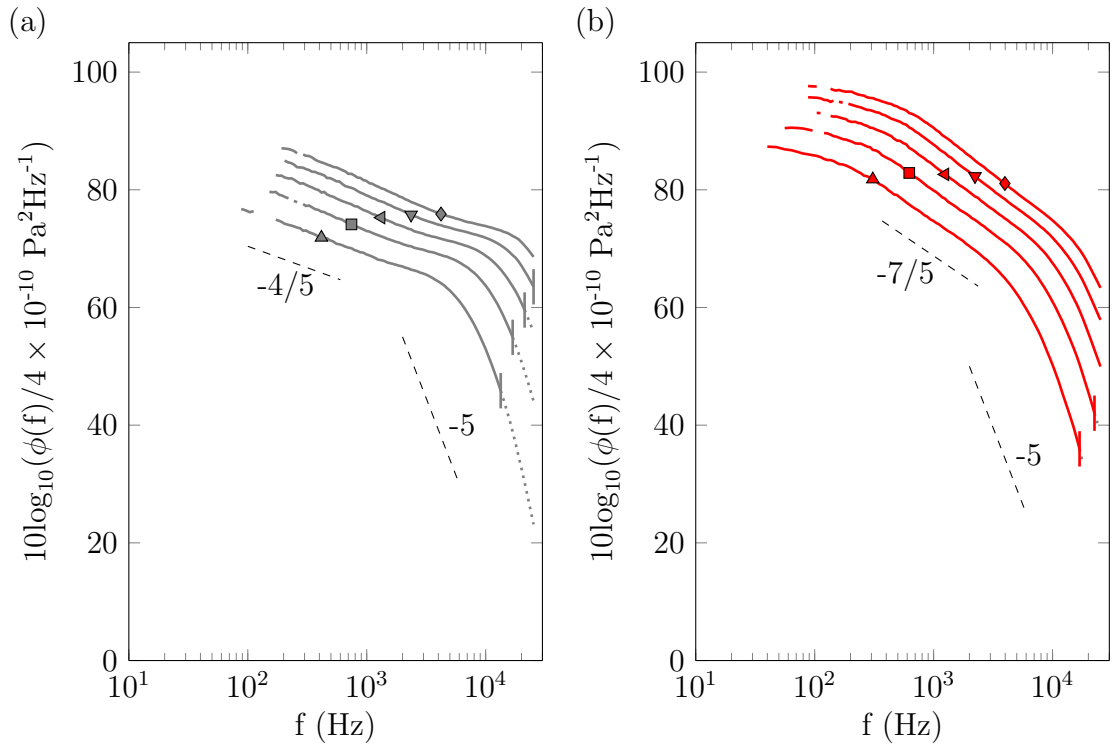

Figure 3.12: Raw pressure spectra for (a) smooth wall and (b) cylinders at △ 30-ms^{-1}, □ 40-ms^{-1}, ◁ 50-ms^{-1}, ▽ 60-ms^{-1}, and ◇ 70-ms^{-1}. Vertical lines on plot delineate the frequency limit for each surface at each speed, as outlined in table 2.5.

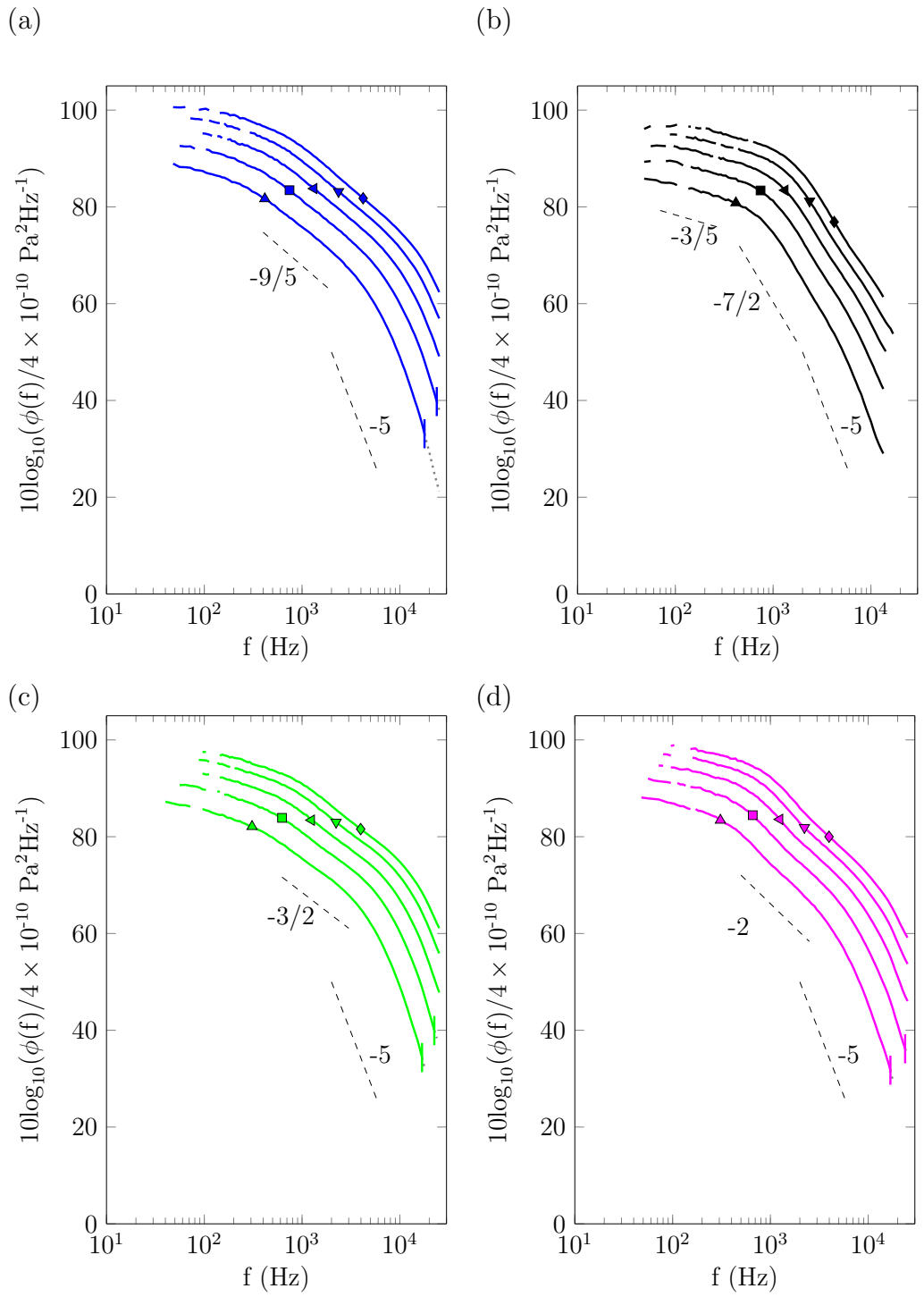

Figure 3.13: Raw pressure spectra for (a) intermediately-spaced rough surface (b) densely-spaced rough surface (c) multi-height surface (in place of 1-mm hemisphere) and (d) multi-shape surface (behind cylinder) at △ 30-ms^{-1}, □ 40-ms^{-1}, ◁ 50-ms^{-1}, ▽ 60-ms^{-1}, and ◇ 70-ms^{-1}. Vertical lines on plot delineate the frequency limit for each surface at each speed, as outlined in table 2.5.

after this initial increase is evident in all but the smooth wall case of fig. 3.12. We also notice that the magnitude and frequency at which this peak occurs increases slightly with speed. To the right of the peak, the spectrum begins to decrease. Then a clear change in slope is observed for all six cases, at all speeds. Again the frequency at which this occurs varies from case to case. We will define the content before this change in slope as the *low-frequency* region. The nearly constant slope region we will refer to as the *mid-frequency* region. The plots show that this mid-frequency region has quite different slopes from surface to surface, ranging from $f^{-0.8}$ in the case of the smooth wall to $f^{-3.5}$ on the densely packed rough surface. For a given surface the slope of the mid-frequency region is constant at all speeds. The mid-frequency region ends at the point where the spectrum begins to roll off under the influence of viscosity. This *high-frequency* portion of the pressure spectrum has a slope of roughly -5 on all surfaces and at all speeds. The frequency at which the roll off begins however, varies with both edge velocity and surface roughness geometry.

The existence of the -5 slope region at high frequencies is supported by figs. 3.14 and 3.15. The spectra in these figures have been pre-multiplied by f^5. This is based on the fact that the power law relationship is constant on a logarithmic scale with a slope equal to the index of the power relationship. Hence pre-multiplying by $f^{\text{-slope}}$ will result in any region with that slope appearing as a flat line. Figs. 3.14 and 3.15 shows that in the case of all surfaces, the very highest frequencies (above 10-kHz) level off to a shallow maximum or roughly flat region. While the identification of -5 regions is not unequivocal in all these plots, it is also important to bear in mind the uncertainties in this region associated with the (up to 2-dB) effect of pinhole resolution.

We can do the same for the mid-frequency region, using the slopes identified in figs. 3.12 and 3.13. We define m_{mid} as the mid-frequency slope. The pre-multiplied plots are presented in figs. 3.16 and 3.17. The smooth wall and surface of cylinders presented in fig. 3.16 both show an almost completely flat line in the mid-freqeuncy region when multiplied by the slopes from fig. 3.12. This is also true of the intermediate roughness and multi-height surface (measured in place of 1-mm element) shown in fig. 3.17a,c respectively. The dense roughness and mutli-shape surfaces are not as well behaved in the mid-frequency region. Fig. 3.17b,d appear to show that there are multiple mid-frequency slopes for these surfaces.

It is important to acknowledge that the primary reason that these spectra show three (at least) distinct regions is because of the high Reynolds numbers at which the experiments were carried out. There is ample scale separation allowing the different frequency regions to be clearly identified. For this reason, studies done at lower Reynolds numbers may not have been able to capture distinct regions.

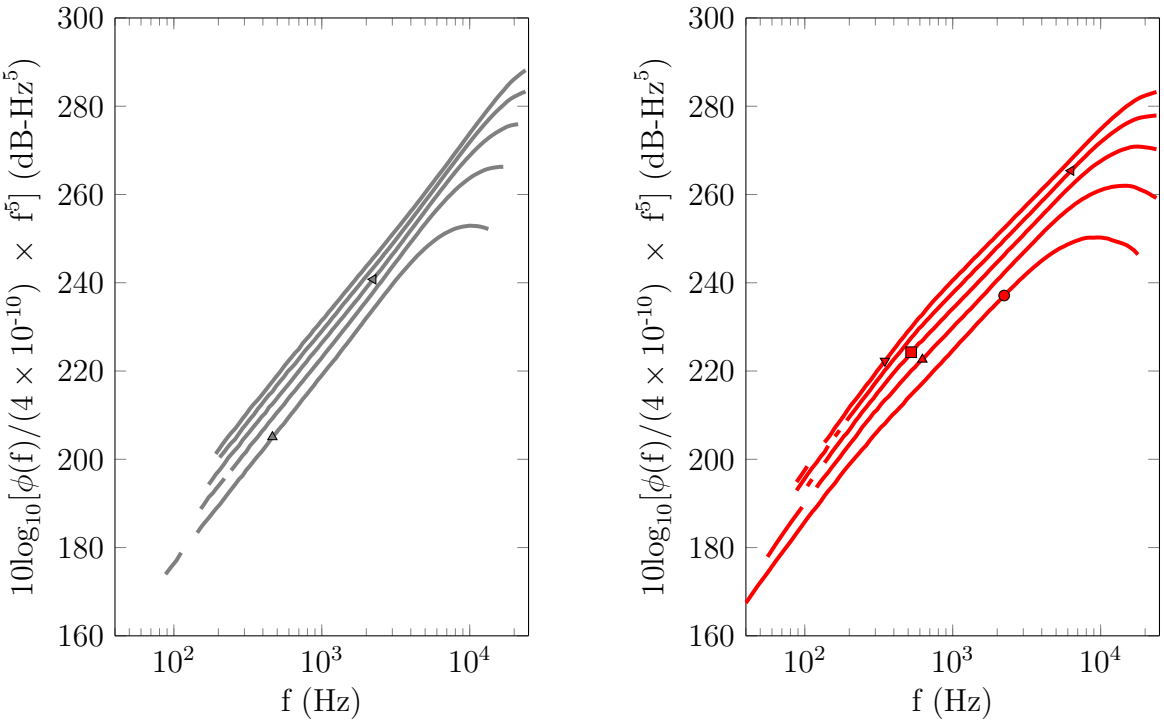

Figure 3.14: Raw pressure spectra pre-multiplied by f^5 to make high-frequency region of -5 slope apparent. (a) smooth wall and (b) cylinders at $\triangle$ 30-ms^{-1}, $\square$ 40-ms^{-1}, $\triangleleft$ 50-ms^{-1}, $\triangledown$ 60-ms^{-1}, and $\Diamond$ 70-ms^{-1}.

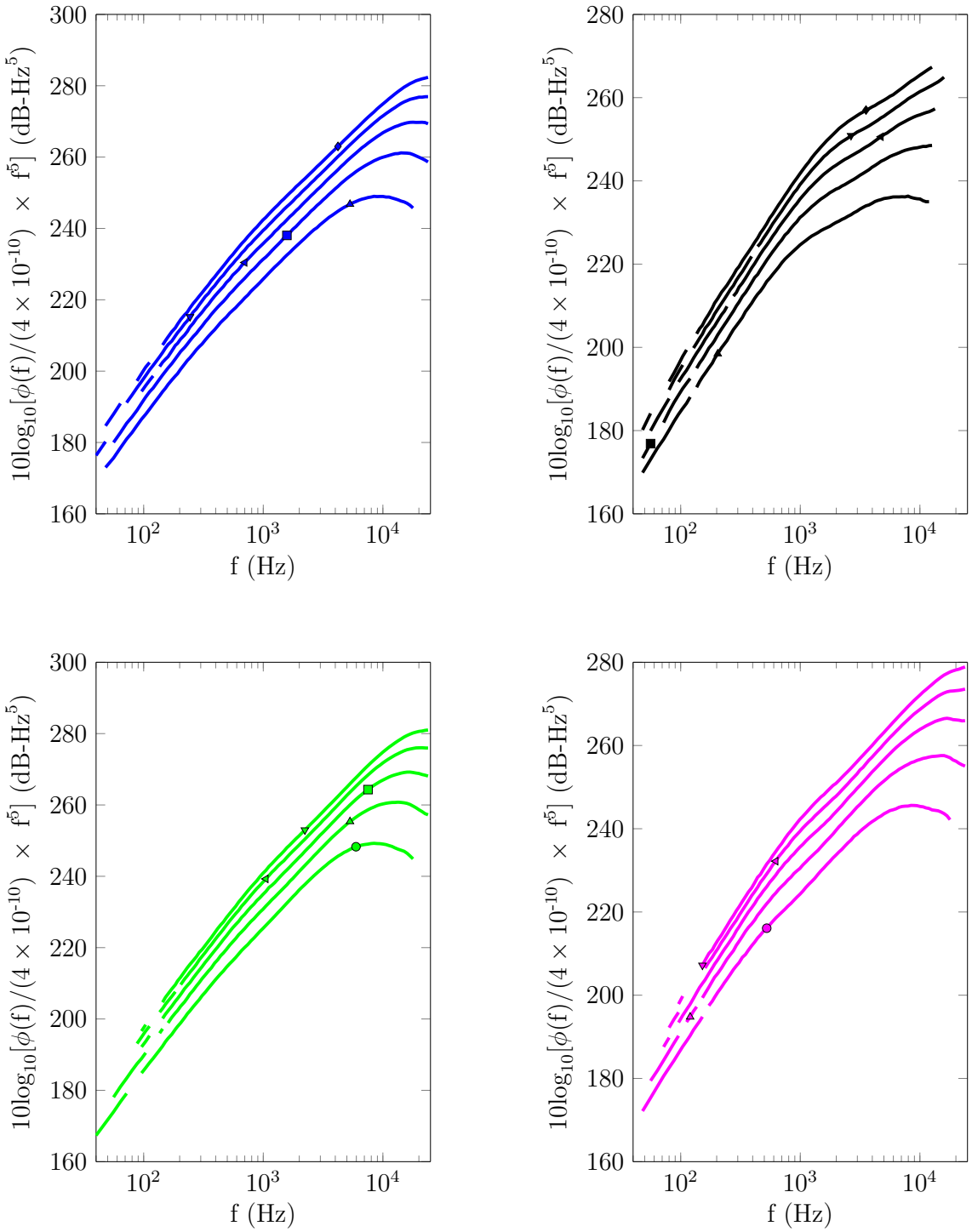

Figure 3.15: Raw pressure spectra pre-multiplied by f^5 to make high-frequency region of -5 slope apparent. (a) intermediately-spaced rough surface (b) densely-spaced rough surface (c) multi-height surface (in place of 1-mm hemisphere) and (d) multi-shape surface (behind cylinder) at $\triangle$ 30-ms^{-1}, $\square$ 40-ms^{-1}, $\triangleleft$ 50-ms^{-1}, $\triangledown$ 60-ms^{-1}, and $\Diamond$ 70-ms^{-1}.

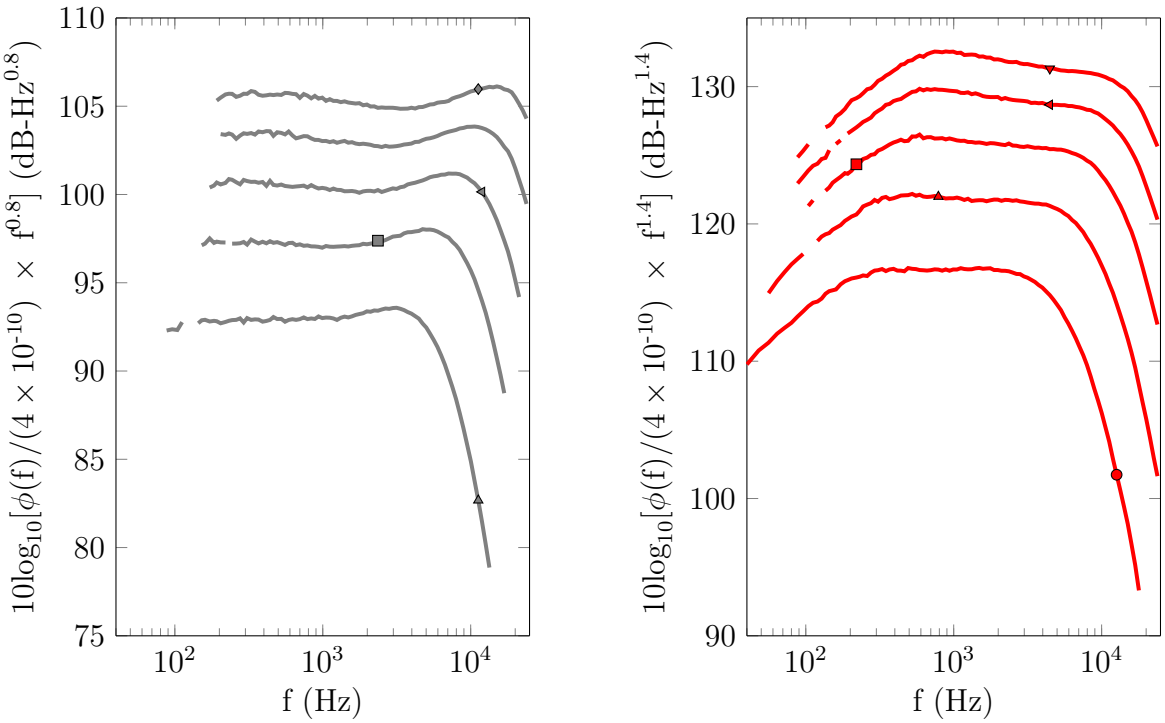

Figure 3.16: Raw pressure spectra pre-multiplied by $f^{m_{mid}}$ to make apparent the mid-frequency region of slope, m_{mid}. (a) smooth wall and (b) cylinders at $\triangle$ 30-ms^{-1}, $\square$ 40-ms^{-1}, $\triangleleft$ 50-ms^{-1}, $\triangledown$ 60-ms^{-1}, and $\Diamond$ 70-ms^{-1}.

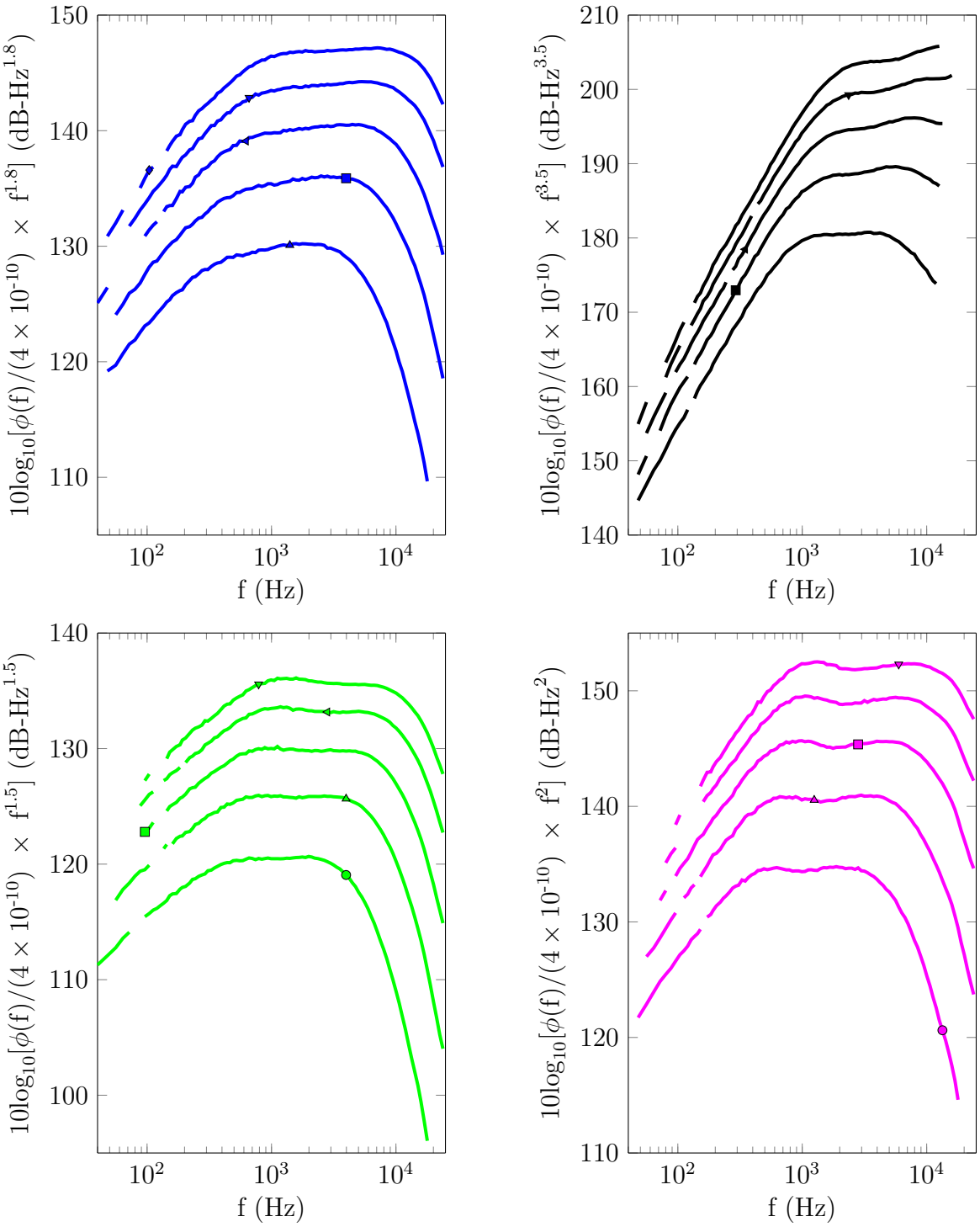

Figure 3.17: Raw pressure spectra pre-multiplied by $f^{m_{mid}}$ to make apparent the mid-frequency region of slope, m_{mid}. (a) intermediately-spaced rough surface (b) densely-spaced rough surface (c) multi-height surface (in place of 1-mm hemisphere) and (d) multi-shape surface (behind cylinder) at $\triangle$ 30-ms^{-1}, $\square$ 40-ms^{-1}, $\triangleleft$ 50-ms^{-1}, $\triangledown$ 60-ms^{-1}, and $\diamond$ 70-ms^{-1}.

The effect of speed on the pressure spectrum is to increase the magnitude and the frequency at which characteristic changes occur. For example in the case of the cylinders the mid-frequency region begins at roughly 200-Hz at 30-ms^{-1} whereas at 70-ms^{-1} it begins at approximately 700-Hz. Essentially the curves are shifted up and to the right as speed increases.

The smooth wall case presented in fig. 3.12a is distinct from the rough wall cases in that the absolute magnitude of the spectrum is lower than that of all the rough cases, at all frequencies. This is due to the more intense pressure fluctuations on the rough walls, as discussed in § 1.7. It is also noted that the mid frequency region of this case has a slope which is much shallower than that of the rough walls - approximately $f^{-0.8}$. This existence of the -0.8 slope is proven by fig. 3.16a where we see the mid-frequency region is a flat line when multiplied by $f^{0.8}$. In addition the roll off to the high frequency is not as smooth as with the rough surfaces. There appears to be a small increase in slope before the roll off begins. This was also observed by Forest [87].

Another case which does not conform perfectly with the general form described above is that of the multi-shape surface (measured behind the cylinder) shown in fig. 3.13d. In the mid-frequency region there is a subtle change in slope, which is proven by fig. 3.17d. Initially the mid-frequency region has a slope of f^{-2}. However this decreases slightly to $f^{-1.8}$ at approximately the middle of the mid-frequency range. For 30-ms^{-1} the change is seen at 1-kHz. Fig. 3.18 plots the pre-multiplied spectra for this surface with both these slopes side by side – (a) f^{-2} and (b) $f^{-1.8}$. In Fig. 3.18a we see that the first part of the mid-freqeuncy region forms an acceptably flat line when multiplied by f^2. The second part has some positive slope. Conversely, Fig. 3.18b shows that the second part of the spectrum is almost completely flat when multiplied by $f^{1.8}$ while the first half has some negative slope. This representation of the spectra makes it clear that there is actually a slope change occurring and the mid-frequency is made up of two regions, one of slope f^{-2} and another of slope $f^{-1.8}$. So it seems that for this combination rough surface the mid-frequency region appears to be a combination of two smaller regions of slightly different slope. This is particularly interesting as it points toward a further separation of scales based on type of roughness on the surface – two roughness scales means two mid-frequency regions. This possibility will be explored further in § 3.8.4 where we will also consider the effects of different microphone locations on this surface.

Additionally, the general form of the spectrum described above is less distinct in the case of the densely packed hemispheres. In fig. 3.13b while the low and the high frequency regions are well defined, the mid-frequency region is less clear cut. In fact there appears to be two slope changes between the low and the high frequency regions. The first region has a constant slope -3/5 (almost the same as the smooth wall case) and occurs just after the low frequency peak. Thereafter the rapid roll off of the spectrum begins. However on closer observation we notice that there is a subtle slope change in this roll-off region. The spectrum initially has a slope of -7/2 which later increases to the typical -5. The slope change is much more distinct at low speeds than at high speeds, most likely because most of the highest frequency

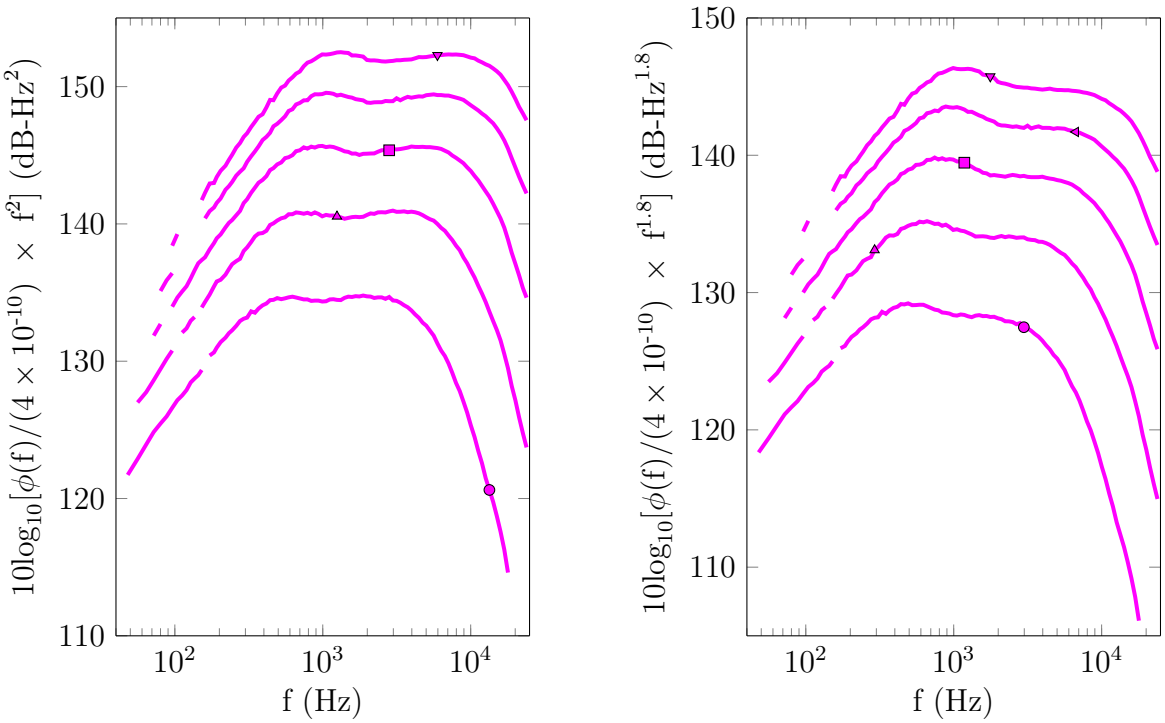

Figure 3.18: Raw pressure spectra for the multi-shape surface (behind cylinder) pre-multiplied with (a)f^2 and (b) $f^{1.8}$.

content is no longer visible within the measurement range at higher speeds. Fig. 3.17 clearly shows the differences in slope when the spectrum is pre-multiplied by the existing slope from fig. 3.13b.

A possible explanation for the slope changes is that the dense roughness, which has k_g larger than the space between elements, behaves like d-type roughness (see § 1.3.2 for detailed discussion). Vortical structures around the elements do not have room to convect downstream and evolve. In fact, they most likely remain in the cavity between elements and recirculate. The result is that the flow over the rough surfaces will essentially skim over the roughness tops and the cavity. This scenario can be thought of as a pseudo-wall existing at the roughness tops. The eddies on the order of δ and the viscous scales are unaffected by this. However, the mid-frequency region, which comprises eddies on the order of k_g, is highly impacted. These eddies are either displaced above the roughness height due to the formation of the pseudo-wall, or are trapped in the interstitial flow within the cavity where they are weakened from recirculation. Both these scenarios lead to a diminished mid-frequency pressure spectrum since eddies are either weakened or their pressure fluctuations are filtered through the layer below the pseudo-wall.

However the current scenario is much more complicated than the simplified, two-dimensional concept of d-type roughness. In our case flow is able to move around the elements and

through the streamwise channels between elements. Therefore the prospect of trapped recirculating eddies is not as likely. What is more probable is that the measured spectrum reflects the fact that the microphone on this dense rough surface is *always* in the wake of an upstream element. The complex separation zone and high shear stress which exists in the wake result in much higher mid-frequency roll off than regions outside the wake. In fact, Hopkins [24] found that for his dense roughness ($\lambda = [0.208, 0.277]$) the entire near wall region consisted of low-momentum, separated fluid. This explains why the spectrum of the dense roughness has a much steeper mid-frequency slope than the other rough surfaces. Again the eddies on the order of δ and the viscous scales would not be directly affected by this.

The idea of the pseudo-wall described above is still valid here because the element spacing is still sufficiently small that the flow has the tendency to 'ride' atop the elements. The result is a filtering of the pressure fluctuations through an additional shear layer. In this way the dense roughness behaves more realistically than idealised d-type roughness (which is governed solely by streamwise element separation) but retains some semblance of d-type behaviour.

The prospect of the mid-frequency region being sensitive to transducer location is intriguing and warrants further analysis which will be undertaken in § 3.7.

3.7 Pressure Field Around Discrete Roughness Elements

Some of the discussion of the past few sections has highlighted the prospect of transducer location being an important influence on the measured pressure spectrum. In particular, effects seem to be predominant in the mid-frequency portion of the spectrum. The following section will delve into the possible physics behind the variations in pressure field observed at different locations around rough elements on three of the five rough surfaces investigated. The cylinders and densely packed hemispheres will not be analysed because all microphones on these surfaces were installed approximately the middle of four elements. We will focus our analysis on the mid-frequency portion of the spectrum since this is where the influence of transducer location is most apparent.

Fig. 3.19 presents sections of the selected rough surfaces showing the variation in pinhole locations relative to rough elements. View is from the top and the maps are to scale. Each pinhole is coloured based on the magnitude of the pressure spectrum measured at that location relative to the other locations. As the magnitude of the spectrum decreases, the pinhole colour progresses from black to red and then green. Uncertainty values for the spectrum were carefully accounted for during the process of ranking the magnitudes of the pressure fluctuations. Flow is from left to right. This figure was developed by overlaying

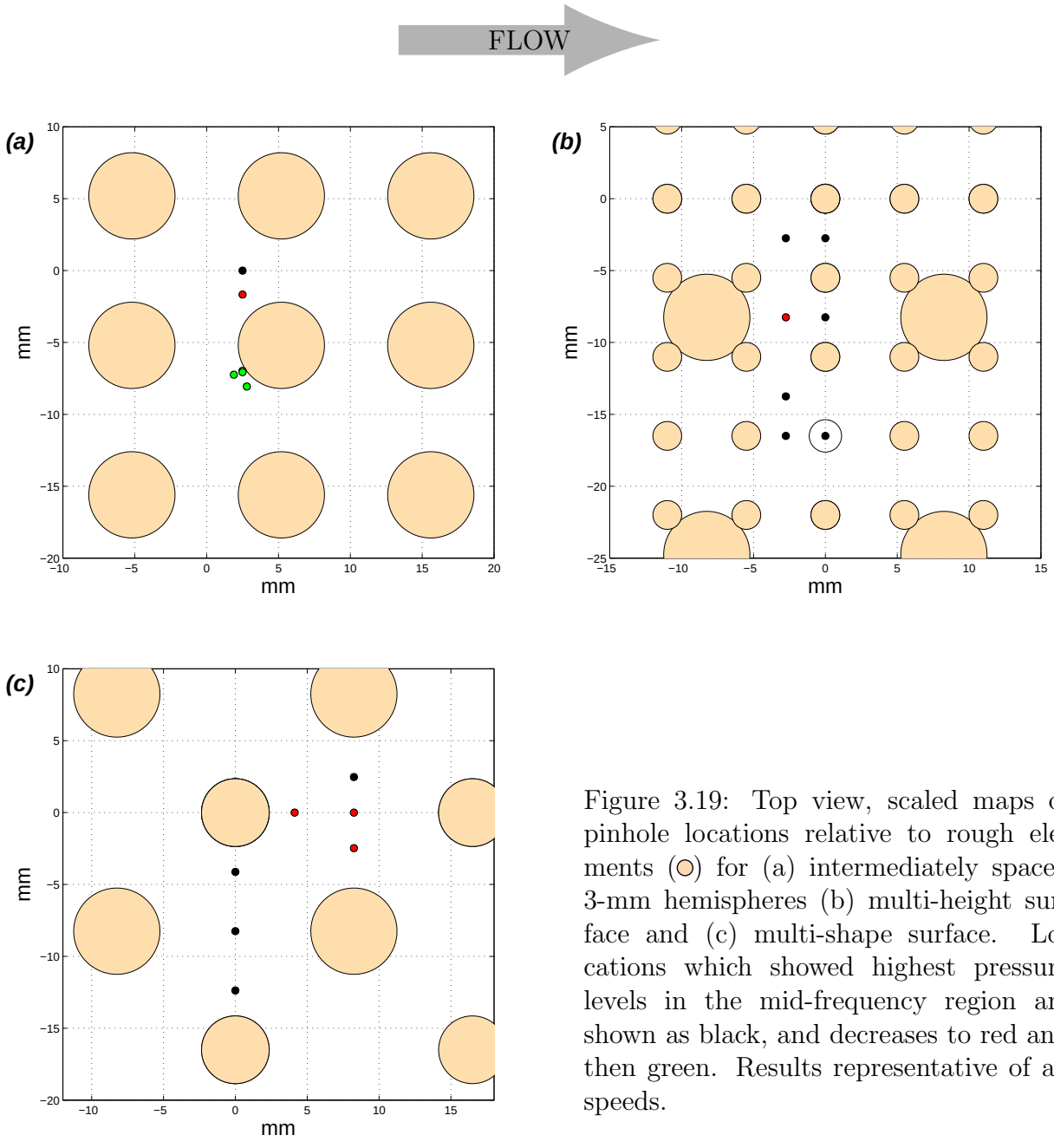

Figure 3.19: Top view, scaled maps of pinhole locations relative to rough elements (○) for (a) intermediately spaced 3-mm hemispheres (b) multi-height surface and (c) multi-shape surface. Locations which showed highest pressure levels in the mid-frequency region are shown as black, and decreases to red and then green. Results representative of all speeds.

a grid on the images in figs. 2.32, 2.34 and 2.35. In this way approximate distances could be obtained from the centre of the element to the microphone location. Based on the grid resolution used the estimated uncertainty in the locations presented in fig. 3.19 is 1.5-mm.

3.7.1 Intermediately-Packed Hemispheres

Fig. 3.19a shows that microphones were installed in three general locations on the intermediately spaced rough surface – (1) in the middle of two spanwise-adjacent elements, in-line with the front of the elements; (2) in-line with the front of the element, about 2-mm away in the spanwise direction; (3) at the front, left point of the element. The highest pressure fluctuation is experienced at location (1) in the middle of two spanwise-adjacent elements, in-line with the front of the elements. This is the pressure fluctuation which is most representative of the flow when not in the wake or separation region of an element. The lowest pressure fluctuation exists at location (3) the front, left point of the element. The pressure spectrum at location (2) lies between that of locations (1) and (3). The maximum difference between the highest and lowest pressure fluctuation level is approximately 2-dB (between locations 1 and 3).

Varano [36] measured the pressure fluctuations in this same general region relative to his hemispherical roughness. As with the present result, he found that the pressure fluctuation intensity in channels between elements was higher than aft of the hemispherical element. It should be borne in mind that Varano's sparseness ratio (λ=0.098) was slightly less than that of the intermediate roughness so there was more space between his elements. On the the other hand, the DNS results of Yang *et al.* [50] found that the power spectral density of surface pressure fluctuations in the channels between elements was actually lower at all frequencies than the results at the foot of the hemispheres. They attributed this to the locations further away from the elements being less 'perturbed' by the roughness and therefore having weaker pressure fluctuations. This discrepancy is most likely because their rough elements were very sparse (λ=0.045) and because their Reynolds numbers were relatively low. However, their results did not show a low pressure region at the foot of the hemispheres which is an expected rough-wall feature and not related to roughness density.

In fact, the existence of a small region of separated flow upstream of rough elements has been identified in both experiment and simulation. This phenomenon accounts for the region of particularly weak pressure fluctuations at location (3). There is likely an adverse pressure gradient here [53] which results in the lift up and slowing of the flow. This is closely linked to the formation of horseshoe vortices which have been widely reported at the base of roughness elements of varying shapes and sizes [29, 51, 38, 25, 52]. They exist very close to the wall and vary in size based on the size of the roughness element from which they emanate [51].

It is tempting to attribute the results of fig. 3.19a to the existence of horseshoe vortices. After all the interactions of adjacent legs of the vortices is a likely explanation for the high pressure region at location (1). However, as rightly stated by Yang *et al.* [50], it is unlikely

that horseshoe vortices exist at such a large downstream location in a fully developed flow. In all likelihood these coherent structures have evolved over the length of the wall as adjacent legs and wakes of elements merge. Add to this the fact that the elements are fairly tightly packed and we almost certainly will not have the characteristic form of a horseshoe. Yang *et al.* saw this in their DNS results – aft of the first few rows of rough elements, the horseshoe vortices were not as defined as before. This is not to say that vortical structures are non-existent. We simply cannot presume to know the exact shape and structure of these from the present data.

What we can say with some level of certainty is that the region of separated flow results in a low pressure fluctuation zone at the front base of the element. As we move away from this region, in the spanwise direction, the pressure fluctuation fluctuation rises until it reaches a maximum at the location equidistant between two spanwise-adjacent elements. This is what the map of fig. 3.19a shows, and these trends were the same for all speeds.

In scaling the pressure spectrum of the intermediately-spaced rough surface, we will average these spectra to obtain a single averaged spectrum. The reason for this choice, as opposed to treating the spectra from each location separately, is that the overall shape of the spectra at all locations were identical. There were no significant slope changes (as we found for the dense roughness at the beginning of this chapter) and the difference in pressure fluctuation levels (2-dB), despite being larger than the uncertainty, is fairly small.

3.7.2 Multi-Height Roughness

The microphone locations on the multi-height rough surface are presented in fig. 3.19b. Microphones were installed at different locations relative to both the 1-mm elements and the 3-mm elements. In most cases the microphones were in the vicinity of the 1-mm elements, except one location directly behind the 3-mm element.

Fig. 3.19b shows that apart from the microphone which was directly behind the 3-mm element, the pressure spectrum was approximately the same for all locations. This is true when the microphone was installed (1) streamwise behind the 1-mm element, (2) in the middle of four 1-mm elements, (3) equidistant between two spanwise-adjacent 1-mm elements, and (4) in the place of a 1-mm element (so that the pinhole is in the middle of four 3-mm hemispheres). Note that to achieve the latter position a 1-mm element was removed and the microphone installed in its place. The outline of the 1-mm element (empty black circle) and the pinhole in its place is shown on fig. 3.19b. So despite the specific locations being slightly different, all the microphones which are in the vicinity of the 1-mm elements have about the same pressure spectrum.

Lower pressure fluctuation is experienced directly behind the 3-mm hemisphere. This is most likely because in this location the microphone is in the wake of the 3-mm element where the flow is separated. This region of separation with strong updraft of fluid has been proposed

in conceptual models by Bennington [51], George [38], Stewart [94] and Varano [36]. The reason that the microphone installed behind the 1-mm element does not also show signs of a similar region of lower pressure fluctuation is because the wake of the 1-mm element is smaller than that of the 3-mm elements. Thus even though the microphone was behind the 1-mm element, it was most likely not in its wake.

To determine whether we can average these data, we look at the pressure spectra at these two general locations. This is presented in fig. 3.20. This figure shows that the slope in the mid-frequency region varies markedly between the spectra in the vicinity of the 1-mm elements and that behind the 3-mm element. The slope is much higher behind the 3-mm element, and varies, in the mid-frequency region, as $f^{-2.2}$. Fig. 3.21 is the pre-multiplied plots for both these locations showing that the slopes are indeed -1.5 and -2.2, respectively. As with the dense roughness we discussed at the beginning of this chapter, this slope increase is possibly because the microphone is in the wake of the element. So we will divide the spectra obtained on the multi-height surface into two groups based on these general locations. One group will be the spectrum obtained from the microphone installed directly behind the 3-mm element. The other group is the average spectra obtained from the microphones in the vicinity of the 1-mm elements. A third group can be made for the microphones which were installed in place of a 1-mm element, despite the spectra of this being about the same for as the latter group, as we can see in fig. 3.20. These three sets will be considered independently when scaling the pressure spectra of the multi-height rough surface.

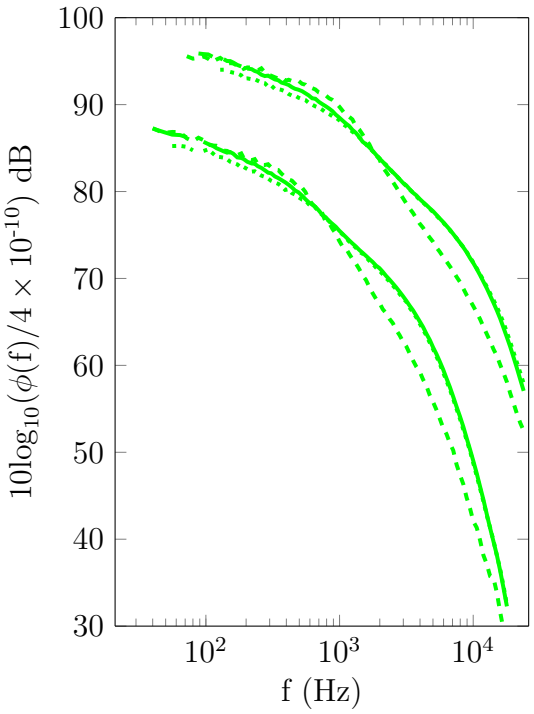

Figure 3.20: Raw pressure spectra for the multi-height surface at different locations – in place of 1-mm element (——), in vicinity of 1-mm element (·····), and behind 3-mm element (- - - -) at 30-ms^{-1} and 60-ms^{-1}.

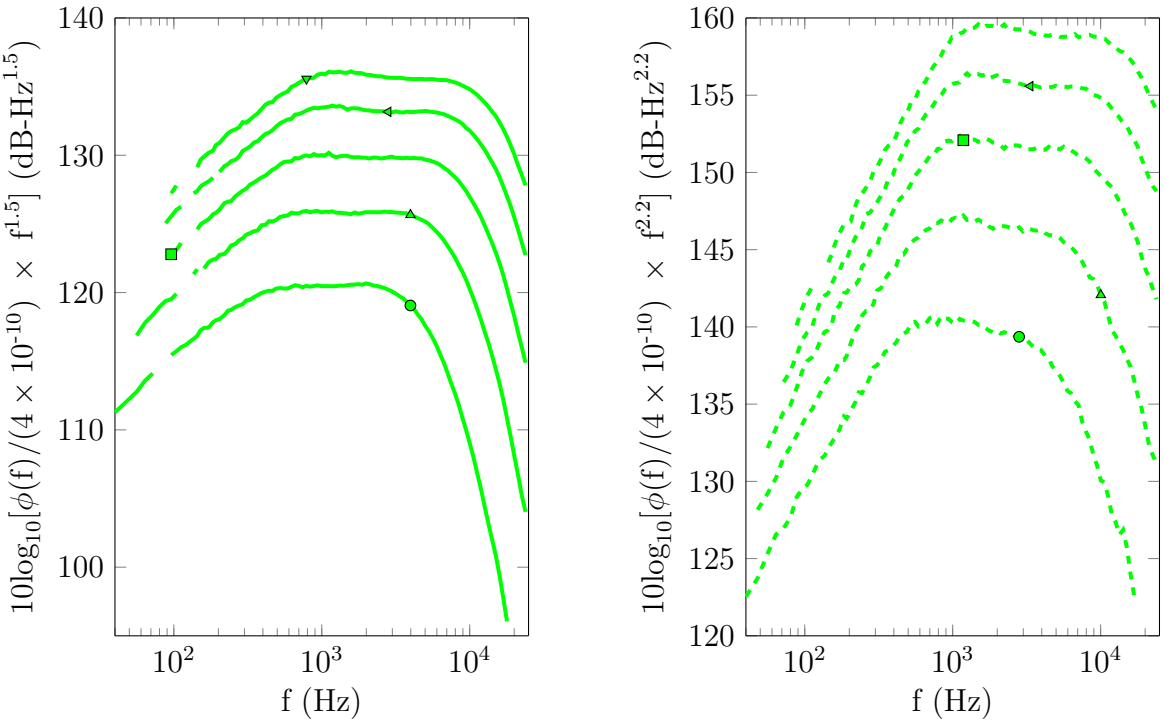

Figure 3.21: Raw pressure spectra pre-multiplied with f^2 for the multi-height surface measured (a) in the vicinity of the 1-mm elements and (b) behind the 3-mm element

3.7.3 Multi-Shape Roughness

Fig. 3.19c presents the microphone locations on the multi-shape rough surface. The larger diameter elements (6-mm) on this plot are the hemispheres and the smaller diameter elements (4.71-mm) are the cylinders. In general the microphones were installed (1) behind the cylinders, equidistant in the spanwise direction between two hemispheres; (2) behind the hemispheres, equidistant the in spanwise direction between two cylinders; (3) about 2-mm downstream the cylinders.

Behind the hemispheres the spectrum is approximately the same whether measured inline with the middle of the hemisphere, or offset in the spanwise location. These locations will therefore be averaged and treated as a single spectrum representing the pressure field behind the hemispheres. Similarly, behind the cylinders the spectrum is about the same for small variations in streamwise and spanwise locations. This is true of 3 of the 4 points measured behind the cylinders. The fourth point actually had a spectrum which was closer in magnitude to the pressure spectrum behind the hemispheres. It is interesting that the spectrum obtained 2-mm behind the cylinder matches that 5.5-mm downstream the cylinder. This tells us that the wake of the cylinder persists as far as 5.5-mm (1.2 cylinder diameters) downstream.

Fig. 3.19c portrays the locations downstream of the hemispheres as having a higher pressure fluctuation than the locations downstream of the cylinders (by approximately 3.5-dB) in the mid-frequency region. This is the opposite of what one would expect. Intuitively one would think that the sharp edges of the cylinders would generate more turbulence and push the spectral level up. In turn the spectrum close to cylinders would have more energy at high frequencies due to the added turbulence generated by the element edges. Instead the spectrum has less energy at high frequencies. The reason for the decreased pressure field aft of the cylinders, when compared to the hemispheres, is most likely because the cylinders produce greater downstream separation than the hemispheres.

Recall from the beginning of the chapter that the multi-shape surface has a unique mid-frequency region which appears to be a combination of two smaller mid-frequency regions (see fig. 3.13d). The conclusions of fig. 3.19c were made based on the maximum differences in the entire mid-frequency region, and does not necessarily capture the full effect of having multiple mid-frequency slopes. So we take a closer look at the actual pressure spectrum from each location.

The averaged pressure spectra downstream each of the cylinder and the hemisphere are presented in fig. 3.22. This figure also includes the pressure spectrum measured directly behind the cylinder as a separate line, even though this agrees well with the other data measured behind the cylinders. A fourth data set included in fig. 3.22 is the average of the spectrum from behind the cylinder with that from behind the hemisphere. Focusing on the mid-frequency region we see that data from all four 'locations' agree well initially ($400 \leq f \leq 1200$ at 30-ms^{-1} and $1200 \leq f \leq 2500$ at 60-ms^{-1}), having a slope of $f^{-1.8}$. In the second half of this region however ($1200 \leq f \leq 3000$ at 30-ms^{-1} and $2500 \leq f \leq 6000$ at 60-ms^{-1}), there is a marked change in slope. The spectra measured behind the hemispheres show decreases in slope to $f^{-1.5}$ while the spectra measured behind the cylinders show slight increases in slope to f^{-2}. It was implied earlier that this change in slope in the mid-frequency region is a consequence of the two different rough scales present on the surface. Fig. 3.22 supports this theory because it shows that the slope varies based on location relative to the different kinds of elements. Essentially, the flow around each type of element dictates the slope of the latter part of the mid-frequency region.

The fact that the first half of the mid-frequency region is independent of the shape of the roughness might mean that these relatively larger scales are governed by the size or density of the roughness, which is the same for the cylinders and the hemispheres. They are large enough to be unaffected by small variations in geometry, such as the element shape. The second half of the mid-frequency spectrum consists of smaller scales (but not on the order of the viscous scales) and so it makes sense that these would be more sensitive to the shape of the rough elements. Thus this portion of the spectrum would vary based on relative location of the transducer to the elements. Again this is an intriguing prospect which will be explored even further in § 3.8.4.

In order to scale the pressure spectra of the multi-shape rough surface, we will consider

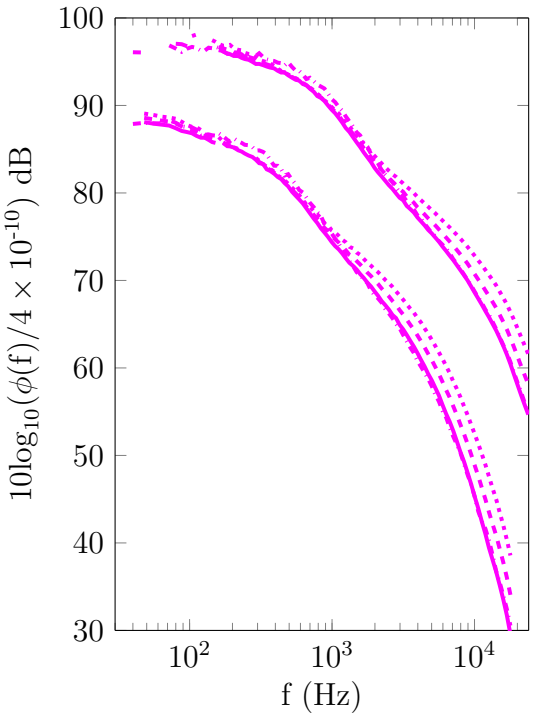

Figure 3.22: Raw pressure spectra for the multi-shape surface at different locations – behind cylinder (——), behind hemisphere (·····), average of spectra of spectra from behind cylinder and hemisphere (- - - -), and directly behind cylinder (-·-·-) at 30-ms^{-1} and 60-ms^{-1}.

the spectra behind the cylinders and behind the hemispheres independently. We will also consider the average of these two spectra and the spectra measured closer to the cylinder during scaling.

3.8 Geometry Effects on Raw Pressure Spectrum

This section examines the effect of geometric features of roughness on the surface pressure spectra. Spectra are presented at the representative speeds of 30-ms^{-1} and 60-ms^{-1}. Since these data are from different test campaigns, differences in atmospheric conditions at the time of the different tests were considered before doing comparisons. These were found to have a negligible effect on the final spectrum. Therefore, the spectra presented are not normalised in any way. In all cases, the presented spectra are averages of the spanwise array of microphones and, unless otherwise indicated, the microphones were located in the middle of a four element array.

3.8.1 Effect of Element Spacing

Fig. 3.23a shows the differences in spectral shape produced by the differences in element spacing. Data from the sparse 3-mm hemispheres of Meyers *et al.* are presented along with the smooth wall, and the intermediately and densely spaced 3-mm hemispheres.

In the low-frequency region the pressure spectrum of all three surfaces differ in magnitude. The intermediately packed surface has the highest spectrum, about 4-dB greater than the dense roughness which has the lowest spectrum in this region. At both speeds the sparse 3-mm hemispheres are closely aligned with the dense roughness, though about 1-dB or so higher in magnitude. The opposite is observed in the high frequency region where the intermediate and sparse rough surfaces show closer agreement than the dense roughness. Nevertheless, all three surfaces have about -5 slope in this region.

In the mid-frequency region the intermediate and sparse surfaces show some agreement and the dense roughness is an outlier. This is mainly due to the large difference in slope for

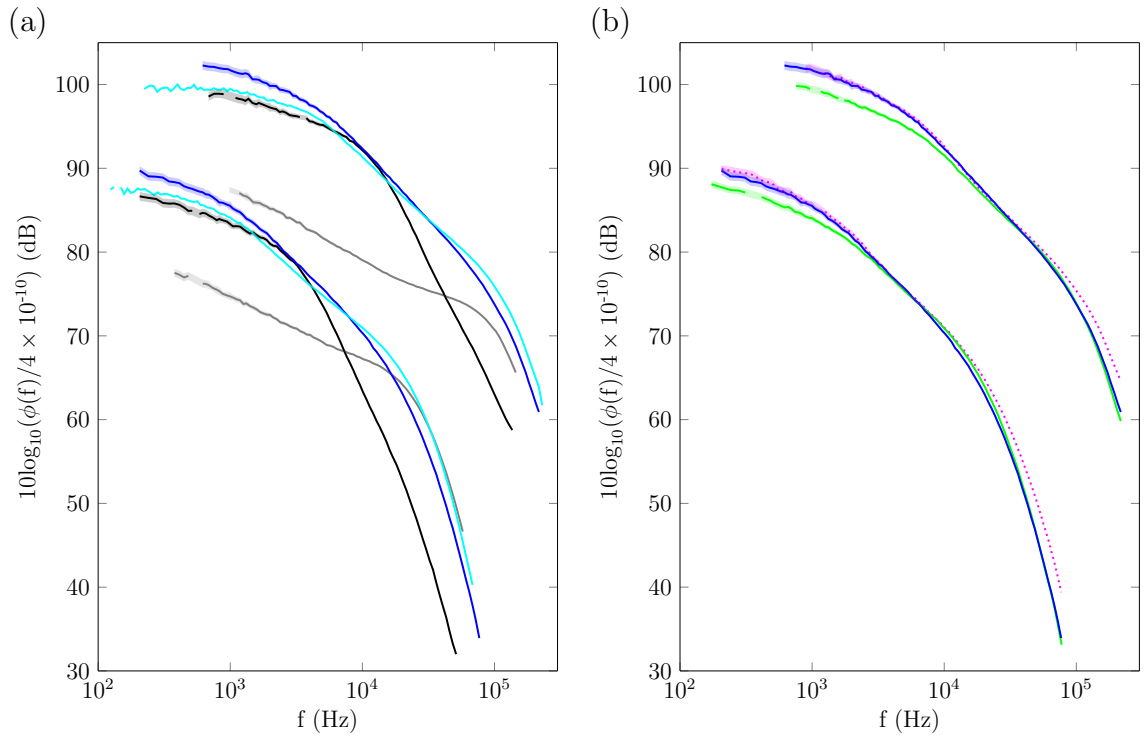

Figure 3.23: (a) Effect of varying the sparseness ratio λ on the pressure spectrum at 30-ms^{-1} and 60-ms^{-1}: smooth wall, sparse 3-mm hemispheres, intermediate 3-mm hemispheres, dense 3-mm hemispheres. (b) Comparison of pressure spectra on surfaces with $\lambda \sim 0.1$ at 30-ms^{-1} and 60-ms^{-1}: intermediate 3-mm hemispheres, multi-height surface (mic vicinity of 1-mm elements), multi-shape surface (mic behind hemispheres).

the dense roughness, as described at the beginning of this chapter. Unlike in the high and low frequency region, the slopes of all cases presented are different in the mid-frequency, the slope change being most severe with the dense roughness. This supports the hypothesis that the mid-frequency region is highly dependent on microphone location relative to the rough elements – different element density would mean different locations relative to the elements. The difference in slope in the mid-frequency then affects the high-frequency magnitude. So element density does not directly affect the scales in the high-frequency. These are only indirectly affected by the change in energy transfer (slope change) which occurs in the mid-frequency thereby affecting the amount of energy transferred to the inner scales.

An important point to note here is that the change in slope is not linearly related to the change in roughness density. The mid-frequency slope of the intermediate roughness is only slightly higher than that of the sparse surface (~ 1.4 times), while the mid-frequency slope of the dense roughness is almost twice that of the intermediate roughness.

This all points toward a threshold in sparseness ratio λ above which the flow behaviour is markedly different, much like the Dvorak-Simpson hypothesis. Fig. 3.24 shows the data from all surfaces, including the 3-mm sparse hemispheres of Meyers *et al.*, plotted with eqs. (1.36) and (1.37). Only speeds of 30-ms^{-1} and 60-ms^{-1} are presented because these are the speeds at which the quadwire data (which produced the estimates of ΔU^+) were obtained. This plot shows that the agreement of the experimental and theoretical roughness function $f(\lambda)$ is fair for all surfaces at these speeds. This further supports the Dvorak-Simpson hypothesis.

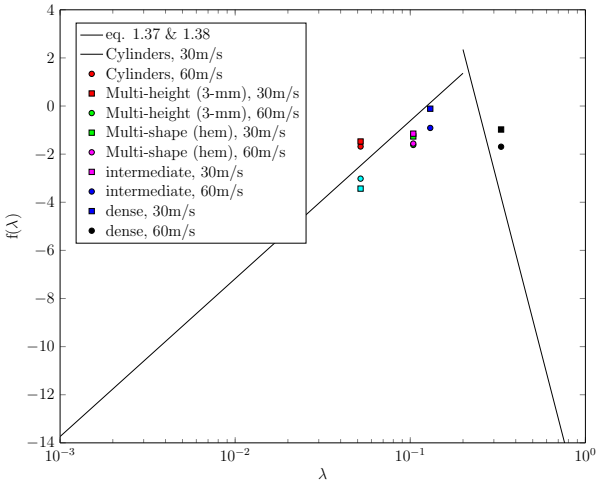

Figure 3.24: Variation of law of the wall intercept with sparseness ratio, λ.

To investigate the effect of density further, we look at the pressure spectra from surfaces which have similar λ but differ in shape and k_g. This is presented in fig. 3.23b. Here we see that the low and high frequency portions of the spectrum are different among the three plots. The mid-frequency however is almost identical in terms of magnitude and slope. It does not appear to be affected by variations in k_g or element shape, as long as λ is about the same. This is an important finding, as it tells us that the mid-frequency region is more sensitive to variations in roughness element density than changes in size and shape.

From fig. 3.23b alone it would not be unreasonable to suggest that the mid-frequency is governed exclusively by roughness element density. However, we will see in fig. 3.26 that on the multi-height surface the larger elements tend to overshadow the effects of the smaller

elements in the mid-frequency region. Thus, it is possible that k_g still plays a role in the mid-frequency which is not apparent in fig. 3.23b because the multi-height surface is dominated by the 3-mm elements in the mid-frequency. For example, we cannot be sure that a surface with $\lambda = 0.13$ (like the intermediate surface) but with uniform k_g of 1-mm would align as well as is observed in fig. 3.23b. Furthermore, the roughness shape may have a small role to play in the mid-frequency as we saw in § 3.7.3. Nevertheless we can conclude that roughness element density is, at the very least, one of the most important parameters governing the mid-frequency region.

3.8.2 Effect of Element Shape

Fig. 3.25 presents the raw pressure spectrum (normalised as in the last section) of the cylinders and the sparse, 3-mm hemispheres at 30-ms^{-1} and 60-ms^{-1}. These were obtained from averaging measurements from the spanwise microphones in middle of a 4 element array.

In the low frequency region the spectra of the different surfaces show good agreement, within the uncertainty (shaded grey area). Additionally both have similar -5 slope in the high frequency region. However the magnitude of the high frequency spectrum of the cylinders

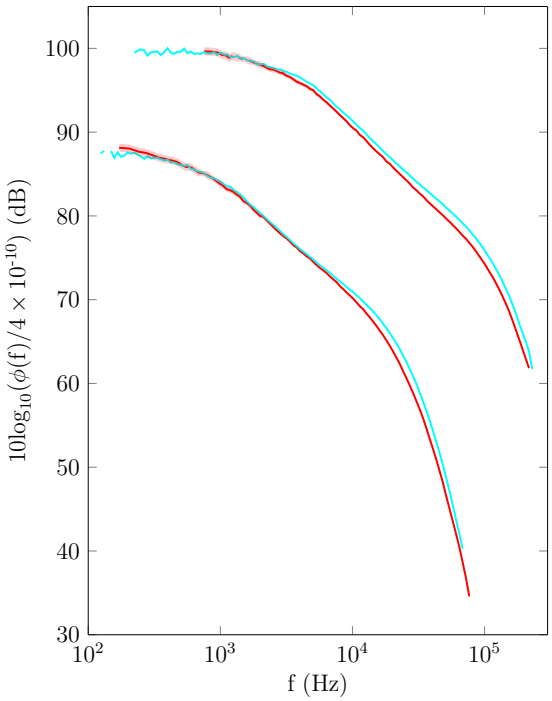

Figure 3.25: Effect of element shape – normalised raw pressure spectrum (averaged from spanwise microphones in middle of 4 element array) of the cylinders (——) and the sparse, 3-mm hemispheres (——) at 30-ms^{-1} and 60-ms^{-1}.

is lower than that of the hemispheres. This suggests that there is a fundamental change in the flow in the mid-frequency region of the cylindrical surface which causes there to be less energy transferred to the inner regions of the flow (less energy in the high frequency region). This is more likely than changes in inner flow itself because (1) the inner viscous scales are likely independent of roughness shape and (2) we would probably see a change of slope in the high frequency region if there were changes in the viscous action of the inner regions.

This brings us to the mid-frequency portion of the spectra. Here we see that there is actually fair agreement between two rough wall cases. However, on closer inspection, there is a slight change in slope which occurs such that the cylinders have a slope of $f^{-1.6}$ while the hemispheres have a slightly shallower slope of $f^{-1.4}$. The slope change is most apparent at 60-ms^{-1}.

According to the DNS studies of Yang *et al.* [52], cylindrical elements produce wider wakes than hemispheres, because the flow on the surface of the cylinder separates sooner. Furthermore, it is reasonable to assume that the edges on the cylinders induce more vortical flow (than the hemispheres) which would in turn create larger pressure fluctuations and result in a more turbulent wake. The effect of this wider, more intense wake would be to reduce the amount of energy transferred from the medium scales to the small scales, without affecting the viscous action close to the wall. This would explain small variation in mid-frequency slope between the two cases.

Another possibility is that the wider, more intense wake of the cylinders displaces the mean streamlines further upward than with the hemispheres. The consequence of this is that the flow now resembles that of a surface with more densely-packed (hemispherical) elements. Naturally this change would be small because this is only an 'effective' increase in roughness density, but it would explain the differences in mid-frequency slope in fig. 3.25 which are also small. And we know from § 3.8.1 that an increase in element density results in an increase in mid-frequency slope.

The most important conclusion is that the edges on the cylinders actually reduce the energy in the near-wall region by slightly increasing the mid-frequency slope. The low frequency content is unaffected, but the high frequency is indirectly affected due to the mid-frequency slope change.

3.8.3 Effect of Height Superposition

Fig. 3.26 presents the pressure spectrum of the multi-height surface, as well as the 1-mm and 3-mm hemispheres of Meyers *et al.* For the multi-height surface, the data presented in fig. 3.26 was collected in the vicinity of the 1-mm elements, and is an average of the measurements from the spanwise microphones at x=7.0-m.

Comparisons show that the 3-mm sparse hemispheres align acceptably with the multi-height surface in the low frequency region, while the spectrum of the 1-mm hemispheres is about

2-dB and 4-dB lower at 30-ms^{-1} and 60-ms^{-1} respectively. This suggests that the 1-mm elements have almost no effect on the outer region of the flow, when the larger 3-mm elements are present. Much the same is seen in the mid-frequency region. It is curious that the effect of roughness density is not observed in these portions of the spectrum. One would not expect the spectrum of two surfaces to be so closely aligned when one surface has twice the λ of the other. We have established in § 3.8.1 that λ is an important factor to consider in the low and mid frequency regions. This leads one to believe that the hypothesis of the outer regions of the flow not 'seeing' the 1-mm elements in the presence of the 3-mm elements is correct. To the outer regions of the flow, the surface does not have twice the λ of the sparse surfaces because it only 'sees' the 3-mm elements.

In the high-frequency region the multi-height surface shows more deviations from the 3-mm hemispheres. The spectrum of the multi-height surface is significantly lower than both the 3-mm hemispheres and the 1-mm hemispheres. Thus it appears that the flow is understandably more sensitive to the presence of the 1-mm elements in this region. The deviation can be attributed to the difference in element density between the sparse surfaces (3-mm and 1-mm) and the multi-height surface. The difference in magnitude we see between the 3-mm elements and the multi-height surface in fig. 3.26 is similar to that observed between the

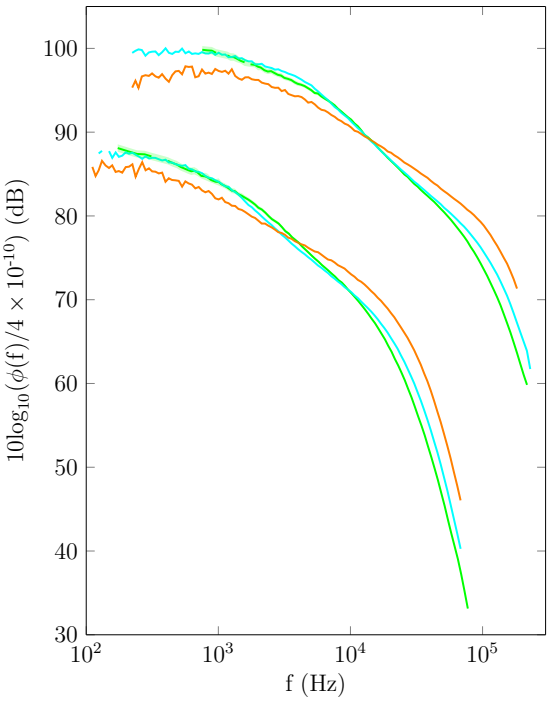

Figure 3.26: Effect of size superposition: normalised raw pressure spectrum (averaged from spanwise microphones in middle of 4 element array) of the multi-height surface (——), the sparse, 3-mm hemispheres (——) and the sparse, 1-mm hemispheres (——) at 30-ms^{-1} and 60-ms^{-1}.

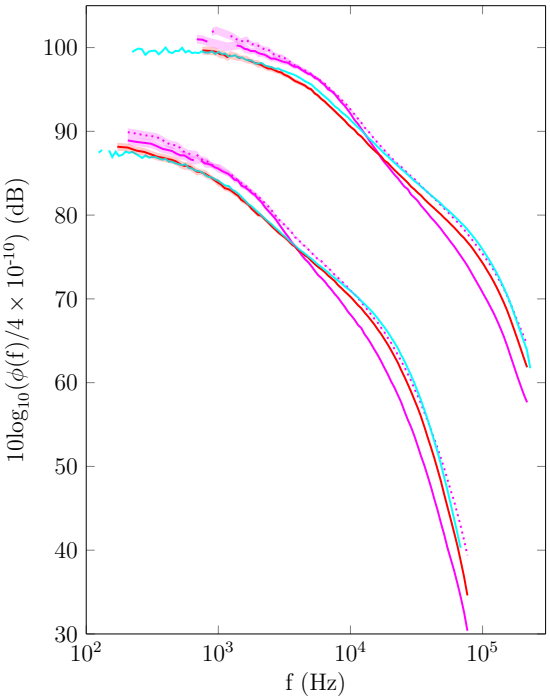

Figure 3.27: Effect of shape superposition: normalised raw pressure spectrum (averaged from spanwise microphones) of the multi-shape surface behind the hemispheres (·····); the multi-shape surface behind the cylinders (——); the sparse, 3-mm hemispheres (——); and the sparse, 3-mm cylinders (——) at 30-ms^{-1} and 60-ms^{-1}.

sparse and intermediate 3-mm hemispheres presented in fig. 3.23a.

The main takeaway here is that the larger elements on the multi-height surface appear to be the predominant source of the pressure fluctuations in the low and mid frequency portions of the spectrum. In the high frequency the effect of the increased element density begins to show as the flow becomes more sensitive to the presence of the 1-mm elements.

3.8.4 Effect of Shape Superposition

Fig. 3.27 presents the pressure spectrum of the multi-shape surface at two locations compared to that of the 3-mm hemispheres of Meyers *et al.* and the 3-mm cylinders. For the multi-shape surface, the data was collected downstream of the hemispherical elements and downstream of the cylinders, and is an average of the measurements from the spanwise microphones at x=7.0-m.

The first observation here is that the low frequency region for the multi-shape surface at both locations has a higher magnitude than the sparse surfaces. This is almost certainly due to the increase in element density of the multi-shape surface compared to the sparse

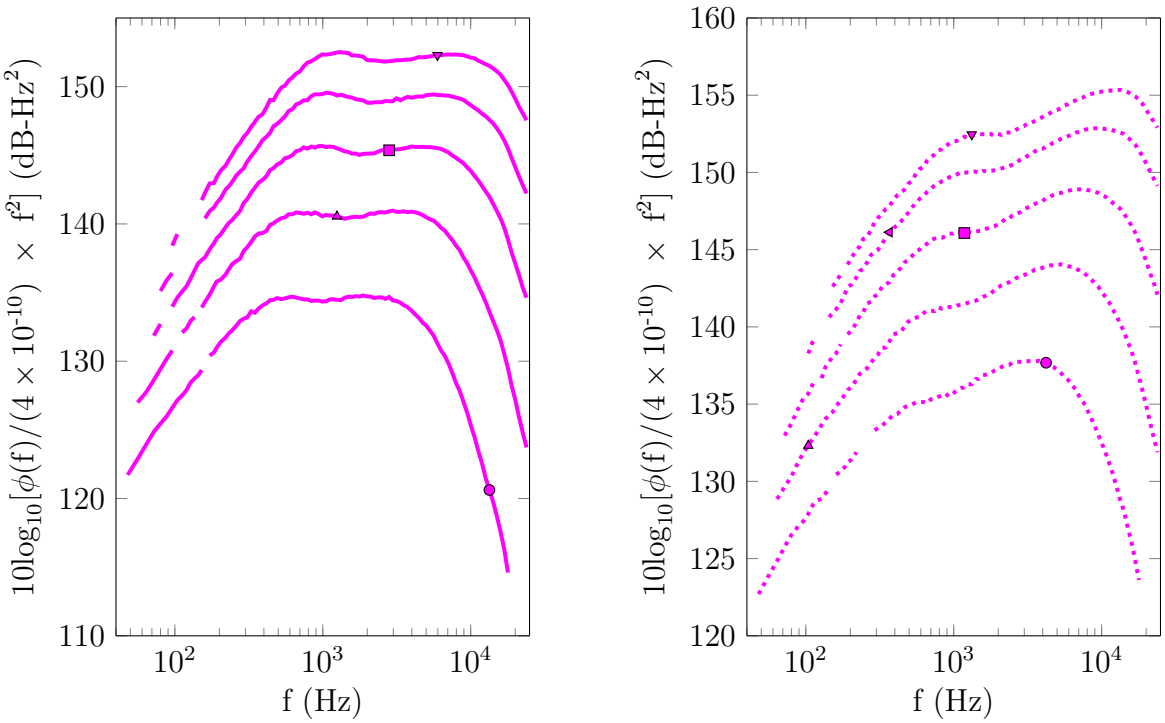

Figure 3.28: Raw pressure spectra pre-multiplied with f^2 for the multi-shape surface measured (a) behind the cylinders and (b) behind the hemispheres

hemispheres and cylinders. Fig. 3.23 clearly depicts this effect.

We have established in previous sections that the mid-frequency portion of the multi-shape surface is comprised of two smaller regions of slightly different slope. Fig. 3.28, which presents the pre-multiplied spectra for both measurement locations, proves that this is true at both measurement locations. We will call the first constant slope region of the mid-frequency (just after the low-frequency region) 'mid-frequency region I'. This portion has a slope of f^{-2}. The second portion of the mid-frequency region which connects to the high-frequency region, we will call 'mid-frequency region II'. This region has a slope of $f^{-1.5}$ when measured behind the hemispheres and $f^{-1.8}$ when measured behind the cylinders.

Fig. 3.22 and fig. 3.28 prove that mid-frequency region I is independent of measurement location. Like the low frequency region, this portion of the spectrum is the same when measured behind the cylinder or behind the hemisphere, having a slope of f^{-2}. Due to the higher magnitude in the low frequency, mid-frequency region I does not line up with the uniform surfaces at either measurement location. Furthermore, we see the characteristic increase in slope in this portion of the spectrum which is associated with increased element density (see § 3.8.1). So we see that the uniform surfaces do not align with the multi-shape surface in this region but the spectra from both measurement locations agree with each other.

On the contrary, mid-frequency region II changes slope dramatically between the two measurement regions such that they do not align at all. Fig. 3.28 clearly shows this with large differences in slope of mid-frequency region II when pre-multiplied by f^2. This means that mid-frequency region II is clearly sensitive to the scales which emanate from a specific kind of element. The spectra measured behind the cylinder have an 'effective element density' which is larger than that of the hemispheres (see§ 3.8.2) and so it has a steeper slope. However the slope difference between the two measurement location is much larger than what we observed due to element shape alone. Furthermore, we observe that mid-frequency region II of the spectrum measured behind the hemispheres aligns well with that of the uniform hemispherical surface. This is surprising considering that $\lambda_{\text{multi-shape}} = 2\lambda_{\text{sparse,hemispheres}}$. One expect that the spectra of the multi-shape surface, irrespective of measurement location, to have a higher slope than the uniform surface.

One explanation for this is that the flow in mid-frequency region II is dependent on local roughness effects. The scales in these regions are smaller in mid-frequency region I and so they are likely to be specific to the particular element from which they emanate. Therefore, the flow measured directly behind the hemispheres will look like the flow measured on the surface of uniform 3-mm hemispheres. This situation is a little more complicated for the spectrum measured behind the cylinder. For some reason the slope of these spectra do not decrease to $f^{-1.6}$ to match the uniform surface. Instead it increases slightly to f^{-2}. This could be due to the more turbulent, wider wake of the cylinders.

Apart from the differences between the cylinders and the hemispheres in the high frequency region which were detailed in § 3.8.2, the high frequency spectra of the uniform surfaces agree well with the multi-shape surface which was measured behind the hemispheres. The high-frequency spectra of the multi-shape surface measured behind the cylinders does not align with the other surfaces. This is simply because of the large slope difference in the mid-frequency region.

It is prudent to again point out that the slope changes that we observe in the mid-frequency region, which leads us to conclude that there are two mid-frequency regions, is only apparent because of the high Reynolds numbers of the current study. This means that the scales from each type of element on the surface are sufficiently separated that we are able to distinguish the two regions.

It seems what the two mid-frequency regions tell us is that the scales on the order of the k_g are dependent on roughness element density, as well as their shape and size. Because we have such clear separation of scales we are able to see that the larger of these structures are dependent on roughness density and the smaller are more sensitive to local features like shape. One might wonder why the dual mid-frequency region is not present in the multi-height surface, which also presents two roughness scales to the flow. The simple answer to this is that the 3-mm elements overshadow the 1-mm elements in the low- and mid-frequency (as discussed in § 3.8.3) which essentially means that from the perspective of the oncoming flow, there was actually only one roughness scale present.

3.9 A Final Note

We have considered variations in the pressure spectrum due to changes in roughness geometry (element size, shape and density), transducer location and the presence of multi-scale roughness on a single surface. All these have informed us that

- The low frequency region is affected by the roughness element density and size. These parameters have the tendency to change the amount of energy present in the outer regions of the flow. The slope of the spectrum is unaffected.
- The mid-frequency region is responsive to changes in the roughness element size, shape and density. There also exists a corresponding sensitivity to transducer placement in this region. Roughness element density and transducer location are closely linked as they dictate where the spectrum is measured, relative to the rough element (in the wake, in upstream separation region, in channel between elements etc.). As such both these parameters affect the slope (energy transfer) in the mid-frequency region. Likewise element shape and k_g tend to also change the slope of the mid-frequency of the spectra but the impact of these parameters is significantly smaller than that of roughness density (element density).
- The high frequency is indirectly affected by roughness element density and transducer placement, because these parameters change the slope in the mid-frequency region. Thus the magnitude of the spectrum in the high frequency portion of the spectrum is indirectly affected. However the action of viscosity is unchanged such that the spectrum in this region is always consistent with a -5 slope.

This new understanding of the flow physics is an important foundation for us as we attempt to scale the pressure spectrum in these three regions.

4. Temporal and Spatial Correlations

4.1 Coherence

The wall surface pressure spectra coherence was calculated using eq. (1.27). The processed wall-pressure cross-spectra (background subtracted, binned to 12 octave bands, and calibrated for the effect of the pinhole cap) for each microphone was used in this equation where x and y are indices of microphone locations. The resulting contours of coherence, γ^2, are presented in fig. 4.1 for the streamwise array of microphones.

Fig. 4.1 includes the coherence of wall-pressure above the smooth and rough walls at distances of up to 0.8-m (maximum streamwise microphone separation) at 30-ms^{-1}. On the abscissa is plotted the frequency, normalised on boundary layer thickness, δ, and edge velocity, U_e. The frequency limit considered is 50 – 25,000-Hz. On the ordinate is the streamwise separation between microphones, ξ, normalised on δ. For the present tests δ is typically between 220 and 240-mm. Actual values of δ for each test case are presented in table 5.12. Plotted on the right y axis are the actual microphone separations using white, dashed lines. Data between these points have been interpolated to produce the complete coherence maps. Recall that at these streamwise locations the flow is considered to be fully developed and homogeneous in layers parallel to the wall (see §§ 3.3 and 3.4).

In general, the coherence contour plots of a turbulent boundary layer have the same pattern – they are wider at the low frequencies and gradually diminish in width to a thin line as the frequency increases. This is true of all the plots presented in fig. 4.1. The reason for this shape is the differences in evolution of the different sized eddies. At the low frequency, there is evidence of streamwise coherence over the largest streamwise separations. This tells us that the larger eddies which exist in this regime persist over longer streamwise distances before evolving. This evolution can be tracked by the various degrees of coherence at a given frequency – structures are highly coherent over short distances but as they convect downstream they gradually become less coherent. Thus the diminishing coherence levels as one moves from the centreline of the plot outward toward the top/bottom. This trend itself gradually decreases as the frequency is increased. The streamwise distance over which the eddies are able to stay coherent becomes smaller and smaller. This is why the plot diminishes in width as the frequency is increased. The small scale eddies which exist in the high frequency region prove to be highly coherent but only over very short distances. These observations support the findings of past researchers [63, 76, 87], and the hypothesis of Bull and Farabee & Cassarella that the coherence of an eddy is proportional to its wavelength.

More specifically contours of coherence for the smooth wall depicted in fig. 4.1a show that for $\omega \leq$600-Hz ($\omega\delta/U_e \approx$0.7) structures are coherent ($\gamma^2 > 0.2$) over a minimum streamwise

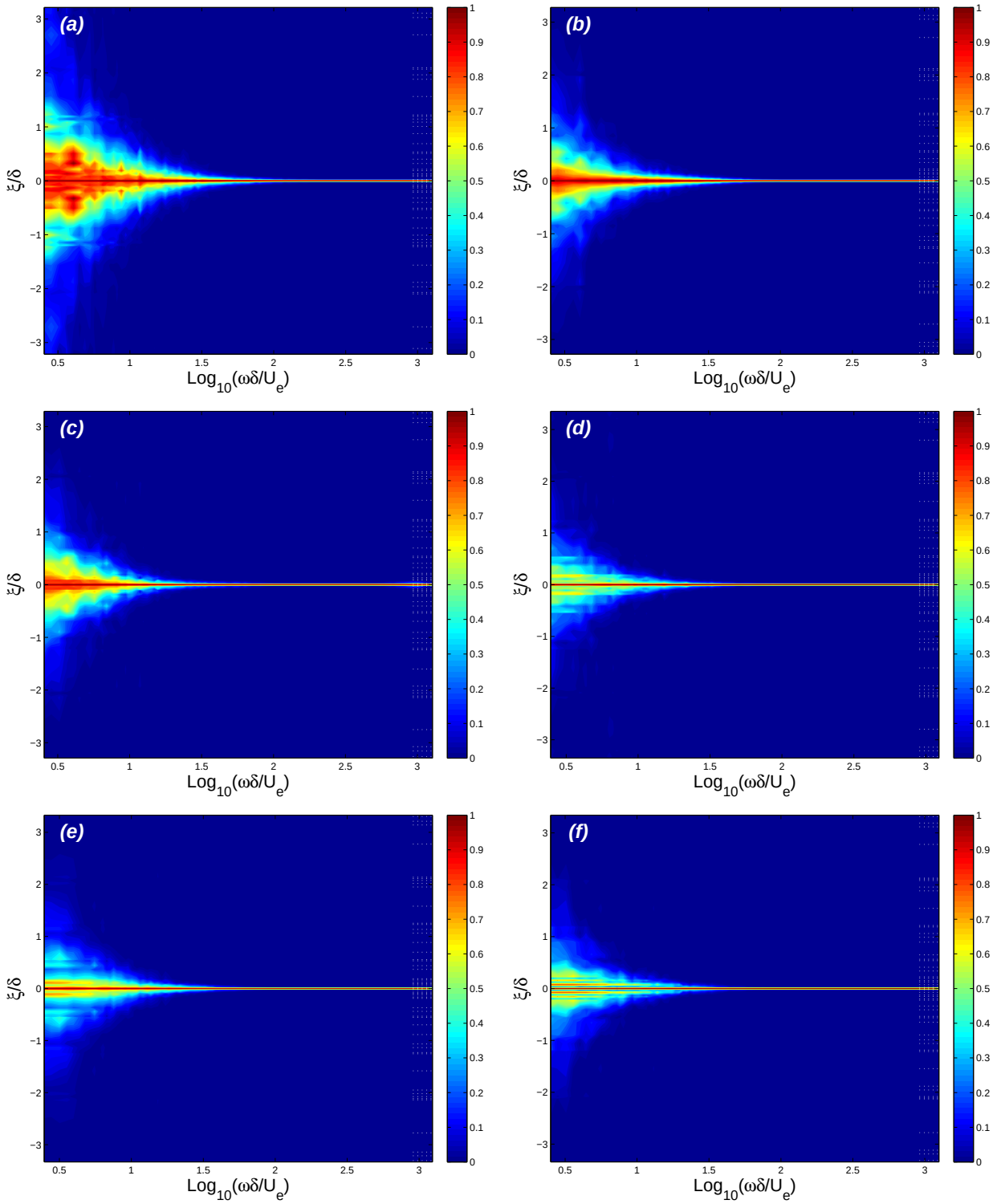

Figure 4.1: Contours of coherence, γ^2, for the streamwise array of microphones on the (a) smooth wall (b) cylinders (c) intermediately-packed rough surface (d) densely-packed rough surface (e) multi-height surface and (f) multi-shape surface at 30-ms^{-1}.

distance equivalent to δ. Larger structures at lower frequencies show coherence up to 2δ. The coherence then progressively decreases over streamwise distance with increasing frequency such that above approximately ω=7700-Hz ($\omega\delta/U_e \approx 1.8$) structures are only coherent over distances of about 2-cm.

We can compare this to the rough wall cases of fig. 4.1b-f to infer the effect that rough elements have on the evolution of eddies in the turbulent boundary layer. On all rough surfaces structures of all sizes are significantly less coherent compared to the structures over the smooth wall. The rough-wall eddies are clearly not able to persist as far downstream as those on the smooth wall before becoming incoherent. This is most likely due to the increased mixing brought on by the presence of the roughness elements. They protrude into the boundary layer essentially breaking up structures which would otherwise have remained coherent. This is the reason that the rough wall coherence contours in fig. 4.1, while having the same characteristic shape, is narrower in the low frequency and diminishes in width more quickly than the smooth wall plot.

This is most apparent on the multi-shape surface. In the low frequency the coherence even at the smallest separations ($\xi <$ 5-cm) is only about $\gamma^2 \simeq 0.8$. At a frequency about 380-Hz ($\omega\delta/U_e \approx 0.5$) structures persist to a distance just about equal to δ. Above this frequency eddies tend to lose coherence fairly quickly. At a frequency of about 2700-Hz ($\omega\delta/U_e \approx 1.35$) structures are coherent over distances of about 2-cm. This did not happen on the smooth wall until about ω=7700-Hz. The cause of the rapid loss of coherence on this surface is threefold. First, this surface consists of hemispheres as well as cylinders which have sharp edges that can break up existing eddies in the flow. Secondly, the multi-shape surface has λ=0.104. This fairly high density means that there is not just a large number of elements on the surface, but they are also closely packed. This means that the likelihood of structures around one element interacting with those of neighbouring elements is increased. This in turn causes the eddies to evolve quickly thereby reducing their coherence. Lastly, the superposition of the cylinders and hemispheres on the multi-shape surface essentially creates a staggered pattern. This, compared to the typical straight orientation, means that eddies can interact even more with the structures surrounding the neighbouring elements.

For similar reasons, the dense roughness and the multi-height surface are second in line for having least coherent structures. In the case of the dense roughness the small scale structures are more coherent than on the multi-shape surface, most likely because there are no sharp edges on the hemispheres to break them up. However the trends for the larger structures are about the same on all three of these rough surfaces.

The cylinders and intermediate surface have the highest coherence of all the rough surfaces. While these values are lower than the smooth wall, and eddies clearly do not persist for as long as is seen on the smooth wall, these two surfaces have more coherent structures than the other rough surfaces. Looking at the cylinders we see that the eddies at $\omega\delta/U_e \approx 0.5$ are preserved over a distance of about δ. These large scale structures are also more coherent for longer distances than all other rough surfaces. It is not until ω=4800-Hz ($\omega\delta/U_e \approx 1.6$) that

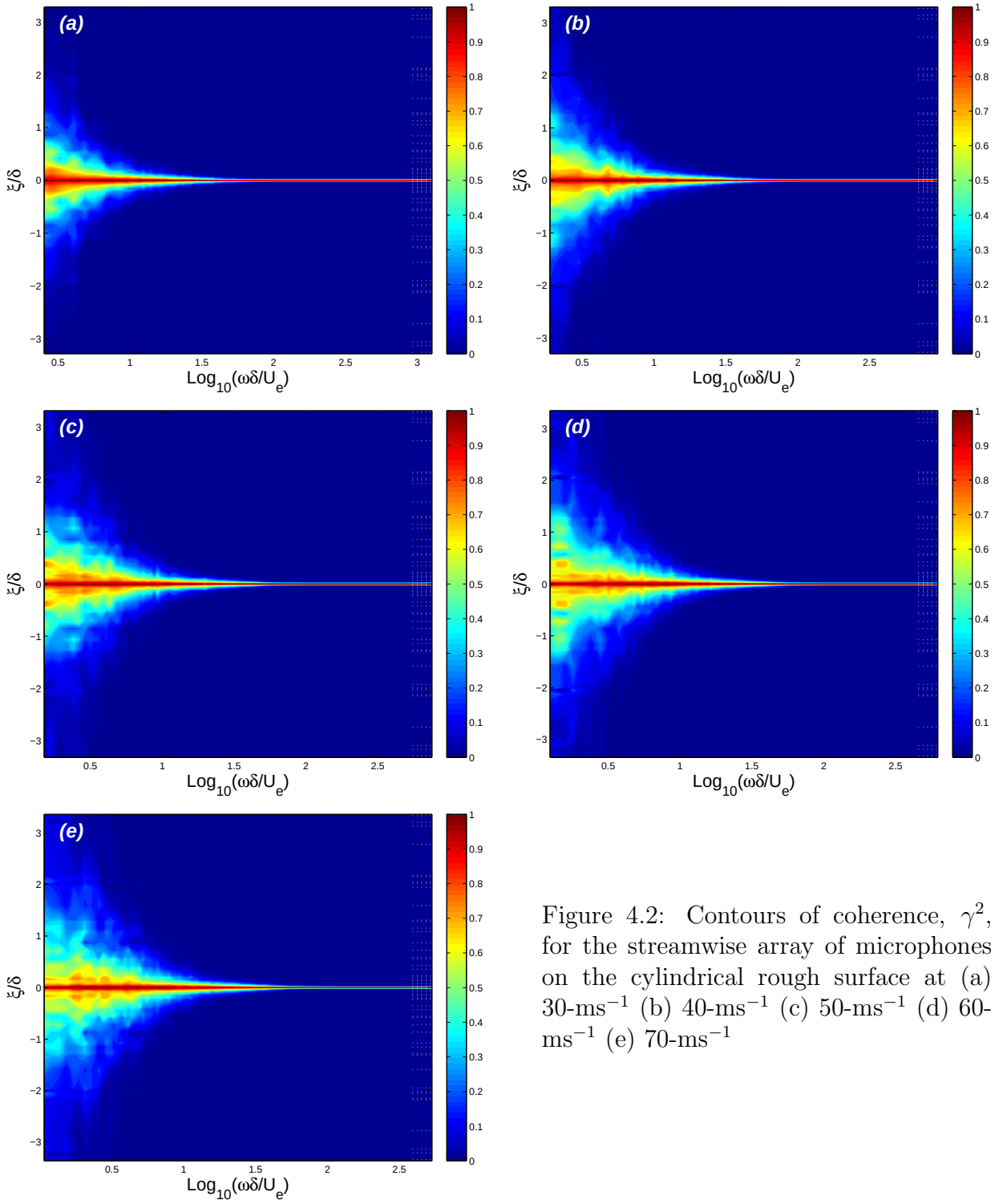

Figure 4.2: Contours of coherence, γ^2, for the streamwise array of microphones on the cylindrical rough surface at (a) 30-ms^{-1} (b) 40-ms^{-1} (c) 50-ms^{-1} (d) 60-ms^{-1} (e) 70-ms^{-1}

the eddies are no longer coherent over distances larger than 2-cm. Similar trends are seen for the intermediate surface except that the large scale structures are not able to convect as far as on the cylindrical surface before they become incoherent. Furthermore the frequency where eddies lose coherence over lengths greater than 2-cm is slightly lower (ω=3800-Hz).

The effect of increased speed on the coherence maps is presented in fig. C.4 for the representative rough-wall case of the cylinders. The primary observation is that as speed increases the eddies are able to maintain their coherent structure over longer distances. The reason behind this is that increased edge velocity means increased convection velocity which translates to larger convection distances. Additionally the increases Reynolds number means that a wider range of scales exist in the boundary layer at higher speeds.

In the spanwise direction there is rapid decrease in coherence due to increasing spanwise separation distances, η. In both the smooth and rough wall cases presented in fig. 4.3 there is no significant coherence above 0.2δ. The larger structures in the low frequency persist over this maximum distance but the smaller structures at the higher frequencies are coherent over very much smaller lengths. The results presented in fig. 4.3 for the smooth wall and the cylinders are representative of the results found on all surfaces.

The coherence maps of the full data set at all speeds, in both streamwise and spanwise configurations, can be reviewed in appendix C.

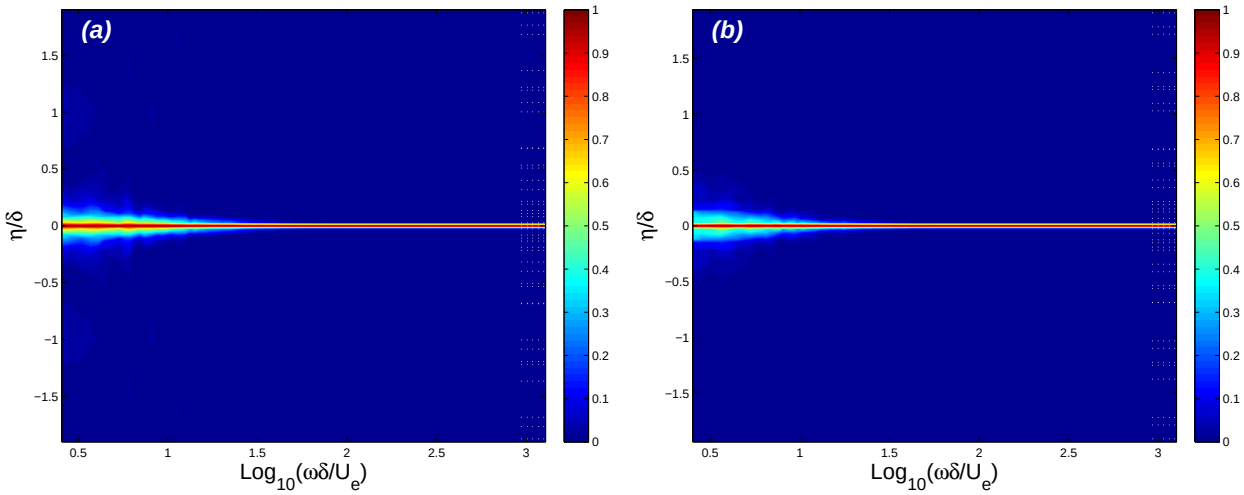

Figure 4.3: Contours of coherence, γ^2, for the spanwise array of microphones on the (a) smooth wall and (b) surface of cylinders at 30-ms^{-1}.

4.2 Space-Time Correlations

Equation (1.33) defines the the wall pressure space-time correlation, R_{pp}, between the pressure at a location x and time t, and the pressure at location $x + s$ and time $t + \tau$ in a homogeneous, stationary flow. We have proven in §§ 3.3 and 3.4 that the flows under study can be considered to be homogeneous in layers parallel to the wall. Therefore we can use eq. (1.33) to obtain contours of the wall-pressure space-time correlation.

Fig. 4.4a depicts the space-time correlations of the wall surface pressure from the streamwise array of microphones on the smooth wall at 30-ms^{-1}. In this figure streamwise separations, ξ, normalised on boundary layer thickness, δ, are plotted on the y axis. On the x axis is the time delay, τ, normalised on the ratio of edge velocity to the boundary layer thickness, U_e/δ. Again microphone separations are plotted on the right y axis of the figures as horizontal white lines.

The elongated convective ridge along the diagonal of the plot is immediately clear in these figures. These contours show that the wall pressure space-time correlation, R_{pp}, is highest for small streamwise separations ξ and time delays τ. As ξ and τ increase the structures are less and less correlated. This corresponds to our findings from the coherence plots in § 4.1. This is the expected form because, as discussed in § 1.6.2, at small ξ and τ the eddies have only travelled a short distance and have not evolved very much. Therefore structures have large R_{pp}. We can expect that the high correlation at small ξ and τ is also because both the small eddies and large eddies contribute to the correlation map here.

As ξ and τ increase the small scale structures decorrelate and no longer contribute to R_{pp}. This results in a lower magnitude of R_{pp} at the extremes of the convective ridge. The larger structures account for the correlation we see at the edges of the convection ridge simply because they are able to persist over larger distances. However, there is evolution of these large eddies as they convect downstream so they also have lower R_{pp} in general. The most strongly correlated eddies ($R_{pp} \geq 0.25$) exist within a separation distance of about 17-cm (0.75δ) while more weakly correlated structures ($0.05 \leq R_{pp} \leq 0.1$) persist over longer distances.

In accordance with the findings of Bull [111] and Choi [78], the contours at large separations are oval shaped. The average width of the convective ridge is $U_e\tau/\delta \sim 0.7$. However this increases slightly as we move from the centre of the plot toward the extrema. Since the width of the convection ridge is tied to the range of eddy sizes existing over a given distance [87], we can say that at short distances there is a large range of eddy sizes which are strongly correlated. At the edges of the ridge, where it is wider, there is a smaller range of eddy sizes which are correlated (albeit weakly) over the larger distances.

In addition to differences in magnitude of R_{pp}, the slope appears to be variable along the convection ridge. As streamwise separations ξ increase, the slope of the convective ridge with streamwise separation and time also increases. The reason behind this is that the slope

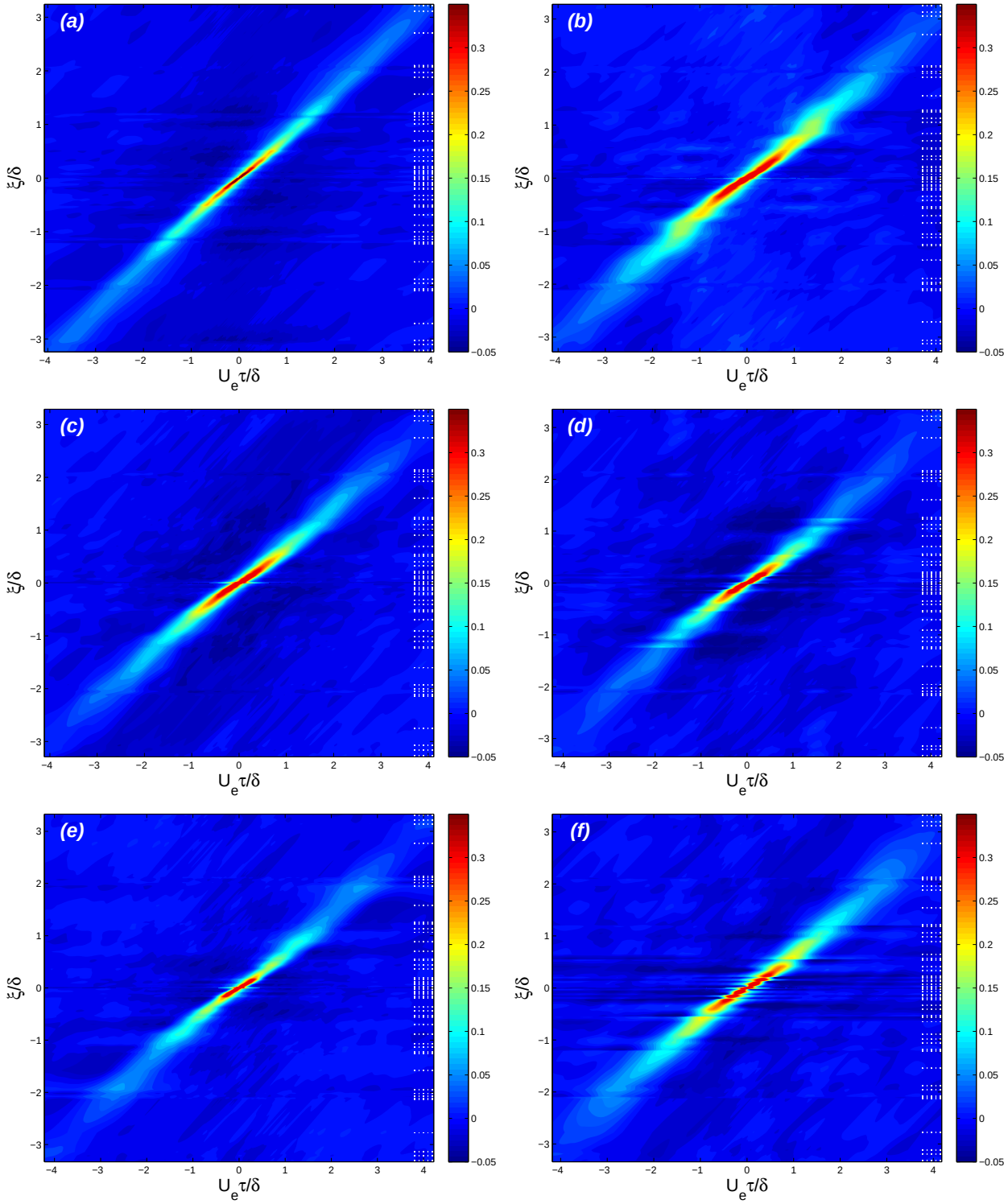

Figure 4.4: Space-time correlation of the streamwise array of microphones on the (a) smooth wall (b) cylinders (c) intermediately-packed rough surface (d) densely-packed rough surface (e) multi-height surface and (f) multi-shape surface at 30-ms^{-1}.

is a measure of the convection velocity (U_c/U_e based on our normalisation) of the respective scales. The smaller scales, which are captured toward zero time-delay, exist in the inner regions of the flow and are therefore slow-moving. This is the reason that the slope close to ξ=0 is shallow, in our case approximately $U_c \approx 0.64U_e$.

The slope increases toward the edges of the convective ridge at larger spatial separations because the eddies represented are those that are larger and exist further away from the wall where the flow velocities are greater. In our present smooth wall case, of the convective ridge asymptotes to $U_c \approx 0.864U_e$ for large streamwise spacing.

The general shape and trends of the correlation plot for the smooth wall are also characteristic of the rough wall correlation contours. However, there are some key differences in terms of the slope and the width of the convection ridge, as well as the magnitude of R_{pp} itself. Fig. 4.4b-f presents the space-time correlations of the wall surface pressure for the rough surfaces tested during campaigns I and II.

The slope of the convective ridge of all the rough surfaces is lower than that of the smooth wall case. This makes sense as the rough elements tend to impede the convection of the eddies over the wall. The slope of the intermediately packed rough surface as well as the multi-scale surfaces appear to be highest at all spacings. The densely packed surface actually has a slope that is slightly lower than that of the intermediately spaced roughness, as is the case with the sparse cylinders.

Variations in the width of the convective ridge appear to be as significant as the slope of the ridge itself. For small separations all surfaces have about the same convective ridge width, except for the cylinders which is just slightly wider in this region. The variation at the edges of the ridge are much more substantial. In all the rough-wall cases the outer width is larger than that of the smooth wall. This widening is due to the increase in the range of scales which exists over the rough wall compared to the smooth wall. The presence of the roughness elements also interferes with the convection speed of the eddies resulting in more variation in rate at which eddies advect. Thus the wider convection ridge over rough wall compared to smooth walls.

The intermediate and dense surfaces have the smallest width of the rough surfaces (they are about the same), followed by the multi-height surface. A marked increase in width is then seen on the multi-shape surface and an even wider ridge exists at the edges of the surface of cylinders. This progression tells us that the intermediate and dense surfaces do not interrupt the flow of the turbulent structures as much as one would expect. In fact, we see that these surfaces show a widening of the convective ridge over small streamwise separations but at large separations the width is fairly close to that of the smooth wall. This was also observed by Forest [87] on his sparse hemispheres. This tells us that the hemispherical roughness promotes mixing primarily in the inner layers of the boundary layer, increasing the range of convection velocities of the smaller eddies.

Furthermore, despite having at least twice as many elements as the cylinders, these denser

surfaces do not affect the convection velocity of the different scales as much as the cylinders do. The obvious reason for this is that the edges on the cylinders have the ability of breaking up and slowing down eddies as well as creating vortical flow both of which produce a varied range of convection speeds in the boundary layer. This reasoning is further supported by the fact that the multi-shape surface, which also comprises of cylinders, also has a significantly wider convective ridge than the multi-height surface, despite both surfaces having the same λ. So we surmise that the shape of the elements is more influential on the instantaneous convection velocities than the density of the elements.

The shape of the contours are quite similar for all the rough surfaces but the magnitude of R_{pp} is significantly different. Consider, for example, the highest correlated structures on each surface (the deep red streak at the centre of the convection ridge). Not only is the width of this ridge larger on the rough walls relative to the smooth wall but the extent of this band is markedly different from surface to surface. A larger region of highly correlated flow means that eddies remain correlated over longer times and distances. This is most evident on the cylindrical surface where we see that there is strong correlation ($R_{pp} \geq 0.2$) to up to ξ=32-cm. Compare this to the smooth wall where the correlation over a distance ξ=32-cm is only $R_{pp} \simeq 0.1$. The correlation on the multi-shape surface is lower than that of the uniform cylindrical roughness having $R_{pp} \simeq 0.13$ at ξ=32-cm. Curiously, the multi-height surface has a remarkably short extent of $R_{pp} \geq 0.25$, even smaller than that of the smooth wall. This is most likely because the smaller 1-mm elements create small scale structures which are only correlated over short distances. This is corroborated by the correlation maps of Meyers [103] for his 1-mm uniform surface.

The space-time correlations from the spanwise array of microphones from the smooth wall and the dense roughness at 30-ms^{-1} is presented in fig. 4.5. Spanwise separations, η, normalised on boundary layer thickness, δ, are plotted on the y axis as a function of normalised time delay, $\tau U_e/\delta$ which is on the x axis. Spanwise microphone separations are again plotted on the right y axis in white.

Flow over spanwise separations, η, appear to be largely uncorrelated and independent of time (all positive correlations lie near to the zero time delay axis τ=0). This is clear from the cases presented in fig. 4.5. This is not surprising as we saw in chapter 3 that the flow is two-dimensional. The absence of spanwise flow means that there should be no strong correlation in time in this direction. The small level of correlation that we do observe is, as rightly conjectured by Forest, due to the intermittent passage of eddies which span a certain η. For the smooth wall the highest correlation ($R_{pp} \geq 0.09$) exists within a spanwise distance of 30-mm. This tells us that eddies over the smooth wall are not elongated above this length. The presence of roughness will increase this effect such that the dense roughness shows correlations up to 0.1 over spanwise distances of 53-mm.

Again these results are representative of all surfaces and speeds, and the full set of plots for every condition can be reviewed in appendix C.

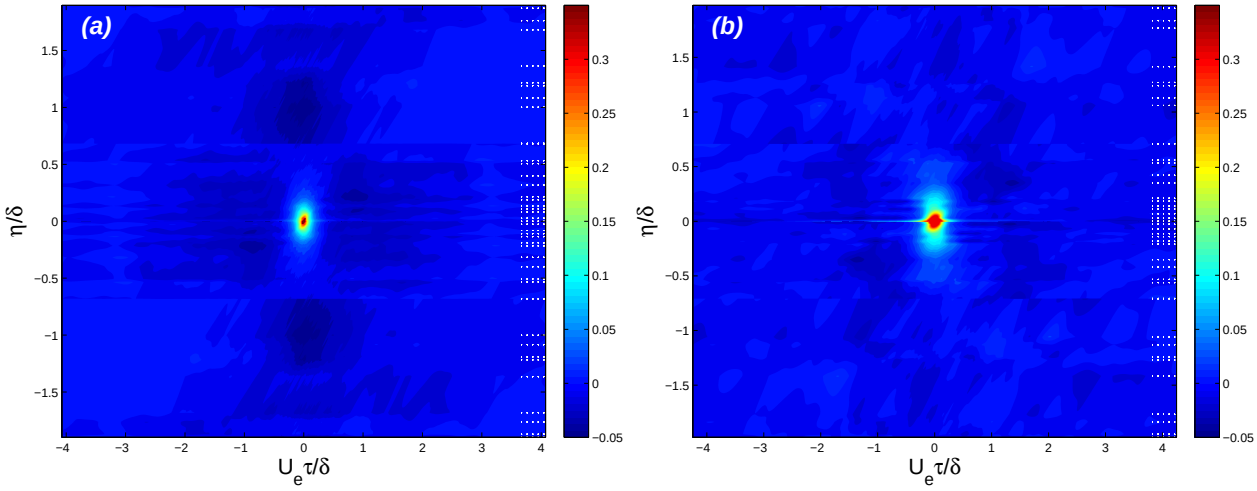

Figure 4.5: Space-time correlation of the spanwise array of microphones on the (a) smooth wall and (b) densely-packed rough surface at 30-ms^{-1}

4.3 Broadband Convection Velocity

The mean convection velocity is the ratio of the separation distance, s, to the time delay, τ.

$$\overline{U}_c(s) = \frac{s}{\tau} \tag{4.1}$$

$\overline{U}_c$ was obtained from the slope of the convection ridge as depicted in fig. 4.6. Here the smooth wall and cylinders at 30-ms^{-1} are used as representative cases. These are the same streamwise correlation maps discussed in § 4.2 but here they include markers (●) at the point of maximum correlation for each ξ. We consider the streamwise correlation because eq. (4.1) are most useful in the streamwise direction ($s \equiv \xi$) where we can track the evolution of eddies as they convect downstream. Thus the streamwise R_{pp} was analysed in this way for all surfaces and at all speeds to provide the local slopes of the convective ridge for each test case.

Recall that the slope varies along the convection ridge such that one can obtain the convection velocity of different sized eddies. To obtain broadband convection velocities, we look at the slope of the outer edges of the convection ridge (largest streamwise separation distances).

The convection velocity of the ridge for all streamwise separations was collected from 30 – 70-ms^{-1} on each surface. These normalised mean convection velocities over the smooth wall and the rough surfaces are presented in fig. 4.7 plotted against ξ. $\overline{U}_c$ is normalised on edge velocity U_e and streamwise separations ξ are normalised on the boundary layer thickness. In all cases there is a rapid increase in $\overline{U}_c$ over short streamwise separations. This is in accordance with previous findings that $\overline{U}_c$ is most sensitive to probe separation at small ξ.

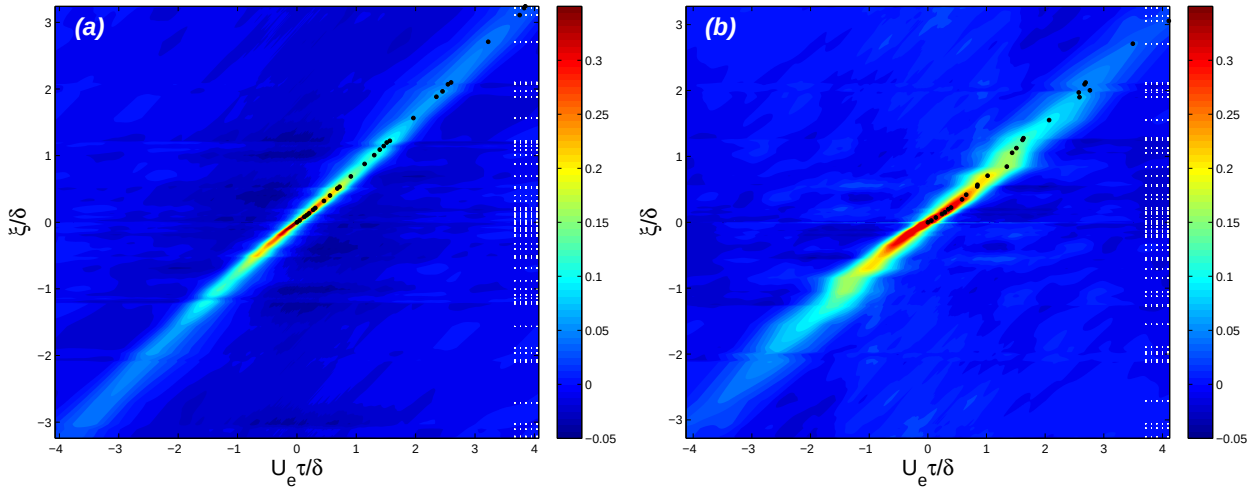

Figure 4.6: Space-time correlation map including maximum points (●) on the convection ridge for the (a) smooth wall and (b) the surface of cylinders at 30-ms^{-1}

The curve then slowly levels off and appears to asymptote to a constant value as streamwise distance increases. At the largest streamwise separations, the trend has already reached its constant value. The broadband convection velocity normalised on edge velocity ($\overline{U}_c/U_e$) can be taken as the final constant value.

It is clear from fig. 4.7 that values of $\overline{U}_c/U_e$ are independent of absolute edge velocity. On every surface we see that the data essentially overlay each other to form a single curve. Thus the final $\overline{U}_c/U_e$ value will be the same for every speed. Determining this constant value is somewhat challenging. In the present work, an equation of the form

$$\frac{\overline{U}_c}{U_e} = \frac{a(\xi/\delta) + b}{(\xi/\delta) + c} \tag{4.2}$$

was fitted to the data. This form produces horizontal asymptotes and was selected for this reason. It should be noted that the fitting was done numerically using the MATLAB curve fitting toolbox, ezyfit©, developed at University Paris-Sud. The final fit of the data at all speeds is shown as a dashed line on the plots of fig. 4.7. The constant value for each surface was then easily selected.

Considering the scatter of the data, the fit appears to be quite consistent and effective for all the rough wall cases shown in fig. 4.7b-f. However, fig. 4.7a shows that this curve fit did not work as well for the smooth wall case, especially considering this data shows very little scatter. The smooth wall fit lies approximately 0.017 units below the apparent centreline of the data. This is most likely due to a slight difference in the form of the equation needed for the fit for the smooth wall compared to the rough wall – a fact that suggests a fundamental difference in the variation of convection velocity over these types of surfaces. This is not surprising, as we saw indications of this from the difference in width of the convection ridge

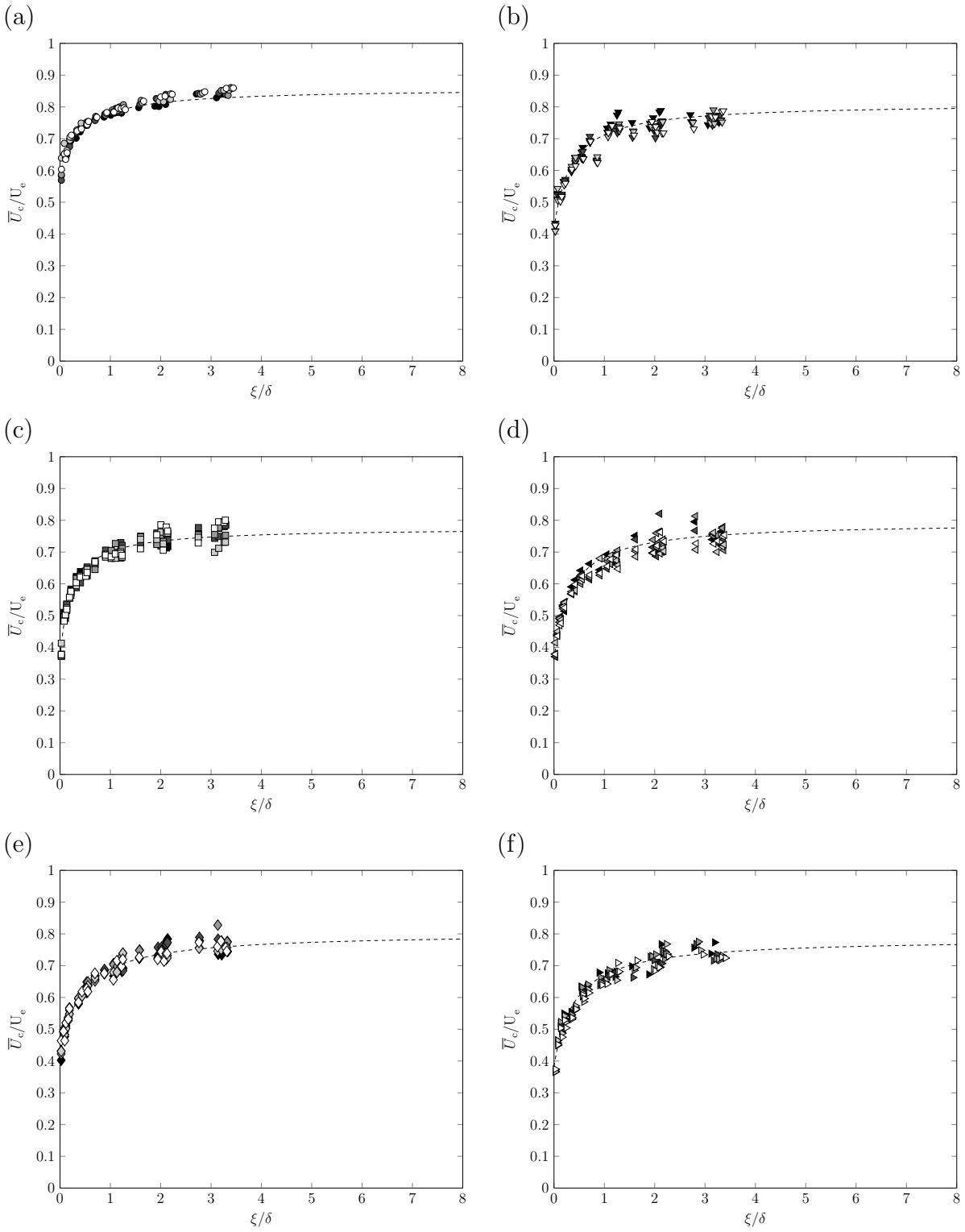

Figure 4.7: Ratio of convection velocity to edge velocity as a function of streamwise distance on the (a) smooth wall (b) cylinders (c) intermediately-packed rough surface (d) densely-packed rough surface (e) multi-height surface and (f) multi-shape surface.

Table 4.1: Ratio of large-scale asymptotic values of mean convection velocity, $\overline{U_{c_b}}$, to edge velocity, U_e for each surface under consideration in the present work. Values obtained from the outer slope of the convection ridge on the correlation map.

Surface	$\overline{U_{c_b}}/U_e$	$\delta(\overline{U_{c_b}}/U_e)$
smooth wall	0.864	$\pm$0.010
intermediately-spaced	0.766	$\pm$0.021
densely-spaced	0.778	$\pm$0.029
cylinders	0.797	$\pm$0.015
multi-height surface	0.787	$\pm$0.031
multi-shape surface	0.769	$\pm$0.025
sparse, 3-mm hemispheres [87]	0.781	-
sparse, 1-mm hemispheres [103]	0.796	-
sparse, 3-mm random hemispheres [103]	0.790	-

in § 4.2. To account for this we will simply add 0.017 to the smooth wall value of $\overline{U}_c/U_e$ obtained from the fit.

The uncertainty associated estimating the convection velocity was approximated based on the variance in the $\overline{U}_c/U_e$ data in fig. 4.7 at large separations. The deviations in the data capture the inherent uncertainty in the value of R_{pp} and in finding the slope of the maxima. This is proven by the fact that we see more scatter in the data on the rough surfaces, where a wider convection ridge means more uncertainty in obtaining the slope, than on the smooth wall. Therefore, these variations in the data are a sufficient indicator of the uncertainty in the $\overline{U}_c/U_e$ estimates.

The large-scale asymptotic values of broadband $\overline{U}_{c_b}/U_e$ values, and their associated uncertainties, are presented in table 4.1. Results from the studies of Forest [87] and Meyers [103] were also estimated from their correlation contours and are included in table 4.1. From these values we see that the present study produced markedly higher convection velocities than the studies of Blake [41] and Bull [63]. This was also observed by Forest [87] in his study. The differences are most likely due to uncertainties in each data set as well as residual pressure gradients and variations in Reynolds number. The present smooth wall $\overline{U}_{c_b}$=0.864U_e for large scale structures, which is closer to that found by Forest, Choi & Moin [78], and Farabee & Casarella [76]. The slope at the smallest separations show that the smaller structures range in $\overline{U}_{c_b}$ from 0.58 – 0.63.

The rough wall values are also significantly larger than that of Blake [41], by as much as 9% in the case of the cylinders.

5. Boundary Layer Velocity and Turbulence

This chapter will focus on the velocity and turbulence results of the single hotwire, the quadwire and the flattened Pitot. As detailed in § 2.3 all three of these instruments were used to collect the velocity data on the rough walls. This was in an effort to validate the results presented here. In addition, two quadwires were mounted side by side and collected data simultaneously. This process produced a dataset which is independently obtained from four sources (hotwire, flattened Pitot and two quadwires) at two speeds: 30-ms^{-1} and 60-ms^{-1}.

As with the microphones, the aim was to obtain measurements on each rough surface in the middle of a four element array. However, on some surfaces in order for one quadwire to obtain measurements at a specific location, it was not possible for the second probe to be in the same element-relative location as the first. The fixed probe separation of 25.4-mm and the presence of the elements themselves determined where the second probe would be placed. Moreover, in the case of the multi-scale surfaces measurements were strategically made at multiple locations relative to the roughness elements. The result is that, in addition to the assortment of transducers used to measure data, we were also able to make measurements at a range of positions relative to the roughness elements.

Images showing the probe location relative to the roughness elements are presented, for each surface, in figs. 5.1 to 5.5.

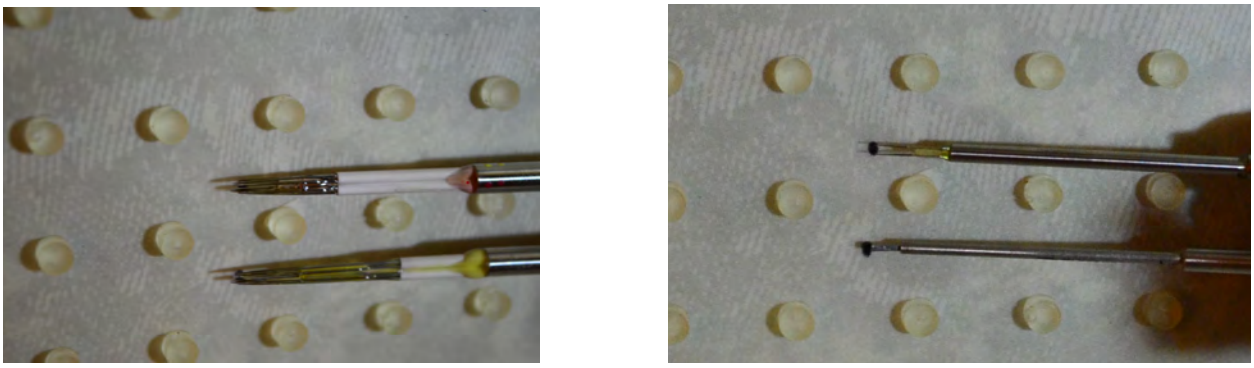

Figure 5.1: Vertically aligned quadwires (left) and vertically aligned single hotwire (top probe of right picture) and flattened Pitot (bottom probe of right picture) measuring velocity on cylindrical rough surface (flow moving left to right)

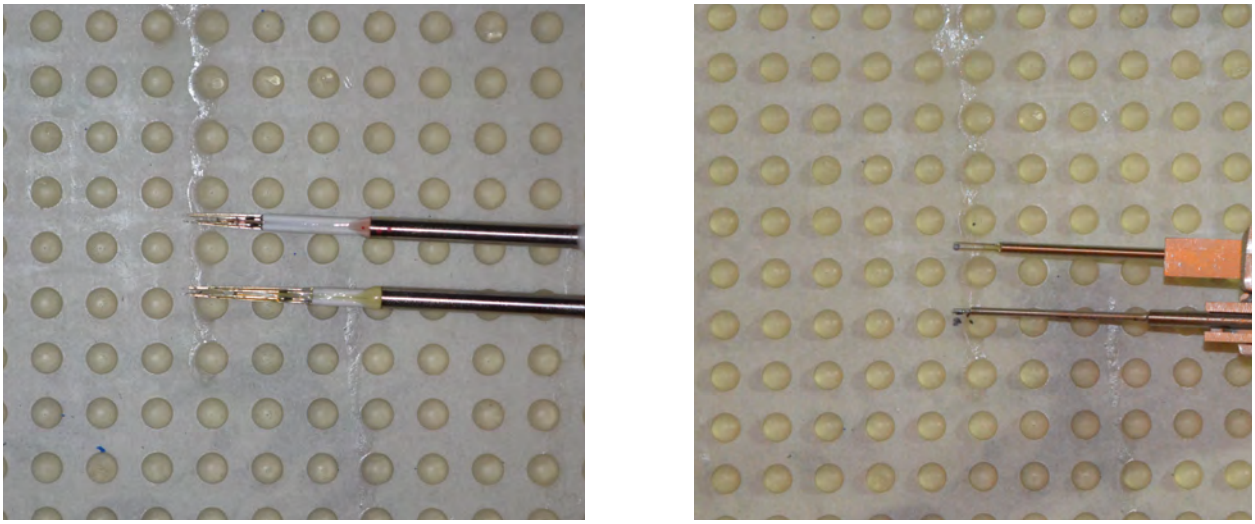

Figure 5.2: Vertically aligned quadwires (left) and vertically aligned single hotwire (top probe of right picture) and flattened Pitot (bottom probe of right picture) measuring velocity on intermediate rough surface (flow moving left to right)

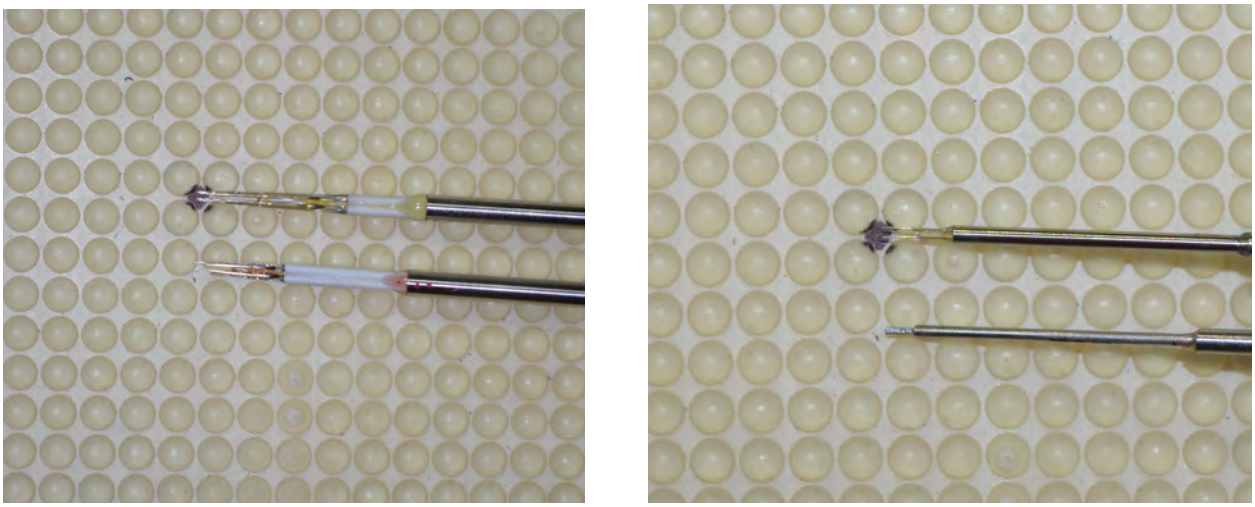

Figure 5.3: Vertically aligned quadwires (left) and vertically aligned single hotwire (top probe of right picture) and flattened Pitot (bottom probe of right picture) measuring velocity on dense rough surface (flow moving left to right)

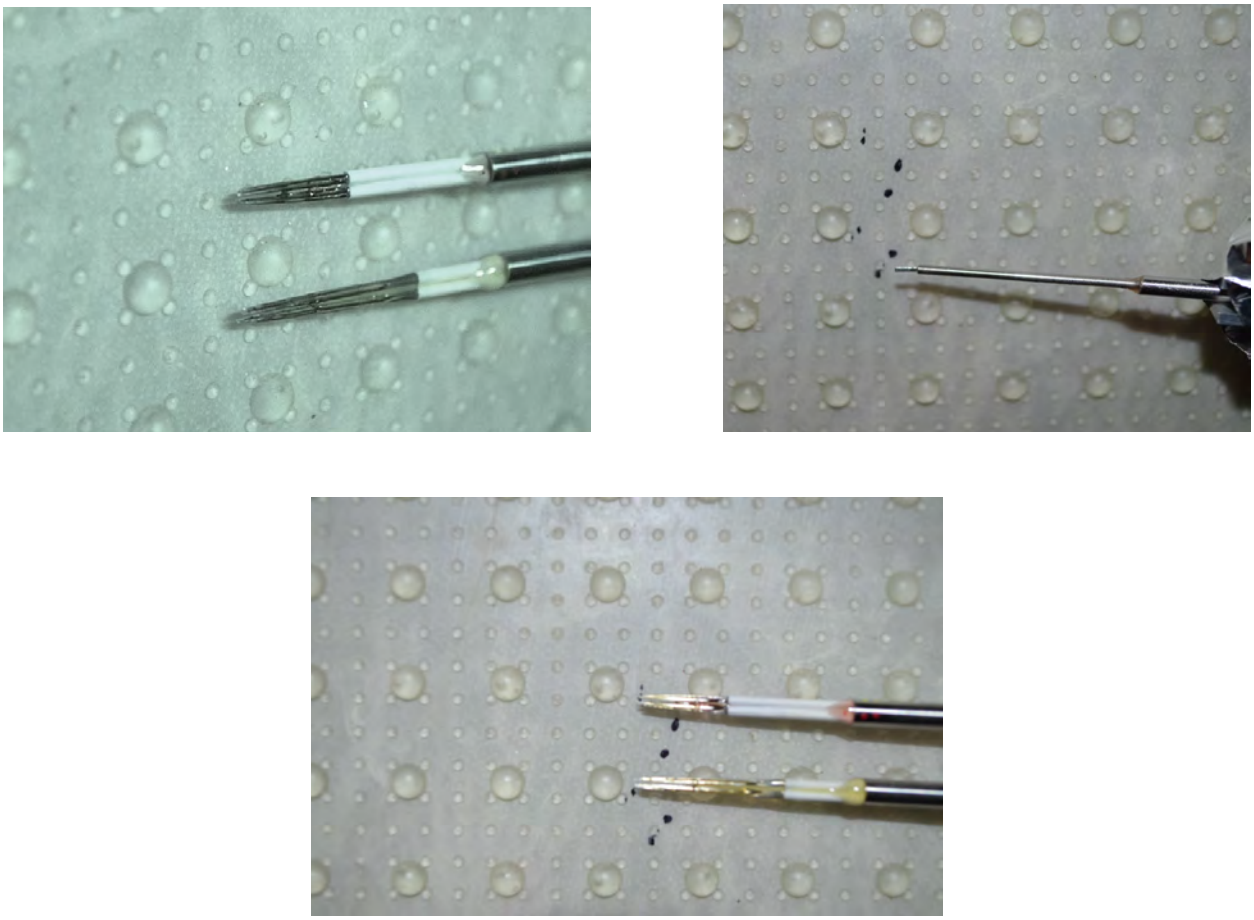

Figure 5.4: Vertically aligned quadwires (top left) and flattened Pitot (top right) measuring velocity on multi-height rough surface (flow moving left to right). Single hotwire not used for this surface.

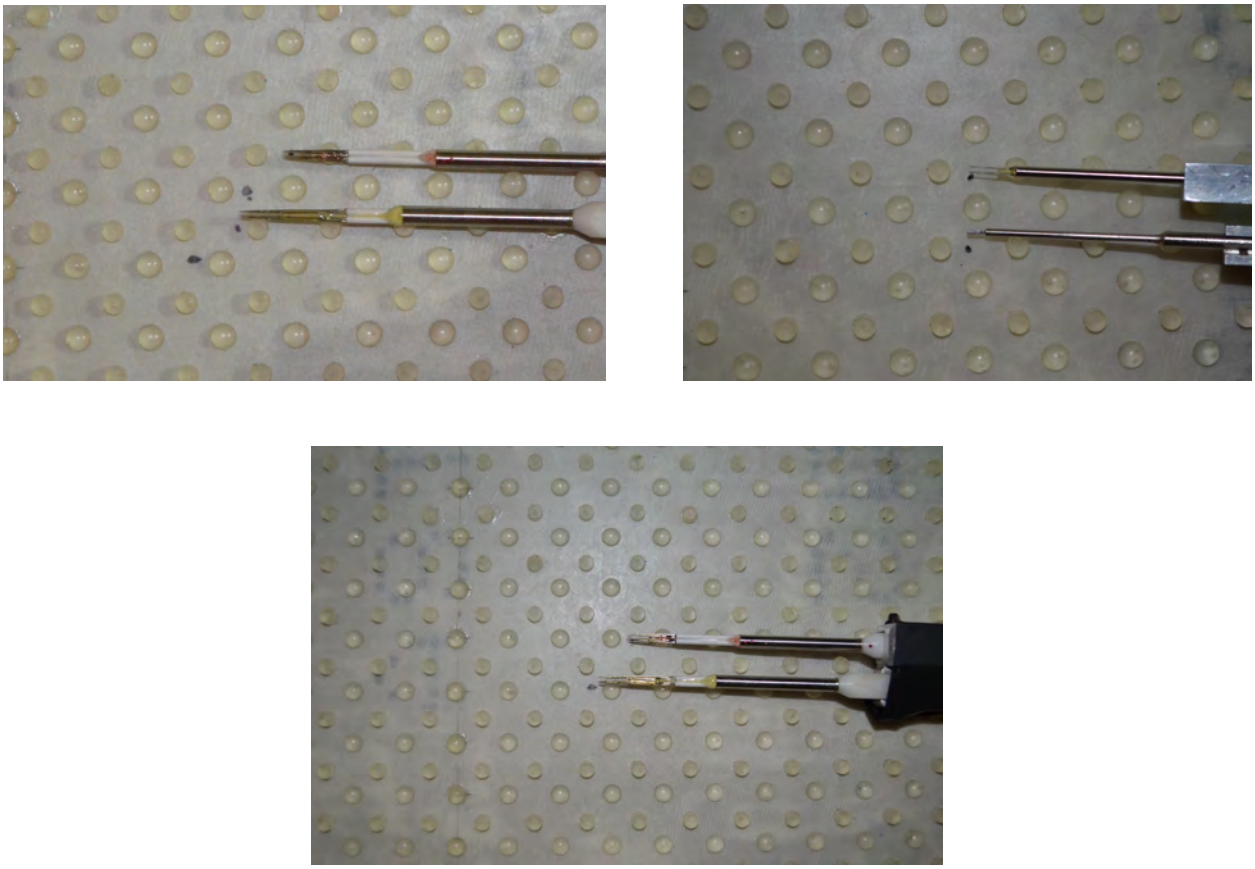

Figure 5.5: Parallel quadwires (top left) and vertically aligned single hotwire (top probe of right picture) and flattened Pitot (bottom probe of right picture) measuring velocity on mixed-shape rough surface (flow moving left to right)

Table 5.1: Summary boundary layer velocity measurements made with different transducers and at different measurement locations

Surface	Measurement Location	Traducer/Measurement Type	Speeds, ms^{-1}
Smooth wall	-	1 Quadwire	[30,60]
	-	Single Hotwire	
	-	Flattened Pitot	
Intermediately-spaced	$\sim$ middle of four element array	2 Quadwires	30
		1 Quadwire	60
		Single Hotwire	[30,60]
		Flattened Pitot	
Densely-spaced	$\sim$ middle of four element array	1 Quadwire	[30,60]
		Single Hotwire	
		Flattened Pitot	
Cylinders	$\sim$ middle of four element array	2 Quadwires	[30,60]
		Single Hotwire	
		Flattened Pitot	
Composite height	near/downstream 1-mm hemisphere	2 Quadwires	[30,60]
	downstream 3-mm hemisphere	2 Quadwires	
	near/downstream 1-mm hemisphere	Flattened Pitot	
Composite shape	downstream 3-mm cylinder	2 Quadwires	[30,60]
	downstream 3-mm hemisphere	2 Quadwires	
	downstream 3-mm cylinder	Single Hotwire	
	downstream 3-mm cylinder	Flattened Pitot	

In the case of the multi-scale surfaces, the selected locations ensured that data was obtained in the vicinity of each type of element on the surface. For the multi-height surface, measurements were made behind the 1-mm and 3-mm elements independently. This is depicted in the images of fig. 5.4. Likewise for the multi-shape surface measurements were obtained behind the cylinder and behind the hemisphere independently, as shown in fig. 5.5. Note again that the apparent spread of probe locations shown in figs. 5.4 and 5.5 is because adjustment of the second probe was limited once the first probe location was set. The goal of these measurements was to gain insight into the way in which the different elements affect (if they affect) the flow on the surface.

The measurement locations, the measurements taken at each location, and the speeds at which data was collected are outlined in table 5.1. In the case of the intermediate and dense roughness, only one quadwire probe was used because the other required repairs.

5.1 Boundary Layer Parameters

Boundary layer parameters were estimated from all four sources of velocity data: two quadwires, single hotwire, and the flattened Pitot.This was in an effort to validate the data presented in this work. Obtaining the most accurate values for these boundary layer parameters is incredibly important for scaling the pressure spectrum, as we will see later.

The boundary layer thickness was calculated from the velocity data based on two criteria: (1) by definition at the boundary layer height the velocity is approximately $0.99U_e$ and (2) from experiments the turbulence intensity, $\overline{u}/U_{ref}$, has been found as approximately 2% [11]. Through a user-interactive program the data was examined to determine the best y location which simultaneously met both criteria most closely. This was done for all the data sets, from all instruments. Once δ was estimated the other characteristic thicknesses, δ^* and θ, were calculated using eqs. (1.14) and (1.15) respectively. Data close to the wall were estimated by linear extrapolation of the measured data in order to complete these numerical integrations.

The friction velocity, U_τ, is independently estimated using the two methods described in § 1.4. In the integral momentum balance method U_τ is adjusted interactively until the $\overline{uv}/U_\tau^2$ profile peaks at 1 (the justification for this is discussed in § 1.4). The Reynolds shear stress plot which resulted from this process is shown in fig. 5.6, for speeds of 30-ms^{-1} and 60-ms^{-1}. This method obviously uses only the quadwire data as the single hotwire and flattened Pitot cannot produce Reynolds stress data. We will revist this plot in § 5.4 when we take a closer look at the Reynolds stresses in our boundary layers.

Two sample cases of the Schlichting fit method are shown in fig. 5.7 where the solid line is the curve produced from eq. (1.9) and the symbols represent the smooth and rough wall data as defined in fig. 5.15. Table 5.2 presents the estimates U_τ, and its derivative parameters, from the Schlichting method and the integral momentum balance method (see § 1.4 for details

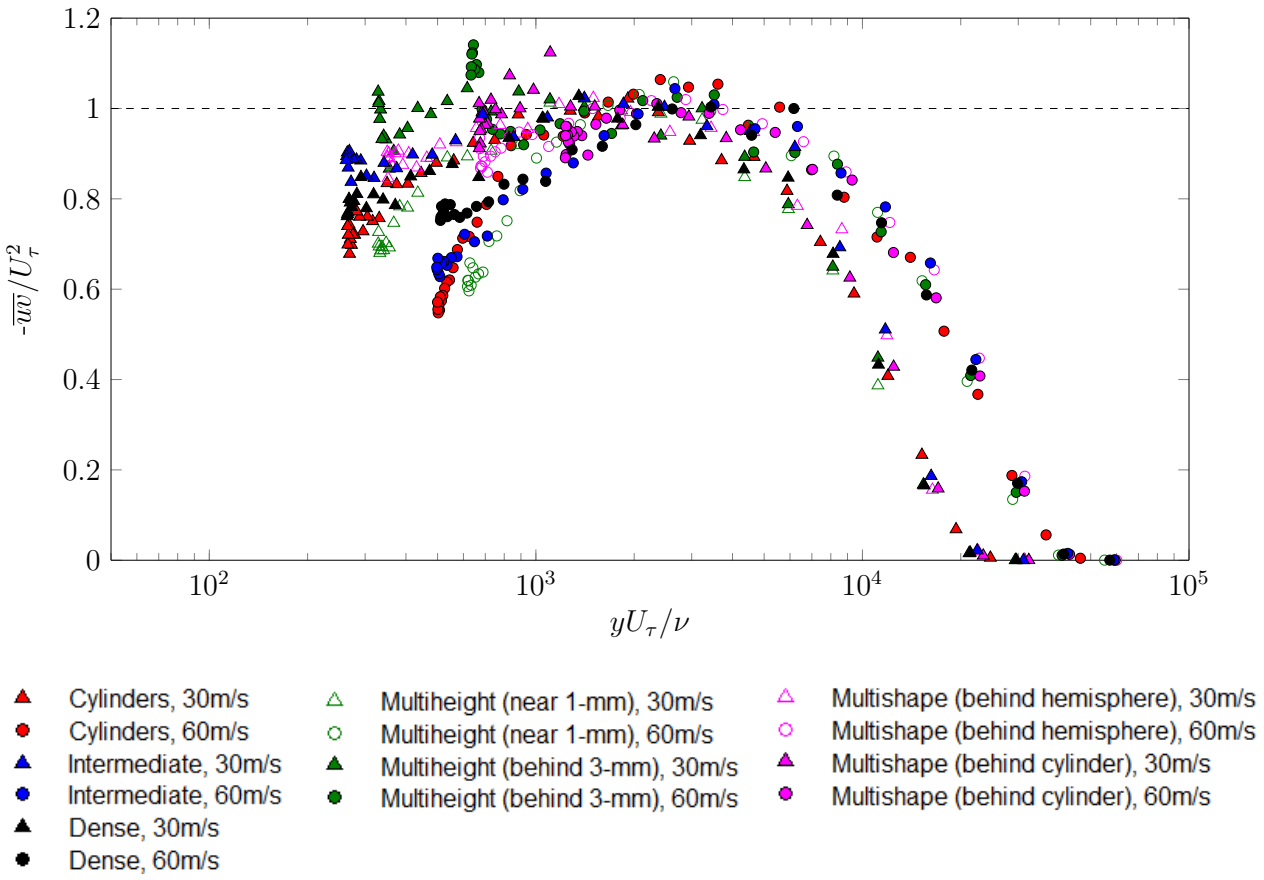

Figure 5.6: Reynolds shear stress, $\overline{uv}$, normalised on friction velocity, U_τ

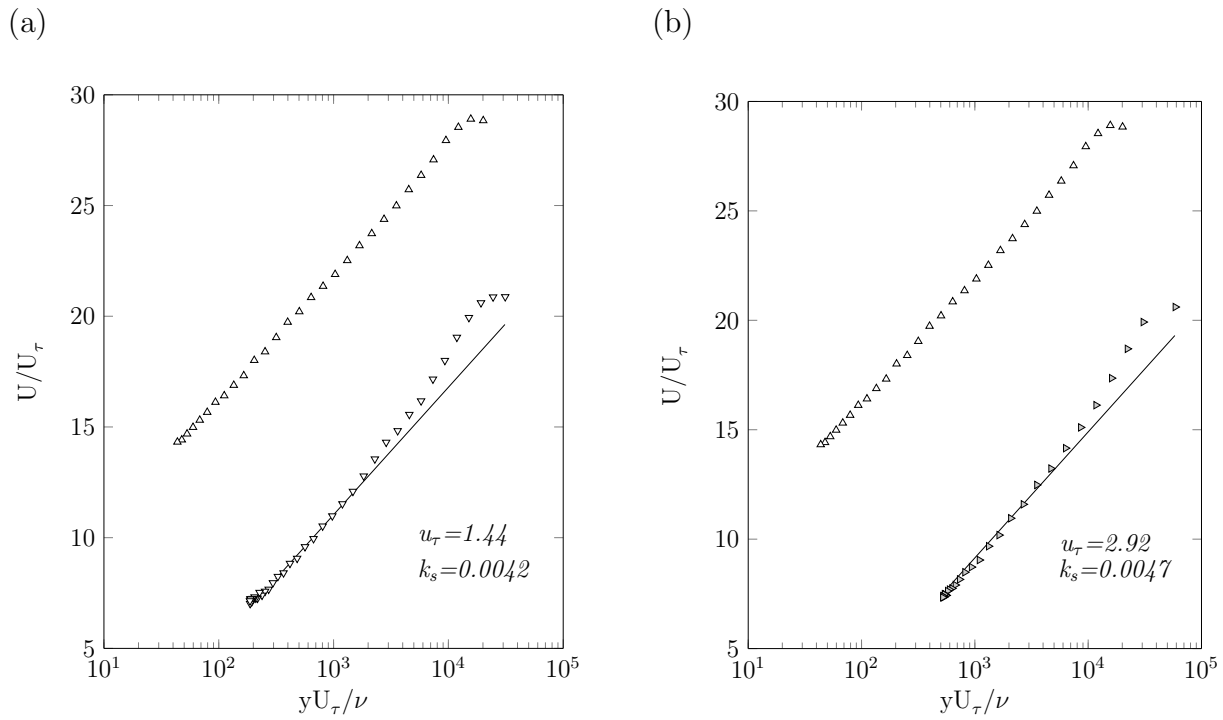

Figure 5.7: Representative plots showing the Schlichting [58] method for estimating U_τ to compare with the results of the integral momentum balance. (a) Cylinders at 30-ms^{-1} (b) Multi-shape surface at 60-ms^{-1}. Solid line is the curve produced from eq. (1.9), $\triangle$ is the smooth wall and $\triangledown$ is the respective rough wall case

of the procedure for each method). Values of U_τ from both methods have an average of 6% difference (maximum difference is 30%), with only the intermediate roughness showing a marked difference between the two methods. Hence the resultant values of U_τ (k_s, τ_w, ΔU^+), are also similar for both methods.

Like Varano [36], we also see that the Schlichting fit method consistently over predicts U_τ. We also know that compared with the integral momentum balance method, there is more uncertainty associated with the Schlichting fit method simply because a fit is more user-subjective than ascertaining when $\overline{uv}$ peaks at 1. We will therefore use the values obtained from the integral momentum balance moving forward.

It would only be possible to use the Schlichting fit method to estimate U_τ from the single hotwire data and the flattened Pitot data. Due to Varano's and our finding that the integral momentum balance is a more reliable method for obtaining U_τ than the Schlichting method, and the fact the two quadwires produced independent useful results, U_τ was not estimated from these other data.

Table 5.2: Comparisons of the boundary layer parameters from Schlichting [58] method versus from $\overline{uv}$ of fig. 5.6. Ambient conditions outlined in table 5.1.

	Schlichting	$\overline{uv}$	Schlichting	$\overline{uv}$	Schlichting	$\overline{uv}$	Schlichting	$\overline{uv}$
	U_τ (ms^{-1})		k_s (m)		τ_w (N-m^{-2})		ΔU^+	
Cylinders, 30-ms^{-1}	1.44	1.44	0.0042	0.0052	2.30	2.31	11.3	11.9
Cylinders, 60-ms^{-1}	2.89	2.88	0.0040	0.0056	8.89	8.88	12.9	13.7
Multi-height (behind 1-mm), 30-ms^{-1}	1.48	1.38	0.0038	0.0043	2.40	2.09	11.1	11.3
Multi-height (behind 1-mm), 60-ms^{-1}	2.93	2.77	0.0038	0.0060	8.98	8.01	12.6	13.7
Multi-height (behind 3-mm), 30-ms^{-1}	1.48	1.39	0.0033	0.0054	2.40	2.10	10.8	11.8
Multi-height (behind 3-mm), 60-ms^{-1}	2.92	2.78	0.0033	0.0061	9.04	8.20	12.4	13.7
Multi-shape (behind hemisphere), 30-ms^{-1}	1.47	1.46	0.0045	0.0055	2.36	2.35	11.5	12
Multi-shape (behind hemisphere), 60-ms^{-1}	2.92	2.98	0.0047	0.0063	8.99	9.37	13.2	14
Multi-shape (behind cylinder), 30-ms^{-1}	1.45	1.49	0.0035	0.0035	2.32	2.44	10.9	10.9
Multi-shape (behind cylinder), 60-ms^{-1}	2.9	2.97	0.0039	0.0039	8.81	9.21	12.7	12.8
Intermediate, 30-ms^{-1}	1.85	1.43	0.0140	0.0071	3.80	2.28	15	12.6
Intermediate, 60-ms^{-1}	3.74	2.88	0.0155	0.0096	14.87	8.83	16.9	15
Dense, 30-ms^{-1}	1.44	1.38	0.0039	0.0052	2.28	2.10	11.1	11.8
Dense, 60-ms^{-1}	2.89	2.84	0.0040	0.0068	8.79	8.49	12.8	14

Once U_τ is ascertained the wall shear stress τ_w is approximated from eq. (1.16) which in turn produces the skin friction coefficient, C_f, from eq. (1.17). From here all other parameters can be ascertained. The actual values of the boundary layer parameters will be presented and discussed in subsequent chapters when we explore the results of each probe and each measurement location.

Table 5.3 lists the uncertainty associated with the boundary layer parameters for the present work. The uncertainty estimates detailed in § 2.3.5 were used in a jitter analysis to determine the uncertainties in the boundary layer parameters. For the special case of U_τ the uncertainty was determined by comparing the user-selected U_τ values from multiple attempts of fitting the $\overline{uv}/U_\tau^2$ plot. The maximum variation in the final results was taken as the uncertainty and presented in table 5.3.

Table 5.3: Absolute uncertainty estimates for boundary layer parameters presented in table 5.12

Quantity	Absolute Uncertainty
U_e (ms^{-1})	0.05
ρ (kgm^{-3})	0.0011
ν (m^{2}s^{-1})	2.8E-08
δ (mm)	1.51
δ^* (mm)	1.53
θ (mm)	1.52
U_τ (ms^{-1})	0.05
τ_w (Nm^{-2})	0.18
C_f	0.0003

5.2 All Velocity & Turbulence Data

This section explores the raw data obtained from the quadwires, single hotwire and flattened Pitot. We will make comparisons in order to validate and select the best quality data for use in the subsequent analysis.

5.2.1 Comparisons between two quadwires

We start by looking at the agreement of the mean velocity obtained from different quadwire probes. In these subsequent plots the mean velocity and Reynolds stresses will be presented. The data are represented by symbols and the shaded grey area represents the uncertainty band for the data. In comparing data sets throughout this chapter, it should be borne in

mind that if any portion of the shaded regions overlap then the data are within range of each other, whether or not the data points themselves overlay.

The quadwire data obtained on the cylindrical surface are shown in figs. 5.8 and 5.9 for 30-ms^{-1} and 60-ms^{-1}, respectively. The top plots are the mean velocities with the plot on the right being a zoomed in version of the plot on the left. The bottom left plot is the normal Reynolds stresses and the bottom right plot is the Reynolds shear-stresses. The data from the different probes are within the uncertainty bounds for the mean velocities. The variation is larger for the Reynolds stresses, especially closer to the wall where instrumentation errors are larger, but still within the uncertainty.

Table 5.5 presents the boundary layer parameters calculated from the data of each probe. In this table the absolute difference between the values, $|\Delta|$, are stated as well as the combined uncertainty associated with each parameter ($\sqrt{2} \times \delta()$). These two values can be compared to determine whether the parameters from the different probes agree within the uncertainty – as long as the absolute difference is less than the combined uncertainty. With this in mind, it is clear that all the parameters from each probe in table 5.5 agree to within their respective uncertainties.

The case of the cylindrical surface is a good representation of the small differences observed between the two quadwires mounted side by side. The results from these measurements on the other surfaces are included in appendix B for further review.

Table 5.4: Legend for figs. 5.8 and 5.9

●	x velocity component for bottom probe
▲	x velocity component for top probe
●	y velocity component for bottom probe
▲	y velocity component for top probe
●	z velocity component for bottom probe
▲	z velocity component for top probe
▬	uncertainty bands for the data

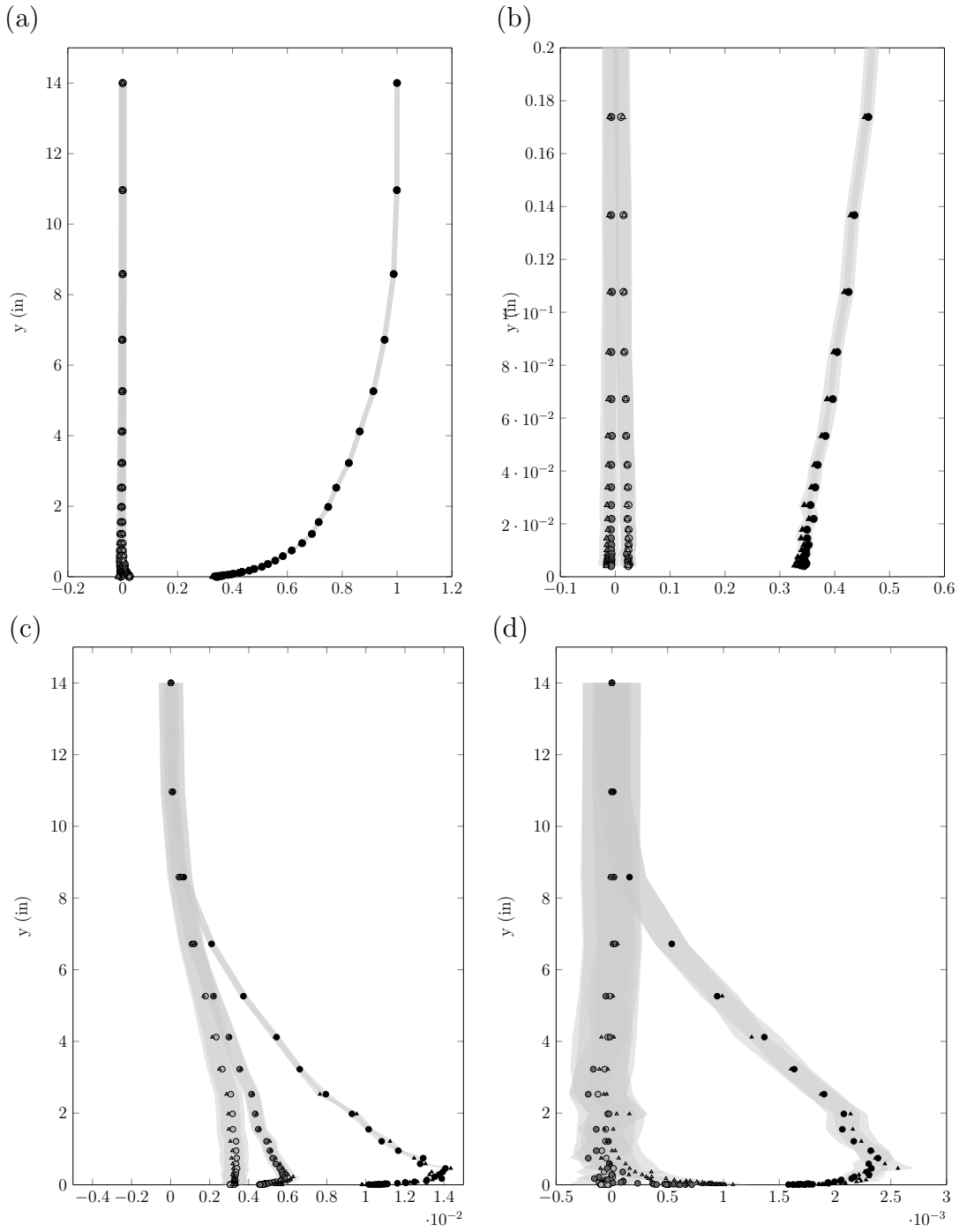

Figure 5.8: Velocity results for cylinders at 30-ms^{-1}. (a) Mean velocity profiles (b) Expanded mean velocity profiles showing the bottom 1.5% of the boundary layer (c) Normal Reynold's stress profiles (d) Reynolds shear-stress profiles.

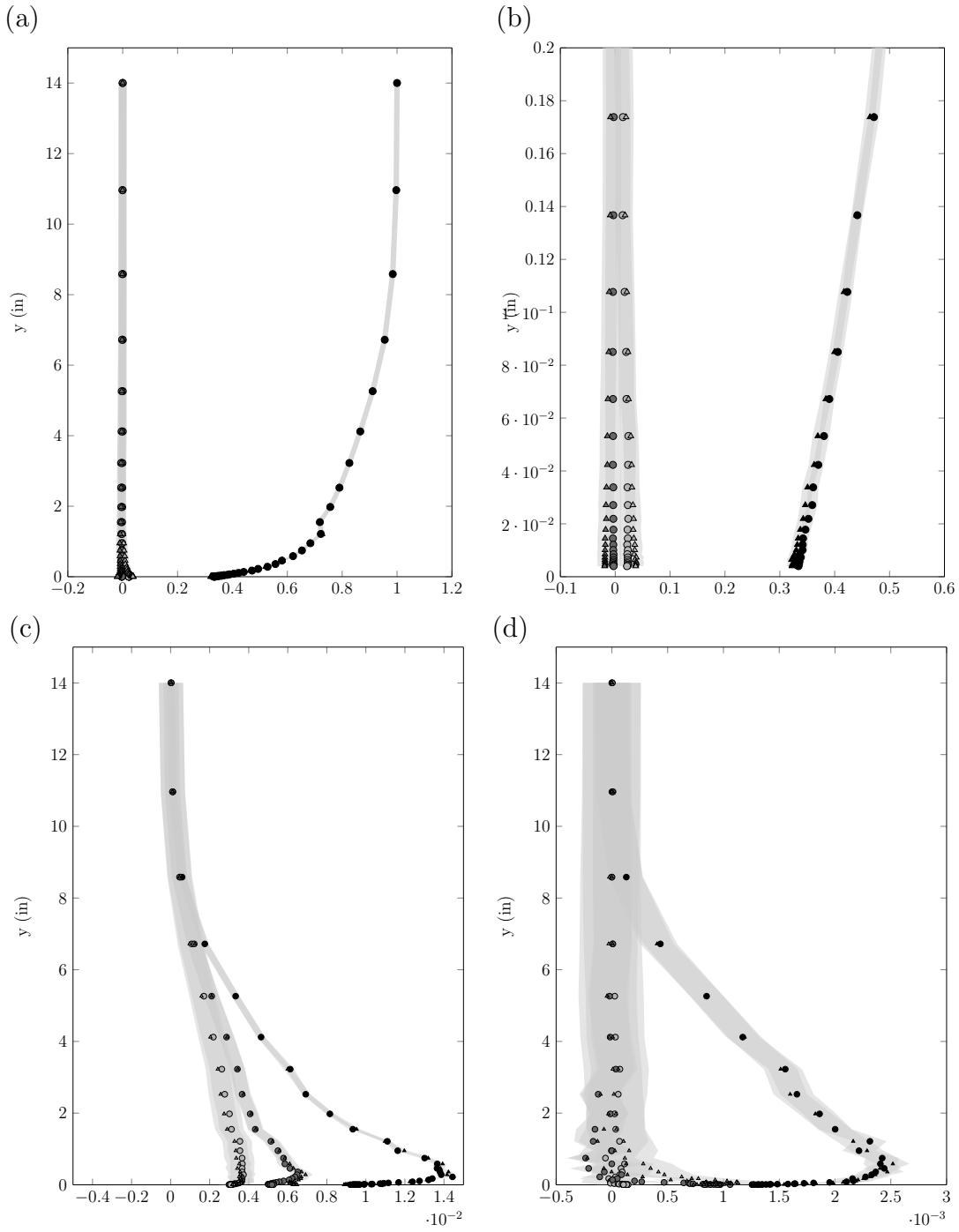

Figure 5.9: Velocity results for cylinders at 60-ms^{-1}. (a) Mean velocity profiles (b) Expanded mean velocity profiles showing the bottom 1.5% of the boundary layer (c) Normal Reynold's stress profiles (d) Reynolds shear-stress profiles.

Table 5.5: Comparisons of the boundary layer parameters for the cylindrical surface from data of two quadwires. $\delta()$ is the uncertainty in a parameter

	$\sqrt{2} \times \delta()$		30-ms^{-1}			60-ms^{-1}		
	30-ms^{-1}	60-ms^{-1}	bottom probe	top probe	$\lvert\Delta\rvert$	bottom probe	top probe	$\lvert\Delta\rvert$
δ (m)	0.0021		0.243	0.242	0.001	0.238	0.238	0
δ^* (m)	0.0032		0.039	0.039	0	0.037	0.037	0
Re_θ	3917	7396	47951	48006	55	88584	88487	97
U_τ (ms^{-1})	0.07		1.44	1.48	0.04	2.88	2.88	0
C_f	0.0004		0.0047	0.0049	0.0002	0.0046	0.0046	0
k_g^+	20.2	31.7	263	269	6	496	496	0
δ^+	1061	1027	21261	21811	550	39511	39355	156
δ/k_g	4.8		80.9	80.8	0.1	79.4	79.3	0.1
ΔU^+	0.6		11.9	12.2	0.3	13.7	13.8	0.1

5.2.2 Comparisons at different element-relative locations (same surface)

The data obtained at different locations on the multi-height surface are presented in figs. 5.10 and 5.11. The top plots are the mean velocities with the plot on the right being a zoomed in version of the plot on the left. The bottom left plot is the normal Reynolds stress and the bottom right plot is the Reynolds shear stresses. The measurement locations shown in the top left image and the bottom middle image of fig. 5.4 are compared.

The data from the different locations show good agreement, within the uncertainty bounds, for the mean velocities. Closer to the wall there are larger variations the agreement is not as good as further away from the wall. Nevertheless the agreement is within the uncertainty band. The variations are larger for the Reynolds stresses but again, still acceptable within the uncertainty. Note that to obtain results for different locations it was necessary to use data from different quadwire probes (see § 5.2.1) so some of the variations observed here are the same as that observed and discussed in § 5.2.1. Hence it appears that we have the more or less the same velocity and Reynolds stresses in the boundary layer over the multi-height surfaces, no matter where you make the measurements.

Table 5.7 outlines the boundary layer parameters obtained from both these measurement locations. At 30-ms^{-1} all parameters agree within the stated uncertainty. However, discrepancies arise at 60-ms^{-1}. δ values are consistently larger behind the 3-mm elements than behind the 1-mm element. This is indicative of some error in one of the measurements – for the same surface at the same streamwise location the boundary layer thickness should be consistent. The estimates of δ behind the 3-mm elements increase with increasing speed, which is not the expected trend. The other discrepancy in table 5.7 is that ΔU^+ for the top probe, at 60-ms^{-1} do not agree for the different measurement locations. The estimate behind the 3-mm element is significantly larger than the others at this speed.

Table 5.6: Legend for figs. 5.10 and 5.11

●	behind 1-mm element
▲	behind 3-mm element
■	middle of four 1-mm element array
▬	uncertainty bands for the data

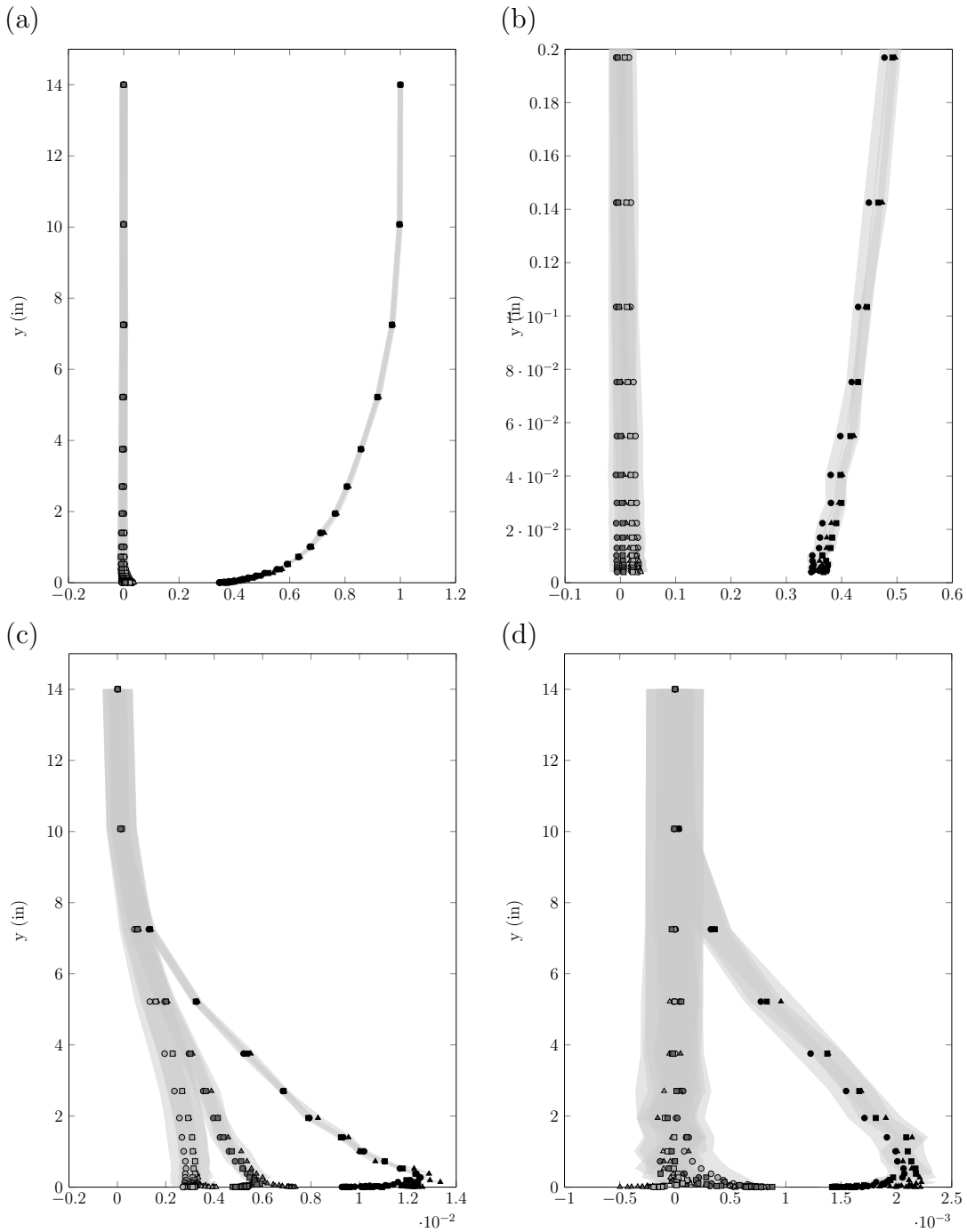

Figure 5.10: Compare results at different measurement locations on the multi-height surface at 30-ms^{-1}: (a) Mean velocity profiles (b) Expanded mean velocity profiles showing the bottom 1.5% of the boundary layer (c) Normal Reynold's stress profiles (d) Reynolds shear stress profiles.

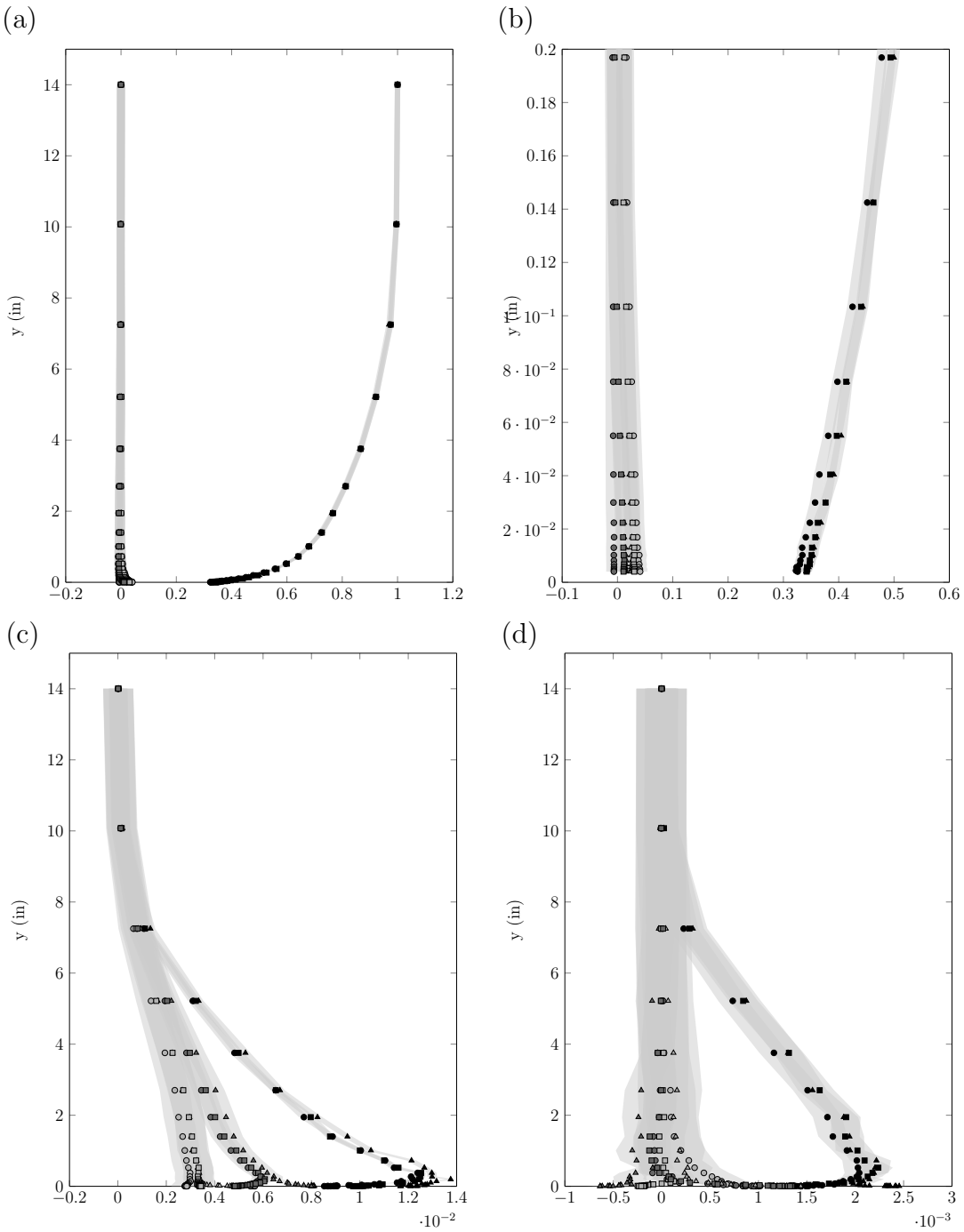

Figure 5.11: Compare results at different measurement locations on the multi-height surface at 60-ms^{-1}: (a) Mean velocity profiles (b) Expanded mean velocity profiles showing the bottom 1.5% of the boundary layer (c) Normal Reynold's stress profiles (d) Reynolds shear stress profiles.

Table 5.7: Comparisons of the boundary layer parameters for the multi-height surface for different measurement locations and measurement probes. $\delta()$ is the uncertainty associated with a parameter

		bottom probe				top probe			
		behind 1-mm	behind 3-mm	$\sqrt{2} \times \delta()$	$\lvert\Delta\rvert$	behind 1-mm	behind 3-mm	$\sqrt{2} \times \delta()$	$\lvert\Delta\rvert$
30-ms^{-1}	δ (m)	0.238	0.237	0.002	0.0015	0.238	0.236	0.003	0.0018
	δ^* (m)	0.037	0.037	0.002	0.0006	0.037	0.036	0.003	0.0004
	Re_θ	44922	44088	3808	834	44629	43984	5386	645
	U_τ (ms^{-1})	1.38	1.39	0.07	0.0043	1.35	1.37	0.1	0.02
	C_f	0.0042	0.0043	0.0004	0.0001	0.0041	0.0042	0.001	0.0001
	k_g^+	245	245	19	0.1	240	242	27	2.5
	δ^+	19498	19419	1007	79	19116	19152	1419	36
	δ/k_g	79.5	79.0	4.7	0.5	79.3	78.7	6.7	0.6
	ΔU^+	11.2	11.8	0.57	0.5	11.8	12.0	0.8	0.18
60-ms^{-1}	δ (m)	0.232	0.238	0.002	*0.006**	0.231	0.237	0.003	*0.006**
	δ^* (m)	0.036	0.036	0.002	0.0007	0.035	0.036	0.003	0.0013
	Re_θ	80527	83998	7222	3471	80163	84518	10213	4355
	U_τ (ms^{-1})	2.77	2.78	0.04	0.02	2.70	2.78	0.1	0.0803
	C_f	0.0042	0.0043	0.001	0.0001	0.0040	0.0043	0.001	0.0003
	k_g^+	460	472	30	12	450	471	42	22
	δ^+	35670	37505	990	1835	34630	37215	1390	2585
	δ/k_g	77.3	79.3	4.7	2	77.1	78.9	6.6	1.8
	ΔU^+	13.7	13.8	0.57	0.09	13.8	14.7	0.8	*0.95**

*shows no agreement between probes

The data obtained behind the cylinder and behind the hemisphere on the multi-shape surface are presented in figs. 5.12 and 5.13. These locations are shown in the top left image and bottom middle image of fig. 5.5, respectively. The top plots are the mean velocities with the plot on the right being a zoomed in version of the plot on the left. The bottom left plot is the normal Reynolds stress and the bottom right plot is the Reynolds shear stresses.

V and W at the different locations show good agreement, averaging to zero. However U values between the probes diverge 3-in above the wall with an average difference of 14% at 30-ms^{-1} and 13% at 60-ms^{-1}. The mean velocities close to the wall are clearly dependent on measurement location. The Reynolds normal stresses also show variations larger than the uncertainty at both speeds. Interestingly, the Reynolds normal stresses appear to agree for both measurement locations at both speeds.

So it appears that the velocity and turbulence statistics are dependent on the measurement locations relative to the roughness elements.

Table 5.8: Legend for figs. 5.12 and 5.13

●	behind hemisphere
▲	behind cylinder
▬	uncertainty bands for the data

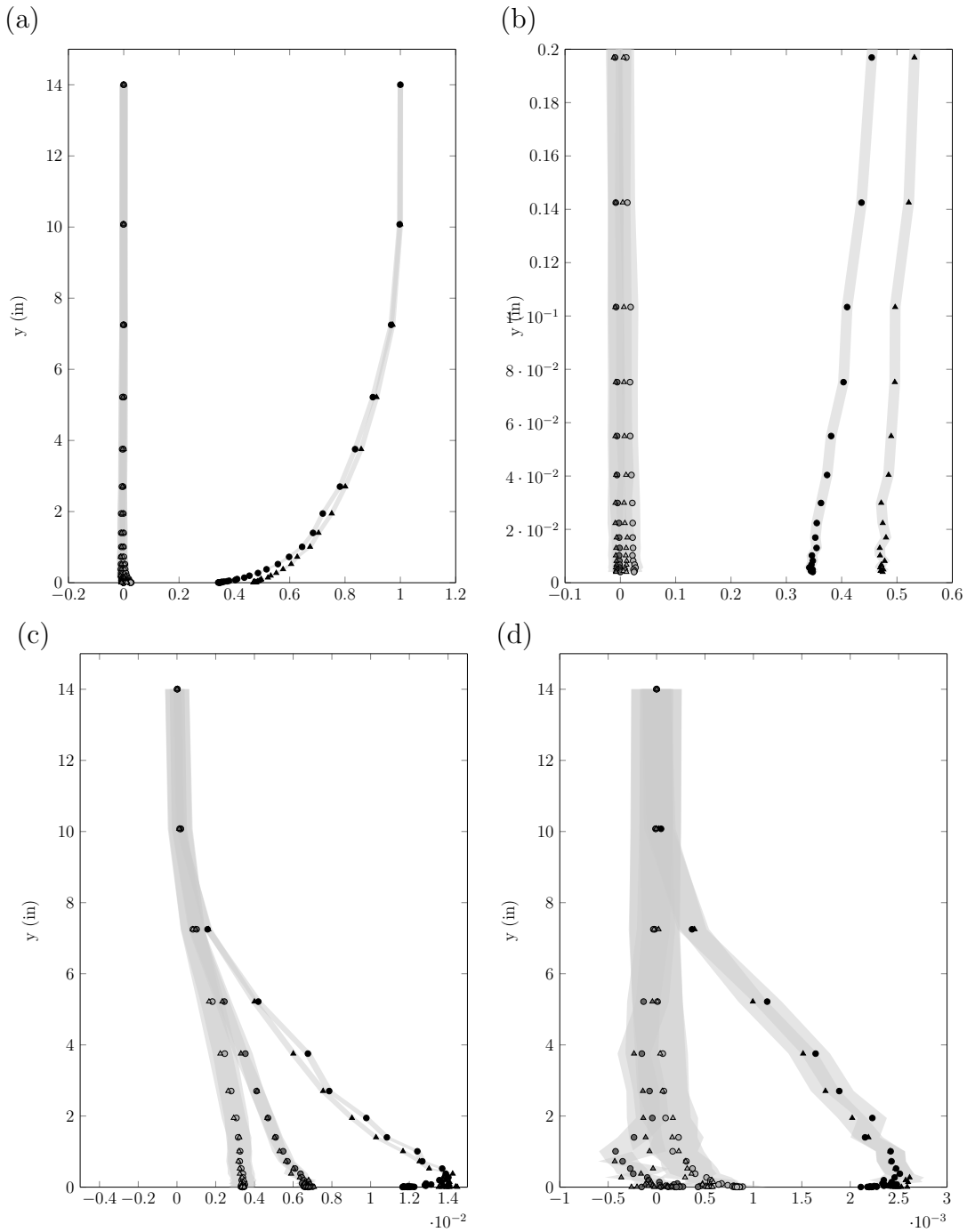

Figure 5.12: Compare results at different measurement locations on the multi-shape surface at 30-ms^{-1}: (a) Mean velocity profiles (b) Expanded mean velocity profiles showing the bottom 1.5% of the boundary layer (c) Normal Reynold's stress profiles (d) Reynolds shear stress profiles.

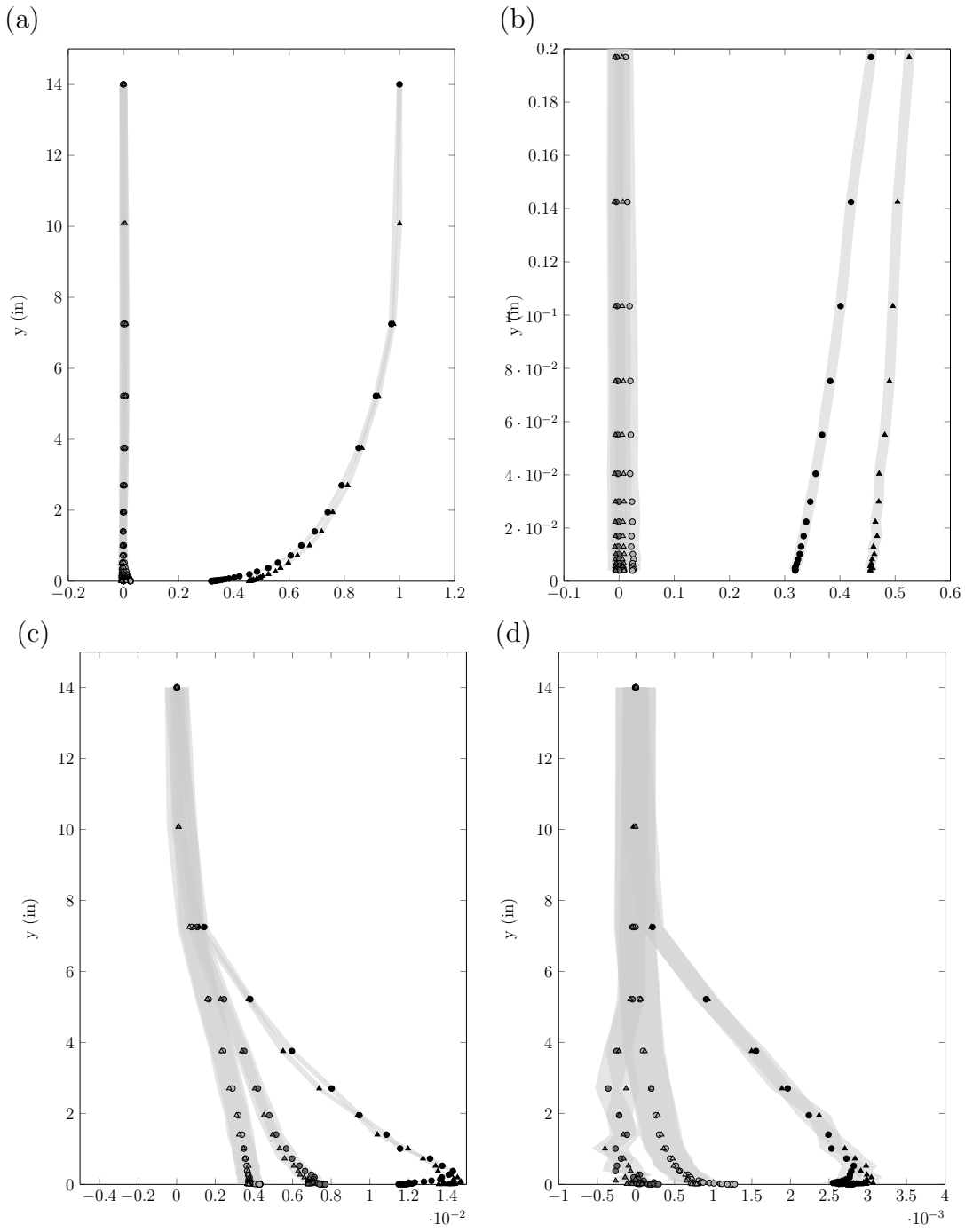

Figure 5.13: Compare results at different measurement locations on the multi-shape surface at 60-ms^{-1}: (a) Mean velocity profiles (b) Expanded mean velocity profiles showing the bottom 1.5% of the boundary layer (c) Normal Reynold's stress profiles (d) Reynolds shear stress profiles. ● behind hemisphere; ▲ behind cylinder. Shaded region represents uncertainty bands for the data

Table 5.9: Comparisons of the boundary layer parameters for the multi-shape surface for different measurement locations and measurement probes. $\delta()$ is the uncertainty associated with a parameter

		bottom probe				top probe			
		behind hemisphere	behind cylinder	$\sqrt{2} \times \delta()$	$\lvert\Delta\rvert$	behind hemisphere	behind cylinder	$\sqrt{2} \times \delta()$	$\lvert\Delta\rvert$
30-ms^{-1}	δ (m)	0.243	0.239	0.002	*0.0036**	0.243	0.239	0.003	*0.0042**
	δ^* (m)	0.041	0.038	0.002	*0.0035**	0.041	0.037	0.003	*0.0034**
	Re_θ	49473	46461	7693	3012	49295	46449	10879	2846
	U_τ (ms^{-1})	1.46	1.49	0.07	0.0272	1.49	1.50	0.1	0.01
	C_f	0.0047	0.0049	0.0007	0.0002	0.0049	0.0050	0.001	0.0001
	k_g^+	261	267	20	5.8	265	269	28.6	3.8
	δ^+	21245	21632	1034	387	21491	21830	1462	339
	δ/k_g	81.0	79.8	4.8	1.2	81.1	79.7	6.8	1.4
	ΔU^+	12.0	11.7	0.57	0.3	12.8	12.0	0.8	0.8
60-ms^{-1}	δ (m)	0.284	0.228	0.002	*0.0560**	0.283	0.228	0.003	*0.05**
	δ^* (m)	0.042	0.037	0.002	*0.005**	0.040	0.036	0.003	*0.0041**
	Re_θ	95511	83205	7171	12306	91727	81949	10141	9778
	U_τ (ms^{-1})	2.98	2.97	0.07	0.0134	3.14	3.21	0.1	0.07
	C_f	0.0049	0.0049	0.001	0	0.0055	0.0057	0.0007	0.0002
	k_g^+	501	491	31.5	10.5	528	531	47	2.5
	δ^+	47712	38900	1068	8812	48740	41186	1519	7554
	δ/k_g	94.7	76.0	5.1	*18.7**	94.3	76.1	7	*18**
	ΔU^+	14.1	13.3	0.57	0.8	15.2	14.6	0.8	0.6

*shows no agreement between probes

5.2.3 Comparisons among all probes

The data obtained from the quadwire, single hotwire and flattened Pitot on the surface of cylinders are shown in fig. 5.14. All these data were collected at close to the centre of the four element array. The top plots are the streamwise mean velocities U/U_{ref} with the plot on the right being a zoomed in version of the plot on the left. The bottom left plot is the streamwise normal Reynolds stress u^2/U_{ref}^2 and the bottom right plot is the zoomed in version of this. Note that there is only data from the hotwires in the bottom plots.

The data from the different probes show good agreement, within the uncertainty bounds for the mean velocities. The variation is larger for the Reynolds stresses, especially closer to the wall. These results are representative of the results obtained on all the surfaces, which are included in appendix B for further review. Table 5.11 presents a comparison of the boundary layer parameters for each surface for each probe. This table shows that the results from the different probes are consistent.

Table 5.10: Legend for fig. 5.14

●	quadwire results from top probe
■	single hotwire results
▲	flattened Pitot results
▬	uncertainty bands for the data

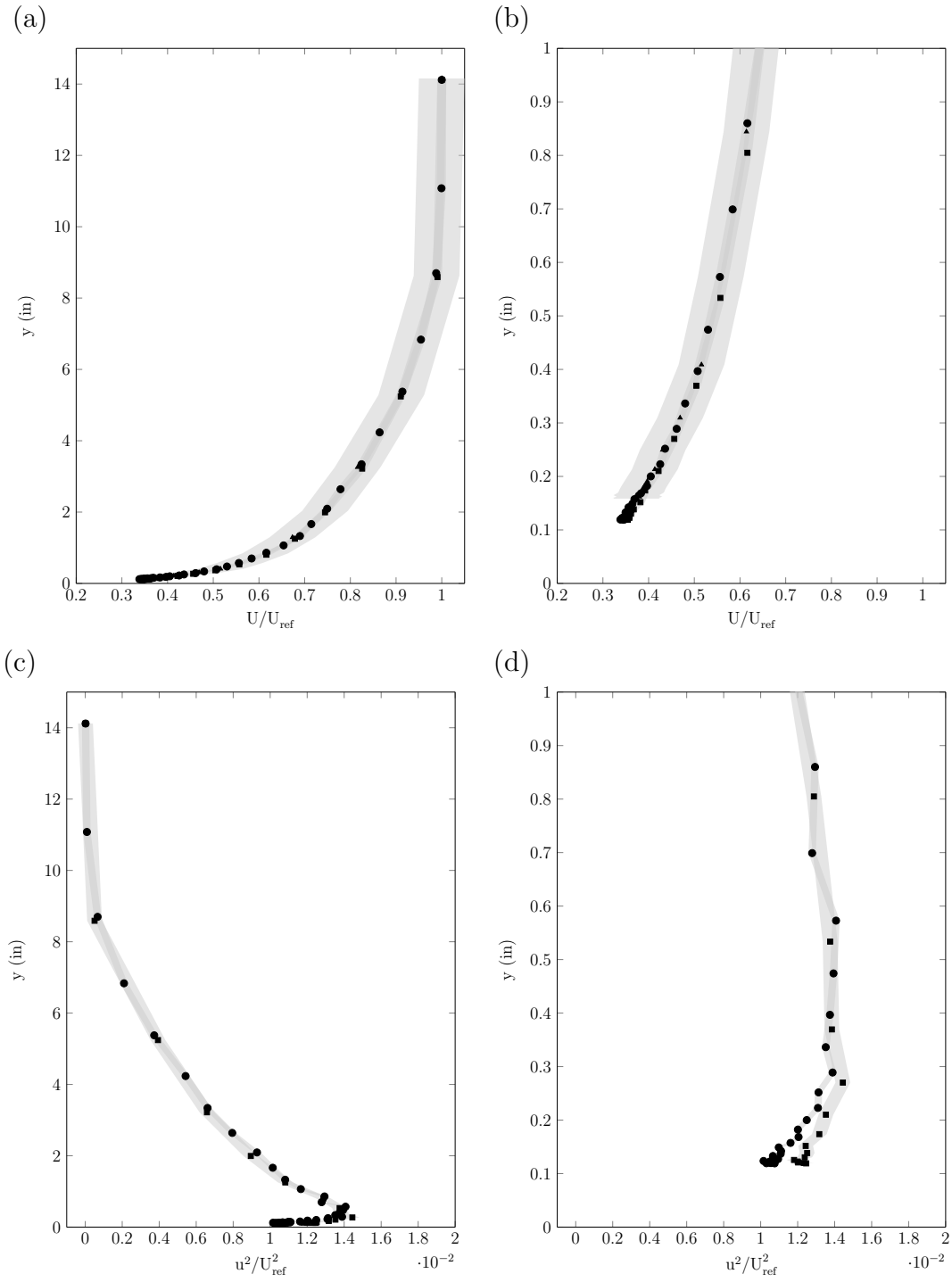

Figure 5.14: Results for cylinders at 30-ms^{-1}: (a) Streamwise mean velocity profiles (b) Expanded streamwise mean velocity profiles (c) Streamwise normal Reynolds stress profiles (d) Expanded streamwise normal Reynolds stress profiles.

Table 5.11: Comparisons of the boundary layer parameters for all surface for different measurement probes: quadwire (QHW), single hotwire (SHW), and flattened Pitot (FP)

	δ (m)			δ^* (m)			θ (m)			Re_θ		
	QHW	SHW	FP	QHW	SHW	FP	QHW	SHW	FP	QHW	SHW	FP
Cylinders, 30-ms^{-1}	0.243	0.225	0.233	0.039	0.038	0.039	0.026	0.026	0.027	47951	43200	44100
Cylinders, 60-ms^{-1}	0.238	0.230	0.231	0.037	0.026	0.039	0.026	0.019	0.027	88584	59800	85100
Multi-height, 30-ms^{-1}	0.237	-	0.239	0.037	-	0.038	0.025	-	0.026	44088	-	44400
Multi-height, 60-ms^{-1}	0.238	-	0.234	0.036	-	0.039	0.024	-	0.026	83998	-	84700
Multi-shape, 30-ms^{-1}	0.239	0.230	0.269	0.038	0.042	0.045	0.026	0.028	0.029	46461	46700	50100
Multi-shape, 60-ms^{-1}	0.228	0.230	0.235	0.037	0.040	0.044	0.025	0.027	0.029	83205	86700	93800
Intermediate, 30-ms^{-1}	0.243	0.231	0.261	0.041	0.041	0.044	0.028	0.027	0.029	50052	47000	50000
Intermediate, 60-ms^{-1}	0.243	0.231	0.278	0.041	0.041	0.046	0.027	0.027	0.030	91856	90100	99200
Dense, 30-ms^{-1}	0.236	0.232	0.259	0.037	0.039	0.041	0.025	0.026	0.028	45490	48300	50300
Dense, 60-ms^{-1}	0.234	0.232	0.261	0.037	0.037	0.041	0.025	0.025	0.028	84393	87300	95500

5.2.4 Final Data

The preceding sections have informed us that the measurements obtained from two quadwire probes, a single hotwire and a flattened Pitot produce velocity and turbulence profiles that agree for most surfaces and under most flow conditions, within the uncertainty. The agreement between the results the three different types of probes is good down to $\sim$ 2.54-mm from the wall (limit for the probes). Spurious results were obtained for the single hotwire in some instances, casting some doubt on the reliability of this instrument. The data from the different quadwire probes show good agreement The variation is larger closer to the wall where instrumentation errors are larger, but still within the uncertainty. Data obtained from different locations relative to the elements show some variations close to the wall but the boundary layer parameters derived from the velocity profiles are consistent.

The final boundary layer parameters for this work are presented in table 5.12. These are derived from the quadwire probes for several reasons: (1) the quadwire provides all the data necessary to obtain these parameters (unlike the flattened Pitot, for example), (2) quadwires have the smallest uncertainty among the instruments (see tables 2.2 to 2.4), (3) when installed in parallel at the same streamwise locations the quadwires produced similar results (within uncertainty) and (4) the single hotwire probe showed clear signs of erroneous data for some cases.

For the surfaces with single scale elements, the quadwire probe selected for further processing was whichever one was closest to the middle of four elements. For the multi-scale surfaces, the decision was a little more complicated because the two locations showed marked differences in results. However, as mentioned before, it is believed that the measurements behind the 3-mm hemisphere are less reliable than those made behind the 1-mm hemisphere. In the end, the probe which was in the vicinity of the 1-mm elements was selected for use on the multi-height surface. For the multi-scale surface, the probe installed behind the cylinders was used instead of the probe installed behind the hemispheres. Moving forward, the data of table 5.12 will be the only boundary layer parameters used for scaling the pressure spectrum. Furthermore, these values are linearly interpolated to obtain the Reynolds numbers at each speed between 30-ms^{-1} and 70-ms^{-1}. Thus the values listed in table 5.12 are not the maximum.

The overall trend in table 5.12 is that for a single surface the boundary layer height decreases with increased speed and the displacement thickness remains about constant. This is true for all but the multi-height surface which has δ =0.237 at 30-ms^{-1} and 0.238 at 60-ms^{-1}. The difference between these values is within the uncertainty of this estimate and so the deviation is not enough to say that the trend does not hold.

Table 5.12: Boundary layer parameters for the surfaces considered in this work

Surface	k_g (m)	λ	U_e ms^{-1}	δ (m)	δ^* (m)	Re_θ	k_s (m)	U_τ ms^{-1}	C_f	k_g^+	k_s^+	δ^+	δ/k_g	ΔU^+
Smooth wall	-	-	30-ms^{-1}	0.246	0.023	31990	-	1.05	0.0024	-	-	14420	-	-
Sparse hemispheres [1]	0.003	0.052		0.219	0.032	43500	0.0033	1.50	0.0050	283	315	21600	73.0	9.6
Sparse 1-mm hemispheres [1]	0.001	0.052		0.212	0.030	39600	0.0011	1.48	0.0049	91	102	19200	212.0	9.2
Random, sparse hemispheres [1]	0.003	0.052		0.222	0.034	45200	0.0033	1.51	0.0051	260	289	19300	74.0	9.7
Intermediate hemispheres	0.003	0.13		0.243	0.041	50052	0.0072	1.43	0.0046	260	624	21065	81.0	12.7
Dense hemispheres	0.003	0.33		0.236	0.037	45490	0.0052	1.38	0.0043	248	428	19590	78.7	11.7
Cylinders	0.003	0.052		0.243	0.039	47951	0.0052	1.44	0.0047	263	456	21261	80.9	11.9
Multi-height hemispheres	0.001, 0.003	0.104		0.238	0.037	44922	0.0043	1.38	0.0042	245	351	19498	79.5	11.2
Multi-shape	0.003	0.104		0.239	0.038	46451	0.0047	1.49	0.0049	267	420	21632	79.8	11.7
Smooth wall	-	-	60-ms^{-1}	0.233	0.023	61966	-	1.98	0.0021	-	-	25070	-	-
Sparse hemispheres [1]	0.003	0.052		0.228	0.032	80200	0.0034	2.90	0.0047	507	566	42500	76.0	11.2
Sparse 1-mm hemispheres [1]	0.001	0.052		0.210	0.027	72100	0.0011	2.84	0.0044	172	195	36200	210.0	10.4
Random, sparse hemispheres [1]	0.003	0.052		0.220	0.031	82700	0.0033	2.84	0.0047	492	548	36100	73.0	11.2
Intermediate hemispheres	0.003	0.13		0.243	0.041	91856	0.0096	2.88	0.0047	493	1582	40000	81.1	15.0
Dense hemispheres	0.003	0.33		0.234	0.037	84393	0.0072	2.84	0.0045	478	1144	37458	78.1	14.2
Cylinders	0.003	0.052		0.238	0.037	47951	0.0056	2.88	0.0046	496	922	39511	79.4	13.7
Multi-height hemispheres	0.001, 0.003	0.104		0.232	0.036	80527	0.006	2.77	0.0042	460	923	35670	77.3	13.7
Multi-shape	0.003	0.104		0.228	0.037	83205	0.0049	2.97	0.0049	491	797	38900	76.0	13.3

The thickest boundary layers are produced by the intermediate rough surface, which shows an increase in δ from the sparse 3-mm hemispheres of 11% at 30-ms^{-1} and 6.6% at 60-ms^{-1}. With a further increase in roughness density from the intermediate to the dense rough surface, δ actually begins to decrease slightly, as is seen by the 3% decrease at 30-ms^{-1} and the 3.7% at decrease at 60-ms^{-1}. This result is in alignment with our previous observations of the mean velocity profiles in § 5.3. The multi-height surface is another example of the influence of roughness density as we see an 8% increase in δ from the sparse, single-element surfaces to the denser multi-height surface at 30-ms^{-1}. This is also true at 60-ms^{-1} where a 4.4% increase is observed.

Compared to the 3-mm sparse hemispheres, the cylinders have significantly larger δ values at both speeds – 10% larger at 30-ms^{-1} and 4.2% larger at 60-ms^{-1}. This is most likely due to the increase in turbulence intensity brought on by the vortices trailing off the edges of the cylinders. The boundary height is larger because the increased $\overline{u}/U_{ref}$ falls to 2% further away from the wall than with the hemispheres.

δ for the multi-shape surface shows a similar behaviour as the cylindrical surface. This overshadows the effect of the increase in element density (from the single element surfaces to the multi-shape surface). At both speeds the cylinders produce a thicker boundary layer than the multi-shape surface. This is not to say that δ for the multi-shape surface is small. It is about as large as the other surfaces with the same element density. The cylindrical surface however produces a larger boundary layer again due to the increase in $\overline{u}/U_{ref}$.

In general as the free-stream velocity is doubled, U_τ also increases by approximately $\times$ 2 and the skin friction remains fairly constant (considering the value of the uncertainty). This is in accordance with the expectation that U_τ be a constant multiple of the free stream velocity [61, 112]. As roughness density increases from sparse to intermediate, U_τ decreases by 4.7% and by 3.5% from intermediate to dense roughness, at 30-ms^{-1}. This reduction in U_τ with increasing density is also reflected in the multi-height surface which has U_τ values which are as much as 8% less than that of the single element surfaces at 60-ms^{-1}. U_τ is also less for the cylinders than for the hemispheres, by about 4% at 30-ms^{-1}.

For all surfaces δ/k_g is larger than 50 which, following Jiménez's [42] criteria would suggest that the roughness does not disrupt the log-layer and, according to Raupach *et al.* [8], the boundary layer should also display wall-similarity. All cases studied here can be categorised as fully-rough wall flows, according to Jiménez's criteria, since the roughness Reynolds numbers ($k_g^+ = k_g U_\tau/\nu$) are all much greater than 80. Therefore, all the present rough-wall flows reach conditions at which we might expect universal scaling behaviour to become apparent.

5.3 Normalised Velocity Profiles

The streamwise velocity profiles, normalised on inner and outer variables, are presented in fig. 5.15 for every surface tested, including multiple locations on the multi-scale surfaces. In fig. 5.15a the effect of increased shear stress is clear for the rough wall profiles versus the smooth wall profile. This is most evident in the bottom 60% of the boundary layer where there is a marked velocity decrease at every y location for the rough wall cases, compared to the smooth wall. In the upper 40% of both the smooth and rough wall boundary layers the velocity is close to the free stream and the effect of the increased wall shear stress is much smaller.

The effect of wall shear stress can also be seen in fig. 5.15b. Just as with fig. 1.8 of § 1.3.1 the rough wall velocity profiles are shifted down from the smooth wall profile. As one would expect, the downward shift is greater for the higher speed than for the lower speed. The magnitude of the shift (ΔU^+) varies with rough configuration. The overall shape of the profiles in fig. 5.15b suggest that the data considered here is in the semi-logarithmic and outer regions of the boundary layer. As noted by Marusic [60] it is indeed difficult to denote from most of these profiles the y location at which the logarithmic region ends. In other cases it is quite clear. The determining factor behind such differences in behaviour lies in the pressure gradient – profiles measured with larger favourable pressure gradients tend to have smaller wake components than the zero-pressure gradient wall [60, 1].

First we look at the effect of element spacing (roughness density) on the mean velocity, as presented in fig. 5.16. Initially the magnitude of the downward shift in the logarithmic region increases when λ is increased from the sparse hemispheres to the intermediate hemispheres ($\Delta U^+ = 12.7$ at 30-ms^{-1} and 15.0 at 60-ms^{-1}). This is due to the increase in wall shear stress from the increased roughness density. As λ is further increased this effect reverses and we see that the downward shift for the dense roughness ($\Delta U^+ = 11.7$ at 30-ms^{-1} and 14.2 at 60-ms^{-1}) is actually less than for the intermediate roughness. This is in accordance with the element sheltering hypothesis discussed in § 1.8.

Considering the effect of element shape, fig. 5.17 depicts the velocity profiles for the 3-mm sparse cylinders and the 3-mm sparse hemispheres. There appears to be some effect of element shape on the shape of velocity profiles, which is inconsistent with the wall similarity hypothesis. In fig. 5.17a the profiles align well at just about all y locations. Furthermore, the relative downward shift for the cylinders and the hemispheres shown in fig. 5.17b are about the same for each speed.

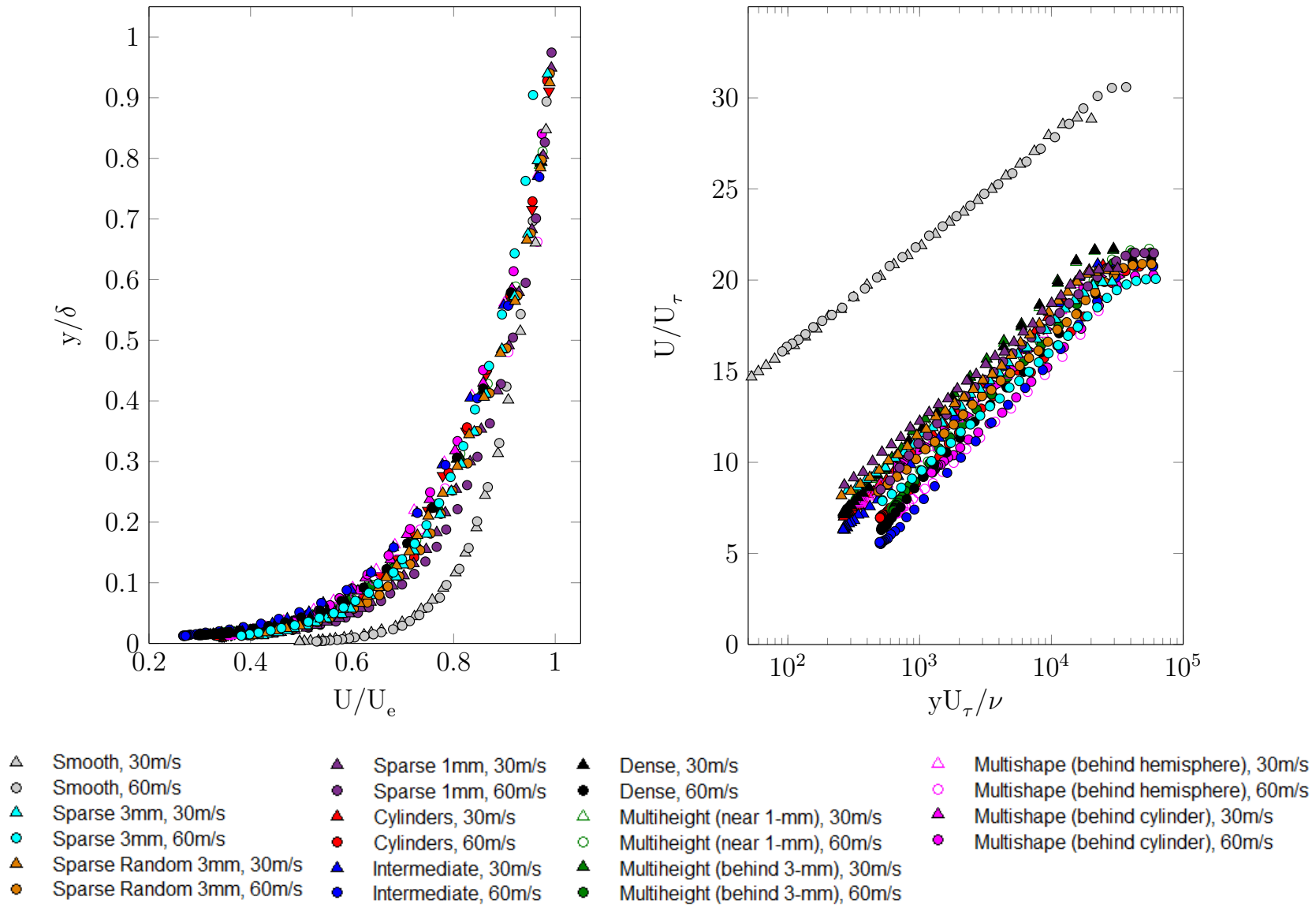

Figure 5.15: Mean streamwise velocity (measured by quadwire) normalised on (a) outer variables and (b) inner variables for all test cases

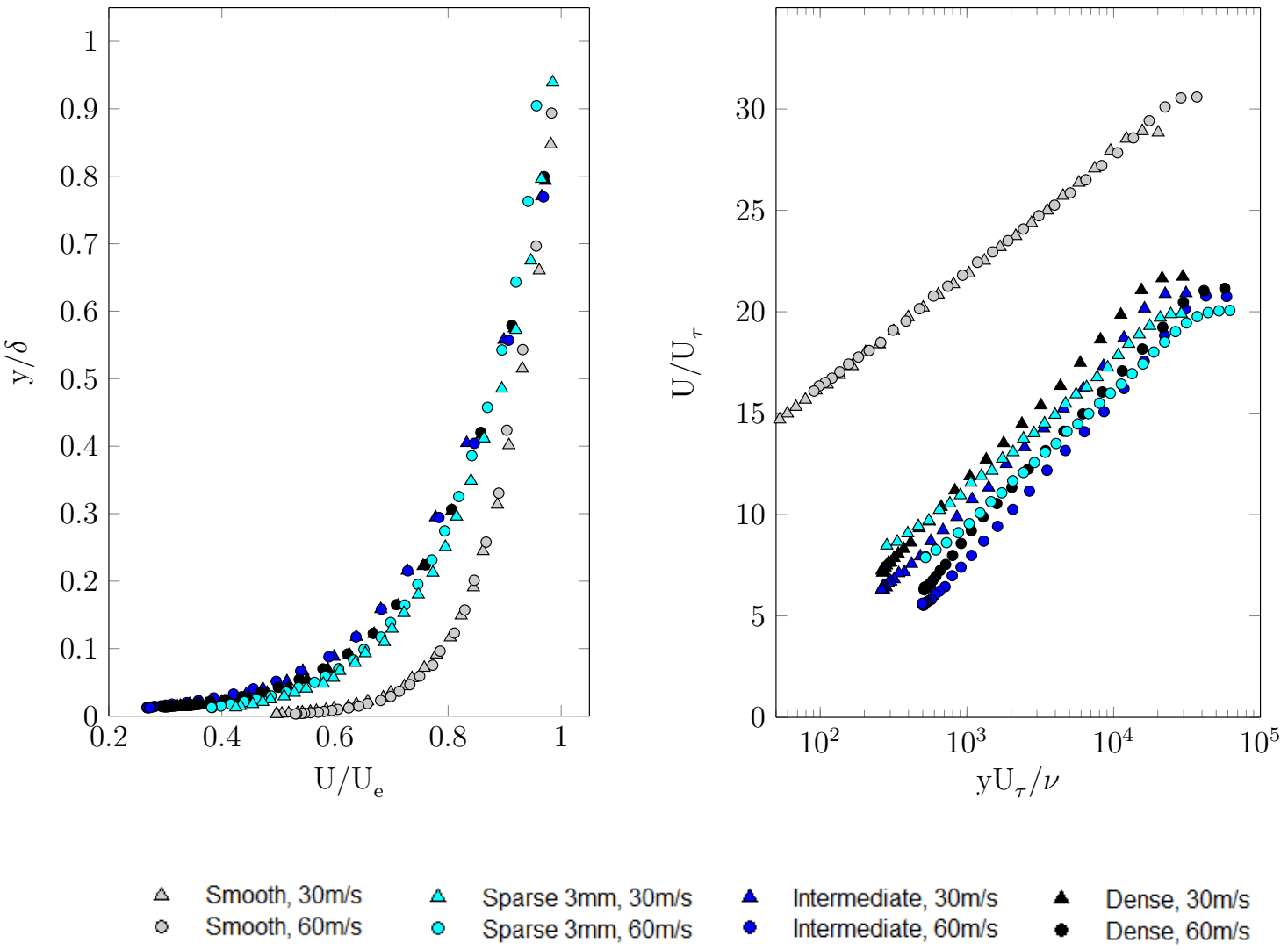

Figure 5.16: Mean streamwise velocity (measured by quadwire) normalised on (a) outer variables and (b) inner variables for roughness of different densities (as outlined in fig. 2.10).

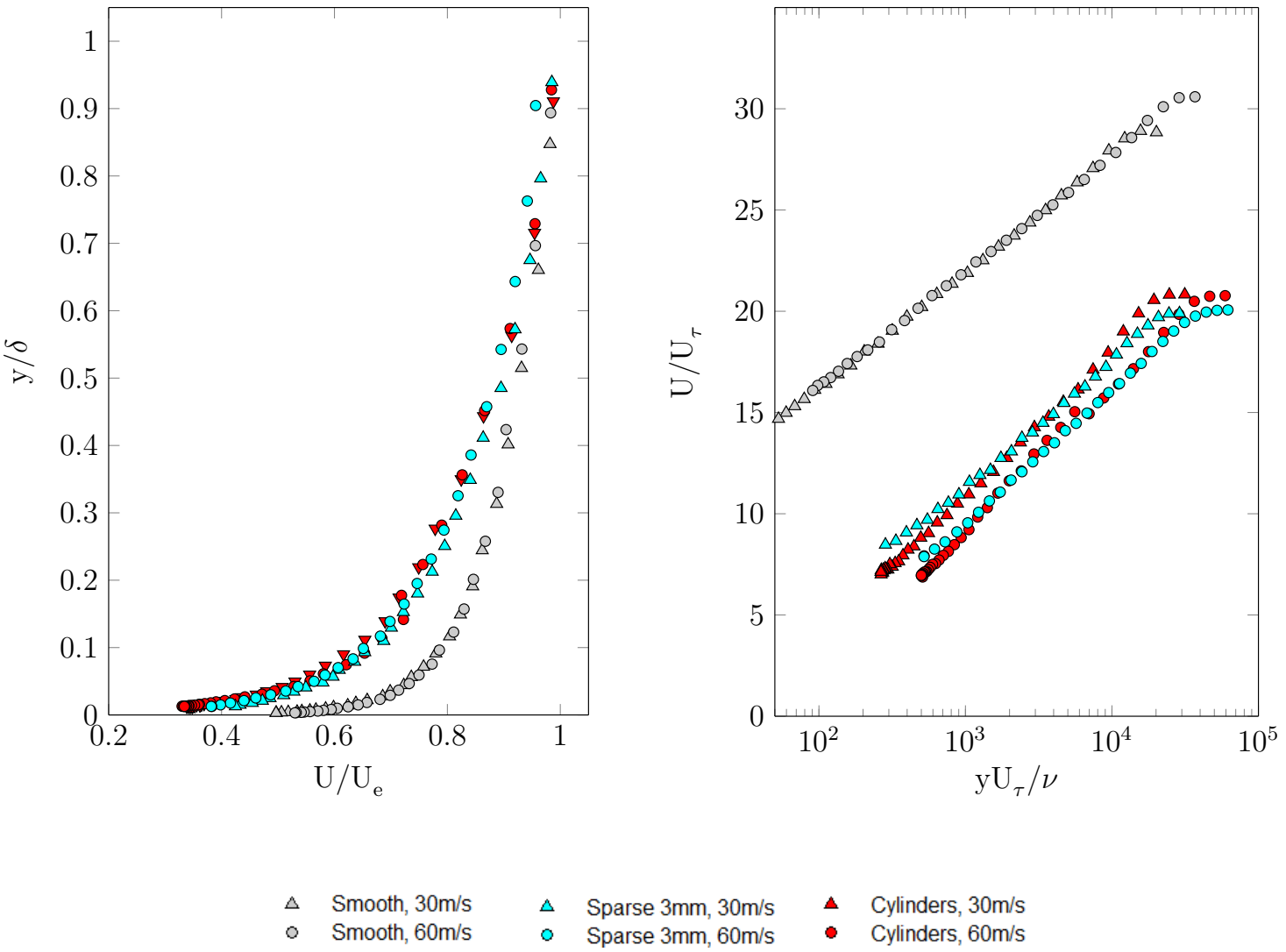

Figure 5.17: Mean streamwise velocity (measured by quadwire) normalised on (a) outer variables and (b) inner variables for roughness of different shape (as outlined in fig. 2.10)

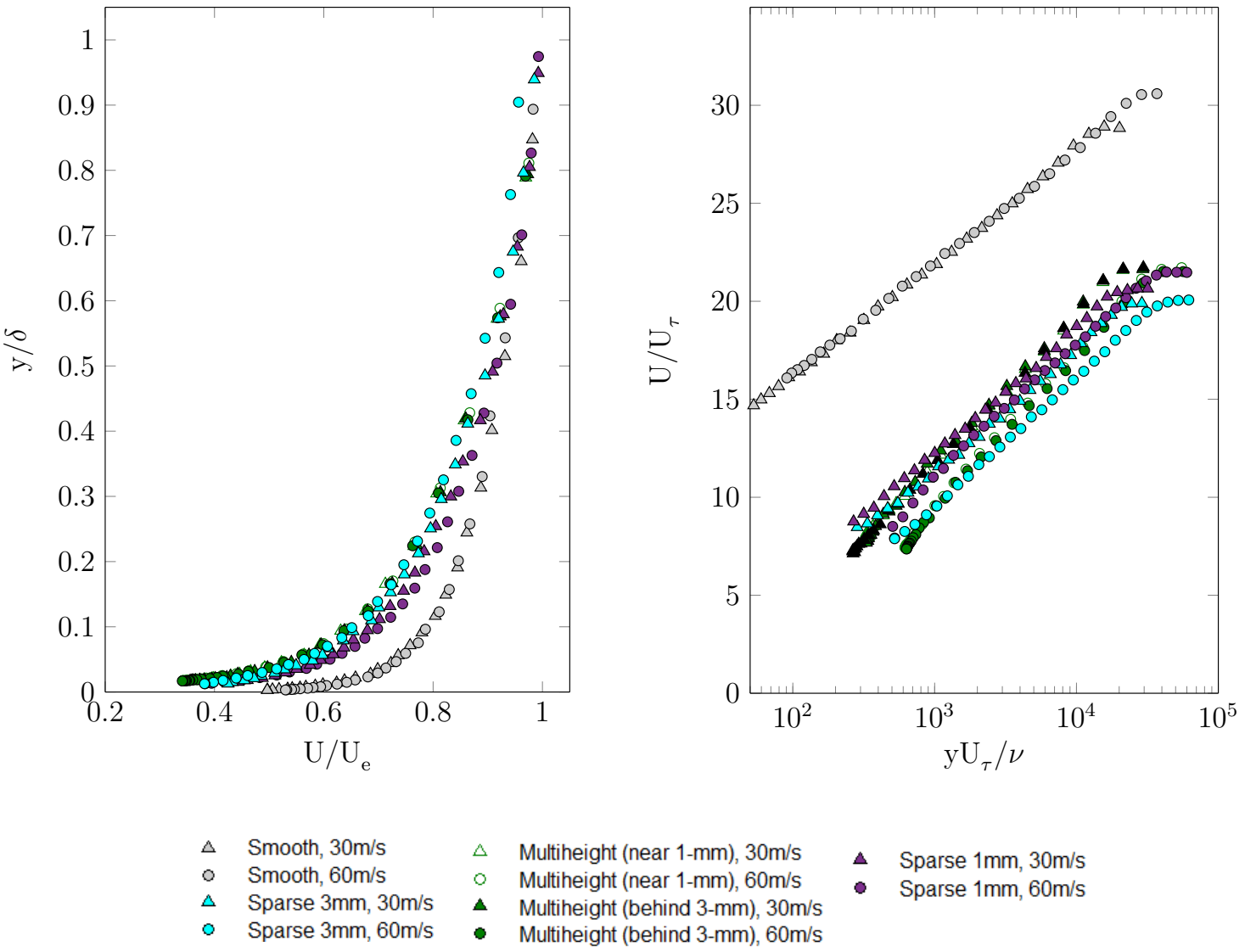

Figure 5.18: Mean streamwise velocity (measured by quadwire) normalised on (a) outer variables and (b) inner variables for size superposition (as outlined in fig. 2.10).

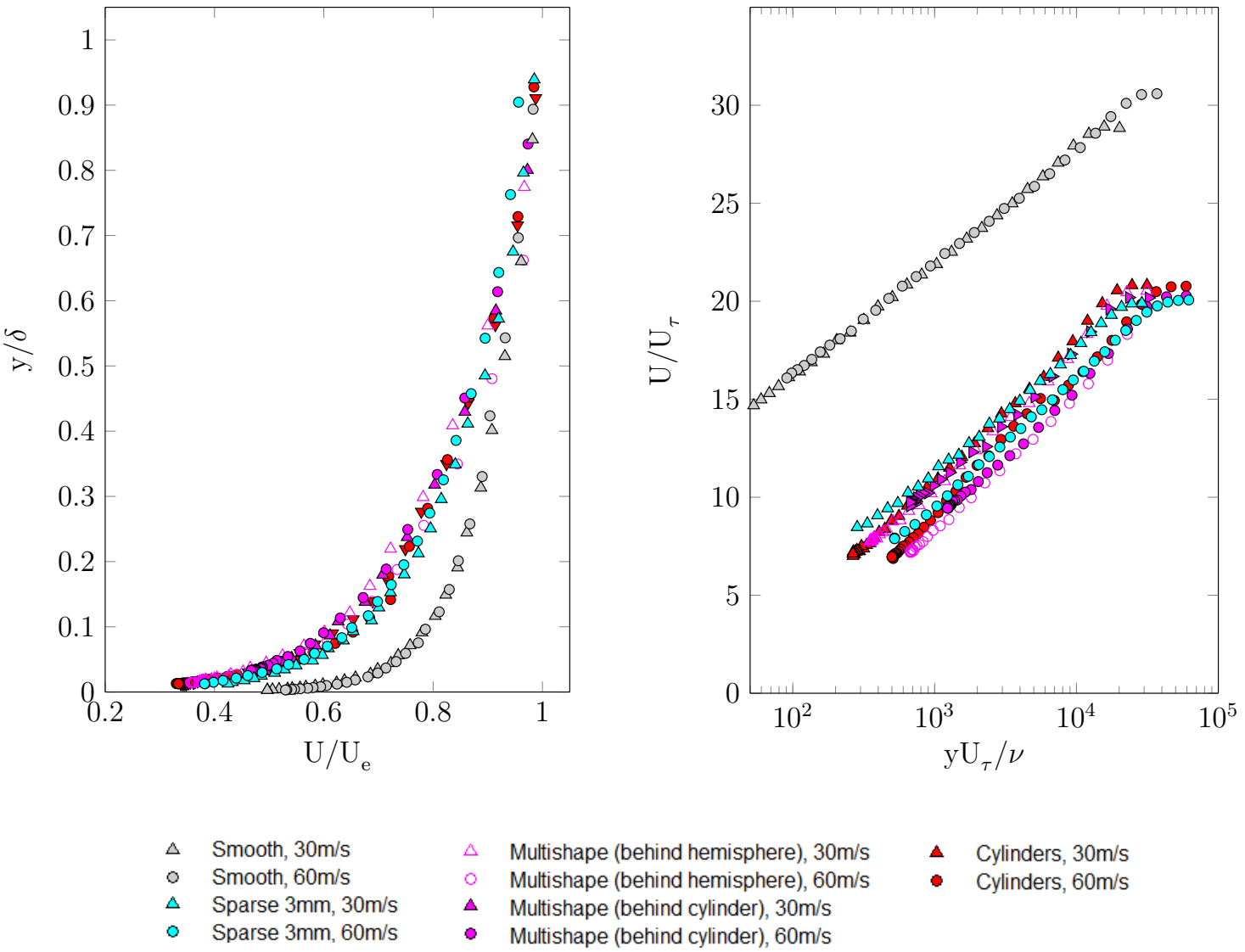

Figure 5.19: Mean streamwise velocity (measured by quadwire) normalised on (a) outer variables and (b) inner variables for shape superposition (as outlined in fig. 2.10)

The velocity profiles for the multi-height surface appear to be in agreement with the profile of the sparse 3-mm hemispheres more so than with the sparse 1-mm hemispheres. Fig. 5.18 shows that in general the differences between all three profiles at the same speed are small, but there is more agreement between the multi-height surface and the 3-mm hemispheres. This is an interesting result as it points toward the dominance of the larger roughness elements on a surface with mixed element sizes.

Fig. 5.19 presents the velocity profiles of the multi-shape surface, compared to the single element surfaces. Here we see that the multi-shape surface appears to have a larger downward shift than both the 3-mm cylinders and the 3-mm hemispheres at both speeds. The velocity profiles of the cylinders and hemispheres show fair alignment (as discussed above) and the multi-shape surface appears to combine the effect of these individual surfaces thereby having a larger downward shift. This effect is greater at 60-ms^{-1} than at 30-ms^{-1}.

Being mean velocity profiles, for a single surface the plots of fig. 5.15 should be independent of measurement location except very close to the wall. This is exactly what is observed on the multi-scale surfaces where quadwire measurements were collected at different locations relative to the elements. Despite some small deviations the profiles measured at different locations on the same surface at the same speed align fairly well.

5.4 Reynolds Stress Profiles

This section explores the Reynolds stress profiles for all surfaces considered in this work. These profiles were derived from quadwire data because the single hotwire $\overline{u^2}/U_\tau^2$ data was found to be relatively unreliable (see appendix B). Of the two parallel mounted quadwire probes, the probe which is closest to the centre of four roughness elements is used in the subsequent analysis. However, it was found in § 5.2.1 that the two quadwires agree fairly consistently so the results of either one can be used.

Reynolds normal stress profiles are presented in fig. 5.20 for all the surfaces under consideration. The symbols are as defined in fig. 5.15. The dashed line represents the -1.26 slope in terms of the natural logarithm, as postulated by Marusic [60], and the dash-dot line represents 30% of this slope, as described by the data of Fernholz and Finley [61]. Note that the present instrumentation could not obtain data close enough to the wall to capture the well-known inner characteristic peak of the $\overline{u^2}/U_\tau^2$ profile.

The presence of the logarithmic region on these profiles, like with the mean profiles of § 5.3, is evident as a linear portion of the plots. The point at which the outer region begins is also more clear than with the mean profiles. The effect of speed on the profiles is most noticeable in the outer region where higher speeds produce higher magnitude normal stresses. This is indicative of the increased turbulence levels in the flow at 60-ms^{-1} compared to 30-ms^{-1}. So we examine these two cases individually to ascertain the effects of the roughness geometry.

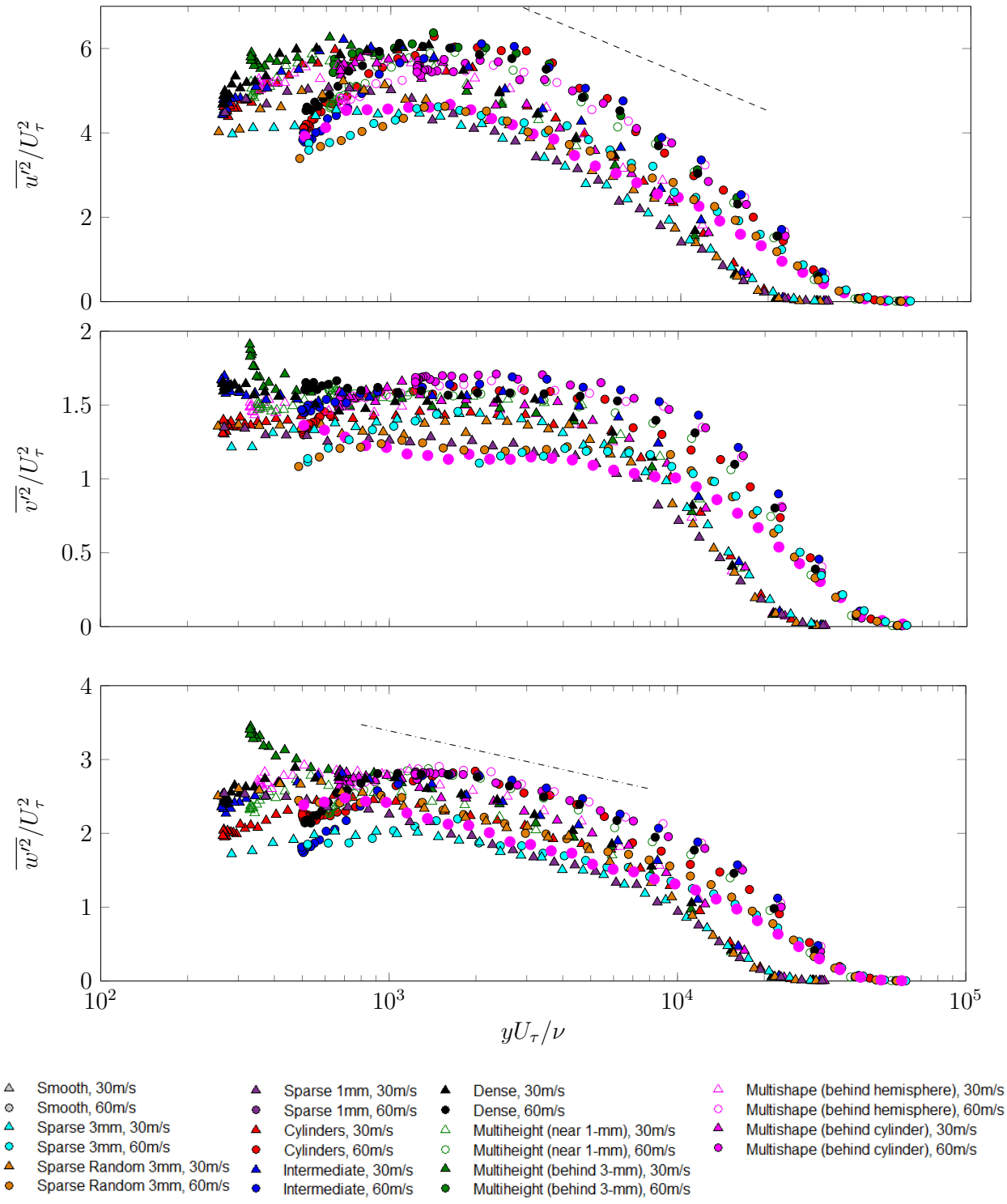

Figure 5.20: Normal Reynolds stress profiles normalised on inner variables for all test cases (including data of Meyers *et al.* [1]). Also shown on the $\overline{uv}$ profile is a -1.26 slope in terms of the natural logarithm (- - - -) as proposed by Marusic [60]. Also shown on the $\overline{uv}$ profile is 30% of this slope (-·-·-·) as found by Fernholz & Finley [61]

Fig. 5.21 presents the Reynolds normal stresses at 30-ms^{-1} while fig. 5.22 presents the Reynolds normal stresses at 60-ms^{-1} for all test cases. At both speeds, the data of Meyers *et al.* has lower magnitude within the semi-logarithmic region. This is especially evident in the $\overline{u^2}/U_\tau^2$ and $\overline{w^2}/U_\tau^2$ profiles at 30-ms^{-1} and all profiles at 60-ms^{-1}. However, the outer region shows some similarity for all cases, pointing toward the free-stream turbulence levels being about the same for both experiments. Looking closer at the current data set, there does appear to be significant differences among the rough and even the smooth wall data. The profiles presented are normalised on local values of U_τ and yet we still observe deviations. This calls into question the effectiveness of U_τ as the velocity scaling parameter in the outer regions of the flow.

The Reynolds shear stress $-\overline{uv}$ is important in the two-dimensional turbulent boundary layer as it is a dominant part of the overall shear stress and a major contributor to the production of turbulent kinetic energy. The other shear stresses, as with V and W in § 5.3, are considered to be zero because they are negligibly small compared to the uncertainty. Proof of this can be explored in § 5.2.1. So we focus on $-\overline{uv}$ which is presented, normalised on inner variables, in fig. 5.6.

There appears to be some dependence on roughness geometry for the Reynolds shear stress evident as scatter at the lower end of the semi-logarithmic region. Despite instrumentation associated errors being larger as we approach the wall and y^+ decreases, from our discussion in § 2.3.5 we know that these are negligible in the present measurement region. Thus the scatter closer to the wall is likely a real rough-wall flow effect. After the peak in the profile there appears to be similarity among all surfaces, for each speed, up to the edge of the boundary layer.

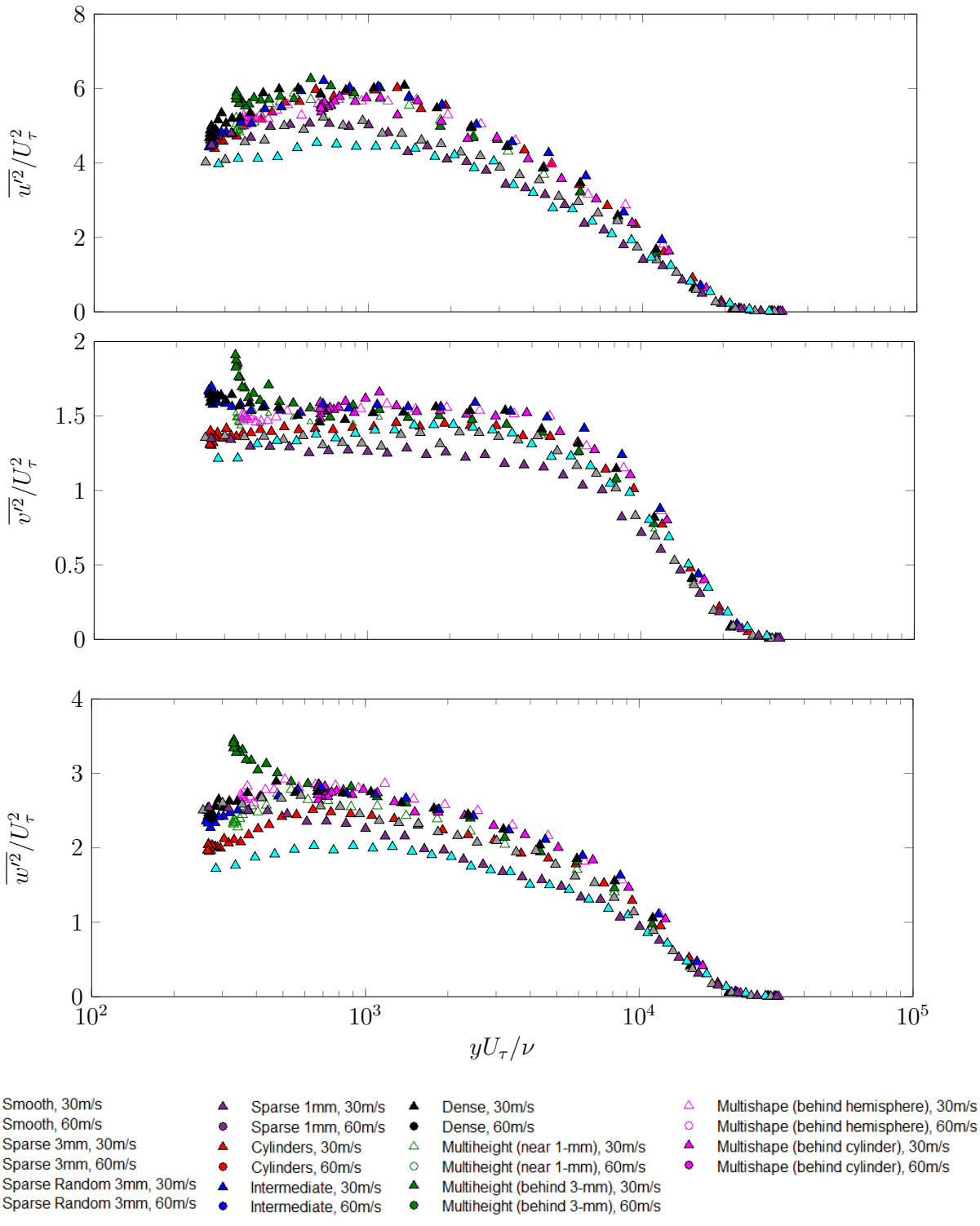

Figure 5.21: Normal Reynolds stress profiles normalised on inner variables for all test cases measured at 30-ms^{-1}. Symbols as defined in fig. 5.15

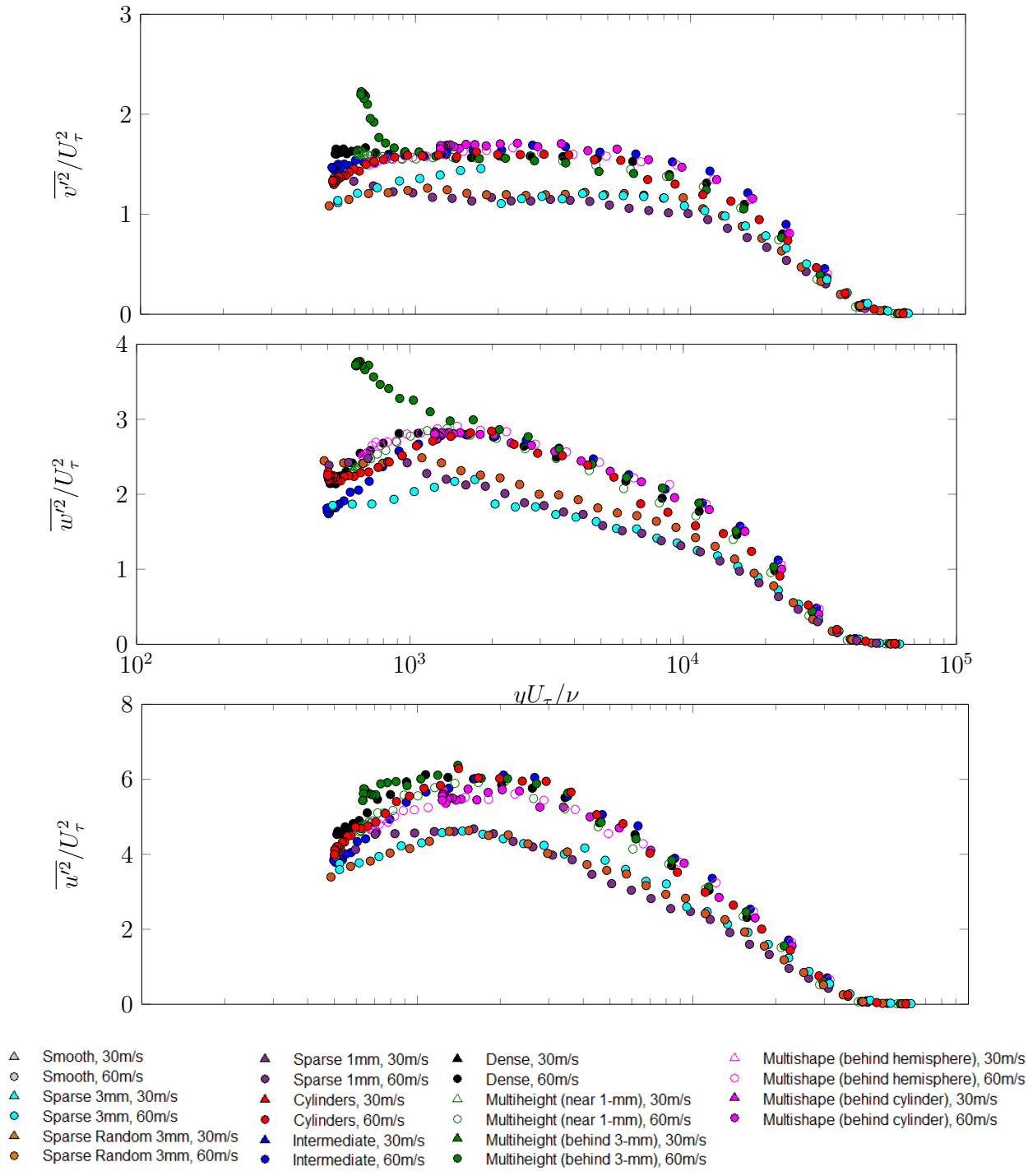

Figure 5.22: Normal Reynolds stress profiles normalised on inner variables for all test cases measured at 60-ms^{-1}. Symbols as defined in fig. 5.15

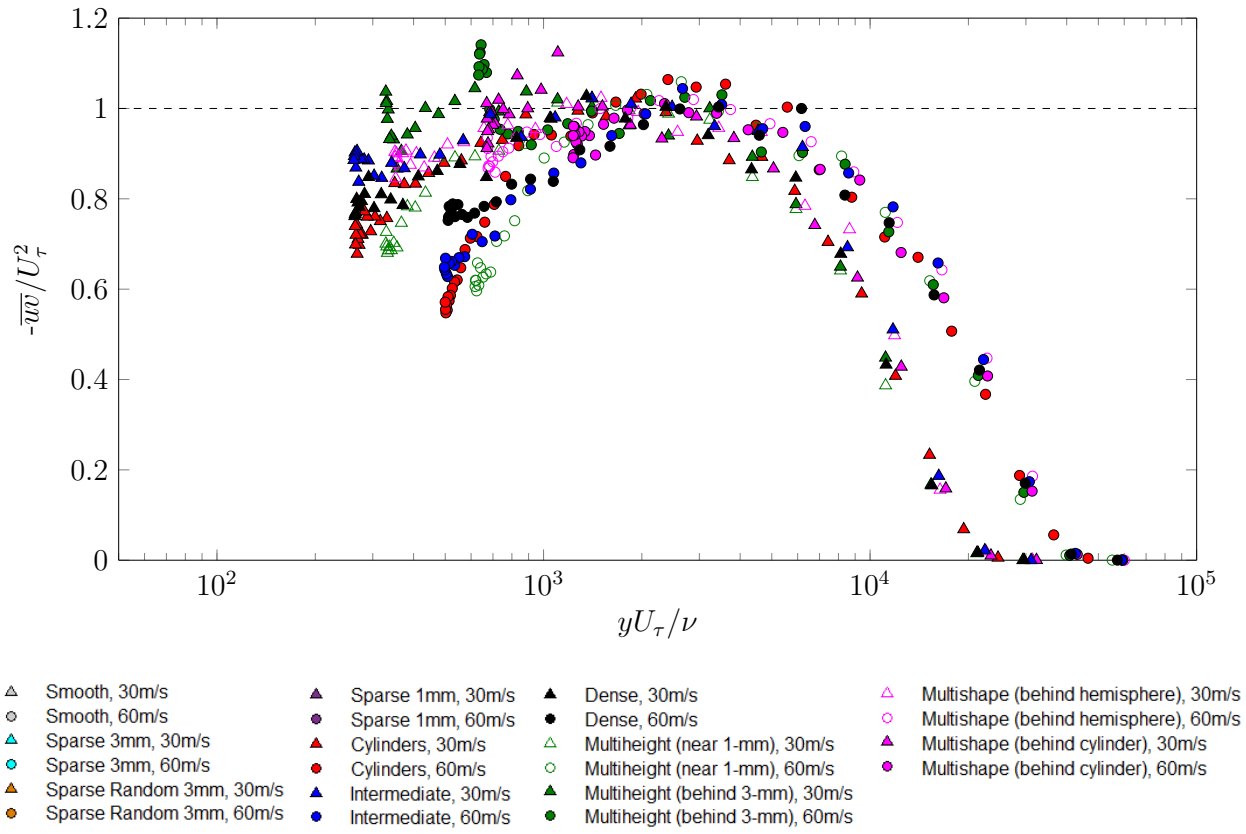

Figure 5.23: Reynolds shear stress, $\overline{uv}$, normalised on friction velocity, U_τ. Symbols as defined in fig. 5.15

6. Scaling Laws

The last three chapters have shed light on the nature of the pressure and turbulence field in the turbulent boundary layer over different rough surfaces. With this understanding we attempt to uncover universal scaling laws which may exist for the pressure spectrum. Correctly scaling the pressure spectrum means identifying the parameters which govern the behaviour of the different scales. For this process we will start by assuming that the triple scaling hypothesis of Meyers *et al.* [1] holds. Therefore, we explore scaling laws for the low-, mid- and high-frequency portions of the spectrum independently.

6.1 High Frequency Scaling

The high frequency region is the part of the pressure spectrum where viscous action induces a rapid roll-off of slope $\sim \omega^{-5}$. Prior to 2015 this was considered to be part of an inner region where roughness effects were dominant. Meyers *et al.* [1], as part of their triple scaling hypothesis, proposed that at the highest frequencies, the flow would be governed entirely by viscosity. They went on to prove this by developing a high frequency scaling based exclusively on viscosity. The *Meyers et al.* high frequency scaling is discussed at length in § 1.7. It employs a time scale ν/U_ν^2 and the spectrum is normalised on $U_\nu/\tau_\nu^2\nu$, where U_ν is the part of U_τ which does not include pressure drag on the elements. It is called the shear friction velocity and τ_ν is the corresponding shear stress. While this scaling appeared successful and is based on a well-reasoned hypothesis, it is untested when it comes to changes in roughness shape, density and composite element surfaces.

Fig. 6.1 applies this high frequency scaling to the full data set from the present study as well as the data of *Meyers et al.* Presented are the averaged pressure spectra from the spanwise array of microphones for hemispherical roughness of 3-mm ordered hemispheres, 3-mm randomly distributed hemispheres, 1-mm hemispheres, 3-mm cylinders, intermediate and dense 3-mm hemispheres as well as surfaces with more than one type of element. Furthermore, cases where microphones are installed at different element-relative locations are also included for the multi-scale surfaces. Each case is shown at five speeds between 20-70-ms^{-1}. In total, fig. 6.1 presents 65 individual rough wall cases. Add in the smooth wall case of the present study and that of Forest [87] and the total rises to 75 curves.

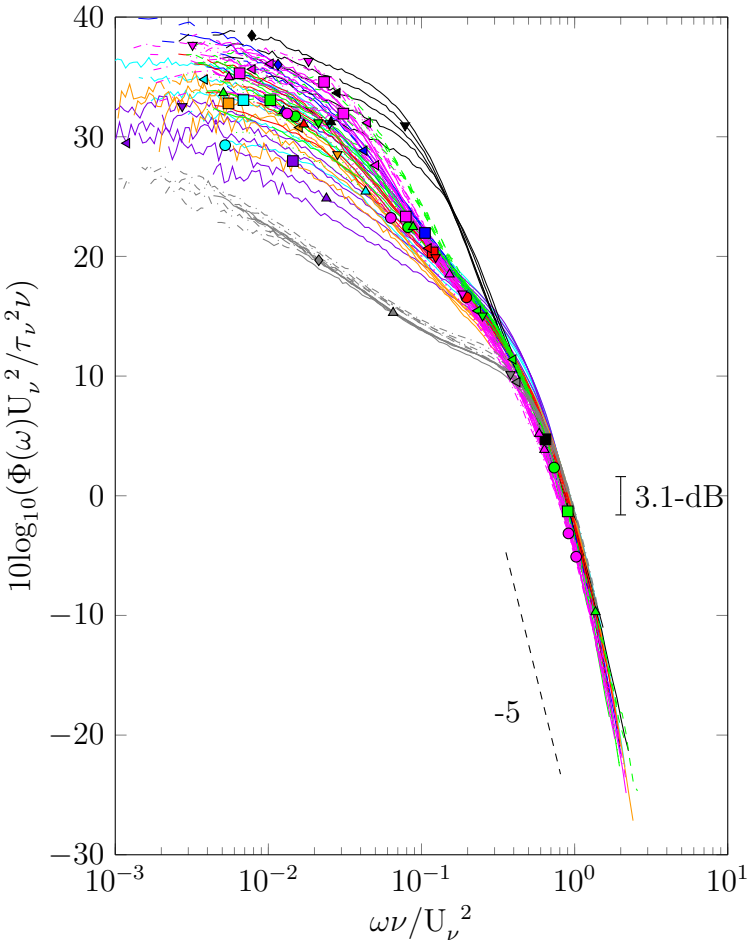

Figure 6.1: High frequency scaling of Meyers *et al.* [1] applied to present data and the data of Forest [87] and Meyers [103]

Table 6.1: Symbols used in scaling plots for each test case under study

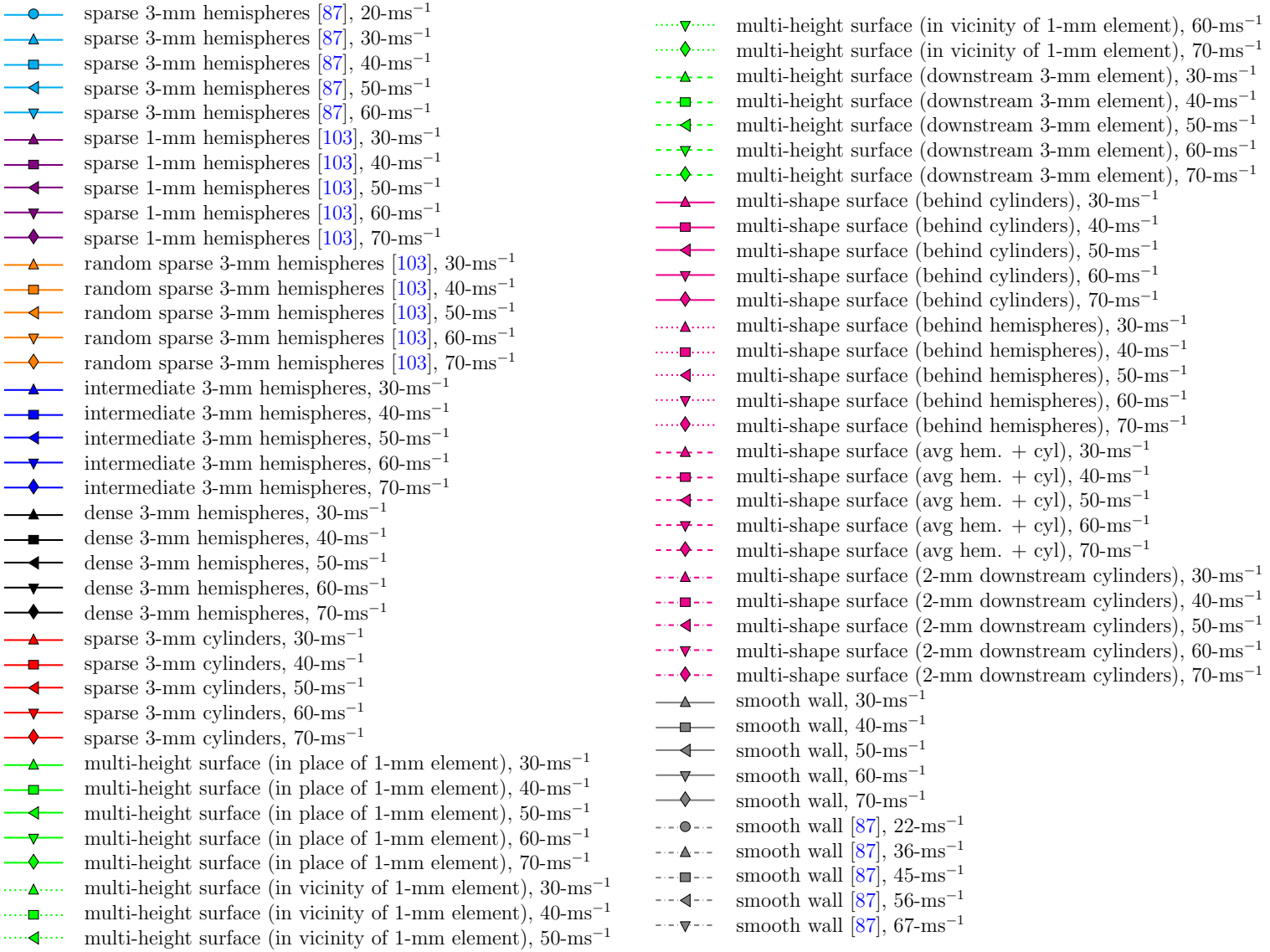

The values of U_ν for each data set were determined through an iterative adjustment of U_ν to obtain the best fit in fig. 6.1. This involved carefully varying U_ν/U_τ down to two decimal points. Finer adjustments to U_ν/U_τ did not result in noticeable changes in the fit. The values for the rough wall data were adjusted in order to align with the smooth wall data, which will, by definition, have U_ν/U_τ=1. In this way the smooth wall served as an anchor case for alignment and fit. As rightly stated by Meyers *et al.*, this iterative approach is sufficient in producing appropriate values of U_ν since it involves changing only a single parameter to satisfy a two degree of freedom fit. An uncertainty of $\pm$0.05 is associated with U_ν/U_τ. This value is based on the maximum difference between two estimates of U_ν/U_τ which both produce a user-defined fit.

At first sight, the collapse of all 75 curves in the high frequency region appears convincing. However, it would not be wise to judge whether the spectra are indeed scaled from simple subjective inspection. A reliable criteria is required. We can consider the uncertainty associated with the high-frequency portion of the spectrum and the uncertainty of the scaling variables to do this. The maximum uncertainty of all the scaled spectra was found to be $\pm$2.2-dB which means that if 95% of the curves exists within a 3.1-dB band, a collapse is achieved. We can therefore impose the criteria that 95% of the curves must be within this dB band (vertically) in order for this scaling to be deemed successful.

Based on this criteria, we can state with certainty that the high-frequency portions of the 75 curves presented in fig. 6.1 have been successfully scaled by the Meyers *et al.* scaling.

At frequencies above $\omega\nu/U_\nu^2$=0.5, all curves converge to a narrow band about 3.5-dB wide. The slope of this line is very close to the theoretical -5 slope. At highest frequencies there does appear to be some evidence of scatter of the data but this is most likely due to lingering microphone resolution issues.

Interestingly, each surface appears to be collapsed individually over different speeds in the mid-frequency region as well. The dense roughness for example, is converged down to $\omega\nu/U_\nu^2$=0.1 and the smooth wall is similarly converged to as low as $\omega\nu/U_\nu^2$=0.006. However the slopes of the collapsed mid-frequency regions vary significantly from surface to surface. The slope appears to drop-off with roughness density, decreasing from the dense roughness of slope $(\omega\nu/U_\nu^2)^{-3}$ to the smooth wall cases of slope $(\omega\nu/U_\nu^2)^{-0.8}$. This is true for all cases except the multi-height case when the microphone was directly behind a 3-mm element, and the multi-shape surface when the microphone was directly behind a cylinder. In each of these special cases, the slope of the collapsed mid-frequency region is higher than the slope of the spectrum measured in the middle of a four element array on the same surface. So it appears that the slopes in the mid-frequency are in fact ordered by closeness of the microphone to the rough elements (which is tied to roughness density, as discussed in chapter 3), and not λ.

The importance of this observation is not just that the mid-frequency region appears to be governed by transducer placement. The fact that each case collapses independently (on speed) but does not collapse universally into a narrow band suggests that the concept of an

'overlap' region may not applicable to rough surfaces. There is likely a distinct mid-frequency region which is dependent on roughness geometry. This finding supports the triple scaling hypothesis and thus we will continue with our initial assumption of three scaling regions.

6.1.1 The Shear Friction Velocity

Recall that the shear friction velocity, U_ν, has been defined as the portion of the friction velocity U_τ which is due to friction and not the pressure drag on the rough elements as defined in eq. (6.1) from Meyers *et al.*

$$U_\tau^2 = U_\nu^2 + \lambda C_{D_p} \overline{q}/\rho \tag{6.1}$$

where C_{D_p} is the pressure drag coefficient on the roughness elements, $\overline{q}$ is the dynamic pressure averaged over the height of the element and ρ is the flow density. Thus U_ν is associated with the viscous component of drag. Since C_{D_p} and U_τ are not local quantities, we expect that U_ν in eq. (6.1) will also be an area averaged quantity, and therefore a global parameter.

Recall from our discussion in § 3.7 that there is a strong dependence of the viscous scales (the high frequency portion of the spectrum) on the transducer location. It therefore follows that the viscous shear, and the shear friction velocity which is the relevant scaling velocity, would vary at different locations on a given surface. The shear friction velocity, in this view, is therefore a local quantity. Thus we will define U'_ν as the local values of the non-local parameter U_ν. Recasting U_ν in this way is not just physically consistent, but it matches the results of fig. 6.1.

Table 6.2 lists both local and global values of the shear friction velocity for each surface. U_ν is found as the root mean square (RMS) of the local U'_ν values. The RMS was used as opposed to an arithmetic average to eliminate bias for values close to the mean value. $U'_\nu = U_\nu$ for surfaces where measurements were made at only one element relative location. Data from similar locations, such as in the vicinity of the 1-mm elements and in place of a 1-mm element on the multi-height surface, collapsed on the same values of U'_ν. Data from locations which put microphones in markedly different parts of the flow, such as behind a cylinder versus behind a hemisphere on the multi-shape surface, collapsed on slightly different values of U'_ν (13% difference in the largest case). The fact that the spectra collapse using local values supports our proposal that U'_ν is in fact a local representation of the viscous effects on the wall.

The local values of shear friction velocity, U'_ν, used for each data set in fig. 6.1 are plotted against roughness Reynolds number in fig. 6.2. These element-relative locations are discussed in depth in figs. 2.31 to 2.35. An estimated uncertainty of ± 0.05 is associated with U_ν/U_τ. Additionally k_g^+ for the multi-height surface is calculated using a characteristic length, l_c, which is the average of the two k_g which exist on the surface (l_c=2-mm).

Table 6.2: List of local (U'_ν) and area-averaged (U_ν) shear friction velocities for each surface tested during the present study

		30-ms^{-1}	40-ms^{-1}	50-ms^{-1}	60-ms^{-1}	70-ms^{-1}
Intermediately-spaced	U_ν U'_ν	0.96	1.22	1.46	1.73	1.95
Densely-spaced	U_ν U'_ν	0.75	0.94	1.13	1.30	1.45
Cylinders	U_ν U'_ν	1.25	1.61	1.94	2.29	2.62
Multi-height Surface	U_ν	0.94	1.19	1.43	1.67	1.88
– in place of 1-mm element		0.98	1.24	1.48	1.73	1.94
– in vicinity of 1-mm element	U'_ν	0.98	1.24	1.48	1.73	1.94
– downstream 3-mm element		0.85	1.09	1.34	1.55	1.75
Multi-shape Surface	U_ν	0.97	1.24	1.48	1.71	1.96
– downstream cylinder		0.93	1.19	1.41	1.63	1.87
– downstream hemisphere	U'_ν	1.05	1.34	1.61	1.87	2.15
– 2-mm downstream cylinder		0.93	1.19	1.41	1.63	1.87

In fig. 6.2 all data except that of the dense roughness form a narrow band, considering the ± 0.05 uncertainty. This curve initially decreases with k_g^+ then begins to flatten out at $k_g^+ \approx 300$, gradually decreasing through a constant value of U_ν/U_τ of about 0.6. This is an interesting result because these data comprise of rough elements of different heights, shapes, and densities, yet they all lie within 15% of each other. This is true also for the multi-scale surfaces measured at different locations. The dense roughness is not part of the pack, even though the sparse and intermediate surfaces are within 4% of each other. This tells us that the element density is only a consideration above a certain point. This again supports the Dvorak-Simpson theory of a roughness density threshold above which the drag on the surface is markedly different.

Consider now the global, area-averaged shear friction velocity, U_ν. This single value, when used for all locations on the same surface, produces a high frequency collapse that is as convincing as in fig. 6.1 despite not being as tight – a spread of 4-dB instead of 3.5-dB. Trends in U_ν are presented in fig. 6.3.

As in fig. 6.2, fig. 6.3 all the data appear to form almost a single curve which initially decreases with k_g^+ then begins to flatten at $k_g^+ \approx 300$. That is, all the data except for the dense roughness. These averaged data show less scatter causing the outlying dense roughness case to become even more apparent.

It seems that whether one uses the area-averaged U_ν or the local U'_ν values for a single surface, the ultimate outcome is about the same. Either estimate of shear friction velocity is able to scale the high frequency portion of the pressure spectrum measured at different

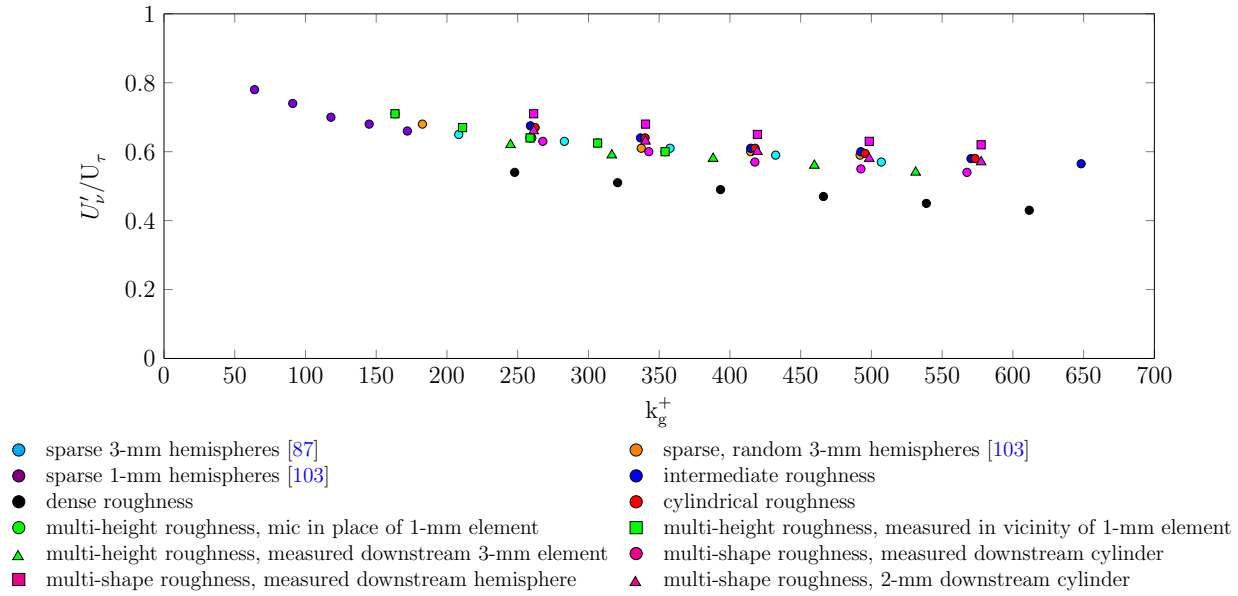

Figure 6.2: Ratio of local shear friction velocity, U'_ν, to friction velocity as a function of Reynolds Number, k_g^+

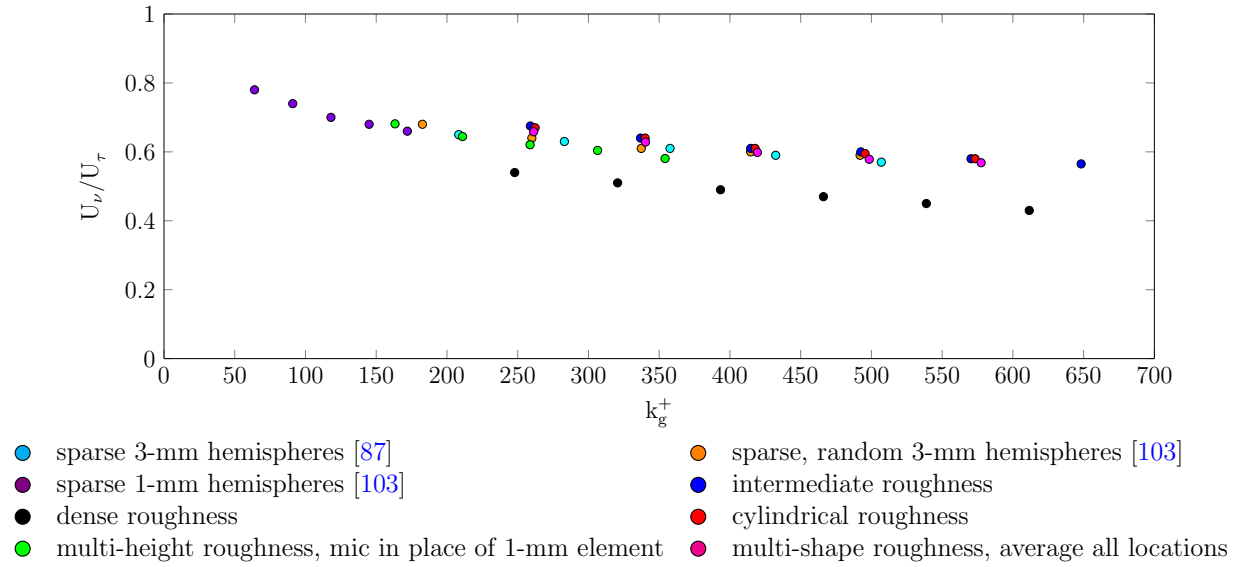

Figure 6.3: Ratio of area-averaged shear friction velocity,U_ν, to friction velocity as a function of Reynolds Number, k_g^+.

locations as well as reveal the effect of element density on estimates of U_ν/U_τ. This reinforces our hypothesis from § 3.7: the high frequency region is indirectly affected by differences in the flow field caused by relative distance to the rough element. The fact that both the local and global estimates of shear friction velocity are effective in scaling, does not mean that the distinction between the two parameters is not important. There are implications of this distinction for the viscous flow, for example, the rough wall drag.

6.1.2 Implications for Rough-Wall Drag

The relationship between drag and viscosity in the turbulent boundary layer is an important topic. The role of roughness in drag production is a further complication which is not adequately understood. The apparent success of the Meyers *et al.* high frequency scaling suggests that the shear friction velocity is an important parameter in this process.

Equation (6.1) can be re-written as

$$1 = \frac{\overline{U}_\nu^2}{U_\tau^2} + \frac{U_p^2}{U_\tau^2} \tag{6.2}$$

where U_p is the area-averaged pressure term from eq. (6.1). In this form eq. (6.2) allows us to compare the contributions to total drag from pressure drag and from the friction drag. We can plot this for the rough wall cases under study to produce fig. 6.4. Here roughness Reynolds number is on the x axis and the y axis represents the fraction of the total drag which is due to viscous shear. The dashed line marks the point where pressure and viscous drag are equal such that above this line the drag is mostly due to viscous action, and below this line pressure drag is predominant. The uncertainty in $\overline{U}_\nu^2/U_\tau^2$ is estimated as ± 0.1.

fig. 6.4 shows substantial viscous contribution to the friction well beyond Reynolds numbers at which the flow is normally assumed fully rough. Furthermore, the gradual rate of decrease of viscous friction suggests it is likely to remain a substantial contributor to the drag at Reynolds numbers representative of full scale. If we define 'fully rough' behaviour as the regime in which the skin friction is predominantly due to form drag on the roughness elements [46], then according to fig. 6.4 fully rough behaviour doesn't begin until $k_g^+ \approx$ 150-250 (conservatively due to uncertainty). This is in contrast to the criteria of Jiménez [42] which cites $k_g^+ \sim 80$ as the minimum Reynolds number for fully rough behaviour, based on the practical observation that k_s/k_g becomes constant at this Reynolds number. This disagreement is most likely because the present study and that of Forest [87] and Meyers [103] have been able to achieve experimental Reynolds numbers higher than most previous studies. As such the increased scale separation allows the true behaviour of the viscous scales to become apparent. It is also possible that the discrepancy in the 'fully rough' limit lies in the fact that the Jiménez criteria is based on k_s which we have come to see is not the appropriate length scale for the high frequency region.

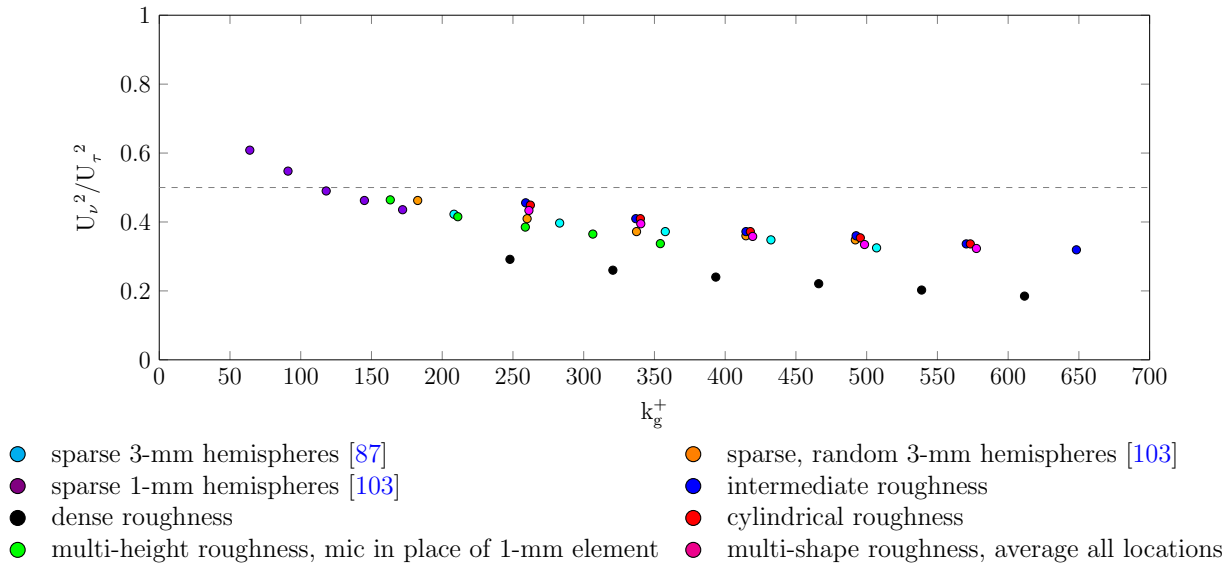

Figure 6.4: Ratio of the square of the area-averaged shear friction velocity to friction velocity, U_ν, as a function of Reynolds Number, k_g^+. - - - - demarcates where pressure drag and friction drag on elements are equal.

In almost all cases the pressure drag is greater than the friction drag. All the rough wall cases presented in fig. 6.4 are within 15% of each other, behaving almost as a single curve. This, despite comprising of surfaces with different element shapes, heights and densities. To investigate this further, we attempt to isolate the pressure drag from the total drag using U'_ν.

Consider the partition of the area-averaged friction on a rough wall into viscous and pressure drag components

$$\tau_w = \tau_\nu + \tau_p \tag{6.3}$$

$$C_f = C_{f_v} + C_{f_p} = 2\frac{U_\tau^2}{U_e^2} \tag{6.4}$$

where C_{f_v} is the viscous component and C_{f_p} is the pressure component. From the high-frequency scaling, the viscous term is

$$C_{f_v} = \frac{\tau_\nu}{1/2\rho U_e^2} \tag{6.5}$$

$$= 2\frac{U_\nu^2}{U_e^2} \tag{6.6}$$

Expanding the pressure term we get

$$C_{f_p} = \frac{\tau_p}{1/2\rho U_e^2} \tag{6.7}$$

$$= \frac{D_p/A_w}{1/2\rho U_e^2} \tag{6.8}$$

$$= \frac{\frac{D_p}{A_f} \times \frac{A_f}{A_w}}{1/2\rho U_e^2} \tag{6.9}$$

$$= C_{D_p}\lambda \tag{6.10}$$

Here A_w and A_f are the planform and frontal projected areas of a single element, as defined in fig. 2.7. C_{D_p} is the pressure drag coefficient over a single element. So eq. (6.4) becomes

$$C_f = 2\frac{U_\nu^2}{U_e^2} + C_{D_p}\lambda \tag{6.11}$$

such that the element pressure drag coefficient can be obtained from the friction and shear friction velocities as

$$C_{D_p} = \frac{2}{\lambda}\left(\frac{U_\tau^2}{U_e^2} - \frac{U_\nu^2}{U_e^2}\right) \tag{6.12}$$

This represents the average pressure drag over all the elements within A_w. Which means that the global values of shear friction velocity should be used in eq. (6.12) such that

$$C_{D_p} = \frac{2}{\lambda}\left(\frac{U_\tau^2}{U_e^2} - \frac{\overline{U}_\nu^2}{U_e^2}\right) \tag{6.13}$$

.

Fig. 6.5 plots eq. (6.13) as a function of Reynolds Number for all surfaces. This includes the averaged results for the multi-scale surfaces. At low k_g^+ (below 200), the average pressure drag coefficient on the elements increases with k_g^+. This increase is slow and eventually disappears as the data plateaus. The point of asymptote occurs earlier for the more densely packed surfaces (so much so that the densest case shows about constant C_{D_p} for all k_g^+ tested) compared to the sparsely packed surfaces.

The most interesting feature of this plot is the clear separation of the data sets into distinct groups based on λ. The group with the highest C_{D_p} coincides with λ=0.052. This set includes data of from surfaces with k_g = 1-mm and 3-mm, random and ordered distribution of elements, cylindrical and hemispherical shaped elements. Despite these marked differences in geometry, the average pressure drag coefficient on the rough elements is within the uncertainty (denoted by error bars) for a given Reynolds number. Again this suggests that the variations in geometry may not be important to the small scale structures of the flow.

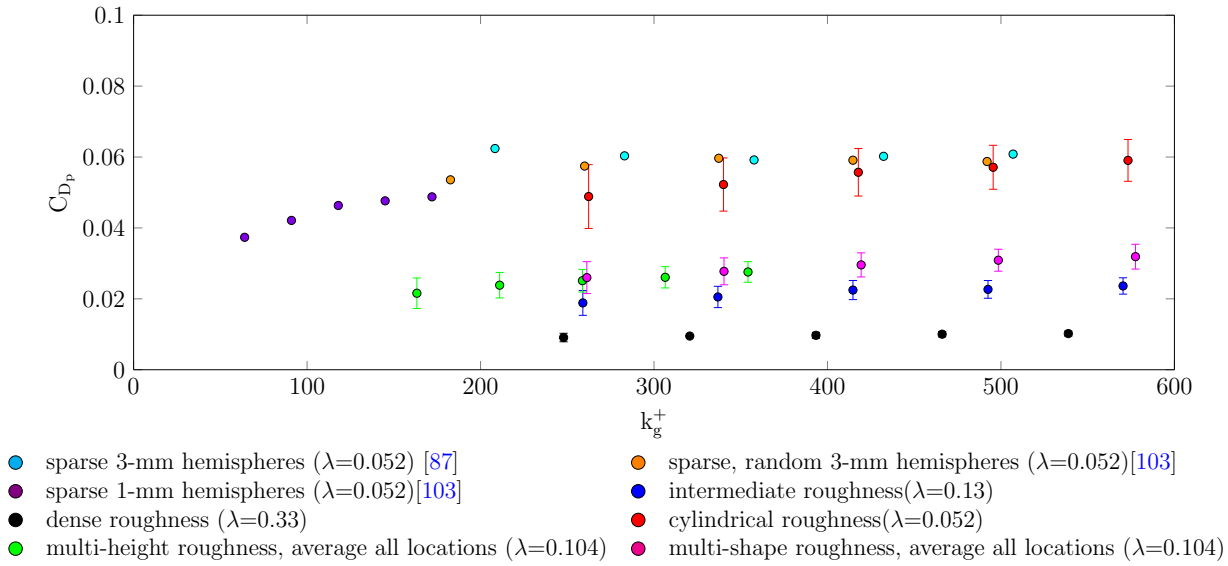

Figure 6.5: Average pressure drag coefficient on rough elements as a function of Reynolds number, k_g^+.

The second group of data range in C_{D_p} from 0.02 to 0.034 and all have $\lambda \approx 0.1$ (0.104 for the multi-scale surfaces and 0.13 for the intermediate surface). The multi-height and multi-shape surfaces have higher pressure drag coefficient than the intermediate surface because these data have slightly lower λ. It must again be highlighted that the multi-scale surfaces are significantly different in terms of element shape and size yet they have about the same C_{D_p} at a given k_g^+.

The smallest C_{D_p} is experienced on the densely packed surface. In this case we can say that C_{D_p} remains fairly constant (considering the uncertainty) at ≈ 0.009 for the Reynolds numbers tested ($250 < k_g^+ < 540$). Assuming that this case did initially have a more pronounced C_{D_p} rise, as is seen with the sparse cases, this would have occurred at small Reynolds numbers.

The main take away from fig. 6.5 is that the pressure drag coefficient increases with Reynolds number, at least up to a certain point but decreases as the elements are more closely packed. The physical basis for this density effect lies in the fact that as the elements are packed increasingly closer, they begin to shelter each other which reduces the pressure drag coefficient on the adjacent elements [46]. In this way the pressure drag coefficient is a function of only k_g and λ. This figure also validates the observations we have made in previous chapters and sections: the density of the roughness elements is more influential on the inner flow than element shape, height, and distribution.

An empirical formula developed based on the trends observed in fig. 6.5 is given in eq. (6.14).

$$C_{D_p} = 0.0009\lambda^{-1}(k_g^+)^{1/5} \tag{6.14}$$

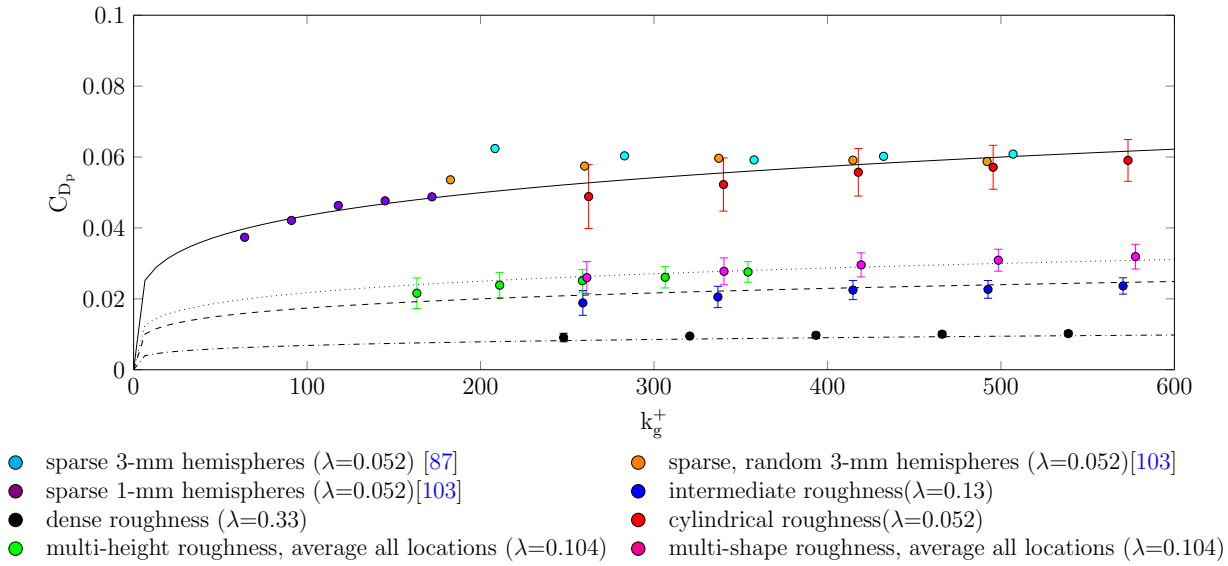

Figure 6.6: Average pressure drag coefficient on rough elements from experiment compared to the results of eq. (6.14) for different λ: ——λ=0.052; ·····λ=0.104; - - - -λ=0.13; -·-·-λ=0.33.

This formula emphasises our main finding that the pressure drag coefficient is a function of only two variables – k_g and λ. In the function C_{D_p} is made to vary as λ^{-1} because pressure drag coefficient will decrease as elements are more tightly packed. At the same time the $^1/_5$ power on k_g^+ enforces a gradual increase of the function with increasing k_g^+, just as is seen in the data in fig. 6.5.

The effectiveness of eq. (6.14) can be gaged from fig. 6.6. This includes the same data as fig. 6.5 but with the results of eq. (6.14) added in (lines). Equation (6.14) was evaluated with the λ values for each data set (0.052, 0.104, 0.13, 0.33) and roughness Reynolds numbers ranging from 0 to 600 to obtain these results.

The empirical results follow the data fairly well for each λ, considering the uncertainty associated with C_{D_p}. The formula is able to predict the pressure drag coefficient for all element geometries (shape, size, densities, composite geometries) up to roughness Reynolds number of 600. This is promising but it would be useful to further validate this formula with data obtained at different facilities and conditions or computations.

Bennington [51] is one of the few researchers who has done drag measurements and calculations on rough wall elements. At U_e=27.5-ms^{-1} he found that a single Gaussian shaped element had a total drag of 1.96×10^{-4}-N. He produced an equation that could isolate the pressure drag from the total drag (using a control volume and momentum balance approach) such that C_{D_p}=0.0299. Since eq. (6.14) is an estimate of average C_{D_p} on a single element, it is reasonable to compare Bennington's result for the single element, with results from eq. (6.14)

providing the data used in the equation is for a fetch of the same elements under the same flow conditions. Luckily, Bennington also tested a fetch of these same Gaussian elements under the same flow conditions. This fetch had λ=0.088 and k_g^+=217. Using eq. (6.14) we find that the estimated average C_{D_p} on a single element on this fetch is 0.03. This matches well with Bennington's estimate for a single element.

6.2 Low Frequency Scaling

The low-frequency region, frequently referred to as the outer region, is the part of the wall pressure spectrum which is unaffected by viscous action. Here the spectrum increases as ω^2 to a shallow maximum [77] and then begins to decrease. At high Reynolds numbers, it might be assumed that the behaviour of the spectrum in this region does not vary with changes in wall boundary conditions such as roughness configuration. This is the principle of wall-similarity (discussed at length in § 1.3.3). Instead this region is thought to be governed by the mechanics of the large scale structures and therefore responds to changes in parameters such as δ and U_e. This has been the basis of a number of proposed low frequency scalings.

6.2.1 Previously Proposed Low Frequency Scalings

Presently, the scalings which are considered to be most effective in the low-frequency region are the so-called *classical outer scaling* shown in eq. (6.15) and *Blake's outer scaling* [41] shown in eq. (6.16).

$$\phi(\omega)U_\tau/\tau_w^2\delta \text{ versus } \omega\delta/U_\tau \tag{6.15}$$

$$\phi(\omega)U_e/\tau_w^2\delta^* \text{ versus } \omega\delta^*/U_e \tag{6.16}$$

The physical merits of both of these normalisations have been discussed in §§ 1.6 and 1.7. They are rooted in the idea that the wall shear stress controls the velocity gradient in the outer portion of the boundary layer through the defect law. Therefore the intensity of the outer region eddies are also controlled by the wall shear stress.

We now apply these scalings to our data set with the aim of testing their universality. As with the high frequency scaling, we will use the averaged pressure spectra from the spanwise array of microphones for all surfaces including that of Forest [87] and Meyers [103]. We will also include the cases where microphones are installed at different element-relative locations and the smooth wall cases. Edge velocities range from 20 to 70-ms^{-1}. The results are shown in fig. 6.7 with the classical outer scaling in plot (a) and Blake's scaling in plot (b).

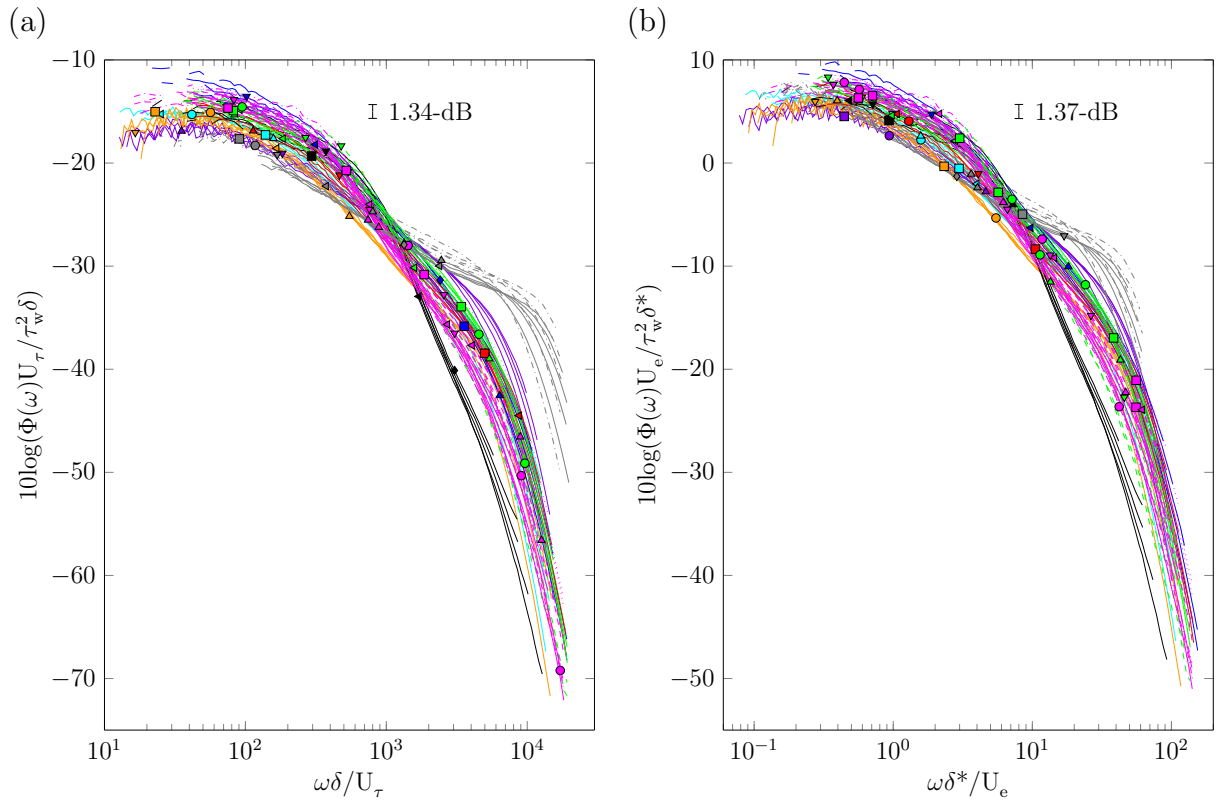

Figure 6.7: (a) Classical and (b) Blake's [41] low frequency scalings applied to present data and the data of Forest [87] and Meyers [1].

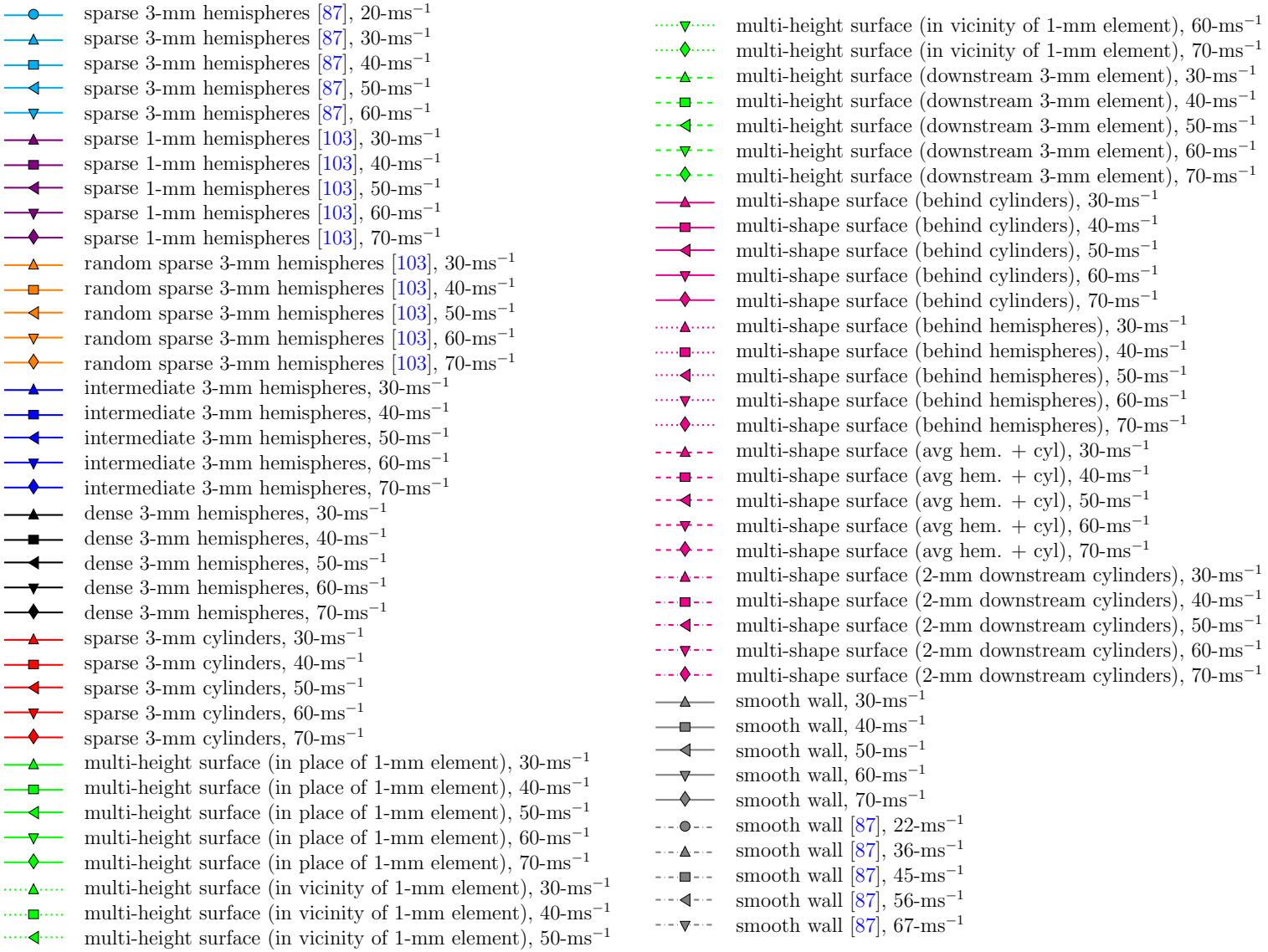
sparse 3-mm hemispheres [87], 20-ms^{-1}
sparse 3-mm hemispheres [87], 30-ms^{-1}
sparse 3-mm hemispheres [87], 40-ms^{-1}
sparse 3-mm hemispheres [87], 50-ms^{-1}
sparse 3-mm hemispheres [87], 60-ms^{-1}
sparse 1-mm hemispheres [103], 30-ms^{-1}
sparse 1-mm hemispheres [103], 40-ms^{-1}
sparse 1-mm hemispheres [103], 50-ms^{-1}
sparse 1-mm hemispheres [103], 60-ms^{-1}
sparse 1-mm hemispheres [103], 70-ms^{-1}
random sparse 3-mm hemispheres [103], 30-ms^{-1}
random sparse 3-mm hemispheres [103], 40-ms^{-1}
random sparse 3-mm hemispheres [103], 50-ms^{-1}
random sparse 3-mm hemispheres [103], 60-ms^{-1}
random sparse 3-mm hemispheres [103], 70-ms^{-1}
intermediate 3-mm hemispheres, 30-ms^{-1}
intermediate 3-mm hemispheres, 40-ms^{-1}
intermediate 3-mm hemispheres, 50-ms^{-1}
intermediate 3-mm hemispheres, 60-ms^{-1}
intermediate 3-mm hemispheres, 70-ms^{-1}
dense 3-mm hemispheres, 30-ms^{-1}
dense 3-mm hemispheres, 40-ms^{-1}
dense 3-mm hemispheres, 50-ms^{-1}
dense 3-mm hemispheres, 60-ms^{-1}
dense 3-mm hemispheres, 70-ms^{-1}
sparse 3-mm cylinders, 30-ms^{-1}
sparse 3-mm cylinders, 40-ms^{-1}
sparse 3-mm cylinders, 50-ms^{-1}
sparse 3-mm cylinders, 60-ms^{-1}
sparse 3-mm cylinders, 70-ms^{-1}
multi-height surface (in place of 1-mm element), 30-ms^{-1}
multi-height surface (in place of 1-mm element), 40-ms^{-1}
multi-height surface (in place of 1-mm element), 50-ms^{-1}
multi-height surface (in place of 1-mm element), 60-ms^{-1}
multi-height surface (in place of 1-mm element), 70-ms^{-1}
multi-height surface (in vicinity of 1-mm element), 30-ms^{-1}
multi-height surface (in vicinity of 1-mm element), 40-ms^{-1}
multi-height surface (in vicinity of 1-mm element), 50-ms^{-1}
multi-height surface (in vicinity of 1-mm element), 60-ms^{-1}
multi-height surface (in vicinity of 1-mm element), 70-ms^{-1}
multi-height surface (downstream 3-mm element), 30-ms^{-1}
multi-height surface (downstream 3-mm element), 40-ms^{-1}
multi-height surface (downstream 3-mm element), 50-ms^{-1}
multi-height surface (downstream 3-mm element), 60-ms^{-1}
multi-height surface (downstream 3-mm element), 70-ms^{-1}
multi-shape surface (behind cylinders), 30-ms^{-1}
multi-shape surface (behind cylinders), 40-ms^{-1}
multi-shape surface (behind cylinders), 50-ms^{-1}
multi-shape surface (behind cylinders), 60-ms^{-1}
multi-shape surface (behind cylinders), 70-ms^{-1}
multi-shape surface (behind hemispheres), 30-ms^{-1}
multi-shape surface (behind hemispheres), 40-ms^{-1}
multi-shape surface (behind hemispheres), 50-ms^{-1}
multi-shape surface (behind hemispheres), 60-ms^{-1}
multi-shape surface (behind hemispheres), 70-ms^{-1}
multi-shape surface (avg hem. + cyl), 30-ms^{-1}
multi-shape surface (avg hem. + cyl), 40-ms^{-1}
multi-shape surface (avg hem. + cyl), 50-ms^{-1}
multi-shape surface (avg hem. + cyl), 60-ms^{-1}
multi-shape surface (avg hem. + cyl), 70-ms^{-1}
multi-shape surface (2-mm downstream cylinders), 30-ms^{-1}
multi-shape surface (2-mm downstream cylinders), 40-ms^{-1}
multi-shape surface (2-mm downstream cylinders), 50-ms^{-1}
multi-shape surface (2-mm downstream cylinders), 60-ms^{-1}
multi-shape surface (2-mm downstream cylinders), 70-ms^{-1}
smooth wall, 30-ms^{-1}
smooth wall, 40-ms^{-1}
smooth wall, 50-ms^{-1}
smooth wall, 60-ms^{-1}
smooth wall, 70-ms^{-1}
smooth wall [87], 22-ms^{-1}
smooth wall [87], 36-ms^{-1}
smooth wall [87], 45-ms^{-1}
smooth wall [87], 56-ms^{-1}
smooth wall [87], 67-ms^{-1}

Both plots in fig. 6.7 show that all 75 curves converge in the low frequency when normalised on each respective scaling. For the classical outer scaling in fig. 6.7a, the convergence occurs below $\omega\delta/U_\tau \approx 5$ and for Blake's scaling in fig. 6.7b the alignment occurs below $\omega\delta^*/U_e \approx 5$. For both normalisations the low frequency peaks align over each other suggesting that the frequency scaling is effective.

Nevertheless the low frequency collapse itself is less than convincing. The average width of the band formed by the curves after applying the classical scaling is approximately 7-dB. The Blake scaling is slightly more successful, having an average width of 5-dB. However we should not conclude from this subjective inspection that these scalings are not successful.

As we did with the high frequency scaling, the uncertainty of the data and the scaling parameters were used to produce an independent standard for scaling success. All curves must be within their respective uncertainty band in order for the scaling to be deemed successful. Using jitter analyses the uncertainty in both scalings were ascertained for each surface at each speed. The maximum uncertainty obtained in each case was selected as the benchmark for the success of the scaling. These values are included as an error bar on each plot in fig. 6.7. Due to the fairly low uncertainty of the pressure data and the corresponding boundary layer parameters (see table 5.3), the maximum uncertainties of both normalisations are small: $\pm$1.34-dB for the classical scaling and $\pm$1.37-dB for Blake's outer scaling.

The imposed uncertainty criteria proves that neither of these scalings truly collapse the data. The average width of the band formed by the curves after applying the classical scaling is approximately 7-dB. This is over three times as large as the limits determined from the uncertainty. The Blake scaling, despite being slightly more successful, is still above the upper limit imposed by the uncertainty. So even if we err on the conservative side and relaxed our uncertainty estimate by as much as 20%, the final conclusions would be the same for both these scalings.

Two other low-frequency scalings are presented in fig. 6.8. These scalings were shown to have marginal success by Meyers *et al* [1]. The first of these is a scaling inspired by the $\overline{u'}$ scaling of DeGraaff & Eaton [113]. Their velocity scaling was developed for smooth wall turbulent boundary layers and essentially mixes the inner and outer velocity scales to collapse the streamwise fluctuating velocity. We have elected to use a time-scale of $\omega\delta/U_e$ and incorporate the DeGraaff & Eaton mixed velocity into the pressure scale as $(\rho U_e U_\tau)^2$. The full DeGraaff & Eaton scaling is

$$\phi(\omega)/U_e U_\tau^2 \rho^2 \delta \text{ versus } \omega\delta/U_e \tag{6.17}$$

The second scaling is based on the work of Klewicki [114] and is another mixed inner-outer scaling. This one is based on an inner-outer layer length-scale normalisation for smooth walls: $\delta\nu/U_\tau$. Klewicki explains that this intermediate length scale represents an average property of the underlying layer width distribution. In this way it can better characterise statistical

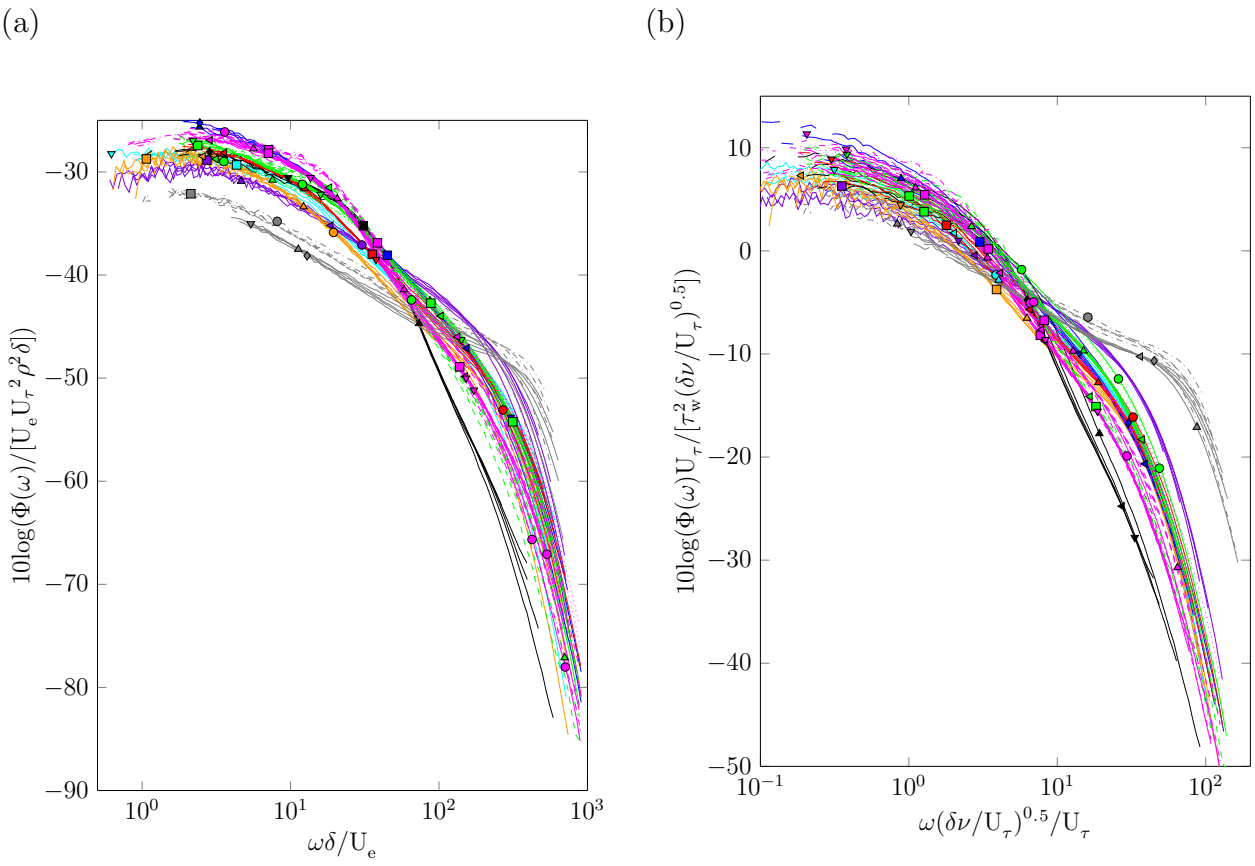

Figure 6.8: (a) DeGraaff & Eaton [113] and (b) Klewicki [114] mixed low frequency scalings applied to present data and the data of Forest [87] and Meyers [1]. Symbols as defined in fig. 6.1.

properties of the flow. Using this length scale with U_e and τ_w we obtain the following hybrid scaling:

$$\phi(\omega)U_\tau/(\tau_w^2\sqrt{\delta\nu/U_\tau}) \text{ versus } \omega\sqrt{\delta\nu/U_\tau}/U_\tau \tag{6.18}$$

It is evident that these two candidate scalings are not ideal. In fig. 6.8a the DeGraaff & Eaton type scaling does not scale the smooth wall data. These lie about 5 to 6-dB below the rough-wall data, which incidentally align fairly well in terms of frequency despite not having a tight collapse. Furthermore, the two smooth wall cases do not collapse on each other. At the very least, a successful scaling should collapse the smooth wall cases into a single curve. The most likely reason that the DeGraaff & Eaton type scaling is unsuccessful is the use of a pressure scale based on U_τ, which is not necessarily the velocity of relevance in the low-frequency region. The time scale on U_e and δ seems appropriate because the curves are aligned horizontally. However the pressure scale may not be appropriate resulting in issues

with the vertical alignment. Unfortunately the lack of collapse in fig. 6.8a disqualifies this as a possible low frequency scaling.

The hybrid Klewicki mixed length-scale normalisation shows even less collapse than that derived from the DeGraaff & Eaton normalisation, with a spread of about 8-dB at the lowest frequency. It actually appears that the curves diverge as the frequency decreases, which is the opposite of what one would expect from a low frequency scaling. Again the most likely reason for this is that this scaling uses a pressure scale based on U_τ, which may be more appropriate for the mid-frequency region than the low frequency region. This is possibly why the mid-frequency of the rough wall data in both plots in fig. 6.8 show a tighter collapse than the low frequency.

6.2.2 Low Frequency Scaling on $\overline{U}_{c_b}$

We know from chapter 4 that the low frequency content of the wall pressure spectrum comprises of large eddies in the outer region of the flow. This means that we are attempting to ascertain the time and pressure scales which govern how these large, fast moving structures behave. A good place to start would be with the classical outer scaling which has shown some success in scaling the smooth wall turbulent boundary layer [69]. This scaling uses δ as the length scale, which is probably the most appropriate parameter for this regime. After all, it makes physical sense that the largest structures in the boundary layer would have sizes on the order of the boundary layer thickness.

It is less likely that, in high Reynolds number flows, the characteristic velocity would be the friction velocity, U_τ. Indeed the defect law does suggest that the intensity of the pressure fluctuations are related to wall shear stress but this does not mean that the velocity of interest in the region is U_τ. Since we are dealing with the eddies close to the edge of the boundary layer, U_e might appear to be a more suitable velocity scale. However, we know for certain that none of the eddies are actually advecting at the velocity U_e. In fact it is known that eddies move at a convection velocity relative to their size. This convection velocity, U_c, is therefore the logical choice as a velocity-scale. The issue here is the wide range of U_c which exist in the turbulent boundary layer, especially over the rough wall (see §§ 4.2 and 4.3). Turbulent convection velocity depends not only on the position of the structures within the boundary layer but also on the type of event occurring (ejections, sweeps etc.) [115]. Considering this it would be most prudent to use the mean broadband convection velocity, $\overline{U}_{c_b}$, for scaling the pressure spectrum. This parameter was discussed at length in § 4.3, which includes uncertainty estimates and a detailed description of how values were extracted from the space-time correlations.

Finding the appropriate pressure scale is slightly more challenging. The classical outer scaling uses τ_w^2 based on the defect law. However at high Reynolds number it is somewhat improbable that the outer regions of the flow would be governed by the shear stress at the wall. It is more likely that the intensity of the pressure fluctuations is dependent on a shear

stress which is local to the outer layers of the boundary layer. Such a shear stress could be defined by the fluid density and the local velocity of the flow such that

$$\tau_{outer} = \rho U_{outer}^2 \tag{6.19}$$

where U_{outer} is the velocity which creates shear in the outer region. Understandably one might take this velocity to be the mean broadband convection velocity, per our discussion above. However, shear stress is by definition created and sustained by a velocity gradient. We propose therefore that the difference between the edge velocity and the mean broadband convection velocity would best account for the velocity gradient in the outer flow:

$$U_{outer} \equiv U_e - \overline{U}_{c_b} \tag{6.20}$$

This produces an outer region pressure scale of

$$\rho^2 (U_e - \overline{U}_{c_b})^4 \tag{6.21}$$

Putting it all together, we hypothesise that a reasonable low frequency scaling would be

$$\phi(\omega)\overline{U}_{c_b}/\rho^2 (U_e - \overline{U}_{c_b})^4 \delta \text{ versus } \omega\delta/\overline{U}_{c_b} \tag{6.22}$$

It is believed that this is the appropriate low frequency scaling because it uses outer layer parameters which also capture some of the effects of the roughness. This last point is important because we know from § 3.9 that the magnitude of the low frequency spectrum is dependent on roughness element spacing and size. In the proposed scaling this is achieved by using $\overline{U}_{c_b}$ which we know from the discussions of chapter 4 indirectly includes the effects of roughness geometry.

We can easily test this new scaling hypothesis on our data set by plotting fig. 6.9. Just as before, we take into account the uncertainties of the data, δ, U_e and $\overline{U}_{c_b}$ (outlined in table 4.1) to develop a criteria for success of this scaling.

From table 5.3 we know that

$$\begin{aligned} \delta(\rho) &= 0.0011 - \text{kg m}^{-3} \\ \delta(\delta) &= 0.00151 - \text{m} \\ \delta(U_e) &= 0.05 - \text{ms}^{-1} \end{aligned} \tag{6.23}$$

We also know $\delta(\overline{U}_{c_b}/U_e)$ for each surface from table 4.1. So the uncertainty in $\overline{U}_{c_b}$ is given by

$$\delta(\overline{U}_{c_b}) = U_c \sqrt{\left(\frac{\delta(\overline{U}_{c_b}/U_e)}{Uc/Ue}\right)^2 + \left(\frac{\delta(U_e)}{U_e}\right)^2} \tag{6.24}$$

The uncertainty associated with the scaling in eq. (6.22) is

$$\delta(\text{scaling})=\sqrt{\left(-\delta(\overline{U}_{c_b})\frac{3\overline{U}_{c_b}+U_e}{\delta\rho^2(\overline{U}_{c_b}-U_e)^5}\right)^2+\left(-4\delta(U_e)\frac{\overline{U}_{c_b}}{\delta\rho^2(U_e-\overline{U}_{c_b})^5}\right)^2+\left(-2\delta(\rho)\frac{\overline{U}_{c_b}}{\delta\rho^3(U_e-\overline{U}_{c_b})^4}\right)^2+\left(-\delta(\delta)\frac{\overline{U}_{c_b}}{\delta^2\rho^2(U_e-\overline{U}_{c_b})^4}\right)^2}$$

From here we add in the uncertainty in taking the base 10 logarithm of the scaling. The last step is to account for the uncertainty in the pressure spectrum when multiplied by the scaling. The result is that the data must collapse within a 3.4-dB wide band in order for the scaling to be considered successful. This single value was obtained from taking the maximum uncertainty across all the roughness cases in the low frequency region. This dB band is included on fig. 6.9 as a single error bar.

Fig. 6.9 shows that the low frequency peaks of the data all overlay each other, suggesting that our frequency scaling is sound. There also appears to be convergence of the data up to $\omega\delta/\overline{U}_{c_b} \simeq 40$. This includes the smooth wall and the extreme case of the dense roughness. The collapse itself spans about 2.5-dB on average. We know that this spread is due to

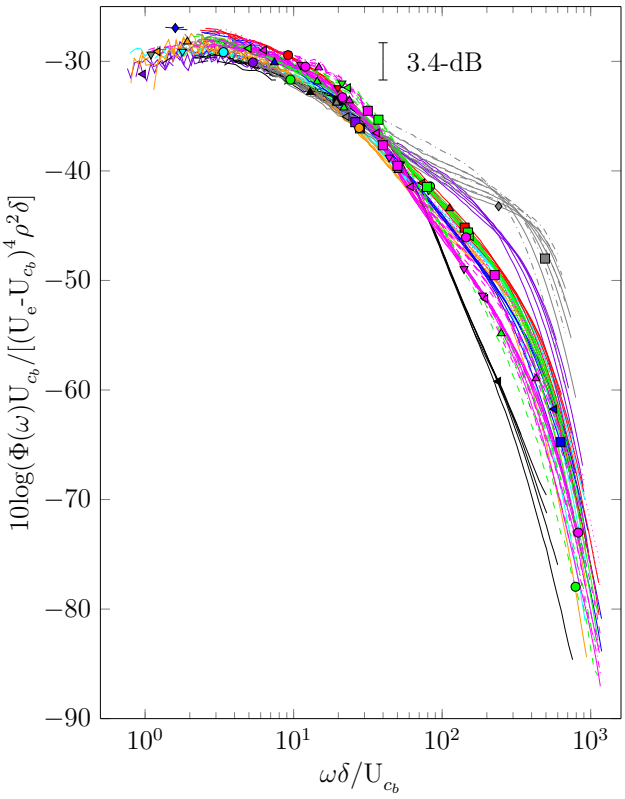

Figure 6.9: New low frequency scaling based on mean broadband convection velocity, $\overline{U}_{c_b}$, applied to present data and the data of Forest [87] and Meyers [1]. Symbols as defined in fig. 6.1.

the uncertainty in the data and scaling parameters since it is less than the pre-determined maximum of 3.4-dB.

It should be noted that the uncertainty band for this scaling is over twice as wide as for the previous scalings we examined. This is due to the high uncertainty associated with $\overline{U}_{c_b}$. Obtaining the slope of the convection ridge is not a precise process (see discussion of §§ 4.2 and 4.3). Furthermore, the new scaling raises $U_e - \overline{U}_{c_b}$ to the fourth power, magnifying the already significant uncertainties. The result is a fairly high overall uncertainty. This is not to say that the scaling isn't successful – it still lies well within the limits of the uncertainty. What we acknowledge here is that care must be taken in estimating $\overline{U}_{c_b}$ and uncertainties must be accounted for during this process.

Considering all this, we can say that to within the uncertainty, the present measurements are successfully scaled in the low frequency using the new low frequency scaling on $\overline{U}_{c_b}$. It is interesting that once scaled in the low frequency, the mid- and high frequency portions of the data are ordered by element density – the smooth wall data are at top and dense roughness data are at bottom. Recall that this was also observed with the high frequency scaling back in § 6.1, granted the order of the curves were reversed. The fact that the fluctuating pressure data naturally show a progression based on element density hints at the existence of a strong correlation between these two variables.

6.2.3 Low Frequency Scaling on $\overline{U}$

Fig. 6.9 is a very promising result, but there is a practical issue to consider – $\overline{U}_{c_b}$ cannot be obtained *a priori*. So while there may be some scientific merit in this scaling, its engineering impact is limited. In this way, we are still in need of a low-frequency scaling for practical applications such as predicting the pressure spectrum. What we can take away from the $\overline{U}_{c_b}$ scaling, apart from a new understanding of the workings of the outer region of the high Reynolds number turbulent boundary layer, is that it *is* possible to scale the low frequency region of the pressure spectrum.

An alternative velocity that one would expect to closely reflect $\overline{U}_{c_b}$ is the mean boundary layer velocity, $\overline{U}$, defined as

$$\overline{U} \equiv U_e(1 - \delta^*/\delta) \tag{6.25}$$

Replacing $\overline{U}_{c_b}$ with $\overline{U}$ in our previous scaling and in eq. (6.19), our second submission for the low frequency scaling law becomes $\omega\delta/\overline{U}$ versus $\phi(\omega)\overline{U}/\rho^2(U_e\delta^*/\delta)^4\delta$. This is applied to the data in fig. 6.10 with an associated maximum uncertainty band of 2.1-dB.

In fig. 6.10 the low frequency peaks are overlaid and the vertical collapse includes the extreme cases of the smooth wall and the dense roughness. It is worth noting that the smooth wall case does not appear to be well collapsed on itself (different speeds for same surface). There is about a 2-dB spread for this data set alone, which suggests that $\overline{U}$ may not be the ideal

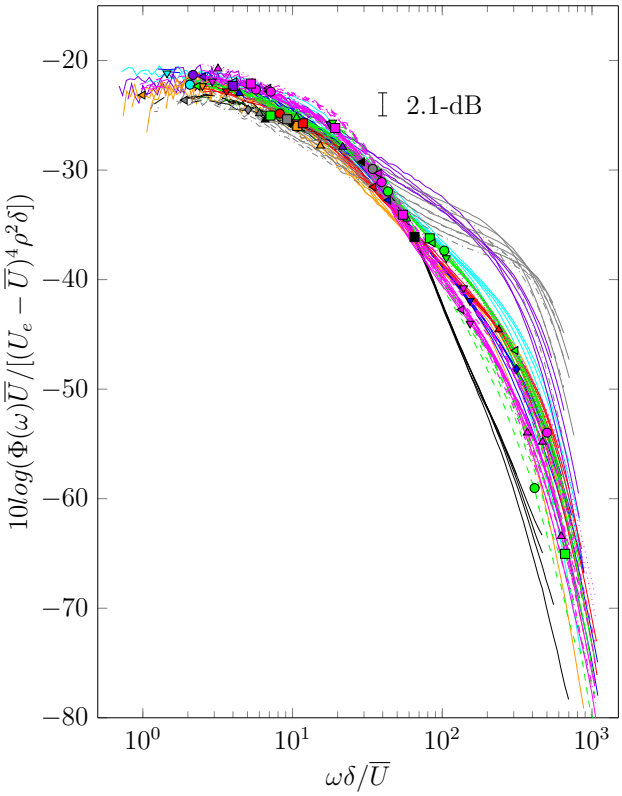

Figure 6.10: New low frequency scaling based on mean boundary layer velocity, $\overline{U} = U_e(1 - \delta^*/\delta)$, applied to present data and the data of Forest [87] and Meyers [1]. Symbols as defined in fig. 6.1.

velocity scale. The smooth wall data is also slightly lower ($\sim$ 2-dB) than the rough wall data.

In general, the curves of fig. 6.10 are not as tightly collapsed as that in fig. 6.9. The average spread is about 3.5-dB. Coincidentally, the maximum spread which we can attribute to uncertainty is 2.1-dB. This is acceptable when we acknowledge that there is a 95% confidence level associated with the uncertainty band which means that the smooth wall data does not have to be included in the analysis. This reduces the spread of the data to 2-dB which is within the uncertainty band.

6.2.4 Implications for Wall Similarity

The success of our two new low frequency scalings have informed us that the outer region of the turbulent boundary layer is dependent on the mean shear in that region, which can be estimated from either $U_e - \overline{U}_{c_b}$ or $U_e - \overline{U}$. This directly contradicts the wall similarity hypothesis which proposes that the outer region of the flow is independent of the boundary

conditions at the wall. This means that the velocity defect law on U_τ should collapse the velocity in the outer regions of the flow, and in this way the outer region is governed by the wall shear stress.

Fig. 6.11a shows that for the present data the velocity defect law on U_τ does not actually collapse the data into a single curve. Normalising the velocity defect on $U_e - \overline{U}$ instead of U_τ produces a more convincing collapse as shown in fig. 6.11b. Therefore it appears that the wall similarity hypothesis may need to be revisited. The new low frequency scalings, along with the velocity and turbulence data, do not appear to support this hypothesis.

The defect law on U_τ has been found to work well on both smooth and rough surfaces by researchers like Flack and Schultz [45]. On the other hand, the work of Krogstad *et al.* [48] has found that the wall similarity hypothesis is not definitive, as we see in fig. 6.11a. Krogstad *et al.* found that outside the near-wall region, smooth and rough wall boundary layers show deviations over a significant portion of the layer, not just within the near-wall region. So it seems that wall similarity at high Reynolds numbers is still an open question in the literature.

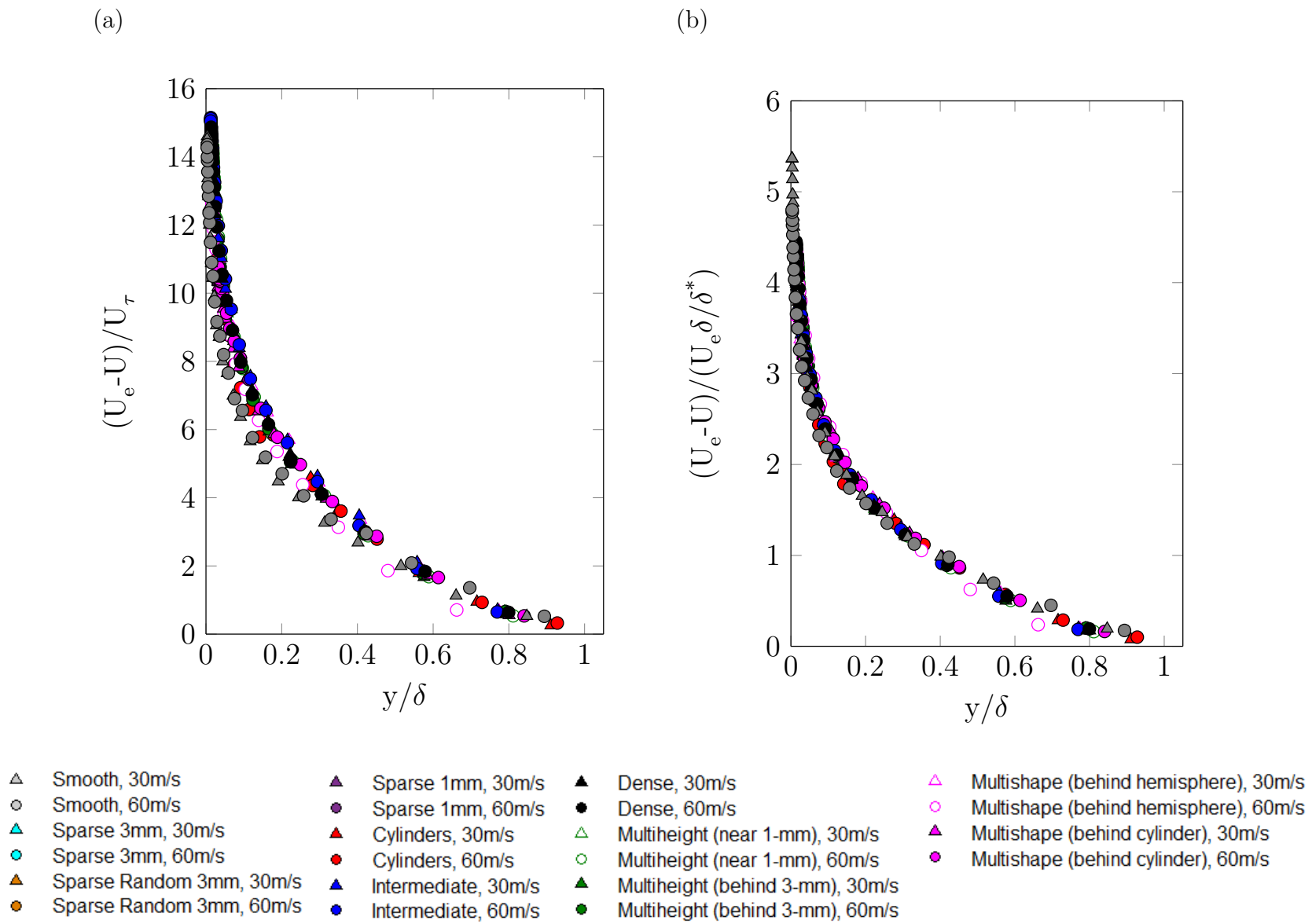
(a)
(b)
$(U_e-U)/U_\tau$
y/δ
$(U_e-U)/(U_e\delta/\delta^*)$
y/δ
Smooth, 30m/s
Smooth, 60m/s
Sparse 3mm, 30m/s
Sparse 3mm, 60m/s
Sparse Random 3mm, 30m/s
Sparse Random 3mm, 60m/s
Sparse 1mm, 30m/s
Sparse 1mm, 60m/s
Cylinders, 30m/s
Cylinders, 60m/s
Intermediate, 30m/s
Intermediate, 60m/s
Dense, 30m/s
Dense, 60m/s
Multiheight (near 1-mm), 30m/s
Multiheight (near 1-mm), 60m/s
Multiheight (behind 3-mm), 30m/s
Multiheight (behind 3-mm), 60m/s
Multishape (behind hemisphere), 30m/s
Multishape (behind hemisphere), 60m/s
Multishape (behind cylinder), 30m/s
Multishape (behind cylinder), 60m/s

Figure 6.11

6.3 Mid-Frequency Scaling

Several previous researchers have proposed scalings for the 'inner' region which were based on some roughness parameter (k_g and k_s for example). It was anticipated that scaling the 'inner' and 'outer' regions would automatically take care of the scaling of this overlap region.

The triple scaling hypothesis contradicts this assumption in that it identifies the 'overlap' region as a scaling region unto itself. It essentially splits the formerly known 'inner' region into a mid-frequency and a high frequency region. We have dealt with the high-frequency region in § 6.1 and proved that is governed by viscous scales. The mid-frequency region should therefore be governed by roughness scales such that the previous 'inner' scalings are in actuality mid-frequency scalings.

6.3.1 Previously Proposed Mid Frequency Scalings

It is clear from our discussion in chapter 3 that the mid-frequency regions have different slopes for different rough surfaces, and thus any scheme to relate these spectra through scaling will be of limited success and value. Mathematics dictates that the slope of the spectrum (logarithmic scale) at any point cannot be changed by normalising the spectrum alone. A change of slope would require dividing the spectrum by a constant value. Nevertheless in this section we attempt to scale the spectra measured in this region in order to shed insight on the underlying physics of the flow in this region and provide the basis for correlating the roughness geometry to the observed variations in slope.

We assess the universality of the 'inner' scalings by applying them to our diverse, high Reynolds number data set. In fig. 6.12 we examine the mid-frequency ('inner') scalings of Blake [41](eq. (6.26)), Aupperle & Lambert [59] (eq. (6.27)), Varano [36] (eq. (6.28)) and Forest [87] (eq. (6.29)). The physical basis for these have been discussed in § 1.7.

$$\phi(\omega)U_\tau/\tau_w^2 k_g \text{ versus } \omega k_g/U_\tau \tag{6.26}$$

$$\phi(\omega)U_\tau/\tau_w^2 k_s C_f \text{ versus } \omega k_s/U_\tau \tag{6.27}$$

$$\phi(\omega)/\rho^2 U_e^3 k_g \text{ versus } \omega k_g/U_e \tag{6.28}$$

$$\phi(\omega)U_\tau^{1.5}/\tau_w^2 \nu^{0.5} k_g^{0.5} \text{ versus } \omega\nu^{0.5}k_g^{0.5}/U_\tau(1.5 \tag{6.29}$$

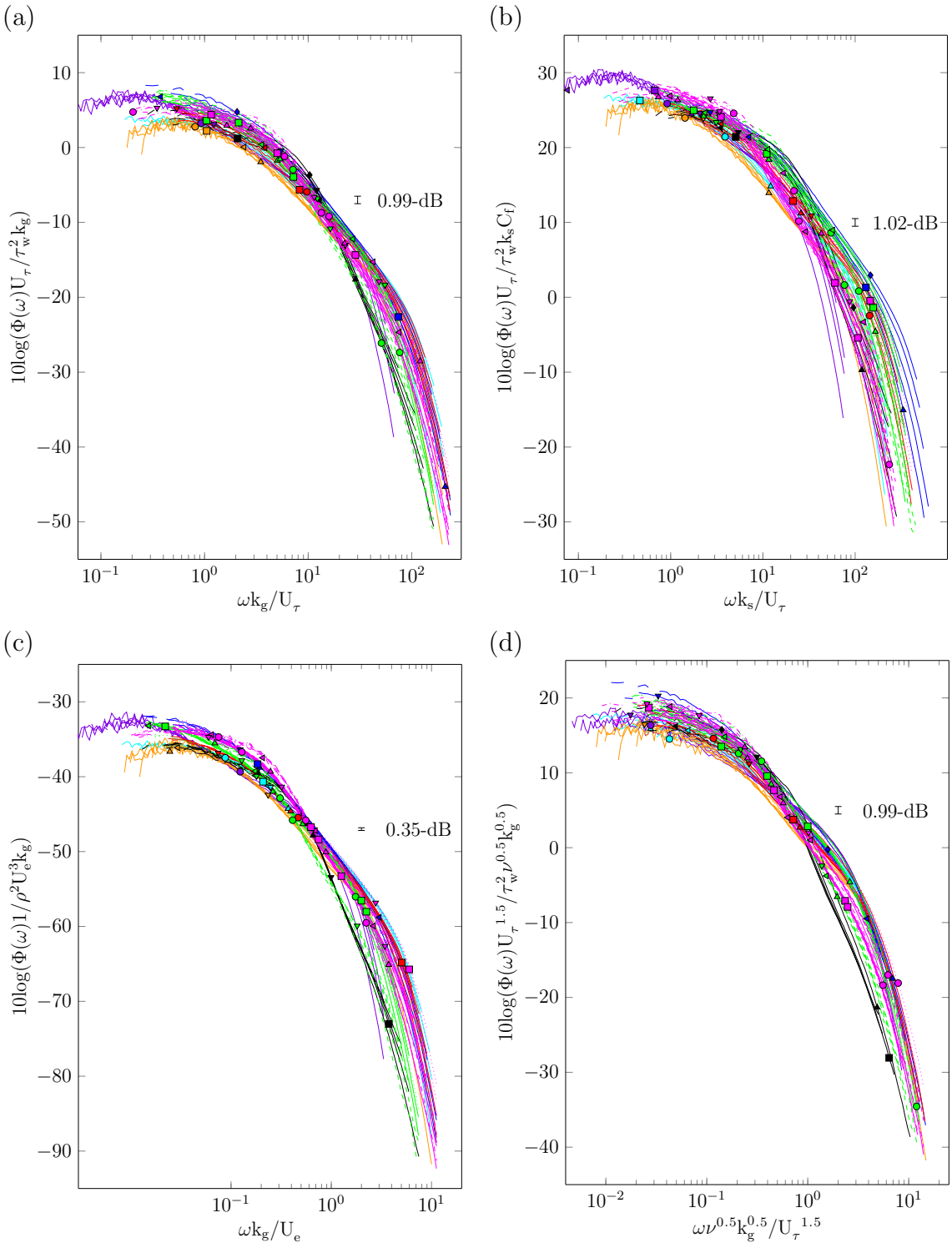

Figure 6.12: (a) Blake's [41] (b) Aupperle & Lambert [59] (c) Varano [36] and (d) Forest [87] mid-frequency ('inner') scalings applied to present data and the data of Forest [87] and Meyers [1].

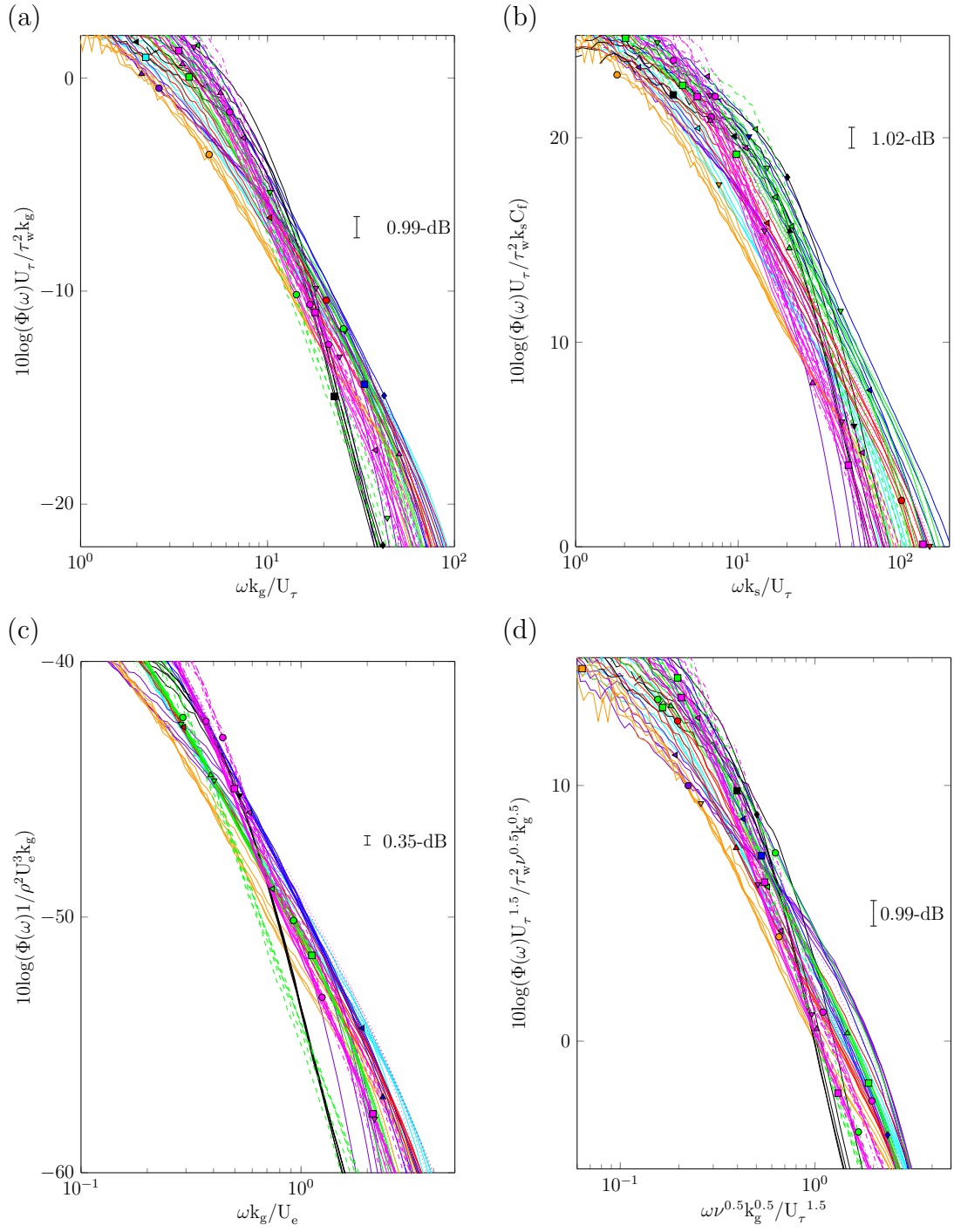

Figure 6.13: Expanded view of the mid-frequency collapse achieved by the mid-frequency ('inner') scalings of (a) Blake [41] (b) Aupperle & Lambert [59] (c) Varano [36] and (d) Forest [87].

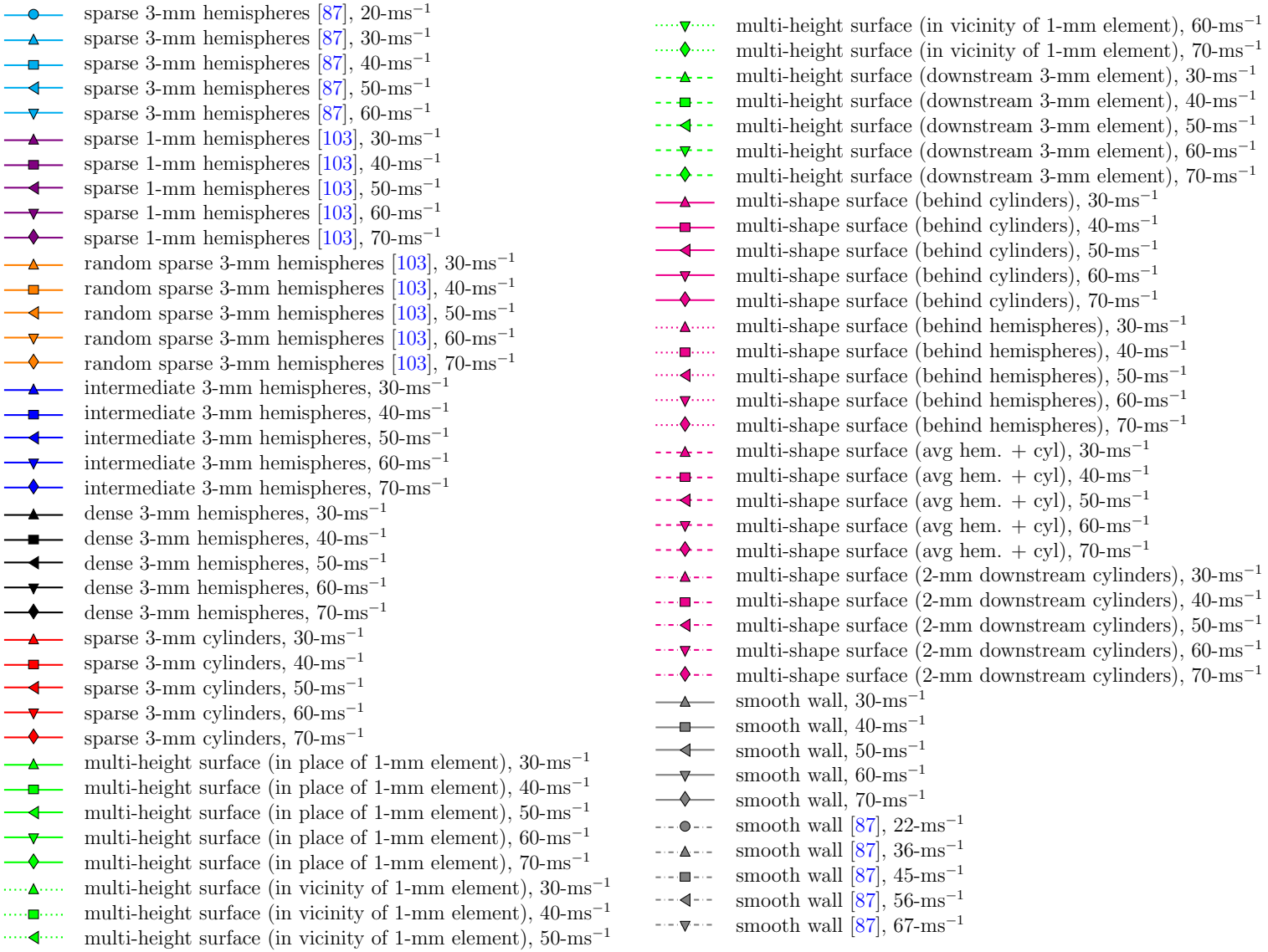
sparse 3-mm hemispheres [87], 20-ms^{-1}
sparse 3-mm hemispheres [87], 30-ms^{-1}
sparse 3-mm hemispheres [87], 40-ms^{-1}
sparse 3-mm hemispheres [87], 50-ms^{-1}
sparse 3-mm hemispheres [87], 60-ms^{-1}
sparse 1-mm hemispheres [103], 30-ms^{-1}
sparse 1-mm hemispheres [103], 40-ms^{-1}
sparse 1-mm hemispheres [103], 50-ms^{-1}
sparse 1-mm hemispheres [103], 60-ms^{-1}
sparse 1-mm hemispheres [103], 70-ms^{-1}
random sparse 3-mm hemispheres [103], 30-ms^{-1}
random sparse 3-mm hemispheres [103], 40-ms^{-1}
random sparse 3-mm hemispheres [103], 50-ms^{-1}
random sparse 3-mm hemispheres [103], 60-ms^{-1}
random sparse 3-mm hemispheres [103], 70-ms^{-1}
intermediate 3-mm hemispheres, 30-ms^{-1}
intermediate 3-mm hemispheres, 40-ms^{-1}
intermediate 3-mm hemispheres, 50-ms^{-1}
intermediate 3-mm hemispheres, 60-ms^{-1}
intermediate 3-mm hemispheres, 70-ms^{-1}
dense 3-mm hemispheres, 30-ms^{-1}
dense 3-mm hemispheres, 40-ms^{-1}
dense 3-mm hemispheres, 50-ms^{-1}
dense 3-mm hemispheres, 60-ms^{-1}
dense 3-mm hemispheres, 70-ms^{-1}
sparse 3-mm cylinders, 30-ms^{-1}
sparse 3-mm cylinders, 40-ms^{-1}
sparse 3-mm cylinders, 50-ms^{-1}
sparse 3-mm cylinders, 60-ms^{-1}
sparse 3-mm cylinders, 70-ms^{-1}
multi-height surface (in place of 1-mm element), 30-ms^{-1}
multi-height surface (in place of 1-mm element), 40-ms^{-1}
multi-height surface (in place of 1-mm element), 50-ms^{-1}
multi-height surface (in place of 1-mm element), 60-ms^{-1}
multi-height surface (in place of 1-mm element), 70-ms^{-1}
multi-height surface (in vicinity of 1-mm element), 30-ms^{-1}
multi-height surface (in vicinity of 1-mm element), 40-ms^{-1}
multi-height surface (in vicinity of 1-mm element), 50-ms^{-1}
multi-height surface (in vicinity of 1-mm element), 60-ms^{-1}
multi-height surface (in vicinity of 1-mm element), 70-ms^{-1}
multi-height surface (downstream 3-mm element), 30-ms^{-1}
multi-height surface (downstream 3-mm element), 40-ms^{-1}
multi-height surface (downstream 3-mm element), 50-ms^{-1}
multi-height surface (downstream 3-mm element), 60-ms^{-1}
multi-height surface (downstream 3-mm element), 70-ms^{-1}
multi-shape surface (behind cylinders), 30-ms^{-1}
multi-shape surface (behind cylinders), 40-ms^{-1}
multi-shape surface (behind cylinders), 50-ms^{-1}
multi-shape surface (behind cylinders), 60-ms^{-1}
multi-shape surface (behind cylinders), 70-ms^{-1}
multi-shape surface (behind hemispheres), 30-ms^{-1}
multi-shape surface (behind hemispheres), 40-ms^{-1}
multi-shape surface (behind hemispheres), 50-ms^{-1}
multi-shape surface (behind hemispheres), 60-ms^{-1}
multi-shape surface (behind hemispheres), 70-ms^{-1}
multi-shape surface (avg hem. + cyl), 30-ms^{-1}
multi-shape surface (avg hem. + cyl), 40-ms^{-1}
multi-shape surface (avg hem. + cyl), 50-ms^{-1}
multi-shape surface (avg hem. + cyl), 60-ms^{-1}
multi-shape surface (avg hem. + cyl), 70-ms^{-1}
multi-shape surface (2-mm downstream cylinders), 30-ms^{-1}
multi-shape surface (2-mm downstream cylinders), 40-ms^{-1}
multi-shape surface (2-mm downstream cylinders), 50-ms^{-1}
multi-shape surface (2-mm downstream cylinders), 60-ms^{-1}
multi-shape surface (2-mm downstream cylinders), 70-ms^{-1}
smooth wall, 30-ms^{-1}
smooth wall, 40-ms^{-1}
smooth wall, 50-ms^{-1}
smooth wall, 60-ms^{-1}
smooth wall, 70-ms^{-1}
smooth wall [87], 22-ms^{-1}
smooth wall [87], 36-ms^{-1}
smooth wall [87], 45-ms^{-1}
smooth wall [87], 56-ms^{-1}
smooth wall [87], 67-ms^{-1}

Apart from the normalisation of Forest in fig. 6.12d, the frequency alignment of the scalings appear to be slightly off. The data from the 1-mm tall roughness is consistently offset to the left by as much as half a decade in frequency. This suggests that the time-scale normalisation on k_g, which is utilised by the scalings of fig. 6.12a-c, is not optimum.

The effectiveness of each pressure scaling is more varied. In all cases the mid-frequency region collapse is larger than the uncertainty-based dB limit (shown as error bar on each plot). The largest deviation appears with Aupperle & Lambert's scaling in fig. 6.12b. Here the mid-frequency spread is approximately 8-dB, a value which is almost six times larger than the maximum allowable spread. The collapse on speed is consistently about 1-dB wide, for the different surfaces. These details can be seen in fig. 6.13b. As discussed in § 1.7, the short-comings of this scaling are probably rooted in the use of k_s and C_f which appear to be selections of convenience.

The mixed inner scaling of Forest, presented in fig. 6.12d and fig. 6.13d, shows a collapse with an average spread of 6-dB in the mid-frequency region. This spread is four times larger than is needed to conclusively determine success. The scaling on U_τ does not appear to produce the tightest fit for different speeds such that the spread for a single surface has an average value of 1-dB. This wide spread obscures the misalignment of the curves in the mid-frequency which is the result of the variations in slope. Closer inspection of fig. 6.13d reveals that curves cross over each other and thus the scaling is less successful than is implied by fig. 6.12d.

Varano's scaling in fig. 6.12c shows the most successful *local* collapse of data for different edge velocities. The data from each rough surface is tightly merged into a thin ($\sim$0.5-dB wide) line in the mid-frequency region. This is shown clearly in fig. 6.13c and is probably the result of using U_e as the velocity scale. What we also see is that the individual cases do not converge to a single line. This scaling particularly highlights the differences in slope of the mid-frequency region for each surface. As a result there is significant cross over of curves in this region. The variations in slope are mostly due to differences in microphone location and roughness element density, as discussed in chapter 3. Overall the data converge into a curve about 3.5-dB wide when normalised on Varano's scaling, approximately seven times larger than the spread required for success.

A similar spread is seen for the scaling of Blake shown in fig. 6.12a and fig. 6.13a. The spread of the collapse is approximately 4-dB, which despite being larger than the width of the Varano collapse, is only three times larger than the maximum allowable spread. This makes the Blake scaling the most successful of the four scalings presented in fig. 6.12. As with Forest's scaling, the use of U_τ as a velocity scale proves to be less than optimum for collapsing the data of each surface. On average, the width of the collapse for a single surface is about 1-dB.

Nevertheless we take a closer look at the Blake 'inner' scaling by separating the different rough cases in fig. 6.14. Here the true behaviour of each dataset can be observed. The 1-dB wide collapse for individual surfaces discussed above is also clearer. Fig. 6.14a shows

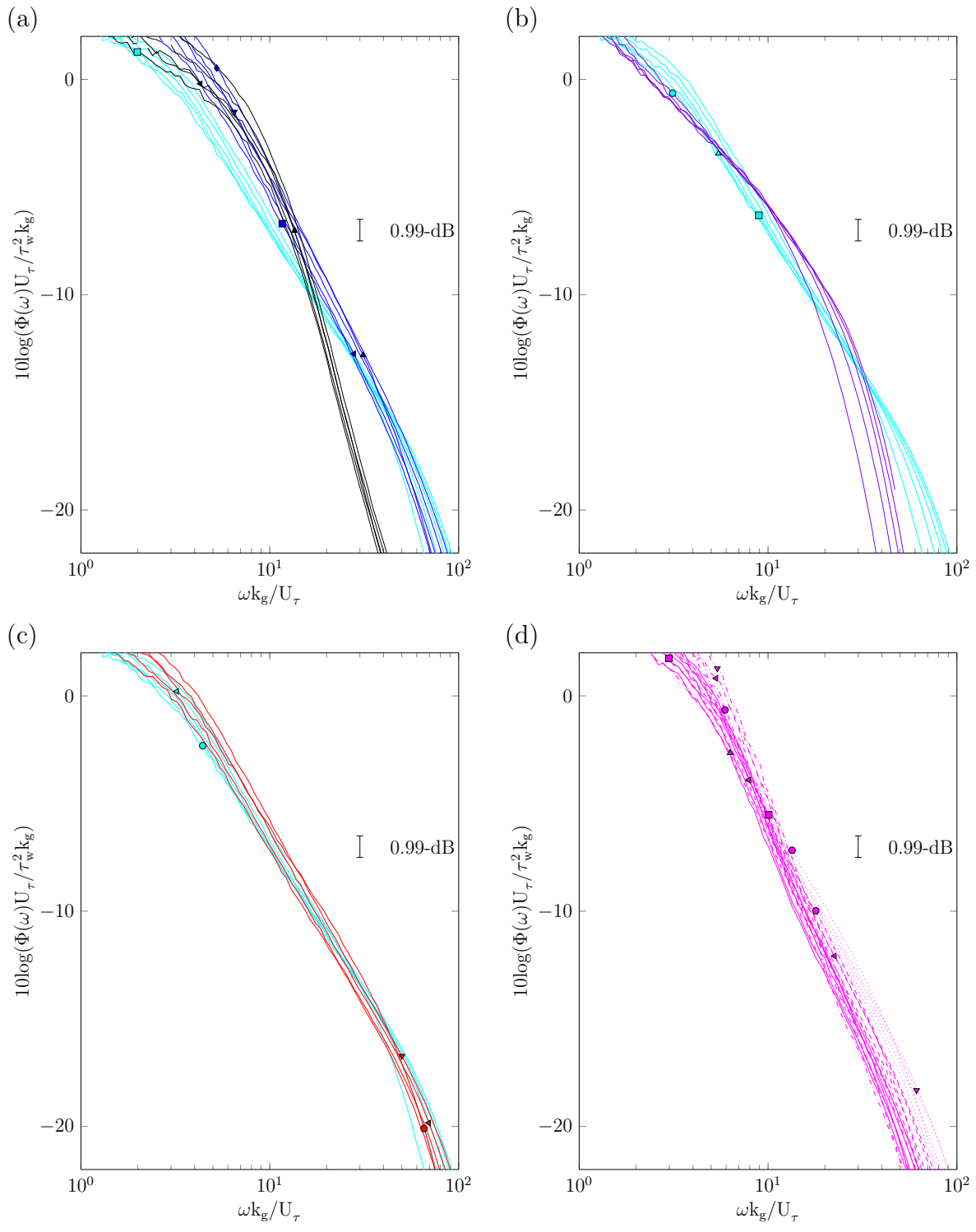

Figure 6.14: Expanded view of the mid-frequency collapse achieved by Blake's [41] mid-frequency scaling for data of various (a) roughness density, (b) size (c) shape and (d) microphone location. Symbols as defined in fig. 6.12.

the scaled mid-frequency spectrum of the sparse, intermediate and dense hemispheres. The slope of each of these is different, increasing from the sparse to the intermediate to the dense case. The differences in slope are also highlighted in fig. 6.14d where we present the data collected at different locations on the multi-shape surface. In mid-frequency region I (defined in § 3.8.4) the collapse is acceptable at approximately 2.5-dB wide. The slope varies slightly with transducer location such that data collected in the middle of four elements have a slope of -2 and data collected about 2-mm behind the cylinders have a slope of about -2.3. In mid-frequency region II the collapse is 4-dB on average and the slope of the curves range between -1.5 and -2. The scaling of Blake cannot account for such variations. Another issue is brought to light by fig. 6.14b which presents the data from all the sparse surfaces – 3-mm hemispheres, random hemispheres, 3-mm cylinders and 1-mm hemispheres. While the collapse is about 2-dB wide, the data of the 1-mm hemispheres is offset to the left by $\omega k_g/U_\tau \sim 40$ units. As mentioned before, this casts some doubt on the appropriateness of k_g as the length scale of choice for the mid-frequency. Lastly we consider how the Blake scaling handles differences in element shape in fig. 6.14(c). For the most part the data of the sparse, 3-mm hemispheres and sparse, 3-mm cylinders converge to an acceptable band about 0.8-dB wide. The slight slope difference which was discussed in § 3.8.2 is evident here as well.

Due to these issues, we can conclude that Blake's 'inner' scaling is not ideal for the mid-frequency. It is the best available scaling for this region but it does not adequately account for changes in the spectrum due to roughness density, height and transducer location.

As a final note, we must acknowledge that it is somewhat unfair to assess the existing mid-frequency scalings using data sets of different mid-frequency slopes. In truth, the scalings of Blake, Varano and Aupperle & Lambert were developed based on fairly low Reynolds number data. Hence these could not uncover much about the mid-frequency behaviour. The scaling of Forest was developed for a uniformly sparse surface which does not show the slope changes that the current data set reveals. These scalings were undoubtedly useful for the data available at the time. Knowing now that variations in roughness density and transducer location result in changes in the slope of the spectrum, we must expand our considerations to include phenomenon which are not captured by simply scaling the spectrum on constant, non-dimensional parameters.

6.3.2 Slope of the Mid-Frequency Region

In an effort to understand how the slope of the mid-frequency region varies with roughness, we will examine each data set individually. This includes data from different microphone locations on the same surface. In §§ 6.1 and 6.2 we mentioned that the high frequency scaling and the low frequency scaling each scale the mid-frequency region as well. We will therefore look at the slope of the mid-frequency when both these scalings are applied.

The mid-frequency slope, which we define as m_{mid}, was obtained by inserting a best fit line through the mid-frequency region. The slope of this line is then found by determining the

number of decades on the y-axis which corresponds to one decade on the x-axis. This is done using horizontal grid lines 0.1 units apart. Thus the uncertainty associated with m_{mid} is ± 0.1. Figs. 6.15 to 6.18 show the individual surfaces scaled on both the low- (left) and high- (right) frequency scalings.

What is most interesting about these plots is that for every case presented, irrespective of roughness geometry or transducer location, both the high and the low frequency scalings effectively scale the mid-frequency. The slope of the mid-frequency is expectedly unchanged for both scalings. In the case of the multi-shape surface we know that there are two mid-frequency 'sub-regions'. Fig. 6.18 shows that mid-frequency region I is dependent on transducer location relative to the roughness element because plots (a) and (b), which present data obtained 5.25-mm downstream an element, have the same slope of m_{mid} =-2 while plot (c), which presents data obtained only 2-mm behind the cylinder, shows a higher slope of m_{mid} =-2.3. These three cases have different slopes in mid-frequency region II, with the data 5.25-mm downstream the hemisphere having the shallowest slope and the data 2-mm downstream the cylinder having the steepest.

The slope in the mid-frequency region is dependent on the structures present at the measurement location. This means that the roughness density and the measurement location will both affect the mid frequency slope. When the microphone is placed at different locations relative to an element then it will encounter different structures (example the trailing legs of horseshoe-like vortices, low pressure region in a separation zone etc.). This does not directly affect the low-frequency or high-frequency content of the spectrum because the only scales affected by the roughness are those on the order of the roughness size. This means that the mid-frequency content is very sensitive to microphone location. In fact the slope of the mid-frequency region is clearly shown to vary based on microphone location in fig. 6.17c-f and fig. 6.18.

Similarly as the space between elements is decreased (roughness density is increased) the microphone is placed closer and closer to the elements, meaning it will be in the wake of the element where different structures exist than the in the middle of the four element array. Furthermore, decreasing the roughness spacing means that vortical structures surrounding the elements begin to merge and interact with each other, thereby forming new structures which would otherwise not exist. Hence the flow is very different than that on a surface with sparser roughness. It is for these reasons that the mid-frequency slope varies so markedly with roughness element spacing as seen when we compare fig. 6.15a-b and fig. 6.15c-f. These figures show that as λ is increased $\times$ 2.5 from 0.052 (sparsely packed hemispheres) to 0.13 (intermediately pacjed hemispheres), the mid-frequency slope steepens from -1.4 to -1.8 ($\times$ 1.3 or 29% increase). A further increase in λ from 0.13 (intermediately spaced hemispheres) to 0.33 (densely packed hemispheres) results in more steepening of the slope of about 67% ($\times$ 1.7 original slope). Thus the increase in mid-freqeuncy slope with λ is not linear.

The mid-frequency slopes for every surface are tabulated in table 6.3. For the case of the multi-shape surface which has multiple m_{mid}, the average slope was taken over the entire

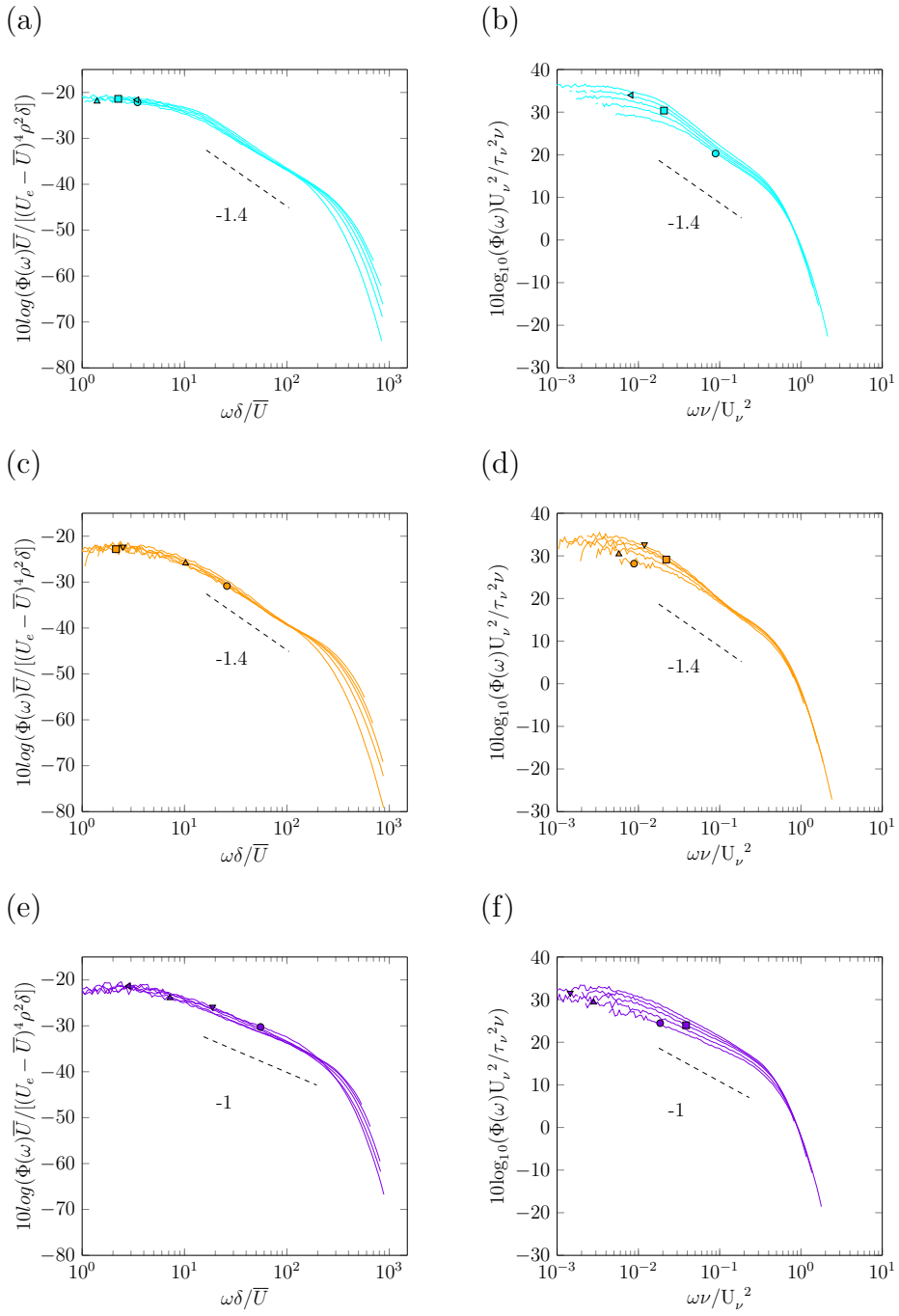

Figure 6.15: Mid-frequency slope, m_{mid}, of the (a) 3-mm sparse hemispheres normalised on low frequency scaling (b) 3-mm sparse hemispheres normalised on high frequency scaling (c) 3-mm random hemispheres normalised on low frequency scaling (d) 3-mm random hemispheres normalised on high frequency scaling (e) 1-mm sparse hemispheres normalised on low frequency scaling (f) 1-mm sparse hemispheres normalised on high frequency scaling.

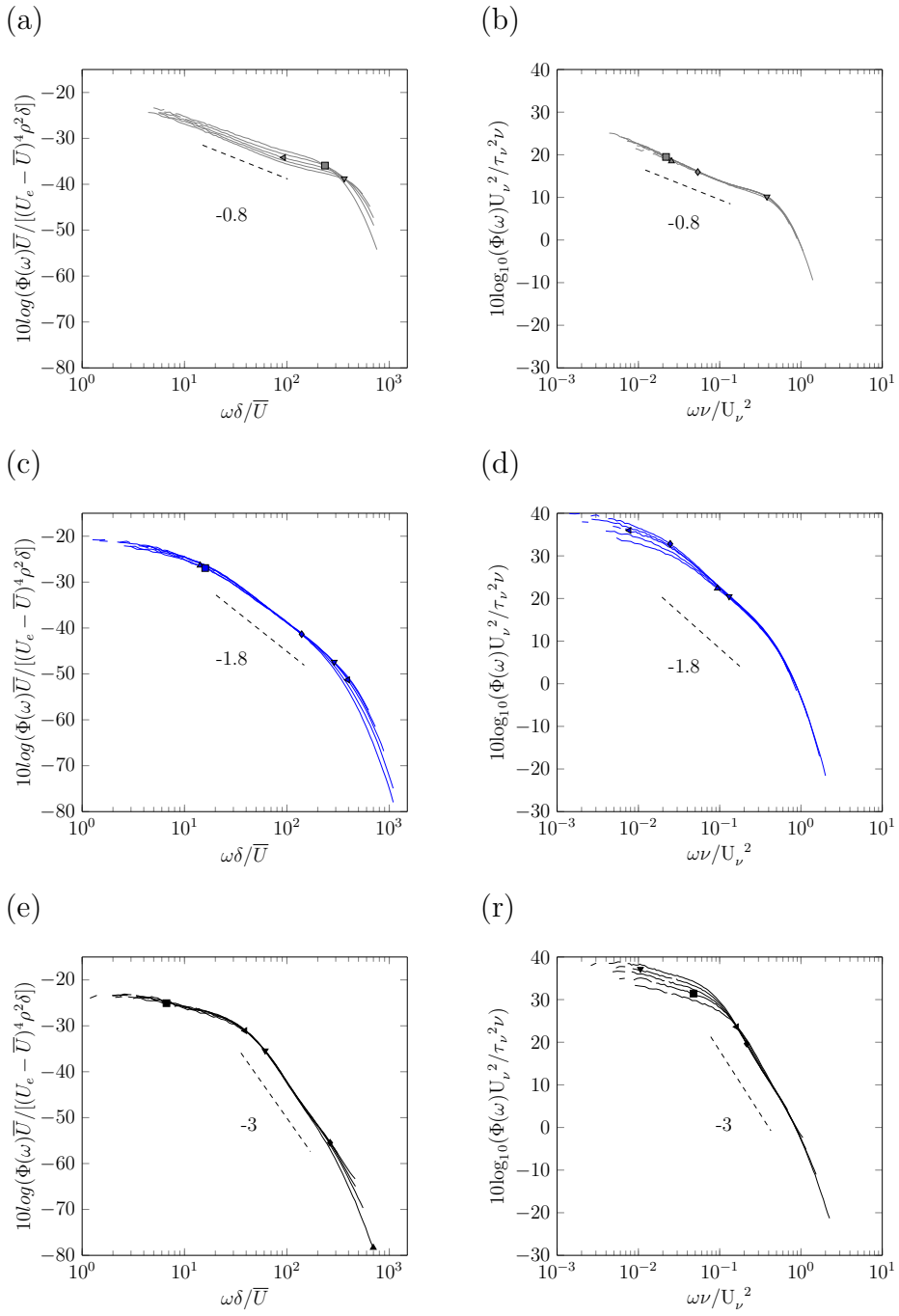

Figure 6.16: Mid-frequency slope, m_{mid}, of the (a) smooth wall normalised on low frequency scaling (b) smooth wall normalised on high frequency scaling (c) 3-mm intermediate hemispheres normalised on low frequency scaling (d) 3-mm intermediate hemispheres normalised on high frequency scaling (e) 3-mm dense hemispheres normalised on low frequency scaling (f) 3-mm dense hemispheres normalised on high frequency scaling.

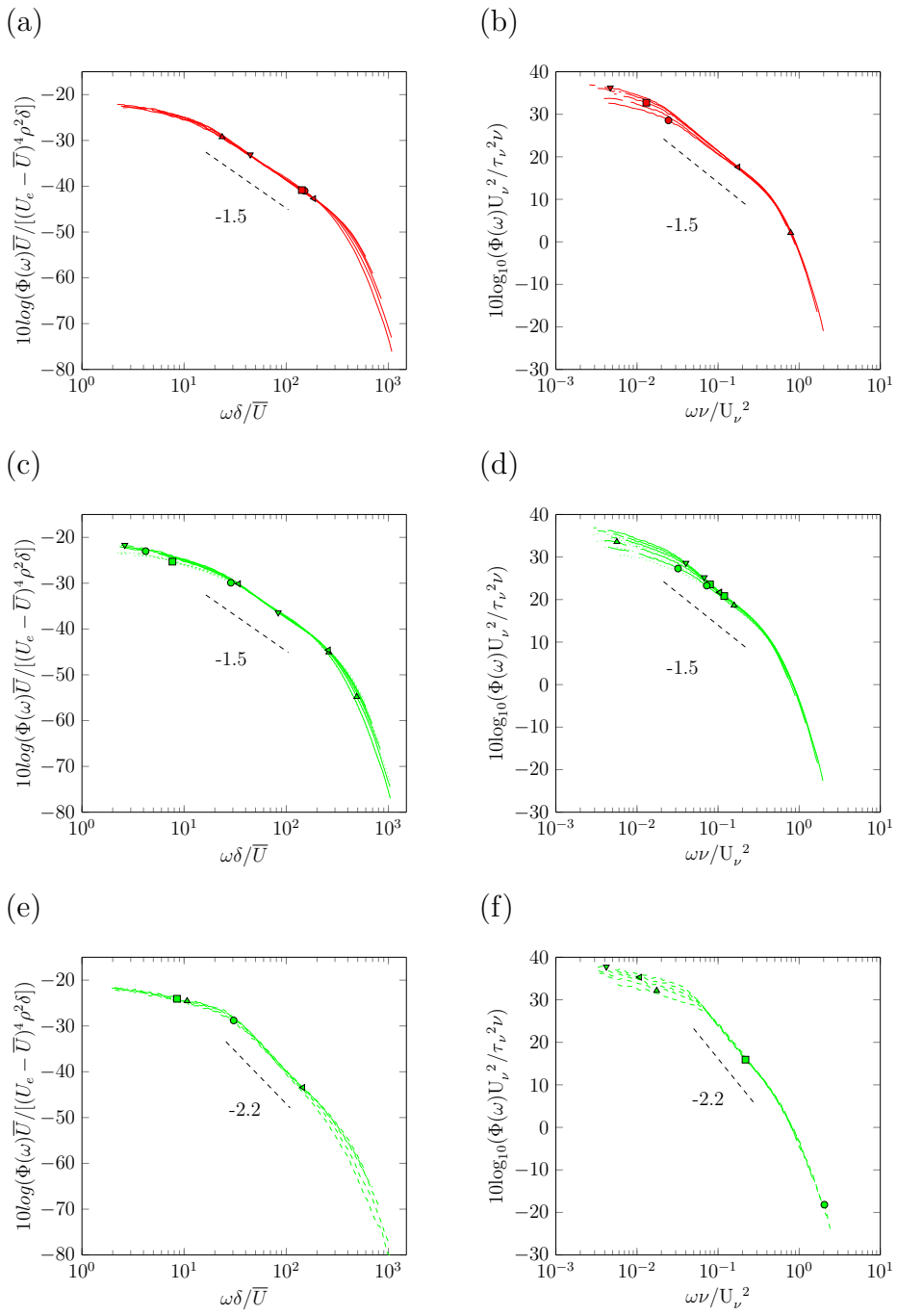

Figure 6.17: Mid-frequency slope, m_{mid}, of the (a) 3-mm sparse cylinders normalised on low frequency scaling (b) 3-mm sparse cylinders normalised on high frequency scaling (c) multi-height surface, measured in vicinity of 1-mm element, normalised on low frequency scaling (d) multi-height surface, measured in vicinity of 1-mm element, normalised on high frequency scaling (e) multi-height surface, measured behind 3-mm element, normalised on low frequency scaling (f) multi-height surface, measured behind 3-mm element, normalised on high frequency scaling.

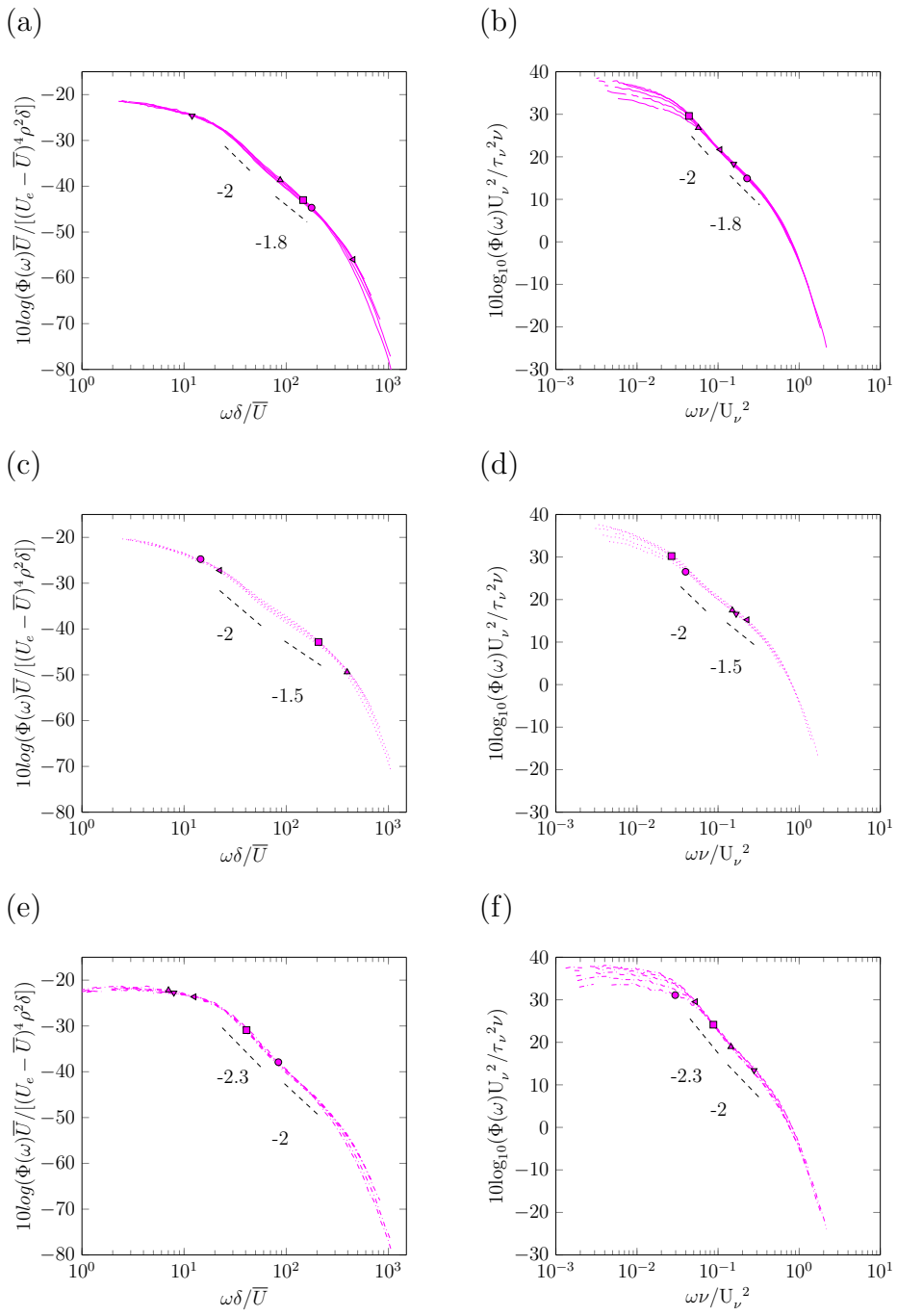

Figure 6.18: Mid-frequency slope, m_{mid}, of the (a) multi-shape surface, measured behind cylinder, normalised on low frequency scaling (b) multi-shape surface, measured behind cylinder, normalised on low frequency scaling (c) multi-shape surface, measured behind hemisphere, normalised on low frequency scaling (d) multi-shape surface, measured behind hemisphere, normalised on high frequency scaling (e) multi-shape surface, measured 2-mm behind cylinder, normalised on low frequency scaling (f) multi-shape surface, measured 2-mm behind cylinder, normalised on high frequency scaling.

Table 6.3: Slope of the mid-frequency region, m_{mid}, for each surface, including different microphone locations

Surface	m_{mid}	
	Low Freq.	High Freq.
Sparse hemispheres [87]	-1.4	-1.4
Random, sparse hemispheres [103]	-1.4	-1.4
Sparse 1-mm hemispheres [103]	-1	-1
Smooth wall	-0.8	-0.8
Intermediate hemispheres	-1.8	-1.8
Dense hemispheres	-3	-3
Cylinders	-1.5	-1.5
Multi-height hemispheres (vicinity of 1-mm elements)	-1.5	-1.5
Multi-height hemispheres (2-mm behind 3-mm element)	-2.2	-2.2
Multi-shape (behind cylinders)	-1.9	-1.9
Multi-shape (behind hemispheres)	-1.75	-1.75
Multi-shape (2-mm behind cylinder)	-2.15	-2.15

mid-frequency region. These values are further plotted versus different geometric parameters in fig. 6.19 in order to uncover the governing parameter(s) controlling m_{mid}. Also included on these plots are the best fit curves through the data and the corresponding formula for the fit. Note that these formulae are represented in general form such that x and $f(x)$ represent whatever quantity is on the abscissa and ordinate, respectively.

Fig. 6.19a shows that m_{mid} is not directly related to k_g because surfaces with the same k_g have widely varying m_{mid}, ranging from -1.4 to -3. Similarly, λ is not correlated with m_{mid} because fig. 6.19b shows that surfaces with the same λ have slopes which vary by as much as -0.7 (in the case of λ=0.104). Furthermore, surfaces with different λ show similar m_{mid} such as the cylinders and the multi-height surface when measured in the vicinity of the 1-mm elements. The product k_g and λ was also considered as the basis for a relationship with m_{mid}. The best correlation is presented in fig. 6.19c where it is clear that this parameter is not ideal. The multi-scale surfaces all have the same value of $k_g\lambda$ but widely different slopes.

Another parameter considered is the modified displacement height, ε^*. Recall that this parameter represents the apparent upward shift in the y origin due to the presence of the roughness, and is a representation of the total volume of the elements present on the surface. Therefore this parameter includes information about the roughness height as well as the element spacing. It is plotted versus m_{mid} in fig. 6.19d. The relationship revealed by this plot suggests that m_{mid} can be roughly estimated from ε^* by a second order polynomial. Data of different roughness element shape, height and density are represented in this function. The outliers in fig. 6.19d are the intermediate rough surface, the multi-height surface data measured 2-mm downstream the 3-mm element, and the multi-shape data measured 2-mm downstream the cylinder. These outliers show that the relationship presented in fig. 6.19d

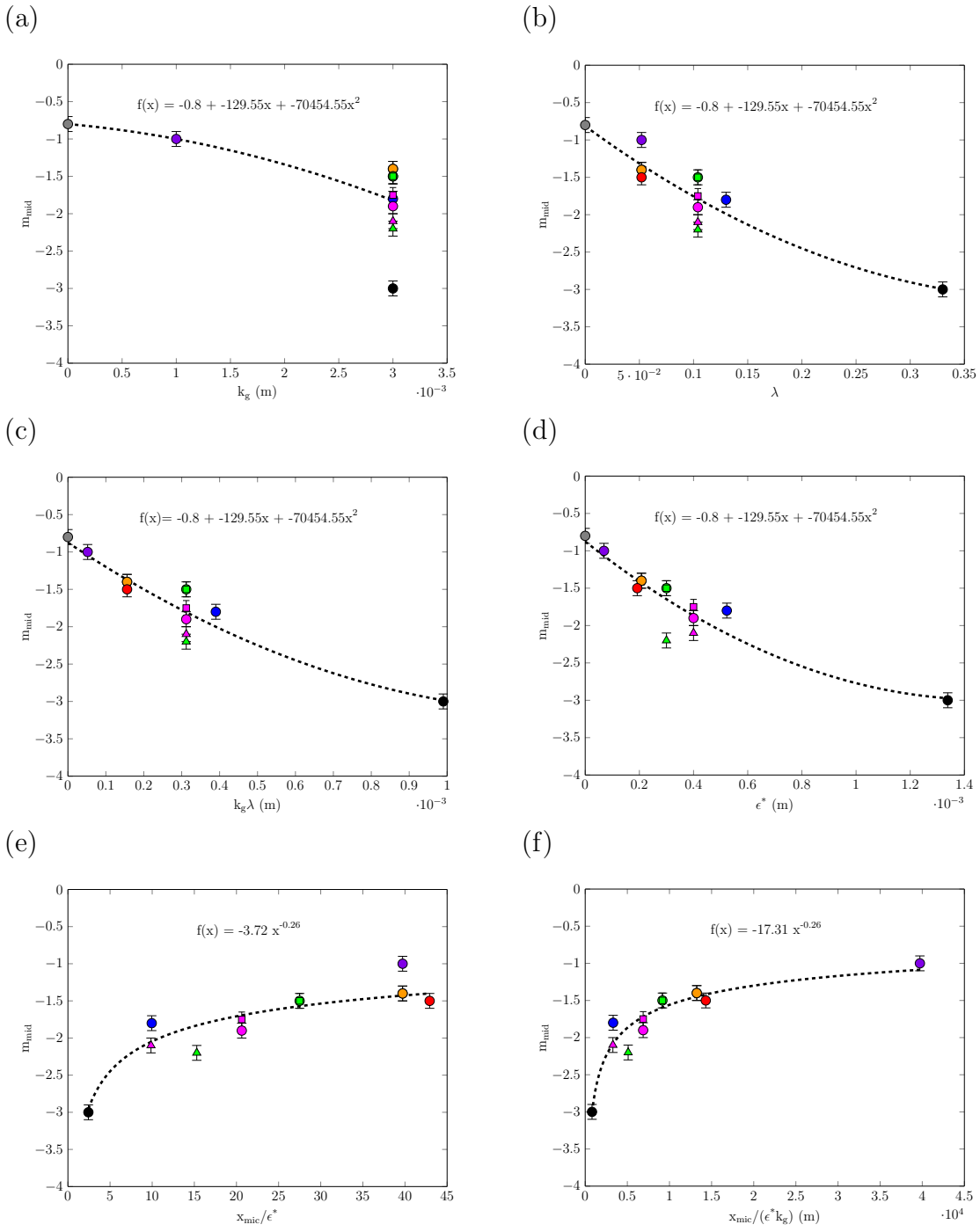

Figure 6.19: Slope of the mid-frequency region (m_{mid}) for each surface, and different microphone locations, plotted versus roughness geometric parameters: (a) k_g (b) λ (c) $k_g\lambda$ (d) ε^* (e) x_{mic}/ε^* (f) $x_{mic}/(\varepsilon^* k_g)$

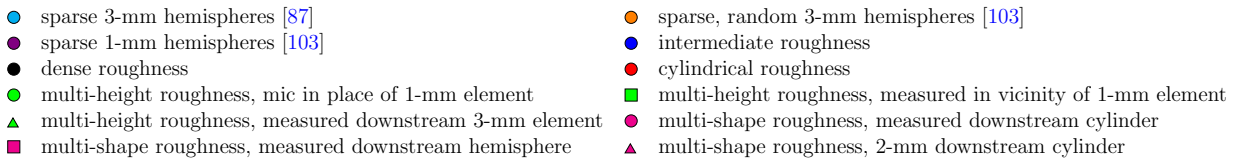

does not account for differences in transducer location. Furthermore, it does not completely account for element density considering the intermediate surface is also an outlier.

We therefore include in this analysis the streamwise distance of the microphone measured from the centre of an element, x_{mic}. This parameter, normalised on ε^* is plotted against m_{mid} in fig. 6.19e. The power-law relationship obtained shows that the slope is steep for transducers close to the elements and, correspondingly, for closely packed roughness elements. As the transducer is further away from the element the slope slowly levels off. Intuitively this curve tells us that m_{mid} should approach the smooth wall value at infinite x_{mic}/ε^*. However, the 1-mm hemisphere contradicts this. It has a value of x_{mic}/ε^* which is the same as the other sparse surfaces, yet its slope (-1) is closer to that of the smooth wall (-0.8) than that of the sparse surfaces (-1.4). Furthermore, the multi-height surface measured 2-mm downstream the 3-mm element, the multi-shape surface measured downstream the cylinder and the intermediate surface are also outliers.

In an effort to account for the discrepancy with the 1-mm rough surface, we incorporate k_g into the previous parameter to obtain $x_{mic}/(\varepsilon^* k_g)$. This parameter is plotted against m_{mid} in fig. 6.19f. The resulting relationship is a power law similar to that in fig. 6.19e. However, the 1-mm surface is now in agreement with the curve and the expected trend described above. The agreement of the other data remain the same as in fig. 6.19e. Normalising $x_{mic}/(\varepsilon^* k_g)$ by multiplying by δ was considered in the hopes that including actual flow data would change the relationship. However, apart from a reduction in the power-law constant, the overall trends were identical to that of fig. 6.19f.

Admittedly, $x_{mic}/(\varepsilon^* k_g)$ is not an intuitive parametric quantity despite representing all the important geometric parameters in the roughness regime. It is essentially a portion of the roughness height corresponding to the ratio of ε^*/x_{mic}. And ε^*/x_{mic} is an estimate of how much smaller the effect of the roughness is in the wall-normal y direction compared to the streamwise x direction (at the microphone location). Moreover, determining the streamwise microphone location relative to a roughness element will be almost impossible on a realistically rough surface. So while fig. 6.19f is informative and pinpoints the important parameters which affect the mid-frequency slope, it is impractical in terms of predicting the mid-frequency slope.

6.3.3 The 'Overlap' Hypothesis

The premise of an overlap region connecting the low and the high frequency regions is based on the same principle as the overlap region for the velocity in the turbulent boundary layer. The hypothesis proposes that there *must* exists a region between the low and high frequency regions where both scalings apply. This region is collapsed when the low frequency scaling is applied to the spectrum as well as when the high frequency scaling is applied. In both these cases the 'overlap' region will itself collapse into a single curve or common form. the triple scaling hypothesis states that there is no 'overlap' region but instead an independent, mid-frequency region controlled by scales on the order of the roughness geometry. We seek here to determine which of these hypotheses is supported by the data.

The present results partially support the premise of an 'overlap' region in that the mid-frequency region is scaled by both the high and the low frequency scaling, for all surfaces investigated. This is clear in figs. 6.15 to 6.18. However, these figures also show that the form of the scaled mid-frequency region is not universal. The slopes vary significantly as is outlined in table 6.3. This latter finding contradicts the 'overlap' hypothesis.

Table 6.3 has also provided us with a somewhat obvious, yet very significant result – the rough-wall mid-frequency slope is not -1. We discussed in § 1.6 that it is believed that the mid-frequency region of smooth wall boundary layers should vary as ω^{-1}. It is suggested by some that experiments are not able to achieve this slope because it is approached slowly with increasing Reynolds number. The following is the basis for the ω^{-1} expectation, which was first developed by Bradshaw [86] and expanded upon by Panton & Linebarger [82]. Note that in this analysis parentheses are used to denote arguments of a function, while square brackets are used for grouping terms in a function.

Previous pressure spectrum normalisations [77] have utilised U_τ such that in the low frequency region we have

$$\frac{\Phi(\omega)}{[\rho U_\tau^2]^2}\frac{U_e}{\delta} = g_L\left(\frac{\omega\delta}{U_e}\right) \tag{6.30}$$

and in the high frequency region we have

$$\frac{\Phi(\omega)}{[\rho U_\tau^2]^2}\frac{U_\tau^2}{\nu} = g_H\left(\frac{\omega\nu}{U_\tau^2}\right) \tag{6.31}$$

Both these normalisation utilise the pressure scale $(\rho U_\tau^2)^2$ because they are based on the principle that τ_w, represented by U_τ, controls the intensity of the pressure fluctuations throughout the boundary layer. This assumption is derived from the success of the defect law when applied to smooth walls. In the mid-frequency region, the overlap hypothesis dictates that eq. (6.30) is equal to eq. (6.31) such that

$$g_L\left(\frac{\omega\delta}{U_e}\right)\frac{\delta}{U_e} = g_H\left(\frac{\omega\nu}{U_\tau^2}\right)\frac{\nu}{U_\tau^2} \tag{6.32}$$

The functions g_L and g_H can have any form and eq. (6.32) must be true for all forms if the overlap hypothesis holds. Since the arguments of the functions g_L and g_H are the same, the only way that the two sides can be equal is if

$$g_L\left(\frac{\omega\delta}{U_e}\right) \propto \left(\frac{\omega\delta}{U_e}\right)^{-1} \tag{6.33}$$

$$g_H\left(\frac{\omega\nu}{U_\tau^2}\right) \propto \left(\frac{\omega\nu}{U_\tau^2}\right)^{-1} \tag{6.34}$$

To further prove this, we elect to use the power law functional form as an example because it is not only simple but it also produces a linear region on the logarithmic scale. Equation (6.32) becomes

$$A_L\left[\frac{\omega\delta}{U_e}\right]^m\frac{\delta}{U_e} = A_H\left[\frac{\omega\nu}{U_\tau^2}\right]^m\frac{\nu}{U_\tau^2} \tag{6.35}$$

which can only be true if m = -1.

This analysis is sound, but completely dependent on the initial assumption that τ_w controls the intensity of the pressure fluctuations throughout the boundary layer. This enforces the use of U_τ in both the low and high frequency pressure normalisation, which is the only way m= -1.

From § 6.1 and § 6.2, we know that the optimum pressure scaling for the high and the low frequency regions is not $(\rho U_\tau^2)^2$. This is proven by fig. 6.11 where the defect law normalisation on U_τ is shown to be inappropriate for rough walls. Furthermore, we have found that the pressure scale for these regions is not the same. Using our new scalings, we can re-work the preceding analysis to investigate the validity of the ω^{-1} argument.

For the low frequency region, the scaling on $\overline{U}$ dictates that

$$\frac{\Phi(\omega)}{[\rho[U_e-\overline{U}]^2]^2}\frac{\overline{U}}{\delta} = g_L\left(\frac{\omega\delta}{\overline{U}}\right) \tag{6.36}$$

and in the high frequency region U_ν scaling gives

$$\frac{\Phi(\omega)}{[\rho U_\nu^2]^2}\frac{U_\nu^2}{\nu} = g_H\left(\frac{\omega\nu}{U_\nu^2}\right) \tag{6.37}$$

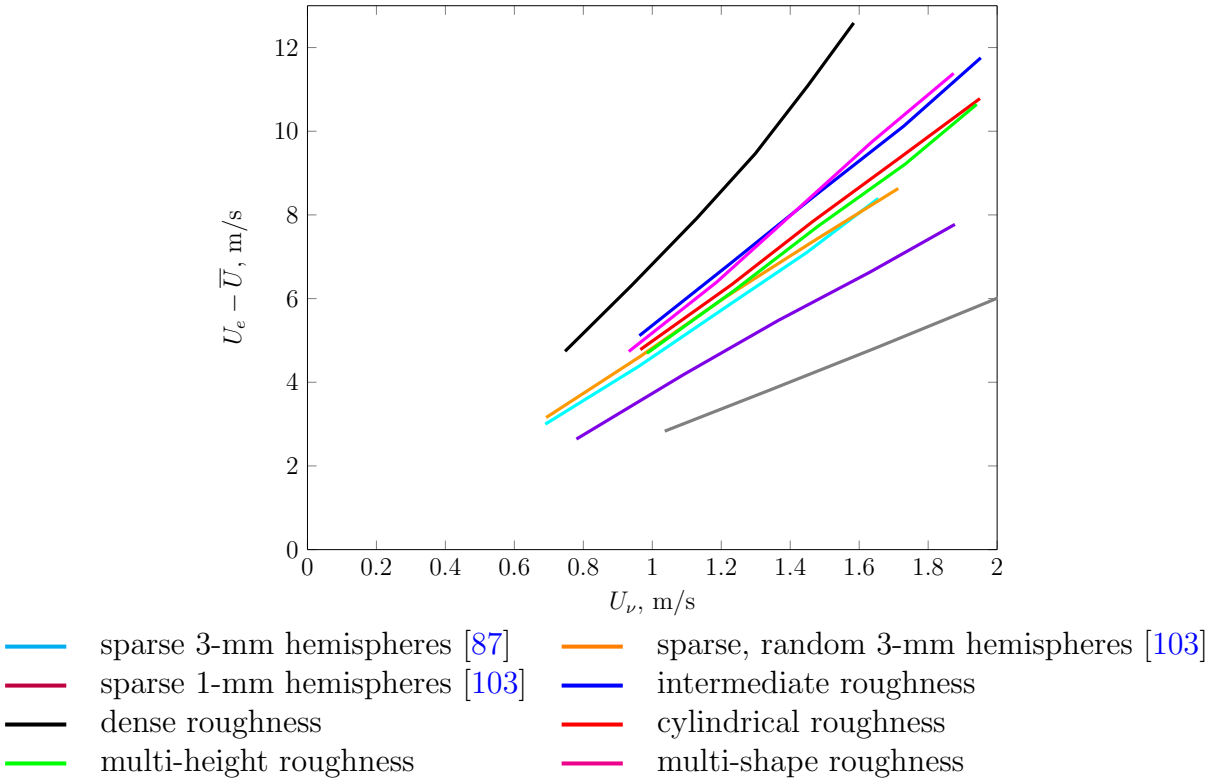

Figure 6.20: Variation of $(U_e - \overline{U})^4$ with U_ν^4 for all surfaces.

Equating these as required by the 'overlap' hypothesis, we get

$$g_L\left(\frac{\omega\delta}{\overline{U}}\right)[U_e - \overline{U}]^4\frac{\delta}{\overline{U}} = g_H\left(\frac{\omega\nu}{U_\nu^2}\right)U_\nu^4\frac{\nu}{U_\nu^2} \tag{6.38}$$

In the most general sense, eq. (6.38) shows that for ω to decay with a slope of -1, eq. (6.39) must *always* be true.

$$[U_e - \overline{U}]^4 \propto U_\nu^4 \tag{6.39}$$

The variation of $(U_e - \overline{U})$ with U_ν for all surfaces is plotted in fig. 6.20. This figure proves that the two parameters are not proportional for any surface, not even the smooth wall.This explains why it has been difficult to achieve, or come within 20% of, the ω^{-1} slope in rough-wall experiments. It appears that this expectation is not valid.

All in all, removing the expectation of the ω^{-1} slope does not invalidate the 'overlap' hypothesis. All it tells us is that the mid-frequency region does not vary as ω^{-1}. It is possible that an overlap exists but that it varies with a different slope. We investigate this possibility

considering eq. (6.38). An 'overlap' slope would have to exist universally for all surfaces, and for all forms of the functions g_L and g_H. Therefore we can utilise the simple power-law relationship as before.

$$A_L\left[\frac{\omega\delta}{\overline{U}}\right]^m[U_e-\overline{U}]^4\frac{\delta}{\overline{U}}=A_H\left[\frac{\omega\nu}{U_\nu^2}\right]^m U_\nu^4\frac{\nu}{U_\nu^2} \tag{6.40}$$

Solving eq. (6.40) to obtain an estimate for the slope produces

$$\left[\frac{\delta U_\nu^2}{\overline{U}\nu}\right]^m=\frac{\nu\overline{U}U_\nu^2}{\delta[U_e-\overline{U}]^4} \tag{6.41}$$

$$m=m_{\text{theoretical}}=\frac{\log\left[\frac{\nu\overline{U}U_\nu^2}{\delta[U_e-\overline{U}]^4}\right]}{\log\left[\frac{\delta U_\nu^2}{\overline{U}\nu}\right]} \tag{6.42}$$

In order for the 'overlap' hypothesis to be true, eq. (6.42) must be constant for all surfaces and Reynolds numbers. This is highly unlikely considering $m_{theoretical}$ is a function of δ, ν, U_ν, U_e and $\overline{U}$. Nevertheless, we explore the values of $m_{theoretical}$, obtained from eq. (6.42), using the present dataset. Table 6.4 shows that the variation in $m_{theoretical}$ with speed for a single surface is minimal – the maximum standard deviation observed is 0.026 in the case of the 1-mm sparse hemispheres. This makes sense considering the curves for each speed, for a given surface, collapse into a thin line. We therefore average the values of $m_{theoretical}$ over speed to produce a single value for each surface. Table 6.5 presents the slopes predicted from eq. (6.42) compared with that extracted from the data itself (from table 6.3).

The differences between the observed and theoretical slopes are significant as evidenced by the % differences included in table 6.5. The simple reason for these differences is that the 'overlap' region is not a complete view of the phenomenon occuring within the boundary layer. Real effects of the roughness elements affect the way in which energy is transferred from larger to smaller scales. The theoretical value of the slope does not take into account these roughness effects but simply assumes that the high and the low frequency scalings contain the roughness information implicitly, which is only partly true. Table 6.5 indicates that the theoretical slope for different microphone locations on the same surface varies. This means that eq. (6.42) captures at least some of the effect of roughness geometry (including element density) and transducer location. This finding is significant because it confirms that at least one of the high and low frequency scalings implicitly accounts for these effects.

Table 6.4: Mid-freqeuncy slope predicted by eq. (6.42), $m_{theoretical}$, for each speed on each surface

Surface	20-ms^{-1}	30-ms^{-1}	40-ms^{-1}	50-ms^{-1}	60-ms^{-1}	70-ms^{-1}
Sparse hemispheres [87]	-1.98	-1.97	-1.97	-1.97	-1.98	-
Random, sparse hemispheres [103]	-2.03	-2.02	-2.02	-2.00	-1.99	-
Sparse 1-mm hemispheres [103]	-1.79	-1.84	-1.85	-1.84	-1.84	-
Smooth wall	-	-1.64	-1.64	-1.64	-1.65	-1.65
Intermediate hemispheres	-	-2.06	-2.06	-2.06	-2.05	-2.06
Dense hemispheres	-	-2.29	-2.29	-2.30	-2.31	-2.33
Cylinders	-	-2.02	-2.01	-2.02	-2.02	-2.01
Multi-height hemispheres (vicinity of 1-mm elements)	-	-2.00	-2.00	-2.01	-2.00	-2.01
Multi-height hemispheres (2-mm behind 3-mm element)	-	-2.13	-2.13	-2.10	-2.11	-2.11
Multi-shape (behind cylinders)	-	-2.05	-2.06	-2.08	-2.10	-2.09
Multi-shape (behind hemispheres)	-	-1.94	-1.94	-1.96	-1.97	-1.97
Multi-shape (2-mm behind cylinder)	-	-2.05	-2.06	-2.08	-2.10	-2.09

Table 6.5: Comparison of mid-freqeuncy slope predicted by eq. (6.42), $m_{theoretical}$, with the mid-frequency slope from the data, $m_{observed}$ for each surface, including different microphone locations

Surface	$m_{observed}$ (from table 6.3)	$m_{theoretical}$ (from eq. (6.42))	% difference
Sparse hemispheres [87]	-1.4	-1.97	41%
Random, sparse hemispheres [103]	-1.4	-2.01	44%
Sparse 1-mm hemispheres [103]	-1	-1.83	83%
Smooth wall	-0.8	-1.64	105%
Intermediate hemispheres	-1.8	-2.06	14%
Dense hemispheres	-3	-2.31	23%
Cylinders	-1.5	-2.02	35%
Multi-height hemispheres (vicinity of 1-mm elements)	-1.5	-2.01	34%
Multi-height hemispheres (2-mm behind 3-mm element)	-2.2	-2.12	4%
Multi-shape (behind cylinders)	-1.9	-2.08	9%
Multi-shape (behind hemispheres)	-1.75	-1.96	12%
Multi-shape (2-mm behind cylinder)	-2.15	-2.08	03%

This is the only way that they could be translated into a mid-frequency slope based solely on equating the two scalings. But there is still some mechanism in play controlling the slope of the mid-frequency region which has not been identified.

We also find from fig. 6.21 that $m_{\text{theoretical}}$ is not proportional to m_{observed}. There exists a linear relationship such that

$$m_{theoretical} = 0.25 m_{observed} - 1.58 \tag{6.43}$$

So it appears that the mid-frequency region is not an 'overlap' region in the traditional sense. While the low frequency scaling and the high frequency scaling both effectively scale this portion of the pressure spectrum, the resulting slope varies with roughness geometry and transducer location. There is no universal form for the scaled mid-frequency region.

However, the fact that both the high and low frequency scalings work in the mid frequency region for a given rough surface suggests that an explicit mid-frequency scaling may not be necessary. The effect of roughness geometry and transducer location appear to be implicit in the already established high and/or low frequency scalings. This is why they are both able to independently scale the mid-frequency region. It is worth exploring the possibility

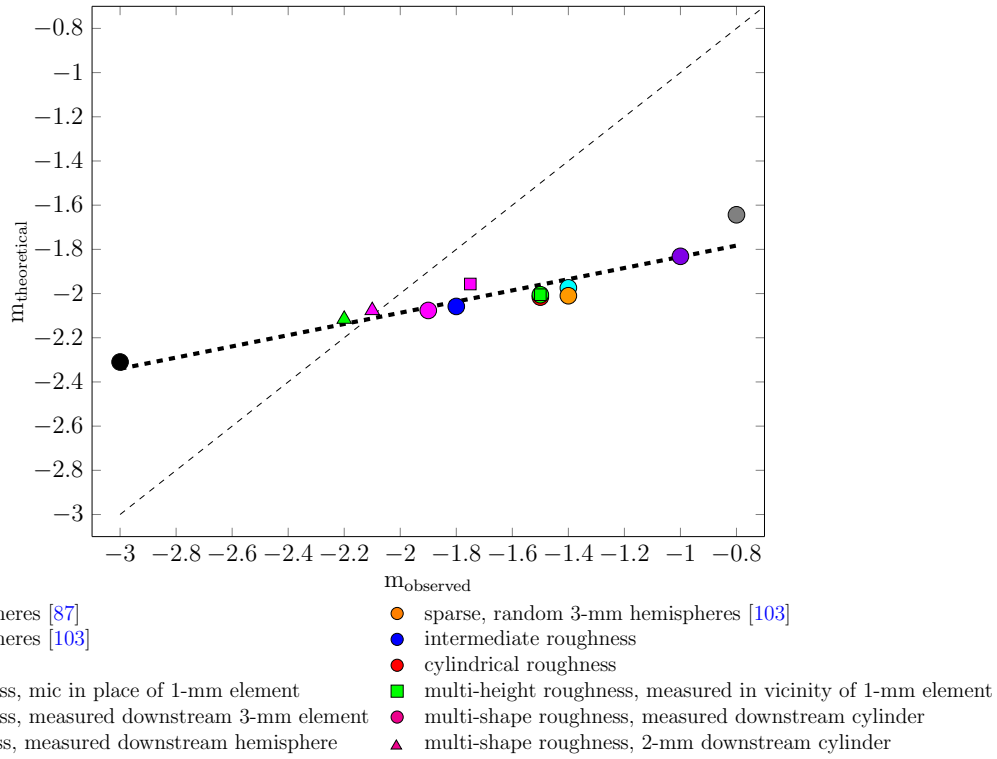

Figure 6.21: Variation of mid-freqeuncy slope predicted by eq. (6.42), $m_{\text{theoretical}}$, with the mid-frequency slope from the data, m_{observed}, for all surfaces.

of connecting (using some form of an equation) the scaled high and low frequency portions of the spectrum to yield the appropriate mid-frequency spectrum. We will investigate this further in chapter 7.

6.3.4 Evanescent Pressure Decay Hypothesis

The last two sections have implied that the processes occurring within the interstitial flow are responsible for the slope of the mid-frequency region. However, the exact mechanism which controls the slope is still unknown. To gain insight into this, measurements were taken at various distances, y, above the wall for four of the five surfaces tested in the present work. For 0-mm $\leq y \leq$ 5-mm a single microphone was inserted into the flow and data was taken at y increments of 1-mm. Fig. 6.22 shows the microphone at different y locations on the four different surfaces (densely-packed, cylinders, multi-height, and multi-shape). In the case of the multi-height surface the microphone was installed in place of a 1-mm element, which is in the middle of a four element array of 3-mm elements. In the case of the multi-shape surface, the microphone was installed downstream a cylinder.

Fig. 6.22e shows the microphone inserted 3-mm above the wall into the flow. In this case it is outfitted with a rapid-prototype bushing which is 3-mm high and has an outer diameter of 4.71-mm. This bushing ensures that the part of the microphone seen by the flow has the same dimensions as a cylindrical element. A front view of the microphone inside the bushing is included at the bottom left corner of fig. 6.22e. Essentially, this configuration allows us to measure the pressure field at the top of a cylindrical element. The only difference here is that, due to mounting constraints, the microphone inside the bushing had to be installed in the middle of a four element array, as opposed to replacing an actual cylinder on the surface. This means that it was in the channel between elements, and not downstream or upstream any other elements.

We must bear in mind that inserting the microphone into the flow as shown in fig. 6.22 presents special issues. The blockage effect of the microphone itself will affect the measurements made at locations greater than y=0-mm. Vortical flow emanating from flow around the microphone artificially adds to the naturally occurring structures in the flow. Furthermore, only a single microphone was used for these measurements which means that we do not benefit from the reduction in uncertainty which comes from averaging the data from different microphones. While these considerations do not allow us to capture an accurate quantitative picture of the pressure spectrum, we are still able to qualitatively assess the spectrum inside and outside the interstitial region, which is our primary aim.

Figs. 6.23 to 6.26 present the pressure spectra measured over each of the four surfaces investigated at speeds ranging from 30-ms^{-1} to 70-ms^{-1}. In these figures the spectrum measured at the wall is presented as a solid black line. The spectra measured above the roughness elements, at 4-mm $\leq y \leq$ 5-mm, are presented as grey lines and the spectra measured within the interstitial flow, at 1-mm $\leq y \leq$ 3-mm, are presented as dark grey

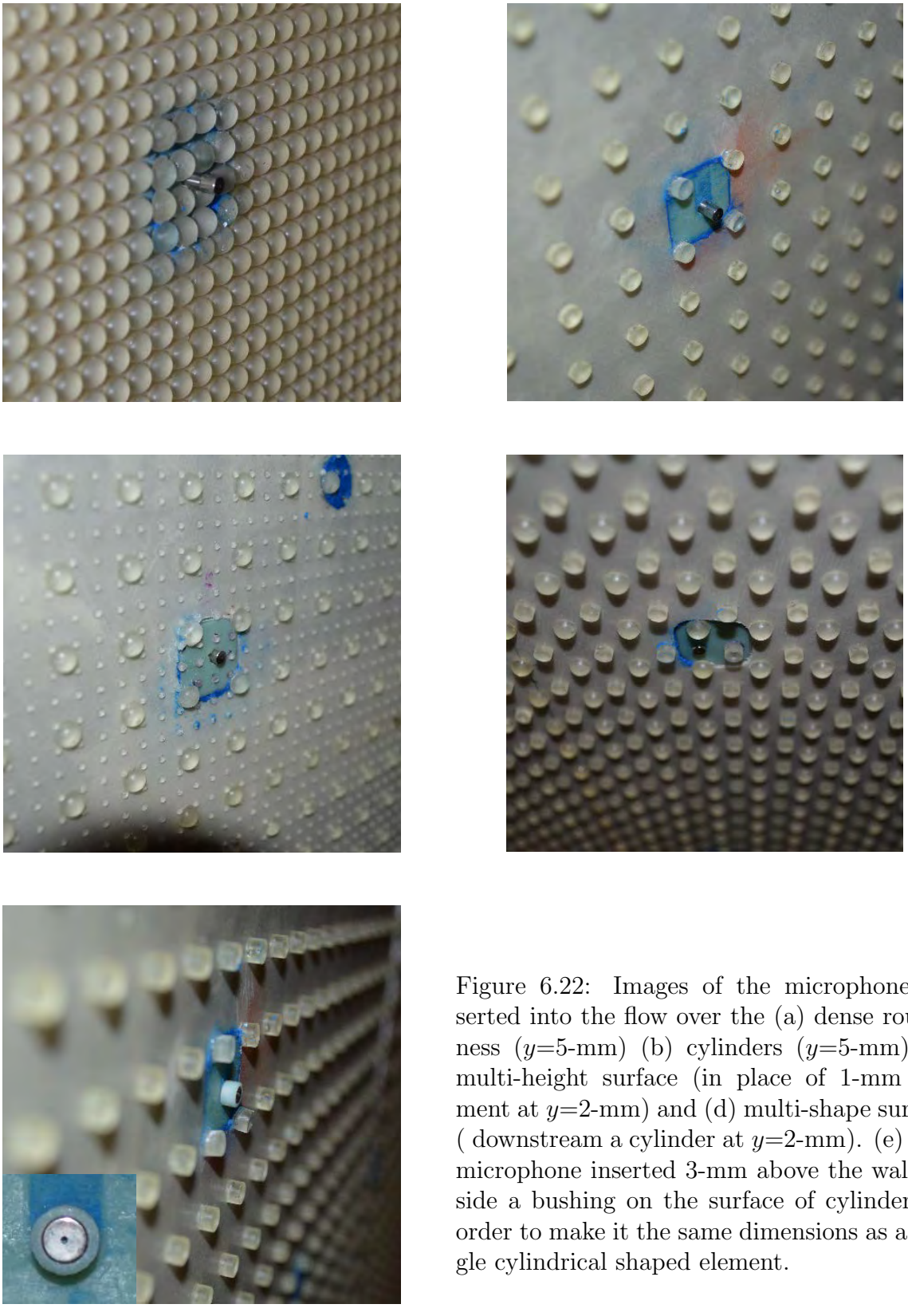

Figure 6.22: Images of the microphone inserted into the flow over the (a) dense roughness (y=5-mm) (b) cylinders (y=5-mm) (c) multi-height surface (in place of 1-mm element at y=2-mm) and (d) multi-shape surface (downstream a cylinder at y=2-mm). (e) The microphone inserted 3-mm above the wall inside a bushing on the surface of cylinders in order to make it the same dimensions as a single cylindrical shaped element.

lines. Different line styles (dash, dot, solid) further depict various y locations within each region of the flow. Also included on these plots is the spectrum of the smooth wall at the given speed. This serves as a reference point in our analysis because the smooth wall has no interstitial flow. For reasons discussed before, the rough wall spectra are all higher in magnitude than the smooth wall at low frequencies. However we can compare the form of the spectra between the two cases. Note that figs. 6.23 to 6.26 emphasise the 30-ms^{-1} case (shown in sub-figure (a) on all plots) because the trends shown in these cases are representative of all speeds, which the reader can confirm by inspecting sub-figures (b)-(e).

Fig. 6.23 shows that the pressure spectra, for the dense roughness, obtained outside the interstitial flow, at 4-mm $\leq y \leq$ 5-mm, bear a strong resemblance to the smooth wall spectra. For these two cases the mid-frequency slopes are almost identical to that of the smooth wall, approximately -0.8, despite having different magnitudes. Furthermore, the high-frequency roll off begins at about the same frequency for both the smooth wall and the measurements outside the interstitial flow. Together, these observations suggest that the flow above the roughness tops behaves *like* a smooth wall flow (but is not identical to the smooth wall case). We discussed in chapter 3 that the elements of the dense roughness are packed so closely that the flow above them are likely to skim over their tops. In this way there exists a 'pseudo-wall' at around y=k_g. This premise is supported by the above observations. The pseudo-wall separates the interstitial flow from the flow above the roughness tops such that the flow outside the interstitial region acts like a smooth-wall flow over the pseudo-wall.

An interesting observation is that the high-frequency portion of the smooth wall aligns well with that measured at y=3-mm on the densely-packed rough surface. This is interesting because the flow at y=3-mm does not include the pressure fluctuations nearest the wall, which are thought to be the majority of the high-frequency portion of the spectrum. While possible, it is unlikely that this is just a coincidence because we see this at all five speeds in fig. 6.23. A more likely explanation is that the pseudo-wall at the roughness tops is well formed because the elements are so closely packed.

Within the interstitial flow, at 3-mm $\leq y \leq$ 0-mm, we observe progressive changes to the form of the spectra among the different y locations. All cases below y=4-mm have about the same low and mid-frequency magnitude – between 79-dB to 82-dB. Nevertheless the mid-frequency slope and the high-frequency roll off point for each y location within the interstitial flow are substantially different. The slope of the mid-frequency region of the spectrum measured at y=3-mm is approximately -0.8, as is the case at larger y locations. However at y=2-mm the mid-frequency slope rises to approximately -0.9 and further increases to -1.2 at y=1-mm. Between y=1-mm and 0-mm, there is a large steepening of the slope from -1.2 to -3. The frequency at which the roll off begins also varies with y distance from the wall. Above y=4-mm the high frequency roll-off begins at appropriately 9-kHz. At y=3-mm and 2-mm, the roll off begins closer to 4-kHz. At y=1-mm the roll off frequency drops to about 1.5-kHz and decreases further to 600-Hz at the wall. At locations above y=2-mm, the roll-off region appears to include only the high frequency portion of the spectrum. As we move closer to the wall, the roll-off region increasingly extends to lower frequencies such that it includes

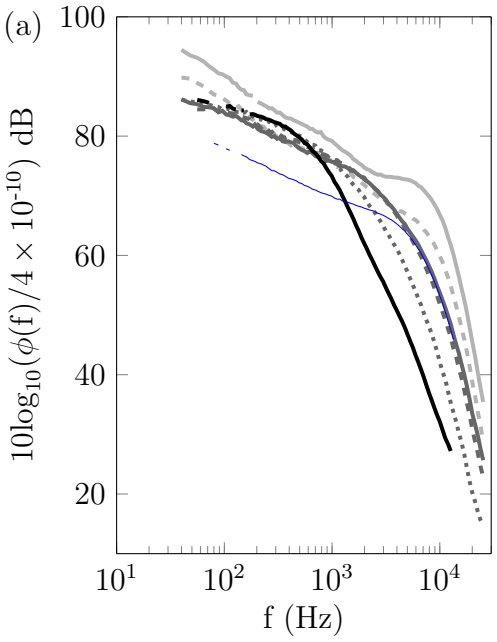

Figure 6.23: Pressure spectra measured over the densely-packed hemispheres at (a) 30-ms^{-1} (b) 40-ms^{-1} (c) 50-ms^{-1} (d) 60-ms^{-1} and (e) 70-ms^{-1}. In these figures the measurement height above the wall is denoted by: ——0-mm; ·····1-mm; - - - -2-mm; ——3-mm; - - - -4-mm; ——5-mm. The pressure spectrum over the smooth wall, measured at the wall, at each speed is also included as ——

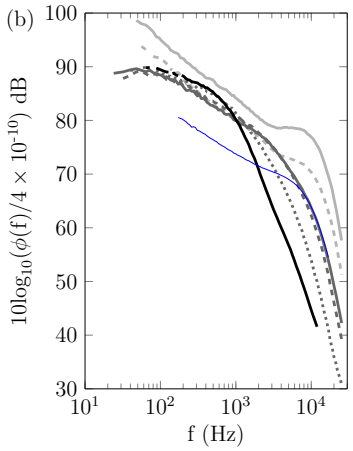

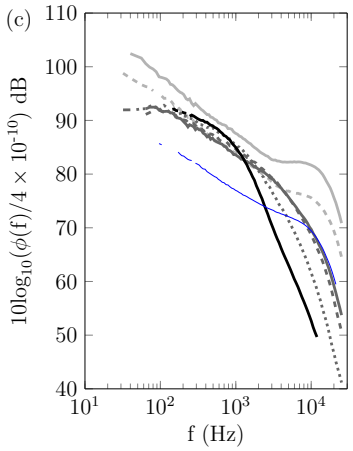

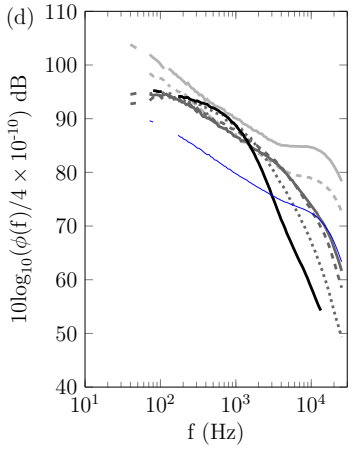

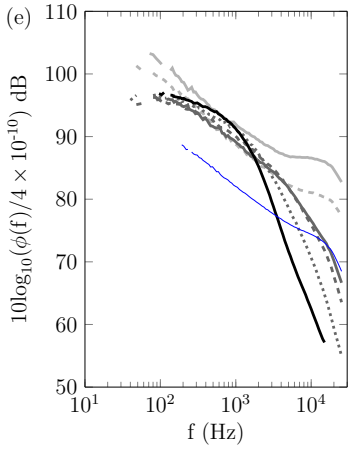

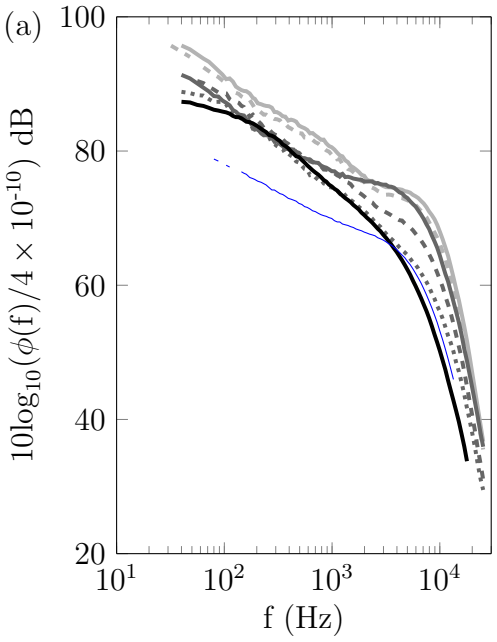

Figure 6.24: Pressure spectra measured over the surface of cylinders at (a) 30-ms^{-1} (b) 40-ms^{-1} (c) 50-ms^{-1} (d) 60-ms^{-1} and (e) 70-ms^{-1}. In these figures the measurement height above the wall is denoted by: ——0-mm; ·····1-mm; - - - -2-mm; ——3-mm; - - - -4-mm; ——5-mm. The pressure spectrum over the smooth wall, measured at the wall, at each speed is also included as ——

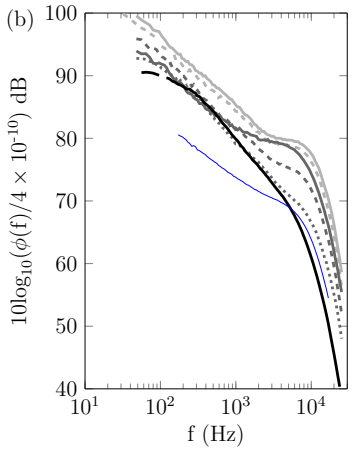

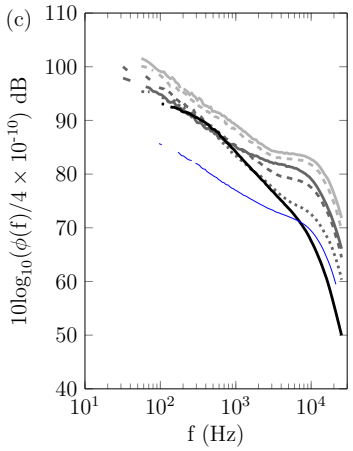

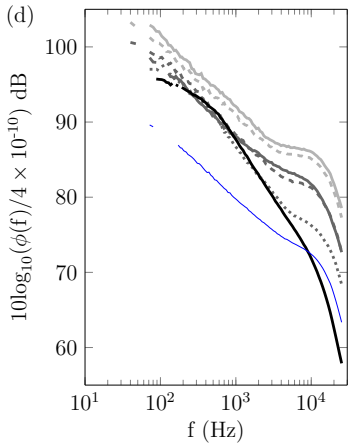

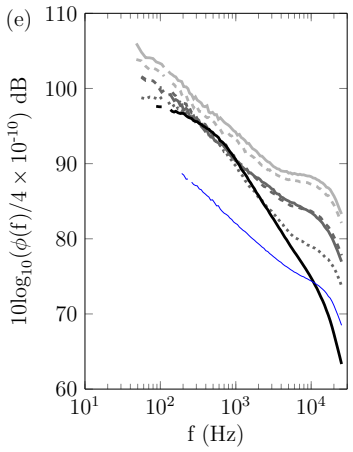

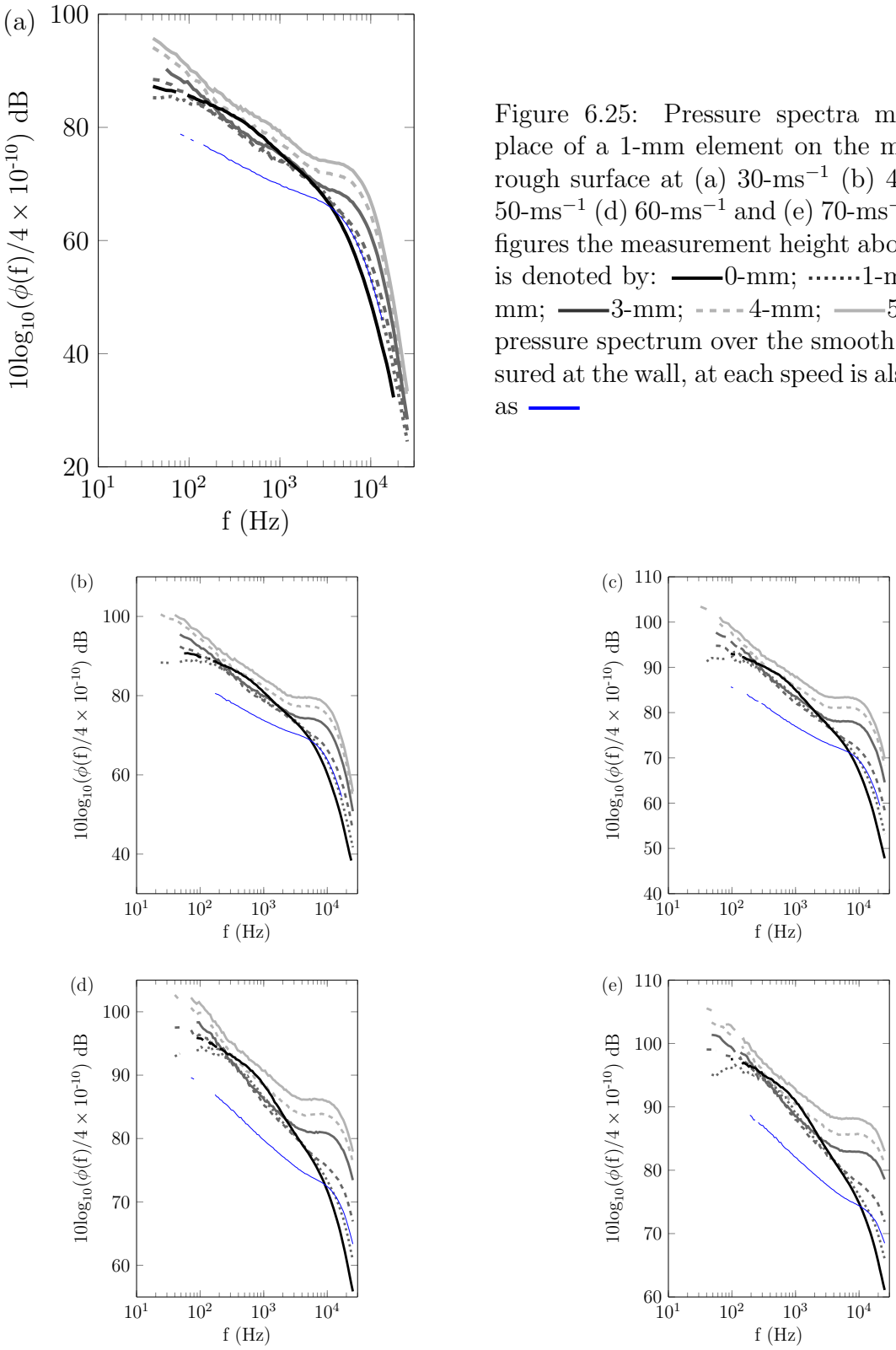

Figure 6.25: Pressure spectra measured in place of a 1-mm element on the multi-height rough surface at (a) 30-ms^{-1} (b) 40-ms^{-1} (c) 50-ms^{-1} (d) 60-ms^{-1} and (e) 70-ms^{-1}. In these figures the measurement height above the wall is denoted by: ——0-mm; ·····1-mm; - - - -2-mm; ——3-mm; - - - -4-mm; ——5-mm. The pressure spectrum over the smooth wall, measured at the wall, at each speed is also included as ——

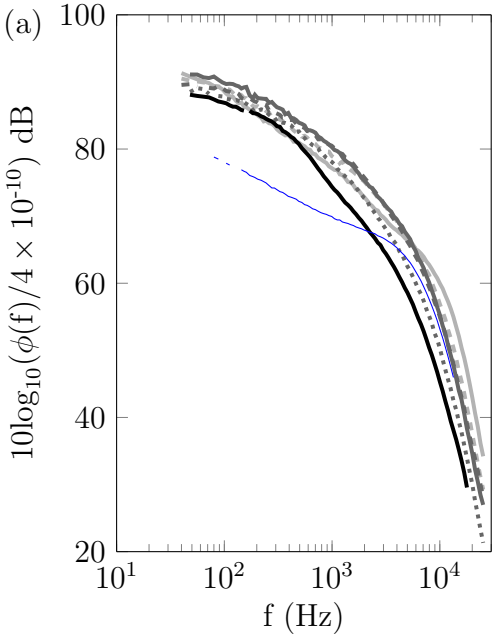

Figure 6.26: Pressure spectra measured downstream a cylindrical element on the multi-shape rough surface at (a) 30-ms^{-1} (b) 40-ms^{-1} (c) 50-ms^{-1} (d) 60-ms^{-1} and (e) 70-ms^{-1}. In these figures the measurement height above the wall is denoted by: ——0-mm; ·····1-mm; - - - -2-mm; ——3-mm; - - - -4-mm; ——5-mm. The pressure spectrum over the smooth wall, measured at the wall, at each speed is also included as ——

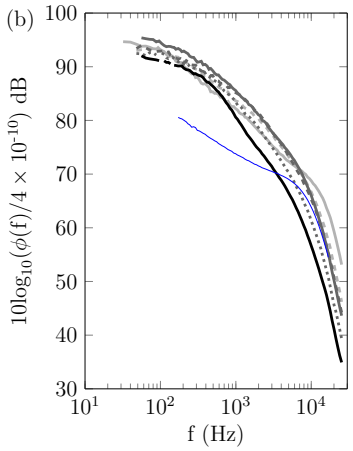

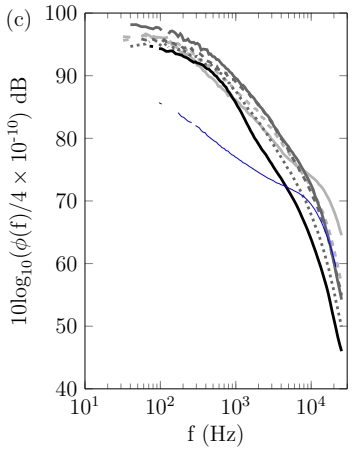

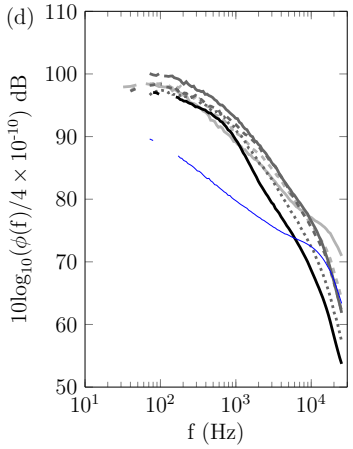

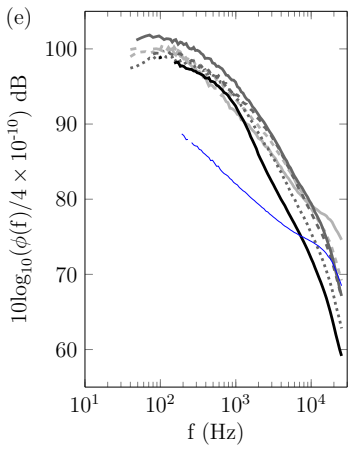

parts of the mid-frequency region. The observation that the rapid roll-off region includes parts of the mid-frequency region on the denser roughness was also discussed in chapter 3 where we speculated that the low momentum fluid in the near-wall region was the reason for the steeper mid-frequency slope. This idea appears to be valid when we consider that the mid-frequency slope becomes increasingly steeper as we move closer to the wall. One would expect that regions closest to the wall would contain the slowest moving, lowest-energy flow because of the blockage of roughness elements and the imposition of the no-slip condition.

This gradual, progressive decay of energy and turbulent structures from the region above the roughness, through the interstitial flow, to the wall is suggestive of an evanescent pressure decay phenomenon occurring through the lower layers of the turbulent boundary layer. The increased shear and vorticity within the interstitial flow tends to decay the pressure fluctuations from the what they would be if there were no roughness (such as exists over the smooth wall and just above the roughness tops). It is curious that the y=4-mm case also shows a decrease in magnitude of about 4-dB from y=5-mm. It is in fact closer in magnitude to the spectrum measured at the wall than that at y=5-mm. This suggests that the evanescent decay may also be applicable some distance above the roughness tops.

The proposition of a pseudo-wall existing at the top of the roughness elements is obviously most suited to surfaces on which the elements are closely-packed. However, the premise of an evanescent pressure decay through the interstitial flow is not restricted to such cases. In fact, figs. 6.24 and 6.25 also show evidence of the evanescent pressure decay behaviour on the surface of cylinders and on the multi-height surface.

In the case of the cylinders, presented in fig. 6.24, we see much the same behaviour as for the dense roughness. Above the roughness tops, outside the interstitial region, the pressure spectra resembles the smooth wall. The mid-freqeuncy slope is approximately -0.8 and the freqeuncy at which the rapid-roll off begins is approximately 7-kHz. The shape of the spectrum at y=3-mm is similar to that at larger y locations except that the magnitude of the spectrum drops by approximately 4-dB in the low and mid-frequency regions. Below y=3-mm the spectrum begins to decay with decreasing y such that the mid-frequency slope at y=2-mm is -1 (compared to -0.8 at y=3-mm) and -1.2 at y=1-mm. The slope further steepens to -1.5 at the wall. The frequency at which the rapid roll-off begins also becomes smaller, occurring at 7-kHz, 6.3-kHz and 3.5-kHz for y=2-mm, y=1-mm and y=0-mm respectively. These rapid-roll off region does not extend into the mid-frequency region as we saw with the dense roughness, most likely because there is more space between elements so the flow is not retarded as much as on the densely packed rough surface. The high frequency portion of the smooth wall spectrum lies about 2.5-dB above the spectrum measured at the wall on the surface of cylinders, and 2-dB below the spectrum measured y=1-mm above the wall. This means that at this microphone location ($\sim$ 8-mm from the centre of the element) the eddies are only displaced a fraction of a millimetre above the wall. Furthermore, the increased viscous action which accompanies the addition of cylindrical roughness results in a 2.5-dB decrease in the pressure levels in the high frequency region.

Fig. 6.25 shows that the mid-frequency slope of the spectra measured between y=1-mm and 5-mm over the multi-height roughness have the same slope – -1.1. The mid-frequency slope then steepens to -1.5 at the wall. This still supports the evanescent pressure decay hypothesis because we see a gradual change in slope (despite the initial slope being 37% steeper than that of the smooth wall) closer to the wall. The progressive decrease in the frequency at which roll-off begins is also evident at y below 2-mm. Above the roughness tops rapid roll-off begins at a frequency of 8.5-kHz. A y=2-mm roll off starts at 7.5-kHz versus 5.6-kHz at y=1-mm. At the wall the roll off frequency drops to 3.8-kHz. The high frequency portion of the smooth wall spectrum aligns within 0.3-dB with the spectrum measured at y=1-mm above the multi-height surface. Again this tells us that eddies are displaced about 1-mm above the wall and that the increase in viscous action compared to the smooth wall results in a 4-dB decrease in the pressure levels in the high frequency region.

The case of the multi-shape surface is presented in fig. 6.26. As with the multi-height surface the slopes of the mid-frequency spectra above the wall are not the same as the smooth wall. In fact, they are only 10% shallower than the slope at the wall. Nevertheless we do see evidence of an evanescent decay of pressure as the slopes progressively, granted slowly, become steeper as we move closer to the wall.

An analytical method for modelling the evanescent pressure decay which would occurs between the roughness tops and the wall was developed based on Lighthill's acoustic analogy. The author is indebted to Prof. Stewart Glegg of Florida Atlantic University for providing the analysis below.

We begin with the momentum equation written in the form used by Lighthill

$$\frac{\partial(\rho\nu_i)}{\partial t} + \frac{\partial p}{\partial y_i} + \frac{\partial(\rho\nu_i\nu_j - \sigma_{ij})}{\partial y_i} = 0 \tag{6.44}$$

If we assume that the flow is incompressible and divergence-free, we can take the divergence of eq. (6.44) to obtain a Poisson's equation of the form

$$\frac{\partial^2 p}{\partial y_i^2} = \frac{\partial T_{ij}}{\partial y_i \partial y_j} \tag{6.45}$$

where T_{ij} is Lighthill's stress tensor for an incompressible fluid, and includes the viscous effects of the stress tensor, such that

$$T_{ij} = \rho_0\nu_i\nu_j - \sigma_{ij} \tag{6.46}$$

The Green's function which satisfies the Poisons equation is

$$\frac{\partial^2 G}{\partial y_i^2} = -\delta(\mathbf{x}-\mathbf{y}) \tag{6.47}$$

which is used to obtain Curle's solution for a flow in the presence of rigid surfaces

$$p(\mathbf{x},t) = \int_S \left(p(\mathbf{y},t)\frac{\partial G(\mathbf{x}|\mathbf{y})}{\partial y_i} n_i - \sigma_{ij}(\mathbf{y},t)\frac{\partial G(\mathbf{x}|\mathbf{y})}{\partial y_i} n_j \right) dS + \int_V T_{ij}(\mathbf{y},t)\frac{\partial G(\mathbf{x}|\mathbf{y})}{\partial y_i \partial y_j} dV \tag{6.48}$$

n_i in eq. (6.48) is the unit normal pointing into the fluid. Equation (6.48) is a result for the mean flow which can be transformed to include perturbation quantities by subtracting the time average quantities such as $p' = p - \overline{p}$. The result is

$$\begin{aligned} p'(\mathbf{x},t) = &\int_S \left(p'(\mathbf{y},t)\frac{\partial G(\mathbf{x}|\mathbf{y})}{\partial y_i} n_i - \left[\sigma_{ij}(\mathbf{y},t) - \overline{\sigma_{ij}(\mathbf{y})}\right]\frac{\partial G(\mathbf{x}|\mathbf{y})}{\partial y_i} n_j \right) dS \\ &+ \int_V \left[T_{ij}(\mathbf{y},t) - \overline{T_{ij}(\mathbf{y})}\right]\frac{\partial G(\mathbf{x}|\mathbf{y})}{\partial y_i \partial y_j} dV \end{aligned} \tag{6.49}$$

If we now define the rough surface by the function $y_2 = \zeta(y_1, y_3)$, the unit normal to the surface is obtained as $\mathbf{n} = \nabla f/|\nabla f|$ where $f = y_2 - \zeta(y_1, y_3)$. Similarly, the surface can be projected until its planform, Σ, in the plane y_2=0, integrating over y_1 and y_3. Since $dS = Jd\Sigma$ and $J = |\nabla f|$, the surface integral reduces to

$$p_s(\mathbf{x},t) = \int_\Sigma \left(p(\mathbf{y},t)\frac{\partial G(\mathbf{x}|\mathbf{y})}{\partial y_i}\frac{\partial f}{\partial y_i} - \sigma_{ij}(\mathbf{y},t)\frac{\partial G(\mathbf{x}|\mathbf{y})}{\partial y_i}\frac{\partial f}{\partial y_i} \right) d\Sigma \tag{6.50}$$

This solution requires that the traducer lie in the flow. In the case where the sensor is close to the wall, a rough surface that consists of a uniform flat plate in the plane y_2=0 with elements that protrude into the flow in the region $y_2 > 0$ is assumed. The measurement location is defined just above the flat surface where there are no roughness elements and the surface normal is in the y_2 direction.

Choosing $\partial G/\partial y_2$=0 on the surface in the vicinity of the microphone sensor, a suitable Greens function is given as

$$G = \int_{-\infty}^{\infty}\int_{-\infty}^{\infty} \left(\frac{e^{ik_1(x_1-y_1)+ik_3(x_3-y_3)}}{4\pi^2} \right) \left(\frac{e^{-\gamma|x_2-y_2|} + e^{-\gamma(x_1+y_1)}}{2\gamma} \right) dk_1 dk_3 \tag{6.51}$$

where $\gamma = \sqrt{k_1^2 + k_3^2}$

This ensures that $\partial G/\partial y_2$=0 ont he flat part of the surface, prociding $x_2 = \varsigma > 0$.. However, on the roughness elements and in the flow above the flat surface, $y_2 > x_2$ of ς tends to zero. In this case

$$G = \int_{-\infty}^{\infty}\int_{-\infty}^{\infty}\left(\frac{e^{ik_1(x_1-y_1)+ik_3(x_3-y_3)-\gamma y_2}}{4\pi^2}\right)\left(\frac{\cosh(\gamma\varepsilon)}{\gamma}\right)dk_1dk_3 \tag{6.52}$$

Substituting eq. (6.52) into eq. (6.50) we get

$$\begin{aligned} p_s(\mathbf{x},t) = \sum_n \int_{\Sigma_n}\int_{-\infty}^{\infty}\int_{-\infty}^{\infty}\left(p(\mathbf{y},t)\kappa_i\frac{\partial f}{\partial y_i} - \sigma_{ij}(\mathbf{y},t)\kappa_i\frac{\partial f}{\partial y_i}\right) \\ \times\left(\frac{e^{ik_1(x_1-y_1)+ik_3(x_3-y_3)-\gamma y_2}}{4\pi^2}\right)\left(\frac{\cosh(\gamma\varepsilon)}{\gamma}\right)dk_1dk_3d\Sigma \end{aligned} \tag{6.53}$$

where the wavevector is defined as $\boldsymbol{\kappa} = (ik_1, \gamma, ik_3)$.

From eq. (6.53) we get the surface wavenumber spectrum as

$$\begin{aligned} \hat{p}_s(k_1,k_3,\boldsymbol{\omega}) = -\sum_n \int_{\Sigma_n}\left(\tilde{p}(\mathbf{y},\boldsymbol{\omega})\kappa_i\frac{\partial f}{\partial y_i} - \tilde{\sigma_{ij}}(\mathbf{y},\boldsymbol{\omega})\kappa_i\frac{\partial f}{\partial y_i}\right) \\ \times\left(\frac{e^{ik_1(x_1-y_1)+ik_3(x_3-y_3)-\gamma\zeta(y_1,y_3)}}{4\pi^2}\right)\left(\frac{\cosh(\gamma\varepsilon)}{\gamma}\right)dk_1dk_3d\Sigma \end{aligned} \tag{6.54}$$

and

$$\hat{p}_v(k_1,k_3,\boldsymbol{\omega}) = \int_V\left(\kappa_i\kappa_j\tilde{T_{ij}}(\mathbf{y},\boldsymbol{\omega})\left(\frac{e^{ik_1(x_1-y_1)+ik_3(x_3-y_3)-\gamma\zeta(y_1,y_3)}}{4\pi^2}\right)\left(\frac{\cosh(\gamma\varepsilon)}{\gamma}\right)dV\right. \tag{6.55}$$

To model the results, it is assumed that the pressure over each rough element is spatially uniform and viscous effects are ignored. If the pressure fluctuations are uncorrelated on each element, and homogeneous, then the wavenumber frequency spectrum is given by

$$S_{pp}^{(s)}(k_1,k_3,\omega) = S_{pp}(\omega)\sum_n\left|\Lambda_n(k_1,k_3)\right|^2 \tag{6.56}$$

where

$$\Lambda(k_1,k_3) = -\int_{\Sigma_n}\left(\kappa_i\frac{\partial f}{\partial y_i}\right)\left(\frac{e^{ik_1(x_1-y_1)+ik_3(x_3-y_3)-\gamma\zeta(y_1,y_3)}}{4\pi^2}\right)\left(\frac{\cosh(\gamma\varepsilon)}{\gamma}\right)d\Sigma \tag{6.57}$$

Similarly the wavenumber spectrum from the volume sources can be defined in terms of the wavenumber frequency spectrum of T_{ij} in planes of constant elevation above the surface, providing that they are zero below the maximum height, Δy, so

$$S_{pp}^{(V)}(k_1,k_3,\omega)=\int_{\Delta y}^{\infty}\int_{\Delta y}^{\infty}\kappa_i\kappa_j\kappa_p\kappa_s\left(\frac{\pi}{T}E\left[\hat{T}_{ij}(k_1,k_3,\omega,y_2')\hat{T}^*{}_{ps}(k_1,k_3,\omega,y_2)\right]\right)$$
$$\times\left(\frac{\cosh(\gamma\varepsilon)}{\gamma}\right)^2 e^{-\gamma(y_2+y_2')}dy_2dy_2' \tag{6.58}$$

This indicates an exponential decay if the turbulent sources are raised above the surface by the mean flow. In the absence of roughness this would be the only term that contributes. This integral is evaluated over the limits k_g to infinity and so it is more appropriate to specify the previous equation using the coordinate $\xi_2 = y_2 - k_g$ so that the integral is independent of the roughness height. The surface pressure as a function of $x_2 = \varepsilon < k_g$ is then

$$S_{pp}^{(V)}(k_1,k_3,\omega)=\left(\frac{\cosh(\gamma\varepsilon)}{\gamma}e^{-\gamma h}\right)^2\int_0^{\infty}\int_0^{\infty}\kappa_i\kappa_j\kappa_p\kappa_s\left(\frac{\pi}{T}E\left[\hat{T}_{ij}(k_1,k_3,\omega,\xi_2')\hat{T}^*{}_{ps}(k_1,k_3,\omega,\xi_2)\right]\right)$$
$$\times\, e^{-\gamma(\xi_2+\xi_2')}d\xi_2d\xi_2' \tag{6.59}$$

In eq. (6.59) if we replace ε with x_2 then the terms outside the integral show that the surface pressure spectrum will be proportional to

$$\left(\frac{\cosh(\gamma\varepsilon)}{\gamma}e^{-\gamma h}\right)^2=\left(\frac{e^{-\gamma(\Delta y-x_2)}+e^{-\gamma(\Delta y+x_2)}}{2\gamma}\right)^2 \tag{6.60}$$

So on the surface where x_2=0 the spectrum has an exponential decay $e^(-2\gamma\Delta y)/\gamma^2$. At the tops of the roughness, where x_2=Δy, the spectrum depends on $(1+e^(-2\gamma\Delta y))^2/4\gamma^2$. Therefore, the pressure spectrum at the top of the roughness is related to the pressure spectrum at the wall by a multiplicative factor of

$$\frac{4e^{-2\gamma\Delta y}}{(1+e^{-2\gamma\Delta y})^2} \tag{6.61}$$

Hence a wavenumber frequency spectrum model could be multiplied by this factor in order to estimate the evanescent pressure decay which would occur over the distance Δy.

The choice of Δy is important as it will dictate the exponential decay. The obvious choice would be to use the spectrum measured at the roughness tops, y=k_g, so that we model the evanescent decay through the interstitial flow. However, it is not unreasonable that Δy would vary with roughness configuration (the multi-shape surface, for example, has shown evidence of displacing streamlines further away from the wall than the other surfaces) and microphone location.

Table 6.6: Comparison of the optimum decay height, Δy, and the average roughness height, $k_{g_{avg}}$, on different surfaces

Surface	$k_{g_{avg}}$, mm	Δy, mm
dense roughness	3	2.5
cylinders	3	2.5
multi-height surface (in place of 1mm element)	2	1.5
multi-shape surface (downstream cylinder)	3	2.5

The analytical model of eq. (6.61) was used to compare the attenuation associated with an evanescent decay to the difference between the pressure spectrum of the rough-wall boundary layer measured at the roughness tops (y=3-mm) and at the wall. To do this a Chase model [116], scaled with the boundary layer parameters of the respective roughness case, was used to represent the wavenumber frequency spectrum of the rough-wall boundary layer. The model wavenumber spectrum was evaluated on a wavenumber grid with a spacing of 50 steps and limits of 150-Hz $\leq \omega \leq$ 12000-Hz, 150-m^{-1} $\leq k_1 \leq$ 20000-m^{-1} and -10000-m^{-1} $\leq k_3 \leq$ 10000-m^{-1}. The spectrum was then integrated in wavenumber space to obtain a frequency spectrum both with and without the evanescent decay term of eq. (6.61). The dB difference between the two spectra was then subtracted from the pressure spectrum measured at the roughness tops for comparison with that measured at the substrate. The results at 30-ms^{-1} and 60-ms^{-1} for each of the four rough surfaces tested (densely-packed, cylinders, multi-height, and multi-shape) are shown in fig. 6.27.

Δy was selected by a user-determined algorithm which allows the user to select the value of Δy which produces the closest mid-frequency slope alignment between the spectrum measured at the wall and the decayed spectrum. Values of Δy could be chosen to within a 0.2-mm resolution. The final values for Δy used in fig. 6.27 are listed in table 6.6 for each surface. Here they are compared to the average geometric roughness height, which we stated before is the intuitive choice for Δy. Interestingly, the chosen value for Δy is consistently half a millimetre smaller than $k_{g_{avg}}$. This means that the evanescent pressure decay actually begins a short distance below the roughness tops. The fact that we found this distance to be 0.5-mm is most likely a coincidence and obviously subject to uncertainty. What we can take away though, is that the evanescent pressure decay occurs over a distance smaller than the average roughness height.

The results of fig. 6.27 are quite promising. In the case of the dense roughness, the evanescent pressure decay model is able to adjust the mid-frequency slope of the spectrum measured at the roughness tops to obtain the slope of the spectrum measured at the wall. Using a decay distance of 2.5-mm we see that the model is able to accurately steepen the slope to coincide with the slope measured at the wall. The same is observed for the cylinders and the multi-height surface. In both these cases the spectrum at the roughness tops is successfully modified by the evanescent decay model to obtain a spectrum whose slope matches that measured at the wall. On these three surfaces, not only is the slope matched, but also the

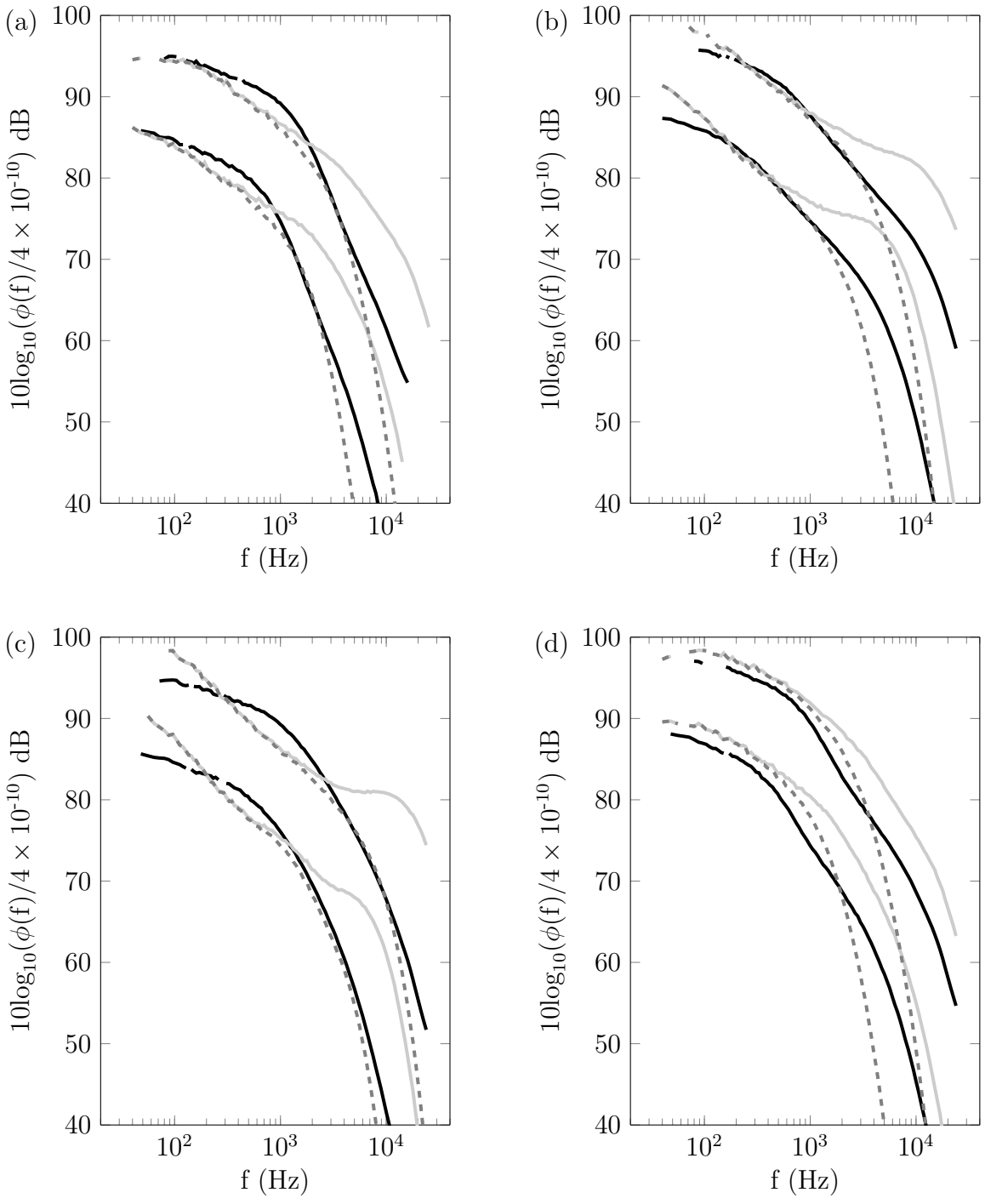

Figure 6.27: Evanescent pressure decay applied to data collected at y=3-mm above the (a) dense roughness (b) surface of cylinders (c) multi-height roughness and (d) multi-shape roughness. Results shown for 30-ms^{-1} and 60-ms^{-1} only. Spectra shown on each plot are: ——spectrum measured at wall; ——spectrum measured 3-mm above wall; - - - -spectrum measured 3-mm above wall decayed using the multiplier in eq. (6.61)

magnitude. In the case of the multi-shape surface, the magnitude of the spectrum measured at the roughness tops is consistently 3-dB higher than that measured at the wall. Since we seek a qualitative result, we can still apply the model of eq. (6.61) to determine whether the slope will be corrected appropriately. Indeed, this is what we find. Fig. 6.27d shows that the mid-freqeuncy slope of the decayed spectrum matches that measured at the wall. The magnitude of the decayed spectrum is 3-dB higher than that measured at the roughness top simply because the initial spectrum measured at the roughness top was also offset by 3-dB. A final observation from fig. 6.27 is that the decay distance, Δy, does not vary with increases in edge velocity. It is the same for 30-ms^{-1} and 60-ms^{-1}.

6.4 Application to Realistic Roughness

The goal of this research is to uncover relationships and physics for realistic rough surfaces. The discrete roughness tested in this work are not realistic. We must therefore seek to apply our findings to rough surfaces of a more practical nature.

As a first step toward applying our findings to more realistic surfaces, we can look at how the high and low frequency scalings work with the spectrum measured at the top of a cylinder on the uniform surface of cylinders. This is possible because we inserted the microphone 3-mm into the flow, inside a bushing, so that the microphone was the same geometry as a cylinder. The only difference was the location of the cylinder which, instead of being in a streamwise line with other elements, was in the middle of a four element array. Nevertheless we attempt to scale the high and the low frequency portions of this spectrum because, on a real rough surface, there would hardly be discrete roughness elements. We would need an ideal scaling which works irrespective of location on the rough surface.

Fig. 6.28 presents the spectra measured at the top of a cylindrical element scaled on the high and the low frequency scalings. We observe in fig. 6.28a that the low frequency scaling appears to work. Apart from some deviations at the lowest frequencies, the low frequency portion of the spectrum falls almost in the middle of the collapsed dataset.

The high frequency scaling applied to the measurements at the roughness top is presented in fig. 6.28b. The results are inconclusive. The slope of the high frequency collapse at the roughness tops appears to be slightly steeper ($\sim$-5.6) than -5. Furthermore, the curves do not all extend to the highest frequencies. So while it apears that there is some alignment with the data at the wall, more investigations need to be done in this regard before we can make any conclusions.

Naturally different values of U_ν were used for the spectra at the roughness tops compared to that at the wall. This is simply because the spectrum at the wall contains more high frequency content because of the additional small eddies existing close to the wall and in the interstitial flow. The spectrum measured at the roughness tops will include some of these

viscous scales which have been displaced from the wall by the roughness, and through events like bursts. However, we cannot expect the two to be the same. To produce the alignment shown in fig. 6.28b all values of U_ν used at the roughness tops were 20% higher than that used at the wall. Using the same values of U_ν which were obtained for the spectra at the wall resulted in a collapse of the data, but the resulting line was approximately 15-dB above the rest of the data.

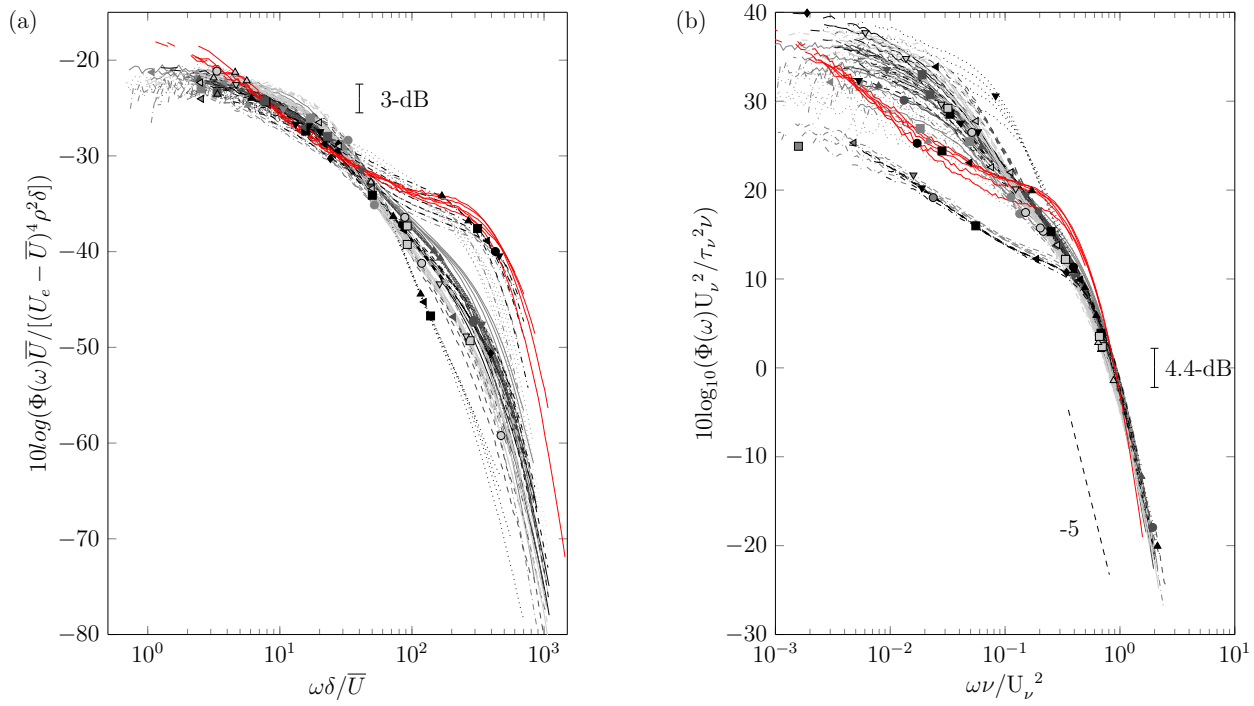

Figure 6.28: (a) Low frequency scaling on $\overline{U}$ and (b) high frequency scaling of Meyers *et al.* [1] applied to the pressure spectra measured at the top of the cylinders (——) at all speeds. Other data included on the plot for reference. Symbols as defined in fig. 6.1

7. Empirical Spectral Model for the Rough-Wall Surface Pressure Spectrum

The Goody model [74], discussed in § 1.6.1 and presented in eq. (1.25), provides a fairly successful empirical fit to the smooth wall turbulent boundary layer pressure spectrum. This formula is repeated here for convenience.

$$\frac{\phi(\omega)U_e}{\tau_w^2\delta} = \frac{C_2(\omega\delta/U_e)^2}{\left[(\omega\delta/U_e)^{0.75}+C_1\right]^{3.7}+\left[C_3R_T^{-4/7}(\omega\delta/U_e)\right]^7} \tag{7.1}$$

There does not exist an equivalent empirical model which can predict the rough wall turbulent boundary layer pressure spectrum. It would be useful to develop such a formulae in order to predict the pressure spectrum from the boundary layer parameters. This task is undertaken in the following sections.

7.1 Modified Goody Model

We began with the generic form of the Goody model normalised on the new low frequency scaling on $\overline{U}$ and shown in eq. (7.2). This is a useful starting point as this form of the model enforces the high and low frequency behaviour we expect for the pressure spectrum.

$$\frac{\phi(\omega)\overline{U}}{(U_e-\overline{U})^4\rho^2\delta} = \frac{C_2(\omega\delta/\overline{U})^a}{\left[(\omega\delta/\overline{U})^p+C_1\right]^b+\left[C_3R_T^q(\omega\delta/\overline{U})\right]^c} \tag{7.2}$$

The first step in developing a functional form was to define $a \equiv 2$ and $c \equiv 7$. This ensures that we achieve a low frequency slope of ω^2 and a high frequency slope of ω^{-5}.

The next step was to ascertain values for the variables C_1, C_2, C_3, b, p and q. No single value for these constants could be found which worked for all the rough wall data. Perhaps the use of constants is suitable for the smooth wall (as was done by Goody), but clear variations in the success of the fit with U_e, k_g and λ were seen. Thus it was necessary to develop relationships for these variables which fully captured the dependencies on U_e, k_g and λ. The resulting relationships are outlined hereafter.

C_2 controls the magnitude of the pressure spectrum which we know is related to the velocity gradient in the different regions of the boundary layer. For this reason, C_2 is defined as the ratio of the outer velocity gradient to the inner velocity gradient such that:

$$C_2 = \frac{U_\tau}{Ue-\overline{U}} \div \frac{U_\nu}{U_\tau} \tag{7.3}$$

Equation (7.3) makes the assumption that the pressure scale in the mid-frequency is U_τ. From our discussions in chapter 6 we know that this may not be the case. However, it is a valid assumption at this point.

C_1 was found to control the low frequency curvature, and indirectly influences the magnitude of the low frequency portion of the spectrum. It should therefore be governed by outer region velocities. It was also observed that this parameter was highly dependent on the sparseness ratio. For this reason, we define C_1 as

$$C_1 = \left(\frac{U_e}{\overline{U}}\right)^{4.5\lambda - 2.9\lambda + 79\lambda} \tag{7.4}$$

The index of eq. (7.4) was determined purely from correlations of λ with the optimum C_1 values which fit the data.

The parameter p controls the mid-frequency slope. Correlations between the slopes from chapter 6 and the outer velocity ratio showed a linear relationship such that

$$p = -1.6(\overline{U}/U_e) + 2.1 \tag{7.5}$$

when b is 5.

C_3 governs the point at which the high frequency roll off begins. It should therefore depend on the ratio of the viscous to outer pressure scales. So we define C_3 as

$$C_3 = \frac{U_e - \overline{U}}{U_\nu} \tag{7.6}$$

The definition given by Goody for R_T was retained: the ratio of the outer timescales to the inner timescales. However, the inner and outer scales from our new low frequency scaling and the Meyers *et al.* high frequency scaling were utilised giving us

$$R_T = \frac{\delta}{\overline{U}} \frac{U_\nu^2}{\nu} \tag{7.7}$$

Lastly, q was found to vary as

$$q = -0.77\left(\frac{k_g \varepsilon^*}{x_{mic}\delta}\right)^{0.015} \tag{7.8}$$

The argument of eq. (7.8) might appear to be a strange formulation. However it is based on the mid-frequency slope correlation we found in fig. 6.19. It takes into account the ratio of the wall-normal to the streamwise effect of the roughness

$$\frac{\varepsilon^*}{x_{mic}} \tag{7.9}$$

as well as the roughness height, k_g normalised on the boundary layer thickness, δ.

Equations (7.3) to (7.8) were defined based on the combined considerations of (1) the parameters which physically govern the flow (in a given region) and (2) correlations with the experimental data. The latter of these considerations was heavily dependent on an iterative process for improving the fit between the data and the model. For example, eq. (7.4) was developed after observing that the low frequency curvature varied with free stream velocity but also with roughness element density.

The results of this model are presented in figs. 7.1 to 7.3 for the present rough wall data and fig. 7.4 shows the predicted spectrum for the data of Forest [87] and Meyers [103]. In these plots, the averaged pressure spectrum (in dB) measured in the experiments are shown in black. The prediction produced by the new model is shown as a red line.

The model appears to have marginal success. The low frequency is predicted to within 1-dB for all surfaces at all speeds except the multi-shape surface. Here we see deviations up to 2-dB. In the high frequency region, there is a fair agreement between the data and the prediction, with differences less than 1-dB between the two curves. However, the multi-shape surface, measured 2-mm downstream of the cylinder, is not well predicted by the model. In this case there is an average magnitude difference of 3-dB. The proposed model has significantly more issues with capturing the mid-frequency regions. The spectra of the intermediately spaced hemispheres, the multi-height surface when measured in place of a 1-mm element, and the multi-height surface when measured in the vicinity of the 1-m elements are well predicted (less than 0.5-dB deviations). All other surfaces show mid-frequency deviations between the data and the prediction. The issue is both with the slope of this region and its magnitude as the free stream velocity increases. In the case of the sparse 3-mm hemispheres, the random 3-mm hemispheres and the sparse 3-mm cylinders we see that the agreement at low speed is better than at higher speeds. As the speed increases, the mid-frequency magnitude also appears to increase. The spectra with steep mid-frequency regions are also poorly predicted, namely the dense roughness, the multi-shape roughness (especially when measured 2-mm downstream the cylinder) and the multi-height surface when measured 2-mm downstream the 3-mm hemisphere. Part of the issue with the multi-shape surface prediction is that the low frequency was poorly correlated with the $\overline{U}$ scaling to begin with. Some efforts were put toward adding a third term to the denominator of eq. (7.2). However, this did not solve the mid-frequency issue and had reduced success in the high and low frequency regions. The mid-frequency issue most likely lies in the definition of q and possibly p. These definitions need to be revisited and improved.

So it seems that the proposed model is able to predict the low and high frequency regions to within 1-dB in most cases. But the mid-frequency region needs work. This is not surprising based on the complexities we uncovered for this region back in chapter 6. Furthermore, the fact that the multi-shape surface is hardest to predict should again be expected when we recall that it shows evidence of having multiple mid-frequency regions.

A fact that must be addressed is the sheer complexity of the proposed relationships for the

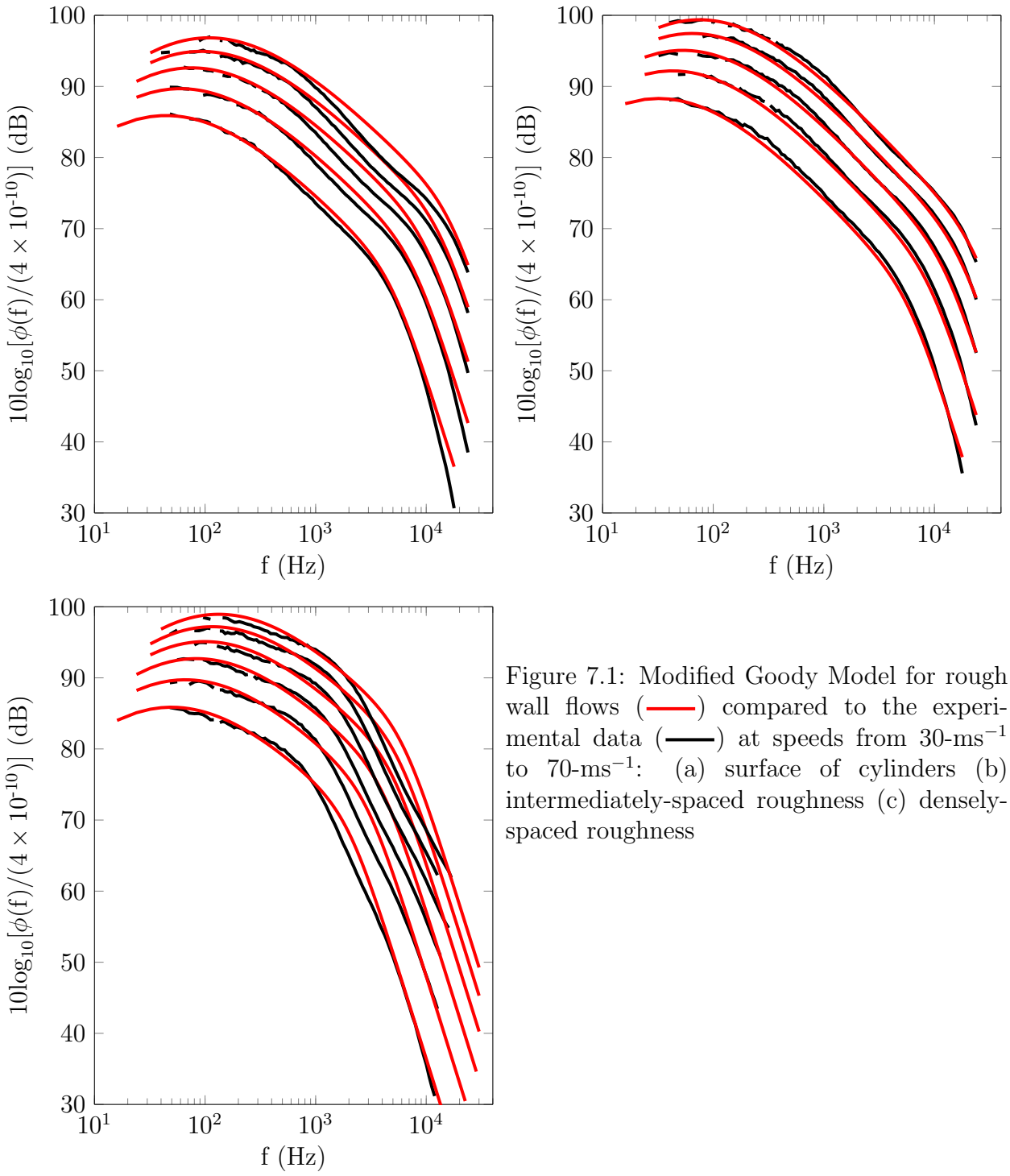

Figure 7.1: Modified Goody Model for rough wall flows (——) compared to the experimental data (——) at speeds from 30-ms^{-1} to 70-ms^{-1}: (a) surface of cylinders (b) intermediately-spaced roughness (c) densely-spaced roughness

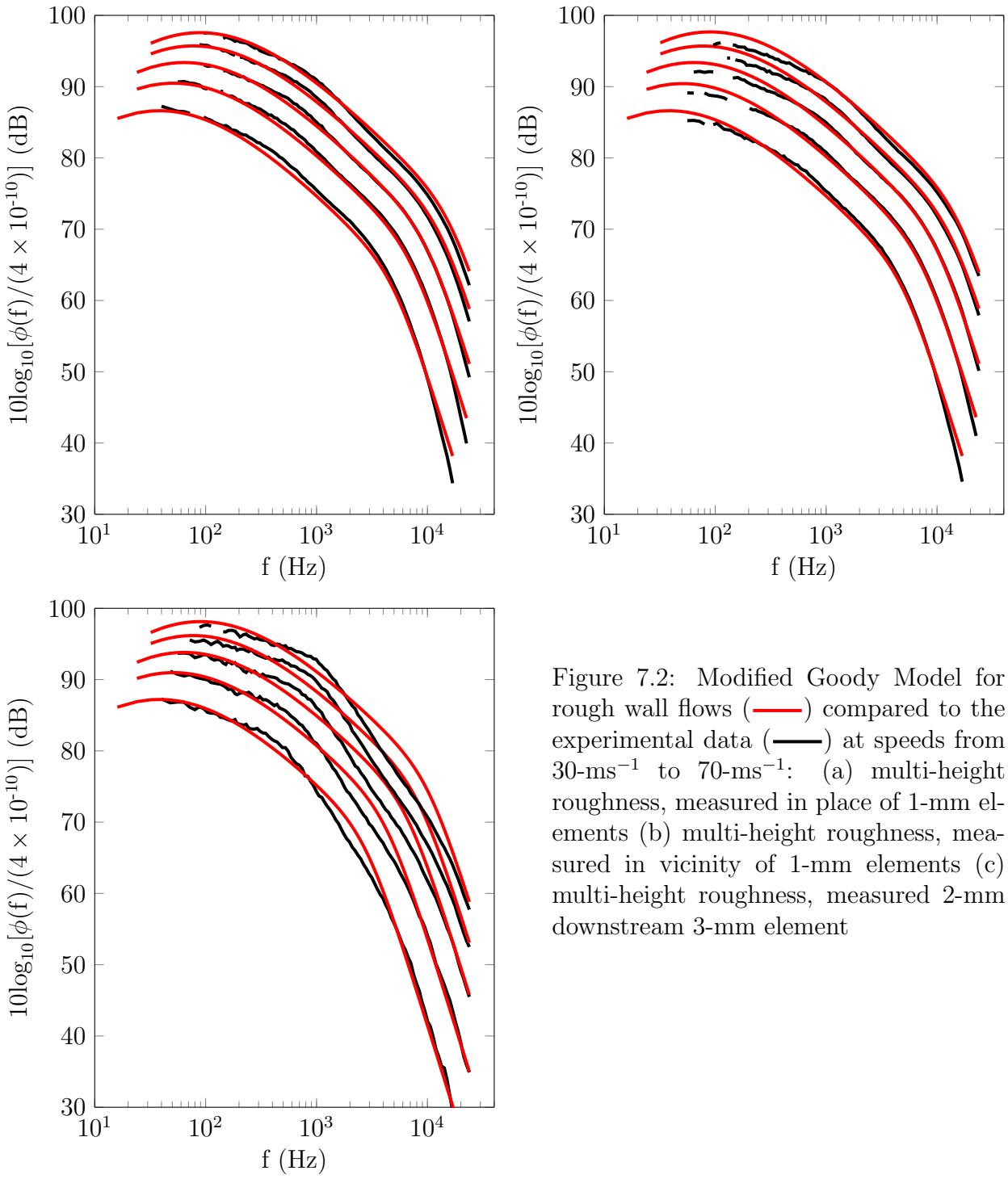

Figure 7.2: Modified Goody Model for rough wall flows (——) compared to the experimental data (——) at speeds from 30-ms^{-1} to 70-ms^{-1}: (a) multi-height roughness, measured in place of 1-mm elements (b) multi-height roughness, measured in vicinity of 1-mm elements (c) multi-height roughness, measured 2-mm downstream 3-mm element

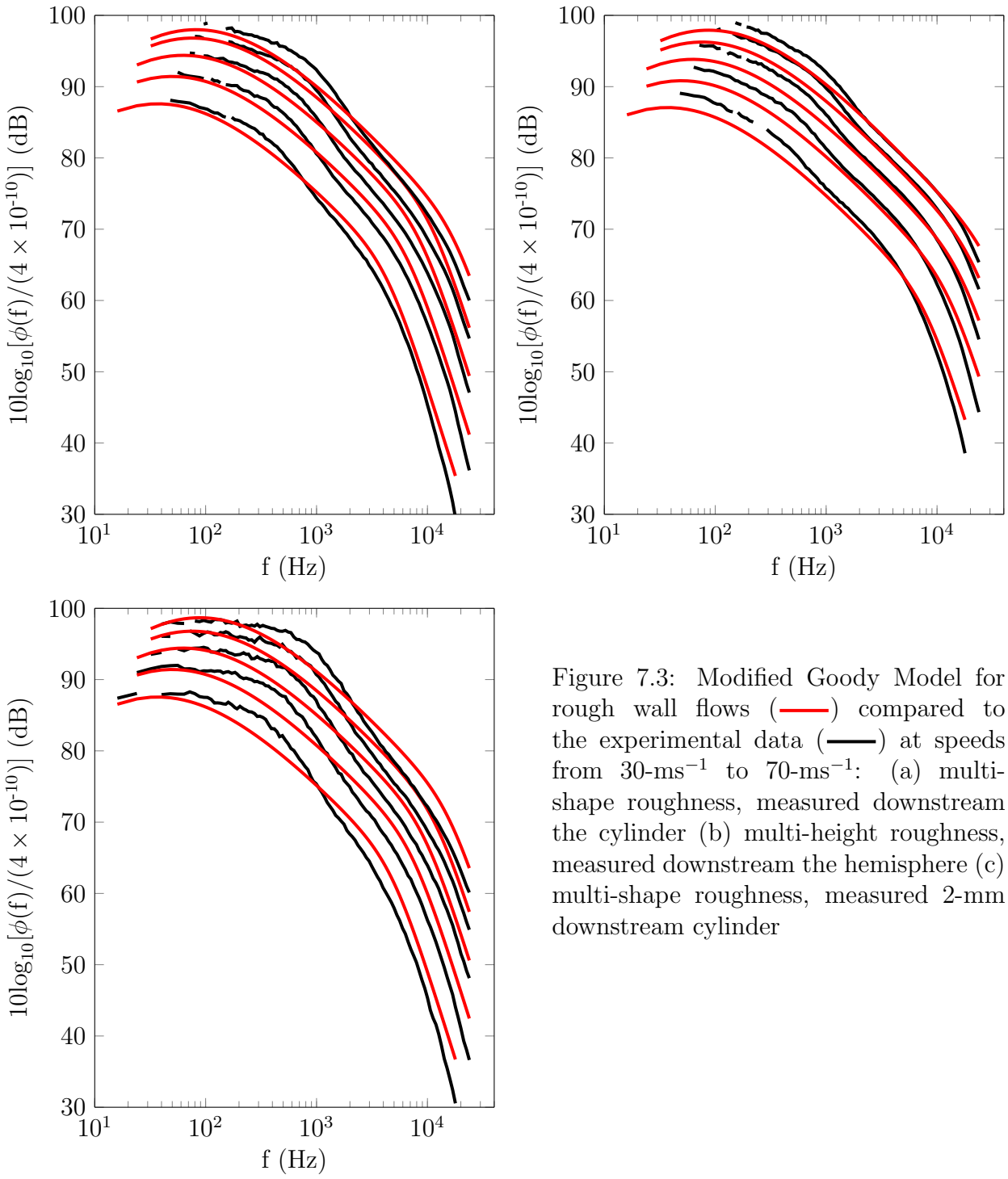

Figure 7.3: Modified Goody Model for rough wall flows (——) compared to the experimental data (——) at speeds from 30-ms^{-1} to 70-ms^{-1}: (a) multi-shape roughness, measured downstream the cylinder (b) multi-height roughness, measured downstream the hemisphere (c) multi-shape roughness, measured 2-mm downstream cylinder

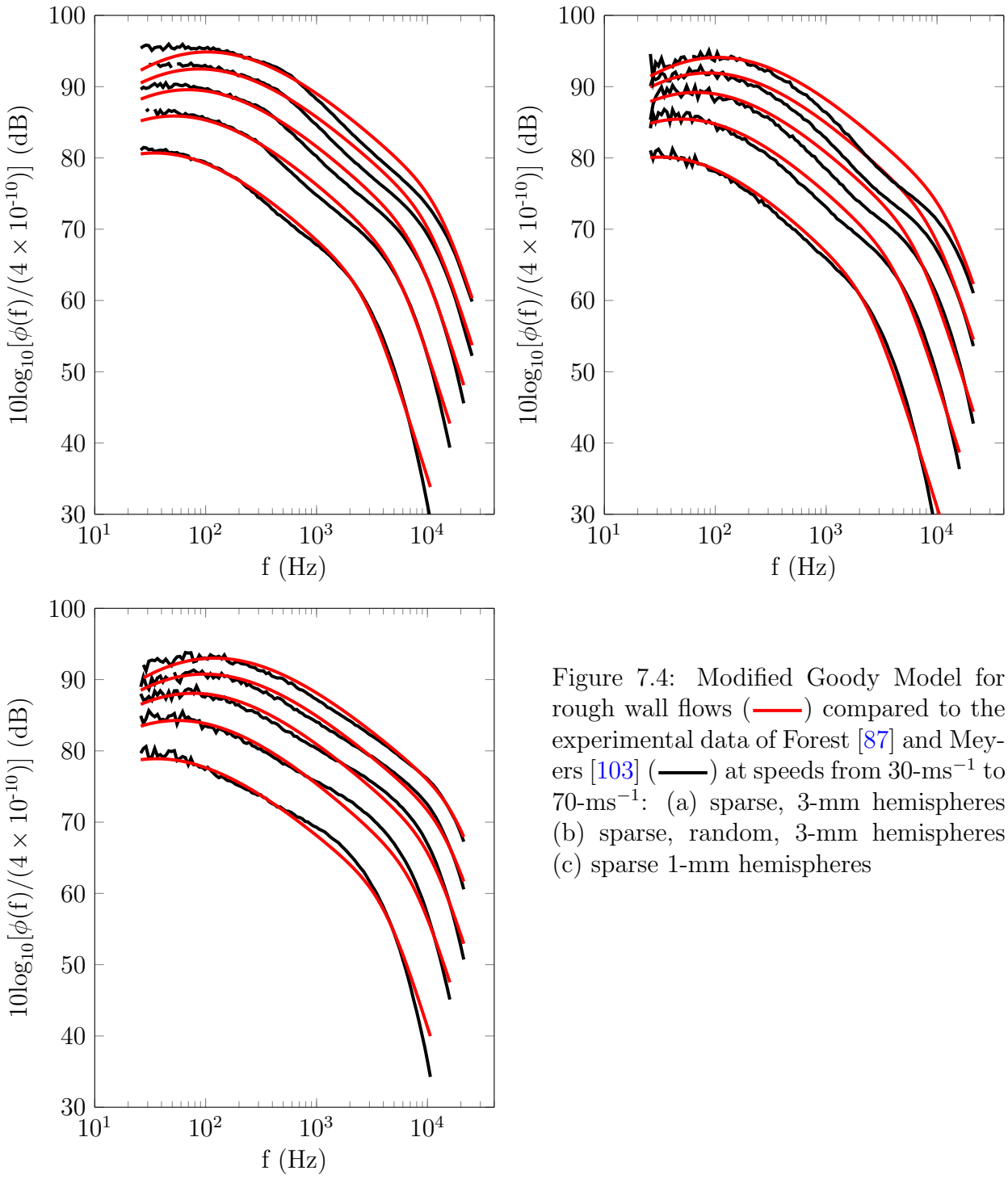

Figure 7.4: Modified Goody Model for rough wall flows (——) compared to the experimental data of Forest [87] and Meyers [103] (——) at speeds from 30-ms^{-1} to 70-ms^{-1}: (a) sparse, 3-mm hemispheres (b) sparse, random, 3-mm hemispheres (c) sparse 1-mm hemispheres

variables in eq. (7.2). While each variable is defined with the physics of the flow in mind, these are also heavily dependent on data correlations. The index of eq. (7.4) for example, has no physical basis other than the observation that the low frequency curvature was dependent on both free stream speed and roughness element density. This is a valid observation, and one we made when looking at the raw pressure spectra in chapter 3, but the equation itself is not the most intuitive formulation. So while it is true that the model is able to predict, to within 1-dB, the low frequency spectrum of 55 cases and the high frequency spectrum of 45 cases, the complexity of some of the proposed terms casts some doubt on its overall versatility.

7.2 Piece-wise Model

A simpler approach than modifying the Goody model to account for rough walls is developing a piece-wise function based solely on a curve fit through the successful high frequency and low frequency collapsed data. This fitting must be done carefully in order to retain the theoretically proven low frequency form of ω^2 and high frequency form of ω^{-5}.

The form of the equation usually used is

$$y = \frac{ax^p}{b + cx^q} \tag{7.10}$$

This form relates two portions of a curve based on values of x. At low x the function y will go as x^p and at high x it will go as x^{p-q}. For the present analysis, y is the scaled pressure spectrum and x is the scaled frequency.

Considering the low frequency and mid-frequency regions, we must set $p \equiv 2$. We choose to use -0.8 (smooth wall result) for the mid-frequency slope. Therefore, q =2.8. Substituting the low frequency scaling for frequency, our low frequency fit is

$$\phi(\omega)\frac{\overline{U}}{(U_e - \overline{U})^4 \rho^2 \delta} = \frac{0.05(\omega\delta/\overline{U})^2}{8 + 3(\omega\delta/\overline{U})^{2.8}} \tag{7.11}$$

Similarly, for the high and mid-frequency regions we define $p \equiv m_{mid}$ where m is the observed mid-frequency slope, as described in § 6.3.2. It therefore follows that $q = 5 - m_{mid}$ in order to ensure that at high frequencies the slope is -5. So our high frequency fit is

$$\phi(\omega)\frac{U_\nu^2}{\tau_\nu^2 \nu} = \frac{0.6(\omega\nu/U_\nu^2)^{m_{mid}}}{0.15 + (\omega\nu/U_\nu^2)^{5-m_{mid}}} \tag{7.12}$$

In using m_{mid} in eq. (7.12) we can match the mid-frequency slope of any data set without affecting the high frequency fit.

The coefficients of eqs. (7.11) and (7.12) were determined by iteratively adjusting the input values until the fit passed through the centre of the scaled data band. Equations (7.11) and (7.12) are plotted over the scaled data in fig. 7.5. The plot on the left shows the fit of eq. (7.11) in green with the data (grey) scaled on $\overline{U}$ data. The plot on the right shows the fit of eq. (7.12) in red with the data (grey) scaled using the high frequency scaling. In fig. 7.5b m_{mid} = -1.4 to match the sparse hemispheres.

The low-frequency scaling is not reliable past $\omega\delta/\overline{U} \geq 10$. Similarly the high-frequency scaling is not effective below $\omega\nu/U_\nu^2 \leq 0.5$. Between these frequencies, a mid-frequency fit is required. However, we do not have a mid-frequency scaling from which to extract a useful fit. What do know is that information relating to roughness geometry which is important in the mid-frequency is implicit in the high and low frequency scalings. Therefore, we can simply connect the high and the low frequency fits to produce an estimate of the mid-frequency region.

We attempt to do this first by using a simple linear connection between the high and low frequency portions of the spectrum. The resulting plots are shown in figs. 7.6 to 7.8 for the present data (including the smooth wall), and in fig. 7.9 for the data of Forest [87] and Meyers [103]. In these plots the data is the black line, the low frequency prediction from eq. (7.11) is shown as a red line, the high frequency prediction of eq. (7.12) is the green line and the mid-frequency linear connection is the magenta line.

Both the low and the high frequency fits show deviations from surface to surface. The 3.5-dB spread of the low frequency collapse means that some data are over-predicted and others are under-predicted. The low frequency fit best predicts the smooth wall data, the intermediate roughness, the multi-height surface and the sparse random hemispheres. Because of the tighter collapse on the high frequency scaling, the predicted high frequency spectra show less deviations than the low frequency. The sparse 3-mm and sparse 1-mm hemispheres are the only cases which show deviations above 1-dB.

Also there is a clear fall off in the success of the fit as edge velocity is increased. This is true for the low frequency where we see an effect on the low frequency curvature, and it is also true in the high frequency where we see less alignment with the data at higher speeds. These observations are true for all the data presented and speaks toward the dependence on edge velocity. This is the same dependence on speed that the modified Goody Model in § 7.1 attempted to capture.

The mid-frequency linear connection is poor for all surfaces except the smooth wall where the deviation is 1.5-dB at its maximum. The linear mid-frequency connection on the other surfaces do not produce the correct slope and consequently the magnitude is as much as 4-dB off. Furthermore, the transition from one region to another is quite abrupt. It appears that the frequency limits on the high and low frequency regions dictate the success of the linear connection and, if it were possible to have these limits vary from surface to surface then this method would be more successful. This leads to the conclusion that a simple linear connection of the high and low frequency predicted curves is inadequate for rough walls.

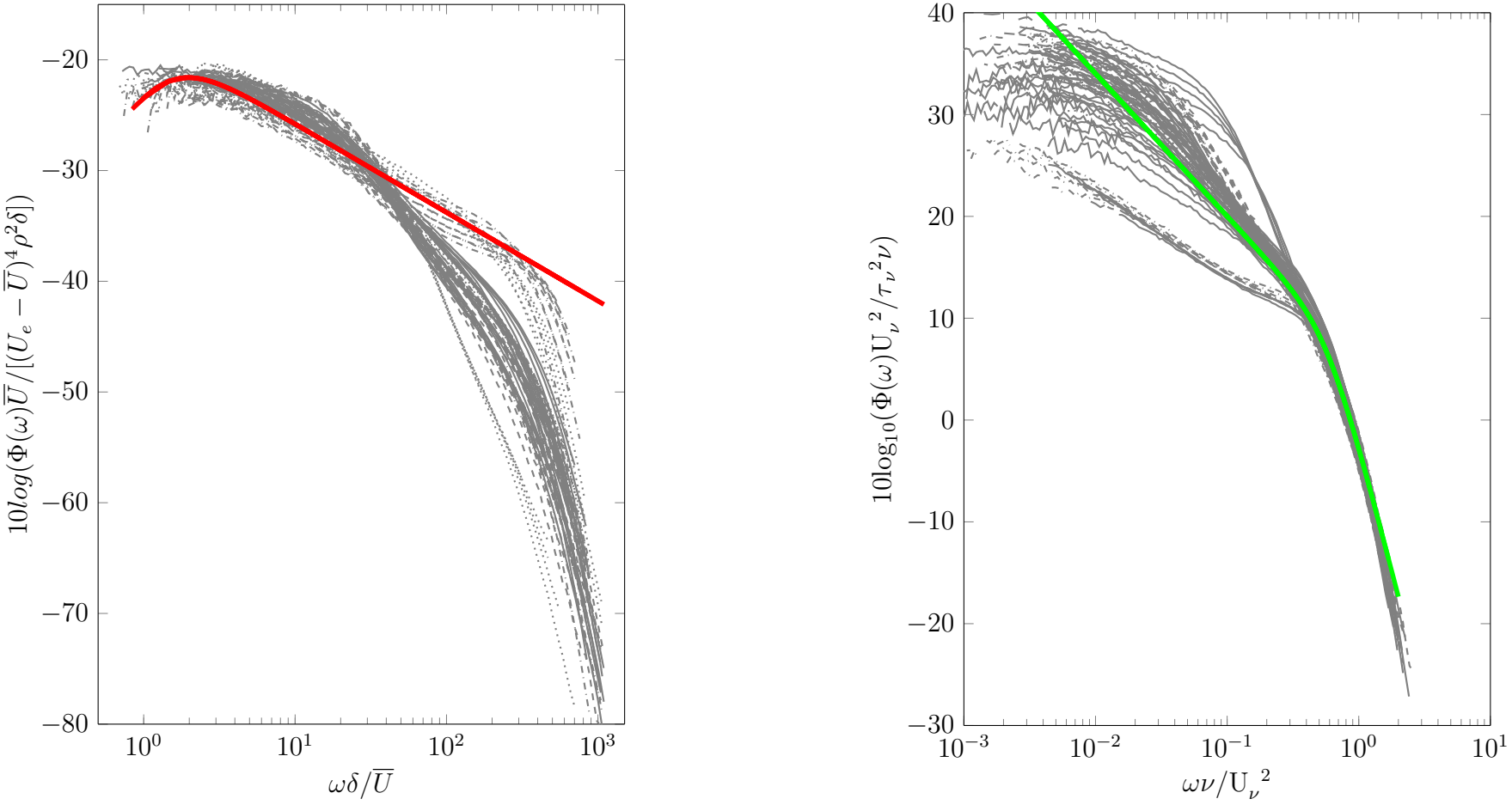

Figure 7.5: Fit through the (a) scaled low frequency data as defined by eq. (7.11) and the (b) scaled high frequency data as defined by eq. (7.12)

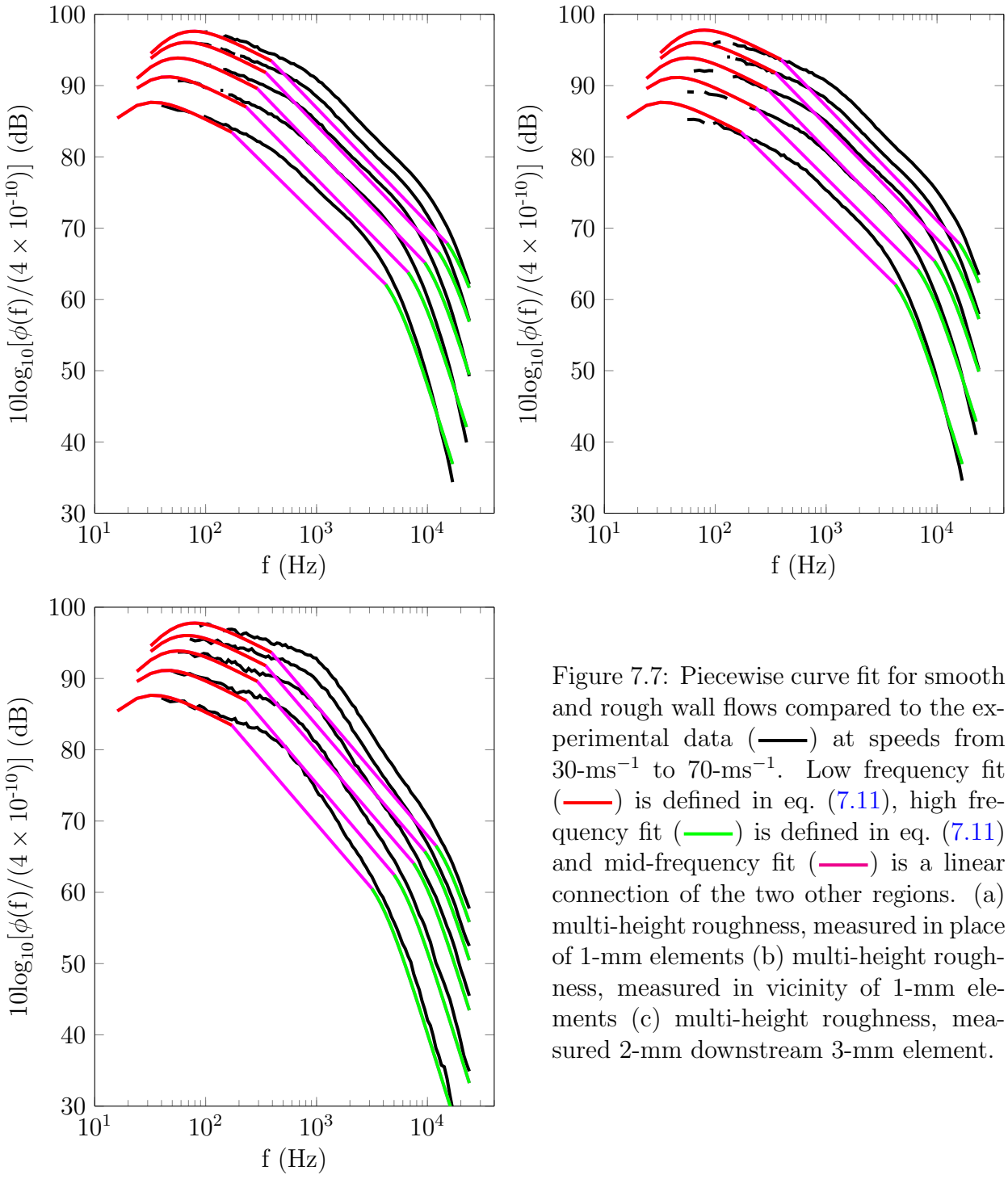

Figure 7.7: Piecewise curve fit for smooth and rough wall flows compared to the experimental data (——) at speeds from 30-ms^{-1} to 70-ms^{-1}. Low frequency fit (——) is defined in eq. (7.11), high frequency fit (——) is defined in eq. (7.11) and mid-frequency fit (——) is a linear connection of the two other regions. (a) multi-height roughness, measured in place of 1-mm elements (b) multi-height roughness, measured in vicinity of 1-mm elements (c) multi-height roughness, measured 2-mm downstream 3-mm element.

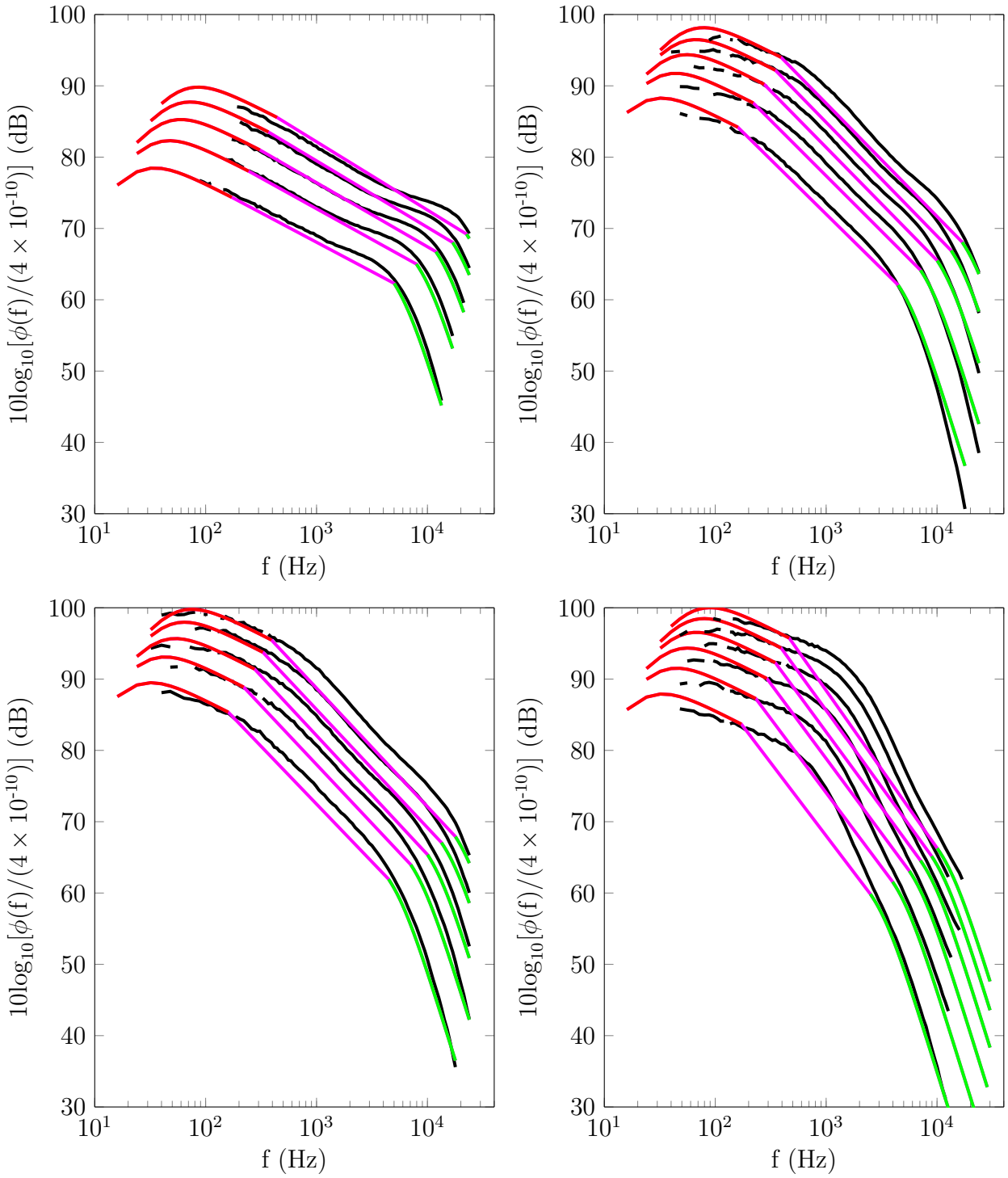

Figure 7.6: Piecewise curve fit for smooth and rough wall flows compared to the experimental data (——) at speeds from 30-ms^{-1} to 70-ms^{-1}. Low frequency fit (——) is defined in eq. (7.11), high frequency fit (——) is defined in eq. (7.11) and mid-frequency fit (——) is a linear connection of the two other regions. (a) smooth wall (b) surface of cylinders (c) intermediately-spaced roughness (d) densely-spaced roughness.

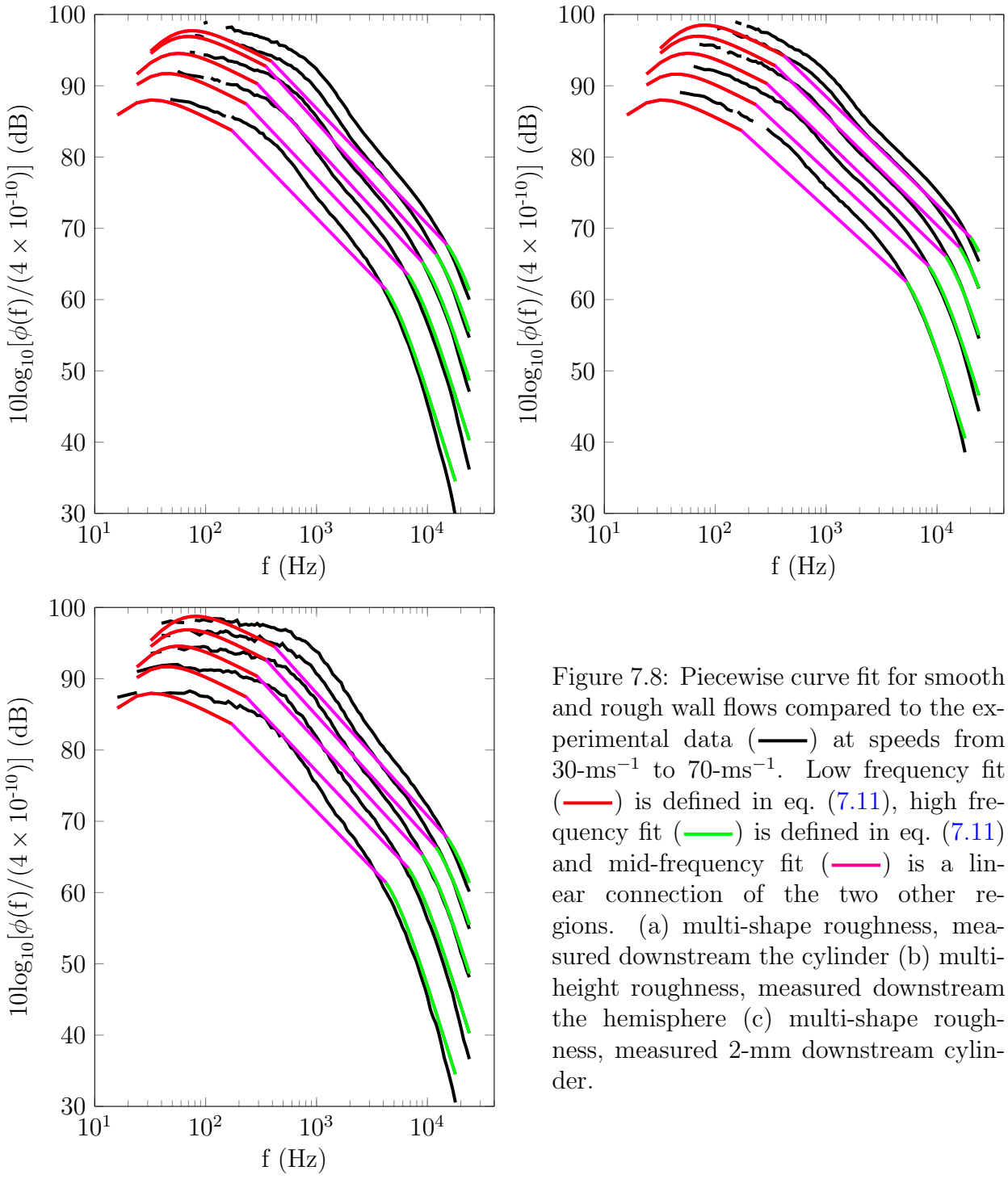

Figure 7.8: Piecewise curve fit for smooth and rough wall flows compared to the experimental data (——) at speeds from 30-ms^{-1} to 70-ms^{-1}. Low frequency fit (——) is defined in eq. (7.11), high frequency fit (——) is defined in eq. (7.11) and mid-frequency fit (——) is a linear connection of the two other regions. (a) multi-shape roughness, measured downstream the cylinder (b) multi-height roughness, measured downstream the hemisphere (c) multi-shape roughness, measured 2-mm downstream cylinder.

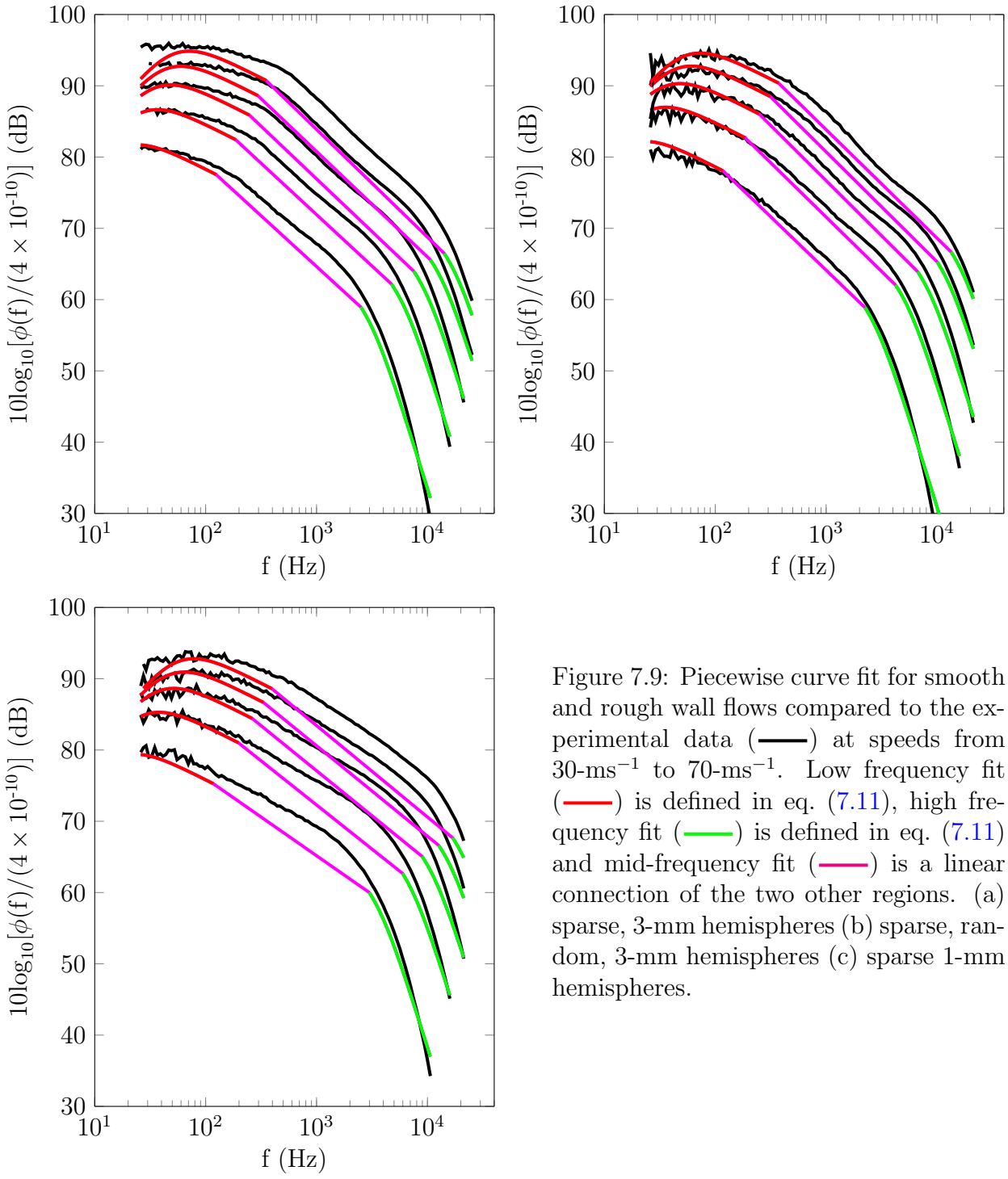

Figure 7.9: Piecewise curve fit for smooth and rough wall flows compared to the experimental data (——) at speeds from 30-ms^{-1} to 70-ms^{-1}. Low frequency fit (——) is defined in eq. (7.11), high frequency fit (——) is defined in eq. (7.11) and mid-frequency fit (——) is a linear connection of the two other regions. (a) sparse, 3-mm hemispheres (b) sparse, random, 3-mm hemispheres (c) sparse 1-mm hemispheres.

Instead of a linear connection, we can use a spline interpolation scheme between the high and low frequency spectra in order to connect the high and low frequency piecewise functions. The interpolated mid-frequency values are based on a cubic interpolation of the values at neighbouring grid points in each respective dimension. The result of this analysis is presented in figs. 7.10 to 7.12 for the present data and in fig. 7.13 for the data of Forest [87] and Meyers [103]. In these curves we use the same colour scheme as in figs. 7.6 to 7.9. The high and low frequency piecewise functions are unchanged so their success is also the same as in figs. 7.6 to 7.9.

This approximation of the mid-frequency region is more successful than with the simple linear connection. The cylinders, intermediate roughness, multi-height surface (in place of and in vicinity of 1-mm elements), the multi-shape surface (behind cylinder and behind hemisphere), and the sparse random 3-mm hemispheres show deviations of less than 1-dB in the mid-frequency. The slope and curvature is also adequately predicted by the spline interpolation.

The smooth wall is not well approximated by the spline interpolation as is the case for the spectra with steep mid-frequency slopes – the dense roughness, the multi-height surface 2-mm downstream the 3-mm hemisphere, and the multi-shape surface 2-mm downstream the cylinder. It must be noted that in the case of the multi-shape surface, the sparse 3-mm hemispheres and the sparse 1-mm hemispheres, the mid-frequency issues observed are due to issues with the low frequency piecewise function. This function under-predicts the low frequency spectra of the multi-scale surface and produces erroneous low frequency curvature for the sparse 3-mm and sparse 1-mm hemispheres. These problems are the source of the issues seen in the spline interpolation in the mid-frequency in these cases.

Despite its limitations, the high and low-frequency piecewise function of eqs. (7.11) and (7.12) are simple and able to produce an estimate of the spectrum to within 3-dB for most surfaces. This is a useful starting point for predicting the pressure spectrum over both smooth and rough walls, and, can be expected to be more rigorous than the modified Goody Model presented in § 7.1. Furthermore, the mid-frequency region can be estimated in most cases using a spline interpolation of the low frequency and high frequency piecewise functions. In this way we can obtain a complete, albeit rough, prediction of the smooth and rough wall turbulent boundary layer pressure spectra.

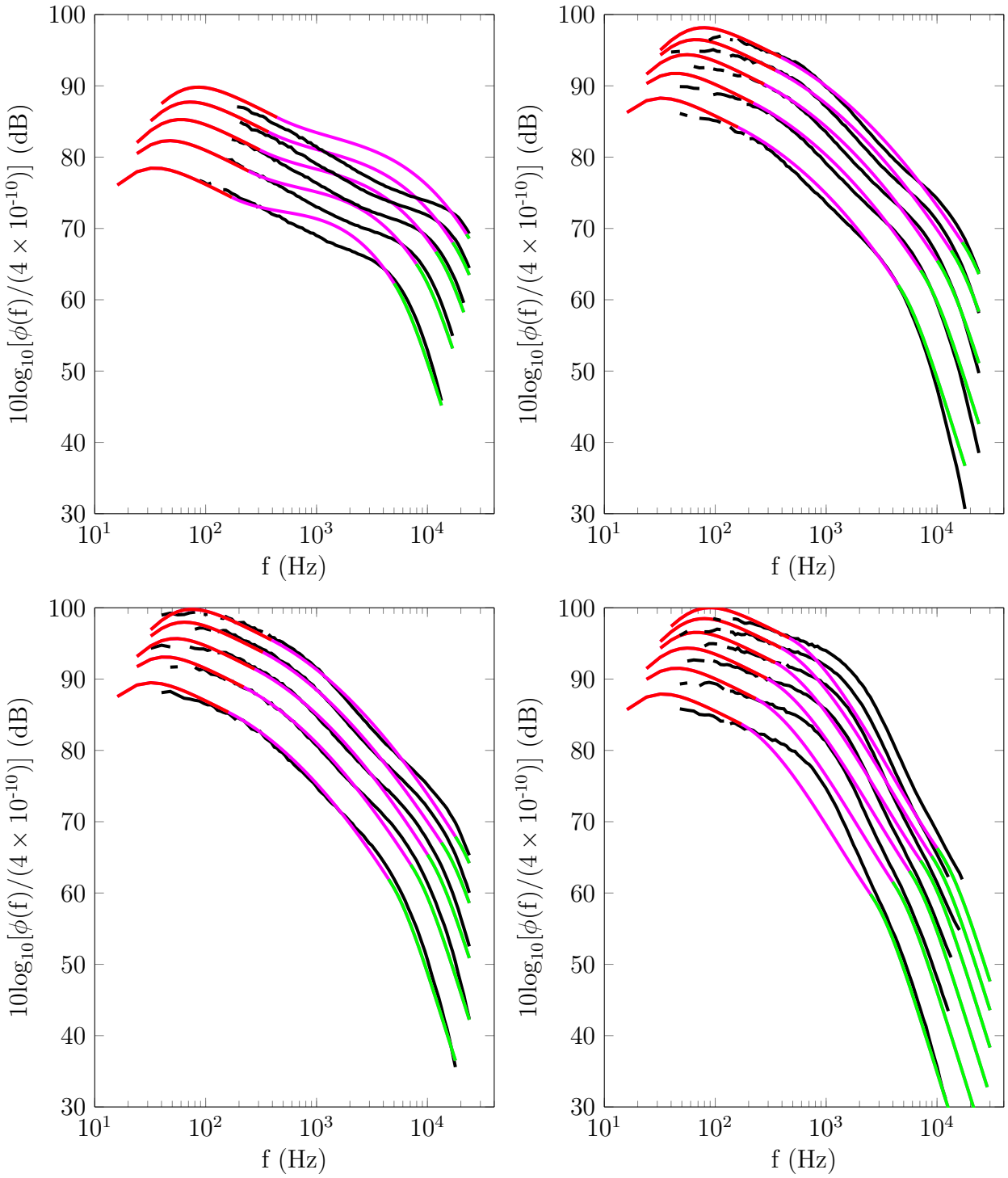

Figure 7.10: Piecewise curve fit for smooth and rough wall flows compared to the experimental data (——) at speeds from 30-ms^{-1} to 70-ms^{-1}. Low frequency fit (——) is defined in eq. (7.11), high frequency fit (——) is defined in eq. (7.11) and mid-frequency fit (——) is a spline interpolation between the two other regions. (a) smooth wall (b) surface of cylinders (c) intermediately-spaced roughness (d) densely-spaced roughness.

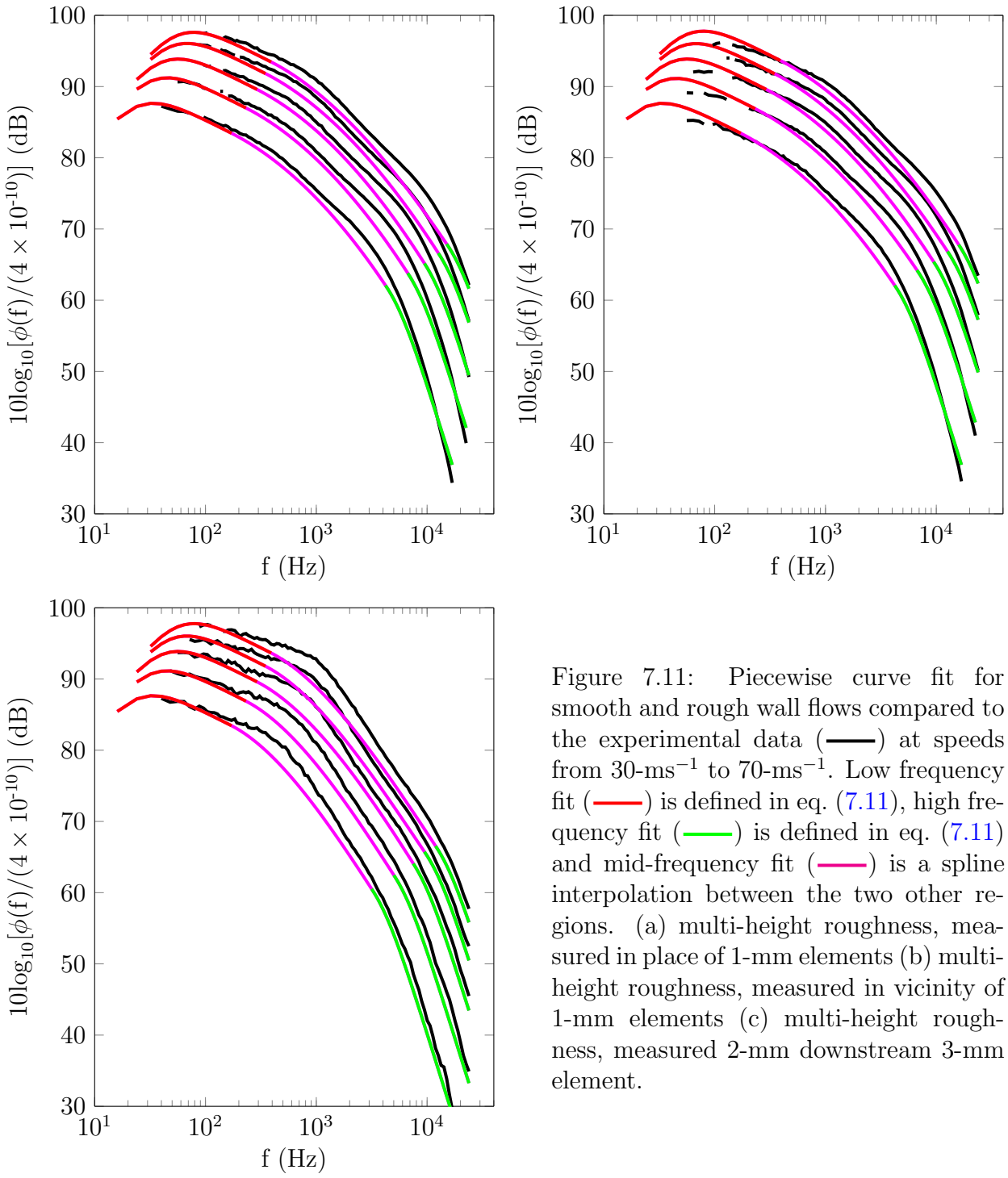

Figure 7.11: Piecewise curve fit for smooth and rough wall flows compared to the experimental data (——) at speeds from 30-ms^{-1} to 70-ms^{-1}. Low frequency fit (——) is defined in eq. (7.11), high frequency fit (——) is defined in eq. (7.11) and mid-frequency fit (——) is a spline interpolation between the two other regions. (a) multi-height roughness, measured in place of 1-mm elements (b) multi-height roughness, measured in vicinity of 1-mm elements (c) multi-height roughness, measured 2-mm downstream 3-mm element.

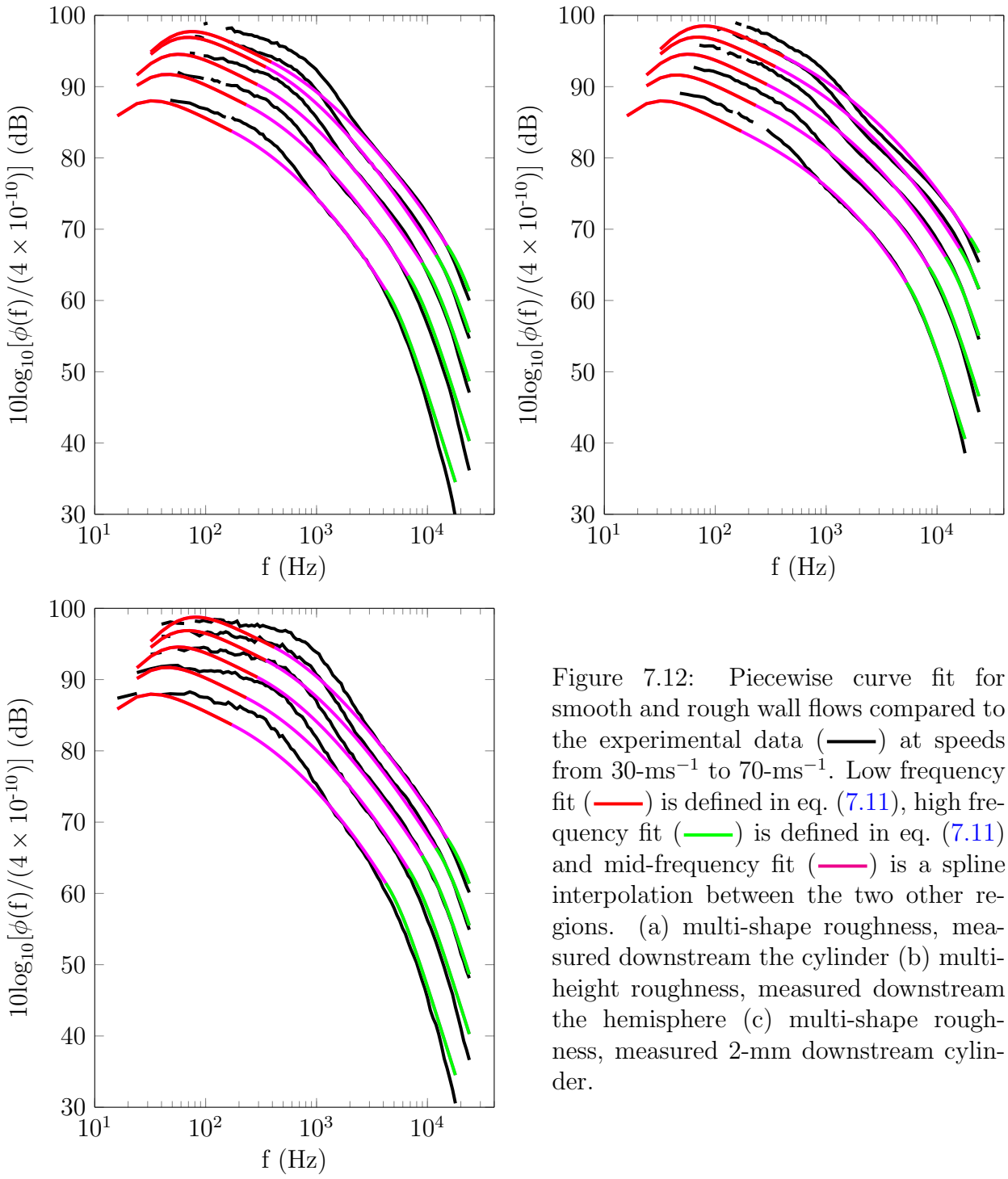

Figure 7.12: Piecewise curve fit for smooth and rough wall flows compared to the experimental data (——) at speeds from 30-ms^{-1} to 70-ms^{-1}. Low frequency fit (——) is defined in eq. (7.11), high frequency fit (——) is defined in eq. (7.11) and mid-frequency fit (——) is a spline interpolation between the two other regions. (a) multi-shape roughness, measured downstream the cylinder (b) multi-height roughness, measured downstream the hemisphere (c) multi-shape roughness, measured 2-mm downstream cylinder.

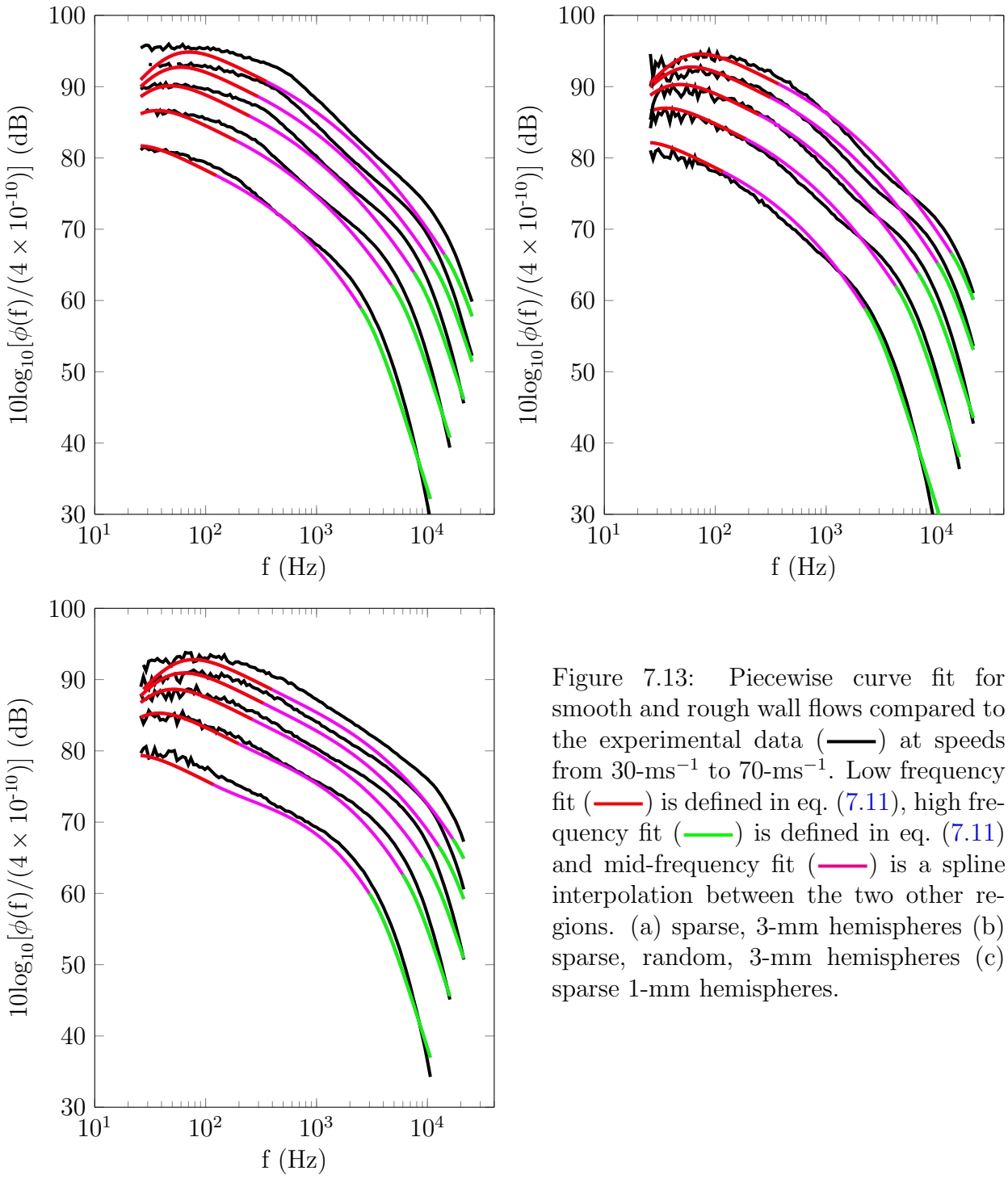

Figure 7.13: Piecewise curve fit for smooth and rough wall flows compared to the experimental data (——) at speeds from 30-ms^{-1} to 70-ms^{-1}. Low frequency fit (——) is defined in eq. (7.11), high frequency fit (——) is defined in eq. (7.11) and mid-frequency fit (——) is a spline interpolation between the two other regions. (a) sparse, 3-mm hemispheres (b) sparse, random, 3-mm hemispheres (c) sparse 1-mm hemispheres.

8. Conclusions

8.1 Summary of Experiments

Experiments have been carried out in the Virginia Tech Stability Wind Tunnel to measure the turbulence and pressure fluctuations in a high Reynolds Number turbulent boundary layer over zero-pressure gradient rough walls. These tests were run at Re_θ upwards of 40,000 and well over 100,000 at the highest speeds. This corresponds to k_g^+ well over 200 and δ/k_g ratios above 73.

A total of five surfaces were fabricated and tested. These include a surface of cylinders, a surface of intermediately-spaced 3-mm hemispheres, a surface of densely-spaced 3-mm hemispheres, a surface of mixed 1-mm and 3-mm hemispheres, and a surface of mixed 3-mm cylinders and 3-mm hemispheres. Together with the 3-mm hemispheres of Forest [87] and the 1-mm and random 3-mm hemispheres of Meyers [103], we obtain a set of surfaces which offer variations in roughness height, shape, and density. We are also able to determine the effect of superposing roughness of different heights and shapes.

Velocity and turbulence measurements were obtained using quadwires, a single hotwire and a flattened Pitot. These data were used to validate the quadwire data and provide insights into the effect of roughness on the mean velocity and Reynolds stress profiles. The boundary layer parameters for each rough wall configuration were also derived from this data. Pinhole microphones were used to measure the pressure fluctuations at the wall and at incremental distances above the wall. The pressure spectrum was calculated from the microphone pressure data and calibrated (for pinhole effect), binned, background subtracted, and averaged.

Following the triple scaling hypothesis of Meyers *et al.* [1], attempts were made to scale the pressure spectrum in the low frequency, mid-frequency and high-frequency regions. A method for predicting the pressure spectrum of the turbulent boundary layer over a rough wall was also proposed.

8.2 Conclusions

The present study has revealed that changing the roughness element shape from a hemisphere to a cylinder appears to have only a small effect on the pressure spectrum. This is seen as a small slope change ($\sim$-0.1) in the mid-frequency region. On the other hand, the roughness element density influences the entire pressure spectrum at all frequencies. At the low frequencies this parameter changes the magnitude of the spectrum. In the mid-frequency

element density strongly impacts the slope of the spectrum which means that it affects the energy transfer mechanism between different scales. This in turn affects the magnitude of the high frequency region. Similarly, the location at which measurements are made appears to be significant for the pressure spectrum. As with element density, this parameter strongly affects the mid-frequency slope and thus indirectly affects the high-frequency portion of the spectrum.

Superposing roughness elements of different geometry unto a single surface uncovered some interesting insights. On a surface with elements of different heights, the pressure spectrum appears to be influenced most by the larger element. The effect of increased element density is diminished over such a surface because the flow only 'sees' the larger elements. These observations are true at least for elements of k_g 3-mm and 1-mm. Superposing roughness elements of different shapes on the same surface results in a pressure spectrum which is markedly different from that of its individual, component geometries. The slope of the mid-frequency region was not constant but appeared to be a combination of two constant slope regions. One of these regions was invariant with traducer location while the other was very sensitive to where measurements were taken on the surface.

We have also confirmed that the high-frequency portion of the pressure spectrum is governed by the shear friction velocity as defined by Meyers *et al.* [1]. They defined this parameter as an area-averaged measure of the viscous drag. The present work has uncovered that the shear friction velocity is actually a local value which varies based on position on the wall relative to the roughness elements. Applying the high frequency scaling proposed by Meyers *et al.* with the local values of shear friction velocity to the pressure spectrum of rough surfaces of varying element height, shape and density results in a collapse 3.5-dB wide. This scaling is also able to collapse data from different element-relative locations, on the multi-scale surfaces as well as the smooth wall data. The collapse is most effective when local values of shear friction velocity are used. However, the area-averaged shear friction velocity defined by Meyers *et al.* is also able to collapse the data to within a 4-dB band. The implications of the local and global shear friction velocity on the element pressure drag was explored. It was found that the element pressure drag coefficient can be expressed as a function of two variables – the roughness element height and the sparseness ratio. An empirical formula was proposed which defines this relationship.

Two new scalings have been proposed for the low frequency region. Both scalings are based on the idea that a velocity defect between the local velocity and the edge velocity controls the pressure scales in the outer regions of the flow. The first scaling uses the broadband convection velocity as the local velocity and is $\phi(\omega)\overline{U}_{c_b}/\rho^2(U_e - \overline{U}_{c_b})^4\delta$ versus $\omega\delta/\overline{U}_{c_b}$. This scaling collapsed all data below $\omega\delta/\overline{U}_{c_b}$=40 into a narrow band about 2.5-dB wide. The second scaling uses the mean velocity in the boundary layer as the local velocity for the defect. This scaling is $\omega\delta/\overline{U}$ versus $\phi(\omega)\overline{U}/\rho^2(U_e\delta^*/\delta)^4\delta$. This scaling was able to collapse the data below $\omega\delta/\overline{U}$=20 into a narrow band about 3.5-dB wide. While both these scalings appear promising, the scaling on $\overline{U}$ is better suited for practical purposes because $\overline{U}_{c_b}$ cannot be obtained *a priori* and there are substantial uncertainties associated with this parameter when

obtained from space-time correlations. The success of the new low frequency scalings, along with the observations from the averaged pressure spectra and the velocity and turbulence profiles, indicates that the wall similarity hypothesis may not be valid for rough walls.

The mid-frequency region has proven to be quite complex. At this time, there is no normalisation which adequately scales this region. The main reason for this is the dramatic changes in slope we observe as a result of variations in transducer location and element spacing. The slopes observed in the spectrum did not vary with any single geometric parameter. Instead they showed a power law relationship with a parameter that combined the streamwise microphone location, the modified displacement height and the roughness height.

It has also been shown that the slope of the mid-frequency region should only vary as -1 when the pressure scales for the high- and low- frequency regions are the same. Based on our proposed high and low frequency scalings, we cannot expect to see a -1 slope in the data. The hypothesis of the mid-frequency region being an 'overlap' region was also explored because it was found that the low frequency scaling and the high frequency scaling both collapse the mid-frequency region. Mid-frequency slopes were predicted assuming that the overlap hypothesis was valid. These predicted slopes were not the same as those observed in the data, suggesting that the overlap hypothesis is not valid. However, there does exist a linear relationship between the observed slope and the predicted slope. This correlation suggests that the current analysis needs to be expanded for the mid-frequency region.

A piecewise model for predicting the pressure spectrum over rough walls has been proposed. This model uses the new low frequency scaling on mean velocity and the high frequency scaling on shear friction velocity to approximate the spectrum in these regions. In lieu of an actual mid-frequency scaling, the mid-frequency is predicted using a spline interpolation between the low and high frequency regions. This model is able to predict the pressure spectrum to within 4-dB. A modified version of the Goody empirical model for smooth walls was also presented. While this model showed promise, it is quite complex which casts doubt on its versatility.

Bibliography

[1] T. Meyers, J. B. Forest, and W. J. Devenport. The wall-pressure spectrum of high-reynolds-number turbulent boundary-layer flows over rough surfaces. *Journal of Fluid Mechanics*, 768:261–293, 2015.

[2] L. S. G. Kovasznay. Structure of the turbulent boundary layer. *Physics of Fluids*, 10(9):S25–S30, 1967.

[3] J. A. Schetz. *Boundary layer analysis*. American Institute of Aeronautics and Aeronautics, Reston, Va, 2010.

[4] S. B. Pope. *Turbulent flows*. Cambridge University Press, Cambridge;New York;, 2000.

[5] P. J. Mulhearn. Boundary layer wall-pressure fluctuations near an abrupt change in surface roughness. In *5th Australasian Conference on Hydraulics in Fluid Mechanics*, pages 568–574, Christchurch, NZ.

[6] T.A. Brungart, G.C. Lauchle, S. Deutsch, and E.T. Riggs. Outer-flow effects on turbulent boundary layer wall pressure fluctuations. *Journal of the Acoustical Society of America*, 106(4):2097–2106, 1999.

[7] P. S. Klebanoff. *Characteristics of turbulence in a boundary layer with zero pressure gradient*. National Advisory Committee for Aeronautics, 1954.

[8] M. R. Raupach, R. A. Antonia, and S. Rajagopalan. Rough-wall turbulent boundary layers. *Applied Mechanics Reviews*, 44(1):1–25, 1991.

[9] S. K. Robinson. A perspective on coherent structures and conceptual models for turbulent boundary layer physics. Technical report, 1990.

[10] B. J. McKeon, J. Li, W. Jiang, J. F. Morrison, and A. J. Smits. Further observations on the mean velocity distribution in fully developed pipe flow. *Journal of Fluid Mechanics*, 501:135–147, 2004.

[11] M. Awasthi. High reynolds number turbulent boundary layer flow over small forward facing steps. Thesis, Virginia Polytechnic Institute and State University, 2012.

[12] D. Coles. The law of the wake in the turbulent boundary layer. *Journal of Fluid Mechanics*, 1(2):191–226, 1956.

[13] C. C. Chu and R. E. Falco. Vortex ring/viscous wall layer interaction model of the turbulence production process near walls. *Experiments in Fluids*, 6(5):305–315, 1988.

[14] R. Falco. The production of turbulence near a wall. In *13th Fluid and PlasmaDynamics Conference*, Fluid Dynamics and Co-located Conferences. American Institute of Aeronautics and Astronautics, 1980.

[15] A. J. Grass. Structural features of turbulent flow over smooth and rough boundaries. *Journal of Fluid Mechanics*, 50(2):233–255, 1971.

[16] S. J. Kline, W. C. Reynolds, F. A. Schraub, and P. W. Runstadler. The structure of turbulent boundary layers. *Journal of Fluid Mechanics*, 30(4):741–773, 1967.

[17] S. K. Robinson. *The kinematics of turbulent boundary layer structure*. Phd thesis, Stanford University, 1991.

[18] C. Liu. *An Experimental Study of Turbulent Boundary Layer on Rough Walls*. PhD thesis, Stanford University, 1966.

[19] B. Lagraa, L. Labraga, and A. Mazouz. Characterization of low-speed streaks in the near-wall region of a turbulent boundary layer. *European Journal of Mechanics - B/Fluids*, 23(4):587–599, 2004.

[20] M. J. Lee, J. Kim, and P. Moin. Structure of turbulence at high shear rate. *Journal of Fluid Mechanics*, 216(1):561–583, 1990.

[21] C. D. Tomkins. *The structure of turbulence over smooth and rough walls*. PhD thesis, Virginia Polytechnic and State University, 2001.

[22] D. K. Oldaker and W. G. Tiederman. Spatial structure of the viscous sublayer in drag-reducing channel flows. *Physics of Fluids*, 20(10):S133–S144, 1977.

[23] P. M. Ligrani and R. J. Moffat. Structure of transitionally rough and fully rough turbulent boundary layers. *Journal of Fluid Mechanics*, 162(1):69–98, 1986.

[24] A. Hopkins. *Fluid Dynamics and Surface Pressure Fluctuations of Two-Dimensional Turbulent Boundary Layers Over Densely Distributed Surface Roughness*. PhD thesis, Virginia Polytechnic Institute and State University, 2010.

[25] M. T. Rusche and R. L. Simpson. Structure of turbulent boundary layers and surface pressure fluctuations on a patch of roughness elements. 50th AIAA Aerospace Sciences Meeting Including the New Horizons Forum and Aerospace Exposition, Nashville, TN, United states, 2012. American Institute of Aeronautics and Astronautics Inc.

[26] J. M. Witting. A spectral model of pressure fluctuations at a rigid wall bounding an incompressible fluids based on turbulent structures in the boundary layer. *Noise Control Engineering Journal*, 26(1):28–43, 1986.

[27] T. Theodorsen. Mechanism of turbulence. In *Proceedings of the Second Midwestern Conference on Fluid Mechanics*, pages 1–18. Ohio State University.

[28] M. R. Head and P. Bandyopadhyay. New aspects of turbulent boundary-layer structure. *Journal of Fluid Mechanics*, 107(1):297–338, 1981.

[29] P. R. Bandyopadhyay and R. D. Watson. Structure of rough-wall turbulent boundary layers. *Physics of Fluids*, 31(7):1877–1883, 1988.

[30] B. K. Ahn, J. M. R. Graham, and S. A. Rizzi. Modelling unsteady wall pressures beneath turbulent boundary layers. *10th AIAA/CEAS Aeroacoustics Conference*, 2004.

[31] R. J. Adrian, C. D. Meinhart, and C. D. Tomkins. Vortex organization in the outer region of the turbulent boundary layer. *Journal of Fluid Mechanics*, 422:1–54, 2000.

[32] T. J. Black. *An analytical study of the measured wall pressure field under supersonic turbulent boundary layers*. National Aeronautics and Space Administration, 1968.

[33] M. P. Schultz and K. A. Flack. The rough-wall turbulent boundary layer from the hydraulically smooth to the fully rough regime. *Journal of Fluid Mechanics*, 580:381–405, 2007.

[34] D. Bettermann and Paris Faculté des sciences de. *Contribution à l'étude de la couche limite turbulente le long de plaques rugueuses*. 1965.

[35] F. A. Dvorak. Calculation of turbulent boundary layers on rough surfaces in pressure gradient. *AIAA Journal*, 7(9):1752–1759, 1969.

[36] N. D. Varano. *Fluid Dynamics and Surface Pressure Fluctuations of Turbulent Boundary Layers Over Sparse Roughness*. PhD thesis, Virginia Polytechnic Institute and State University, 2010.

[37] J. Nikuradse. Laws of flow in rough pipes. Technical report, 1950.

[38] J. George. *Structure of 2-D and 3-D Turbulent Boundary Layers with Sparsely Distributed Roughness Elements*. PhD thesis, Virginia Polytechnic Institute and State University, 2005.

[39] R. A. Antonia and P. Å Krogstad. Turbulence structure in boundary layers over different types of surface roughness. *Fluid Dynamics Research*, 28(2):139–157, 2001.

[40] J. Klewicki, P. Fife, and T. Wei. On the logarithmic mean profile. *Journal of Fluid Mechanics*, 638:73–93, 2009.

[41] W. Blake. Turbulent boundary-layer wall-pressure fluctuations on smooth and rough walls. *Journal of Fluid Mechanics*, 44(4):637–660, 1970.

[42] J. Jimenez. Turbulent flows over rough walls. *Annual Review of Fluid Mechanics*, 36(1):173–196, 2004.

[43] P. R. Bandyopadhyay. Rough-wall turbulent boundary layers in the transition regime. *Journal of Fluid Mechanics*, 180(1):231–266, 1987.

[44] D. H. Wood and R. A. Antonia. Measurements in a turbulent boundary layer over a d-type surface roughness. *Journal of Applied Mechanics*, 42(3):591, 1975.

[45] K. A. Flack, M. P. Schultz, and T. A. Shapiro. Experimental support for townsend's reynolds number similarity hypothesis on rough walls. *Physics of Fluids (1994-present)*, 17(3):035102, 2005.

[46] R. L. Simpson. A generalized correlation of roughness density effects on the turbulent boundary layer. *AIAA Journal*, 11(2):242–244, 1973.

[47] K. Bhaganagara, G. Coleman, and J. Kim. Effect of roughness on pressure fluctuations in a turbulent channel flow. *Physics of Fluids*, 19(2), 2007.

[48] P. A. Krogstad, R. A. Antonia, and L. W. B. Browne. Comparison between rough-wall and smooth-wall turbulent boundary-layers. *Journal of Fluid Mechanics*, 245:599–617, 1992.

[49] H. Nakagawa and I. Nezu. Prediction of the contributions to the reynolds stress from bursting events in open-channel flows. *Journal of Fluid Mechanics*, 80(1):99–128, 1977.

[50] Q. Yang and M. Wang. Boundary-layer noise induced by arrays of roughness elements. *Journal of Fluid Mechanics*, 727:282–317, 2013.

[51] J. L. Bennington. *Effects of Various Shaped Roughness Elements in Two-Dimensional High Reynolds Number Turbulent Boundary Layers*. PhD thesis, Virginia Polytechnic Institute and State University, 2004.

[52] Q. Yang and M. Wang. Statistical analysis of acoustic-source field in rough-wall boundary layers. In *17th AIAA/CEAS Aeroacoustics Conference, Portland, Oregon*, June 5-8 2011.

[53] R. L. Simpson. Junction flows. *Annual Review of Fluid Mechanics*, 33(1):415–443, 2001.

[54] S. A. L. Glegg and W. Devenport. *Aeroacoustics of low Mach number flows: fundamentals, analysis, and measurement*. Academic Press, London, 2017.

[55] N. J. Molinaro. The two point correlation structure of a cylinder wake. Master's thesis, Virginia Polytechnic Institute and State University, 2017.

[56] B. S. Smith. *Wall Jet Boundary Layer Flows Over Smooth and Rough Surfaces*. PhD thesis, Virginia Polytechnic Institute and State University, 2008.

[57] K. S. Wittmer, W. J. Devenport, and J. S. Zsoldos. A four-sensor hot-wire probe system for three-component velocity measurement. *Experiments in fluids*, 24(5-6):416–423, 1998.

[58] H. Schlichting. *Boundary-layer theory*. McGraw-Hill, New York, 7th edition, 1979.

[59] F. A. Aupperle and R. F. Lambert. Effects of roughness on measured wall-pressure fluctuations beneath a turbulent boundary layer. *Journal of the Acoustical Society of America*, 47(1):359–370, 1970.

[60] I. Marusic, J. P. Monty, M. Hultmark, and A. J. Smits. On the logarithmic region in wall turbulence. *Journal of Fluid Mechanics*, 716:np–np, 2013.

[61] H. H. Fernholz and P. J. Finley. The incompressible zero-pressure-gradient turbulent boundary layer: An assessment of the data. *Progress in Aerospace Sciences*, 32(4):245–311, 1996.

[62] W. W Willmarth. Pressure fluctuations beneath turbulent boundary layers. *Annual Review of Fluid Mechanics*, 7:13–38, 1975.

[63] M. K. Bull. Wall-pressure fluctuations associated with subsonic turbulent boundary layer flow. *Journal of Fluid Mechanics*, 28(4):719–754, 1967.

[64] G. Schewe. On the structure and resolution of wall-pressure fluctuations associated with turbulent boundary-layer flow. *Journal of Fluid Mechanics*, 134(1):311–328, 1983.

[65] Y. Lee, W. K. Blake, and T. M. Farabee. Modeling of wall pressure fluctuations based on time mean flow field. *Journal of Fluids Engineering*, 127(2):233, 2005.

[66] W. W. Willmarth and C. E. Wooldridge. Measurements of the fluctuating pressure at the wall beneath a thick turbulent boundary layer. *Journal of Fluid Mechanics*, 14(2):187–210, 1962.

[67] W. Blake. Turbulent velocity and pressure fields in boundary-layer flows over rough surfaces. *Symposium on Turbulence in Liquids*, 1971.

[68] M. K. Bull. Wall pressure fluctuations beneath turbulent boundary layers: Some reflections on forty years of research. *Journal of Sound and Vibration*, 190(3):299–315, 1996.

[69] M. C. Goody and R. L. Simpson. An experimental investigation of pressure fluctuations in three-dimensional turbulent boundary layers. Technical report, DTIC Document, 1999.

[70] M. K. Bull and A. S. W. Thomas. High frequency wall-pressure fluctuations in turbulent boundary layers. *Physics of Fluids*, 19(4):597–599, 1976.

[71] G. M. Corcos. Resolution of pressure in turbulence. *Journal of the Acoustical Society of America*, 35(2):192–199, 1963.

[72] G. M. Corcos. The resolution of turbulent pressures at the wall of a boundary layer. *Journal of Sound and Vibration*, 6(1):59–70, 1967.

[73] S. P. Gravante, A. M. Naguib, C. E. Wark, and H. M. Nagib. Characterization of the pressure fluctuations under a fully developed turbulent boundary layer. *AIAA Journal*, 36(10):1808–1816, 1998.

[74] M. Goody. Empirical spectral model of surface pressure fluctuations. *AIAA Journal*, 42(9):1788–1794, 2004.

[75] R. L. Panton. Scaling turbulent wall layers. *Journal of Fluids Engineering*, 112(4):425, 1990.

[76] T. M. Farabee and M.J. Casarella. Spectral features of wall pressure fluctuations beneath turbulent boundary layers. *Physics of Fluids A*, 3(10):2410–2420, 1991.

[77] W. K. Blake. Mechanics of flow-induced sound and vibration, volume ii: Complex flow-structure interactions. *Applied Mathematics and Mecahnics*, 17-11, 1986.

[78] H. Choi and P. Moin. On the space-time characteristics of wall-pressure fluctuations. *Physics of Fluids*, 2(8):1450–1460, 1990.

[79] A. V. Smol'yakov. Calculation of the spectra of psuedosound wall-pressure fluctuations in turbulent boundary layers. *Acoustical Physics*, 46(3):342–347, 2000.

[80] R. Panton, A.L. Goldman, R.I. Lowery, and M.M. Reischman. Low-frequency pressure fluctuations in axisymmetric boundary layers. *Journal of Fluid Mechanics*, 97(2):299–319, 1980.

[81] J. C. Klewicki, P. J. A. Priyadarshana, and M. M. Metzger. Statistical structure of the fluctuating wall pressure and its in-plane gradients at high reynolds number. *Journal of Fluid Mechanics*, 609:195–220, 2008.

[82] R. Panton and J.H. Linebarger. Wall pressure spectra calculations for equilibrium boundary layers. *Journal of Fluid Mechanics*, 65(2):261–287, 1974.

[83] B. 'E. McGrath and R. Simpson. Some features of surface pressure fluctuations in turbulent boundary layers with zero and favorable pressure gradients. Technical report, NASA, 1987.

[84] Y. Lee, W. K. Blake, and T. Farabee. Prediction of wall pressure spectrum using a rans calculation. In *43rd AIAA Aerospace Sciences Meeting and Exhibit*, pages 2005–802, 2005.

[85] J. B. Forest and W. Devenport. The wall pressure spectrum of high reynolds number rough-wall turbulent boundary layers. 17th AIAA/CEAS Aeroacoustics Conference 2011 (32nd AIAA Aeroacoustics Conference), Portland, OR, United states, 2011.

[86] P. Bradshaw. 'inactive' motion and pressure fluctuations in turbulent boundary layers. *Journal of Fluid Mechanics*, 30(2):241–258, 1967.

[87] J. B. Forest. The wall pressure spectrum of high reynolds number rough-wall turbulent boundary layers. Master's thesis, Virginia Polytechnic Institute and State University, 2012.

[88] G. M. Corcos. The structure of the turbulent pressure field in boundary-layer flows. *Journal of Fluid Mechanics*, 18(3):353–378, 1964.

[89] T. M. Farabee and F. E. Geib Jr. Measurements of boundary layer pressure fluctuations at low wavenumbers on smooth and rough walls. volume 11, pages 55–68, Atlanta, GA, USA, 1991. ASME.

[90] L. A. Joseph, T. W. Meyers, N. J. Molinaro, and W. J Devenport. Pressure fluctuations in a high-reynolds-number turbulent boundary layer flow over rough surfaces. In *22nd AIAA/CEAS Aeroacoustics Conference*, Aeroacoustics Conferences. American Institute of Aeronautics and Astronautics, 2016.

[91] T. Meyers, W Nathan Alexander, William Devenport, and Stewart AL Glegg. High reynolds number turbulent boundary layer flow over rough walls: Wall pressure spectrum and noise. *19th AIAA/CEAS Aeroacoustics Conference*, 2013.

[92] D. R. Waigh and R. J. Kind. Improved aerodynamic characterization of regular three-dimensional roughness. *AIAA Journal*, 36(6):1117–1119, 1998.

[93] Jacob George and Roger Simpson. Some effects of sparsely distributed three-dimensional roughness elements on two-dimensional turbulent boundary layers. Reston, 2000. American Institute of Aeronautics and Astronautics.

[94] D. O. Stewart. Effects of spacing and geometry of distributed roughness elements on a two-dimensional turbulent boundary layer. Master's thesis, Virginia Polytechnic Institute and State University, 2005.

[95] M. R. Raupach. Conditional statistics of reynolds stress in rough-wall and smooth-wall turbulent boundary layers. *Journal of Fluid Mechanics*, 108(1):363–382, 1981.

[96] M. R. Raupach, A. S. Thom, and I. Edwards. A wind-tunnel study of turbulent flow close to regularly arrayed rough surfaces. *Boundary-Layer Meteorology*, 18(4):373–397, 1980.

[97] X. Zhang, C. Pan, J. Shen, and J. Wang. Effect of surface roughness element on near wall turbulence with zero-pressure gradient. *SCIENCE CHINA Physics, Mechanics Astronomy*, 58(6), 2015.

[98] Q. Yang and M. Wang. Boundary-layer noise induced by a roughness patch. In *16th AIAA/CEAS Aeroacoustics Conference*, Aeroacoustics Conferences. American Institute of Aeronautics and Astronautics, 2010.

[99] A. A. Fontaine and S. Deutsch. Structure of near wall turbulence downstream of a wall mounted protrusion: an interesting reynolds stress suppression phenomena. *Experiments in Fluids*, 20(5), 1996.

[100] R. Balachandar and D. Blakely. Surface roughness effects on turbulent boundary layers on a flat plate located in an open channel. *Journal of Hydraulic Research*, 42(3):247–261, 2004.

[101] I. P. Castro and A. G. Robins. The flow around a surface-mounted cube in uniform and turbulent streams. *Journal of Fluid Mechanics*, 79(2):307–335, 1977.

[102] W. J. Devenport, R. A. Burdisso, A. Borgoltz, P. A. Ravetta, M. F. Barone, K. A. Brown, and M. A. Morton. The kevlar-walled anechoic wind tunnel. *Journal of Sound and Vibration*, 332(17):3971–3991, 2013.

[103] T. W. Meyers. The rough wall high reynolds number turbulent boundary layer surface pressure spectrum. Master's thesis, Virginia Polytechnic Institute and State University, 2014.

[104] R. Ma. *Unsteady turbulence interaction in a tip leakage flow downstream of a simulated axial compressor rotor*. PhD thesis, Virginia Polytechnic Institute and State University, 2003.

[105] P. M. Ligrani and P. Bradshaw. Spatial resolution and measurement of turbulence in the viscous sublayer using subminiature hot-wire probes. *Experiments in Fluids*, 5(6), 1987.

[106] W. J. Devenport, Dustin L. Grissom, W. Nathan Alexander, Benjamin S. Smith, and Stewart A. L. Glegg. Measurements of roughness noise. *Journal of Sound and Vibration*, 330(17):4250–4273, 2011.

[107] P. F. Mish. *An experimental investigation of unsteady surface pressure on single and multiple airfoils*. PhD thesis, Virginia Polytechnic Institute and State University, 2003.

[108] J. S. Bendat and A. G. Piersol. *Random Data: Analysis and Measurement Procedures*. Wiley, 2011.

[109] N. D. Varano and R. L. Simpson. Flow structure and pressure fluctuations of turbulent boundary layers with sparse roughness. 47th AIAA Aerospace Sciences Meeting including the New Horizons Forum and Aerospace Exposition, Orlando, FL, United states, 2009. American Institute of Aeronautics and Astronautics Inc.

[110] P. Horne. Physical and computational investigation of the wall pressure fluctuations in a channel flow. Technical report, Naval Research Laboratory, April 26 1990.

[111] M. K. Bull. Properties of the fluctuating wall-pressure field of a turbulent boundary layer. Technical report, Advisory Group For Aeronautical, Research and Development, Paris, 1963.

[112] K. R. Sreenivasan. *The turbulent boundary layer*, pages 159–209. Springer Berlin Heidelberg, Berlin, Heidelberg, 1989.

[113] D. B. De Graaff and J. K. Eaton. Reynolds-number scaling of the flat-plate turbulent boundary layer. *Journal of Fluid Mechanics*, 422:319–346, 2000.

[114] J. C. Klewicki. Self-similar mean dynamics in turbulent wall flows. *Journal of Fluid Mechanics*, 718:596–621, 2013.

[115] P. Å Krogstad, J. H. Kaspersen, and S. Rimestad. Convection velocities in a turbulent boundary layer. *Physics of Fluids*, 10(4):949–957, 1998.

[116] D. M. Chase. Modeling the wavevector-frequency spectrum of turbulent boundary layer wall pressure. *Journal of Sound and Vibration*, 70(1):29–67, 1980.

[117] R. L. Barger. *A theoretical investigation of forebody shapes designed for natural laminar boundary-layer flow*. Langley Research Center, National Aeronautics and Space Administration, Scientific and Technical Information Office, 1979.

[118] W. J. Devenport and J.A Schetz. Boundary layer codes for students in java. In *ASME 1998 fluids engineering division summer meeting, Washington DC, June 21–25*, number 17, pages 4250–4273, Washington, DC, USA, 1998. Publ by ASME.

Appendices

A. Calibrating for Shear Stress Effect on Microphone Response

Previous studies [1] have shown that the shape of the resonant peak in the calibration curve depends on the flow speed. Due to the decrease in the relative magnitude of the viscous effects, the damping response of the microphones is reduced with increasing Reynolds Number. As we increase flow speed, we increase Reynolds number, which in turn decreases the relative magnitude of the viscous effects. Thus the microphone response will be more damped with no flow than with flow on. However the microphones are only calibrated with flow off. So this effect is not captured in the microphone calibration.An experiment was undertaken to quantify this effect, and establish a suitable correction to account for it.

A laminar forebody was designed according to the work of Barger [117]. His design with 2:1 fineness ratio was selected for this work. It was attached to a cylindrical mid-section and an arbitrarily curved aft-section. The coordinates of the laminar forebody and the attached aft-body are presented in table A.1. The laminar forebody model is shown in fig. A.1a.

A preliminary study was done using online engineering applets which carry out the Thwaites-Walz method to detect where transition and separation would occur on the body. Information about these engineering applets is detailed in Devenport and Schetz [118]. This study was done at speeds up to 70-ms^{-1} and revealed that the flow separates at the junction of the forebody and the cylindrical mid-section. The flow does not transition upstream of this location. Thus a ⅛-in B&K 4138-A-015 test microphone embedded 25.4-mm forward of the junction of the forebody and the mid-section would be immersed in a fully laminar boundary layer. The successful design was fabricated out of a single block of aluminum according to the specifications in table A.1 and is shown in fig. A.1b.

Realistically, machining the model to the exact design specifications is not possible. Surface roughness effects and machining imperfections are expected. Naphthalene sublimation tests were therefore done on the model before any experiments were undertaken. The goal of this test was to

Table A.1: Coordinates of the laminar forebody [117], conjoined cylindrical mid-section and aft-body

x (in)	$f(x)$ (in)
0	0
0.01	0.05
0.03	0.08
0.07	0.121
0.13	0.161
0.23	0.212
0.36	0.263
0.52	0.325
0.71	0.385
0.93	0.454
1.19	0.524
1.47	0.598
1.78	0.669
2.1	0.739
2.44	0.8045
2.78	0.864
3.11	0.9125
3.43	0.954
3.72	0.981
3.99	0.999
4	1
5	1
6	1
6.18	0.992
7.752	0.915
8.565	0.835
9.533	0.676
10.098	0.554
10.677	0.411
11.193	0.25
11.623	0.119
12	0

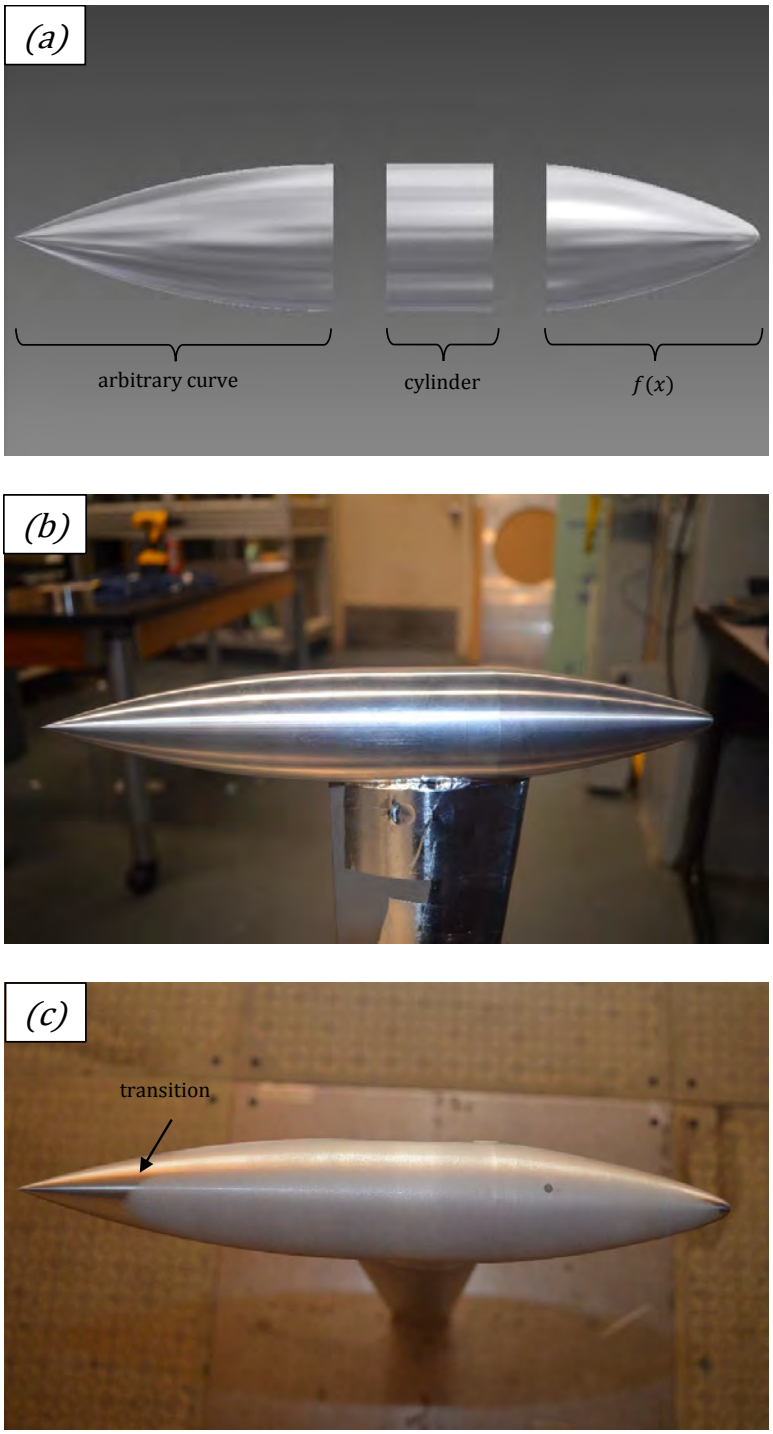

Figure A.1: The laminar forebody (described by function $f(x)$ in table A.1) with attached cylindrical midsection and aft-body. (a) Exploded model (b) test model made from aluminum block (c) Naphthalene sublimation test to detect transition location

ensure that the location of the microphone was in fact in the laminar flow regime at speeds up to 70-ms^{-1}. A dummy microphone was inserted into model creating an upstream step of 3.6-μm$\pm$16-nm and a downstream step of 3.8-μm$\pm$16-nm, as measured using a Mahr PS1 surface profilometer. The pictorial results of this test are presented in fig. A.1c. Despite the steps, transition does not occur upstream of the microphone or anywhere on the laminar forebody at speeds up to 70-ms^{-1}. The calibration could therefore be carried out with confidence that the test microphone was in a laminar boundary layer.

To actually calibrate for shear stress effect on microphone response an experiment was designed in the Virginia Tech Stability Wind tunnel. A test microphone immersed in a laminar boundary layer was used to measure the acoustics of a spark source (impulse) at speeds between 0-ms^{-1} and 70-ms^{-1}. The laminar forebody model was mounted in the middle of the test section using streamlined struts. The spark source was mounted also using a streamlined strut directly above the microphone (x and y separations approximately 0-mm) with a separation in the z direction of approximately 146-mm. The experimental set up is shown in fig. A.2.

Care was taken to ensure that once installed the step between the microphone and the forebody was not greater than 3.8-μm$\pm$16-nm. For each speed (between 0-ms^{-1} and 70-ms^{-1}) data was collected for at least 120-s (divided into 10-s increments so as not to burn

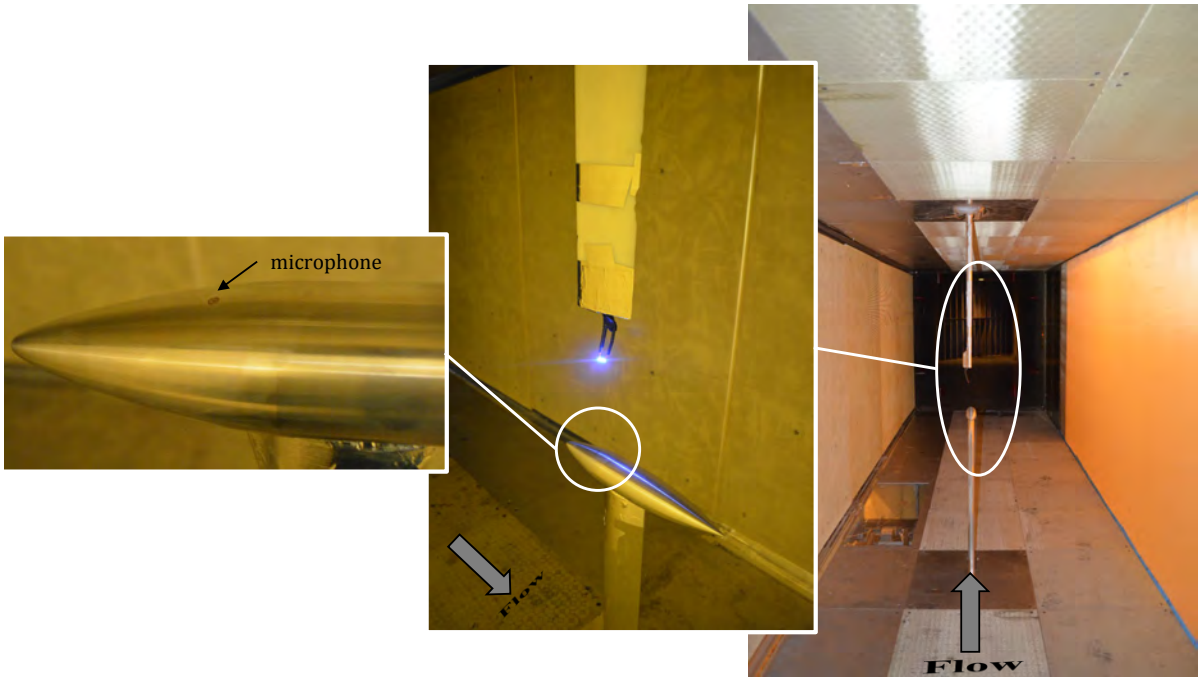

Figure A.2: Experimental setup to calibrate for shear stress effect on microphone response. Laminar forebody and spark source mounted in the test section of the Virginia Tech Stability Wind Tunnel

out the spark source). This was in an effort to obtain at least 1000 impulses per speed, which would make averaging out the background noise possible. Data with no flow was collected before and after the runs at speed in order to ensure that the character of the impulse did not change during the runs.

Recalling that a calibration is essentially

$$\text{output signal} = \text{input signal} \times \text{calibration function}$$

For this specific case we have

$$\text{microphone output} = \text{spark source output (impulse)} \times \text{microphone calibration function}$$

So for the flow on and flow off cases we have

$$\begin{aligned} Y(\omega)_{noflow} &= X(\omega)_{noflow} \times H(\omega)_{noflow} \\ Y(\omega)_{flow} &= X(\omega)_{flow} \times H(\omega)_{flow} \end{aligned} \tag{A.1}$$

where $Y(\omega)$ is the spectrum of the output signal, $X(\omega)$ is the spectrum of the input signal and $H(\omega)$ is the system transfer function. To find the microphone calibration function with flow on, we use system identification methods with a known signal – the impulse. Knowing that the spectrum of the impulse signal is a constant we get

$$\frac{Y(\omega)_{noflow}}{Y(\omega)_{flow}} = \frac{H(\omega)_{noflow}}{H(\omega)_{flow}} \tag{A.2}$$

So the calibration function for the microphone with flow on will be

$$H(\omega)_{flow} = H(\omega)_{noflow} \frac{Y(\omega)_{flow}}{Y(\omega)_{noflow}} \tag{A.3}$$

$H(\omega)_{noflow}$ is the same calibration function obtained from eq. (2.5) by the methods described in § 2.4.3. And $Y(\omega)$ is simply the Fourier transform of the signal measured by the microphone during this calibration test.

To process the measured data for cases with and without flow, the first step was to isolate each impulse. At each speed typically upwards of 2000 impulses were measured. Then we take the Fourier transform of each impulse in order to phase align them. The phase aligning process was done in the frequency domain because this eliminated the dependence of the results of the chosen time step. Phase aligning involved finding the time delay (the slope of the phase versus frequency plot) and adding this to the original Fourier transform. Once the impulses were aligned the arithmetic average was taken. This is $Y(\omega)$.

The laminar boundary layer ensures that the shear stress can be calculated for the test conditions. Again using online engineering applets [118], the Thwaites-Walz method was

used to estimate the shear stress experienced by the microphone which was then used to calculate d^+ values.

Fig. A.3 shows the result of this experiment compared to the calibration obtained in § 2.4.3. The plot shows that there is little difference (at most 1.2-dB) between the calibration function with no shear effects and the calibration function with shear effects. The most likely explanation for this is the small values of wall shear stress experienced. In the typical rough wall turbulent boundary layer, shear stress values range from 2 – 14-N/m^2. In this laminar boundary layer, the maximum shear stress experienced at 70-ms^{-1} was only 1.1-N/m^2. This was not sufficient enough to see the damping effect on the resonant peak.

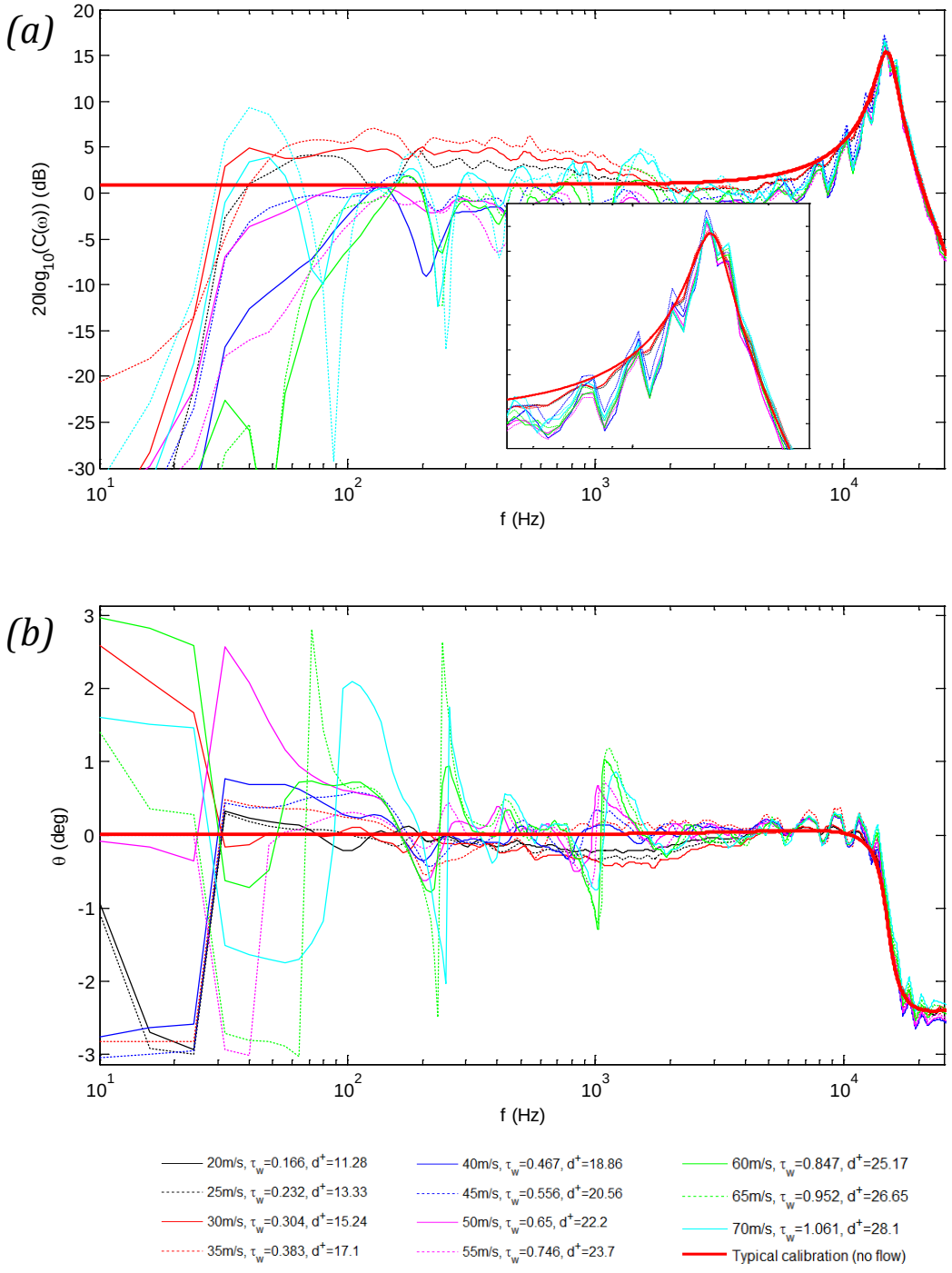

Figure A.3: (a) Amplitude and (b) phase calibration curves at different flow speeds, compared to the calibration curves obtained with no flow (from fig. 2.21)

B. Detailed Velocity & Turbulence Profiles

This appendix includes the detailed velocity and turbulence profiles measured from different probes and at different element-relative locations on different rough surfaces. We compare these results in the following sections.

B.1 Comparisons between two quadwires

The quadwire data obtained on the multi-height surface, downstream of the 1-mm elements, are presented in figs. B.1 and B.2 for 30-ms^{-1} and 60-ms^{-1}, respectively. The locations are shown in the top left image of fig. 5.4. The top plots are the mean velocities with the plot on the right being a zoomed in version of the plot on the left. The bottom left plot is the normal Reynolds stresses and the bottom right plot is the Reynolds shear-stresses.

The data from the different probes appear to show good agreement for the mean velocities, until we look at the profile close to the wall. While the differences are within the uncertainty, there is a larger variation between probes than what was observed for the cylinders. Similarly larger variation are seen in the Reynolds stresses, especially the shear stresses. This could be because the two probes are in slightly different locations relative to the 1-mm elements (see fig. 5.4). The top probe is directly behind the element while the bottom probe is closer to the middle of a 4 element array.

Table B.2 presents the boundary layer parameters calculated from the data of each probe. In this table the absolute difference between the values ($|\Delta|$) are stated as well as the combined uncertainty associated with each parameter ($2\times\delta()$). Just as before, as long as the absolute difference is less than the combined uncertainty we can say that there is agreement. With this in mind, it is clear that all the parameters from each probe in table B.2 agree.

Table B.1: Legend for figs. B.1 and B.2

●	x velocity component for bottom probe
▲	x velocity component for top probe
●	y velocity component for bottom probe
▲	y velocity component for top probe
●	z velocity component for bottom probe
▲	z velocity component for top probe
▬	uncertainty bands for the data

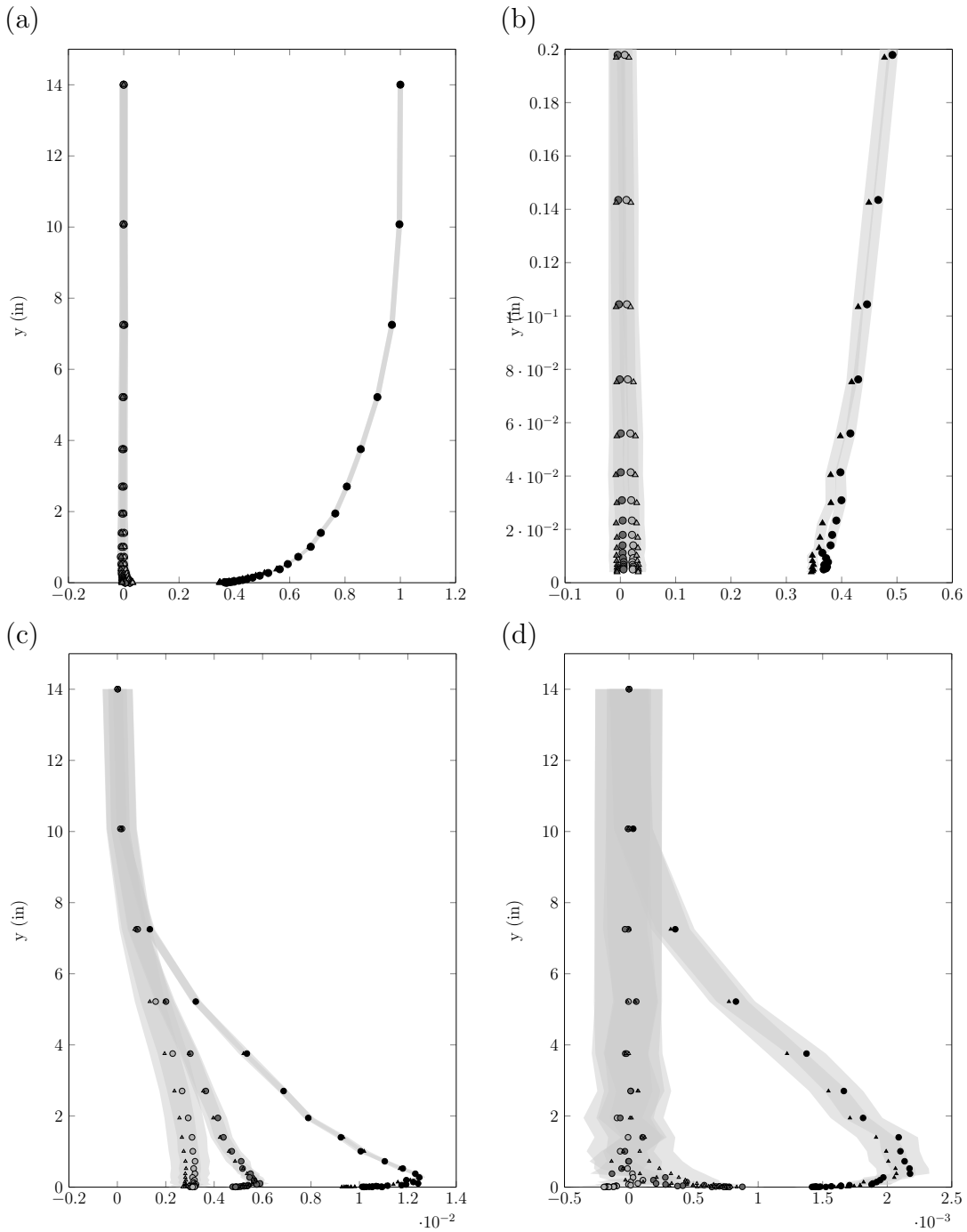

Figure B.1: Velocity results for multi-height surface, in the vicinity of 1-mm element, at 30-ms^{-1}. (a) Mean velocity profiles (b) Expanded mean velocity profiles showing the bottom 1.5% of the boundary layer (c) Normal Reynold's stress profiles (d) Reynolds shear-stress profiles.

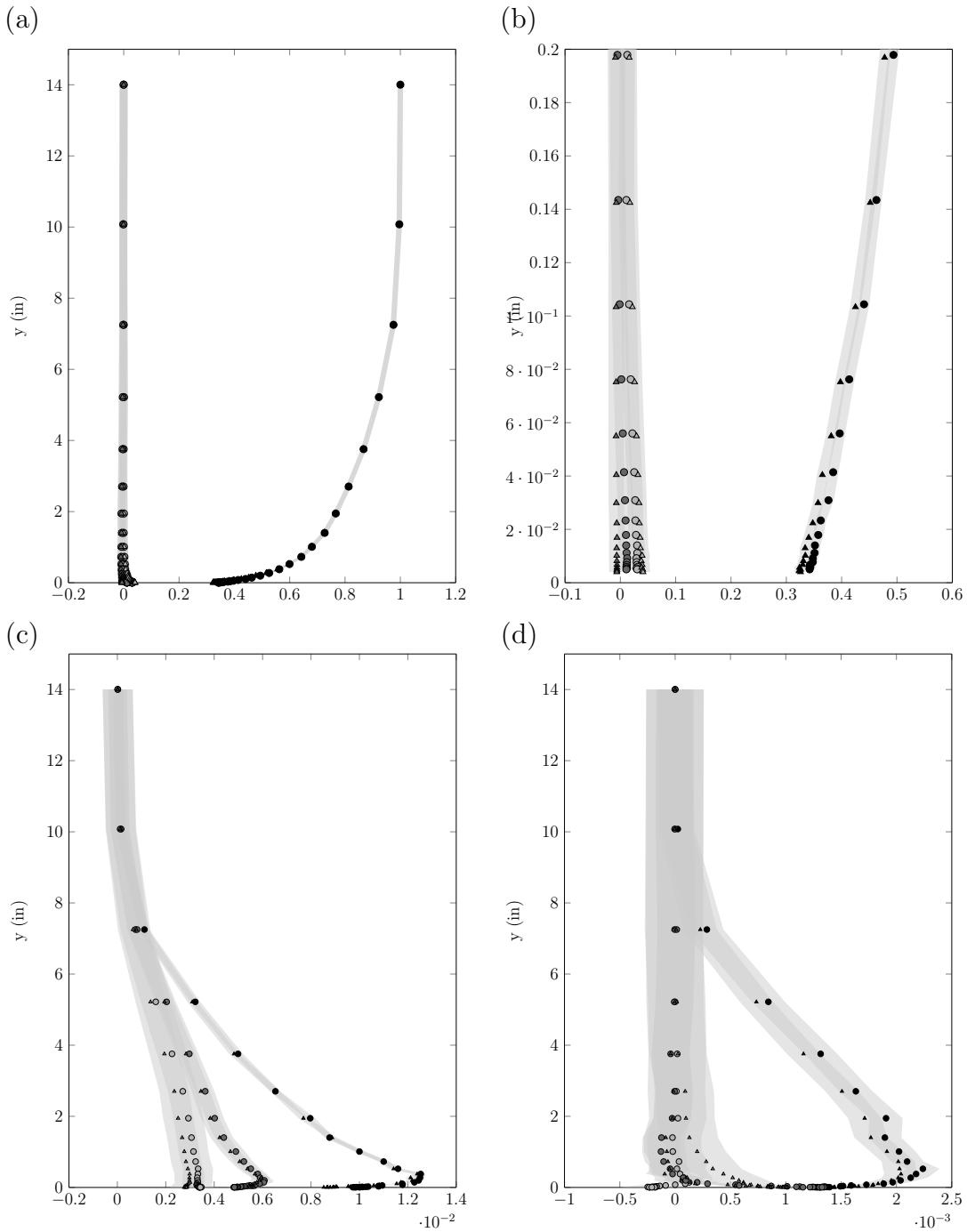

Figure B.2: Velocity results for multi-height surface, in the vicinity of 1-mm element, at 60-ms^{-1}. (a) Mean velocity profiles (b) Expanded mean velocity profiles showing the bottom 1.5% of the boundary layer (c) Normal Reynold's stress profiles (d) Reynolds shear-stress profiles.

Table B.2: Comparisons of the boundary layer parameters for the multi-height surface (measured in the vicinity of the 1-mm elements) from data of two quadwires. $\delta()$ is the uncertainty in a parameter

	$2\times\delta()$		30-ms^{-1}			60-ms^{-1}		
	30-ms^{-1}	60-ms^{-1}	bottom probe	top probe	$\lvert\Delta\rvert$	bottom probe	top probe	$\lvert\Delta\rvert$
δ (m)	0.00302		0.238	0.238	0	0.232	0.231	0.001
δ^* (m)	0.00459		0.037	0.037	0	0.036	0.035	0.001
Re_θ	5400	10120	44922	44629	293	80527	80163	364
U_τ (ms^{-1})	0.1		1.38	1.35	0.03	2.77	2.70	0.07
C_f	0.0006		0.0042	0.0041	0.0001	0.0042	0.0040	0.0002
k_g^+	27	45	230	240	10	494	450	44
δ^+	1430	1268	19498	19116	382	35670	34630	1040
δ/k_g	6.6		79.5	79.3	0.2	77.3	77.1	0.2
ΔU^+	0.8		11.2	11.8	0.6	13.7	13.8	0.1

The quadwire data obtained on the multi-height surface, downstream of the 3-mm elements, are presented in figs. B.3 and B.4 for 30-ms^{-1} and 60-ms^{-1}, respectively. These location correspond to the locations shown in the bottom middle image of fig. 5.4. The top plots are the mean velocities with the plot on the right being a zoomed in version of the plot on the left. The bottom left plot is the normal Reynolds stresses and the bottom right plot is the Reynolds shear-stresses.

There is a larger variation between probes than what was observed in the case of the cylinders but the variations are still within the uncertainty. Similarly larger variations are seen in the Reynolds stresses, especially the shear stresses. The probes are not at the same location relative to the 3-mm element (see fig. 5.4). The bottom probe is directly behind the element while the top probe is closer to the middle of a 4 element array. Nevertheless the profiles are still acceptably close, suggesting that differences are only due to the difference in probe location and not due to erroneous measurements.

Table B.4 presents the boundary layer parameters calculated from the data of each probe. In this table the absolute difference between the values are stated ($|\Delta|$) as well as the combined uncertainty associated with each parameter ($2\times\delta()$). Just as before, as long as the absolute difference is less than the combined uncertainty we can say that there is agreement. With this in mind, it is clear that all the parameters from each probe in table B.4 agree except ΔU^+ at 60-ms^{-1}.

Table B.3: Legend for figs. B.3 and B.4

●	x velocity component for bottom probe
▲	x velocity component for top probe
●	y velocity component for bottom probe
▲	y velocity component for top probe
●	z velocity component for bottom probe
▲	z velocity component for top probe
▬	uncertainty bands for the data

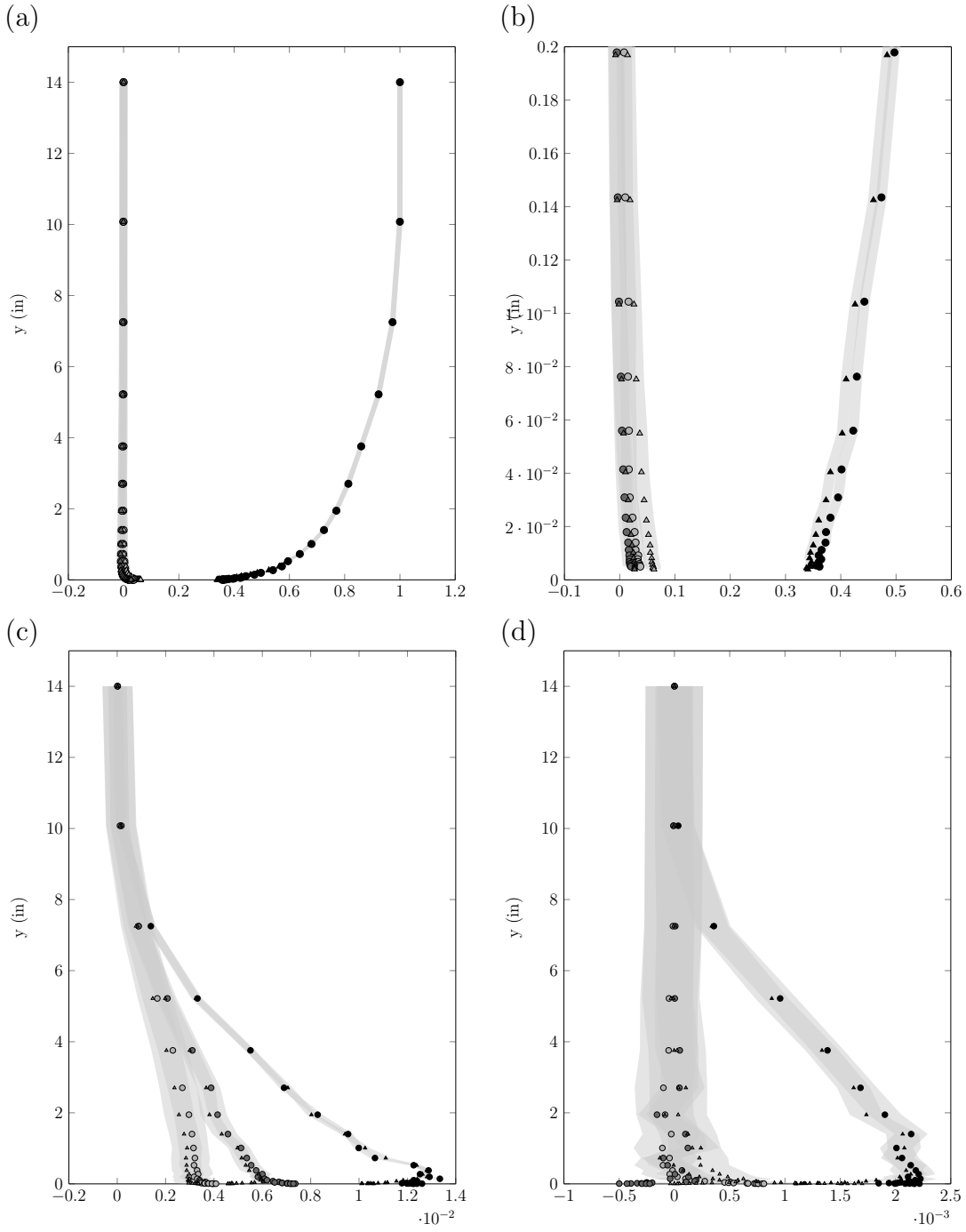

Figure B.3: Velocity results for multi-height surface, behind the 3-mm element, at 30-ms^{-1}. (a) Mean velocity profiles (b) Expanded mean velocity profiles showing the bottom 1.5% of the boundary layer (c) Normal Reynold's stress profiles (d) Reynolds shear-stress profiles.

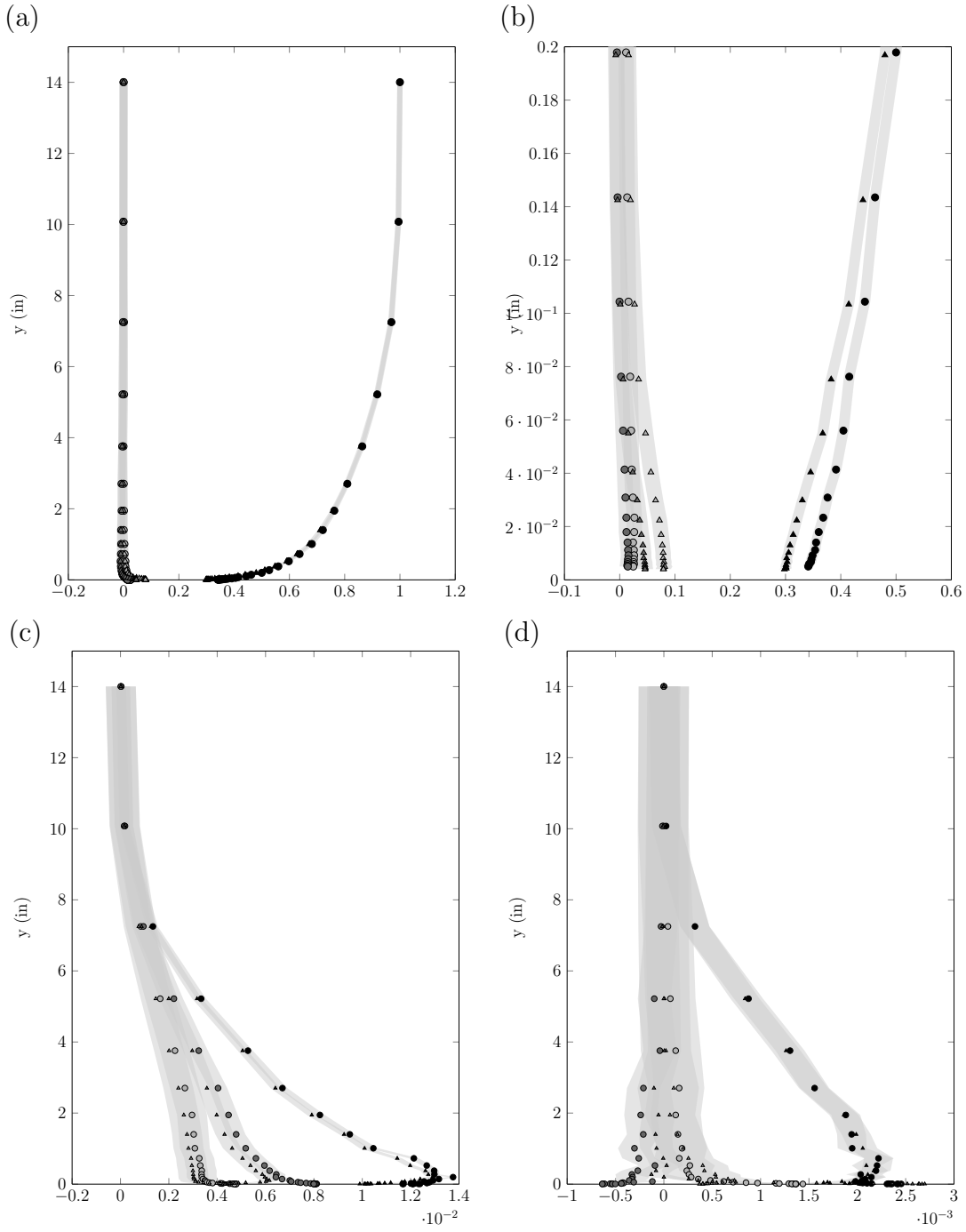

Figure B.4: Velocity results for multi-height surface, behind the 3-mm element, at 60-ms^{-1}. (a) Mean velocity profiles (b) Expanded mean velocity profiles showing the bottom 1.5% of the boundary layer (c) Normal Reynold's stress profiles (d) Reynolds shear-stress profiles.

Table B.4: Comparisons of the boundary layer parameters for the multi-height surface (measured behind the 3-mm elements) from data of two quadwires. $\delta()$ is the uncertainty in a parameter

	$2\times\delta()$		30-ms^{-1}			60-ms^{-1}		
	30-ms^{-1}	60-ms^{-1}	bottom probe	top probe	$\lvert\Delta\rvert$	bottom probe	top probe	$\lvert\Delta\rvert$
δ (m)	0.00302		0.237	0.236	0.001	0.238	0.237	0.001
δ^* (m)	0.00459		0.037	0.036	0.01	0.036	0.036	0
Re_θ	5380	10306	44088	43984	104	83998	84518	520
U_τ (ms^{-1})	0.1		1.39	1.37	0.02	2.78	2.78	0
C_f	0.0006		0.0043	0.0042	0.0001	0.0043	0.0043	0
k_g^+	27	45	245	242	3	472	471	1
δ^+	1420	1425	19419	19152	267	37505	37215	290
δ/k_g	6.6		79.0	78.7	0.3	79.3	78.9	0.4
ΔU^+	0.8		11.8	12.0	0.2	13.8	14.7	*0.9**

*shows no agreement between probes

The quadwire data obtained on the multi-shape surface, downstream of the hemispheres, are presented in figs. B.5 and B.6 for 30-ms^{-1} and 60-ms^{-1}, respectively. These locations correspond to the probe locations shown in the bottom middle image of fig. 5.5. The top plots are the mean velocities with the plot on the right being a zoomed in version of the plot on the left. The bottom left plot is the normal Reynolds stresses and the bottom right plot is the Reynolds shear-stresses.

The data from the different probes show good agreement for the mean velocities, until we look at the profile close to the wall where there is substantial deviation. Similarly larger variation are seen in the Reynolds shear stresses. It is likely that the difference in streamwise location of the probe is the cause of this discrepancy. The top probe is further downstream than the bottom probe and so the characteristics of the boundary layer are slightly different in these two locations, an effect that is compounded as the flow speed is increased. This is probably why the deviation gets larger with larger flow speed.

Table B.6 presents the boundary layer parameters calculated from the data of each probe. In this table the absolute difference between the values ($|\Delta|$) are stated as well as the combined uncertainty associated with each parameter ($2\times\delta()$). Just as before, as long as the absolute difference is less than the combined uncertainty we can say that there is agreement. With this in mind, we find that there are issues with ΔU^+ at 60-ms^{-1}, mainly because there is a discrepancy in U_τ at 60-ms^{-1}. The value produced from the top probe is higher than the value of the bottom probe, most likely due to differences in streamwise location.

Table B.5: Legend for figs. B.5 and B.6

●	x velocity component for bottom probe
▲	x velocity component for top probe
●	y velocity component for bottom probe
▲	y velocity component for top probe
●	z velocity component for bottom probe
▲	z velocity component for top probe
▬	uncertainty bands for the data

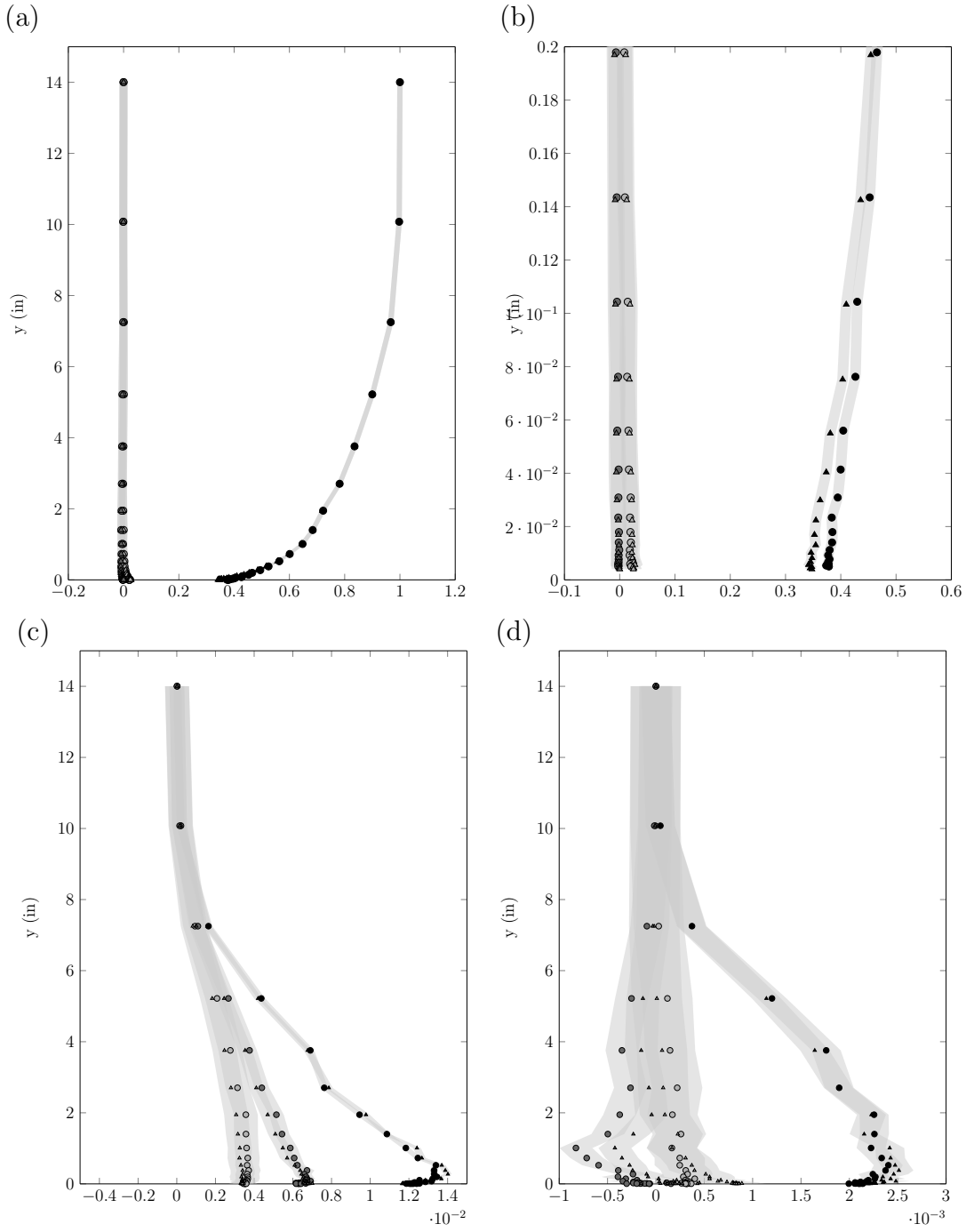

Figure B.5: Velocity results for multi-shape surface, behind the hemisphere, at 30-ms^{-1}. (a) Mean velocity profiles (b) Expanded mean velocity profiles showing the bottom 1.5% of the boundary layer (c) Normal Reynold's stress profiles (d) Reynolds shear-stress profiles.

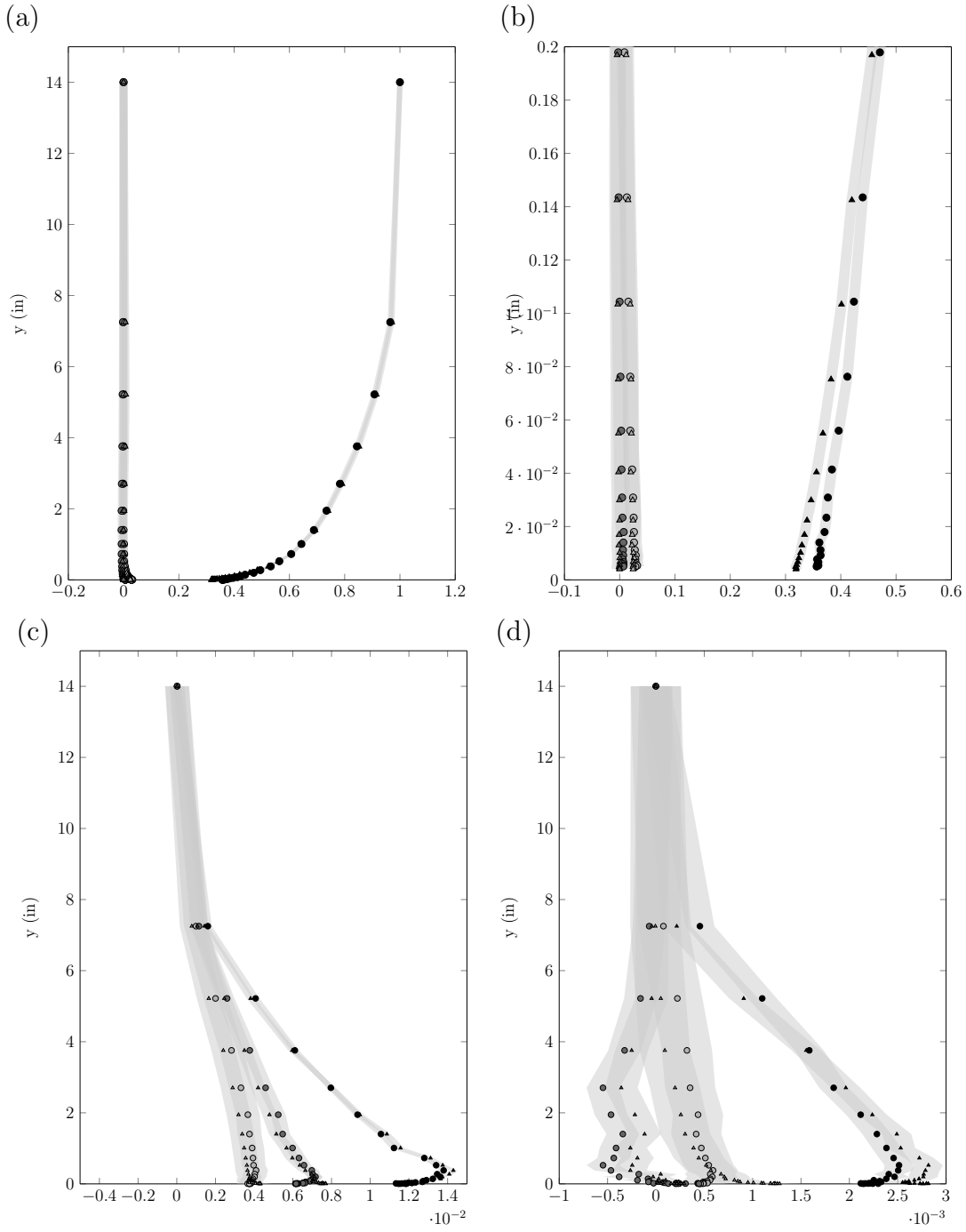

Figure B.6: Velocity results for multi-shape surface, behind the hemisphere, at 60-ms^{-1}. (a) Mean velocity profiles (b) Expanded mean velocity profiles showing the bottom 1.5% of the boundary layer (c) Normal Reynold's stress profiles (d) Reynolds shear-stress profiles.

Table B.6: Comparisons of the boundary layer parameters for the multi-shape surface (measured behind the 3-mm hemispheres) from data of two quadwires. $\delta()$ is the uncertainty in a parameter

	$2\times\delta()$		30-ms^{-1}			60-ms^{-1}		
	30-ms^{-1}	60-ms^{-1}	bottom probe	top probe	$\lvert\Delta\rvert$	bottom probe	top probe	$\lvert\Delta\rvert$
δ (m)	0.00302		0.243	0.243	0	0.284	0.283	0.001
δ^* (m)	0.00459		0.041	0.041	0	0.042	0.040	0.002
Re_θ	5432	9062	49473	49295	178	95511	91727	3784
U_τ (ms^{-1})	0.1		1.46	1.49	0.03	2.98	3.14	*0.16**
C_f	0.0006		0.0047	0.0049	0.0002	0.0049	0.0055	0.0006
k_g^+	28	45	261	265	4	501	528	27
δ^+	1470	1670	21245	21491	246	47712	48740	1028
δ/k_g	7.0		81.0	81.1	0	94.7	94.3	0.4
ΔU^+	0.8		12.0	12.8	0.8	14.1	15.2	*1.1**

*shows no agreement between probes

The quadwire data obtained on the multi-shape surface, downstream of the cylinders, are presented in figs. B.7 and B.8 for 30-ms^{-1} and 60-ms^{-1}, respectively. These locations correspond to the probe locations shown in the top left image of fig. 5.5. The top plots are the mean velocities with the plot on the right being a zoomed in version of the plot on the left. The bottom left plot is the normal Reynolds stresses and the bottom right plot is the Reynolds shear-stresses.

Unlike the data taken behind the hemispheres, these data show good agreement for the mean velocities even close to the wall. Agreement is even seen for the Reynolds stresses including the shear stresses near the wall. At 60-ms^{-1} there is some deviation near the wall for $\overline{uv}/U_{ref}$ which appears to be substantial. Again the likely cause is the difference in streamwise location of the probe is the cause of this discrepancy. The top probe is further downstream than the bottom probe and so the characteristics of the boundary layer are slightly different in these two locations, an effect that is compounded as the flow speed is increased.

Table B.8 presents the boundary layer parameters calculated from the data of each probe. In this table the absolute difference between the values ($|\Delta|$) are stated as well as the combined uncertainty associated with each parameter ($2\times\delta()$). Just as before, as long as the absolute difference is less than the combined uncertainty we can say that there is agreement. With this in mind, there appears to be many more issues with values in this case than previous cases. U_τ at 60-ms^{-1} is again higher for the top probe, leading to values of C_f, δ^+ and ΔU^+ being higher than the bottom probe. Hence we see that the absolute difference in these values between probes is greater than the combined uncertainty.

Table B.7: Legend for figs. B.7 and B.8

●	x velocity component for bottom probe
▲	x velocity component for top probe
●	y velocity component for bottom probe
▲	y velocity component for top probe
●	z velocity component for bottom probe
▲	z velocity component for top probe
▬	uncertainty bands for the data

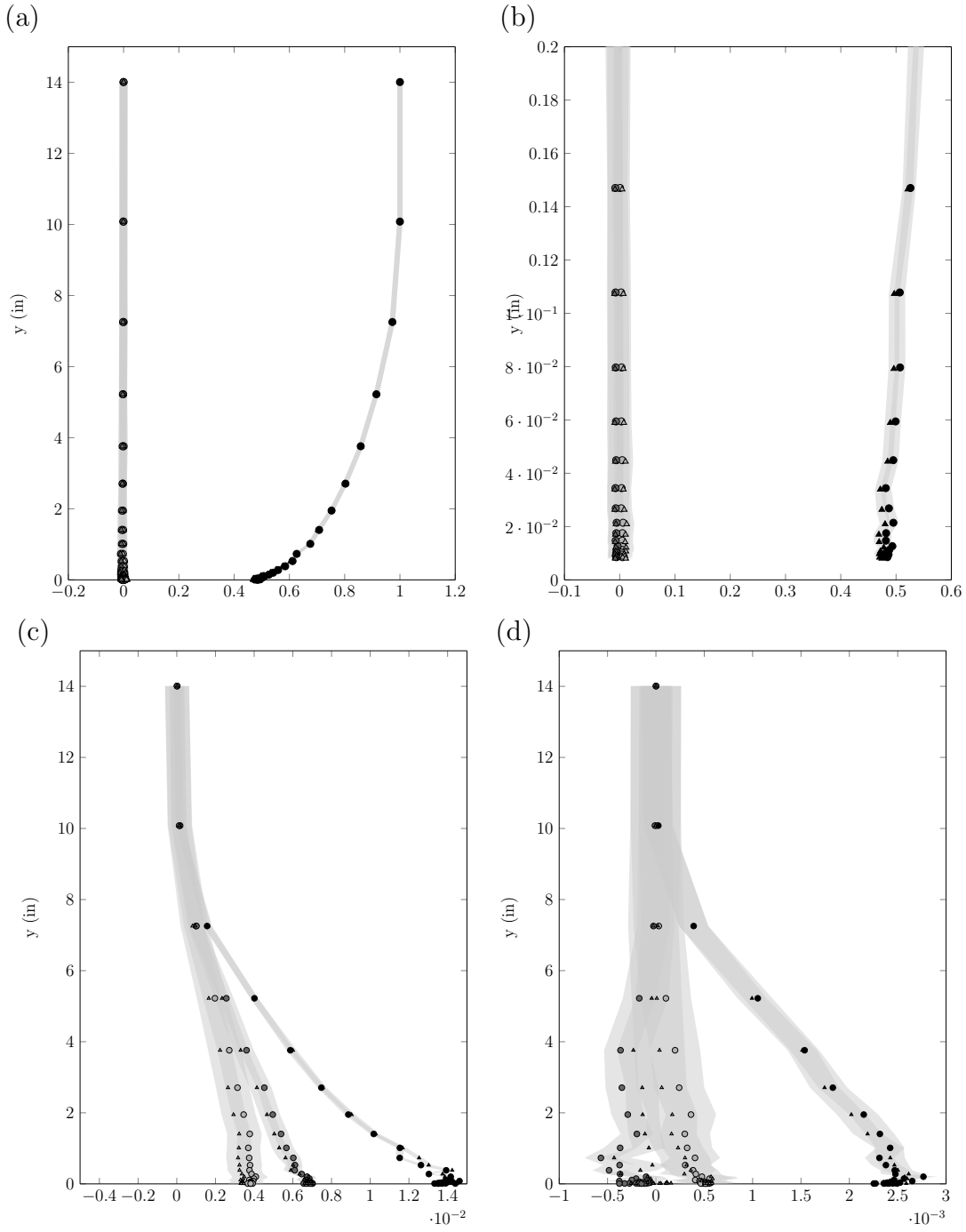

Figure B.7: Velocity results for multi-shape surface, behind the cylinder, at 30-ms^{-1}. (a) Mean velocity profiles (b) Expanded mean velocity profiles showing the bottom 1.5% of the boundary layer (c) Normal Reynold's stress profiles (d) Reynolds shear-stress profiles.

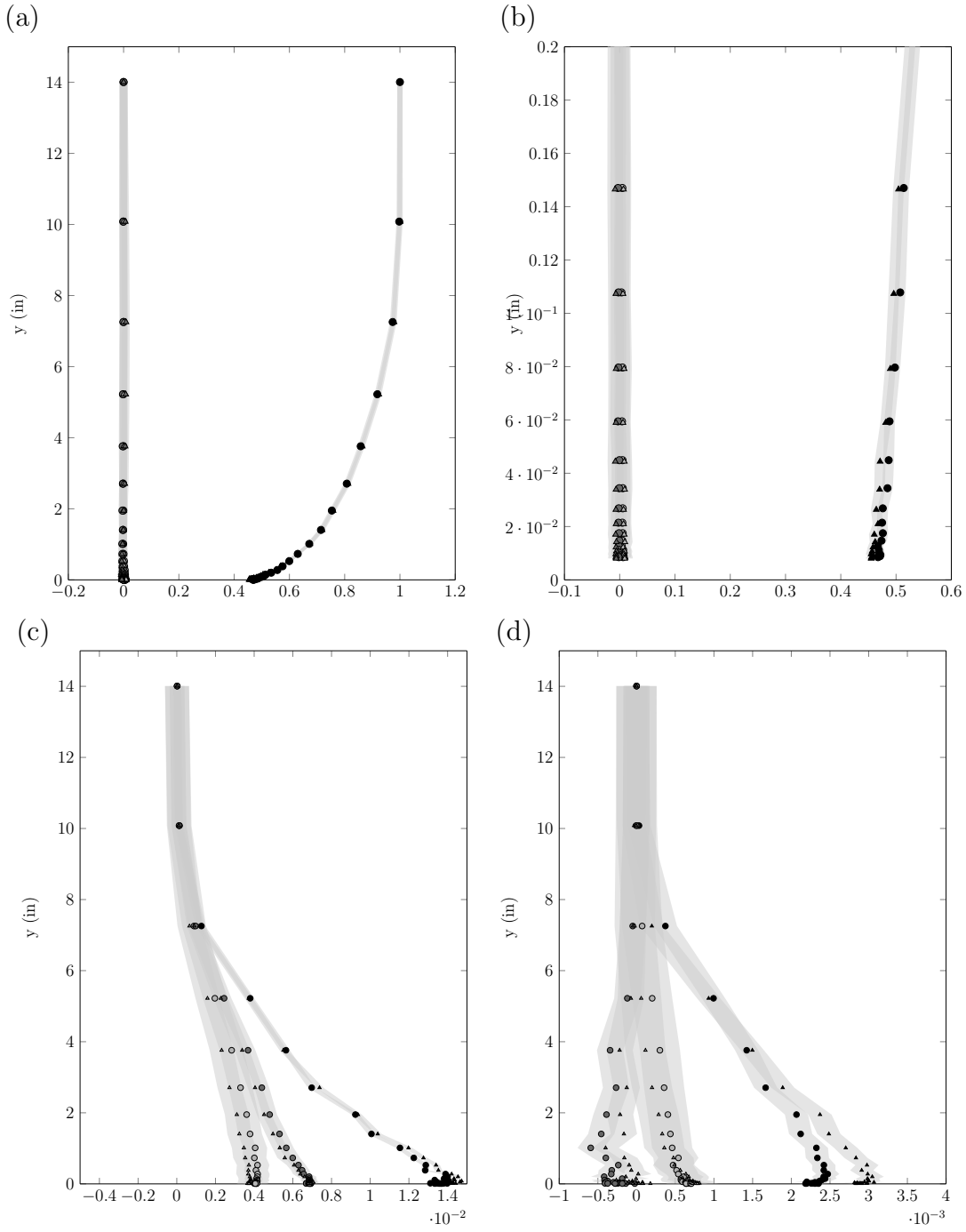

Figure B.8: Velocity results for multi-shape surface, behind the cylinder, at 60-ms^{-1}. (a) Mean velocity profiles (b) Expanded mean velocity profiles showing the bottom 1.5% of the boundary layer (c) Normal Reynold's stress profiles (d) Reynolds shear-stress profiles.

Table B.8: Comparisons of the boundary layer parameters for the multi-shape surface (measured behind the 3-mm cylinders) from data of two quadwires. $\delta()$ is the uncertainty in a parameter

	$2\times\delta()$		30-ms^{-1}			60-ms^{-1}		
	30-ms^{-1}	60-ms^{-1}	bottom probe	top probe	$\lvert\Delta\rvert$	bottom probe	top probe	$\lvert\Delta\rvert$
δ (m)	0.00302		0.239	0.239	0	0.228	0.228	0
δ^* (m)	0.00459		0.038	0.037	0.001	0.037	0.036	0.001
Re_θ	5432	9062	46461	46449	12	83205	81949	1256
U_τ (ms^{-1})	0.1		1.49	1.50	0.01	2.97	3.21	*0.24**
C_f	0.0006		0.0049	0.0050	0.0001	0.0049	0.0057	*0.0008**
k_g^+	28	45	267	269	2	491	531	40
δ^+	1470	1670	21632	21830	198	38900	41186	*2286**
δ/k_g	7.0		12.6	12.5	0.1	12.3	12.0	0.3
ΔU^+	0.4		11.7	12.0	0.3	13.3	14.6	*1.3**

*shows no agreement between probes

The quadwire data obtained on the intermediately spaced surface is shown in fig. B.9 for 30-ms^{-1} because data could not be collected with the bottom probe at 60-ms^{-1}. These locations correspond to the probe locations shown in the left image of fig. 5.3. The top plots are the mean velocities with the plot on the right being a zoomed in version of the plot on the left. The bottom left plot is the normal Reynolds stresses and the bottom right plot is the Reynolds shear-stresses.

The data from the different probes show good agreement, within the uncertainty bounds for the mean velocities. The variation is larger for the Reynolds stresses, especially closer to the wall where errors are larger, but still within the uncertainty.

Table B.10 presents the boundary layer parameters calculated from the data of each probe. In this table the absolute difference between the values ($|\Delta|$) are stated as well as the combined uncertainty associated with each parameter ($2\times\delta()$). Just as before, as long as the absolute difference is less than the combined uncertainty we can say that there is agreement. With this in mind, we see that all parameters for each probe agree at 30-ms^{-1}.

Table B.9: Legend for fig. B.9

●	x velocity component for bottom probe
▲	x velocity component for top probe
●	y velocity component for bottom probe
▲	y velocity component for top probe
●	z velocity component for bottom probe
▲	z velocity component for top probe
▬	uncertainty bands for the data

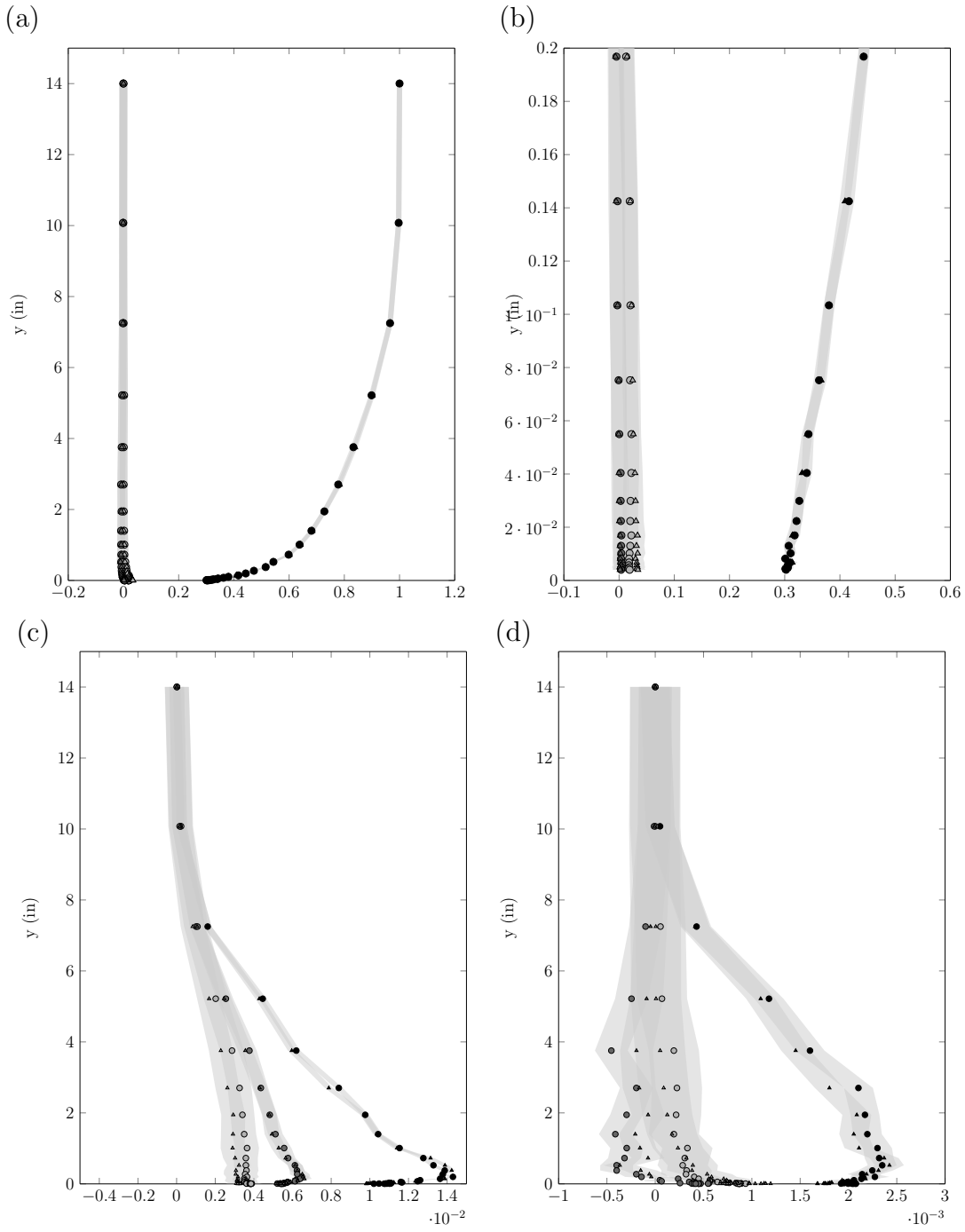

Figure B.9: Velocity results for intermediately spaced surface at 30-ms^{-1}. (a) Mean velocity profiles (b) Expanded mean velocity profiles showing the bottom 1.5% of the boundary layer (c) Normal Reynold's stress profiles (d) Reynolds shear-stress profiles. ● x velocity component for bottom probe, ▲ x velocity component for top probe, ● y velocity component for bottom probe, ▲ y velocity component for top probe, ● z velocity component for bottom probe, ▲ z velocity component for top probe. Shaded region represents uncertainty bands for the data

Table B.10: Comparisons of the boundary layer parameters for the intermediate rough surface from data of two quadwires. $\delta()$ is the uncertainty in a parameter

	$2\times\delta()$	30-ms^{-1}		
		bottom probe	top probe	$\lvert\Delta\rvert$
δ (m)	0.00302	0.243	0.243	0
δ^* (m)	0.00459	0.041	0.041	0
Re_θ	5530	50052	49558	494
U_τ (ms^{-1})	0.1	1.43	1.44	0.01
C_f	0.0006	0.0046	0.0047	0.0001
k_g^+	44.6	260	262	2
δ^+	1454	21065	21296	231
δ/k_g	6.6	81.0	81.1	0.1
ΔU^+	1.4	12.7	12.8	0.1

B.2 Comparisons among all probes

The data obtained from the quadwire, single hotwire and flattened Pitot on the surface of cylinders at 60-ms^{-1} are shown in fig. B.10. All these data were collected at close to the centre of the four element array. The top plots are the streamwise mean velocities U/U_{ref} with the plot on the right being a zoomed in version of the plot on the left. The bottom left plot is the streamwise normal Reynolds stress u^2/U_{ref}^2 and the bottom right plot is the zoomed in version of this. Note that there is only data from the hotwires in the bottom plots.

The data obtained from the quadwire, and flattened Pitot on the multi-height surface are presented in figs. B.11 and B.12. These are the data collected downstream/in the vicinity of the 1-mm elements (shown in the top images of fig. 5.4). The top plots are the streamwise mean velocities U/U_{ref} with the plot on the right being a zoomed in version of the plot on the left. No data is presented for the streamwise normal Reynolds stress u^2/U_{ref}^2 since the single hotwire was not used for this particular surface, and it is not useful to present the quadwire data on its own.

The data from the different probes show good agreement for the mean velocities, even close to the wall. The differences in this region are well within the uncertainty cited.

Table B.11: Legend for figs. B.11 and B.12

●	quadwire results measured downstream/in the vicinity of the 1-mm elements
■	single hotwire results
▲	flattened Pitot results
▬	uncertainty bands for the data

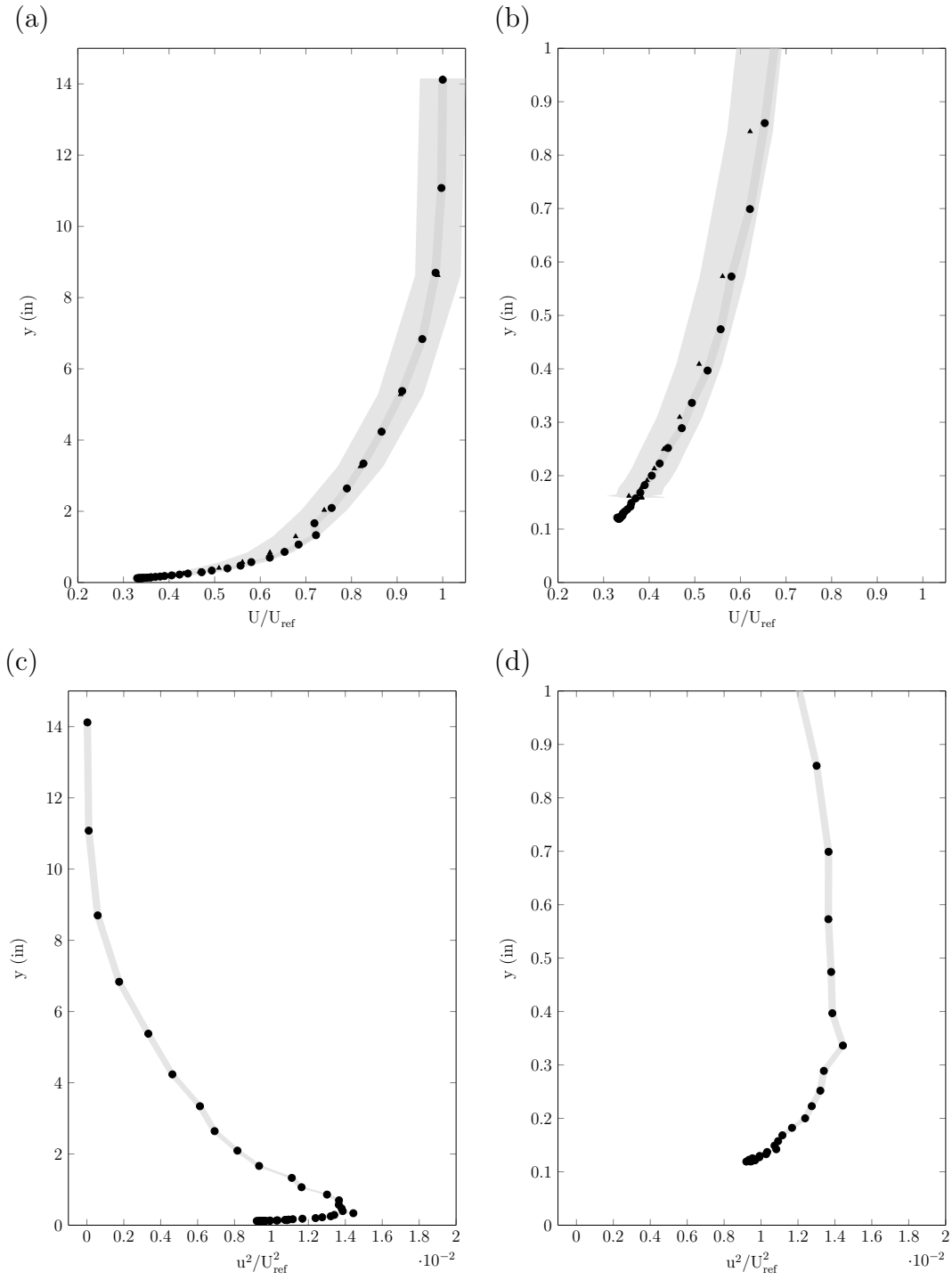

Figure B.10: Results for cylinders at 60-ms^{-1}: (a) Streamwise mean velocity profiles (b) Expanded streamwise mean velocity profiles (c) Streamwise normal Reynolds stress profiles (d) Expanded streamwise normal Reynolds stress profiles.

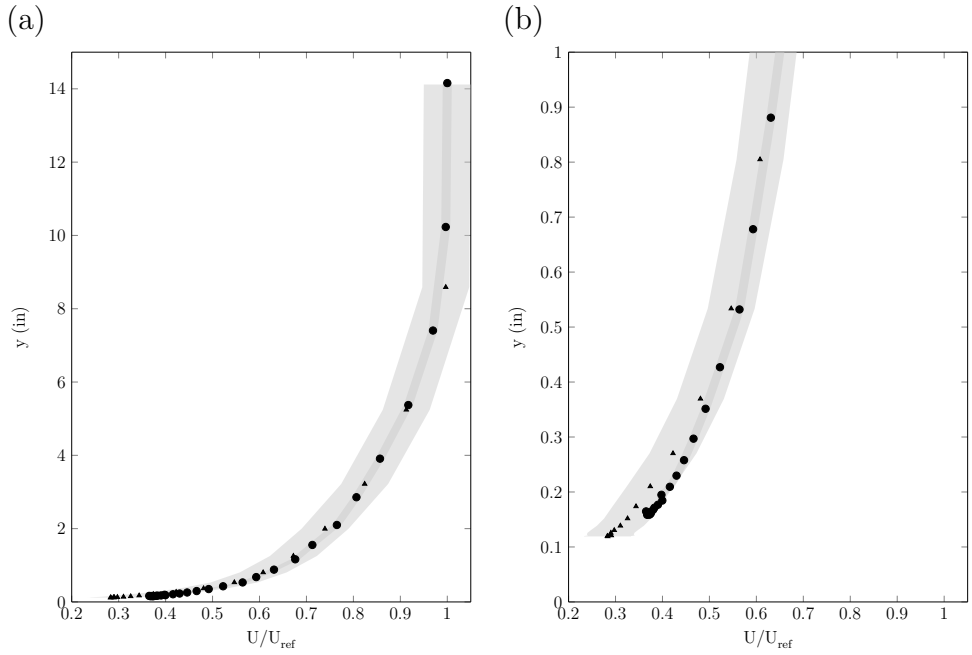

Figure B.11: Results for multi-height surface at 60-ms^{-1}: (a) Streamwise mean velocity profiles (b) Expanded streamwise mean velocity profiles.

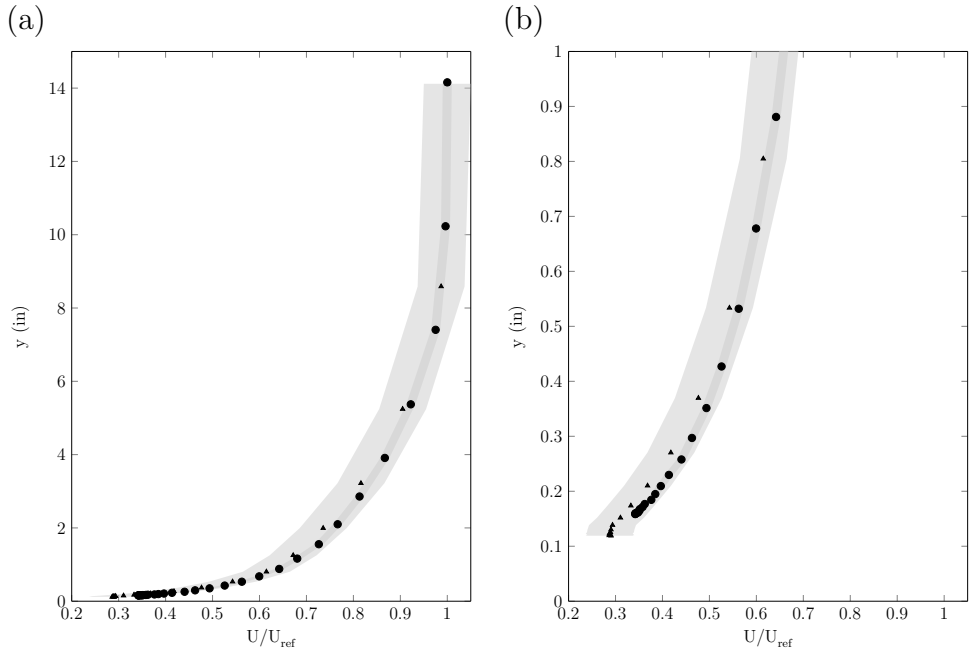

Figure B.12: Results for multi-height surface at 60-ms^{-1}: (a) Streamwise mean velocity profiles (b) Expanded streamwise mean velocity profiles.

The velocity data obtained on the multi-shape surface, from quadwire, single hotwire and flattened Pitot, are presented in figs. B.13 and B.14. The data were collected downstream the cylinder as shown in the top images of fig. 5.5. The top plots are the streamwise mean velocities U/U_{ref} with the plot on the right being a zoomed in version of the plot on the left. The bottom left plot is the streamwise normal Reynolds stress u^2/U_{ref}^2 and the bottom right plot is the zoomed in version of this. Note that there is only data from the hotwires in the bottom plots.

The data from the different probes appear to show good agreement for the mean velocities, except very close to the wall. On the other hand the Reynolds normal stress shows some divergence as far out as 3-inches from the wall, and as large as 15% at 60-ms^{-1}. This suggests that either the quadwire or the single hotwire are in error. From § 5.2.1 we know that the two quadwires agree well for this case. We also know that the uncertainty associated with the single hotwire is larger than that of the quadwire (see tables 2.2 and 2.3) and that the single hotwire has produced erroneous results during this experiment (see fig. B.10). Therefore we surmise that the quadwire produces the more trustworthy data, in this case.

Table B.12: Legend for figs. B.13 and B.14

●	quadwire results measured downstream cylinders
■	single hotwire results
▲	flattened Pitot results
▬	uncertainty bands for the data

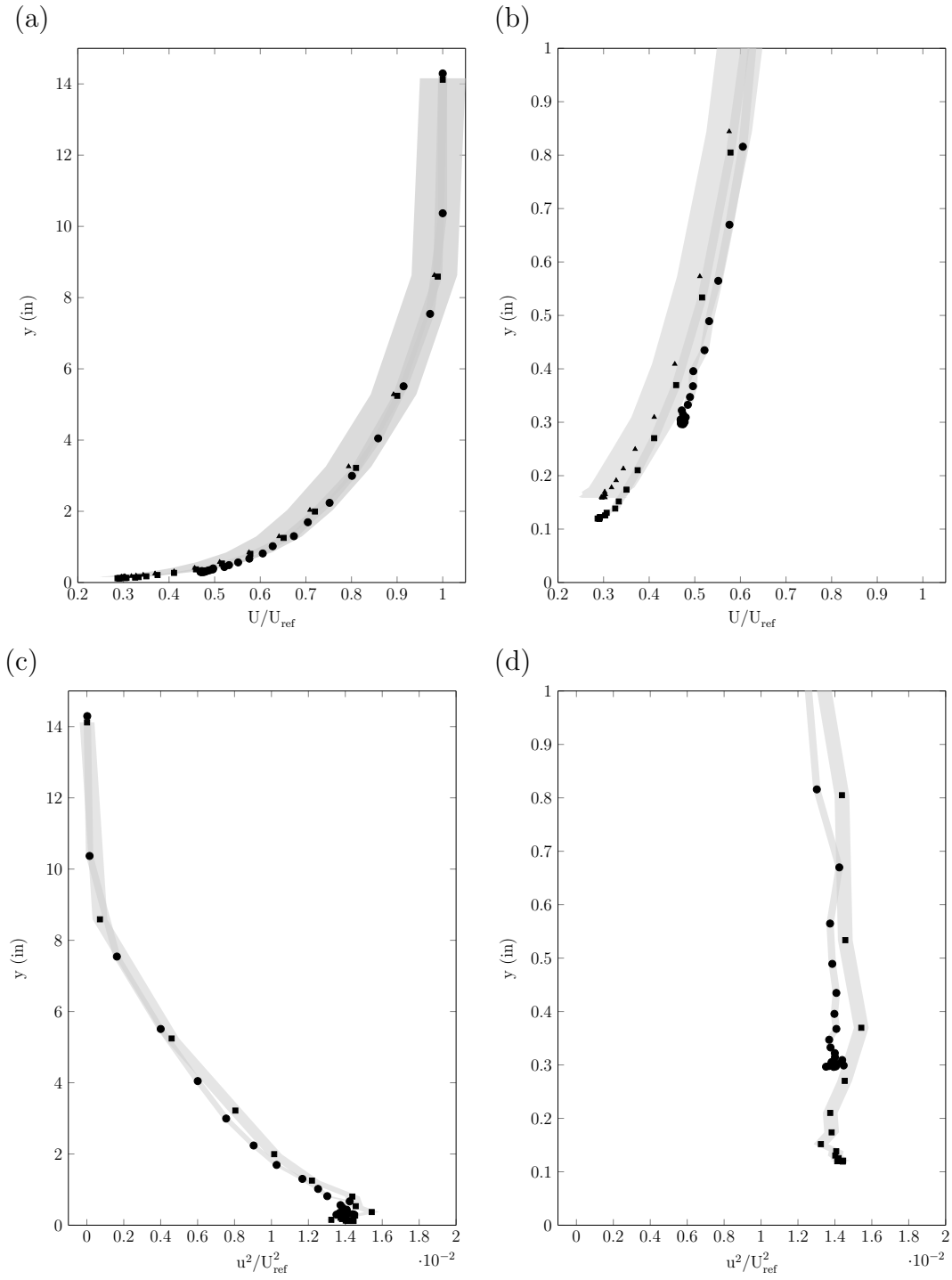

Figure B.13: Results for mixed-shape surface at 30-ms^{-1}: (a) Streamwise mean velocity profiles (b) Expanded streamwise mean velocity profiles (c) Streamwise normal Reynolds stress profiles (d) Expanded streamwise normal Reynolds stress profiles.

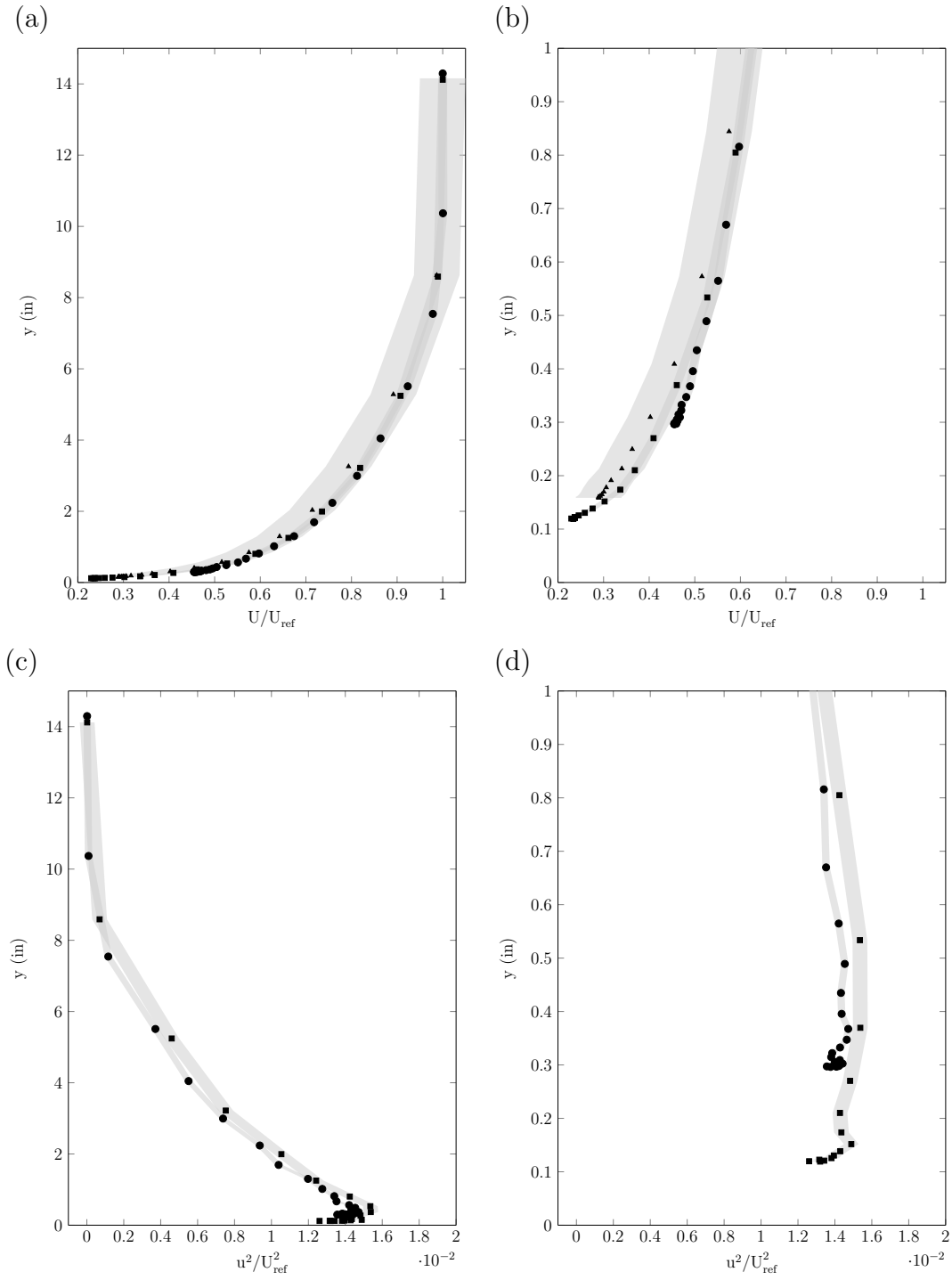

Figure B.14: Results for mixed-shape surface at 60-ms^{-1}: (a) Streamwise mean velocity profiles (b) Expanded streamwise mean velocity profiles (c) Streamwise normal Reynolds stress profiles (d) Expanded streamwise normal Reynolds stress profiles.

The quadwire data obtained on the intermediately spaced surface is shown in figs. B.15 and B.16. These measurements were all taken in approxiamtely the middle of a four element array, as shown in fig. 5.2. The top plots are the streamwise mean velocities U/U_{ref} with the plot on the right being a zoomed in version of the plot on the left. The bottom left plot is the streamwise normal Reynolds stress u^2/U_{ref}^2 and the bottom right plot is the zoomed in version of this. Note that there is only data from the hotwires in the bottom plots.

The data from the different probes show some agreement for the mean streamwise velocity. All variations are well within the uncertainty. The Reynolds normal stress however shows some divergence as far out as 5-inches from the wall, and as large as 20% at 30-ms^{-1}. The variations are actually smaller at 60-ms^{-1}. As in the case of the multi-shape surface, and for the same reasons, we surmise that the quadwire produces the more trustworthy data in this case.

Table B.13: Legend for figs. B.15 and B.16

●	quadwire results
■	single hotwire results
▲	flattened Pitot results
▬	uncertainty bands for the data

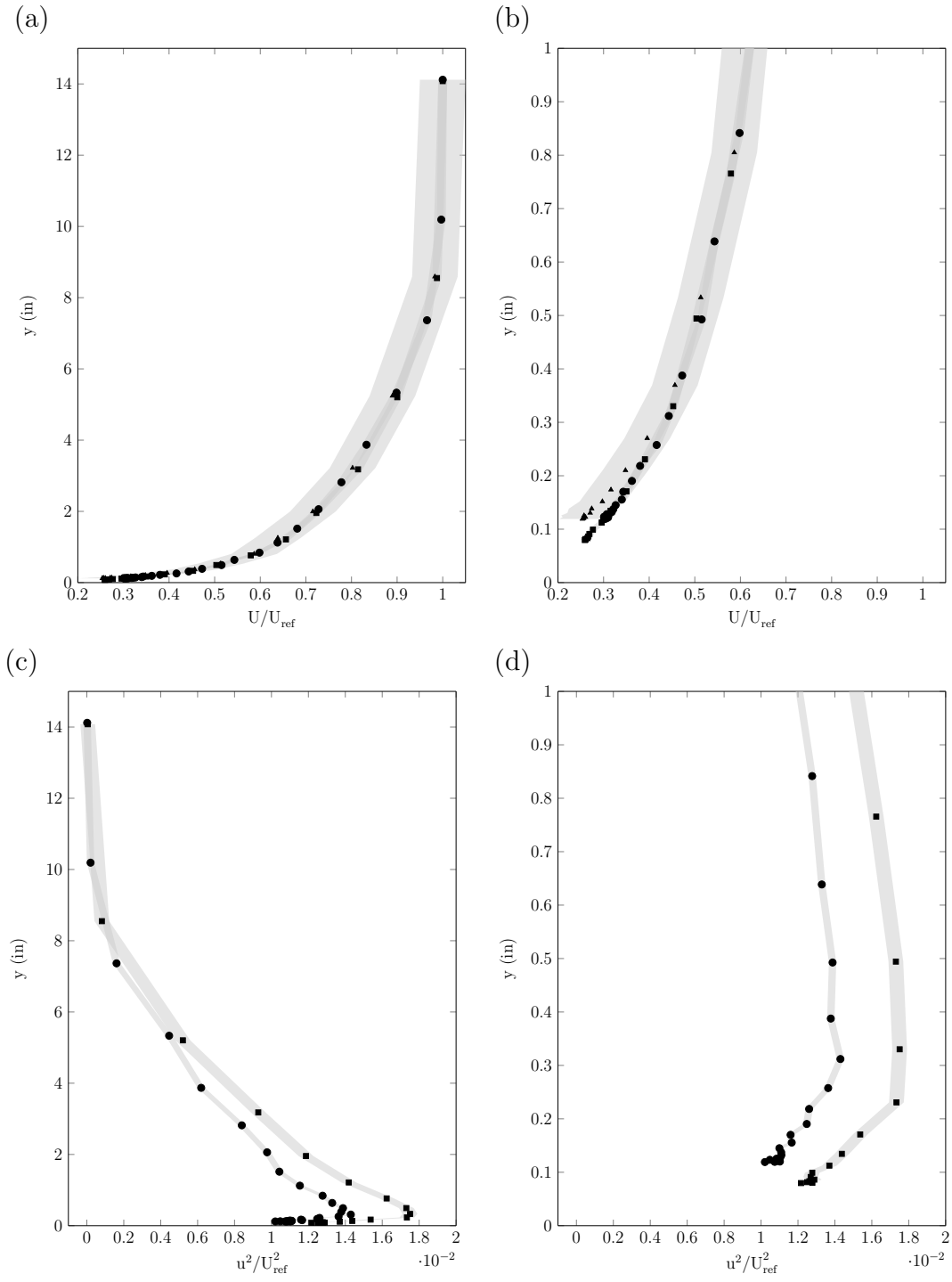

Figure B.15: Results for intermediately spaced surface at 30-ms^{-1}: (a) Streamwise mean velocity profiles (b) Expanded streamwise mean velocity profiles (c) Streamwise normal Reynolds stress profiles (d) Expanded streamwise normal Reynolds stress profiles.

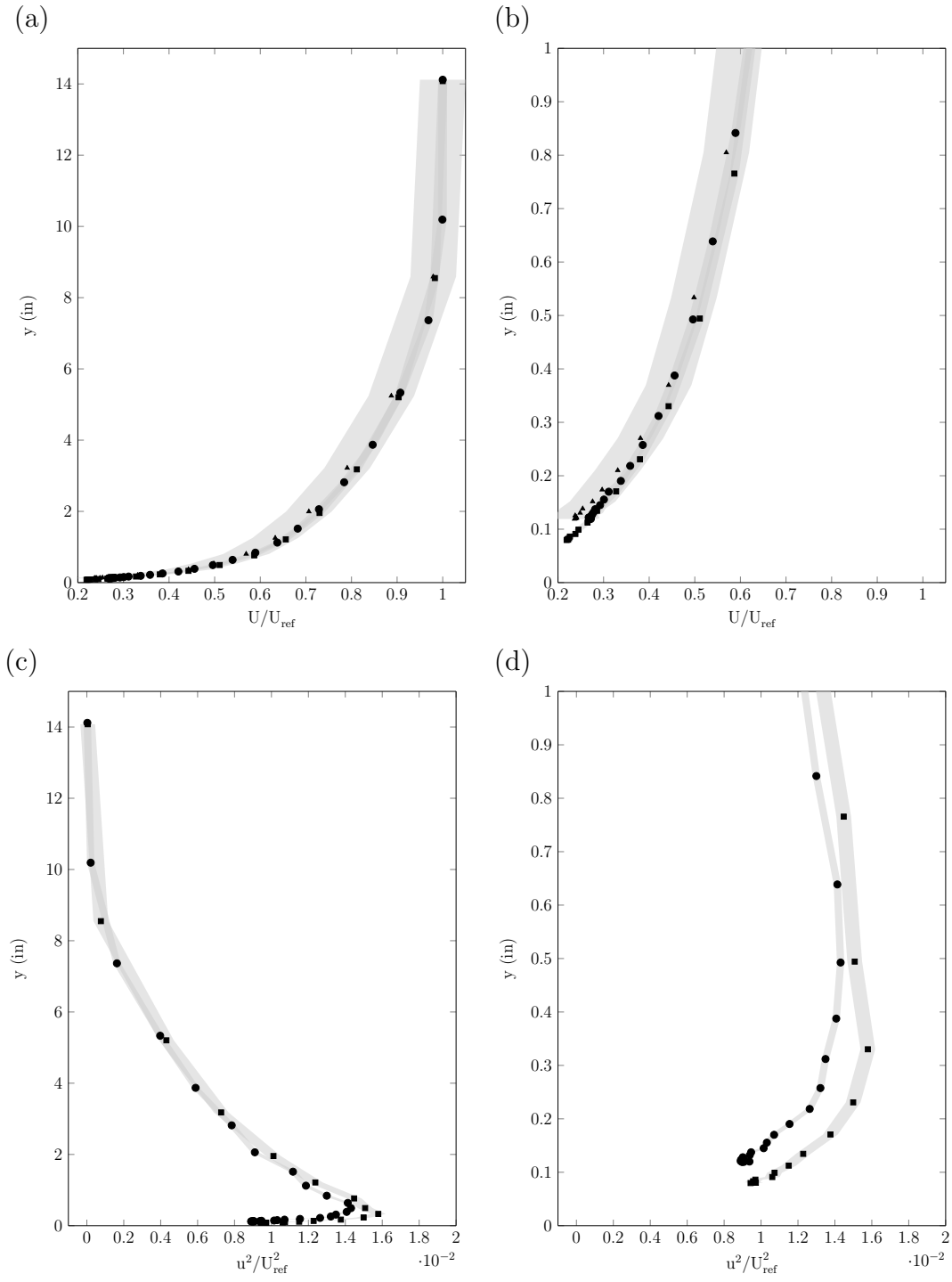

Figure B.16: Results for intermediately spaced surface at 60-ms^{-1}: (a) Streamwise mean velocity profiles (b) Expanded streamwise mean velocity profiles (c) Streamwise normal Reynolds stress profiles (d) Expanded streamwise normal Reynolds stress profiles.

The quadwire data obtained on the densely spaced surface is shown in figs. B.17 and B.18. These measurements were all taken in approxiamtely the middle of a four element array, as shown in fig. 5.3. The top plots are the streamwise mean velocities U/U_{ref} with the plot on the right being a zoomed in version of the plot on the left. The bottom left plot is the streamwise normal Reynolds stress u^2/U_{ref}^2 and the bottom right plot is the zoomed in version of this. Note that there is only data from the hotwires in the bottom plots.

The data from the different probes show fair agreement, within the uncertainty bounds, for the mean streamwise velocity. Variations in the Reynolds normal stress, as with the two previous surfaces, are signifcant. The results diverge as far out as 2-inches from the wall, and are as large as 13% at 60-ms^{-1}. We shall again hypothesize that the quadwire produces the more trustworthy data in this case, for the same reasons discussed for the multi-shape surface and intermediately-spaced surface.

Table B.14: Legend for figs. B.15 and B.16

●	quadwire results
■	single hotwire results
▲	flattened Pitot results
▬	uncertainty bands for the data

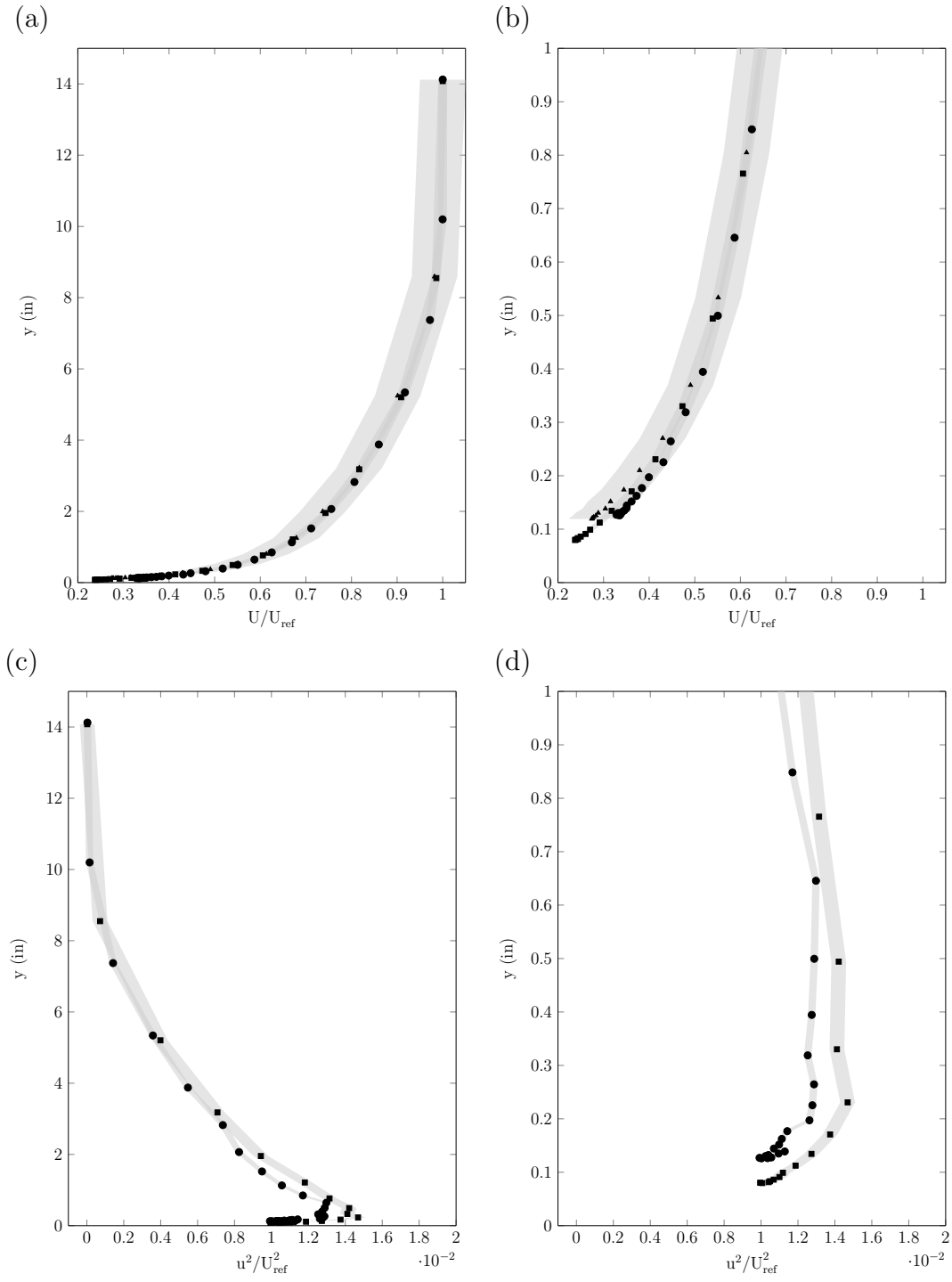

Figure B.17: Results for densely spaced surface at 30-ms^{-1}: (a) Streamwise mean velocity profiles (b) Expanded streamwise mean velocity profiles (c) Streamwise normal Reynolds stress profiles (d) Expanded streamwise normal Reynolds stress profiles.

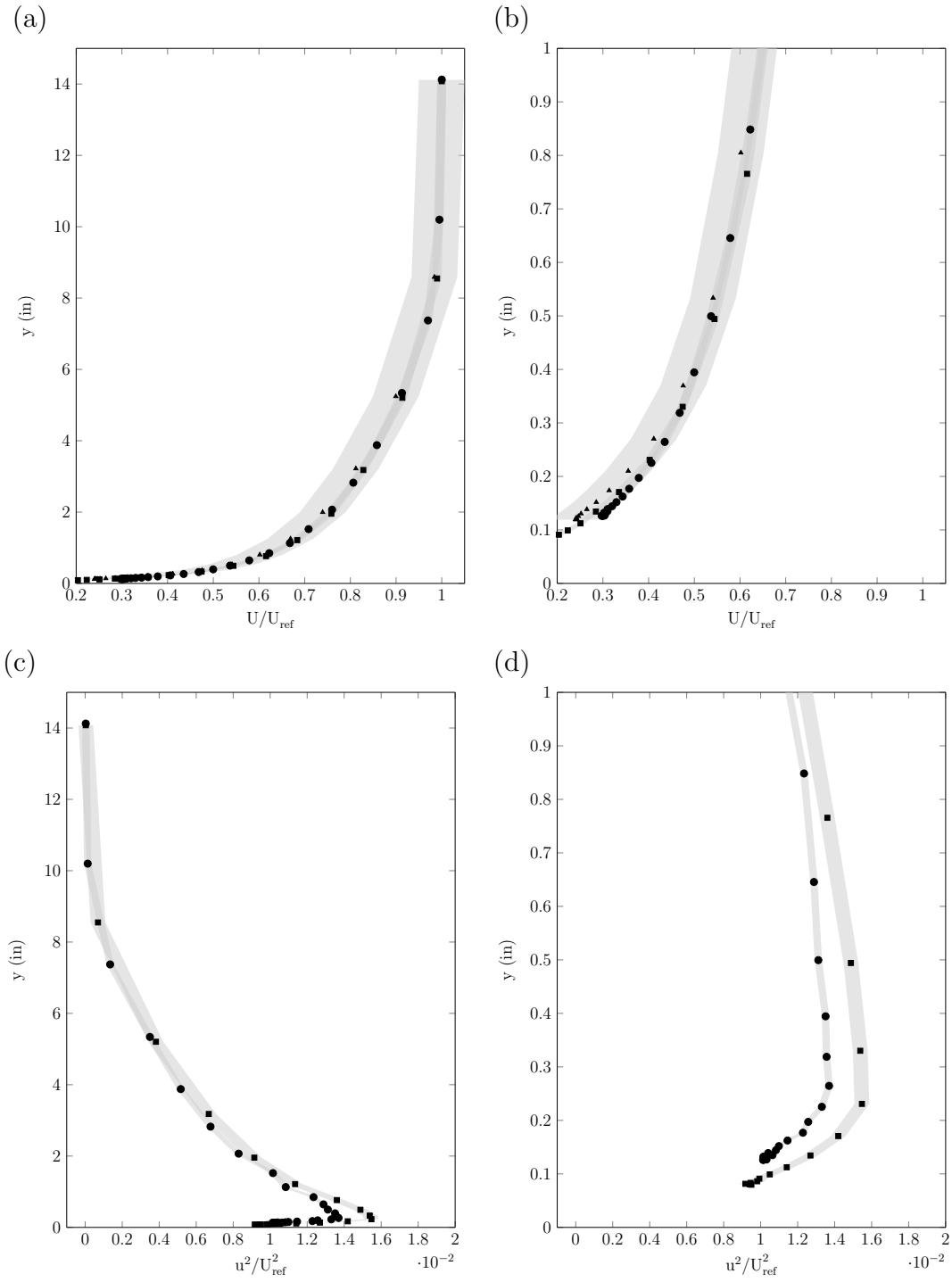

Figure B.18: Results for densely spaced surface at 60-ms^{-1}: (a) Streamwise mean velocity profiles (b) Expanded streamwise mean velocity profiles (c) Streamwise normal Reynolds stress profiles (d) Expanded streamwise normal Reynolds stress profiles.

C. Space-Time Correlations: All Data

This chapter includes the full set of contour maps showing the coherence and correlations for the streamwise and spanwise array of microphones. Each case was tested at speeds from 30-ms^{-1} to 70-ms^{-1}. Refer to chapter 4 for a discussion of these results.

C.1 Coherence: Streamwise Array of Microphones

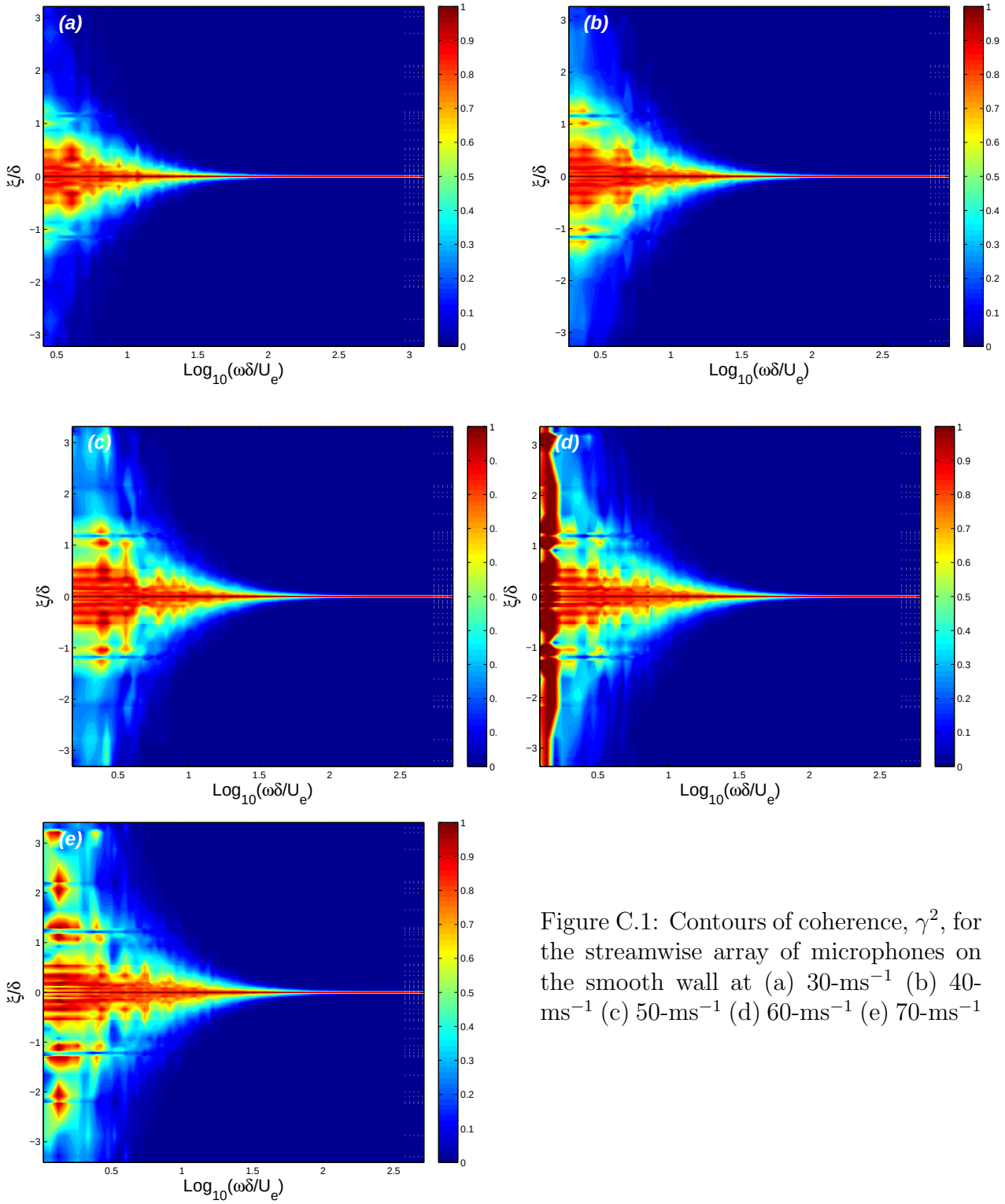

Figure C.1: Contours of coherence, γ^2, for the streamwise array of microphones on the smooth wall at (a) 30-ms^{-1} (b) 40-ms^{-1} (c) 50-ms^{-1} (d) 60-ms^{-1} (e) 70-ms^{-1}

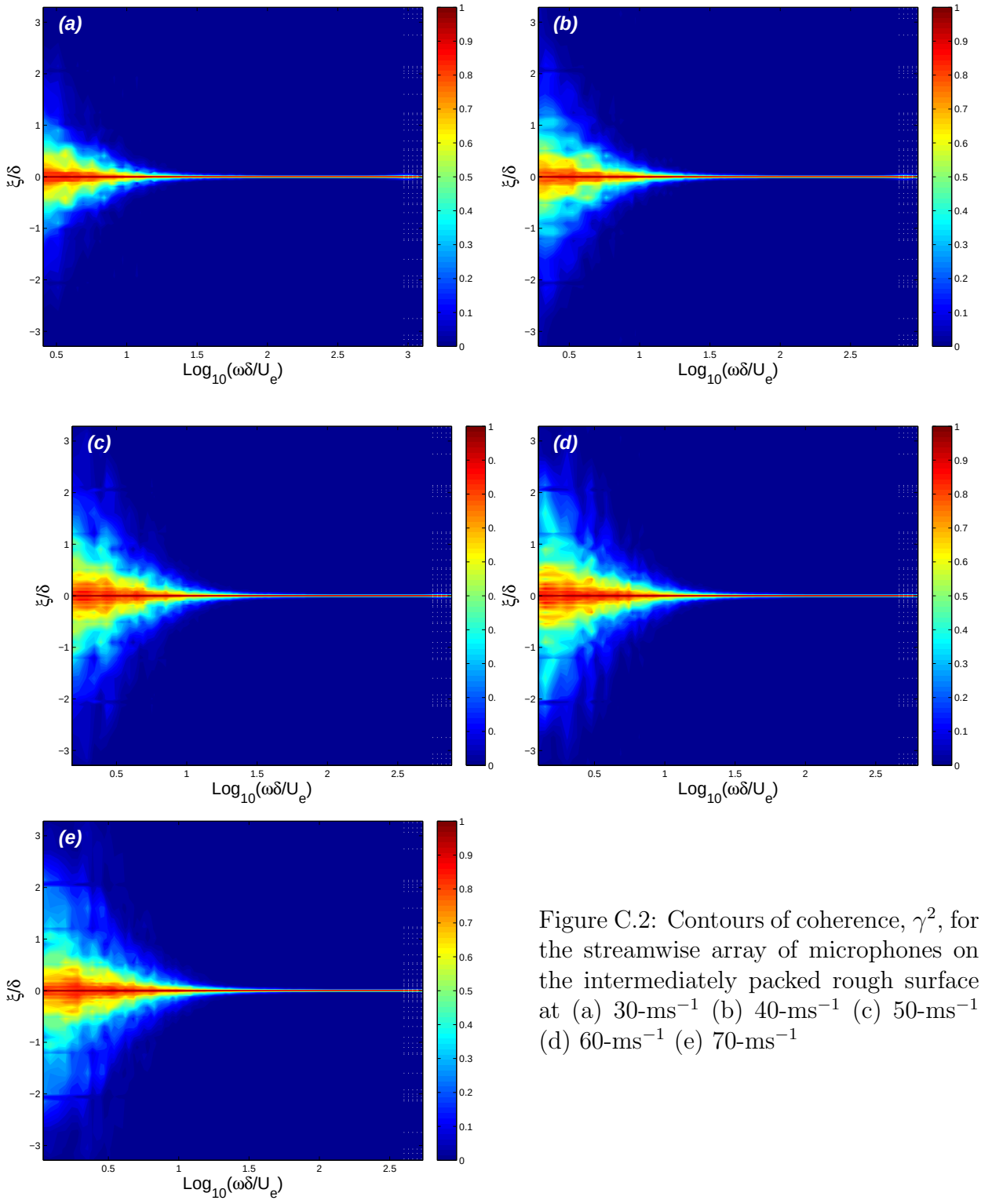

Figure C.2: Contours of coherence, γ^2, for the streamwise array of microphones on the intermediately packed rough surface at (a) 30-ms^{-1} (b) 40-ms^{-1} (c) 50-ms^{-1} (d) 60-ms^{-1} (e) 70-ms^{-1}

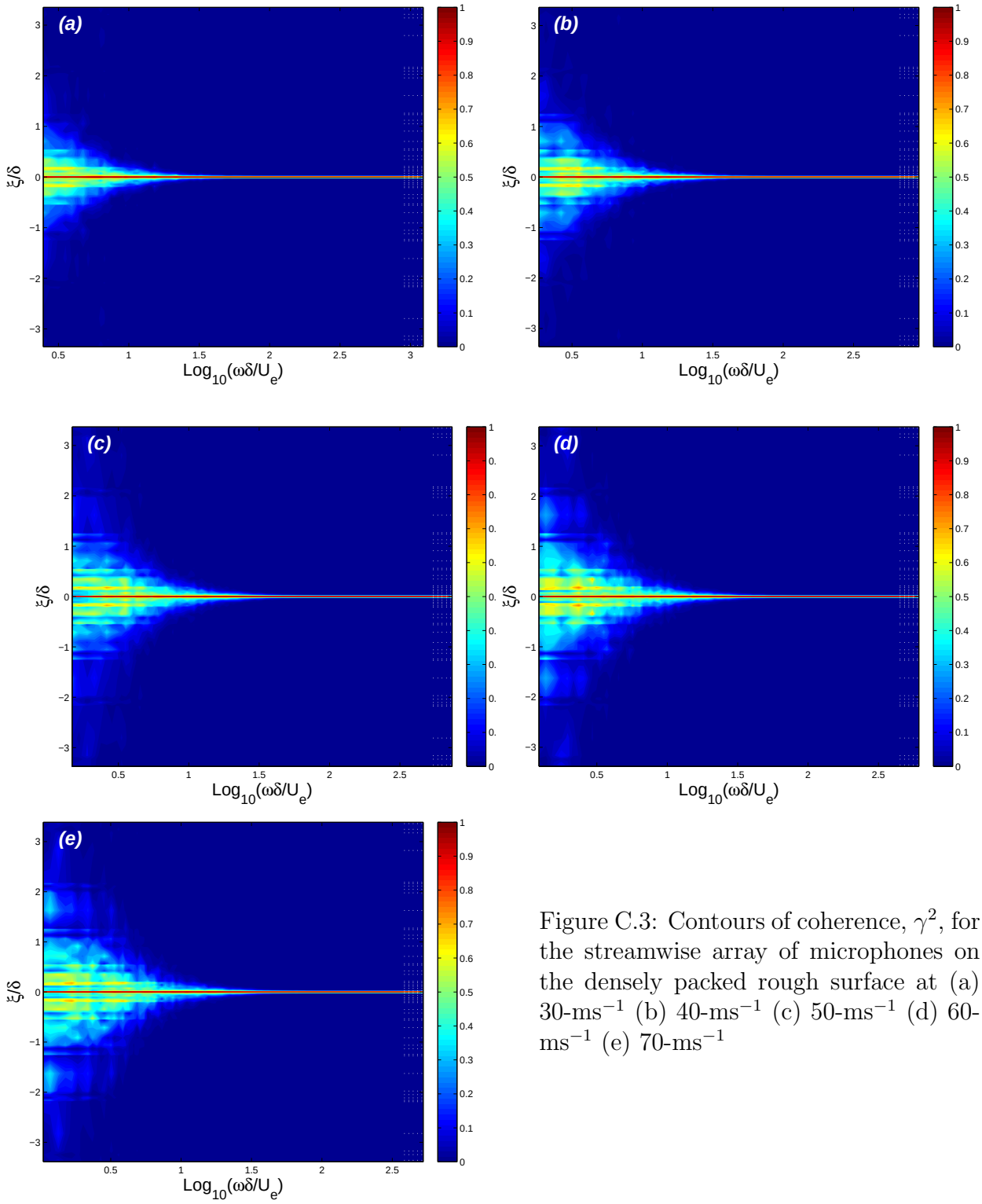

Figure C.3: Contours of coherence, γ^2, for the streamwise array of microphones on the densely packed rough surface at (a) 30-ms^{-1} (b) 40-ms^{-1} (c) 50-ms^{-1} (d) 60-ms^{-1} (e) 70-ms^{-1}

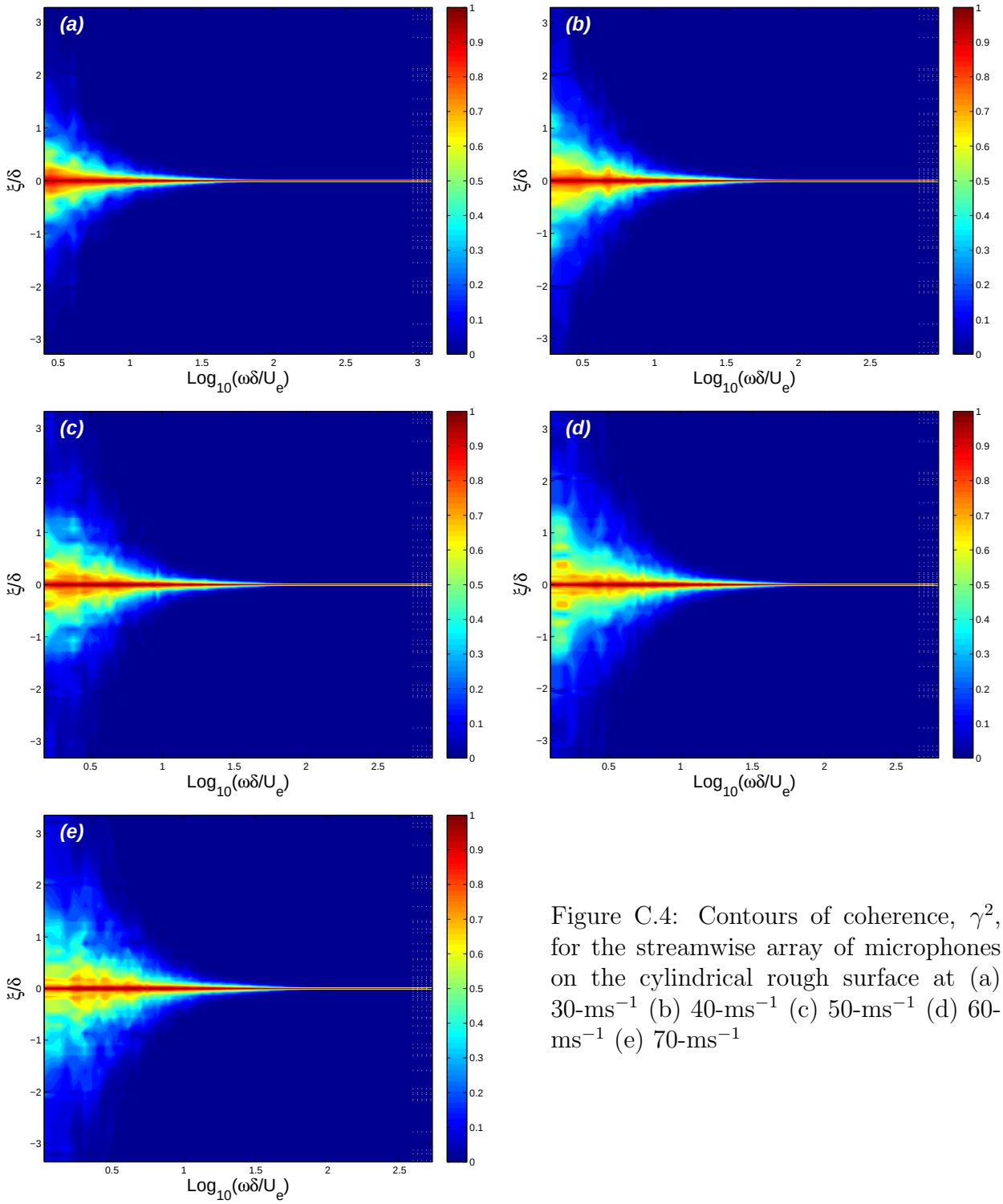

Figure C.4: Contours of coherence, γ^2, for the streamwise array of microphones on the cylindrical rough surface at (a) 30-ms^{-1} (b) 40-ms^{-1} (c) 50-ms^{-1} (d) 60-ms^{-1} (e) 70-ms^{-1}

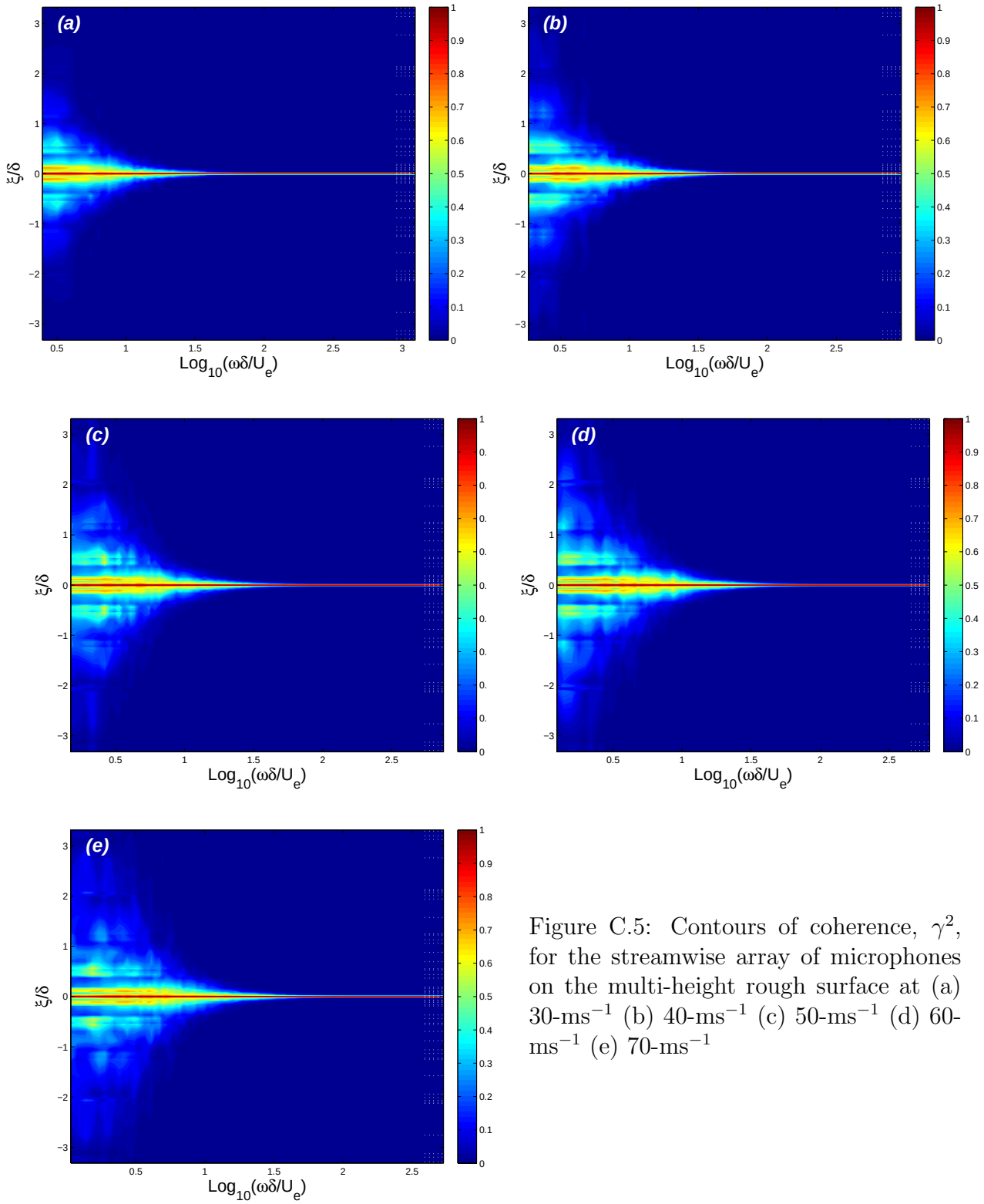

Figure C.5: Contours of coherence, γ^2, for the streamwise array of microphones on the multi-height rough surface at (a) 30-ms^{-1} (b) 40-ms^{-1} (c) 50-ms^{-1} (d) 60-ms^{-1} (e) 70-ms^{-1}

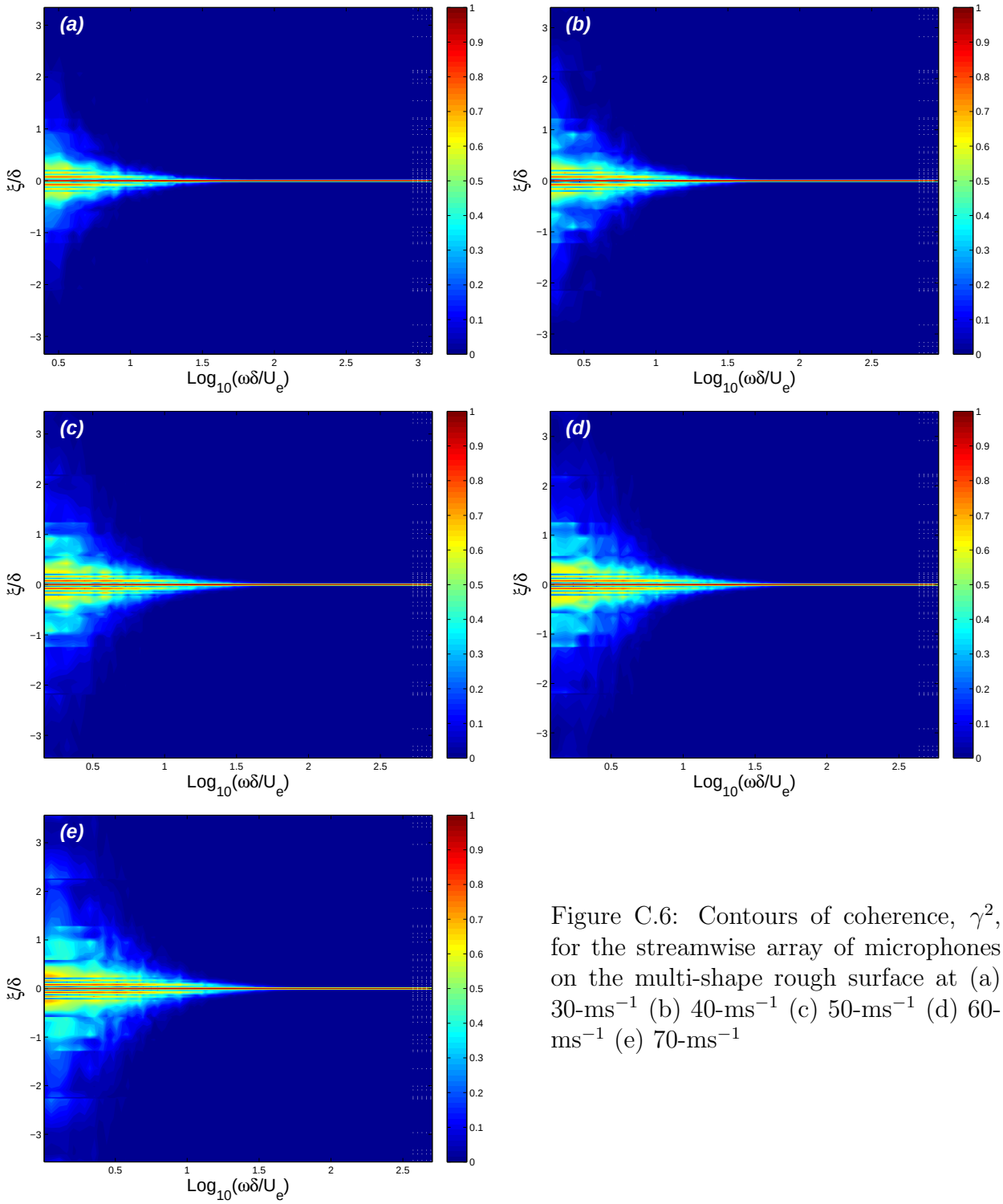

Figure C.6: Contours of coherence, γ^2, for the streamwise array of microphones on the multi-shape rough surface at (a) 30-ms^{-1} (b) 40-ms^{-1} (c) 50-ms^{-1} (d) 60-ms^{-1} (e) 70-ms^{-1}

C.2 Coherence: Spanwise Array of Microphones

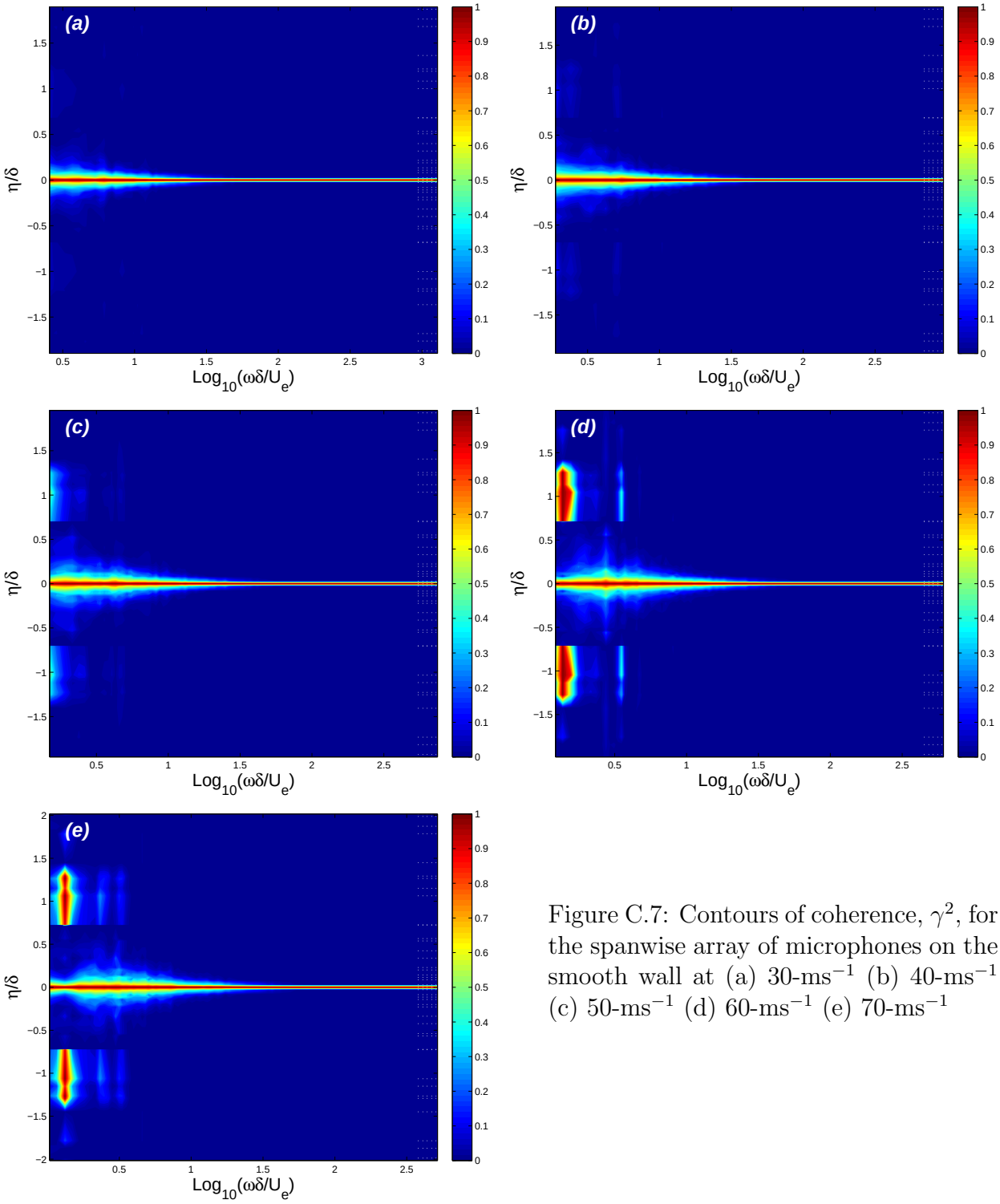

Figure C.7: Contours of coherence, γ^2, for the spanwise array of microphones on the smooth wall at (a) 30-ms^{-1} (b) 40-ms^{-1} (c) 50-ms^{-1} (d) 60-ms^{-1} (e) 70-ms^{-1}

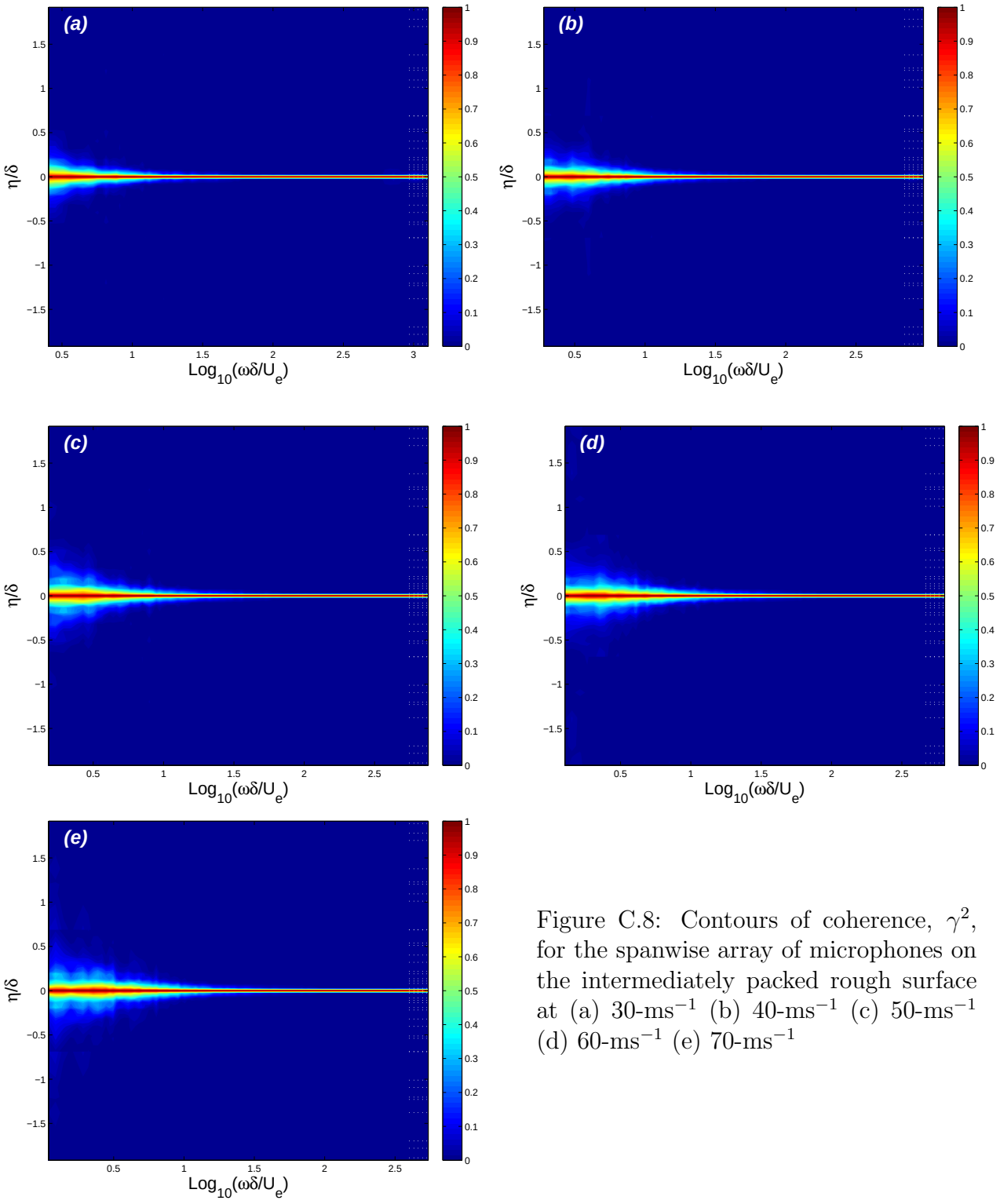

Figure C.8: Contours of coherence, γ^2, for the spanwise array of microphones on the intermediately packed rough surface at (a) 30-ms^{-1} (b) 40-ms^{-1} (c) 50-ms^{-1} (d) 60-ms^{-1} (e) 70-ms^{-1}

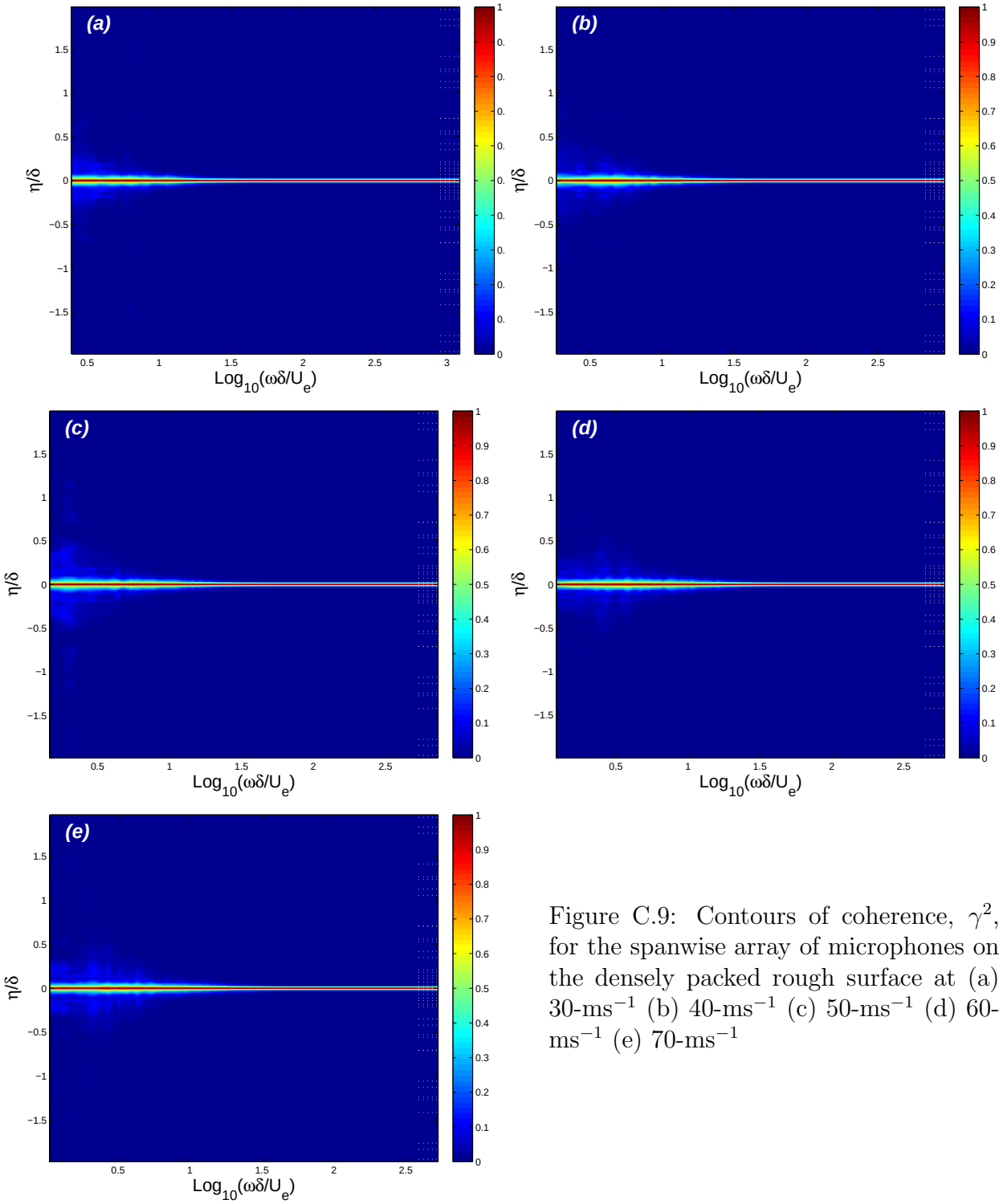

Figure C.9: Contours of coherence, γ^2, for the spanwise array of microphones on the densely packed rough surface at (a) 30-ms^{-1} (b) 40-ms^{-1} (c) 50-ms^{-1} (d) 60-ms^{-1} (e) 70-ms^{-1}

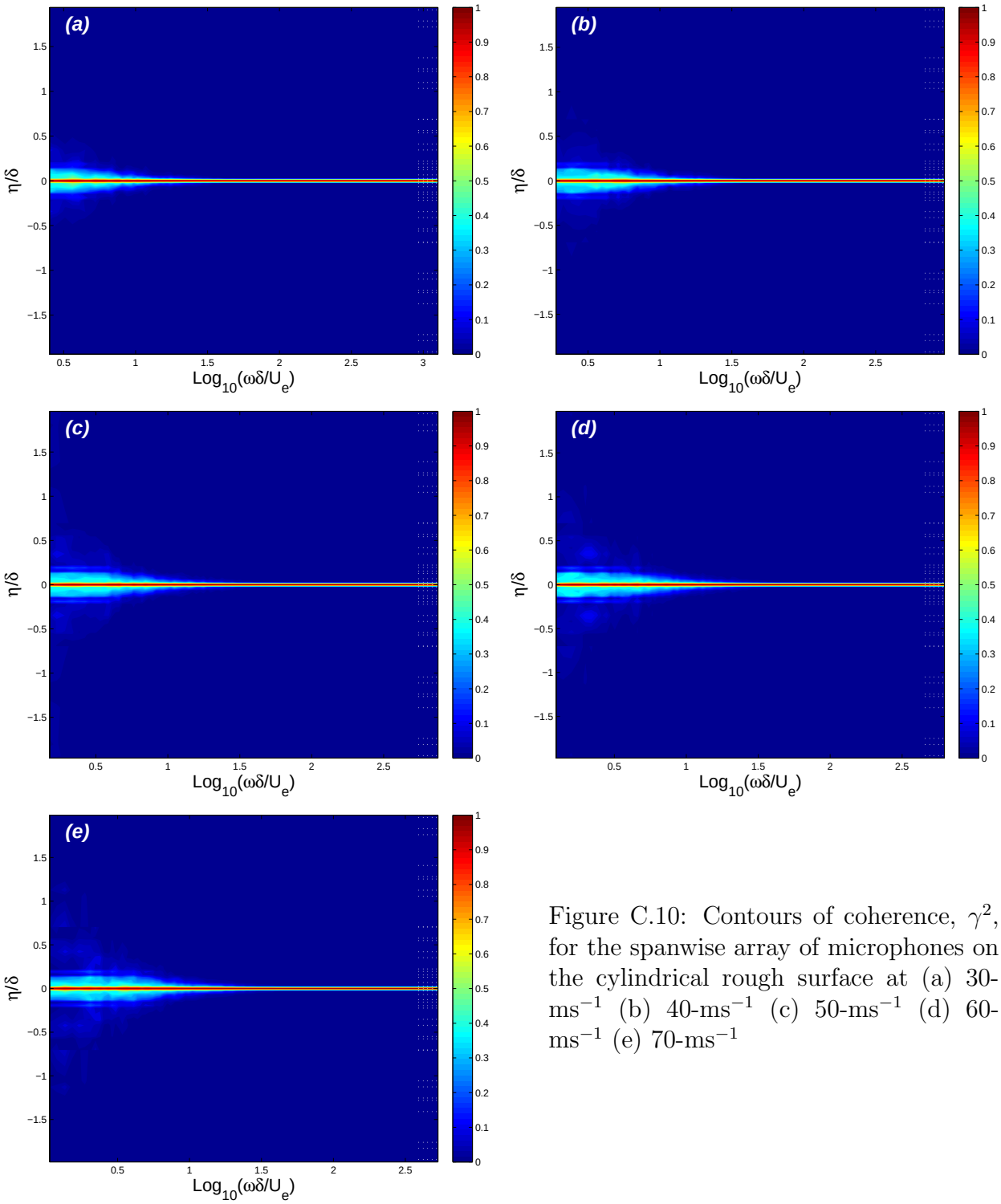

Figure C.10: Contours of coherence, γ^2, for the spanwise array of microphones on the cylindrical rough surface at (a) 30-ms^{-1} (b) 40-ms^{-1} (c) 50-ms^{-1} (d) 60-ms^{-1} (e) 70-ms^{-1}

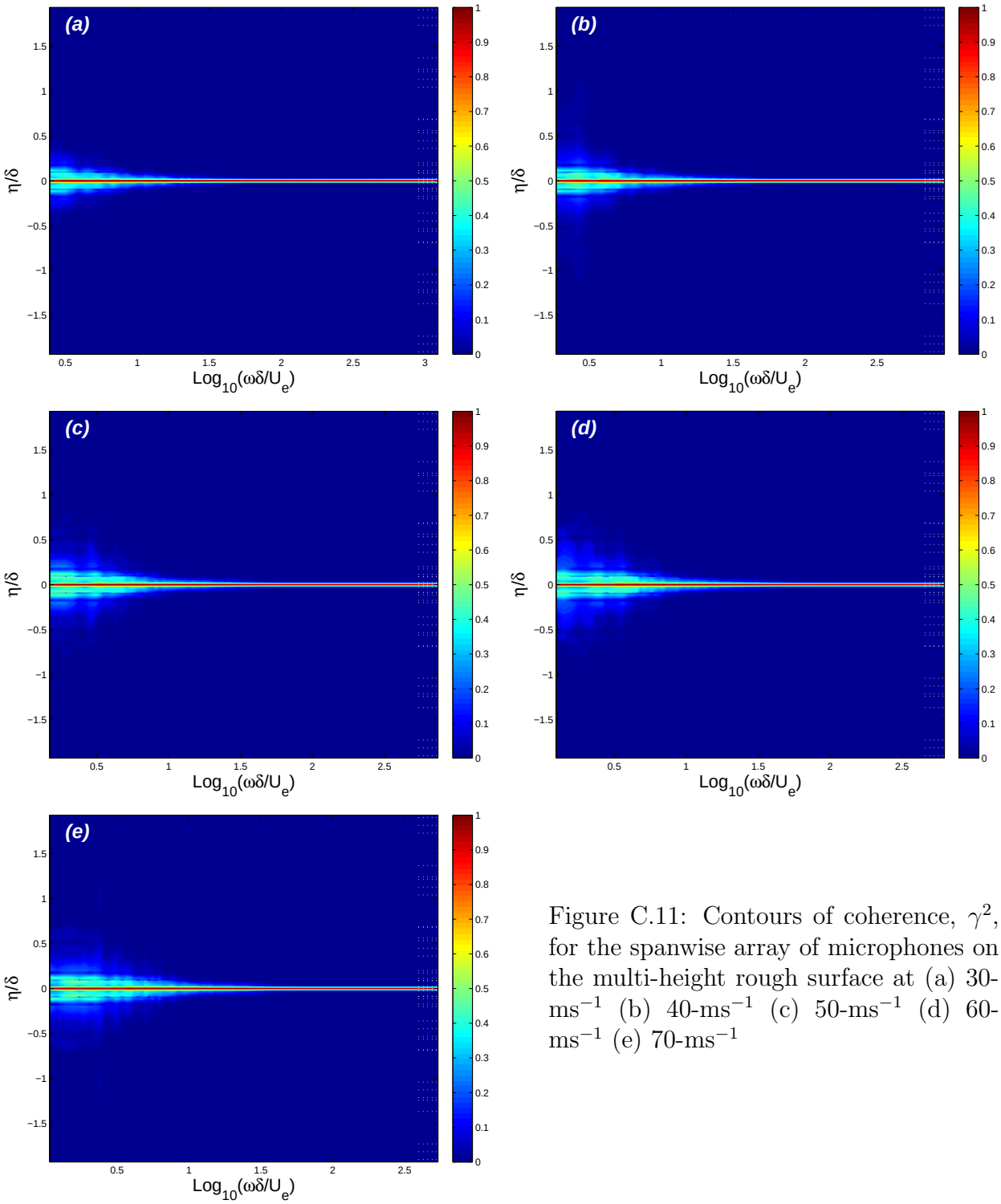

Figure C.11: Contours of coherence, γ^2, for the spanwise array of microphones on the multi-height rough surface at (a) 30-ms^{-1} (b) 40-ms^{-1} (c) 50-ms^{-1} (d) 60-ms^{-1} (e) 70-ms^{-1}

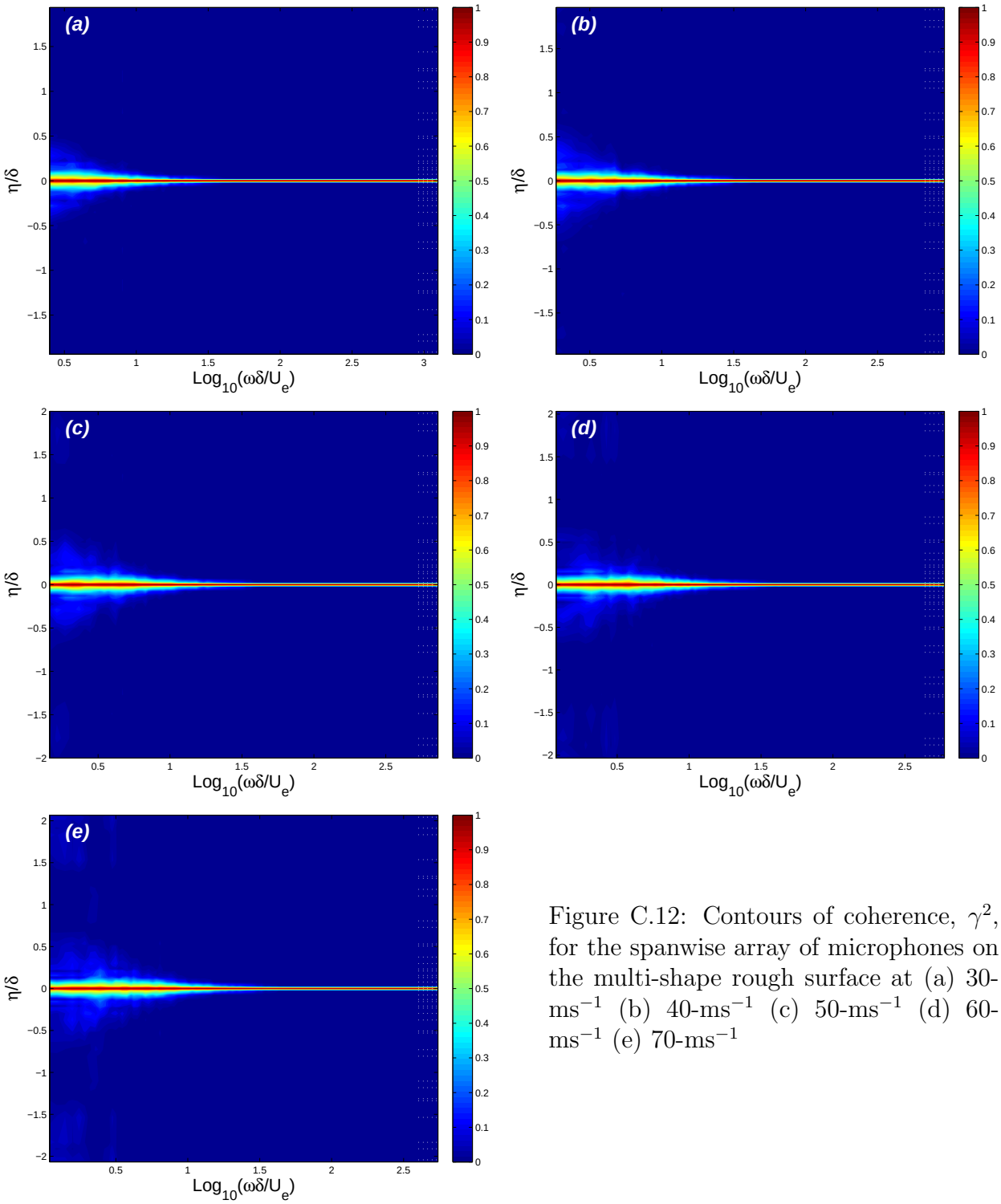

Figure C.12: Contours of coherence, γ^2, for the spanwise array of microphones on the multi-shape rough surface at (a) 30-ms^{-1} (b) 40-ms^{-1} (c) 50-ms^{-1} (d) 60-ms^{-1} (e) 70-ms^{-1}

C.3 Space-Time Correlations: Streamwise Array of Microphones

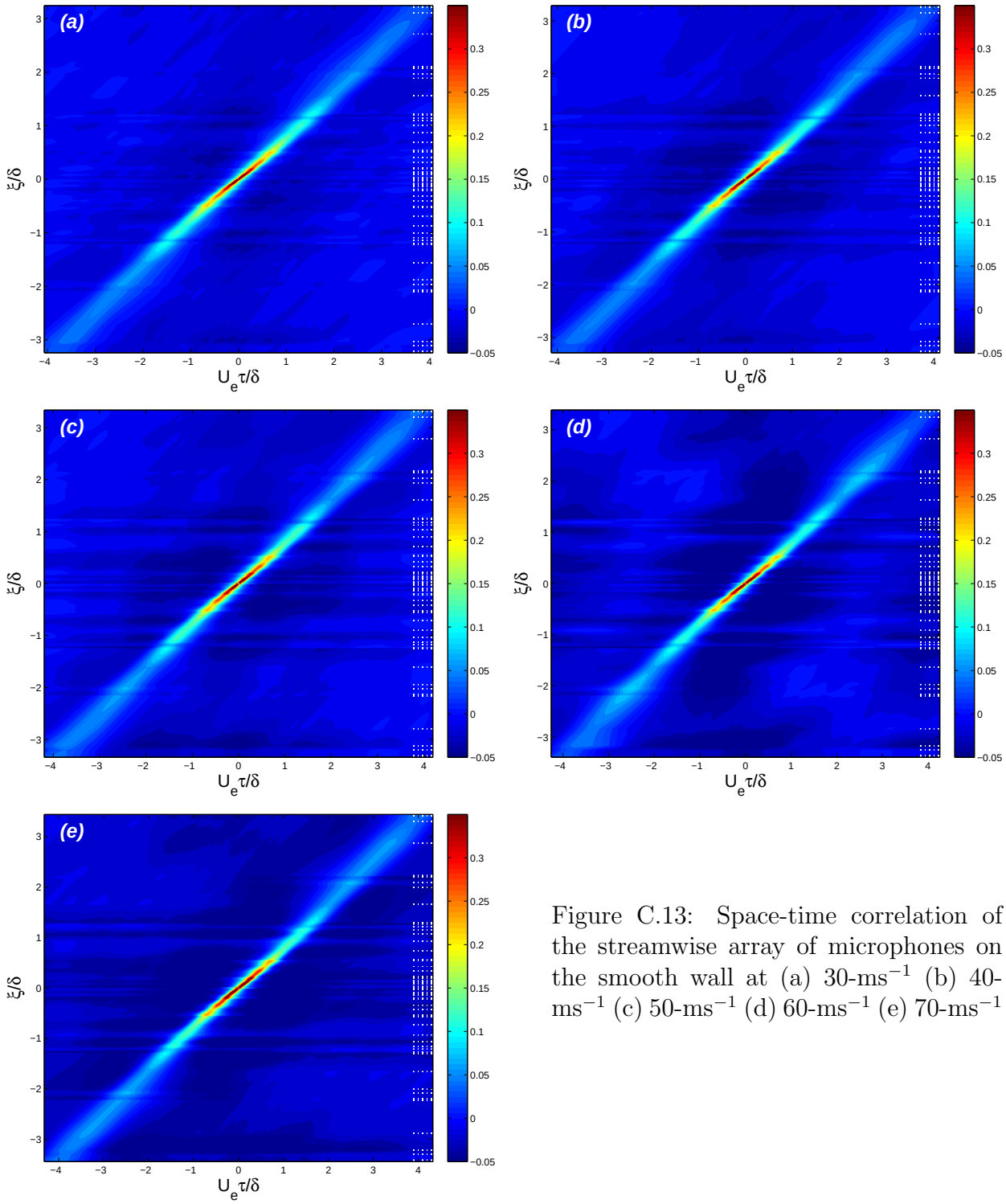

Figure C.13: Space-time correlation of the streamwise array of microphones on the smooth wall at (a) 30-ms^{-1} (b) 40-ms^{-1} (c) 50-ms^{-1} (d) 60-ms^{-1} (e) 70-ms^{-1}

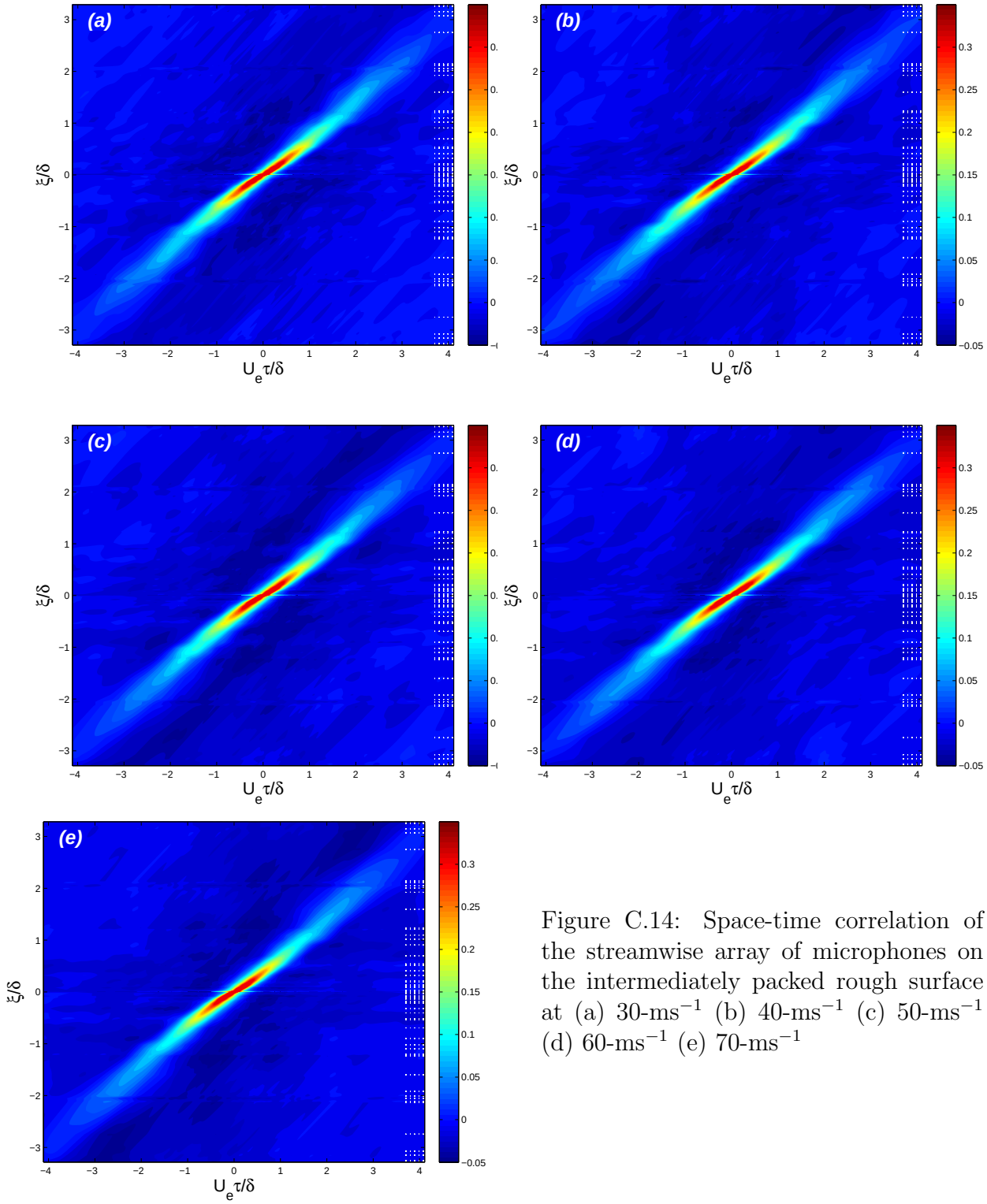

Figure C.14: Space-time correlation of the streamwise array of microphones on the intermediately packed rough surface at (a) 30-ms^{-1} (b) 40-ms^{-1} (c) 50-ms^{-1} (d) 60-ms^{-1} (e) 70-ms^{-1}

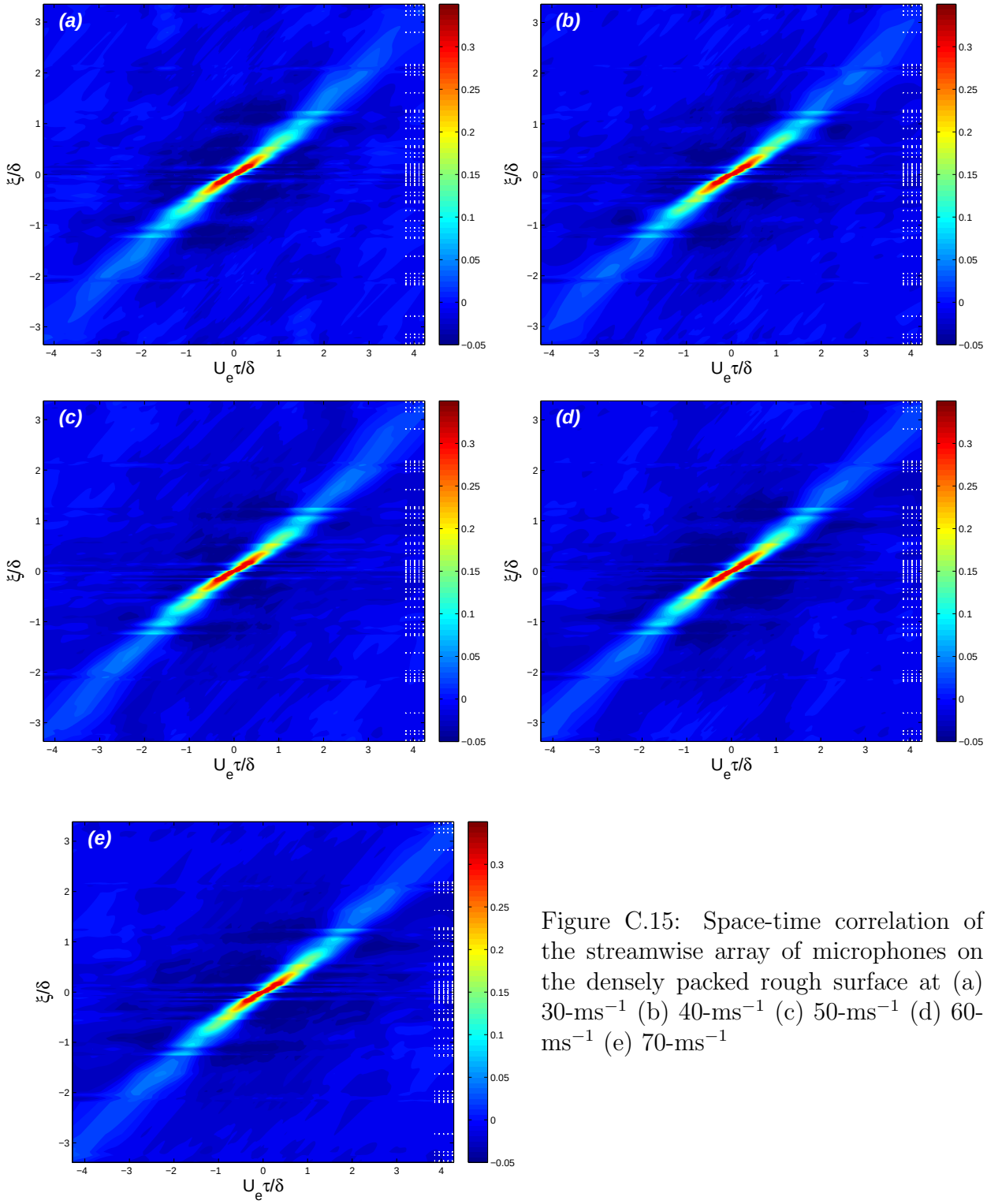

Figure C.15: Space-time correlation of the streamwise array of microphones on the densely packed rough surface at (a) 30-ms^{-1} (b) 40-ms^{-1} (c) 50-ms^{-1} (d) 60-ms^{-1} (e) 70-ms^{-1}

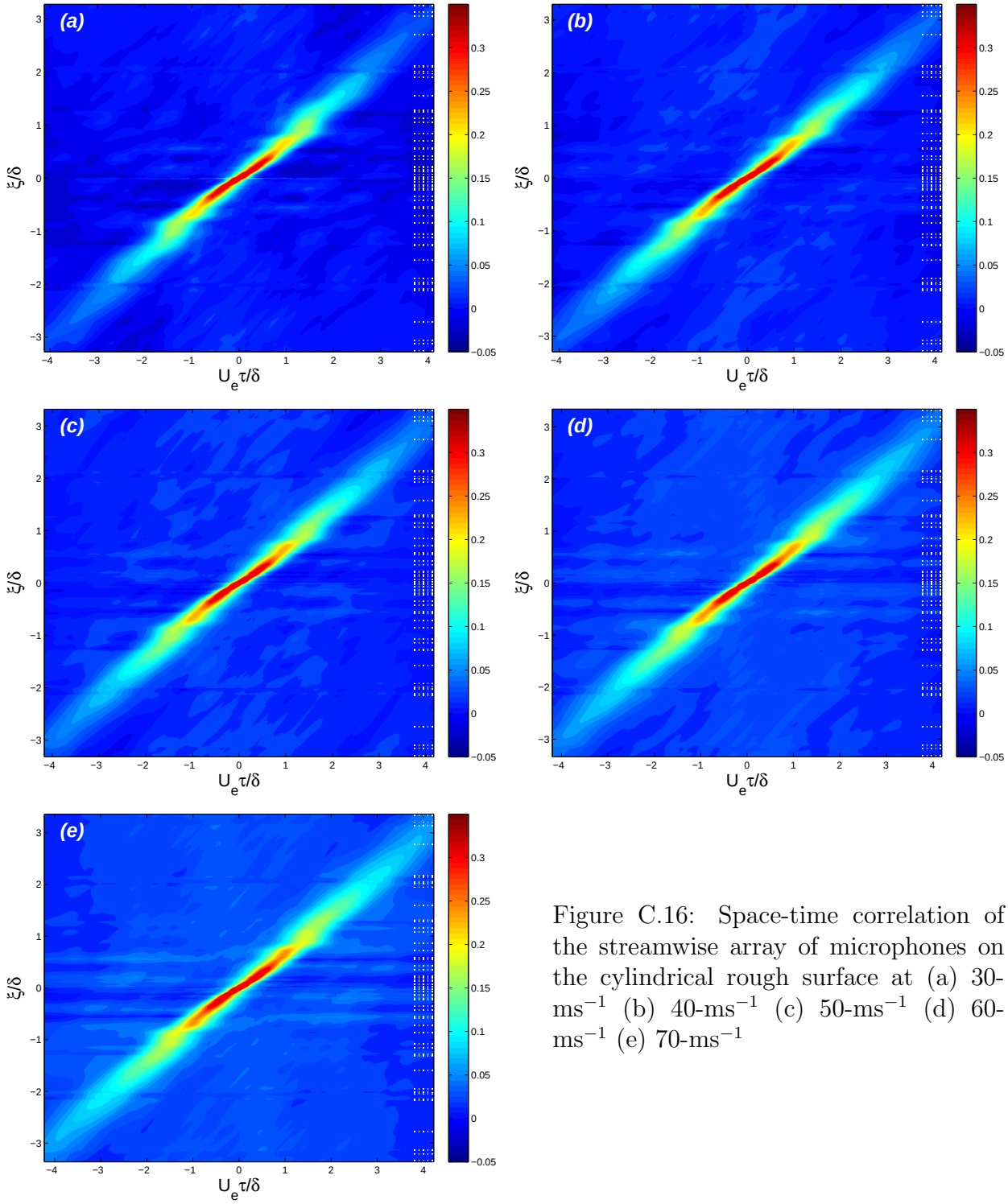

Figure C.16: Space-time correlation of the streamwise array of microphones on the cylindrical rough surface at (a) 30-ms^{-1} (b) 40-ms^{-1} (c) 50-ms^{-1} (d) 60-ms^{-1} (e) 70-ms^{-1}

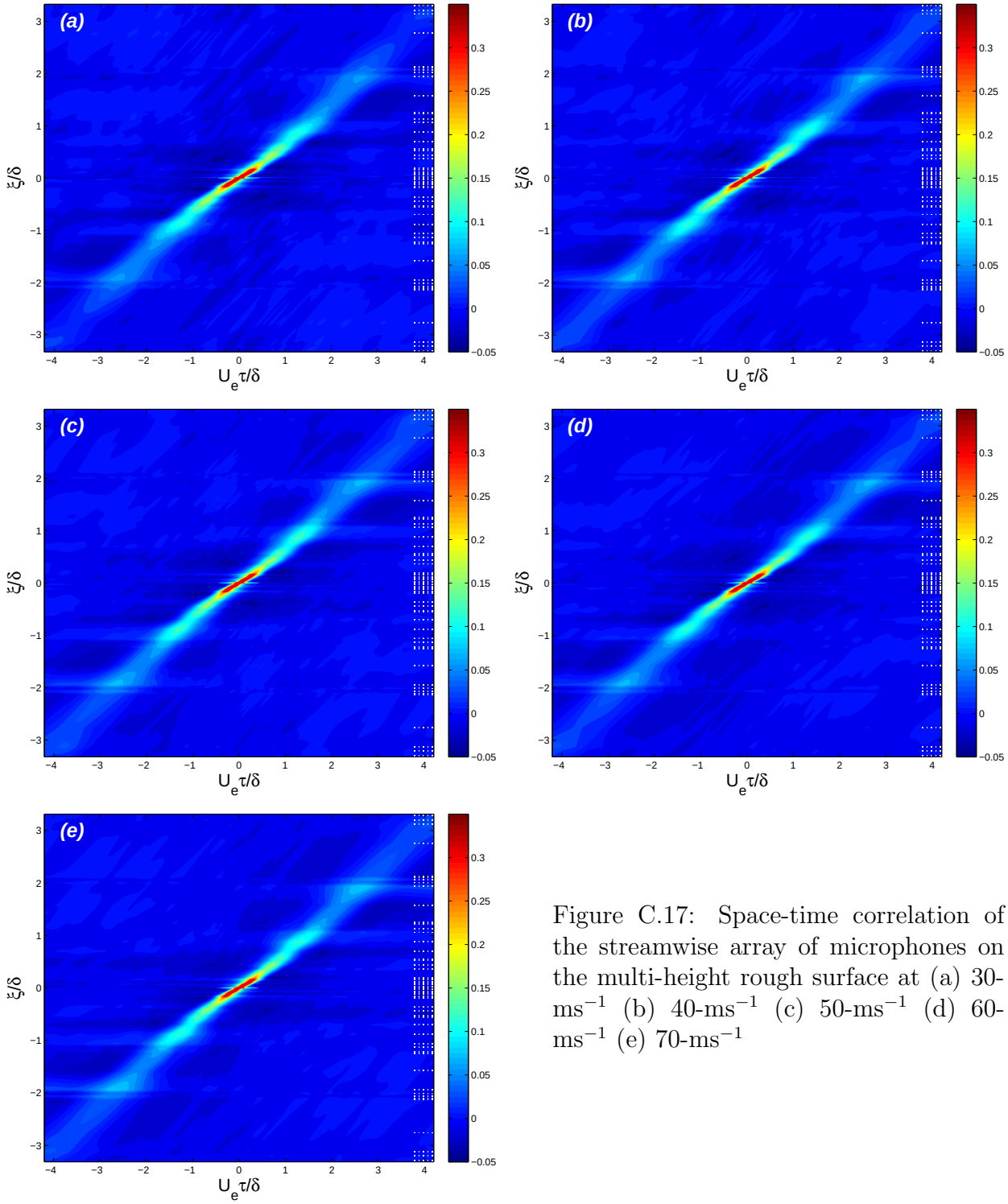

Figure C.17: Space-time correlation of the streamwise array of microphones on the multi-height rough surface at (a) 30-ms^{-1} (b) 40-ms^{-1} (c) 50-ms^{-1} (d) 60-ms^{-1} (e) 70-ms^{-1}

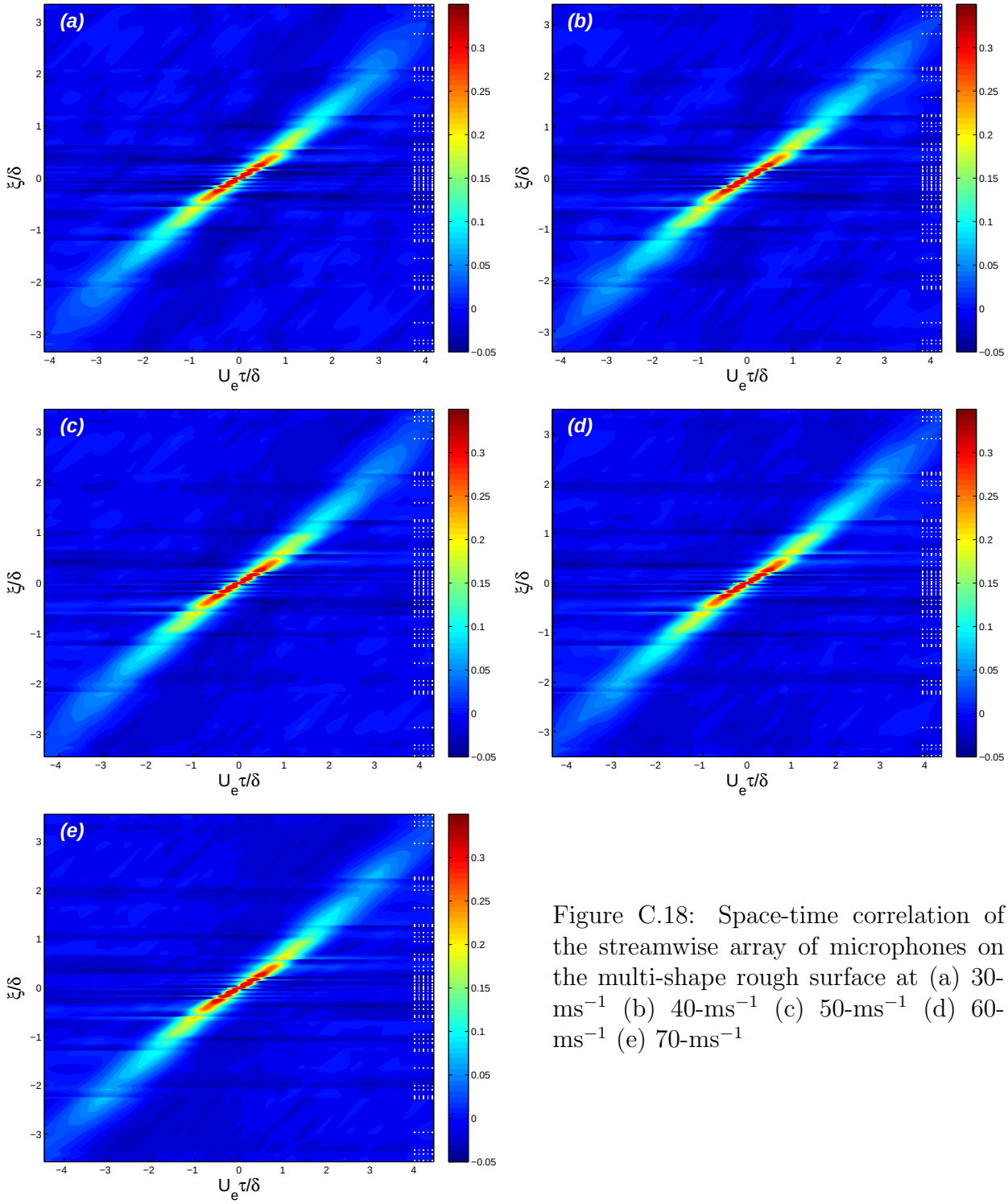

Figure C.18: Space-time correlation of the streamwise array of microphones on the multi-shape rough surface at (a) 30-ms^{-1} (b) 40-ms^{-1} (c) 50-ms^{-1} (d) 60-ms^{-1} (e) 70-ms^{-1}

C.4 Space-Time Correlations: Spanwise Array of Microphones

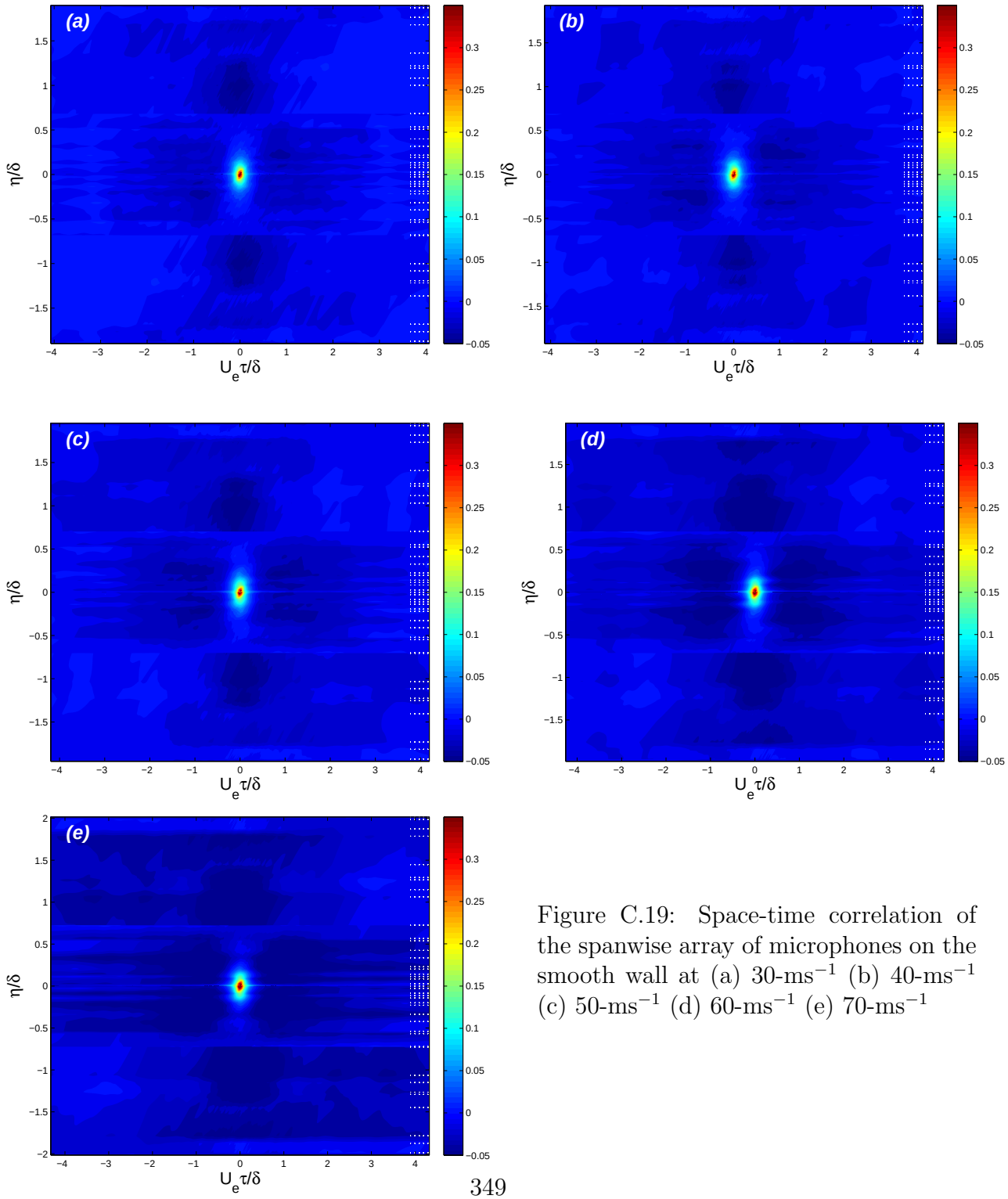

Figure C.19: Space-time correlation of the spanwise array of microphones on the smooth wall at (a) 30-ms^{-1} (b) 40-ms^{-1} (c) 50-ms^{-1} (d) 60-ms^{-1} (e) 70-ms^{-1}

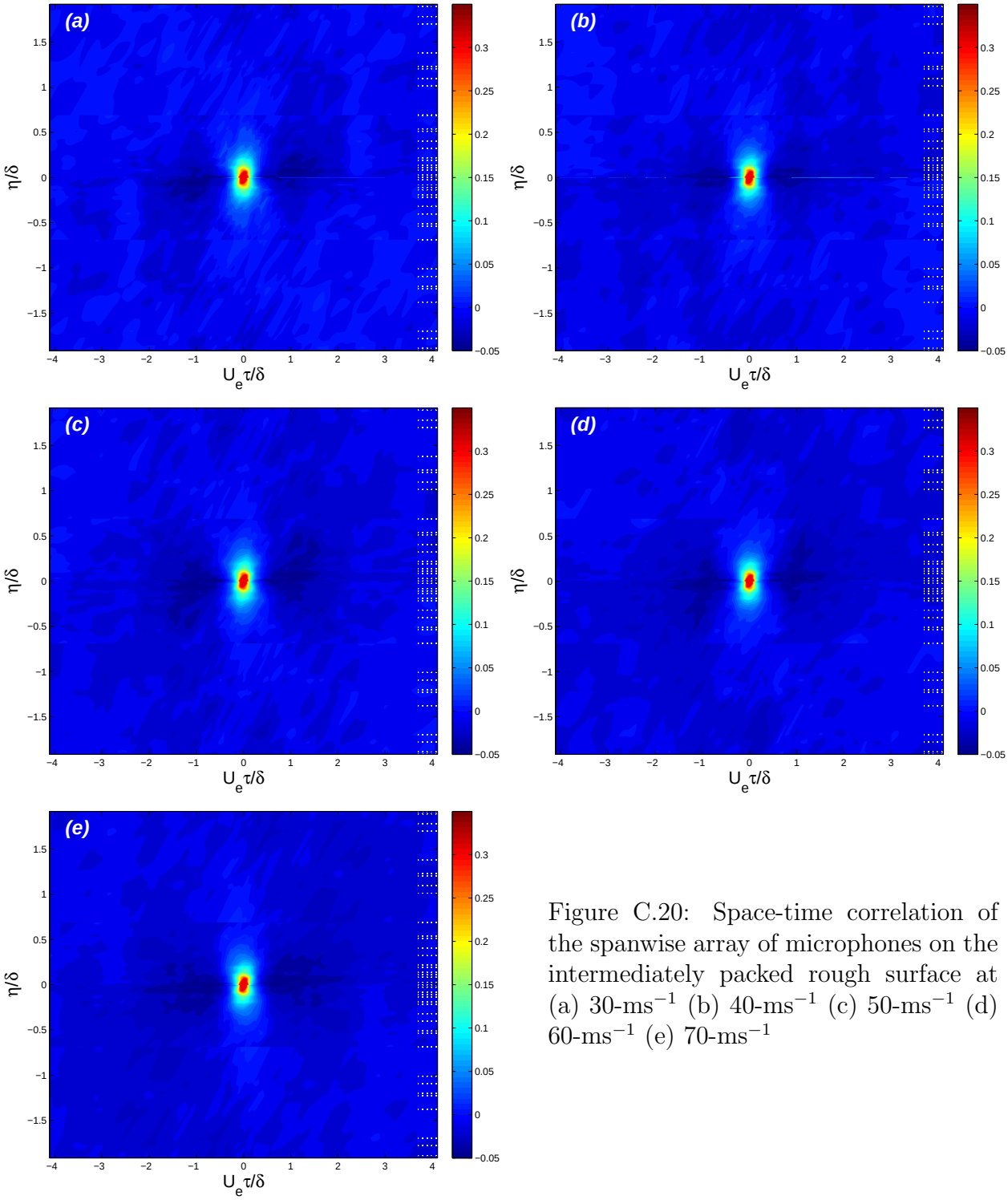

Figure C.20: Space-time correlation of the spanwise array of microphones on the intermediately packed rough surface at (a) 30-ms^{-1} (b) 40-ms^{-1} (c) 50-ms^{-1} (d) 60-ms^{-1} (e) 70-ms^{-1}

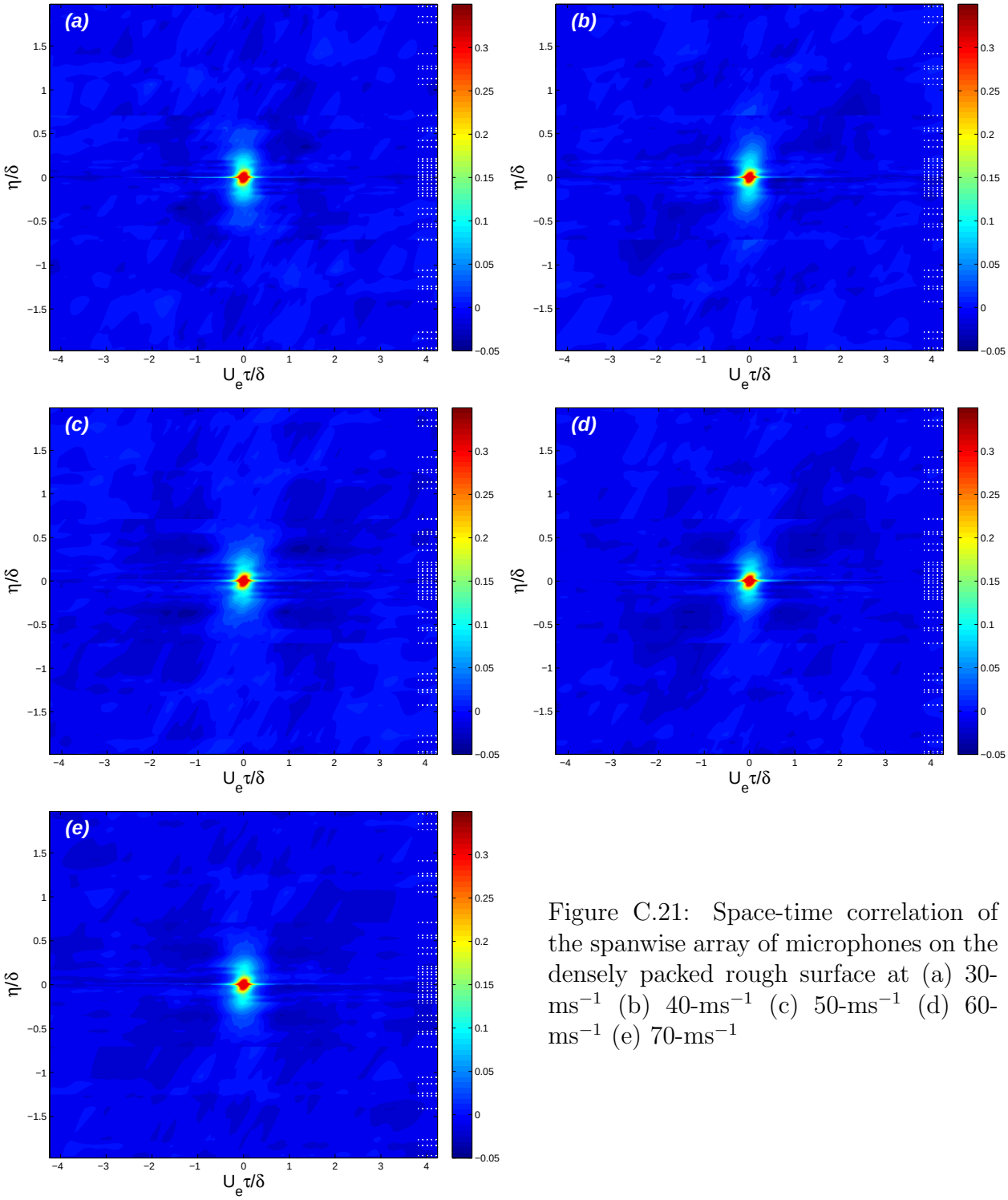

Figure C.21: Space-time correlation of the spanwise array of microphones on the densely packed rough surface at (a) 30-ms^{-1} (b) 40-ms^{-1} (c) 50-ms^{-1} (d) 60-ms^{-1} (e) 70-ms^{-1}

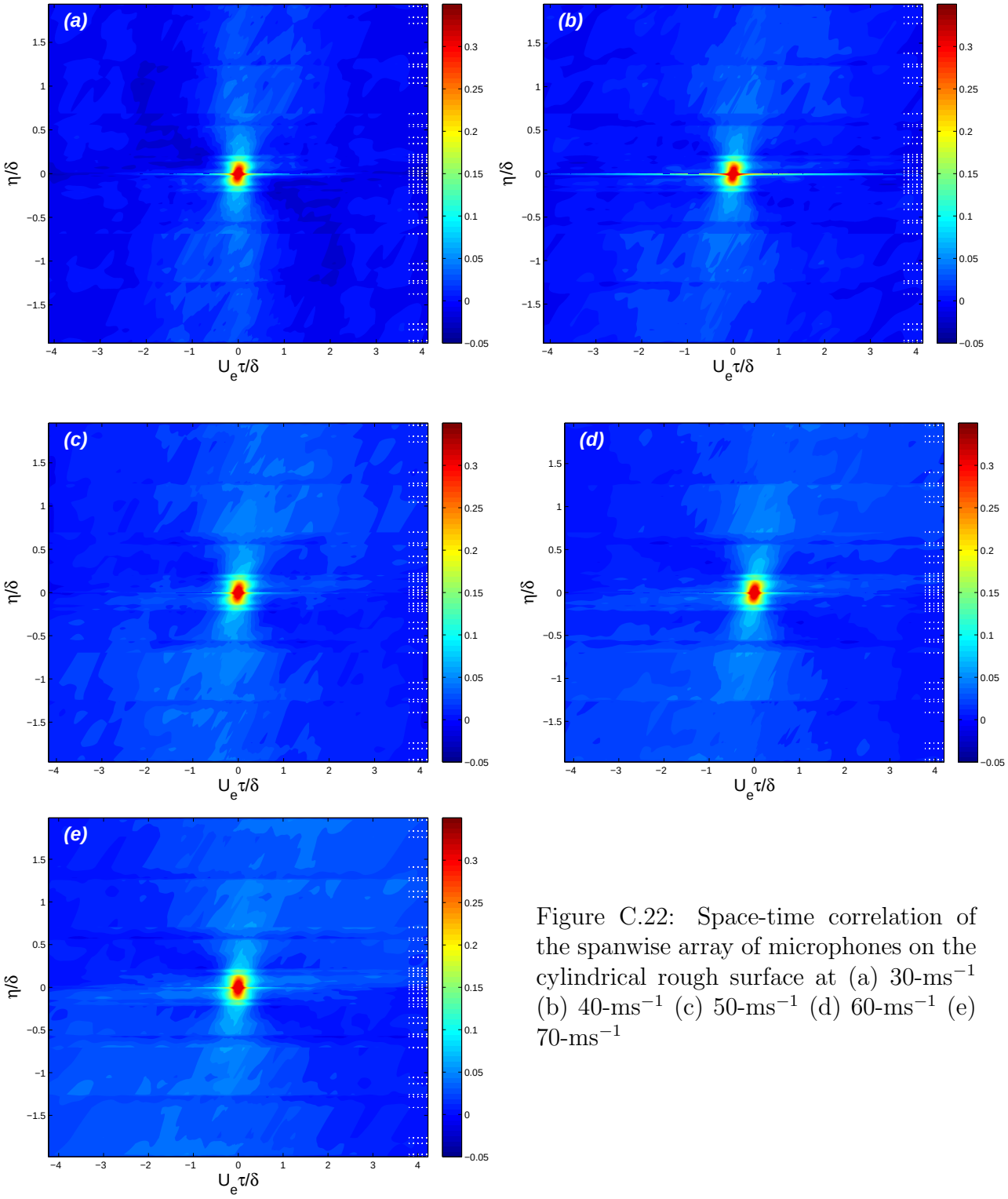

Figure C.22: Space-time correlation of the spanwise array of microphones on the cylindrical rough surface at (a) 30-ms^{-1} (b) 40-ms^{-1} (c) 50-ms^{-1} (d) 60-ms^{-1} (e) 70-ms^{-1}

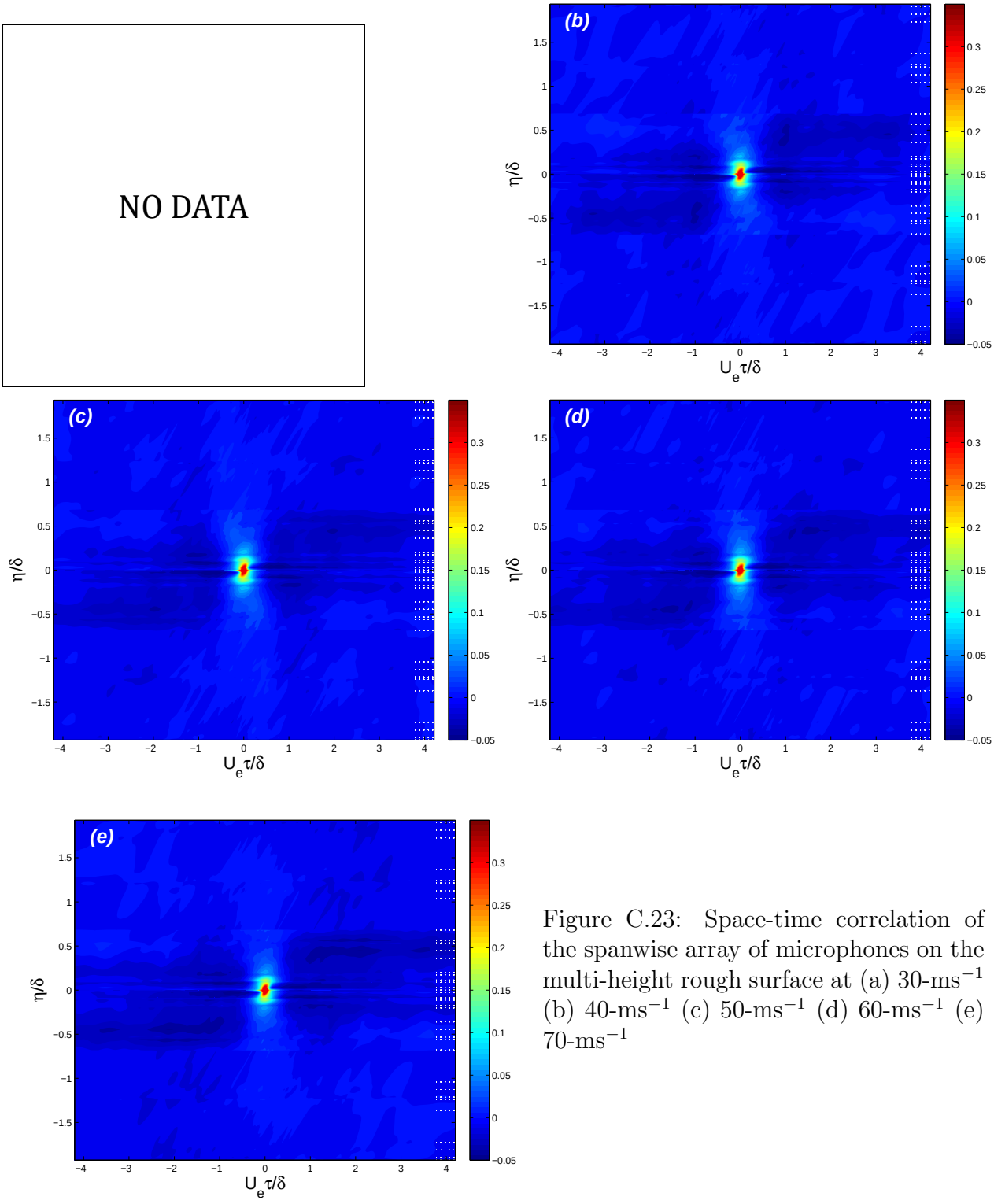

Figure C.23: Space-time correlation of the spanwise array of microphones on the multi-height rough surface at (a) 30-ms^{-1} (b) 40-ms^{-1} (c) 50-ms^{-1} (d) 60-ms^{-1} (e) 70-ms^{-1}

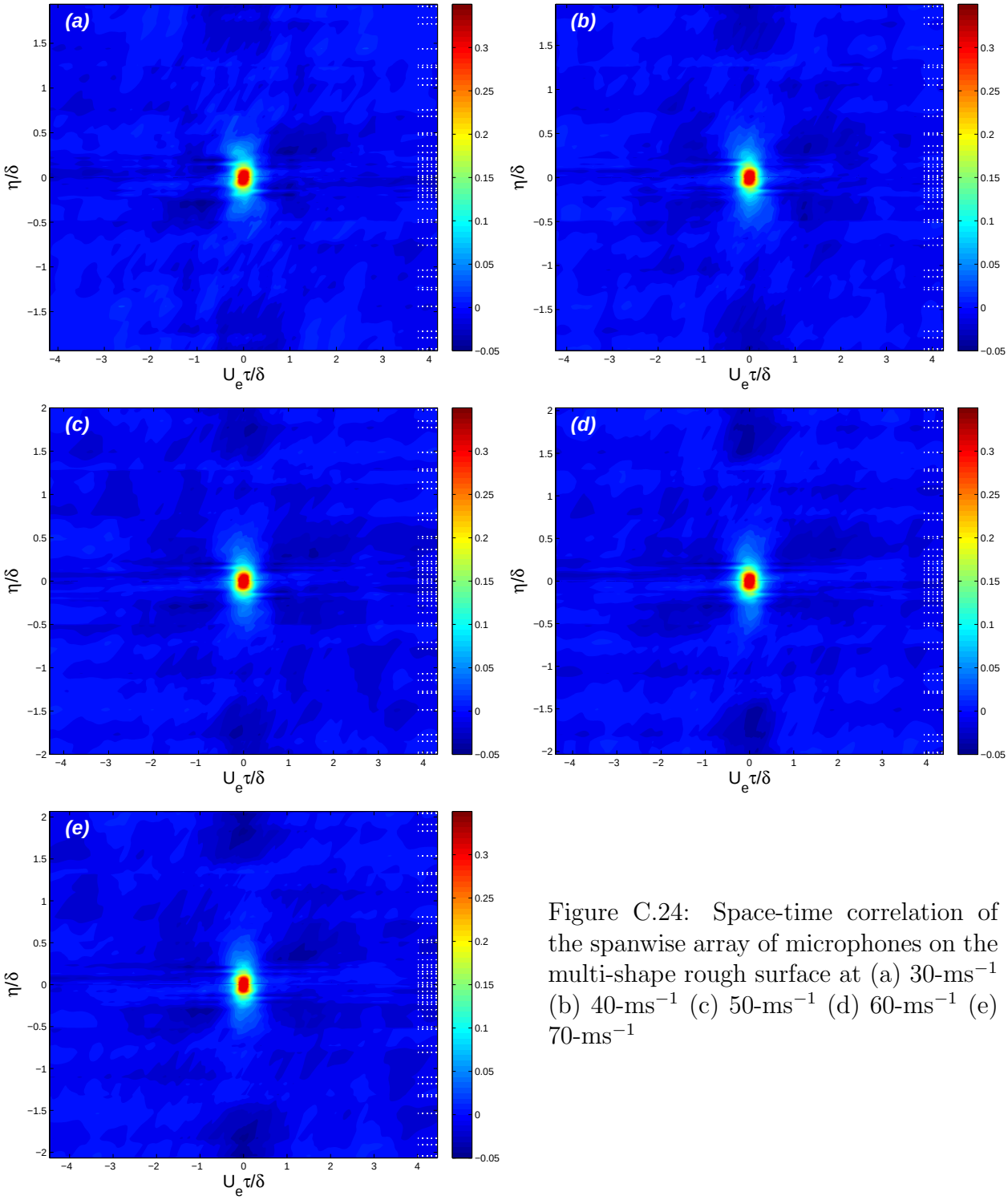

Figure C.24: Space-time correlation of the spanwise array of microphones on the multi-shape rough surface at (a) 30-ms^{-1} (b) 40-ms^{-1} (c) 50-ms^{-1} (d) 60-ms^{-1} (e) 70-ms^{-1}